

# METAL ORGANIC FRAMEWORKS AND THEIR DERIVATIVES FOR HETEROGENEOUS CATALYSIS



विद्यारत्नम् महद्वनम्

Thesis submitted in partial fulfillment

for the award of degree

Doctor of Philosophy

by

**GARGI DEY**

**RAJIV GANDHI INSTITUTE OF PETROLEUM TECHNOLOGY**

**JAIS — 229304**

PC19002

2024



---

## CERTIFICATE

It is certified that the work contained in the thesis titled “**METAL ORGANIC FRAMEWORKS AND THEIR DERIVATIVES FOR HETEROGENEOUS CATALYSIS**” by “**GARGI DEY**” has been carried out under my supervision and this work has not been submitted elsewhere for a degree. It is further certified that the student has fulfilled all the requirements of Comprehensive, Candidacy and SOTA.

---

(Supervisor)  
Dr. Arshad Aijaz

---

## DECLARATION BY THE CANDIDATE

I, “**GARGI DEY**”, certify that the work embodied in this thesis is my own bonafide work and carried out by me under the supervision of “**DR. ARSHAD AIJAZ**” from “AUGUST 2019” to “APRIL 2024”, at Rajiv Gandhi Institute of Petroleum Technology, Jais.

The matter embodied in this thesis has not been submitted for the award of any other degree. I declare that I have faithfully acknowledged and given credits to the research workers wherever their works have been cited in my work in this thesis. I further declare that I have not willfully copied any other’s work, paragraphs, text, data, results, etc., reported in journals, books, magazines, reports dissertations, theses, etc., or available at websites and have not included them in this thesis and have not cited as my own work.

Date:

Place:

---

GARGI DEY  
Roll No. PC 19002

---



---

## CERTIFICATE BY THE SUPERVISOR(S)

It is certified that the above statement made by the student is correct to the best of my knowledge.

---

(Supervisor)

**Dr. Arshad Aijaz**

Signature & Seal of Head of Department

---

## CERTIFICATE

Certified that the work contained in the thesis titled “**Metal Organic Frameworks and Their Derivatives for Heterogeneous Catalysis**” by **Ms. Gargi Dey**” has been carried out under my supervision. It is also certified that she fulfilled the mandatory requirement of TWO quality publications arose out of her thesis work.

It is further certified that the two publications (copies enclosed) of the aforesaid Ms. Gargi Dey have been published in the Journals indexed by —

- (a) SCI
- (b) SCI Extended
- (c) SCOPUS
- (d) \*Non-indexed Journals- (only in special cases) (\*Please enclose DPGC resolution in this regard)

---

(Supervisor)

**Dr. Arshad Aijaz**

---

(Convener, DPGC)

**Dr Praveen Kumar  
Srivastava**

**N.B.:** Please strike out the category (a, b, c, d) that is not applicable.



---

## **COPYRIGHT TRANSFER CERTIFICATE**

**Title of the thesis:** METAL ORGANIC FRAMEWORKS AND THEIR DERIVATIVES FOR HETEROGENEOUS CATALYSIS

**Name of the student:** Gargi Dey

### **Copyright Transfer**

The undersigned hereby assigns to the Rajiv Gandhi Institute of Petroleum Technology, Jais all rights under copyright that may exist in and for the above thesis submitted for the award of the “DOCTOR OF PHILOSOPHY”.

Date:

Place:

---

GARGI DEY

Roll No. PC 19002

**Note:** However, the author may reproduce or authorize others to reproduce material extracted verbatim from the thesis or derivative of the thesis for author’s personal use provided that the source and the Institute’s copyright notice are indicated.





*Dedicated to Ma, Baba, Didi...*  
*for their endless love, support, and encouragement...*







## **Acknowledgement**

It gives me great pleasure and honor to offer my sincere appreciation to everyone who has assisted me in carrying out the research presented in this thesis.

First and foremost, I would like to express my heartfelt gratitude to my supervisor Dr. Arshad Aijaz, for providing necessary infrastructure and resources to accomplish my research. I joined the lab as second PhD student and despite strict deadlines and setbacks at various points, his continuous support in every way enabled me to go forward and complete the journey. I am grateful to Dr. Aijaz for providing me with a dynamic work environment, several opportunities to explore new ideas, and the freedom to do research, debate, and express myself. Apart from the scientific aspects, his numerous insightful words of wisdom will surely help me at different stages of life. Thank you, sir, for your trust and patience on me.

I deeply acknowledge Rajiv Gandhi Institute of Petroleum Technology for financial support and research facilities throughout my PhD journey. I am grateful to Director Sir Prof. A. S. K. Sinha for providing vibrant research environment. I also would like to thank my Research Progress Evolution Committee (RPEC) members Prof. Umapasana Ojha and Dr. Milan kumar for their time-to-time evaluation of my work and valuable suggestions during the presentation which surely help to build up confidence in me.

I also would like to thank Prof. A. K. Choubey (Head, Department of Sciences & Humanities) for maintaining a welcoming and discipline environment in the department. Thanks to all RGIPT faculty members for creating an inspiring atmosphere for research in the institute and for always being available to answer queries. I am thankful to all the faculty who taught me during my course-work study. A special thanks to Dr. Milan

Kumar from whom I have learned a lot about electrochemistry during the period of my doctoral research.

My sincere gratitude to all my collaborators Dr. Debasis Banerjee (Department of Chemistry, IIT Roorkee) & his student Mr. Motahar Sk, Dr. Milan Kumar (Department of Chemical & Biochemical Engineering, RGIPT), Dr. Ayan Datta (Department of Chemical Sciences, IACS Kolkata) & his student Dr. Rajkumar Jana for providing their lab facilities and invaluable inputs to my research work. Special thanks to Prof. Dibyendu Bhattacharyya (BARC Mumbai) for providing XAS facilities for my research. It was a wonderful experience for me to work with them.

I would like to express my enormous gratitude to various institutes in India to allow me to use their CRF facilities. Sincerely thanks to Dr. Prem Lama (CSIR IIP Dehradun) for TGA and NH<sub>3</sub>-TPD analysis, Mr. Ashish K. Tiwari (ACMS building, IIT Kanpur) for PXRD, Ms. Samata samal ma'am (MSE department, IIT Kanpur) for SEM, Mr. Shilankar (MSE department, IIT Kanpur) for Raman, Mr. Jai Kumar (Advance imaging center, IIT Kanpur) for TEM, Mr. Rajesh (CeNs Bangalore) for TEM, Satyajit Dada for GC-MS (CBMR Lucknow), Sujay (IIT Guwahati) for Raman, Riya Ghosh (IIT Guwahati) for EPR and few more institute SAIF facilities such as IIT Bombay for TEM, IIT Madras for ICP-OES. I admire and appreciate all the person of RGIPT Central Instrumentation Facility Lab Dr. Zahoor Alam, Dr. Anuj Prajapati, Mr. Brijesh K. Verma, and Mr. Gourav to help me in various instrumentation analysis. The support of technical and administrative staff is equally crucial for the smooth progression of a long course.

I would like to thank all my teachers from my early years. I want to convey my heartfelt thanks to all my teachers of Department of Chemistry, University of Kalyani. Their passionate teaching and motivations push me to pursue PhD. Specially, I owe Prof.

Shital Kumar Chattopadhyay (Department of Chemistry, University of Kalyani), Prof. Kumaresh Ghosh (Department of Chemistry, University of Kalyani) a debt of appreciation for acquainting me with the world of research. They drilled values into me and gave me a strong feeling of exploration. I will always be grateful for their kindness. My respectable gratitude to all the teachers of Department of Chemistry, Chakdaha College for imparting knowledge to me throughout my B.Sc. programme. Special thanks to Dr. Debaprasad Panda, Mr. Biplab Biswas for their direct and indirect help throughout my college life. I am very deeply indebted to all my school teachers (Basanta Kumari Balika Vidyapith and Bapuji Sishu Niketan) for building the foundations of my learnings in life. The influence of Mr. Swapan Mondal, Mr. Shirshendu Bose, cannot be overstated; without their assistance, I would not have been able to reach this point.

I feel myself tremendously fortunate to be a member of Nanocatalysis group at RGIPT. I want to express my gratitude to all current and former members of my Lab Shadab, Ashish, Parvez for establishing and preserving such a welcoming atmosphere. Special thanks to my senior lab partner, Shadab Saifi for constructive discussions and providing insights in every project. I spent most of the time in this lab with him, and we had a long, unforgettable partnership where we shared highs and lows and encouraged each other to reach our greatest potential.

From my school days to my Ph.D., I would like to extend my warm regards to all my seniors, juniors, and buddies from RGIPT. There is too much on the list to write. Still, some of them are Belal sir, Shama ma'am, Soumendra sir, Athar sir, Subhankar da, Suman da, Pralay, Chandan, Arpan, Santosh, Shrinkhala, Dilraj behen, Rachna di, Ankit, Vikas, and all my PhD batchmates. Thank you all for making this stressful journey so smooth. The list is incomplete without mentioning some name Sulagna (my

childhood friend), Sahanaj, Susmita, Prachi, Moumi, Sangita, Suparna, Riya, Joyanta, Souvik, Dipankar, Abhishek, Monalisa, Astam, Arghya, all my K.U. organic batch-mates. I will always be grateful to them for their love, effortless support, positive outlook, guidance, and encouragement throughout my life. I can't even fault our chemical suppliers, Mukesh Ji, Singh Ji for their unending assistance in everything from chemicals to instruments. Even though many people are not addressed, none are ignored!

Above all, I want to express my gratitude to my parents Ma, Baba for always supporting me in following my passions and desires and for believing in my goals. I am grateful to my beloved sister Parvi for her unwavering support in every circumstance which I can't express in words. I express my gratitude to all my relatives specially my Mejo masi, Sejo masi, Sejo meso, Nabab dada for instilling self-belief in me and motivating me to pursue this doctoral programme. My parents are my never-ending source of strength, and their confidence in me has enabled me to overcome any obstacle quickly. They should get all the credit for all my accomplishments.

Above everything I bow down to the Almighty's grace.

.....Gargi Dey



# Contents

<b>Acknowledgement</b> .....	<b>i</b>
<b>List of Tables</b> .....	<b>ix</b>
<b>List of Figures</b> .....	<b>xi</b>
<b>List of Schemes</b> .....	<b>xxv</b>
<b>List of Abbreviations</b> .....	<b>xxvii</b>
<b>Preface</b>	<b>xxxi</b>
<b>Chapter 1: Introduction And Literature Survey</b> .....	<b>1</b>
1.1 Background .....	1
1.2 Functional porous materials as heterogeneous catalysts .....	3
1.3 Metal organic frameworks (MOFs).....	4
1.3.1 Design and strategies for functionalization of MOFs .....	9
1.3.1.1 MOF composites .....	10
1.3.1.2 MOF derivatives.....	17
1.4 Catalytic applications of MOF composites and MOF derivatives .....	25
1.4.1 Catalysis for organic transformation .....	25
1.4.2 Electrocatalysis.....	27
1.4.2.1 Energy conversion technology .....	29
1.4.2.1.1 Electrocatalytic water splitting.....	29
1.4.2.1.2 Fuel Cell .....	31
1.4.2.2 Energy storage technology .....	34
1.4.2.2.1 Zn-air battery .....	35
1.4.2.2.2 Vanadium redox flow battery.....	37
1.5 Conclusions .....	39
<b>Chapter 2: Immobilizing A Homogeneous Manganese Catalyst Into MOF Pores For <math>\alpha</math>-alkylation of Methylene Ketones With Alcohols.....</b>	<b>41</b>
2.1 Abstract .....	41
2.2 Introduction .....	41
2.3 Experimental .....	44
2.3.1 Chemicals .....	44

2.3.2 Synthesis .....	45
2.3.2.1 Synthesis of MnPhen@ZIF .....	45
2.3.2.2 Synthesis of ZIF-8 .....	45
2.3.2.3 Synthesis of Mn-ZIF-8.....	45
2.3.2.4 Synthesis of MnPhen complex .....	46
2.4 Characterization .....	46
2.5 Catalytic measurements .....	47
2.5.1 Synthetic method for the synthesis of $\alpha$ -substituted methylene ketones with alcohol:.....	47
2.5.2 Synthesis of pure MnPhen Complex and its catalytic activity test:.....	48
2.6 Reusability test with MnPhen@ZIF .....	48
2.7 Calculations of lewis acidity using NH <sub>3</sub> -TPD measurements .....	48
2.8 Analytical data .....	49
2.9 Results and discussion .....	52
2.10 Conclusion .....	73
<b>Chapter 3: Carbon Nanofibers Coated With MOF-Derived Carbon Nanostructures For Vanadium Redox Flow Batteries With Enhanced Electrochemical Activity And Power Density .....</b>	<b>75</b>
3.1 Abstract.....	75
3.2 Introduction.....	76
3.3 Experimental.....	78
3.3.1 Chemicals.....	78
3.3.2 Synthesis .....	79
3.3.2.1 Synthesis of Zn-LDH/CF:.....	79
3.3.2.2 Synthesis of ZIF-8/CF: .....	79
3.3.2.3 Synthesis of N,O/CF:.....	79
3.4 Materials Characterization.....	79
3.5 Electrochemical measurements.....	81
3.6 Results and discussion .....	82
3.6.1 Electrochemical and Flow battery test.....	89
3.7 Conclusion .....	106
<b>Chapter 4: Dual Single-Atomic Co–Mn Sites In Metal–Organic-Framework-Derived N-Doped Nanoporous Carbon For Electrochemical Oxygen Reduction.....</b>	<b>109</b>

4.1 Abstract .....	109
4.2 Introduction .....	110
4.3 Experimental .....	112
4.3.1 Materials:.....	112
4.3.2 Physicochemical characterizations:.....	113
4.3.3 Synthesis: .....	116
4.3.3.1 Synthesis of CoMn-ZIF.....	116
4.3.3.2 Synthesis of Mn-ZIF .....	116
4.3.3.3 Synthesis of Co-ZIF: .....	116
4.3.3.4 Synthesis of CoMn/NC: .....	116
4.3.3.5 Synthesis of CoMn/NC800: .....	117
4.3.3.6 Synthesis of CoMn/NC700: .....	117
4.3.3.7 Synthesis of Co/NC:.....	117
4.3.3.8 Synthesis of Mn/NC: .....	117
4.3.4 Electrochemical measurements: .....	117
4.3.5 Proton exchange membrane fuel Cell (PEMFC) testing.....	120
4.3.6 Fabrication and testing of Zn–Air battery.....	121
4.3.7 Density functional theory (DFT) calculations.....	121
4.4 Results and discussion.....	122
4.5 Conclusion.....	122
<b>Chapter 5: NiO Nanoclusters Supported On Atomically Dispersed Ni single Atom at Mesoporous Carbon Cages For Oxygen Evolution Reaction and Quasi-Solid-State Zn-air Batteries With An Organohydrogel Electrolyte.....</b>	<b>163</b>
5.1 Abstract .....	163
5.2 Introduction .....	164
5.3 Experimental .....	167
5.3.1 Materials.....	167
5.3.2 Physicochemical characterization .....	168
5.3.3 Synthetic methods .....	169
5.3.3.1. Synthesis of ZIF-8.....	169
5.3.3.2. Synthesis of ZIF-8@SiO <sub>x</sub> .....	169
5.3.3.3. Synthesis of Ni/ZIF-8.....	170
5.3.3.4 Synthesis of Ni/ZIF-8@SiO <sub>x</sub> .....	170

5.3.3.5 Synthesis of MOF Derived Catalysts.....	170
5.3.3.5.1 Synthesis of NiO/Ni-SACs/mNC1000 .....	170
5.3.3.5.2 Synthesis of NiO/Ni-SACs/mNC900 .....	171
5.3.3.5.3 Synthesis of mNC1000 .....	171
5.3.3.5.4 Synthesis of Ni-SACs/NC1000 .....	171
5.3.3.5.5 Synthesis of NC1000 .....	171
5.3.3.6 Synthesis of NiO NPs .....	172
5.3.3.7 Synthesis of the hydrogel electrolytes .....	172
5.3.3.7.1 Synthesis of the PAM hydrogel electrolyte (PAM-h) .....	172
5.3.3.7.2 Synthesis of the PAM organohydrogel electrolyte (PAM-dh) .....	172
5.3.3.7.3 Synthesis of the metal salt treated PAM hydrogel electrolyte (PAM-zh) .....	172
5.3.3.7.4 Synthesis of the metal salt treated PAM organohydrogel electrolyte (PAM- zdh) .....	173
5.3.4 d band center calculations.....	173
5.3.5 Electrochemical measurements.....	173
5.3.5.1 TOF calculations for OER .....	175
5.3.5.2 Faradaic efficiency calculations for OER .....	176
5.3.6 Fabrication of Quasi-solid-state Zn-air battery (ZABs) .....	176
5.3.7 Electrolytic cell measurements .....	176
5.4 Binding energy calculations.....	177
5.5 Density functional theory (DFT) calculations .....	177
5.6 Results and discussion .....	179
5.7 Conclusion .....	216
<b>Chapter 6: Summary And Future Directions .....</b>	<b>219</b>
<b>Appendix Section .....</b>	<b>222</b>
<b>Copies of <sup>1</sup>H NMR &amp; <sup>13</sup>C NMR spectra: .....</b>	<b>222</b>
<b>References .....</b>	<b>239</b>
<b>List of Publications .....</b>	<b>281</b>

## List of Tables

<b>Table 2.1</b> Optimization of reaction conditions <sup>a</sup> .....	57
<b>Table 2.2</b> MnPhen@ZIF catalysed alkylation of ketones with alcohols <sup>a,b</sup> . ....	58
<b>Table 2.3</b> Pore size and pore volume of MnPhen@ZIF and supporting catalysts. ....	68
<b>Table 2.4</b> Lewis acidity calculation from NH <sub>3</sub> TPD. ....	71
<b>Table 3.1</b> Equivalent circuit parameters for N,O/CF after fitting EIS. ....	95
<b>Table 3.2</b> Equivalent circuit parameters for bare CF after fitting EIS. ....	96
<b>Table 3.3</b> VE, CE, EE at 40 mA/cm <sup>2</sup> at different flow rates for bare CF and N,O/CF. .....	100
<b>Table 3.4</b> VE, CE, EE at 80 mA/cm <sup>2</sup> at different flow rates for bare CF and N,O/CF. .....	100
<b>Table 3.5</b> Comparison of performance of N,O/CF in VRFB with literature. ....	104
<b>Table 3.6</b> Comparison of performance of N,O/CF in VRFB with literature considering peak potential values.....	105
<b>Table 4.1</b> Comparison of surface area, average pore size and total pore volume for CoMn-ZIF, Co-ZIF and Mn-ZIF. ....	124
<b>Table 4.2</b> Element content distribution for CoMn/NC from XPS analysis.....	135
<b>Table 4.3</b> Bond length, coordination number and disorder factors obtained by EXAFS fitting at Co K- edge. ....	138
<b>Table 4.4</b> Bond length, coordination number and disorder factors obtained by EXAFS fitting at Mn K- edge.....	138
<b>Table 4.5</b> A summary of kinetic parameters derived from the K-L plots of CoMn/NC in 0.1 M KOH. ....	142
<b>Table 4.6</b> A summary of kinetic parameters derived from the K-L plots of Pt/C in 0.1 M KOH. ....	143
<b>Table 4.7</b> A summary of kinetic parameters derived from the K-L plots of Co/NC in 0.1 M KOH. ....	143
<b>Table 4.8</b> A summary of kinetic parameters derived from the K-L plots of Mn/NC in 0.1 M KOH. ....	143
<b>Table 4.9</b> Summary of kinetic parameters derived from the K-L plots of CoMn/NC in 0.5 M H <sub>2</sub> SO <sub>4</sub> . ....	148
<b>Table 4.10</b> Summary of kinetic parameters derived from the K-L plots of Pt/C in 0.5 M H <sub>2</sub> SO <sub>4</sub> . ....	148
<b>Table 4.11</b> Summary of kinetic parameters derived from the K-L plots of Co/NC in 0.5 M H <sub>2</sub> SO <sub>4</sub> . ....	149

<b>Table 4.12</b> Summary of kinetic parameters derived from the K-L plots of Mn/NC in 0.5 M H <sub>2</sub> SO <sub>4</sub> .....	149
<b>Table 4.13</b> Comparison of ORR activities of CoMn/NC with various reported nonprecious electrocatalysts under alkaline conditions. ....	159
<b>Table 4.14</b> Comparison of ORR activities of CoMn/NC with various reported nonprecious electrocatalysts under acidic conditions.....	160
<b>Table 4.15</b> Comparison of potential difference of CoMn/NC catalyst with previously reported dual single-atom based bifunctional electrocatalysts. ....	161
<b>Table 5.1</b> Surface texture characteristics of the NiO/Ni-SACs/mNC1000, NiO/Ni-SACs/mNC900, mNC1000, Ni-SACs/NC1000, NC1000 (a-b) BET method, (c) BJH method. ....	198

## List of Figures

<b>Figure 1.1</b> Important turning points in the discovery of useful porous materials. Reprinted with permission from ref [5]. Copyright 2020 WILEY VCH.....	4
<b>Figure 1.2</b> Schematic representation of MOF through reticular chemistry i.e. linking metal ion and organic linker. ....	5
<b>Figure 1.3</b> a) Representative examples of series of linkers used for the synthesis of iso reticular MOFs IRMOF-n (n =1-8, 10,12, 14,16) where all possess same cubic topology but differ by organic linkers functionalization and its length b) their corresponding single X-ray structures. Reproduced with permission from ref [17]. Copyright 2002 Science. ....	6
<b>Figure 1.4</b> Different types of MOF prepared by using same organic linker terephthalic acid but with different metals. Adopted with permission from ref [20]. Copyright 2019 MDPI.....	7
<b>Figure 1.5</b> Schematic diagram of synthetic methods, properties, and applications of MOF.....	8
<b>Figure 1.6</b> a) Different types of active sites to fabricate functionalized MOF (MOF composites). Reprinted with permission from ref [27]. Copyright 2017 The Royal society of chemistry, b) Schematic illustration to show the strategy for fabrication of metal/carbon composites (MOF derivatives) from MOFs. Adopted with permission from ref [28]. Copyright 2018 Elsevier. ....	9
<b>Figure 1.7</b> Post synthetic modification of node by grafting ligand to the metal sites for MOF a) MIL-101 (Cr). Adopted with permission from ref [29]. Copyright 2018 Elsevier and b) Cu-BDC. Reprinted with permission from ref [30]. Copyright 2016 Elsevier. ....	11
<b>Figure 1.8</b> Examples of post synthetic metalation of nodes: a) Reaction of bridging OH group between two Al center with 1,1'-ferrocenediyl-dimethylsilane. Reproduced with permission from ref [32]. Copyright 2009 American Chemical Society, b) post synthetic metalation of UiO-68 SBUs using CoCl <sub>2</sub> . Reprinted with permission from ref [33]. Copyright 2016 Nature, c) Nonfunctionalized MOF, Zr-NU-1000, and its corresponding inorganic Zr <sub>6</sub> nodes with the reactive -OH/H <sub>2</sub> O terminal groups. Several representative metal binding motifs are also shown including MoO <sub>x</sub> , Rh(C <sub>2</sub> H <sub>4</sub> ) <sub>2</sub> , Co-Al complex, and Rh-Ga complex synthesized by SIM strategy. Reprinted with permission from ref [35]. Copyright 2018 American Chemical Society. d) Activation of Ce-BTC to form CeH-BTC. Adopted with permission from ref [36]. Copyright 2016 American Chemical Society. ....	13
<b>Figure 1.9</b> Examples of linker functionalization: a) Schematic description of immobilizing metallosalen linkers into a Zn-MOF and crystal structure viewed along	

the c-axis (Cu, green; Zn, yellow; C, gray; O, red; N, blue). Reprinted with permission from ref [37]. Copyright 2004 Wiley-VCH, b) Schematic representation of the post-synthesis modification of MIL-101(Cr) and the synthesis of a single-site heterogeneous Ru (III) catalyst. Adopted with permission from ref [38]. Copyright 2015 The Royal Society of Chemistry, c) Synthetic procedure for grafting Mn bipyridine complex Mn(bpydc)(CO)<sub>3</sub>Br to UiO-67 MOF. Adopted with permission from ref [39]. Copyright 2015 American Chemical Society, d) Schematic illustration for grafting mono-catecholato metal complexes into UiO-66 MOF. Reproduced with permission from ref [40]. Copyright 2014 American Chemical Society..... 14

**Figure 1.10** Examples for pore functionalization: a) Encapsulation of Pt nanoparticles into MIL-101 by DSM method. Adopted with permission from ref [49]. Copyright 2012 American Chemical Society, b) Incorporation of size-controlled metal nanoparticles into ZIF-8 pore. Reprinted with permission from ref [50]. Copyright 2012 Nature, c) Silica template protection assisted method for encapsulation of Cu<sub>2</sub>O nanoparticles into ZIF-8 cavity. Reproduced with permission from ref [51]. Copyright 2018 WILEY VCH. d) Schematic representation of formation of rho-ZMOF with encapsulation of porphyrin ring (H<sub>2</sub>TMPyP)<sup>4+</sup> and Mn<sup>+</sup> (Mn<sup>+</sup> = Mn, Co, Cu, Zn). Reprinted with permission from Ref [52]. Copyright 2008 American Chemical society, e) Ligand in dimer strategy for encapsulation of Co(IPr)Br]<sub>2</sub>(μ-Br)<sub>2</sub> (Co<sub>2</sub>) into MOF cage. Adopted with permission from ref [53]. Copyright 2022 WILEY VCH..... 16

**Figure 1.11** a) Temperature induced morphology-controlled synthesis of Fe<sub>3</sub>C@NCNT from MOF. Adopted with permission from ref [69]. Copyright 2016 The Royal Society of Chemistry, b) Diagram illustrating the structural alterations of Cu-BTC calcined in various atmospheres, Reproduced with permission from ref [70]. Copyright 2018 Elsevier, c) Effect of heating rate during pyrolysis for synthesizing ultrasmall NPs with high loading. Reprinted with permission from ref [71]. Copyright 2022 Elsevier, d) Procedures for fabrication of different composition of Co<sub>x</sub>S<sub>y</sub> nanostructures. Adopted with permission from ref [72]. Copyright 2018 WILEY VCH. .... 20

**Figure 1.12** a) Schematic illustration for the designing of core shell ZIF-8@ZIF-67 crystals and conversion into NC@GC upon further calcination. Reprinted with permission from ref [73]. Copyright 2015 American Chemical Society, b) Synthetic procedure to fabricate carbon nanorods and graphene nanoribbons from MOF-74. Reproduced with permission from ref [74]. Copyright 2016 Nature. .... 21

**Figure 1.13** a) Diagram illustrating the steps involved in creating porous MoC<sub>x</sub> nano-octahedrons. Adopted with permission from ref [75]. Copyright 2014 Nature, b) Schematic representation for synthesizing RuIrO<sub>x</sub> oprn nano net cage structures. Reproduced with permission from ref [76]. Copyright 2019 Nature, c) Synthetic scheme for the formation of Co NPs-N/C (top) and Co SAs/N-C (bottom). Reproduced with permission from ref [77]. Copyright 2016 WILEY VCH. .... 23

**Figure 1.14** a) Co,N-CNF synthetic process using the mSiO<sub>2</sub>-protected calcination approach. Reproduced with permission from ref [78]. Copyright 2016 WILEY VCH,



b) Process diagram for preparing Fe SACs supported on a hollow carbon polyhedron co-doped with phosphorus, sulfur, and nitrogen (Fe-SAs/NPS-HC). Reprinted with permission from ref [79]. Copyright 2018 Nature. ....	24
<b>Figure 1.15</b> a) Schematic illustration of salicylaldimine-Cobalt(II) complex supported by a Zr-MOF for selective reduction of Nitro group by organosilanes. Adopted with permission from ref [82]. Copyright 2023 WILEY VCH, b) Schematic representation of UiO-66(L <sub>3</sub> )-Ni-Catalyst for Suzuki-Miyaura cross-coupling reaction. Reprinted with permission from ref [83]. 2018 American Chemical Society, c) Molybdenum (VI) oxide catalyst supported by Zr <sub>6</sub> node of Nu-1000 MOF used for Cyclohexene Epoxidation. Adopted with permission from ref [84]. Copyright 2016 American Chemical Society, d) Schematic graphic depicting the one pot cascade reactions over PdAg@MIL-101. Reproduced with permission from ref [85]. Copyright 2015 American Chemical Society. ....	27
<b>Figure 1.16</b> Schematic representation of various MOF derived nanostructures and their electrochemical properties. ....	29
<b>Figure 1.17</b> a) Diagram illustrating an electrochemical set up for overall water splitting reactions, b) details of HER and OER reaction in acidic and alkaline medium. ....	30
<b>Figure 1.18</b> a) Synthetic approach for NCNHP/CoP, b) HER LSVs, c) OER LSVs in 0.1 M KOH with a scan rate 5 mV S <sup>-1</sup> , d) Utilizing CoP/NCNHP as the positive and negative electrodes in a two-electrode system, a chromatopotentiometric stability test was conducted on the electrolysis of water at different current densities in 1.0 M KOH. Adopted with permission from ref [98]. American Chemical Society. ....	31
<b>Figure 1.19</b> Schematic diagram for overall water splitting reactions. ....	32
<b>Figure 1.20</b> a) Diagram of the ORR mechanism showing the direct and indirect pathways, and b) the ORR mechanism on the catalyst surface (* denotes catalyst surface). Reprinted with permission from ref [105]. Copyright 2023 MDPI. ....	33
<b>Figure 1.21</b> a) Schematic showing the Fe/Ni-N <sub>x</sub> /OC synthesis process, b) SEM images of as synthesized catalyst, c) White dots in HAADF-STEM images confirming the presence of Fe/Ni-N <sub>x</sub> /OC, d) ORR polarization curves of Fe/Ni-N <sub>x</sub> /OC and its comparison with other supporting catalysts in O <sub>2</sub> saturated 0.1 M KOH solution with a rotation of 1600 rpm, e) Catalyst test in PEM-fuel cell conditions under both H <sub>2</sub> /O <sub>2</sub> and H <sub>2</sub> /air. Adopted with permission from ref [108]. Copyright 2020 WILEY VCH. ....	34
<b>Figure 1.22</b> Schematic representation of Zn-air battery. ....	35
<b>Figure 1.23</b> a) Diagram illustrating the Fe-N <sub>x</sub> -C synthesis process, b) LSVs for both OER and ORR reversibility test of Fe-N <sub>x</sub> -C with commercial Pt/C in 0.1 M KOH solution, c) polarization curves for charging and discharging and the accompanying power density plots, d) comparison of specific capacitance of Fe-N <sub>x</sub> -C with commercial Pt/C. Reproduced with permission from ref [113]. Copyright 2019 WILEY VCH. ....	36
<b>Figure 1.24</b> Schematic diagram of vanadium redox flow battery (VRFB). ....	37

<b>Figure 1.25</b> Schematic representation for the synthesis of ZrO <sub>2</sub> @C on graphitic felt electrode and corresponding cyclic voltammetry study and its comparison with without treated graphite felt for vanadium redox reactions. Reproduced with permission from ref [121]. Copyright 2019 ELSEIVER.....	38
<b>Figure 2.1</b> a)-c) SEM images at different scale bars; d)-f) TEM images of the as synthesized MnPhen@ZIF catalyst.....	53
<b>Figure 2.2</b> PXRD patterns of ZIF-8, MnPhen@ZIF, MnPhen, and a mixture of ZIF-8 with MnPhen. ....	53
<b>Figure 2.3</b> N <sub>2</sub> sorption isotherms of ZIF-8 (black) and Mnphen@ZIF (blue), recorded at 77 K. Filled and open circles represent adsorption and desorption, respectively. ...	54
<b>Figure 2.4</b> Solid state UV-Vis spectra of ZIF-8 and MnPhen@ZIF. ....	54
<b>Figure 2.5</b> Dark-field HAADF-STEM image of MnPhen@ZIF with the corresponding elemental mappings.....	55
<b>Figure 2.6</b> Mn 2p XPS spectra of MnPhen@ZIF a) before Ar-etching (left), and b) after Ar etching (right). This Ar-sputtering suggests the presence of more Mn in the bulk of MnPhen@ZIF crystals. ....	55
<b>Figure 2.7</b> Physical appearance of pure ZIF-8, manganese phenanthroline complex (MnPhen) and as-synthesized catalyst MnPhen@ZIF. ....	55
<b>Figure 2.8</b> Physical appearances of Mn-NaOH test for MnPhen@ZIF a) without, and b) with acid.....	56
<b>Figure 2.9</b> The set-up made for the measurement of generated H <sub>2</sub> gas in the reaction. ....	60
<b>Figure 2.10</b> The set-up made for the collection of generated H <sub>2</sub> gas in the reaction (conditioned were same as mentioned in section 5) (above). Gas chromatographs of the collected gas in reaction mentioned as blue line, which has same retention time as pure H <sub>2</sub> shown in pink line (below).....	61
<b>Figure 2.11</b> Recyclability test of MnPhen@ZIF for the synthesis of 2-Methyl-1,3-diphenylpropan-1-one (3a). ....	67
<b>Figure 2.12</b> a)-c) TEM images of MnPhen@ZIF after catalysis.....	67
<b>Figure 2.13</b> a) N <sub>2</sub> adsorption–desorption curves b) PXRD patterns of MnPhen@ZIF before and after catalysis, c) Pore size distribution of ZIF-8, MnPhen@ZIF (before catalysis), and MnPhen@ZIF (after catalysis). ....	68
<b>Figure 2.14</b> HAADF-STEM image of used MnPhen@ZIF with the corresponding elemental mapping of C, N, Zn and Mn.....	69
<b>Figure 2.15</b> Hot filtration test indicating no further formation of branched ketone product 3a after removal of solid MnPhen@ZIF catalyst. Black line curve is product formation vs time plot till completion of the reaction (24 h), while blue curve is for second batch of reaction where catalyst was removed by hot filtration at the time of ~2 h. ....	69

<b>Figure 2.16</b> A comparison of TGA curves of as-synthesized catalyst MnPhen@ZIF, a mixture of MnPhen+ZIF-8 complex, pristine ZIF-8, MnPhen complex, and Phen ligand itself. This data suggests that MnPhen@ZIF and its encapsulated Mn-complex is stable under experimental catalytic reaction temperature ie; at 140 °C. ....	70
<b>Figure 2.17</b> NH <sub>3</sub> -TPD profiles for MnPhen@ZIF before and after catalysis. ....	71
<b>Figure 2.18</b> O 1s XPS spectrum of MnPhen@ZIF after catalysis. ....	72
<b>Figure 2.19</b> a) Formation of product 3a and decrease in concentration of 1a with reaction time in presence of catalyst MnPhen@ZIF, b) Comparison of product 3a formation with respect to initial period of time in presence of catalyst MnPhen@ZIF and ZIF-8. ....	72
<b>Figure 3.1</b> SEM images of bare CF. ....	83
<b>Figure 3.2</b> SEM images of a-b) Zn-LDH/CF. c) SEM image of Zn-LDH/CF with corresponding elemental mappings (C, Zn, O). d) EDX spectrum of Zn-LDH/CF (The peak at ~2.2 eV is from Au coating). ....	83
<b>Figure 3.3</b> a-c) SEM images of ZIF-8/CF at different resolutions. d) Corresponding EDX elemental mappings (C, Zn, N, O). e) EDX spectrum of ZIF-8/CF (The extra peak at ~2.2 eV is from Au coating). ....	84
<b>Figure 3.4</b> a)-b) SEM images of as-synthesized N,O/CF. c) High-resolution SEM image of the area highlighted in yellow in b. ....	85
<b>Figure 3.5</b> Digital photographs of bare CF (left) and as-synthesized N,O/CF (right). ....	85
<b>Figure 3.6</b> a)-d) TEM images of N,O/CF. (e) SEM image of N,O/CF with the corresponding elemental mappings C, N, and O. ....	86
<b>Figure 3.7</b> a) PXRD patterns, (b) Raman spectra of N,O/CF and bare CF. ....	87
<b>Figure 3.8</b> a) N <sub>2</sub> adsorption–desorption isotherms of bare CF and N,O/CF, (b) Pore size distribution of bare CF and N,O/CF calculated from their corresponding N <sub>2</sub> sorption isotherms. ....	87
<b>Figure 3.9</b> XPS of a) C 1s, b) N 1s, and c) O 1s of N,O/CF. ....	88
<b>Figure 3.10</b> Wettability test of bare CF (up) and N,O/CF (down) using a slow motion camera; pictures captured within a gap of milliseconds. ....	89
<b>Figure 3.11</b> H <sub>2</sub> O adsorption–desorption isotherms of bare CF and N,O/CF. ....	89
<b>Figure 3.12</b> a) Cyclic voltammetry in 0.5 M VOSO <sub>4</sub> + 1.0 M H <sub>2</sub> SO <sub>4</sub> at a scan rate 5 mV/s, b) Cyclic voltammograms of bare CF and N,O/CF using 0.01 M V <sub>2</sub> O <sub>3</sub> in 1M H <sub>2</sub> SO <sub>4</sub> with scan rate of 5 mV/s. ....	90
<b>Figure 3.13</b> Schematic representation of vanadium redox flow battery (VRFB). ....	91
<b>Figure 3.14</b> The digital image of interdigitated flow field plate used in our VRFB experiments. ....	91
<b>Figure 3.15</b> The vanadium redox flow battery workstation used for measurements. ....	92

<b>Figure 3.16</b> a) N,O/CF and b) bare CF at electrolyte flow rates of 30, 50, 80, and 120 mL/min in the VRFB.....	93
<b>Figure 3.17</b> Comparative study of polarization and power density curves for the VRFB system with bare CF and as-synthesized N,O/CF at electrolyte flow rates (a) 30, (b) 50, (c) 80, and (d) 120 mL/min. ....	95
<b>Figure 3.18</b> Electrochemical impedance spectroscopy and equivalent circuits for a) N,O/CF and b) bare CF. ....	95
<b>Figure 3.19</b> iR-corrected polarization and power density curves of a) N,O/CF and b) bare CF. ....	97
<b>Figure 3.20</b> Comparative study of polarization and power density curves with iR correction for VRFB system with bare CF and as-synthesized N,O/CF at electrolyte flow rates a) 30, b) 50, c) 80, and d) 120 mL/min.....	97
<b>Figure 3.21</b> Comparative study of potential loss from OCP for VRFB system with bare CF and N,O/CF at electrolyte flow rates (a) 30, (b) 50, (c) 80, and (d) 120 mL/min. ....	98
<b>Figure 3.22</b> Charging–discharging measurement of the battery employed with a) N,O/CF and b) bare CF at 40 mA/cm <sup>2</sup> current density with flow rates of 50 and 100mL/min. ....	99
<b>Figure 3.23</b> Comparative study of charge-discharge curve of VRFB with N,O/CF and bare CF at a) 50 mL/min & b) 100 mL/min at 40 mA/cm <sup>2</sup> ; c) 50 mL/min & d) 100 mL/min at 80 mA/cm <sup>2</sup> .....	100
<b>Figure 3.24</b> Charging–discharging test of the VRFB system with N,O/CF using it as both the anode and cathode at current densities of 40 and 80 mA/cm <sup>2</sup> with a) flow rates of 100 mL/min and b) 50 mL/min. ....	101
<b>Figure 3.25</b> a) Charging–discharging test performed at 40 mA/cm <sup>2</sup> for four cycles with a flow rate of 100 mL/min to show the electrochemical stability. b) Voltage, energy, and coulombic efficiencies calculated for four cycles mentioned in (3.24a). c) Discharge capacity plotted as a function of the cycle number for N,O/CF.....	102
<b>Figure 3.26</b> The proposed surface structure of N, O/CF; Reaction mechanism for, b) V <sup>2+</sup> /V <sup>3+</sup> and c) VO <sub>2</sub> <sup>+</sup> /VO <sup>2+</sup> redox couples at oxygen functional group active sites, d) Reaction mechanism for VO <sub>2</sub> <sup>+</sup> /VO <sup>2+</sup> redox couple at nitrogen functional group active sites. ....	102
<b>Figure 3.27</b> a) SEM image and corresponding elemental mappings of N,O/CF after VRFB charge- discharge stability test, b) XPS spectra of C, N, O of N,O/CF after VRFB charge-discharge stability test. ....	103
<b>Figure 4.1</b> PXRD patterns of simulated ZIF-8, as-synthesized ZIF-8, CoMn-ZIF, Co-ZIF and MnZIF. ....	123
<b>Figure 4.2</b> N <sub>2</sub> sorption isotherms (left) and their corresponding BJH pore size distribution (right) of CoMn-ZIF, Co-ZIF and Mn-ZIF. ....	124

<b>Figure 4.3</b> SEM images of a-c) CoMn-ZIF at different scale bars. d) SEM image with corresponding EDS elemental mappings of CoMn-ZIF. e) High-resolution XPS spectra of C 1s, N 1s, Zn 2p, Co 2p, and Mn 2p acquired from CoMn-ZIF. ....	125
<b>Figure 4.4</b> a) Schematic representation for the synthesis of the CoMn/NC catalyst. b) SEM. c, d) TEM, e) HR-TEM, and f) high-resolution HAADF-STEM image of CoMn/NC. g) Intensity profiles obtained from two sites, site 1 and site 2, in (f). h) HAADF-STEM image of CoMn/NC with the corresponding C, N, Co and Mn EDX elemental mappings. The white encircled two white dots in (f) correspond to the dual single-metal sites.....	127
<b>Figure 4.5</b> a-b) SEM images of CoMn/NC. c-e) TEM images of CoMn/NC at different scale bars. f) SAED pattern of CoMn/NC, revealing absence of any metallic nanoparticle.....	128
<b>Figure 4.6</b> a) HAADF-STEM image of CoMn/NC showing encircled a single Co-Mn pair as two white dots and b) corresponding EELS spectrum. ....	128
<b>Figure 4.7</b> a-c) SEM images of Co/NC at different scale bars. d) TEM image of single polyhedron of Co/NC. e) High-resolution TEM image of Co/NC and corresponding SAED pattern. f) HAADF-STEM image and corresponding EDX elemental mappings of carbon (blue), nitrogen (yellow), and cobalt (green) of Co/NC. ....	129
<b>Figure 4.8</b> a-c) SEM images of Mn/NC at different scale bars. d) TEM image of single polyhedron of Mn/NC. e) High-resolution TEM image of Mn/NC and corresponding SAED pattern. f) HAADF STEM image of Mn/NC and corresponding EDX elemental mappings of carbon (blue), nitrogen (yellow), and manganese (green). ....	129
<b>Figure 4.9</b> a-c) SEM images of CoMn/NC700 at different scale bars. d) TEM image of single polyhedron of CoMn/NC700. e) High-resolution TEM image of CoMn/NC700 and corresponding SAED pattern. f) STEM image of CoMn/NC700. g) SEM image with corresponding EDX elemental mappings of carbon (blue), nitrogen (yellow), manganese (green), cobalt (greenish blue), and zinc (grey).....	130
<b>Figure 4.10</b> a-c) SEM images of CoMn/NC800 at different scale bars. d) TEM image of single polyhedron of CoMn/NC800. e) High-resolution TEM image of CoMn/NC800 and corresponding SAED pattern. f) STEM image of CoMn/NC800. g) SEM image with corresponding EDX elemental mappings of carbon (blue), nitrogen (yellow), manganese (green), cobalt (greenish blue), and zinc (grey).....	131
<b>Figure 4.11</b> a) PXRD patterns, b) Powder X-ray diffraction (PXRD) patterns of CoMn/NC before and after acid (10% H <sub>2</sub> SO <sub>4</sub> ) wash. Two sharp peaks shown in sample (before acid wash) correspond to metallic nanoparticles. These two peaks disappeared in sample (after acid wash), confirming the absence of any metallic or metal oxide nanoparticles within CoMn/NC. ....	132
<b>Figure 4.12</b> a) Raman spectrum of CoMn/NC and other supporting catalysts, b) Raman spectra of CoMn/NC in wider Raman shift range from 500 to 3000 cm <sup>-1</sup> . ....	133
<b>Figure 4.13</b> a) N <sub>2</sub> -sorption isotherms of CoMn/NC and supporting catalysts, b) Pore size distribution of CoMn/NC and supporting samples derived from figure a.....	134

<b>Figure 4.14</b> High-resolution XPS spectra of a) N 1s, b) Co 2p, and c) Mn 2p of CoMn/NC.....	135
<b>Figure 4.15</b> a) Zn 2p XPS spectrum of CoMn/NC, b) XPS survey of CoMn/NC. ..	135
<b>Figure 4.16</b> N 1s XPS spectra of a) NC, b) Co/NC, c) Mn/NC.....	136
<b>Figure 4.17</b> XAS analysis: at Co K-edge, a) normalized XANES spectra of CoMn/NC along with Co-pc (cobalt phthalocyanine) and Co foil, b) $k^3$ -weighted EXAFS spectra of Co K-edge, and c) EXAFS fitting curve of CoMn/NC at R-space. XAS analysis: at Mn K-edge, d) normalized XANES spectra of CoMn/NC along with Mn-pc (manganese phthalocyanine) and Co foil, e) $k^3$ -weighted EXAFS spectra of Mn K-edge, f) EXAFS fitting curve of CoMn/NC at R-space.....	138
<b>Figure 4.18</b> Proposed atomic model of the Co–Mn dual active site present in CoMn/NC with bond length values (Å) using DFT methods.....	139
<b>Figure 4.19</b> CV curves of CoMn/NC in Ar- and O <sub>2</sub> -saturated 0.1 M KOH acquired at scan rate of 50 mV/s. ....	139
<b>Figure 4.20</b> Electrochemical ORR performance in 0.1 M KOH. a) LSV curves of CoMn/NC, Co/NC, Mn/NC, and Pt/C catalysts with a sweep rate of 5 mV/s and a rotation rate of 900 rpm, b) $E_{\text{onset}}$ and $E_{1/2}$ of CoMn/NC, Pt/C, and supporting catalysts. ....	140
<b>Figure 4.21</b> a) Polarization curves of CoMn/NC at different rotation speeds. The inset shows the corresponding K-L plots with e <sup>-</sup> transfer number (n) at different potentials, b) H <sub>2</sub> O <sub>2</sub> yield and n values for CoMn/NC and Pt/C, calculated from RRDE measurements. ....	141
<b>Figure 4.22</b> Tafel slopes of CoMn/NC and other supporting catalysts in 0.1 M KOH. ....	141
<b>Figure 4.23</b> ORR linear sweep voltammograms (LSVs) of CoMn/NC, CoMn/NC700, and CoMn/NC800 in 0.1 M KOH acquired at scan rate of 5 mV/s. ....	142
<b>Figure 4.24</b> RDE polarization curves for a) Co/NC, b) Mn/NC, and c) Pt/C in 0.1 M KOH acquired at scan rate of 5 mV/s. Inset figures are corresponding K-L plots with e <sup>-</sup> transfer numbers at different potentials. ....	142
<b>Figure 4.25</b> a) Nyquist plots, and b) electrochemical double-layer capacitance ( $C_{\text{dl}}$ ) of CoMn/NC and supporting catalysts.....	144
<b>Figure 4.26</b> Cyclic voltammograms for a) CoMn/NC, b) Mn/NC, c) Co/NC in 0.1 M KOH at different electrochemical scan rates 5, 10, 20, 30, 40, 50 mV/s within potential window 1.03-1.13 V (vs RHE) (non-faradaic region).....	144
<b>Figure 4.27</b> Comparative plots for K-L analysis (left) and derived rate limiting currents ( $j_k$ ) & number of e <sup>-</sup> transfer (n) (right) for ORR in 0.1 M KOH using CoMn/NC, Co/NC, Mn/NC, and Pt/C at 0.75 V vs RHE. ....	145
<b>Figure 4.28</b> a) Comparison of methanol tolerances of CoMn/NC and Pt/C at 0.86 V (vs RHE). Methanol was injected into the electrolyte at 3000 s, b) Chronoamperometric durability test for CoMn/NC and Pt/C at 0.89 V (vs RHE), c) ORR LSVs of CoMn/NC	

before and after stability test with continuous run for 24 h at a constant potential of 0.89 V (vs RHE) with electrode rotation of 900 rpm in 0.1 M KOH solution, d) comparison of E<sub>onset</sub> and E<sub>1/2</sub> of CoMn/NC before and after stability test, e) Chronoamperometric ORR stability test of CoMn/NC with continuous run for 72 h at a constant potential of 0.89 V (vs RHE) with electrode rotation of 900 rpm in 0.1 M KOH solution, and f) ORR cyclic voltammetry curves of CoMn/NC before and after 10,000 cycles. .... 146

**Figure 4.29** Electrochemical ORR performance in 0.5 M H<sub>2</sub>SO<sub>4</sub>. a) LSV curves for CoMn/NC, Co/NC, Mn/NC, and Pt/C catalysts with a sweep rate of 5 mV/s and a rotation rate of 900 rpm, b) Onset potentials and half-wave potentials (E<sub>1/2</sub>) of CoMn/NC, Pt/C, and supporting catalysts, c) ORR LSVs of CoMn/NC, CoMn/NC700 and CoMn/NC800 in 0.5 M H<sub>2</sub>SO<sub>4</sub> acquired at scan rate of 5 mV/s..... 146

**Figure 4.30** Comparative plots for K-L analysis (left) and derived rate limiting currents (j<sub>k</sub>) & number of e- transfer (n) (right) for ORR in 0.1 M KOH using CoMn/NC, Co/NC, Mn/NC, and Pt/C at 0.75 V vs RHE..... 147

**Figure 4.31** RDE polarization curves of a) Co/NC, b) Mn/NC and c) Pt/C in 0.5 M H<sub>2</sub>SO<sub>4</sub> solution acquired at scan rate of 5 mV/s. Inset figures are corresponding K-L plots with e- transfer numbers at different potentials. .... 147

**Figure 4.32** a) Tafel slopes, b) mass activities, and c) J<sub>k</sub> values of CoMn/NC and supporting catalysts..... 148

**Figure 4.33** a) Chronoamperometric durability test for CoMn/NC and Pt/C at 0.82 V (vs RHE), b) Chronoamperometric ORR stability test of CoMn/NC with continuous run for 72 h at a constant potential of 0.82 V (vs RHE) with electrode rotation of 900 rpm in 0.5 M H<sub>2</sub>SO<sub>4</sub> solution, c) LSV curves of CoMn/NC before and after the durability test. .... 150

**Figure 4.34** Optimized geometries of CoN<sub>3</sub>-MnN<sub>3</sub>, MnN<sub>3</sub>-MnN<sub>3</sub>, and CoN<sub>3</sub>-CoN<sub>3</sub> DSAC models. .... 150

**Figure 4.35** Optimized structures of various possible CoN<sub>x</sub>C<sub>y</sub>-MnN<sub>x'</sub>C<sub>y'</sub> atomic models (where x, y, x' and y' = 0-3) (blue = Co, pink = Mn, grey = N, and brown = C). .... 152

**Figure 4.36** Relative stability of various possible CoN<sub>x</sub>C<sub>y</sub>-MnN<sub>x'</sub>C<sub>y'</sub> structures (where x, y, x' and y' = 0-3) with respect to the CoN<sub>3</sub>-MnN<sub>3</sub> model..... 152

**Figure 4.37** O<sub>2</sub> activation (bridge mode) on the Co-Mn active site in a) dissociative pathways and b) associative pathways, c) O<sub>2</sub> activation (end on) on one of the metal atoms of Co-Mn active site considering associative path at c) Co atom and d) Mn atom. DFT calculation further added that side on adsorption is more favourable over end on. .... 153

**Figure 4.38** Free energy diagrams for the ORR at Co-Mn DSAC sites for a) dissociative mechanisms and b) associative mechanisms. Elementary reaction steps are shown inside the free energy diagrams. .... 154

**Figure 4.39** Kinetic aspects of the ORR pathway on Co-Mn DSAC sites in the a) dissociative approach and b) associative approach..... 155

**Figure 4.40** Schematic diagram of a PEM fuel cell. .... 156

<b>Figure 4.41</b> A schematic diagram for single PEM fuel cell assembly showing 5-layered MEA. ....	156
<b>Figure 4.42</b> Physical appearance of MEA and single cell PEM fuel cell assembly progress.....	156
<b>Figure 4.43</b> a) Polarization curves and corresponding power densities of CoMn/NC and Pt/C under H <sub>2</sub> /O <sub>2</sub> fuel cell conditions, b) Stability test of CoMn/NC as a cathode in a fuel cell at 0.65 V, c) Polarization curve and corresponding power density of CoMn/NC in H <sub>2</sub> /air fuel cell.....	157
<b>Figure 4.44</b> Bifunctional ORR/OER characteristics of CoMn/NC and the Pt/C + IrO <sub>2</sub> couple showing LSVs for both the ORR and the OER, acquired in 0.1 M KOH at a scan rate of 5 mV s <sup>-1</sup> . ....	157
<b>Figure 4.45</b> a) Schematic diagram of a homemade liquid cell-based rechargeable ZAB. Performance of ZAB using CoMn/NC as the ORR/OER oxygen electrode: b) open circuit voltage, c) discharge polarization curves and corresponding power density curves showing a comparison with the Pt/C + IrO <sub>2</sub> couple, d) charge–discharge polarization curves showing a comparison with the Pt/C + IrO <sub>2</sub> system, e) repeating discharge curves at various current densities, f) long-time discharge at a fixed current density 40 mA cm <sup>-2</sup> , g) cycling performance at 5 mA cm <sup>-2</sup> current density and 20 min duration per cycle, and h) cycling performance with a cycle duration of 2 h at higher current density of 20 mA cm <sup>-2</sup> . ....	159
<b>Figure 5.1</b> PXRD pattern of ZIF-8, Ni/ZIF-8, Ni/ZIF-8@SiO <sub>x</sub> , ZIF-8@SiO <sub>x</sub> . ....	180
<b>Figure 5.2</b> FT-IR analysis of Ni(OAc) <sub>2</sub> ·4H <sub>2</sub> O, ZIF-8, Ni/ZIF-8, Ni/ZIF-8@SiO <sub>x</sub> . ....	180
<b>Figure 5.3</b> N <sub>2</sub> adsorption desorption isotherm of pure ZIF-8, Ni/ZIF-8, Ni/ZIF-8@SiO <sub>x</sub> . ....	181
<b>Figure 5.4</b> a)-c) SEM images of ZIF-8 at different scale bars. d) SEM image with corresponding EDS elemental mappings of ZIF-8. e) XPS spectra of C1s, N1s, Zn 2p, acquired from ZIF-8. ....	182
<b>Figure 5.5</b> a)-c) SEM images of Ni/ZIF-8 at different scale bars. d) SEM image with corresponding EDS elemental mappings of Ni/ZIF-8. e) XPS spectra of C1s, N1s, Zn 2p, Ni 2p acquired from Ni/ZIF-8. ....	183
<b>Figure 5.6</b> a)-c) SEM images of Ni/ZIF-8@SiO <sub>x</sub> at different scale bars. d)-f) HR-TEM images of Ni/ZIF-8@SiO <sub>x</sub> . g) HAADF-STEM image and its corresponding EDX elemental mapping of Silicon (cyan), Oxygen (purple), Carbon (red), Nitrogen (yellow), Nickel (green), Zinc (blue). ....	183
<b>Figure 5.7</b> High resolution XPS spectra of C1s, O1s, Si 2p, N1s, Zn 2p, Ni 2p acquired from Ni/ZIF-8@SiO <sub>x</sub> . ....	184
<b>Figure 5.8</b> a) SEM images of NiO/Ni-SACs/mNC1000. b) TEM images of NiO/Ni-SACs/mNC900. c) HR-TEM images where small NiO nanoclusters distributed over carbon (inset is the SAED pattern of NiO/Ni-SACs/mNC900). d)-e) High resolution HAADF-STEM images. f) d spacing calculations from corresponding fringes of NiO nanoclusters. g) Intensity profiles of the nanoclusters. h) HAADF-STEM image and its	



corresponding EDX elemental mapping of Carbon (blue), Nitrogen (green), Nickel (red), Oxygen (yellow).....	185
<b>Figure 5.9</b> a)-b) SEM images of NiO/Ni-SACs/mNC900 at different scale bars. c)-d) TEM images of NiO/Ni-SACs/mNC900. e) HR-TEM images where small NiO nanoclusters distributed over carbon. f) d spacing calculations from corresponding fringes of NiO nanoclusters. g) SAED pattern of NiO/Ni-SACs/mNC900. h) HAADF-STEM image and its corresponding EDX elemental mapping of Carbon (blue), Nitrogen (green), Nickel (red), Oxygen (yellow). .....	186
<b>Figure 5.10</b> a)-b) SEM images of mNC1000 at different scale bars. c)-d) TEM images of mNC1000. e) SAED pattern of mNC1000. f) HR-TEM images where no metallic particles or clusters are present. g) HAADF-STEM image and its corresponding EDX elemental mapping of Carbon (blue), Nitrogen (green).....	187
<b>Figure 5.11</b> a)-b) SEM images of Ni-SACs/NC1000 at different scale bars. c)-d) TEM images of Ni-SACs/NC1000. e) SAED pattern of Ni-SACs/NC1000. f) HR-TEM images where no metallic particles or clusters are present. g) HAADF-STEM image and its corresponding EDX elemental mapping of Carbon (blue), Nitrogen (green), Nickel (Ni). .....	188
<b>Figure 5.12</b> TGA of ZIF-8 and Ni/ZIF-8@SiO <sub>x</sub> at a ramp rate of 10 °C min <sup>-1</sup> under an N <sub>2</sub> flow. ....	189
<b>Figure 5.13</b> Schematic illustration of the synthesis process of mesoporous carbon cages with more stretched edges.....	190
<b>Figure 5.14</b> a) PXRD of as synthesis NiO/Ni-SACs/mNC1000 and other supporting catalysts. b) PXRD of as synthesized NiO nanoparticles. ....	190
<b>Figure 5.15</b> a) Comparison of Raman spectra of as synthesized NiO/Ni-SACs/mNC1000 with all other supporting catalysts. b) Raman spectra of NiO/Ni-SACs/mNC1000 and NiO/Ni-SACs/mNC900 in a wide range.....	191
<b>Figure 5.16</b> Electron paramagnetic resonance (EPR) spectra measured at 292 K...	192
<b>Figure 5.17</b> Comparison of XPS Ni 2p spectra of NiO/Ni-SACs/mNC1000 with other supporting catalysts.....	193
<b>Figure 5.18</b> Comparison of XPS N 1s spectra of NiO/Ni-SACs/mNC1000 with other supporting catalysts.....	194
<b>Figure 5.19</b> Comparison of XPS O 1s spectra of NiO/Ni-SACs/mNC1000 and NiO/Ni-SACs/mNC900 with pure NiO nanoparticles. ....	195
<b>Figure 5.20</b> a) UPS He I spectra b) Valence band spectra (The white bar shows d-band center) of NiO/Ni-SACs/mNC1000 and Ni-SACs/NC1000.....	197
<b>Figure 5.21</b> N <sub>2</sub> adsorption desorption isotherm comparison between NiO/Ni-SACs/mNC1000 and Ni-SACs/NC1000. ....	198
<b>Figure 5.22</b> a)-c) N <sub>2</sub> adsorption desorption isotherms of NiO/Ni-SACs/mNC900, mNC1000 & without washed sample of NiO/Ni-SACs/mNC1000 respectively. D) BJH	

analysis for pore size distribution of NiO/Ni-SACs/mNC1000 and all other supporting catalysts. ....	198
<b>Figure 5.23</b> Cyclic voltammetry study of NiO/Ni-SACs/mNC1000 catalyst in 1 M KOH solution at scan rate 10 mV/s. ....	199
<b>Figure 5.24</b> a) Linear sweep voltammetry study of NiO/Ni-SACs/mNC1000 and other supporting catalysts in 1 M KOH solution at scan rate 5 mV/s. b) Bar graph corresponding to comparison of overpotential for different catalysts required to achieve 10 mA cm <sup>-2</sup> . ....	200
<b>Figure 5.25</b> Tafel plots of NiO/Ni-SACs/mNC1000 and other supporting catalysts. ....	201
<b>Figure 5.26</b> a) Comparison of Nyquist plots of NiO/Ni-SACs/mNC1000 and other supporting catalysts for OER in 1M KOH. b) & c) Fitting of the Nyquist plot and its corresponding equivalent circuit model used for OER kinetics. ....	201
<b>Figure 5.27</b> CV curves of (a) NiO/Ni-SACs/mNC1000, (b) NiO/Ni-SACs/mNC900, (c) Ni-SACs/NC1000 and (d) IrO <sub>2</sub> in a potential range of 1.028 to 1.128 V vs. RHE at different scan rate in 1 M KOH. ....	202
<b>Figure 5.28</b> Electrochemical double-layer capacitance (C <sub>dl</sub> ) of NiO/Ni-SACs/mNC1000 and supporting catalysts. ....	203
<b>Figure 5.29</b> a) Chronopotentiometric durability test of NiO/Ni-SACs/mNC1000 at different current densities (5, 10, 15, 20, 25 mA cm <sup>-2</sup> ). b) LSV before and after stability test. ....	204
<b>Figure 5.30</b> a) RRDE current-potential response of NiO/Ni-SACs/mNC1000 and Ni-SACs/NC1000 catalysts for OER in O <sub>2</sub> -saturated 1.0 M KOH. b) TOF and FE calculated for OER considering different overpotential values, catalyzed by NiO/Ni-SACs/mNC1000 and Ni-SACs/NC1000. ....	205
<b>Figure 5.31</b> a) Schematic illustration of water splitting electrochemical cell. b) LSV curves of NiO/Ni-SACs/mNC1000 + Pt/C where Pt/C used as cathode and NiO/Ni-SACs/mNC1000 used as anode and compare with conventional catalyst mixture Pt/C + IrO <sub>2</sub> . ....	205
<b>Figure 5.32</b> Electrochemical ORR performance in 0.1 M KOH. a) LSV curves of NiO/Ni-SACs/mNC1000, Ni-SACs/NC1000, Pt/C with a sweep rate of 5 mV/s and a rotation rate of 900 rpm. (b) E <sub>onset</sub> and E <sub>1/2</sub> of NiO/Ni-SACs/mNC1000, Pt/C, and supporting catalysts. ....	206
<b>Figure 5.33</b> The optimized structure for a) Ni-N <sub>4</sub> and b) OH, c) O, and d) OOH adsorbed on Ni-N <sub>4</sub> . ....	207
<b>Figure 5.34</b> The optimized structure for a) Ni-NiO-N <sub>4</sub> and b) OH, c) O, and d) OOH adsorbed on Ni-NiO-N <sub>4</sub> . ....	207
<b>Figure 5.35</b> DOS of (a) Ni-N <sub>4</sub> and (b) Ni-NiO-N <sub>4</sub> . The Fermi energy (E <sub>F</sub> ) is at zero. Calculated free energy diagram for OER on c) Ni-N <sub>4</sub> and (b) Ni-NiO-N <sub>4</sub> at zero applied potential (U = 0). ....	209

<b>Figure 5.36</b> Photograph displaying measured open-circuit voltage of ~1.361 V using PAM-h electrolyte for NiO/Ni-SACs/mNC1000.....	210
<b>Figure 5.37</b> photograph of PAM-zdh electrolyte.....	210
<b>Figure 5.38</b> a) Tensile stress-strain curve of PAM-h, PAM-dh, PAM-zh, PAM-zdh. b) Cycling performance of the symmetric Zn   Zn cells employing PAM hydrogel electrolyte and PAM organohydrogel electrolyte at 5 mA cm <sup>-2</sup> . c) XRD patterns of various Zn samples. It suggests that the discharging and charging/discharging products are Zn(OH) <sub>2</sub> and ZnO, respectively. d) DSC curves of PAM-h, PAM-dh, PAM-zh, PAM-zdh.....	212
<b>Figure 5.39</b> The binding energy between H <sub>2</sub> O, PAM-H <sub>2</sub> O, PAM-DMSO-H <sub>2</sub> O, PAM-Zn (BF <sub>4</sub> ) <sub>2</sub> -H <sub>2</sub> O and PAM-DMSO-Zn(BF <sub>4</sub> ) <sub>2</sub> -H <sub>2</sub> O obtained by DFT simulation using Gaussian.....	213
<b>Figure 5.40</b> a) Photograph displaying measured open-circuit voltage of ~1.454 V, and b) open circuit voltage of 1.454 and 1.446 V using PAM-zdh electrolyte for NiO/Ni-SACs/mNC1000 and Pt/C+IrO <sub>2</sub> couple, respectively. ....	214
<b>Figure 5.41</b> a) Polarization curves and corresponding power densities of NiO/Ni-SACs/mNC1000 and Pt/C + IrO <sub>2</sub> as cathode using PAM-zdh electrolyte for single solid-state ZAB. b) Photograph of a lighted LED powered via connecting two ZABs in a series. c) Comparison of specific capacity between NiO/Ni-SACs/mNC1000 and Pt/C + IrO <sub>2</sub> . d) Comparison of galvanostatic discharge-charge cycling performance of rechargeable solid-state ZAB at a constant discharge-charge current density of 20 mA cm <sup>-2</sup> with a cycle duration of 1h for NiO/Ni-SACs/mNC1000 and Pt/C + IrO <sub>2</sub> . e) Repeating discharge curves three time at various current densities (2, 5, 10 mA cm <sup>-2</sup> ). f) Photograph of Zn-gel interface, fresh Zn plate and Zn plate after long term discharge. g) Charging discharging stability of the battery at with NiO/Ni-SACs/mNC1000 at 10 mA cm <sup>-2</sup> for 110h. Cycling stability at higher current densities h) 60 mA cm <sup>-2</sup> & i) 100 mA cm <sup>-2</sup> . j) Stability test of the battery at different bending conditions. k) Battery performance at ice cold condition: charging discharging test at 2 mA cm <sup>-2</sup> . ....	215



## List of Schemes

<b>Scheme 1.1</b> Schematic diagram of reaction paths a) homogeneous catalysis, b) heterogeneous catalysis.....	2
<b>Scheme 2.1</b> a) Metal catalysed alkylation of branched ketones. b) Mnphen@ZIF catalysed one-step sustainable synthesis of di-substituted ketones. ....	43
<b>Scheme 2.2</b> Schematic representation of the synthesis of the MnPhen@ZIF catalyst. ....	44
<b>Scheme 2.3</b> Proposed mechanism for the Mn-catalyzed alkylation of ketones. ....	59
<b>Scheme 2.4</b> Reaction conditions: propiophenone 1a (0.1 mmol), benzyl alcohol 2a (0.15 mmol), MnPhen@ZIF (20 mg), t-BuOK 1.0 equiv. for (a) and 2.0 equiv. for (b)–(d), toluene (2 mL) under an Ar atmosphere, a Schlenk tube used under an Ar atmosphere, 140 °C, 36 h time.....	62
<b>Scheme 2.5</b> Deuterium labelling experiments between 1a with 2a-d. ....	63
<b>Scheme 2.6</b> Deuterium labelling experiments between 1a with 2a-d <sub>2</sub> . ....	64
<b>Scheme 2.7</b> Deuterium labelling experiments between 1a with mixture of 2a & 2a-d <sub>2</sub> . ....	65
<b>Scheme 2.8</b> Deuterium labelling experiments between 1a-d <sub>2</sub> with 2a. ....	66
<b>Scheme 3.1</b> Schematic representation of the synthesis of N,O/CF from bare CF.....	82
<b>Scheme 4.1</b> Schematic representation for the synthesis of the CoMn/NC catalyst..	123
<b>Scheme 5.1</b> Schematic representation for the synthesis of NiO/Ni-SACs/mNC1000. ....	179



## List of Abbreviations

MOFs	Metal-Organic Frameworks
SACs	Single-Atom Catalysts
MNPs	Metal Nanoparticles
COF	Covalent Organic Framework
PSM	Post Synthetic Metalation
TMs	Transition Metals
POMs	Polyoxometalates
bpy	Bipyridine
ZIFs	Zeolitic Imidazolate Frameworks
MIL	Matériaux de l'Institut Lavoisier
TEM	Transmission Electron Microscopy
SEM	Scanning Electron Microscopy
BET	Brunauer-Emmett Teller
PXRD	Powder X-Ray Diffraction
XAS	X-Ray Absorption Spectroscopy
TGA	Thermogravimetric Analysis
XPS	X-Ray Photoelectron Spectroscopy
$^1\text{H}$ NMR	Proton Nuclear Magnetic Resonance
$^{13}\text{C}$ NMR	Carbon Nuclear Magnetic Resonance
CNTs	Carbon Nanotubes
HAADF-STEM	High Angle Annular Dark Field- Scanning Transmission Electron Microscopy
SEM	Scanning Electron Microscopy
EDS	Energy Dispersive X-Ray Spectroscopy

ICP-OES	Inductively Coupled Plasma-Optical Emission Spectrometry
UV-Vis.	Ultraviolet-Visible Spectroscopy
FTIR	Fourier Transform Infrared
XANES	X-Ray Absorption Near Edge Spectroscopy
2-mIm	2-methylimidazole
N <sub>2</sub>	Nitrogen
Ar	Argon
He	Helium
H <sub>2</sub>	Hydrogen
DMF	Dimethylformamide
MeOH	Methanol
EtOH	Ethanol
H <sub>2</sub> O	Water
BJH	Barrett Joyner Halenda
Hz	Hertz
Å	Angstrom
α	Alpha
°C	Degree Celsius
λ	Lambda
cm <sup>-1</sup>	Centimeter Inverse
mol	Mole(s)
Mg	Milligram(s)
mL	Milliliter(s)
DFT	Density Functional Theory
VASP	Vienna Ab Initio Simulation package



ZAB	Zinc Air Battery
PEMFCs	Proton Exchange Membrane Fuel Cells
ORR	Oxygen Reduction Reaction
OER	Oxygen Evolution Reaction
HER	Hydrogen Evolution Reaction
MEA	Membrane Electrode Assembly
CV	Cyclic Voltammetry
LSV	Linear Sweep Voltammetry
RDE	Rotating Disc Electrode
RRDE	Rotating Ring Disc Electrode
ECSA	Electrochemical Surface Area
RHE	Reversible Hydrogen Electrode
eV	Electron Volt
K-L	Koutechy-Levich
EIS	Electrochemical Impedance Spectroscopy
F	Faraday
E	Potential
$E_{1/2}$	Half-wave Potential
i	Current
J	Current Density
$C_s$	Specific Capacitance
mF	Milli Faraday
mV	Milli Volt
$\text{Dec}^{-1}$	Decade Inverse
Z	Electron Transfer Number
n	Mole

$\Omega$

Ohm

$\text{CDCl}_3$

Deuterated chloroform

KOH

Potassium Hydroxide

$\text{H}_2\text{SO}_4$

Sulfuric Acid

## Preface

Catalysis has sparked intense interest in both scientific research and industrial applications. A catalyst is a material that speeds up a chemical reaction towards equilibrium while consuming relatively little energy. One or more desirable reactions can proceed more quickly and selectively under generally benign conditions by utilizing the right catalyst. Since catalytic processes are used to produce more than 95% of all modern chemical products, the search for better catalytic materials is an exciting and rapidly developing area of study.

Metal-organic frameworks (MOFs) offer significant potential for the rational design of novel catalytic materials as indicated by the several numbers of publications published in the last ten years. The coordination bonds between metal ions/clusters and organic ligands form the foundation of these novel class of crystalline porous materials. MOFs excel as heterogeneous catalysts due to several characteristics, including their remarkable structural diversity, intrinsic hybrid organic–inorganic nature, unsaturated metal sites, potential voids for host guest interactions etc. However, the broadness of catalytic applications using MOFs are quite limited, as MOFs are considered not stable under harsh acidic or basic conditions. In the present thesis, we have discovered a MOF based heterogeneous system which is chemically and thermally stable under harsh basic conditions.

Electrochemical energy storage and conversion technologies have been acknowledged as the most viable solutions to address the world's mounting energy dilemma due to their high levels of energy efficiency and minimal environmental impact. Redox flow batteries, rechargeable Zn -air batteries, proton exchange membrane fuel cells, water electrolyzers are some of the EESC systems that have received the greatest attention and development. Regardless of their various working theories, these

electrochemical systems all aim for the physicochemical properties of materials to determine their ultimate storage capacity and conversion efficiency. These properties include low cost, low overpotential, high electrochemical active surface area, better electronic conductivity or lower charge transfer resistance, well-defined redox couples, long-term stability at higher current density etc.

MOFs are a developing precursor for earth-abundant element-based electrocatalysts. Because of polymeric nature and presence of organic/metal moieties, by calcination/carbonization a MOF can be converted into metal/carbon composite or individually each (refer as MOF-derived materials), depending upon the calcination gaseous environment. Pure MOF electrocatalysts suffer from low stability, nonconductivity, severe environmental sensitivity under extreme acidic/basic electrolytic conditions. Although MOF-derived materials partially address these issues, they nevertheless have certain inherent drawbacks, such as an inability to regulate the pore size during carbonization and dissolution of active sites particularly in acidic media. Therefore, more work is required in this current research to enhance the functionality of MOF derivatives for application in actual EESC devices in the future.

**Chapter 1:** In this chapter, we give a brief introduction of MOF and MOF-derived materials. With an emphasis on structure-property relationships, we discuss key elements of creating MOF catalysts, their atomic-level structural information. We also summarize the MOF catalysts used so far for various organic transformation reactions. A detailed study on the working principles of the electrochemical energy storage and conversion devices, along with that we have discussed the methods for creating unique MOF-derived nanostructured materials with functionalities that are specifically suited for electrocatalysis.

**Chapter 2:** In this chapter, we have developed an earth-abundant Mn based heterogeneous catalyst using the trick of immobilization of homogeneous Mn-Phenanthroline complex into MOF pores. The as synthesized heterogeneous catalysts designated as Mnphen@ZIF demonstrated as first MOF based catalysts for the selective synthesis of functionalized branched ketones where alcohols being used as renewable coupling partner. Superior stability of catalyst under harsh basic conditions well examined by SEM, TEM, BET, PXRD, TGA and EDX elemental mappings. The borrowing hydrogen strategy was validated through mechanistic studies and deuterium labelling experiments. The released hydrogen gas was also measured by water displacement method or quantified by GC. Formation of extra Lewis acid sites, defects, and pore enhancement during catalysis helped in achieving higher activity and selectivity.

**Chapter 3:** In this chapter, a unique synthetic approach has been introduced where nanostructurally grown zinc layered double hydroxide on graphitic carbon felt (CF) is converted into a zeolitic imidazolate framework (ZIF-8), and then, subsequent carbonization resulted in a N/O-functionalized porous carbon electrode (N,O/CF). Because of the presence of N/O-containing functional groups and deposition of ZIF-8-derived nano porous carbon on the CF, the N,O/CF is found to be highly hydrophilic in nature with a large surface area. Cyclic voltammetry measurements with N,O/CF suggest the fast electrochemical kinetics of  $V(IV) \leftrightarrow V(V)$  reactions. Polarization curves and electrochemical impedance spectroscopy measurements of the vanadium redox flow battery (VRFB) assembly illustrate the significant decrease in charge transfer resistance at electrode surfaces. At 50 mL/min electrolyte flow rate, N,O/CF delivers energy efficiencies of 83.11 and 76.66% at current densities of 40 and 80 mA/cm<sup>2</sup>, respectively. The values are 82.59 and 76.39%, respectively, at 100 mL/min, showing the negligible effect of the flow rate. The power density of VRFBs at various electrolyte flow rates is

also presented, which increases with increasing flow rates and is higher for N,O/CF ( $\sim 821 \text{ mW/cm}^2$ ) than for bare CF ( $606 \text{ mW/cm}^2$ ). The stability test confirms the retention of energy, voltage, and coulombic efficiencies after recycling of the electrode. The above-mentioned findings of improved performance of VRFBs with employing the N,O/CF electrode are a cumulative effect of enhanced nano-porosity, an increased number of catalytic active sites, high wettability, and low charge transfer resistance.

**Chapter 4:** In this chapter, we report atomically dispersed Co-Mn dual single atom catalysts anchored on nanostructured N-doped porous carbon polyhedral synthesizing via controlled carbonization of a Co/Mn-doped ZIF-8 MOF. The atomically isolated Co-Mn site in CoMn/NC is recognized by combining microscopic as well as spectroscopic techniques. CoMn/NC exhibited excellent ORR activities in alkaline ( $E_{1/2}$ , 0.89V) as well as in acidic ( $E_{1/2}$ , 0.82 V) electrolytes with long-term durability and enhanced methanol tolerance. Density functional theory (DFT) suggests that Co-Mn site is efficiently activating the O–O bond via bridging adsorption, decisive for the 4e oxygen reduction process. Though the Co-Mn sites favor  $\text{O}_2$  activation via the dissociative ORR mechanism, stronger adsorption of the intermediates in the dissociative path degrades its overall ORR activity. Our DFT studies conclude that ORR on Co-Mn site mainly occurs via bridging side-on  $\text{O}_2$  adsorption following thermodynamically and kinetically favorable associative mechanistic pathways with lower overpotential and activation barrier. CoMn/NC performed excellently as a cathode in proton exchange membrane (PEM) fuel cell and rechargeable Zn-air battery with high peak power densities of  $970 \text{ \& } 176 \text{ mW cm}^{-2}$ , respectively. This work provides the guidelines for the rational design and synthesis of non-precious DSACs for enhancing the ORR activity as well as robustness of DSACs and opens the door to design the multi-functional robust electrocatalysts for energy storage and conversion devices.

**Chapter 5:** In this chapter, we introduce a quasi-solid-state Zinc-Air Battery (ZAB) exhibiting prolonged cycle life and robust stability over a wide temperature range. Our method involves the fabrication of a unique nanostructure through a silica-mediated Metal-Organic Framework (MOF) templated approach. This structure comprises a mesoporous concave carbon cage with elongated edges, facilitating efficient mass transport, and exposing catalytically active sites for oxygen redox reactions. The incorporation of NiO nanoclusters onto isolated nickel atom sites (Ni-N-C) enhances catalytic activity for both Oxygen Evolution Reaction (OER) and Oxygen Reduction Reaction (ORR). Through Density Functional Theory (DFT) calculations, we investigated the role of NiN<sub>4</sub> and cubic NiO in decorating NiN<sub>4</sub> sites, elucidating the mechanism of OER at the atomic level. Our analysis revealed an augmentation of Ni d-orbitals near the Fermi level, promoting H<sub>2</sub>O molecule absorption and subsequent intermediates. The OER activity at Ni of the NiO site surpassed that of the Ni single site of NiN<sub>4</sub>. Furthermore, we improved interfacial stability and low-temperature tolerance of the battery electrolyte by modifying the H-bond network with DMSO and Zn (BF<sub>4</sub>)<sub>2</sub>. This approach enables high-rate cycling at 25 °C and broad temperature adaptability (-70 to 70 °C), providing valuable insights for the advancement of quasi-solid-state ZAB technology.

**Chapter 6:** In this chapter, based on the current studies we have drawn the conclusion. We also discuss the work's potential future directions and important suggestions.

\*\*\*





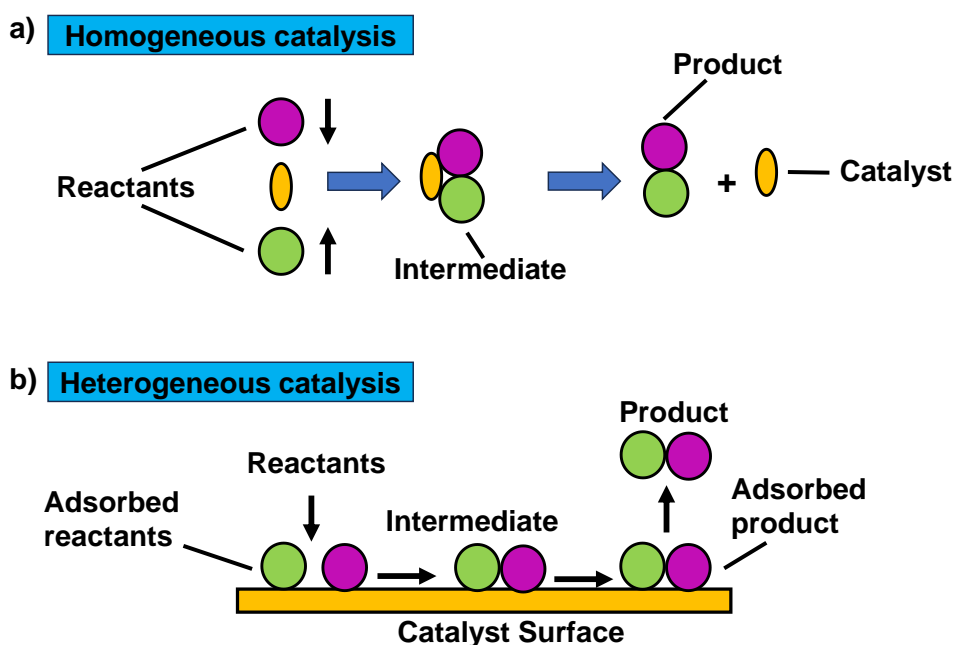
# Chapter 1: Introduction And Literature Survey

## 1.1 Background

The development of sustainable and green chemistry has become a greater focus for scientists during the last ten years of research. Green chemistry, by definition, is the design of safe, effective, and ecologically friendly processes and products with little usage of hazardous materials and production. Out of all the green chemistry principles, catalysis is the most relevant to current research era because it is still a long-term topic of interest in the field of chemical technology [1]. A material that accelerates a chemical reaction towards equilibrium without significantly consuming is called a catalyst. Greek words "κατα," which means "down," and "λυσις," which means "loosening," are the origin of the word "catalysis" [2]. Using the appropriate catalyst, one or more desirable reactions can continue at a higher rate and selectivity under relatively mild circumstances. Because of its importance in many domains, such as industry, energy, environment, and life sciences, catalysis remains a strategic field of chemistry. The production of industrial catalysts accounts for almost \$16 billion of the global market, and catalytic processes are used to produce over 95% (by volume) of all chemical products produced today [3]. These numbers make it easy to see why catalysis research is at the vanguard of chemical engineering, materials science, and chemistry.

These catalysts can be classified as two types one is homogeneous, and the other is heterogeneous. Homogeneous catalysts means where the reactants and catalysts are in same phase. It subsequently exhibits increased activity, excellent selectivity, ease of mechanistic pathway study, etc. Nonetheless, it has a significant disadvantage as catalyst, products, and reactants all stay in the same phase, at the end of the process it is very challenging task to separate all of them. However, heterogeneous catalysts overcome this problem

of separation as the catalyst and reactants are in different phases. Heterogeneous catalysis occurs mostly in liquid-solid and gas-solid systems. Reactants are substances that dissolve in gaseous or liquid media, while the catalyst is typically a solid substance. Nevertheless, it faces some problem due to poor accessibility of active sites. The fundamental of catalysis is, it is a molecular phenomenon like conversion of one molecule to other either it is homogeneous or heterogeneous. Homogeneous catalysis mainly connected with molecular organometallic chemistry and heterogeneous catalysis to surface science or solid-state chemistry. So, scientists are trying to bridge the gap between this two by introducing some nano catalysts with defined active sites i.e., combination of molecular reactivity to the surface science to establish the structure activity correlation more precisely.



**Scheme 1.1** Schematic diagram of reaction paths a) homogeneous catalysis, b) heterogeneous catalysis.

## 1.2 Functional porous materials as heterogeneous catalysts

The field of "pore or space" chemistry is extremely challenging and offers solutions for numerous problems utilizing host-guest interaction. Porous materials are categorized into three kinds based on the size of their pores: micro, meso, and macro porous materials, with pore sizes ranging from 2 nm,  $>2-50$  nm and greater than 50 nm, respectively. Due to its superior qualities in ion-exchange, adsorption, separation, and catalysis, porous materials have widespread applications [4,5]. The aluminosilicate mineral stilbite was the first to be found as naturally containing zeolites in 1756 (Figure 1.1) [6]. After that its artificial synthesis initiated from 1940s. Zeolites are mainly inorganic materials consisting of Si, Al & O where silicon and aluminium are linked by some oxides. The term "molecular sieve" often used for these materials as it contains well-defined sub-nanometric void area ( $d < 2$  nm) which allow guest molecules/ions to enter, disperse, and exchange. These properties also highlight its significance as modern adsorbents and detergents. In addition to this, tunable chemical compositions and acidic sites make zeolites a potential candidate for petrochemical industries, biomass conversion etc. Despite of, zeolites have two main drawbacks: it's hard to change their pore surface at the atomic level and their diffusion of big substrates is constrained. The invention of mesoporous silica in 1992 i.e., an ordered mesoporous material with larger pore size  $2 \text{ nm} < d < 50 \text{ nm}$  and more diverse chemical composition enlighten this research area with their promising applications in catalysis, sensing, electronic devices & drug delivery etc [7]. Still there is lack between these two microporous zeolites and mesoporous silica. Some crystalline porous materials such as metal organic frameworks (MOFs) and covalent organic frameworks (COFs) have been investigated as a new class of heterogeneous catalysts [8,9,10]. In contrast to conventional porous materials, MOFs and COFs have garnered substantial attention to the scientific community with their unique physicochemical properties.

Considerable progress has been made in both basic and applied fields by taking advantage of the special qualities of reticular materials. MOFs generally considered as organic-inorganic hybrid coordination polymers as it is an assembly of metal ions and organic linkers via directional chemical bonding. Whereas COFs considered as porous organic polymers as it is fabricated by covalent bonding of organic building blocks and mainly consists of light elements C, N, O etc. However, the limited thermal stability and absence of permanent porosity, restrict COFs from its wide applicability [11].

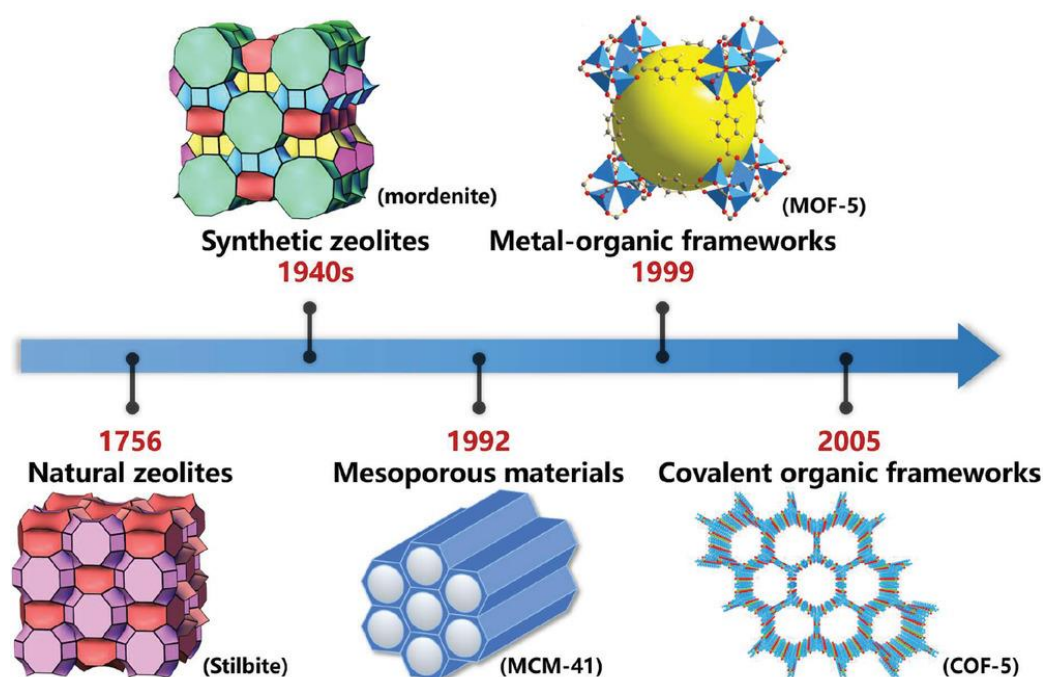


**Figure 1.1** Important turning points in the discovery of useful porous materials. Reprinted with permission from ref [5]. Copyright 2020 WILEY VCH.

### 1.3 Metal organic frameworks (MOFs)

Metal organic frameworks (MOFs) have been evolved as a new class of two- or three dimensional porous crystalline materials with infinite lattices, also known as porous coordination polymers (PCPs). MOFs are mainly fabricated by periodic arrangement of metal cation salts or clusters and polydentate organic ligands with directional coordination bond (Figure 1.2) [12-15].

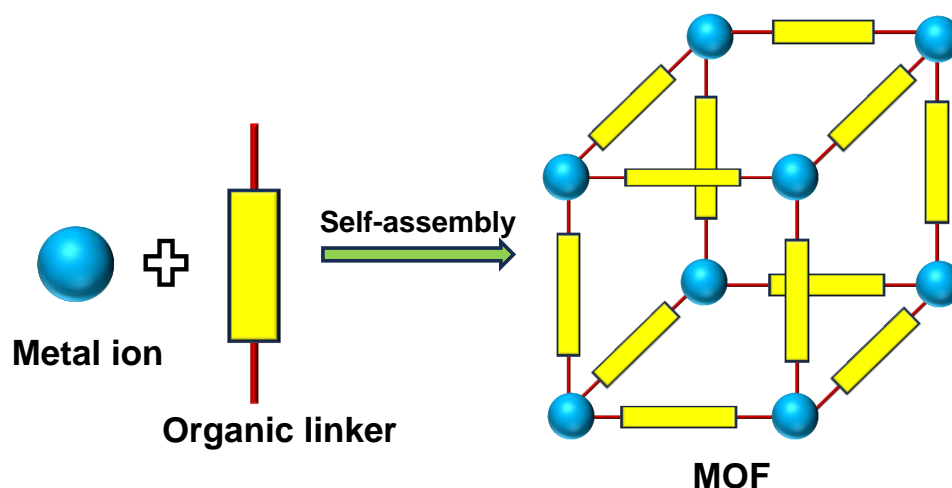


**Figure 1.2** Schematic representation of MOF through reticular chemistry i.e. linking metal ion and organic linker.

MOFs become an ideal platform for heterogeneous catalysis because of their ultrahigh, well-defined porosity, larger pore volume, and unprecedented tunability in chemical and structural property, synthetic versatility, and remarkable host-guest chemistry. Additionally, the presence of uncoordinated metal sites and easily accessible organic struts further contributes to their appeal [16]. In fact, every researcher working on catalytic engineering has these qualities at the top of their list of priorities. In 2002, Yaghi and his co-workers have shown how nicely one can control MOF's porosity and functionality by designing linkers (Figure 1.3) or metals (Figure 1.4) and make MOFs flexible as well as versatile to achieve targeted properties without altering the fundamental topology [17]. Thus MOFs can be able to fill the gap between micro and meso porous materials. Till now, According to BET analysis MOFs attributed surface area up to  $10,000 \text{ m}^2 \text{ g}^{-1}$  which is greater than Zeolites and activated carbon [18].

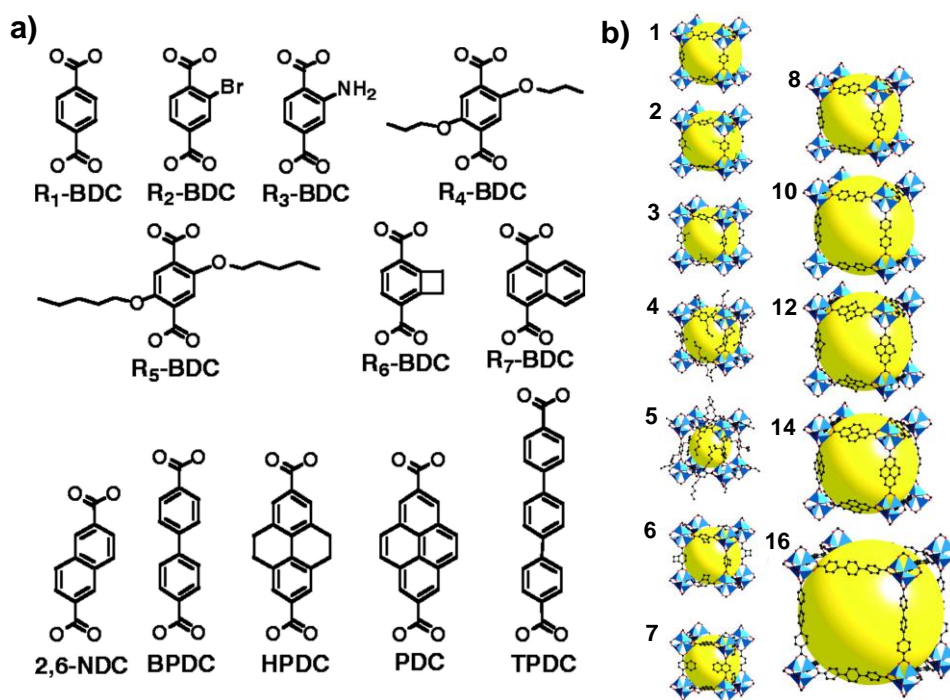


**Figure 1.3** a) Representative examples of series of linkers used for the synthesis of iso reticular MOFs IRMOF-n ( $n = 1-8, 10, 12, 14, 16$ ) where all possess same cubic topology but differ by organic linkers functionalization and its length b) their corresponding single X-ray structures. Reproduced with permission from ref [17]. Copyright 2002 Science.

Only by altering the organic linker portion several zinc-based MOFs, such as MOF-5, MOF-74, and MOF-177, were created with variable surface area and pore volume [19,20]. The imidazolate-based molecules that are commonly referred to as zeolitic imidazole frameworks (ZIFs) were added to the MOF family in 2002. MOF synthesis also plays a crucial role to create an extensive range of exquisite captivating structures. Establishing synthetic condition that will give specific MOF skeleton without the breakdown of the organic linker is the primary objective of MOF synthesis. At the same time, crystallization kinetics must be suitable to permit the nucleation and development of the required phase. Over time, a variety of techniques have been used for MOF synthesis. Solvothermal, or liquid phase/solvent phase approach, is the most utilized technique. Using this procedure, the ligand and metal precursor are individually dissolved in a specific liquid solvent that they can dissolve in. In a reaction vial, both these separate solutions

are combined. They are then moved to a Teflon-lined autoclave and heated in an oven for the appropriate amount of time and temperature. The Solvothermal technique of MOF synthesis is highly dependent on several variables, including temperature, pH, solvents, and the molar ratio of reactants, which affect how distinct MOF structures are formed and how they bind. Apart from the approach mentioned above, there are several techniques for synthesizing MOFs, which include the use of microwave assistance, sonication, mechanochemical processes, and electrochemical synthesis [21].

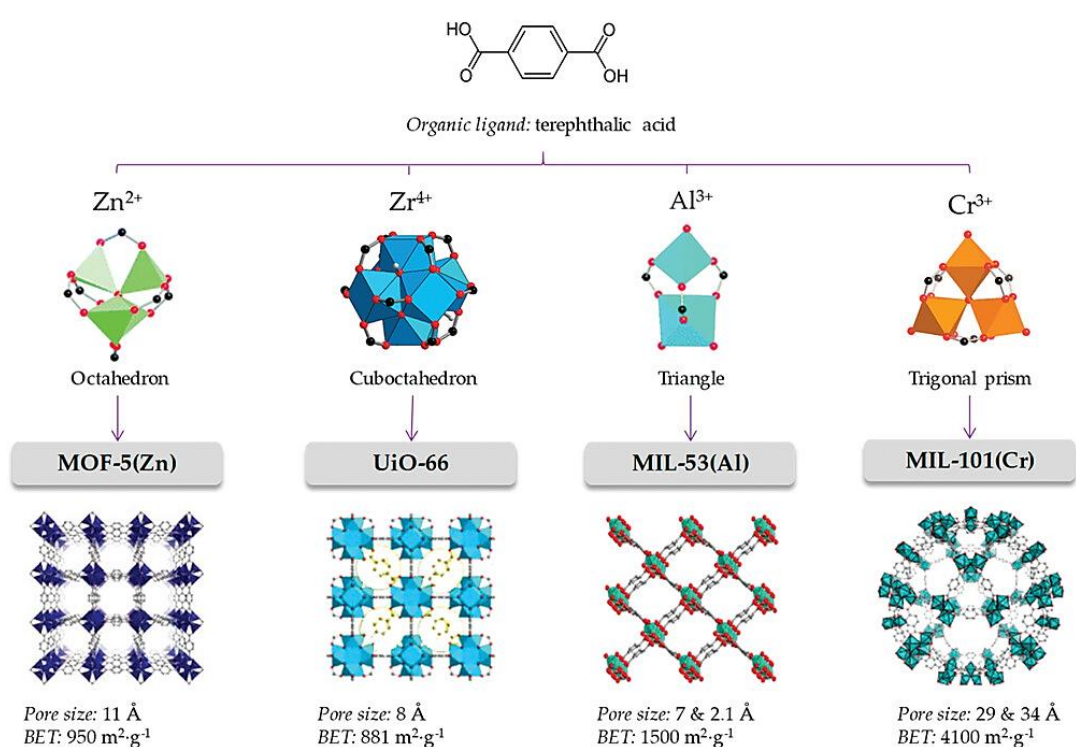


**Figure 1.4** Different types of MOF prepared by using same organic linker terephthalic acid but with different metals. Adopted with permission from ref [20]. Copyright 2019 MDPI.

Beyond the specific surface area, MOFs' thermal and chemical stability is also a crucial characteristic. When a MOF compound is heated to a reasonably high temperature, its thermal stability is typically characterized as its capacity to prevent irreversible changes in its physicochemical properties. Thermal stabilities are primarily determined by the inorganic and organic components, as well as the packing patterns and morphologies of

their structures. MOFs are mainly stable within the range of 350-500 °C [22]. When considering MOFs' applicability in diverse industries, their chemical stability is also a crucial factor. Depending on the application, MOFs are exposed to a range of chemical conditions when used for different purposes. The pH of mediums utilized are the primary factors influencing the chemical stability [23]. Sometimes MOF's application hampered because of their moisture sensitivity, moderate thermal and chemical stability. There are several applications of MOFs like in gas storage, CO<sub>2</sub> capture, separation & purification, food packaging, sensing, biomedicine, drug delivery, proton conduction, membrane, luminescence, environmental, wastewater treatment, energy conversion and storage, catalysis including thermal, electrochemical and photochemical etc. [24-26]. In figure 1.5, a brief outline of MOFs synthetic methods, its properties and application has been sketched.

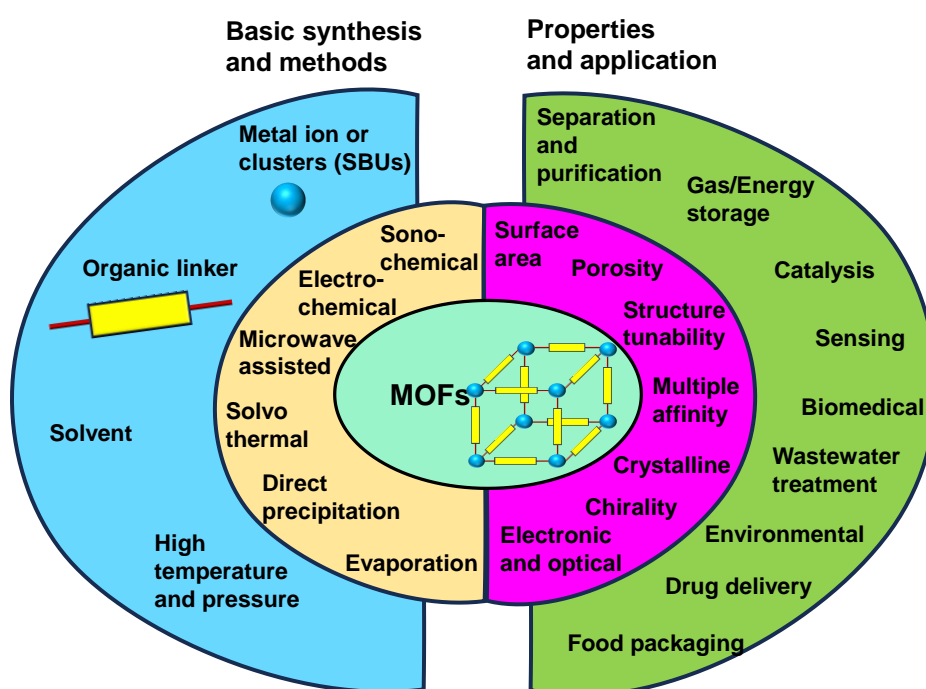


**Figure 1.5** Schematic diagram of synthetic methods, properties, and applications of MOF.



While MOFs have several excellent characteristics that make them a great option for investigation in a variety of applications, some constraints limit pristine MOF's effectiveness. As a result, researchers' focus has recently switched from pristine MOF to the field of functionalized MOFs called as "MOF composites" or "MOF derivatives" due to the significant attention they have received.

### 1.3.1 Design and strategies for functionalization of MOFs

One extremely practical and successful way to further enhance MOF performance or provide additional advantages for real-world applications is to integrate MOFs with various functional species. As depicted in figure 1.6, there are two ways for functionalization of MOFs. 1) MOFs can be functionalized through the modification of metal clusters, pore cavities, or organic linkers mainly known as MOF composites. [27] 2) Due to presence of metal and organic moiety, high temperature treatment converts MOFs into metal/nano porous carbon composites which mainly knows as MOF derivatives. [28]

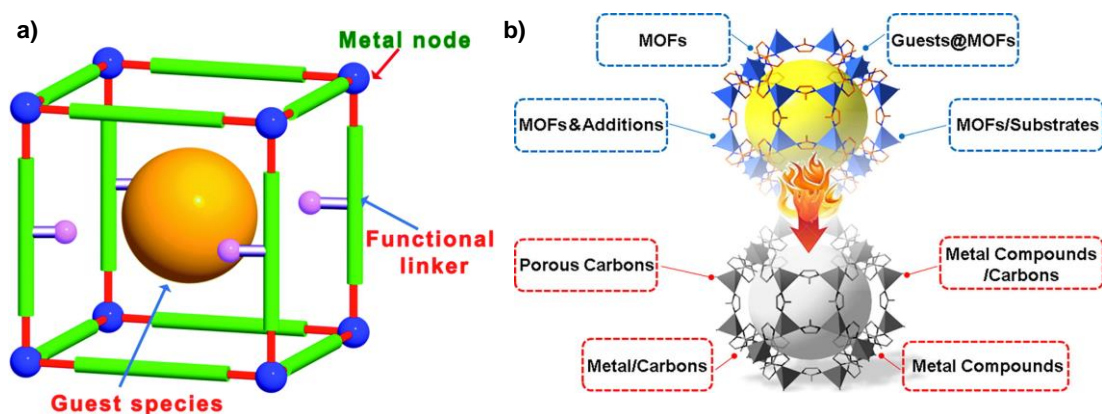


**Figure 1.6** a) Different types of active sites to fabricate functionalized MOF (MOF composites). Reprinted with permission from ref [27]. Copyright 2017 The Royal society of chemistry, b) Schematic illustration to show the strategy for fabrication of metal/carbon composites (MOF derivatives) from MOFs. Adopted with permission from ref [28]. Copyright 2018 Elsevier.

### 1.3.1.1 MOF composites or functional MOFs

MOF composites i.e. combination of MOF with other functional group have several advantages for heterogeneous catalysis over parent MOF as it can use both the properties of MOF and co-catalyst. This can be done either by direct assembly or post synthetic modifications. The synergistic effect between them positively endorses their catalytic potential with enhanced activity, selectivity, and stability. To make it simple, we have divided the active sites of MOF into following category:

**(i) Coordinatively unsaturated open metal sites:** - During initial synthesis of MOF, after successful establishment of coordination between metal and linker, solvent that was employed in the synthesis, fill the MOF pores and remaining metal coordination sites. Thus, the solvent mainly functions as a porogen to aid in the creation of the framework structure and as a ligand at the metal atoms to help them to attain their stable coordination number. Now, in order to create open metal sites in the MOF, solvent molecules need to be removed without altering the framework structure. Several methods and techniques have been proposed in the literature for this challenging task. The most popular method is solvent exchange and removal by thermal activation, where at first the high boiling or less volatile solvent (e.g., DMF) is exchanged by low boiling or more volatile liquid (e.g., ethanol, methanol etc.) and after that followed thermal activation i.e., heat treatment under high vacuum. Other methods include chemical activation and photothermal activation. Following creation, the open metal sites will function as a Lewis acid and be open to absorbing electron density from any potential donor molecule. Those open metal sites can be exchanged or further post functionalized by other active metal ions or by grafting some rich ligands which will further build a new binding site for chelation of some metal ions. Here we mentioned some examples like Ren et al. have developed a chiral MOF CMIL-101 by grafting chiral N-formyl proline derivatives to the open metal Cr sites

(Figure 1.7a) [29]. The above mentioned homogeneous chiral ligand was proved to be a good catalyst for the conversion of imines to amines by using trichlorosilane as hydrogen source. The confined environment of MOF attracts these homogeneous chiral ligands and provide a support to them to make it reusable and boost its activity as compared to its homogeneous counterparts by synergistic interaction. Similarly, Liu and his coworkers create a Cu open metal sites by treating Cu-BDC at high temperature under vacuum and then by agitating the ligand pyridyl-salicylimine (Py-SI) and activated Cu-bdc in dry toluene, they reported a composite Cu-BDC/Py-SI [30]. This composite was then mixed with a PdCl<sub>2</sub>, toluene, and DMF solution to get the final desired catalyst Pd@Cu-BDC/Py-SI for Suzuki coupling (Figure 1.7b).

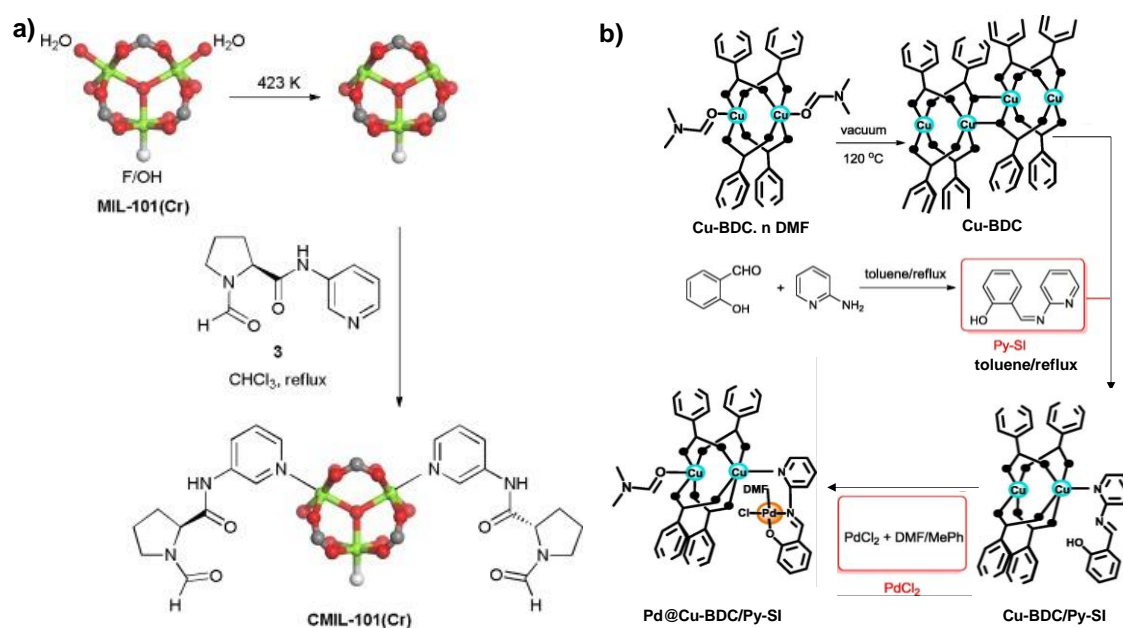


**Figure 1.7** Post synthetic modification of node by grafting ligand to the metal sites for MOF a) MIL-101 (Cr). Adopted with permission from ref [29]. Copyright 2018 Elsevier and b) Cu-BDC. Reprinted with permission from ref [30]. Copyright 2016 Elsevier.

**(ii) Hydroxide containing MOF nodes:** - Hydroxide-containing Secondary building units (SBUs) are found in several MOF structures based on high-valent hard metal centers, such as Ti<sup>4+</sup>, Zr<sup>4+</sup>, Hf<sup>4+</sup>, and Al<sup>3+</sup>, and they could serve as suitable mimics for metal oxide surfaces. These metal-oxo/hydroxo clusters offer new prospects for growing MOF

composites due to their structural variety, thermodynamic and chemical durability [31]. The main driving force for the formation of the metal oxo or hydroxo clusters are the higher Lewis acidity of high valent metal salts which makes them prone to hydrolyze during MOF synthesis. Based on the MOF synthetic conditions, the binding mode of oxo or hydroxo group also differ like some are present as terminal OH or OH<sub>2</sub> whereas some OH groups are present via bridging mode as  $\mu_2$ ,  $\mu_3$ , or  $\mu_4$  coordination. Fisher and coworkers used MIL-53(Al) which possess Al<sub>n</sub>( $\mu_2$ -OH)<sub>n</sub> 1D-chain SBUs. They treated MOF with organometallic complex 1,1'-ferrocenediyl-dimethylsilane. The strong Si-O bonds facilitated the ring opening reaction and graft ferrocene onto MOF SBUs (Figure 1.8a) [32]. Lin et al. have shown another approach for installation of metal on Zr node via deprotonation strategy. First, they have treated UiO-68 MOF containing Zr<sub>6</sub>( $\mu_3$ -O)<sub>4</sub>( $\mu_3$ -OH)<sub>4</sub> SBUs with strong base n-BuLi which abstract the proton from  $\mu_3$ -OH to afford highly nucleophilic ligand M<sub>x</sub>O<sup>-</sup>. This negatively charged ligand, after treatment with CoCl<sub>2</sub> salt form the SBU supported metal complex (Figure 1.8b) [33]. Recently solvothermal deposition of transition metal complexes on MOF SBUs emerged as a promising technique. Farha and his coworkers investigated this strategy not only for Zr/Hf hydroxides but also with other lanthanide actinide MOF SBUs and deposited V complexes. To enable metal deposition on MOF SBUs, solvothermal activation of metal complexes and SBU hydroxides encourages the hydrolysis process and the release of extra dangling ligands [34]. By utilizing a variety of metal precursors in solvothermal settings current research has effectively installed a wide range of distinct, well-defined metal-sites either mono- metal or bi metal on the NU-1000 nodes (Figure 1.8c) [35]. In 2016, Lin et al. have transformed MOF SBUs directly to metal hydrides by reacting Ce-BTC with LiCH<sub>2</sub>Si(CH<sub>3</sub>)<sub>3</sub> followed by HBpin to generate Ce(III)H-BTC (Figure 1.8d) [36].

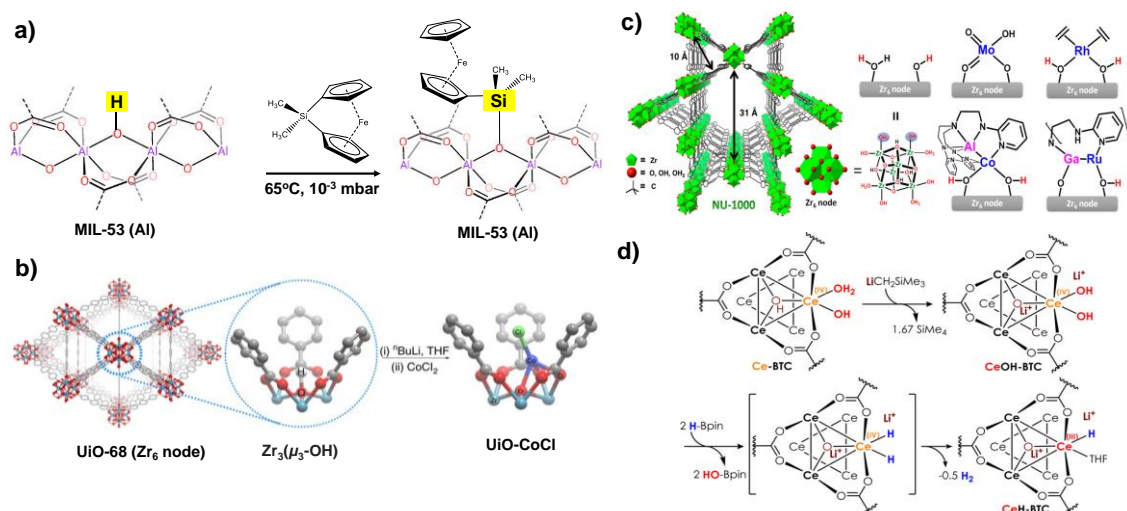


**Figure 1.8** Examples of post synthetic metalation of nodes: a) Reaction of bridging OH group between two Al center with 1,1'-ferrocenediyl-dimethylsilane. Reproduced with permission from ref [32]. Copyright 2009 American Chemical Society, b) post synthetic metalation of UiO-68 SBUs using  $\text{CoCl}_2$ . Reprinted with permission from ref [33]. Copyright 2016 Nature, c) Nonfunctionalized MOF, Zr-NU-1000, and its corresponding inorganic  $\text{Zr}_6$  nodes with the reactive  $-\text{OH}/\text{H}_2\text{O}$  terminal groups. Several representative metal binding motifs are also shown including  $\text{MoO}_x$ ,  $\text{Rh}(\text{C}_2\text{H}_4)_2$ ,  $\text{Co}-\text{Al}$  complex, and  $\text{Rh}-\text{Ga}$  complex synthesized by SIM strategy. Reprinted with permission from ref [35]. Copyright 2018 American Chemical Society. d) Activation of Ce-BTC to form CeH-BTC. Adopted with permission from ref [36]. Copyright 2016 American Chemical Society.

**(iii) Linker with functional group:** - Besides metal nodes, MOF contains organic linker (or extensive modification by covalent bonding with organic functional groups) which offer chelating sites mainly composed of heteroatoms (e.g., N, P, O) to graft targeted metal atoms and form MOF composites. Now, this can be done by two way one is first designing the linker and then prepare the MOF or first make the MOF and then functionalized its linker sustaining their characteristics. Kitagawa et al. have developed a novel synthetic approach to immobilize an unsaturated metal catalytic centers into the channel or pore of MOF using Schiff base linker [37]. First, they designed the desired ligand involving reaction between  $\text{N},\text{N}'$ -phenylene bis (salicylideneimine) dicarboxylic acid ( $\text{H}_4\text{salphdc}$ ) and transition metal ion  $\text{Cu}^{2+}$ ,  $\text{Ni}^{2+}$ ,  $\text{Co}^{2+}$  and then constructed the framework using Zn (II) connector (Figure 1.9a). Instead of direct synthesis of MOF with pre-

designed ligand, Li et al. have done post synthetic functionalization or metalation of MIL-101 (Cr) ligand to incorporate a  $\pi$  conjugated N,N, N chelating site like terpyridyl moiety employing click chemistry and metalated it with Ru salt (Figure 1.9b) [38]. Likewise, in lieu of the conventional solvothermal technique, Cohen et al. also have done post synthetic metalation of Zr (IV) based robust MOF manufactured by open bipyridine ligand with metal chelator property (Figure 1.9c) [39]. Furthermore, Fei and his co-workers established two fundamentally distinct postsynthetic strategies—postsynthetic deprotection (PSD) and postsynthetic exchange (PSE) to generate an isolated metal-monocatecholato moiety in a very robust metal-organic framework (MOF) (Figure 1.9d) [40]. Thus several homogeneous metal complexes with defined active sites enduringly fastened on the ligands and prevent the molecular dissociation or agglomeration in reaction media as MOF backbone decorated isolated individual catalytic sites in a particular fashion.

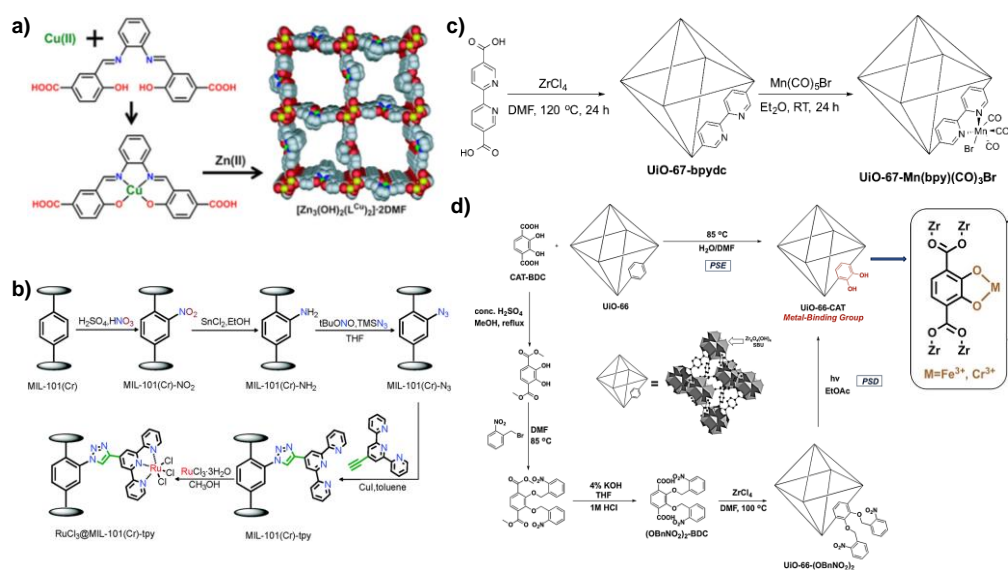


**Figure 1.9** Examples of linker functionalization: a) Schematic description of immobilizing metallosalen linkers into a Zn-MOF and crystal structure viewed along the c-axis (Cu, green; Zn, yellow; C, gray; O, red; N, blue). Reprinted with permission from ref [37]. Copyright 2004 Wiley-VCH, b) Schematic representation of the post-synthesis modification of MIL-101(Cr) and the synthesis of a single-site heterogeneous Ru (III) catalyst. Adopted with permission from ref [38]. Copyright 2015 The Royal Society of Chemistry, c) Synthetic procedure for grafting Mn bipyridine complex  $Mn(bpydc)(CO)_3Br$  to UiO-67 MOF. Adopted with permission from ref [39]. Copyright 2015 American Chemical Society, d) Schematic illustration for grafting mono-

catecholato metal complexes into UiO-66 MOF. Reproduced with permission from ref [40]. Copyright 2014 American Chemical Society.

**(iv) Pore of MOF:** - Some well-known efficient homogenous catalysts include metal or metal oxide nanoparticles, polyoxometalates, and metal complexes suffer due to their greater solubility in protic and aprotic solvents. Researchers were compelled to look for a good support with a strong interaction between them to improve the stability of the catalyst during reaction conditions. Owing to the inherent structure of MOF and its porosity, the problem associated with those homogeneous catalysts has been resolved to some extent. MOFs with linked three-dimensional zeotypic cavities that are accessible through tiny pore windows emerged as a promising host for nucleation and growth like metal precursors enter the cavities through the tiny windows, but after reduction they stop MNPs from escaping or clumping together from the cavities because of the windows' size restrictions. Several approaches have been established for the synthesis of guest@MOF composites such as “Ship in a bottle” which mainly involves CVD, solid grinding, solution impregnation, double solvent approach, one pot synthesis [41-45]. Other methods are “bottle around ship”, colloidal deposition, thermal decomposition, spray drying etc [46-48]. Here we have mentioned some examples of guest/MOF composites. Aijaz et al. for the very first-time developed synthesis of size-controlled and well-dispersed MNPs within a MOF's pores using double solvent approach. n-Hexane served as a hydrophobic solvent in the suspension of activated MIL-101(Cr) (Figure 1.10a). Following sonication, dropwise addition of the  $H_2PtCl_6$  aqueous solution was made while stirring continuously. Well-distributed Pt nanoparticles with an average size of 1.8 nm were found inside the pores following the reduction with  $H_2$  [49]. Huo and his coworkers tailored nanoarchitecture of ZIF-8 involving controlled encapsulation strategy. They have incorporated pre synthesized surfactant capped nanoparticles into the MOF pore. This method provides a promising approach to control the spatial distribution of one or

more nanoparticles, particle size & shape within the cavity (Figure 1.10b). By this way reduction of agglomeration of nanoparticles or complete confinement within MOF cavity can be achieved [50]. But in this “templated synthesis” method complete removal of surfactants like PVP or CTAB is very challenging which sometimes hinders or block the nanoparticles to access. So, Li et al. used sacrificial template synthesis by coating  $\text{Cu}_2\text{O}$  nanoparticle with a removable template shell  $\text{SiO}_2$  (Figure 1.10c) [51]. Eddaoudi et al. and also Cheng et al. reported the insitu encapsulation strategy to fit a large cationic metalloporphyrin or dimer homogeneous complex into MOF cage [52,53]. Thus to impart functionality various MOF composites have been established.

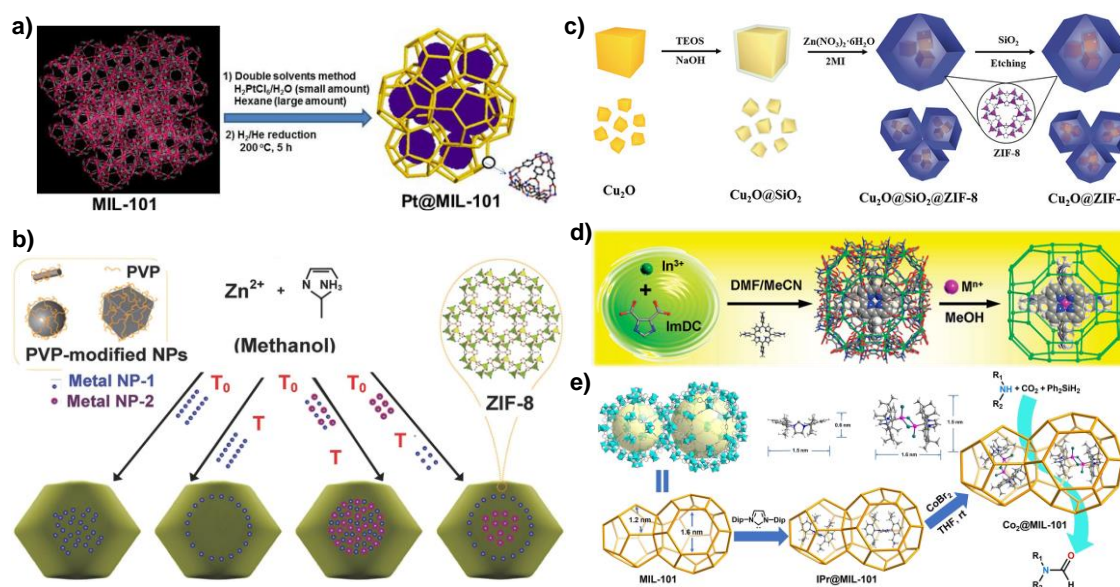


**Figure 1.10** Examples for pore functionalization: a) Encapsulation of Pt nanoparticles into MIL-101 by DSM method. Adopted with permission from ref [49]. Copyright 2012 American Chemical Society, b) Incorporation of size-controlled metal nanoparticles into ZIF-8 pore. Reprinted with permission from ref [50]. Copyright 2012 Nature, c) Silica template protection assisted method for encapsulation of  $\text{Cu}_2\text{O}$  nanoparticles into ZIF-8 cavity. Reproduced with permission from ref [51]. Copyright 2018 WILEY VCH. d) Schematic representation of formation of rho-ZMOF with encapsulation of porphyrin ring ( $\text{H}_2\text{TMPyP}$ ) $^{4+}$  and  $\text{Mn}^+$  ( $\text{Mn}^+ = \text{Mn}, \text{Co}, \text{Cu}, \text{Zn}$ ). Reprinted with permission from Ref [52]. Copyright 2008 American Chemical society, e) Ligand in dimer strategy for encapsulation of  $\text{Co}(\text{IPr})\text{Br}_2(\mu\text{-Br})_2$  ( $\text{Co}_2$ ) into MOF cage. Adopted with permission from ref [53]. Copyright 2022 WILEY VCH.



### 1.3.1.2 MOF derivatives

MOFs have demonstrated as an extensively promising candidate, particularly in catalysis, thanks to their well-defined crystalline structures, tunable pore topology, ultrahigh surface areas, and outstanding tailorability [54-56]. Nevertheless, in some cases, the instability particularly moisture sensitivity and poor electronic conductivity restricts the practical applicability of MOFs [57]. Additionally, one of the most significant issues that heterogeneous catalysis is facing tremendously is creating materials with consistent and precise active sites that provide excellent selectivity and avoid deactivation. Therefore, catalyst research presently uses a combination of computational techniques to forecast the catalyst activity and innovative synthesis processes to create the appropriate structure. However, the path from designing material to real catalyst is very strenuous. For example, in the case of nanoparticle-based catalysis, getting higher metal loadings, maximum metal atom utilization, specific particle size and shape while preventing nanoparticles' inclination to expand into larger crystallites with time via sintering is a difficult task. In this regard, controlled decomposition of MOFs breaks new ground. Merely applying post-treatments, usually pyrolysis or chemical treatment, MOF can be transformed into materials that are significantly more stable and possess distinct benefits over traditional nanoporous materials (Figure 1.6b). In 2008, Xu et al. first ever discovered MOF derived porous carbon with greater surface area [58]. Through the careful adjustment of MOF precursors' size, morphology, structure, and elements, as well as the intentional manipulation of the conversion process, MOF derivatives have been found with a variety of compositions (e.g, porous carbons, metal nanoparticles or single atom/carbons, metal compounds like metal oxide, hydroxide, phosphide, chalcogenides, carbides/carbons hybrid or only metal compounds) [59-61] and structures (porous, yolk-shell, hollow, frame, hierarchical, etc.) [62-64] ranging from zero to three dimensions. In addition to this

majority of synthetic techniques for creating nanoarchitectures from MOF precursors entail morphology-preserved transformations and a templating strategy. These MOF-templated techniques fall into two categories in this regard: self-templating and external-templating techniques. MOF-only precursors are pyrolyzed in the self-templating approach, while MOF composites containing external templates such as graphene, silica, carbon, and metal oxides are used in the external-templating method [65]. Furthermore, a variety of surface/interface regulation techniques, consists of support interaction, defect/doping, surface modification, heterostructure etc. have been flourished for satisfying the need for certain electrocatalytic applications [66-68]. Several numbers of publications are there showcasing different kind of MOF derivatives. Here we have summarized a few of them. Parameters during carbonization namely temperature, heating rate, time and gaseous environment significantly contribute for the nanoengineering of MOF derivatives. Chen and his co-workers have shown the formation of Fe<sub>3</sub>C at carbon nanotube from melamine loaded Fe-MIL-88B. They have observed that temperature plays a crucial role in deciding the final product's morphology, composition, or specific surface area. With rising the temperature from 700 °C to 900 °C, the as formed Nitrogen doped carbon layer (NCL) progressively coiled into N-doped carbon nanotubes (NCNTs). Basically, annealing at 800 °C, formed Fe<sub>3</sub>C metallic compounds which started catalyzing the nano bands to convert into NCNTs (Figure 1.11a) [69]. Pyrolysis can be performed under different gaseous environments like Ar, N<sub>2</sub> air or O<sub>2</sub>, H<sub>2</sub> etc. which also govern to regulate or tune the structure and composition of MOF derived materials. It can be done in two ways i.e., one step calcination with a single gas or multi step calcination with defined gas at each step. Yang et al investigated that even under different gaseous environment like CO, O<sub>2</sub>, H<sub>2</sub> and Ar, Cu-BTC retained its octahedral geometry only the modulation occurred in its surface state and composition. In presence of reaction gases CO or O<sub>2</sub> mostly

the  $\text{Cu}_2\text{O}$  and  $\text{CuO}$  formed while with reducing  $\text{H}_2$  gas they got  $\text{Cu}$  nanoparticles. Calcination under inert gas  $\text{Ar}$  exactly maintained the structural geometry of parent MOF nicely (Figure 1.11b) [70]. Particle size of MOF derivatives and degree of graphitization of carbon components sincerely induced by heating rate. Though MOF is a suitable precursor to get metal-based carbon catalysts by pyrolysis still it has been observed that generation of ultrasmall size nanoparticles with higher metal loading is very hard to achieve specially for non-Nobel metal. In most of the cases after pyrolysis acid etching step often followed to get rid of coarsening caused by nanoparticles, but it reduces the metal loading significantly. Tian and his co-workers proposed a unique method i.e., pulse joule heating which mainly involve rapid pyrolysis such as  $1000\text{ }^\circ\text{C}$  within  $0.3\text{ s}$  to balance both the property ultrasmall size metal particles with greater loading. This technique complies with LaMer model which suggests that rapid pyrolysis only allows the nucleation but prevents Ostwald ripening (Figure 1.11c) [71]. Along with the above-described parameters pyrolysis time also significantly participated for designing or tuning the physical properties of MOF derivatives. A range of  $\text{Co}_x\text{S}_y$  catalysts were produced by Sun et al. using in-situ sulfidation and phase control techniques. After heating at  $700\text{ }^\circ\text{C}$  for one hour in  $\text{Ar}$ , pure  $\text{CoS}_{1.097}$  was produced. However, if the calcination period was increased to two hours, the sublimation of sulfur at a high temperature resulted in the creation of the  $\text{Co}_9\text{S}_8/\text{CoS}_{1.097}$  composite. In addition, the high-temperature generation of  $\text{H}_2\text{S}$  from the interaction between  $\text{H}_2$  and sulfur reduced the product's  $\text{S}$  concentration even more. Consequently, monotype  $\text{Co}_9\text{S}_8$  was produced after two hours of calcination in  $\text{H}_2/\text{Ar}$  environment (Figure 1.11d) [72].

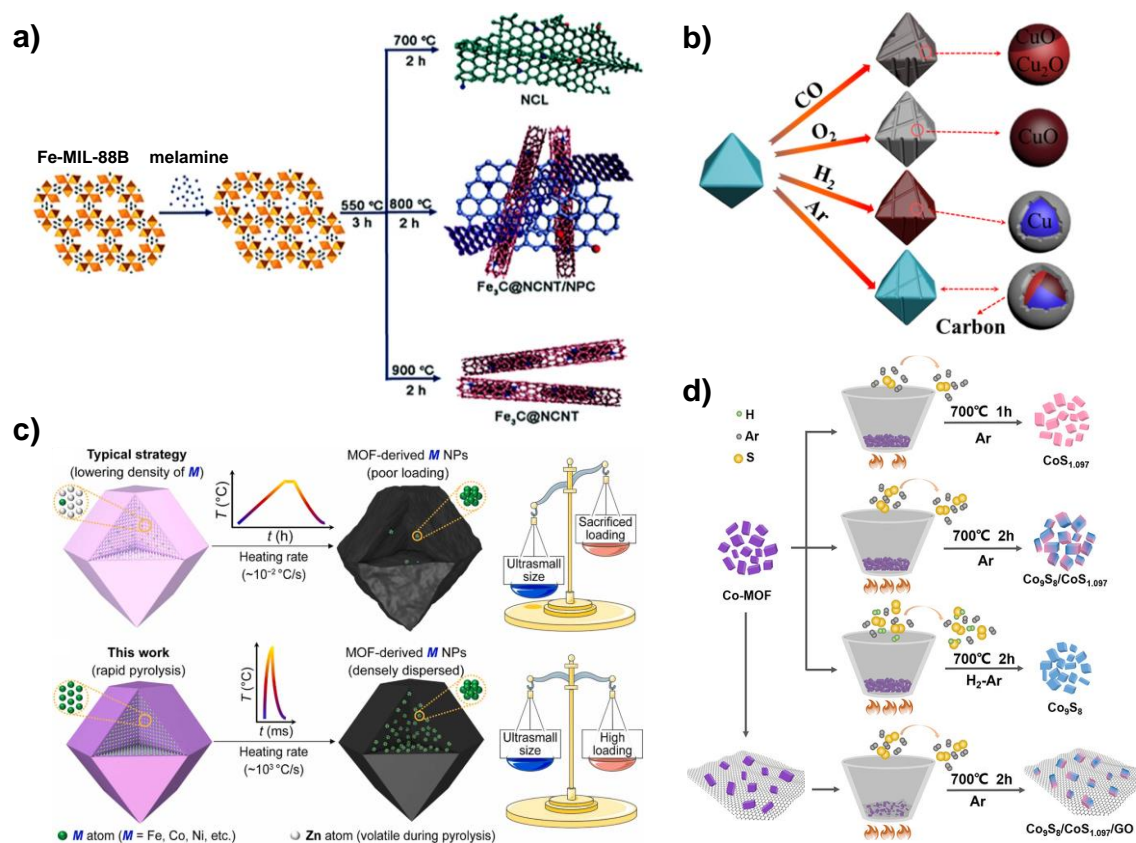


**Figure 1.11** a) Temperature induced morphology-controlled synthesis of Fe<sub>3</sub>C@NCNT from MOF. Adopted with permission from ref [69]. Copyright 2016 The Royal Society of Chemistry, b) Diagram illustrating the structural alterations of Cu-BTC calcined in various atmospheres, Reproduced with permission from ref [70]. Copyright 2018 Elsevier, c) Effect of heating rate during pyrolysis for synthesizing ultrasmall NPs with high loading. Reprinted with permission from ref [71]. Copyright 2022 Elsevier, d) Procedures for fabrication of different composition of Co<sub>x</sub>S<sub>y</sub> nanostructures. Adopted with permission from ref [72]. Copyright 2018 WILEY VCH.

Along with carbonization conditions chemical composition of starting MOF precursor or chemical treatment during pyrolysis played a major role in determining the final structure and composition of MOF derivatives. Tang et al. developed a core-shell carbon nanostructure, where core is N-doped carbon and shell consist of highly graphitic carbon, utilizing a pre-designed core shell MOF made of two isostructural unit ZIF67 and ZIF-8. This work exhibits the simultaneous production of graphitic carbon catalyzed by transition metals and doping of N from N-containing imidazole linkers (Figure 1.12a) [73]. Xu and his co-workers describe a self-templated, catalyst-free method for thermally transforming rod-shaped metal-organic frameworks into one-dimensional carbon nanorods

while preserving their morphology. After the formation of carbon nanorods, they can be chemically activated and sonochemically treated to create two to six-layered graphene nanoribbons (Figure 1.12b). Because of the remarkable electrical, mechanical, and thermal properties, 1D or 2D nanostructured carbons are receiving a lot of interest. These qualities could lead to several significant potential applications [74].

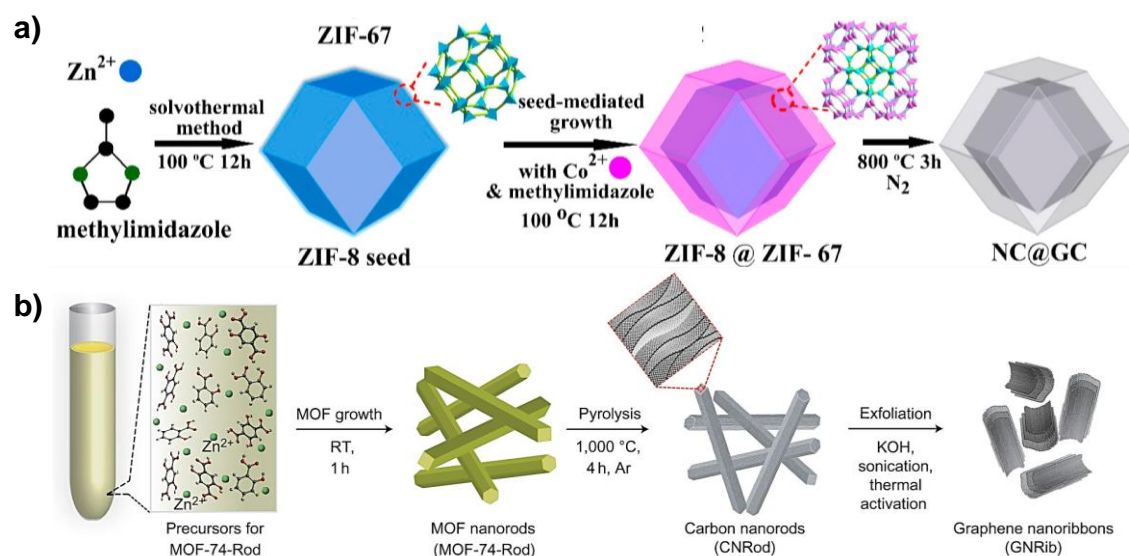


**Figure 1.12** a) Schematic illustration for the designing of core shell ZIF-8@ZIF-67 crystals and conversion into NC@GC upon further calcination. Reprinted with permission from ref [73]. Copyright 2015 American Chemical Society, b) Synthetic procedure to fabricate carbon nanorods and graphene nanoribbons from MOF-74. Reproduced with permission from ref [74]. Copyright 2016 Nature.

However, it can occasionally be challenging to adjust the MOF precursors' composition, particularly the metal centers, to create intended functional materials. Introducing guests carrying metal into the pore channels of MOFs is more practical and adaptable approach. Lou et al. incorporate Mo containing polyoxometalate which upon calcination under inert gas and etching turned into molybdenum carbide (MoC<sub>x</sub>) with retention of octahedral geometry (Figure 1.13a) [75]. Zhuang et al. have devised a dispersing-etching-holing technique for creating a 3D open nano-netcage of RuIrO<sub>x</sub> from ZIF-8. The present methodology involved the dispersion of Ru<sup>3+</sup>/Ir<sup>4+</sup> metals in ZIF-8 to facilitate their exchange with Zn<sup>2+</sup>. The hydrolysis of these sources during the solvothermal reaction resulted in

the etching of the internal ZIF-8 core. RuIrZnO<sub>x</sub> hollow nano boxes were formed by subsequent annealing, and ultimately, by removal of ZnO followed by in-situ electrochemical etching named as hoiling yielded RuIrO<sub>x</sub> with open netcage structure. Such morphology can afford an effective-surface-area ratio much greater than the nanoparticle structure and contributing to greatly increase atomic usage of Ru/Ir noble metals (Figure 1.13b) [76]. In industrial processes, metal nanostructures on a support, are the most commonly utilized as heterogeneous catalyst. The size of the metals plays a major role in determining the catalysts' performance because the specific activity per metal atom typically increases with decreasing particle size. However, when particle size decreases, metals' surface free energy rises substantially, encouraging the aggregation of tiny clusters. A strategy that has been employed by industry for a long time to fabricate stable, finely dispersed metal clusters with high catalytic activity is choosing a support system that will firmly interacts with the metal species to avoid this agglomeration. Single-atom catalysts (SACs), which have individual metal atoms scattered across supports, represent the very small limit of metal particle sizes. As metal ions are the main component and are atomically distributed across MOF structures, MOF is a perfect precursor for building SACs by the reduction of metal ions. One of the best precursors for creating SACs through one-step pyrolysis of mixed metal MOF is the Zn-based zeolitic imidazolate framework-8 (ZIF-8), a subclass of MOF with a high concentration of N dopants in the organic ligands. By direct pyrolysis of Zn/Co bimetallic MOF precursors, Li et al. established a unique method to create Co SACs. A Zn/Co bimetallic MOF with homogeneous distribution of Zn and Co ions was first constructed, in which a specific percentage of Zn<sup>2+</sup> were substituted by Co<sup>2+</sup> sites. This was done because of the comparable coordination of Co<sup>2+</sup> and Zn<sup>2+</sup> with 2-methylimidazole ligands. The Zn<sup>2+</sup> ion acts as a barrier to increase the spacing between neighboring Co atoms in space. The low boiling point of Zn (907 °C) allows

for the selective evaporation at temperatures above 800 °C, leaving the isolated Co atoms associated with nanocarbon support generated from MOF (Figure 1.13c) [77].

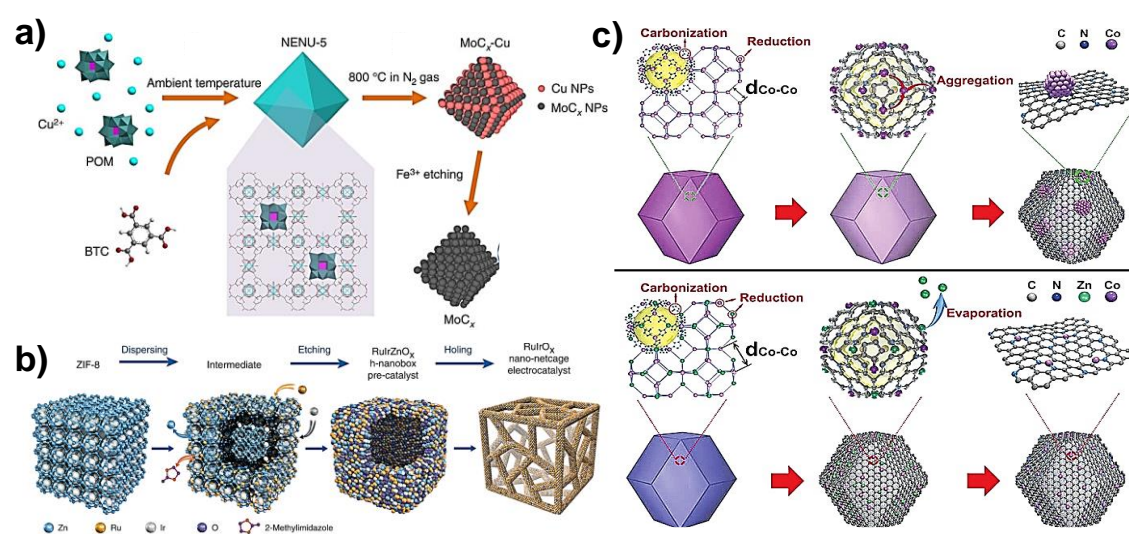


**Figure 1.13** a) Diagram illustrating the steps involved in creating porous MoC<sub>x</sub> nano-octahedrons. Adopted with permission from ref [75]. Copyright 2014 Nature, b) Schematic representation for synthesizing RuIrO<sub>x</sub> open nano net cage structures. Reproduced with permission from ref [76]. Copyright 2019 Nature, c) Synthetic scheme for the formation of Co NPs-N/C (top) and Co SAs/N-C (bottom). Reproduced with permission from ref [77]. Copyright 2016 WILEY VCH.

Instead of direct carbonization of MOF, some external templating method such as silica or polymers also have been elucidated to get more hierarchical porous nanostructured. In 2016, Zhang et al. explored a mesoporous silica protected calcination strategy for synthesizing a hierarchically porous N-doped carbon with atomically dispersed Co atoms. They have uniformly coated Zn, Co bimetallic ZIF with silica shell and calcined it at high temperature under N<sub>2</sub> atmosphere. After carbonization and etching of surface with hydrofluoric acid (HF) they got Co,N-CNF which exhibited greater mesoporous nature as compared to without silica coated N-doped carbon (Figure 1.14a). In order to prevent unwanted particle aggregation during the pyrolysis process and produce MOF-derived carbon materials with a hierarchical pore structure, the mSiO<sub>2</sub> shell is therefore essential [78]. Another unique external templating method was explored by Li et al. to fabricate Fe single atom supported on N, S, P co-doped hollow carbon polyhedra. They have

coated MOF with a polymer. The polymer-based coating makes it easier to manufacture hollow structures through the use of the Kirkendall effect and electronic manipulation of an active metal core through long-range interaction with phosphorus and sulfur (Figure 1.14b) [79].

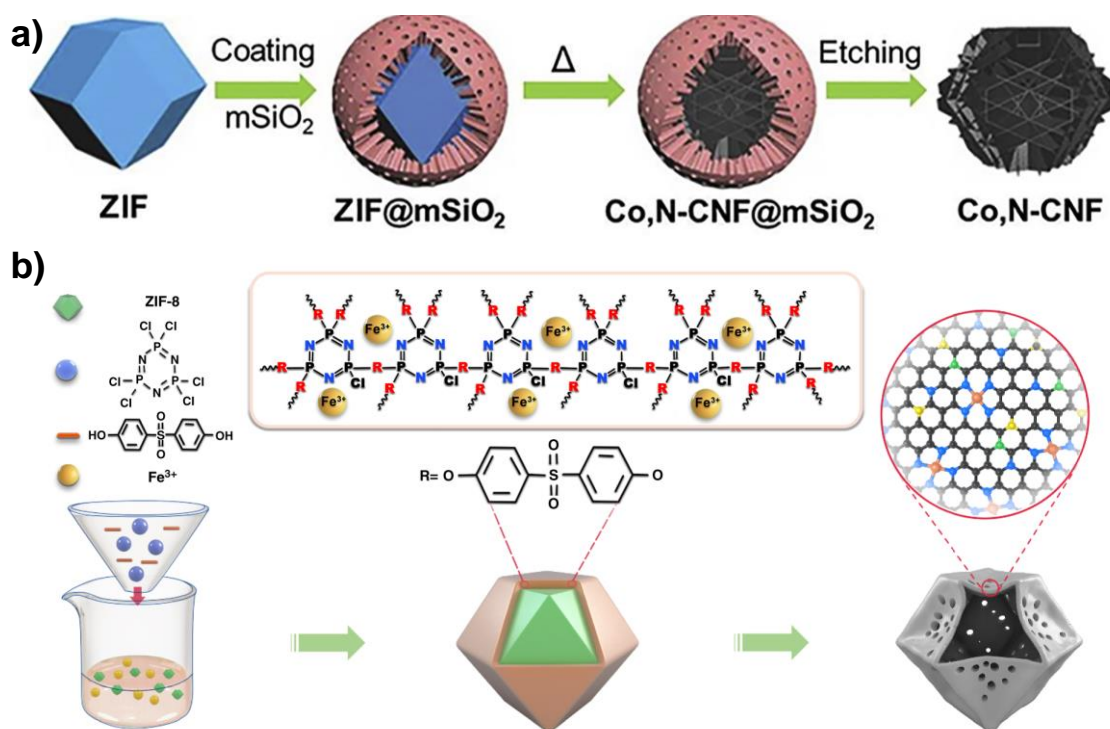


**Figure 1.14** a) Co,N-CNF synthetic process using the  $m\text{SiO}_2$ -protected calcination approach. Reproduced with permission from ref [78]. Copyright 2016 WILEY VCH, b) Process diagram for preparing Fe SACs supported on a hollow carbon polyhedron codoped with phosphorus, sulfur, and nitrogen (Fe-SAs/NPS-HC). Reprinted with permission from ref [79]. Copyright 2018 Nature.



## 1.4 Catalytic applications of MOF composites and MOF derivatives

MOF composites and MOF derivatives both evolved as promising candidates of interest for heterogeneous catalysis. Here we have divided the catalytic reactions into two: one organic transformation reactions and another is electrochemical reactions.

### 1.4.1 Catalysis for organic transformation

As manufacturing prices rise and synthesis approaches become more labor-intensive, numerous researchers have been performing excellent trials using MOF composites as solid catalysts for sustainable environments and economic gains in the fine chemical and pharmaceutical industries [80,81]. Here we shed light on the vital roles that different MOF composites play in the simple organic synthesis. Manna et al. reported a prosperous and facile approach for the grafting of a salicylaldehyde Co(II) catalyst onto the linker of UiO-68 NH<sub>2</sub>. The catalyst showed exceptional activity as well as selectivity for the conversion of nitro group to amine using phenylsilane reducing agent under mild reaction conditions. They also have tested the tolerance of catalyst for wide range of organic compounds containing different electrophilic and nucleophilic moiety including easily reducible functional groups. But the catalyst exhibited no discernible reduction in activity and selectivity even after recycling and reuse for a minimum of 14 times (Figure 1.15 a) [82]. Elumalai and his colleagues tethered N,N type bipyridine ligand or other N,O bidentate ligand to UiO-66-N<sub>3</sub> following azide alkyne cycloaddition reaction. Further they integrated the ligand incorporated MOF with nickel chloride and triphenylphosphine additives which manifested good catalytic activity and recyclability for the Suzuki–Miyaura cross-coupling reaction (Figure 1.15b) [83]. Hupp, Farha and his group investigate the deposition of molybdenum (VI) oxide solvothermally on a Zr<sub>6</sub> node of MOF Nu-1000 (Mo-SIM). Oxomolybdenum is well known homogeneous catalyst as it has shown excellent conversion and selectivity when it comes to the synthesis of epoxides. But

according to reported literature  $\mu$ -oxo oligomerization generally caused deactivation of these catalysts. Using a support such as silica or alumina inhibits the surface deactivation to some extent. Stability is a difficult issue that has not yet been fully overcome because the active species frequently leaks out of the support. However, Mo-SIM have demonstrated remarkable activity for cyclohexene oxide and the ring-opened 1,2-cyclohexanediol and suppress the leaching problem as molybdenum was not found in the reaction mixture before and after catalysis (Figure 1.15c) [84]. Jiang et al. demonstrated the catalytic activity of monometallic Pd NPs as well as bi-metallic PdAg NPs (~1.5 nm) immobilized into MIL-101 for synthesizing secondary arylamines involving hydrogenation of nitrobenzene and reductive amination of benzaldehyde simultaneously. The resulting catalyst PdAg@MIL-101 become a potential candidate in terms of activity and selectivity for this one pot tandem reactions under mild environment due to the host-guest interaction or synergistic interaction of bimetallic NPs. They have shown that each component plays their role like Ag significantly enhance selectivity to the desired product, Pd provides hydrogenation activity, and MIL-101 provides Lewis acidity (Figure 1.15d) [85]. Thus The development of MOF composites has brought the prospect of their implementation as solid catalysts in industrial settings one step closer to reality.

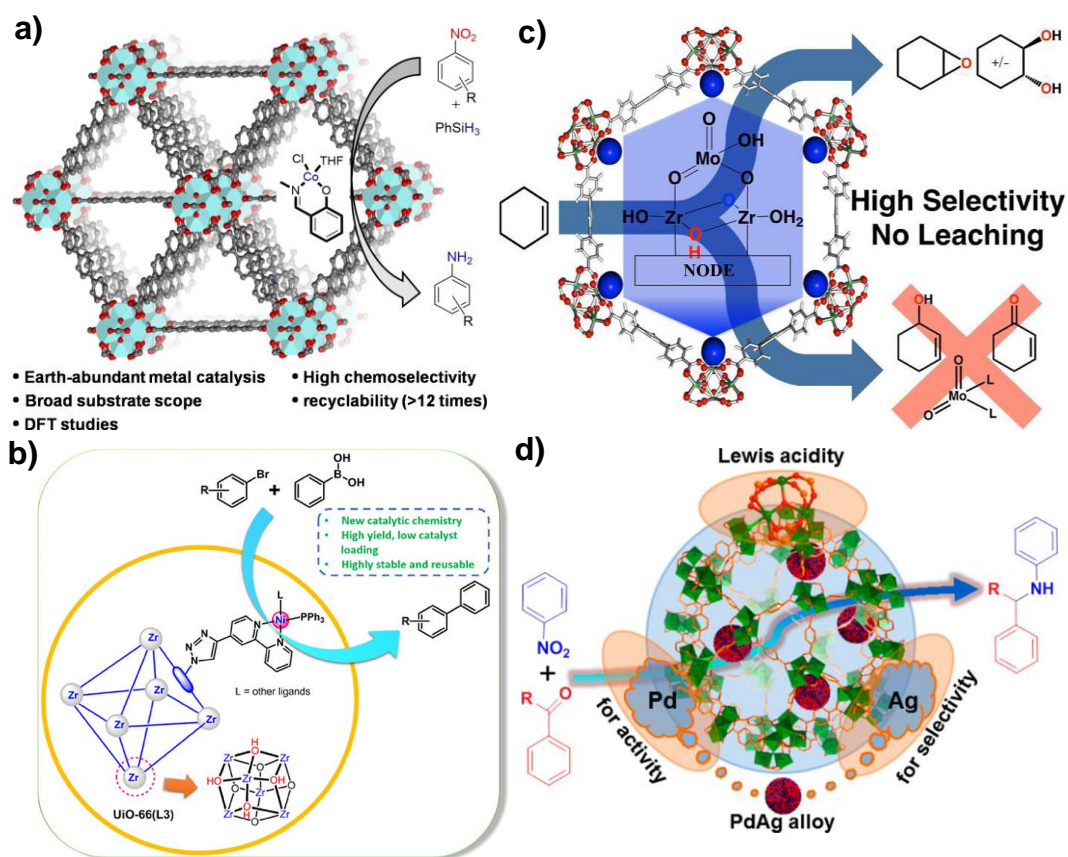


**Figure 1.15** a) Schematic illustration of salicylaldimine-Cobalt(II) complex supported by a Zr-MOF for selective reduction of Nitro group by organosilanes. Adopted with permission from ref [82]. Copyright 2023 WILEY VCH, b) Schematic representation of UiO-66(L<sub>3</sub>)-Ni-Catalyst for Suzuki-Miyaura cross-coupling reaction. Reprinted with permission from ref [83]. 2018 American Chemical Society, c) Molybdenum (VI) oxide catalyst supported by Zr<sub>6</sub> node of Nu-1000 MOF used for Cyclohexene Epoxidation. Adopted with permission from ref [84]. Copyright 2016 American Chemical Society, d) Schematic graphic depicting the one pot cascade reactions over PdAg@MIL-101. Reproduced with permission from ref [85]. Copyright 2015 American Chemical Society.

## 1.4.2 Electrocatalysis

Clean energy conversion relies heavily on electrocatalysis, which greatly advances the development of upcoming sustainable technology [86]. Growing amounts of the overall energy consumed by human society are coming from renewable energy sources, such as wind and solar power. Because of the erratic and sporadic power output of these energy sources electrochemical energy conversion and storage technologies (EESC), such as fuel cells, electrochemical capacitors, electrolyzers, rechargeable batteries, redox flow batteries embellish promising approach for effective and sustainable energy use [87,88].

For instance, produced electricity by wind and solar power can be effectively stored in electrochemical capacitors, rechargeable batteries, redox flow batteries and simultaneously released when needed or and transformed into fuels via electrolyzers and fuel cells [89]. These EESC devices have the same basic functional elements despite having different operating principles: an electrolyte that completes the electric circuit by allowing the transport of ions and blocking electronic conduction, and two electrodes (the cathode and anode), where major electrochemical reactions occur. The performance of devices is essentially determined by the physical (such as electrical and ionic conductivity) and electrochemical (such as redox capability or kinetics, electrode potential etc.) characteristics of the functional materials utilized in these components. High specific capacity and long-lasting improved electrodes are particularly desired in energy storage systems where as high activity, stable, and selective functional electrocatalysts are desperately needed for the cutting edge energy conversion systems. So, for the advancement of these EESC technology researchers mostly focused on the search for superior materials which may show maximum efficiency with minimum overpotential. MOF derivatives have extensively explored in this direction due to its outstanding properties [90,91]. Here we sketched an outline explaining the properties of MOF derivatives for electrocatalytic reactions (Figure 1.16).

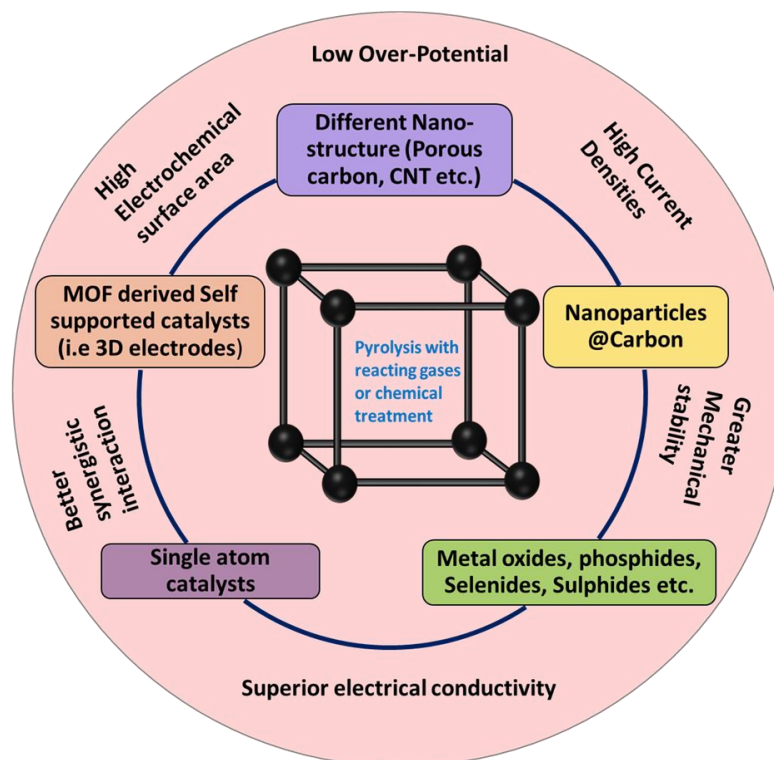


**Figure 1.16** Schematic representation of various MOF derived nanostructures and their electrochemical properties.

## 1.4.2.1 Energy conversion technology

### 1.4.2.1.1 Electrocatalytic water splitting

In order to generate hydrogen from renewable energy sources and move toward a carbon-neutral future, electrochemical water splitting has been proposed as an effective and environmentally friendly method. Two half reactions associated with it: oxygen evolution reaction (OER) at anode and hydrogen evolution reaction (HER) at cathode (Figure 1.17). Pt/C, Ir/RuO<sub>2</sub> are the benchmark catalysts for HER and OER respectively [92]. Ideally, for occurring water splitting in an electrolyzer needs a thermodynamic Gibbs free energy value of  $\sim 237 \text{ kJmol}^{-1}$  which corresponds to standard potential of 1.23 V (vs RHE) [93].

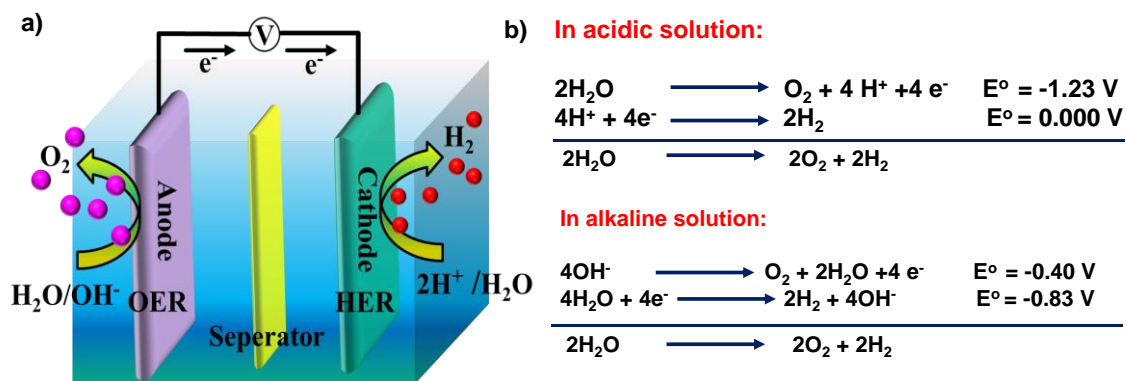


**Figure 1.17** a) Diagram illustrating an electrochemical set up for overall water splitting reactions, b) details of HER and OER reaction in acidic and alkaline medium.

However, scalable application of electro-chemical water splitting is limited because of high activation energy barriers, requiring additional energy to derive these non-spontaneous HER/OER redox reactions [94]. Electrocatalysts need to be applied to fabricate the electrodes to lower the required activation energies resulting in whole process more energy-efficient [95]. Precious-metal-based catalysts have been shown for very high activity for electrochemical water splitting reactions, for example, Pt or Pt-alloys and Ir-/Ru-oxides are well accepted catalysts presently for HER and OER, respectively [96]. However, drawbacks of scarcity, high price, and instability do not allow their long-term applications. After the first work published by Xu and coworkers on MOF-derived porous carbon for capacitance, non-precious MOF-derived materials are continuously being used for both half reactions of water splitting because of their high surface area, better electronic conductivity and low over potential [97]. Recently Pan et al. reported a unique composite nanostructure derived from core-shell ZIF-8@ZIF-67 structure having CoP nanoparticles encapsulated into N-doped carbon nanotube hollow polyhedron (NCNHP) using carbonization, oxidation, and subsequent phosphidation strategy (Figure 1.18) [98]. When as-synthesized catalyst CoP/NCNHP was used as anode and cathode for total water splitting in 1.0 M KOH, a cell potential of 1.64 V was required to attain  $10\text{ mA cm}^{-2}$

current density. This electrolyzer performance was found stable with negligible cell potential decay even after continuous work for 36 h.

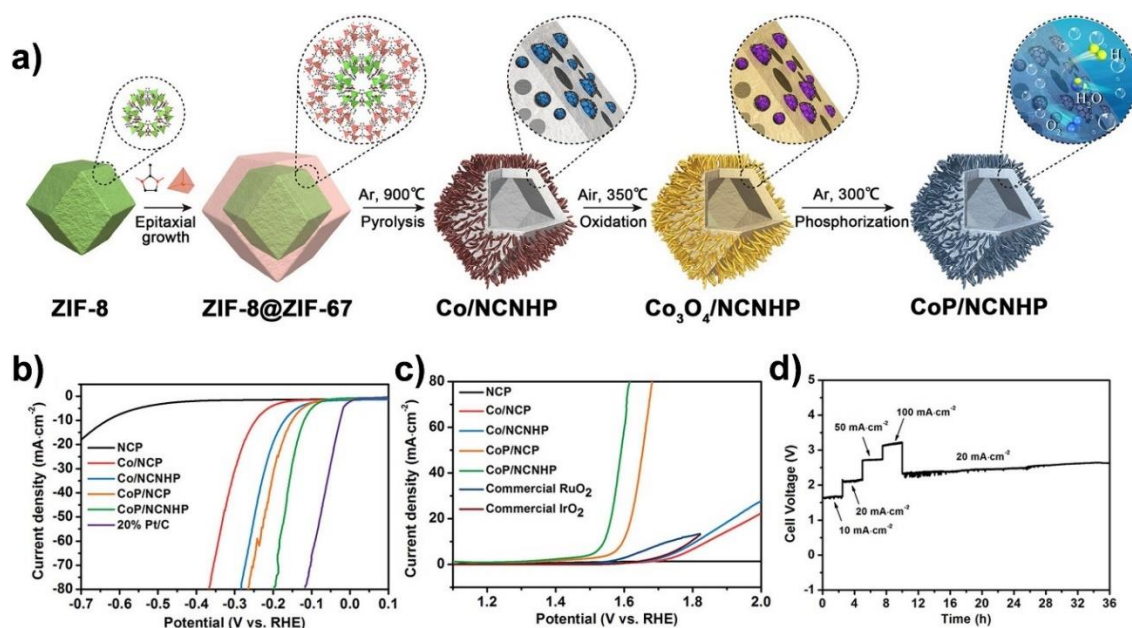


**Figure 1.18** a) Synthetic approach for NCNHP/CoP, b) HER LSVs, c) OER LSVs in 0.1 M KOH with a scan rate  $5 \text{ mV S}^{-1}$ , d) Utilizing CoP/NCNHP as the positive and negative electrodes in a two-electrode system, a chromatopotentiometric stability test was conducted on the electrolysis of water at different current densities in 1.0 M KOH. Adopted with permission from ref [98]. American Chemical Society.

#### 1.4.2.1.2 Fuel Cell

Fuel cells, which are electrochemical cells that transform chemical energy stored in fuel into electricity through chemical reactions with oxygen or other oxidizing agents and various fuels containing proton sources, are another type of highly encouraging and feasible energy conversion technology [99]. Fuel is directed towards the anode, where it undergoes oxidation, releasing hydrogen and electrons named as hydrogen oxidation reaction (HOR). The freed electrons travel to the cathode via an external circuit, while the positive hydrogen ion ( $\text{H}^+$ ) moves through the electrolyte and toward the cathode.  $\text{H}^+$  ions at the cathode participate in reaction with oxygen (or air) named as oxygen reduction reaction (ORR) to produce heat, electricity, and water. Among various types of fuel cell proton exchange membrane fuel cell (PEMFC) arose because of its high-power density,

fast start-up times, and low operating temperatures [100]. However, its practical commercialization is severely limited by the sluggish cathodic ORR reaction as well as the paucity of pricey Pt. Platinum is considered a "state-of-the-art" catalyst as it requires minimum additional energy to cross activation energy barriers for ORR and also proceed through four electron paths. But the main problem associated with, it dissolves very fast in acidic electrolyte. So, several efforts are giving to replace Pt with low cost non precious transition metal based electrocatalysts [101,102].

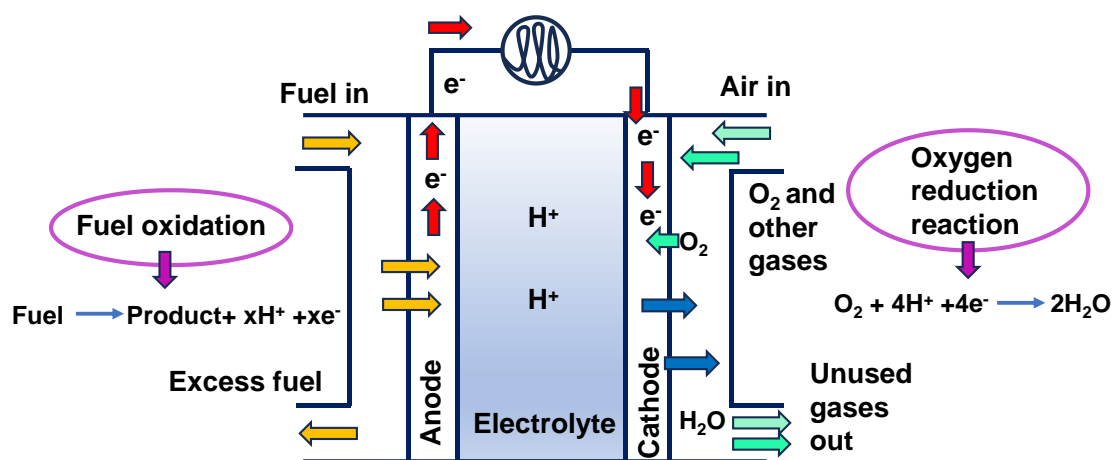


**Figure 1.19** Schematic diagram for overall water splitting reactions.

ORR in aqueous solutions can proceed in one of two ways depending upon the catalyst and pH of the medium. One is the direct 4e<sup>-</sup> path and the other is 2e<sup>-</sup> path which mainly passes through the formation of hydrogen peroxide (H<sub>2</sub>O<sub>2</sub>) as an intermediate [103,104]. This H<sub>2</sub>O<sub>2</sub> reacts with transition metals in most of the cases and cause dissolution of active sites. Along with it the high bond dissociation energy of O-O bond i.e., 498 kJ mol<sup>-1</sup> also contributes to the slower kinetics of ORR. Now depends upon the adsorption of O<sub>2</sub> on the catalytic sites two pathways are possible such as associative & dissociative pathways (Figure 1.20) [105].



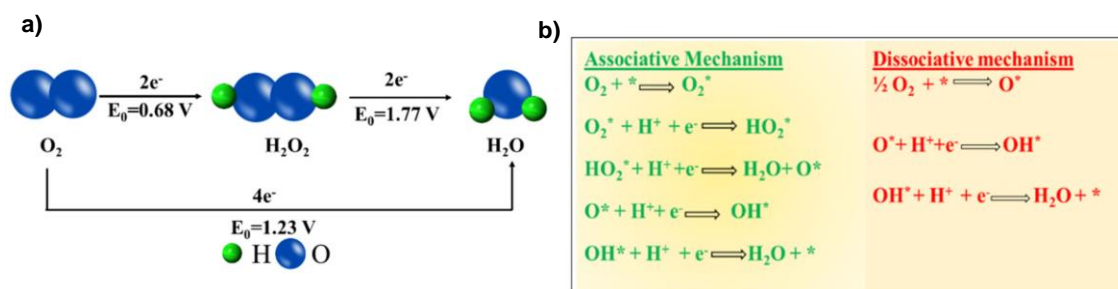


**Figure 1.20** a) Diagram of the ORR mechanism showing the direct and indirect pathways, and b) the ORR mechanism on the catalyst surface (\* denotes catalyst surface). Reprinted with permission from ref [105]. Copyright 2023 MDPI.

MOF derivatives composed of transition metals and heteroatom doped carbon demonstrated exceptional ORR performance, prompting their investigation as potentially effective platinum-group metal-free (PGM-free) catalysts to increase ORR in PEMFCs [106,107]. Zhao et al. presents a novel trimodal-porous structure made up of highly ordered macropores connected by mesopores, encompassing atomically distributed Ni and Fe binded to a microsized nitrogen-doped graphitic carbon substrate. The structure is called hetero-single-atom (h-SA) ORR electrocatalyst. Spectra obtained from extended X-ray absorption reveal that Fe- and Ni-SACs are attached to the carbon support by coordination bonds with NiN<sub>4</sub> and FeN<sub>4</sub>. The resulting Fe/Ni h-SA electrocatalyst outperforms SACs electrocatalysts that solely include Fe- or Ni-SACs as well as the benchmark Pt/C in terms of ORR activity. The obtained experimental results show that the better mass-transfer capability supported by the trimodal-porous-structured carbon support and the synergistic enhancement caused by the coexisting Fe-N<sub>4</sub> and Ni-N<sub>4</sub> sites are responsible for the attained remarkable ORR performance. Under H<sub>2</sub>-O<sub>2</sub> conditions of PEMFC, Fe/Ni-N<sub>x</sub>/OC achieved maximum power densities about 0.58 and 0.36 W cm<sup>-2</sup> at different pressure 1.0 and 0.3 bars, and open circuit voltage 0.96V, 0.95 V, respectively. The catalyst also tested under H<sub>2</sub>-air and again it maintained its activity in those conditions (Figure 1.21) [108].

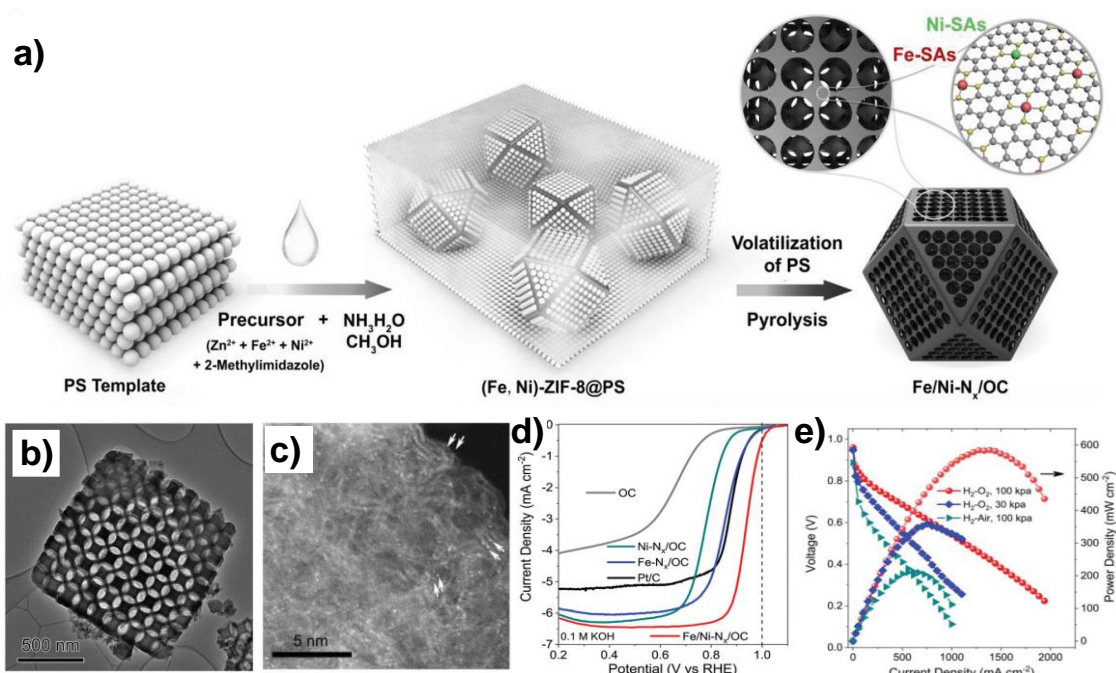


**Figure 1.21** a) Schematic showing the Fe/Ni-N<sub>x</sub>/OC synthesis process, b) SEM images of as synthesized catalyst, c) White dots in HAADF-STEM images confirming the presence of Fe/Ni-N<sub>x</sub>/OC, d) ORR polarization curves of Fe/Ni-N<sub>x</sub>/OC and its comparison with other supporting catalysts in O<sub>2</sub> saturated 0.1 M KOH solution with a rotation of 1600 rpm, e) Catalyst test in PEM-fuel cell conditions under both H<sub>2</sub>/O<sub>2</sub> and H<sub>2</sub>/air. Adopted with permission from ref [108]. Copyright 2020 WILEY VCH.

### 1.4.2.2 Energy storage technology

The issue of energy crisis cannot be solved by just developing extremely efficient energy conversion devices. In addition to energy conversion technology, creating an appropriate energy device in a long-lasting, environmentally responsible manner is crucial. The battery is one of the essential devices made up of electrochemical cells, where chemical potential energy is stored and converted into electricity. The cathode, or positive terminal, and anode, or negative terminal, coupled with the electrolyte, which is an ion-conducting but electronic insulating separator, are the main parts of a battery. Batteries work primarily through two processes: charge and discharge. In the discharge process, oxidation at the anode produces electrons that are consumed at the cathode during reduction; the entire process produces electricity; in the charging process, the opposite process takes place. 109,110 Batteries can be classified as two types. First one is primary battery which

mainly undergo an irreversible change in electrode material upon discharge, necessitating their disposal after a single use. One example of this kind of battery is the alkaline battery used in flashlights. Second one is secondary batteries which are rechargeable and can be used repeatedly since the electrode materials' composition remains unchanged during the charging and discharging process. A typical illustration of this category is the lithium-ion battery due to its utilization practically in every aspect of modern life, beginning with smart devices like laptops and smartphones. These secondary batteries are quickly taking the lead in energy storage technology because of their many cost-effective uses. Here we only discuss about Zn-air battery and vanadium redox flow battery only because it is pertinent to this thesis.

#### 1.4.2.2.1 Zn-air battery

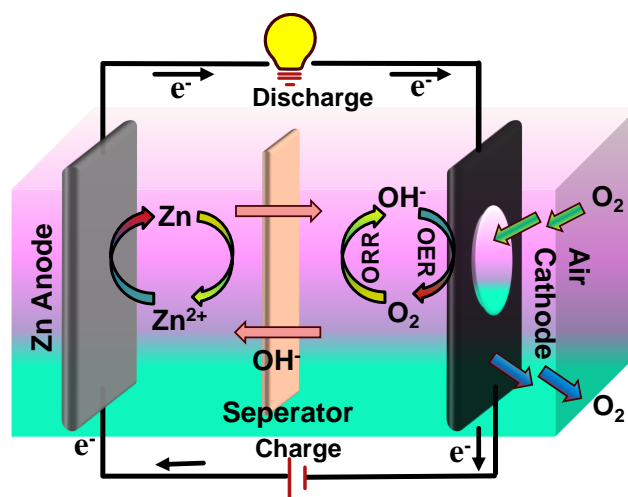


**Figure 1.22** Schematic representation of Zn-air battery.

As depicted in Figure 1.22 rechargeable Zn-air battery composed of Zn anode, air cathode which allows the diffusion of oxygen to the catalytic sites and an electrolyte either aqueous or non-aqueous. Due to high theoretical energy densities, cost effectiveness, safe-operation alkaline aq. Zn-air battery have received widespread attention to the scientific community but still it suffers from some challenges [111,112]. Among several other difficulties associated with it, the main problem is designing cathode catalyst which

will facilitate both OER and ORR reaction. Many MOF derivatives served as bifunctional oxygen electrocatalysts and have shown great applicability as air cathode. Sun et al. synthesized Fe-N<sub>x</sub>-C catalyst where Fe is atomically dispersed on nitrogen doped carbon & coordinated with four nitrogen via thermal treatment of Fe-Phen@ZIF-8 precursor (Figure 1.23) [113]. The as prepared catalyst demonstrated excellent bifunctional activity for both OER and ORR with small potential differences. The catalyst also checked for Zn air battery and it showed outstanding performance & durability with maximum peak power density 96.4 mW cm<sup>-2</sup> or high discharge specific capacity 641 mA.h.g<sup>-1</sup> even greater than Pt/C.

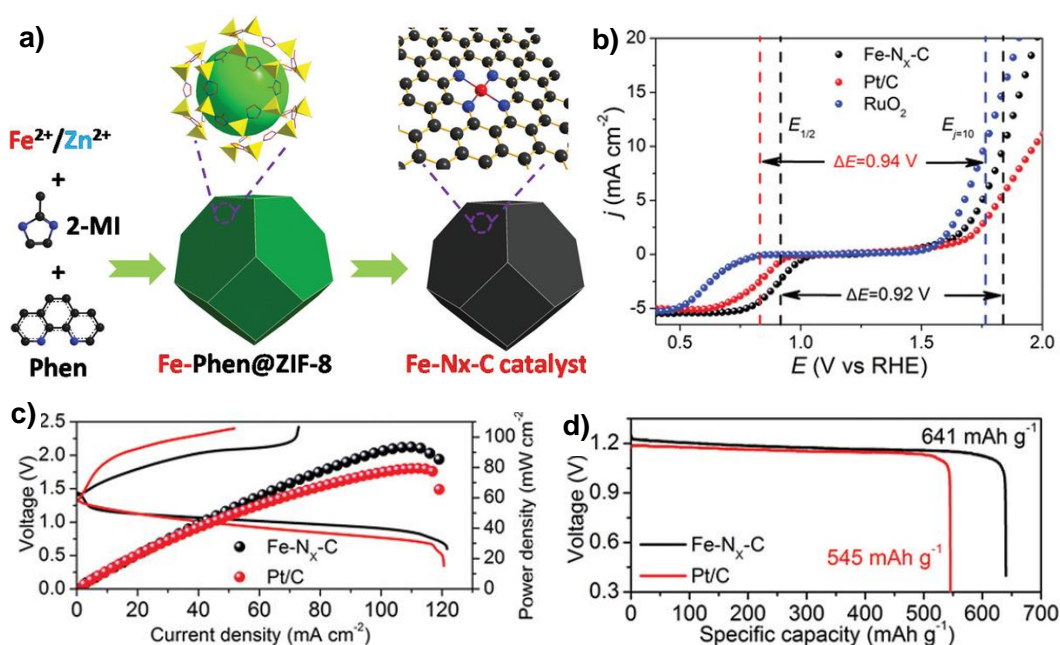


**Figure 1.23** a) Diagram illustrating the Fe-N<sub>x</sub>-C synthesis process, b) LSVs for both OER and ORR reversibility test of Fe-N<sub>x</sub>-C with commercial Pt/C in 0.1 M KOH solution, c) polarization curves for charging and discharging and the accompanying power density plots, d) comparison of specific capacitance of Fe-N<sub>x</sub>-C with commercial Pt/C. Reproduced with permission from ref [113]. Copyright 2019 WILEY VCH.

### 1.4.2.2 Vanadium redox flow battery

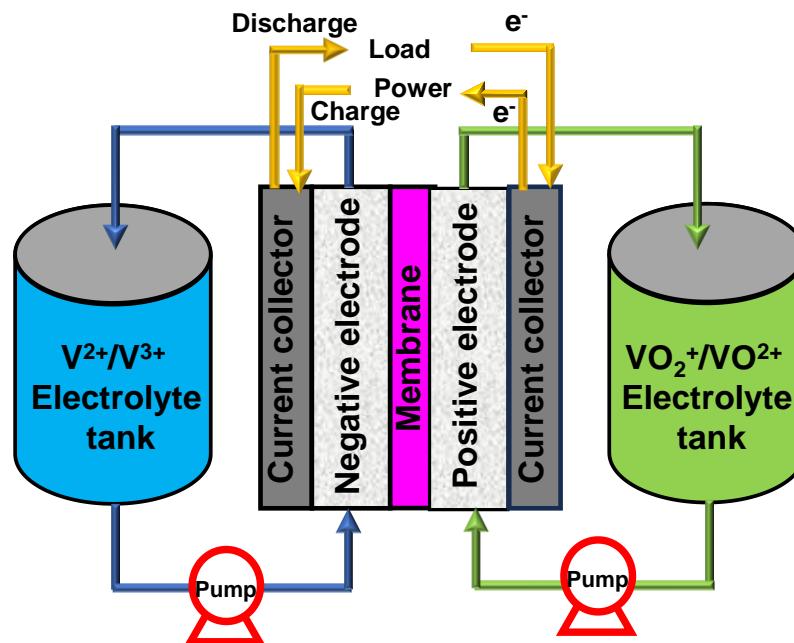


**Figure 1.24** Schematic diagram of vanadium redox flow battery (VRFB).

Among various energy storage systems redox flow battery (RFB) is an important technique to explore the grid energy market as it involves the spatial separation of active species and electrodes. Independent power and energy rating also influenced this RFB system to become a critical component for future. The number of cell stack present in redox flow battery systems regulate the power rating though the energy rating governs by the electrolyte concentration and volume used [114-116]. Among other RFBs, vanadium redox flow battery emerged as a promising technology due to its unique flow cell structure, flexible design, quick response time, long cycling life, better thermal management, and excellent safety [117,118]. It utilizes vanadium ions which can exist in four different oxidation state. At positive side  $V^{4+}$  oxidized to  $V^{5+}$  whereas at negative sides  $V^{3+}$  converts to  $V^{2+}$  and ions are separated by nafion membrane. Due to this it avoids cross contamination of electrolytes as at both sides it possesses same solution. The electrolytic solutions filled in to two tanks reached the cell with the help of pump (Figure

1.24) [119]. So, higher flow rate forced greater amount of solution to reach the cell through MEA, thus it enhances the efficiency of the system also. But still it faces many challenges which hinder its wider exploration and in commercialization due to slow kinetics, low voltage & energy efficiency, low power density. In this regard, electrodes illustrate crucial role by providing active sites for enriching the electrochemical and kinetic activity of vanadium redox reactions. Graphitic or carbon felt was widely used as electrode for VRFB system but due to lesser functionality or greater hydrophobicity many modifications has been introduced to address the above-mentioned problems.120 A very few MOF derivatives known for this VRFB system. Wang and his coworkers deposited UiO-66 MOF on graphitic felt and upon calcination they got ZrO<sub>2</sub> functionalized graphitic felt. It improved the kinetics of both cathodic and anodic redox reactions confirmed by cyclic voltammetry analysis and enhanced the stability of electrode in flow cell station with long charging discharging retention time and better voltage or energy efficiency i.e 77.5% or 75.2% respectively (Figure 1.25) [121].

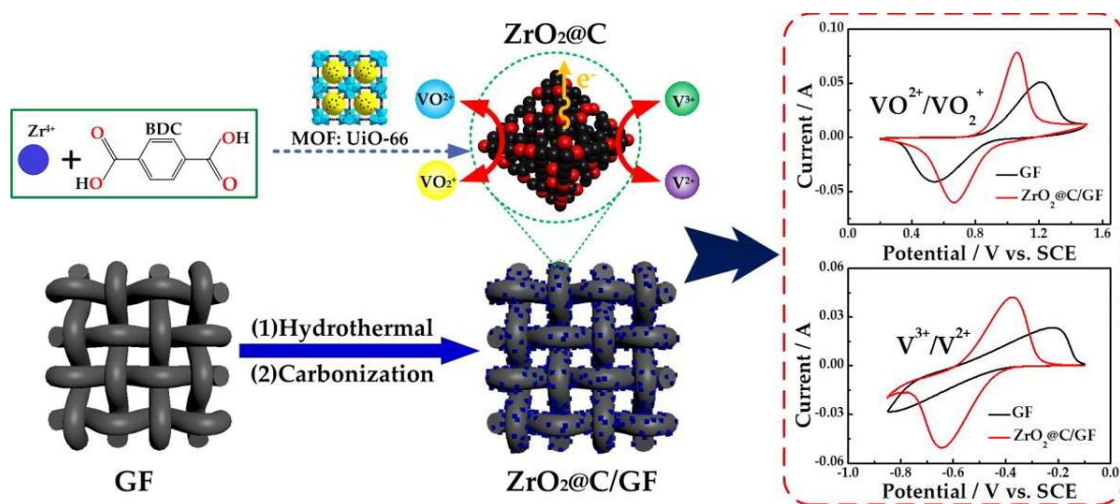


**Figure 1.25** Schematic representation for the synthesis of ZrO<sub>2</sub>@C on graphitic felt electrode and corresponding cyclic voltammetry study and its comparison with without treated graphite felt for vanadium redox reactions. Reproduced with permission from ref [121]. Copyright 2019 ELSEIVER.

## 1.5 Conclusions

The broad applicability of Metal-Organic Frameworks (MOFs) in organic transformations, encompassing processes such as Knoevenagel condensation, acetylation, epoxidation, C–H functionalization, and hydrogenation reactions, has been extensively documented. While various methodologies have been explored to advance MOF-based heterogeneous catalysis, including cation exchange methods, metal deposition on nodes or linkers, and solution impregnation techniques, there remains a scarcity of reports on the in-situ encapsulation of metal complexes within MOF pores suitable for harsh acidic or basic conditions due to inherent limitations in MOF chemical stability. Presently, the foremost challenges lie in the heterogenization of homogeneous catalysts to facilitate reactions under harsh conditions analogous to those encountered in homogeneous catalysis. Conversely, within the realm of electrocatalysis, materials derived from MOFs have demonstrated considerable efficacy in applications related to electrochemical energy storage and conversion, such as fuel cells, water electrolyzers, and metal air batteries. MOFs offer a promising platform for the construction of advanced inorganic functional materials crucial for renewable energy technologies. Specifically, the MOF-derived approach is noteworthy for preserving porous and/or hollow nanostructures/microstructures with precisely defined, strongly coupled metal sites within porous carbon matrices. Although the incorporation of heteroatoms into carbon matrices significantly enhances overall conductivity and alters the electronic structure and surface energy of the material, the self-templated methods, including various MOF-derived strategies, simplify synthetic procedures and enable industrial-scale production. However, the majority of reports in this domain rely on individual systems, and traditional synthetic approaches are often labor-intensive and inherently limited. Thus, from a practical standpoint, MOFs and MOF-derived materials that are low-cost and easily synthesized would hold greater

appeal. With sustained efforts directed towards addressing these challenges, it is anticipated that MOFs and MOF-derived materials will play a revolutionary role in chemical synthesis and the utilization of renewable energy in the future.



## **Chapter 2: Immobilizing A Homogeneous Manganese Catalyst Into MOF Pores For $\alpha$ -alkylation of Methylene Ketones With Alcohols**

### **2.1 Abstract**

Herein, for the first time, a metal-organic framework (MOF) is reported as catalyst for  $\alpha$ -alkylation of ketones with alcohols. Using an encapsulation strategy via nano-confinement of homogeneous Mn-phenanthroline complex into MOF pores selectively produced functionalized branched ketones. Mechanistic investigations, deuterium labelling experiments validate the utilization of borrowing hydrogen strategy. Formation of extra Lewis acid sites, defects, and pore enhancement during catalysis helped in achieving higher activity and selectivity.

### **2.2 Introduction**

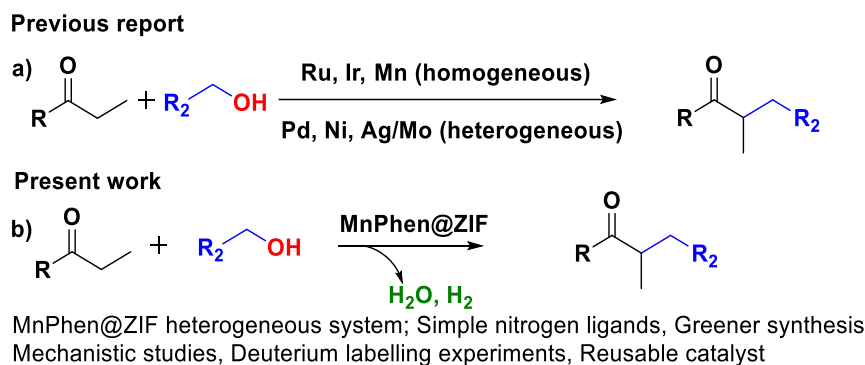
Metal-organic frameworks (MOFs) are porous coordination polymers made up of metal ions and organic linkers [122,123]. These materials are continuously of great interest due to the high possibilities of tuning their pore sizes and pore functionalities which lead to the selective functional applications such as catalysis [124-132]. However, the broadness of catalytic applications using MOFs is quite limited, as MOFs are considered not stable under harsh acidic or basic conditions [133,134]. Therefore, the development of new strategies for important organic transformations using MOFs as heterogeneous catalysts is in great demand.

Manganese (Mn) is the 3rd most Earth-abundant metal and its utilization in catalysis could be a sustainable alternative [135]. Interestingly, in comparison with precious metals and nonprecious metals (Fe, Co, Ni or Cu), Mn has been less explored in MOF-based catalytic systems and it is often limited to conventional catalytic oxidation/reduction reactions [136-145]. For example, Mn-exchanged MOF-5 is demonstrated for olefin

epoxidation [136]; Mn<sub>3</sub>O<sub>4</sub>/MIL-101 for aerobic oxidation [137]; metalloporphyrinic frameworks for olefin epoxidation or oxidation of alkylbenzenes or cyclohexane oxidation [138-140]; MnCo-MOF-74 for substituted toluene oxidation [141]; CPF-5 for allylic oxidation of olefins [142]; MnSO-MOF or (salen)Mn-MOF for epoxidation [143,144]; and MnMIL-88-Me<sub>4</sub> for alcohol oxidation [145]. Cyanosilylation and Knoevenagel condensation reactions are also demonstrated using Mn-MOFs [146]. In these reports, the most common and important finding is the selectivity of products owing to the pore confinement effect. However, a very significant organic transformation, namely the C–C bond formation reaction with Mn-MOFs is rare [147]. This is evident as MOFs' chemical stability is limited under harsh experimental conditions. Therefore, the search for robust MOF-based catalysts with suitable Mn-active sites for important coupling reactions is highly desirable.

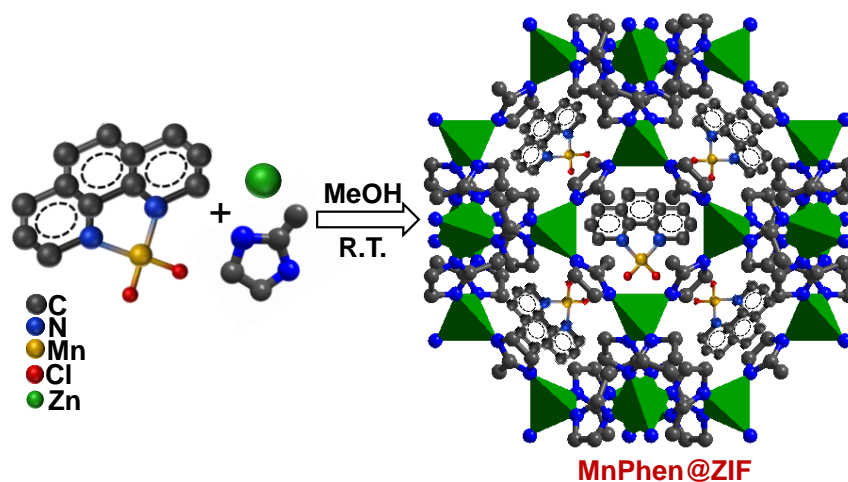
Functionalized branched ketones have high importance in pharmaceuticals and are consistently used as intermediates in organic synthesis [148]. Alkylation of branched ketones with primary alcohols could be an alternative approach for the synthesis of  $\beta,\beta$ -di-substituted ketones [149-155]. Although, a series of precious (Ru, Os, Rh, Ir, Au, and Re) and non-precious (Fe, Co, and Mn) metal-based catalysts have been explored, they are often restricted to linear ketones. Direct access to branched disubstituted ketones using enolate alkylation has been relatively less studied. For example, Ir, Ru, and Mn (homogeneous) catalysts and Pd, Ni, and Ag/Mo (heterogeneous) catalysts are reported for the synthesis of the desired branched ketones (Scheme 2.1a) [156-160]. Since the past few years, we have explored a few interesting catalytic protocols based on non-precious metal catalysts for the synthesis of linear and branched ketones using alcohols as renewable coupling partners [161-164]. However, the catalytic system was not recyclable.

Herein, a homogeneous Mn–phenanthroline complex (MnPhen) was immobilized into MOF (ZIF-8) pores, which selectively produced functionalized branch ketones from the alkylation of ketones with alcohols (Scheme 2.1b). To the best of our knowledge, to date, no MOFs or even no heterogeneous Mn-based catalysts have been reported for the synthesis of branched ketones using alcohols.



**Scheme 2.1** a) Metal catalysed alkylation of branched ketones. b) Mnphen@ZIF catalysed one-step sustainable synthesis of di-substituted ketones.

ZIF-8 is a well-known and high surface area MOF, known for its structural stability under high pH conditions. As the pore window size of ZIF-8 is small (3.4 Å), the MnPhen complex was immobilized into ZIF-8 cavities (11.6 Å) using an in situ nano-confinement strategy (Scheme 2.2) [165]. The resulting catalyst is denoted as MnPhen@ZIF.



**Scheme 2.2** Schematic representation of the synthesis of the MnPhen@ZIF catalyst.

## 2.3 Experimental

### 2.3.1 Chemicals

All reagents and solvents were directly used without further purification. Zinc Acetate dihydrate  $\text{Zn}(\text{CH}_3\text{COO})_2 \cdot 2\text{H}_2\text{O}$  (98%) was purchased from Molychem, 2-methylimidazole (98%) was purchased from Avra, 1,10-phenanthroline monohydrate (AR grade) was purchased from FINAR, Methanol (99%), Benzyl alcohol (99%) were purchased from RANKEM. Toluene HPLC grade (99.7%),  $\text{K}_2\text{CO}_3$  (99.0%), Manganese Chloride tetrahydrate, Manganese acetate tetrahydrate, Hexane (>98%), Ethyl acetate (>98%) were purchased from SDFCL. Deoxybenzoin (97%), 4-chlorobenzyl alcohol (99%),  $\alpha$ -Tetralone were acquired from Alfa Aesar. 4-isopropyl benzylalcohol (98%), Cyclohexanemethanol (>98%) and 4-ethyl benzylalcohol (>98%), 2-thiophenemethanol (98%), 4-methoxy benzylalcohol (98%), 4-fluorobenzyl alcohol (97%), Heptyl alcohol ( $\geq 97\%$ ), Octyl alcohol (98%),  $\beta$ -Citronellol (95%), Furfuryl alcohol (97%), Piperonyl alcohol (98%) were supplied by Sigma-Aldrich. Propiophenone (>98%) was purchased from TCI. Potassium-tert-butoxide t-BuOK (98%) was obtained from Spectrochem. KOH (85%) was acquired from Azytus. Chloroform-d (99.8% min.) was acquired from Merck.

## 2.3.2 Synthesis

**2.3.2.1 Synthesis of MnPhen@ZIF:** In a typical synthesis and at room temperature, 1.0 mmol of  $\text{MnCl}_2$  (197 mg) and 1.0 mmol of phenanthroline (198 mg) were dissolved in two separate 25 mL MeOH solvents. The manganese solution was added into phenanthroline solution with continuous stirring for 24 h at room temperature. A yellow-colored solution was obtained and was filtered. The filtrate was marked as solution 'A'. In continuation, 3.46 mmol of  $\text{Zn}(\text{CH}_3\text{COO})_2 \cdot 2\text{H}_2\text{O}$  (760 mg) was dissolved in 75 mL MeOH solvent, marked as solution 'B'. At the same time, 51.20 mmol of 2-methylimidazole (4.208 g) was also dissolved in 75 mL MeOH solvent and marked as solution 'C'. Solution C was first added into solution A under vigorous stirring. The yellow-colored solution became colorless. To this solution, solution B was transferred quickly with continuous stirring. After 2 h continuous stirring, solution was kept as it for 24 h without any disturbance. A white color solid was precipitated. It was separated by centrifugation and washed with MeOH several times. Sample was dried in vacuum oven at 150 °C and named as MnPhen@ZIF.

**2.3.2.2 Synthesis of ZIF-8:** 3.46 mmol of  $\text{Zn}(\text{CH}_3\text{COO})_2 \cdot 2\text{H}_2\text{O}$  (760 mg) and 51.20 mmol of 2-methylimidazole (4.208 g) were dissolved in 75 mL MeOH solvents separately. Then the zinc solution was added into 2-methylimidazole solution under vigorous stirring. After 2 h continuous stirring, solution was kept as it for 24 h without any disturbance. A white color solid was precipitated. It was separated by centrifugation and washed with MeOH several times. Sample was dried in vacuum oven at 150 °C and stored for further use.

**2.3.2.3 Synthesis of Mn-ZIF-8:** 3.46 mmol of  $\text{Zn}(\text{CH}_3\text{COO})_2 \cdot 2\text{H}_2\text{O}$  and 0.7 mmol  $\text{MnCl}_2$  was dissolved in 75 mL MeOH solvent. At the same time, 51.20 mmol of 2-

methylimidazole was also dissolved in 75 mL MeOH solvent. Then the metal solution was added into 2-methylimidazole solution under vigorous stirring. After 2 h continuous stirring, solution was kept as it for 24 h without any disturbance. A white color solid was precipitated. It was separated by centrifugation and washed with MeOH several times. Sample was dried in vacuum oven at 150 °C and stored for further use.

**2.3.2.4 Synthesis of MnPhen complex:** To synthesize MnPhen complex, 1.0 mmol of MnCl<sub>2</sub> (197 mg) and 2.0 mmol of phenanthroline (396 mg) were dissolved in two separate 25 mL MeOH solvents. The manganese solution was added into phenanthroline solution with continuous stirring for 24 h at room temperature. A yellow-colored precipitate was formed. Then we filter the solution and dried it at room temperature & named as “MnPhen”.

## 2.4 Characterization

PANalytical diffractometer using Cu K $\alpha$  source ( $\lambda = 1.5405 \text{ \AA}$ ) was utilized to measure Powder X-ray diffraction (PXRD) with 2°/min scan rate and 0.05 steps. Cary 5000 UV-Visible-NIR spectrophotometer used to record solid-state UV-VIS spectra with integrating spheres of 105 mm. For analyzing surface area and pore size distribution BELSORP Max sorption analyzer was used at liquid nitrogen temperature 77 K. Before sorption measurements, the samples were degassed 150 °C for 12 h. X-ray photoelectron spectroscopy (XPS) was performed on a Thermo Fisher Scientific (K-Alpha) X-ray photoelectron spectrometer using an Al K $\alpha$  source (10 kV, 10 mA) equipped with ion source (EX06). The Ar sputtering experiments were carried out under the conditions of background vacuum  $\sim 10^{-8}$  Pa, sputtering acceleration voltage of 2 kV and sputtering current of 10 mA. Micromeritics (AUTOCHEM) was used for temperature programmed desorption (TPD) measurements. Thermogravimetric analysis (TGA) was performed on TA

Instrument Q500 thermogravimetric analyzer at under N<sub>2</sub> atmosphere with a heating rate of 10 °C /min from 25 to 700 °C. Scanning electron microscopy (SEM) images were acquired using JEOL (JXA-8230) at 20 KV. Transmission electron microscopy (TEM) images were acquired at 200 kV Talos F200S G2 transmission electron microscope combined with column energy dispersive X-ray spectrometer (EDS) and a CMOS Camera 4K x 4K detector. PERKIN ELMER OPTIMA 5300 DV ICP-OES was used for metals content determination. Nucon GC 5700 gas chromatography (model WINCHROM-1 Spartan) with TCD detector was used for the hydrogen gas analysis. GC-MS were recorded using Agilent Gas Chromatography Mass Spectrometry. <sup>1</sup>H NMR spectral data were collected at 400 MHz, and <sup>13</sup>C NMR were recorded at 100 MHz using JEOL-400 YH NMR spectrometer at 25 °C probe temperature.

## **2.5 Catalytic measurements**

Silica Gel 60 F254 plates with the layer thickness of 0.25 mm were used for thin-layer chromatography. To afford pure product, column chromatography was performed. A gradient of ethyl acetate and hexane was used as a mobile phase and passed through the silica gel with mesh size of 100-200. All the reactions were carried out under Ar atmosphere.

### **2.5.1 Synthetic method for the synthesis of $\alpha$ -substituted methylene ketones with alcohol:**

0.25 mmol ketone, 0.3125 mmol alcohol, 0.25 mmol t-BuOK, 2 mL toluene, 50 mg catalyst were taken in a 25 ml round bottom flask. The reaction was performed in an oil bath under Ar atmosphere. It was heated at 140 °C for 24 h. After the completion of the reaction, the reaction mixture was left to cool down at room temperature. Then 3 mL ethyl acetate was added. The solid catalyst was easily recovered by filtration. The filtrated solution was then concentrated under reduced pressure to make a slurry for purification

process by column chromatography. Hexane and ethyl acetate used as eluent for these purposes.

### **2.5.2 Synthesis of pure MnPhen Complex and its catalytic activity test:**

0.007 mmols of manganese (corresponding to 0.8 wt% Mn in MnPhen@ZIF) and phenanthroline were taken into 25 mL round bottom flask using 2 mL toluene and Ar atmosphere. After stirring for 2 h, ketone (0.25 mmol), alcohol (0.3125 mmol), t-BuOK (0.25 mmol) were placed in that flask and heated at 140 °C for 24 h. When it cooled down to room temperature 3 mL ethyl acetate was added. The concentrated residue was further purified by column chromatography with the eluent system hexane and ethyl acetate.

### **2.6 Reusability test with MnPhen@ZIF**

After completion of the reaction as mentioned in section 2.5.1, the solid product was separated out by filtration and washed with ethyl acetate and dried in oven at room temperature. In 2nd catalytic cycle, solid catalyst was further activated at 150 °C under vacuum and performed same as first cycle. Similarly, 3rd and 4th cycles were measured, and product conversion were determined by GC-MS.

### **2.7 Calculations of lewis acidity using NH<sub>3</sub>-TPD measurements**

Area under the NH<sub>3</sub>-TPD profile of catalyst = A

Number of mmol of NH<sub>3</sub> = 0.294 × A

Catalyst mass = B g

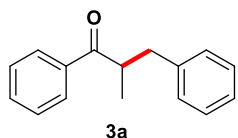
Total acidity of catalyst = mmol of NH<sub>3</sub>/Catalyst mass

= (0.294×A/B) mmol NH<sub>3</sub>/g catalyst.



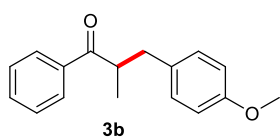
## 2.8 Analytical data

**2-Methyl-1,3-diphenylpropan-1-one (3a):** According to the procedure described in section 2.5.1, the



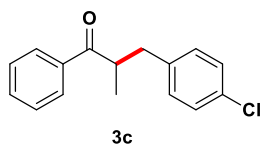
mentioned product obtained as colorless solid (46 mg, 82%);  $^1\text{H NMR}$  (400 MHz,  $\text{CDCl}_3$ )  $\delta$  7.93 (dd,  $J = 8.4, 1.3$  Hz, 2H), 7.57 – 7.52 (m, 1H), 7.45 (t,  $J = 7.5$  Hz, 2H), 7.28 – 7.24 (m, 3H), 7.21 – 7.13 (m, 3H), 3.74 (dq,  $J = 13.5, 6.7$  Hz, 1H), 3.17 (dd,  $J = 13.9, 6.4$  Hz, 1H), 2.69 (dd,  $J = 13.9, 8.0$  Hz, 1H), 1.20 (d,  $J = 7.0$  Hz, 3H).  $^{13}\text{C NMR}$  (101 MHz,  $\text{CDCl}_3$ )  $\delta$  203.77, 139.92, 136.39, 132.92, 129.07, 128.62, 128.35, 128.27, 126.17, 42.74, 39.32, 17.38.

**3-(4-Methoxyphenyl)-2-methyl-1-phenylpropan-1-one (3b):** According to the procedure described in



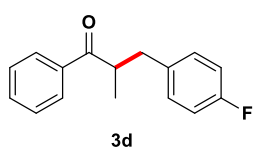
section 2.5.1, the mentioned product obtained as colourless oil (41 mg, 65% yield);  $^1\text{H NMR}$  (400 MHz,  $\text{CDCl}_3$ )  $\delta$  7.92 (d,  $J = 7.3$  Hz, 2H), 7.52 (m, 1H), 7.42 (t,  $J = 7.6$  Hz, 2H), 7.10 (d,  $J = 8.6$  Hz, 2H), 6.80 (d,  $J = 8.6$  Hz, 2H), 3.76 (s, 3H), 3.73-3.65 (m, 1H), 3.10 (dd,  $J = 13.8, 6.4$  Hz, 1H), 2.63 (dd,  $J = 13.8, 7.7$  Hz, 1H), 1.18 (d,  $J = 6.9$  Hz, 3H).  $^{13}\text{C NMR}$  (101 MHz,  $\text{CDCl}_3$ )  $\delta$  207.4, 154.1, 133.0, 132.1, 130.1, 128.7, 128.3, 113.7, 109.5, 55.3, 43.0, 38.6, 17.4.

**3-(4-Chlorophenyl)-2-methyl-1-phenylpropan-1-one (3c):** According to the procedure described in sec-



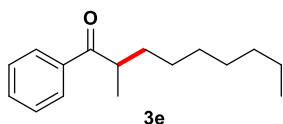
tion 2.5.1, the mentioned product obtained as colorless liquid (34 mg, 53% yield);  $^1\text{H NMR}$  (400 MHz,  $\text{CDCl}_3$ )  $\delta$  7.93 (d,  $J = 8.7$  Hz, 2H), 7.57 (t,  $J = 7.6$  Hz, 1H), 7.44 (t,  $J = 8.3$  Hz, 2H), 7.24 (d,  $J = 8.8$  Hz, 2H), 7.16 (d,  $J = 8.9$  Hz, 2H), 3.81 – 3.70 (m, 1H), 3.18 (dd,  $J = 14.4, 7.2$  Hz, 1H), 2.72 (dd,  $J = 14.4, 7.6$  Hz, 1H), 1.24 (d,  $J = 7.6$  Hz, 3H).  $^{13}\text{C NMR}$  (101 MHz,  $\text{CDCl}_3$ )  $\delta$  203.3, 138.4, 133.0, 132.0, 130.4, 128.7, 128.6, 128.5, 128.2, 42.7, 38.6, 17.6.

**3-(4-Fluorophenyl)-2-methyl-1-phenylpropan-1-one (3d):** According to the procedure described in sec-



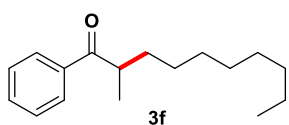
tion 2.5.1, the mentioned product obtained as colorless liquid (29 mg, 48% yield);  $^1\text{H NMR}$  (400 MHz,  $\text{CDCl}_3$ )  $\delta$  7.89 (d,  $J = 8.2$  Hz, 2H), 7.54 (t,  $J = 7.6$  Hz, 1H), 7.43 (t,  $J = 7.9$  Hz, 2H), 7.13 (dd,  $J = 9.0, 5.6$  Hz, 2H), 6.92 (t,  $J = 8.9$  Hz, 2H), 3.70 (dd,  $J = 14.2, 7.1$  Hz, 1H), 3.12 (dd,  $J = 14.1, 7.0$  Hz, 1H), 2.67 (dd,  $J = 14.0, 7.5$  Hz, 1H), 1.19 (d,  $J = 7.1$  Hz, 3H).

**2-methyl-1-phenylnonan-1-one (3e):** According to the procedure described in section 2.5.1, the men-



tioned product obtained as colorless oil (29 mg, 50% yield);  $^1\text{H NMR}$  (400 MHz,  $\text{CDCl}_3$ )  $\delta$  7.98 (d,  $J = 7.3$  Hz, 2H), 7.57 (d,  $J = 6.9$  Hz, 1H), 7.49 (t,  $J = 6.8$  Hz, 2H), 3.49 – 3.47 (m, 1H), 1.82 (dd,  $J = 12.8, 6.5$  Hz, 1H), 1.45 (d,  $J = 5.8$  Hz, 1H), 1.27 (s, 10H), 1.22 (d,  $J = 6.6$  Hz, 3H), 0.89 (s, 3H).

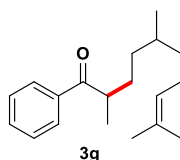
**2-methyl-1-phenyldecan-1-one (3f):** According to the procedure described in section 2.5.1, the mentioned



product obtained as colorless oil (28 mg, 56% yield);  $^1\text{H}$  NMR (400

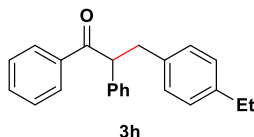
MHz,  $\text{CDCl}_3$ )  $\delta$  7.98 (d,  $J = 7.3$  Hz, 2H), 7.58 (t,  $J = 7.1$  Hz, 1H), 7.49 (t,  $J = 7.5$  Hz, 2H), 3.51 – 3.45 (m, 1H), 1.81 (dd,  $J = 24.3, 13.1$  Hz, 1H), 1.47 (d,  $J = 17.6$  Hz, 1H), 1.28 (d,  $J = 12.9$  Hz, 12H), 1.22 (d,  $J =$

**2,5,9-Trimethyl-1-phenyldec-8-en-1-one (3g):** According to the procedure described in section 2.5.1, the



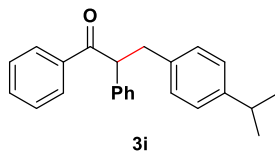
mentioned product obtained as a pale yellow oil (40 mg, 59% yield);  $^1\text{H}$  NMR (400 MHz,  $\text{CDCl}_3$ )  $\delta$  7.93 (d,  $J = 7.9$  Hz, 2H), 7.55 (dd,  $J = 8.2, 6.5$  Hz, 1H), 7.44 (t,  $J = 7.6$  Hz, 2H), 5.05 (ddd,  $J = 12.8, 5.8, 1.3$  Hz, 1H), 3.41 (ddd,  $J = 13.5, 6.7, 2.2$  Hz, 1H), 1.98 – 1.74 (m, 3H), 1.65 (d,  $J = 4.2$  Hz, 3H), 1.57 (d,  $J = 5.0$  Hz, 2H), 1.46 – 1.23 (m, 5H), 1.18 (d,  $J = 6.9$  Hz, 3H), 1.15 – 1.08 (m, 2H), 0.84 (t,  $J = 6.5$  Hz, 3H).  $^{13}\text{C}$  NMR (101 MHz,  $\text{CDCl}_3$ )  $\delta$  204.7, 133.3, 132.8, 131.2, 129.0, 128.7, 128.3, 40.9, 37.0, 36.8, 34.6, 32.57, 31.2, 25.5, 19.5, 17.2

**3-(4-ethylphenyl)-1,2-diphenylpropan-1-one (3h):** According to the procedure described in section



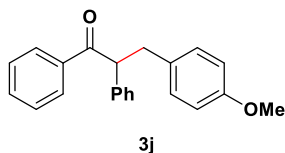
2.5.1, the mentioned product obtained as colorless solid (60 mg, 76%);  $^1\text{H}$  NMR (400 MHz,  $\text{CDCl}_3$ )  $\delta$  7.90 (d,  $J = 7.1$  Hz, 2H), 7.46 (t,  $J = 7.4$  Hz, 1H), 7.34 (t,  $J = 7.6$  Hz, 2H), 7.27 – 7.16 (m, 5H), 7.05 – 6.98 (m, 4H), 4.84 – 4.78 (m, 1H), 3.55 (dd,  $J = 13.8, 7.7$  Hz, 1H), 3.02 (dd,  $J = 13.8, 6.7$  Hz, 1H), 2.56 (q,  $J = 7.6$  Hz, 2H), 1.18 (t,  $J = 7.6$  Hz, 3H).  $^{13}\text{C}$  NMR (101 MHz,  $\text{CDCl}_3$ )  $\delta$  199.29, 141.94, 139.22, 136.92, 136.72, 132.79, 128.99, 128.86, 128.66, 128.43, 128.26, 127.69, 127.07, 55.88, 39.68, 28.38, 15.55.

**3-(4-isopropylphenyl)-1,2-diphenylpropan-1-one (3i):** According to the procedure described in section



2.5.1, the mentioned product obtained as colorless solid (65 mg, 79%);  $^1\text{H}$  NMR (400 MHz,  $\text{CDCl}_3$ )  $\delta$  7.90 (d,  $J = 7.1$  Hz, 2H), 7.44 (t,  $J = 7.4$  Hz, 1H), 7.34 (t,  $J = 7.6$  Hz, 2H), 7.28 – 7.18 (m, 5H), 7.04 (q,  $J = 8.3$  Hz, 4H), 4.82 (t,  $J = 7.9$  Hz, 1H), 3.57 (dd,  $J = 13.8, 7.9$  Hz, 1H), 3.02 (dd,  $J = 13.8, 6.5$  Hz, 1H), 2.88 – 2.75 (m, 1H), 1.19 (d,  $J = 6.9$  Hz, 6H).  $^{13}\text{C}$  NMR (101 MHz,  $\text{CDCl}_3$ )  $\delta$  199.27, 146.57, 139.29, 137.08, 136.73, 132.77, 128.95, 128.86, 128.66, 128.41, 128.25, 127.06, 126.25, 55.82, 39.66, 33.60, 23.97.

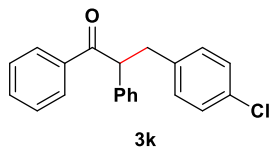
**3-(4-methoxyphenyl)-1,2-diphenylpropan-1-one (3j):** According to the procedure described in section



2.5.1, the mentioned product obtained as colorless solid (48 mg, 61%);  $^1\text{H}$  NMR (400 MHz,  $\text{CDCl}_3$ )  $\delta$  7.89 (d,  $J = 7.1$  Hz), 7.44 (t,  $J = 8.0$  Hz), 7.34 (t,  $J = 7.6$  Hz), 7.24 – 7.22 (m), 6.99 (d,  $J = 8.7$  Hz), 6.73 (d,  $J = 8.7$  Hz), 4.77 (t,  $J = 7.3$  Hz), 3.73 (s), 3.50 (dd,  $J = 13.8, 7.5$  Hz), 3.00 (dd,  $J = 13.8, 7.0$

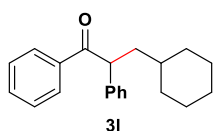
Hz).  $^{13}\text{C}$  NMR (101 MHz, )  $\delta$  199.37, 157.86, 139.09, 136.70, 132.80, 131.79, 130.04, 128.84, 128.63, 128.43, 128.26, 127.06, 113.57, 56.12, 55.12, 39.22.

**3-(4-chlorophenyl)-1,2-diphenylpropan-1-one (3k):** According to the procedure described in section



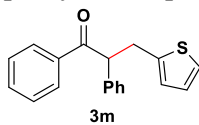
2.5.1, the mentioned product obtained as colorless solid (71 mg, 89%);  $^1\text{H}$  NMR (400 MHz,  $\text{CDCl}_3$ )  $\delta$  7.89 (d,  $J = 7.1$  Hz, 2H), 7.46 (t,  $J = 7.4$  Hz, 1H), 7.35 (t,  $J = 7.6$  Hz, 2H), 7.26 (t,  $J = 7.5$  Hz, 3H), 7.21 (d,  $J = 6.9$  Hz, 2H), 7.16 (d,  $J = 8.4$  Hz, 2H), 7.01 – 6.98 (m, 2H), 4.75 (t,  $J = 7.3$  Hz, 1H), 3.50 (dd,  $J = 13.8, 7.4$  Hz, 1H), 3.03 (dd,  $J = 13.8, 7.2$  Hz, 1H).  $^{13}\text{C}$  NMR (101 MHz,  $\text{CDCl}_3$ )  $\delta$  198.89, 138.66, 138.18, 136.47, 132.98, 130.49, 128.98, 128.66, 128.51, 128.31, 128.22, 127.38, 127.28, 55.83, 39.39.

**3-Cyclohexyl-1,2-diphenylpropan-1-one (3l):** According to the procedure described in section 2.5.1, the



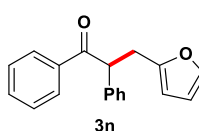
mentioned product obtained as colorless solid (31 mg, 42%);  $^1\text{H}$  NMR (400 MHz, )  $\delta$  7.98 (d,  $J = 8.5$  Hz, 2H), 7.47 – 7.44 (m, 1H), 7.40 – 7.36 (m, 2H), 7.32 – 7.24 (m, 4H), 7.20 – 7.17 (m, 1H), 4.72 (t,  $J = 7.5$  Hz, 1H), 2.15 – 2.04 (m, 1H), 1.74 – 1.69 (m, 6H), 1.20 – 1.08 (m, 4H), 0.96 – 0.90 (m, 2H).  $^{13}\text{C}$  NMR (101 MHz,  $\text{CDCl}_3$ )  $\delta$  199.95, 139.93, 136.83, 132.73, 128.78, 128.56, 128.45, 128.14, 126.79, 50.39, 41.63, 35.20, 33.49, 33.20, 26.43, 26.28, 26.08.

**1,2-diphenyl-3-(thiophen-2-yl)propan-1-one (3m):** According to the procedure described in section



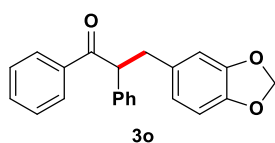
2.5.1, the mentioned product obtained as colorless solid (34 mg, 47%);  $^1\text{H}$  NMR (400 MHz, )  $\delta$  7.94 (d,  $J = 8.3$  Hz, 2H), 7.47 – 7.45 (m,  $J = 7.4$  Hz, 1H), 7.39 (t,  $J = 7.8$  Hz, 2H), 7.29 (dd,  $J = 3.8, 3.3$  Hz, 4H), 7.25 – 7.19 (m, 1H), 7.06 (d,  $J = 5.1$  Hz, 1H), 6.83 (dd,  $J = 5.1, 3.4$  Hz, 1H), 6.69 (d,  $J = 4.5$  Hz, 1H), 4.85 (dd,  $J = 7.9$  Hz, 6.6 Hz, 1H), 3.79 (dd,  $J = 15.5, 7.9$  Hz, 1H), 3.28 (dd,  $J = 14.8, 6.6$  Hz, 1H).  $^{13}\text{C}$  NMR (101 MHz,  $\text{CDCl}_3$ )  $\delta$  198.79, 142.03, 138.58, 136.44, 132.99, 128.98, 128.72, 128.50, 128.20, 127.35, 126.64, 125.68, 123.62, 56.03, 34.10, 22.34, 14.08.

**((S)-3-(furan-2-yl)-1,2-diphenylpropan-1-one (3n):** According to the procedure described in section



2.5.1, the mentioned product obtained as a pale yellow solid (20 mg, 28% yield);  $^1\text{H}$  NMR (400 MHz,  $\text{CDCl}_3$ )  $\delta$  7.93 (dd,  $J = 8.3, 1.2$  Hz, 2H), 7.5 (m, 1H), 7.4 (m, 2H), 7.3 (m, 5H), 7.2 (m, 1H), 6.2 (dd,  $J = 3.1, 1.9$  Hz, 1H), 5.9 (dd,  $J = 3.1, 0.5$  Hz, 1H), 4.98 (dd,  $J = 7.7, 6.9$  Hz, 1H), 3.60 – 3.53 (m, 1H), 3.09 (dd,  $J = 15.1, 6.8$  Hz, 1H).  $^{13}\text{C}$  NMR (101 MHz,  $\text{CDCl}_3$ )  $\delta$  198.8, 153.3, 141.1, 138.7, 136.4, 132.9, 128.9, 128.7, 128.5, 128.0, 110.2, 106.5, 52.5, 32.4.

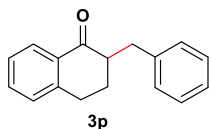
**(S)-3-(benzo[d][1,3]dioxol-5-yl)-1,2-diphenylpropan-1-one (3o):** Following the general procedure 2.5.1,



the title product was obtained as a colorless solid (48 mg, 58% yield); <sup>1</sup>H NMR (400 MHz, CDCl<sub>3</sub>) δ 7.73 – 7.71 (m, 2H), 7.46 (t, *J* = 8.2 Hz, 1H), 7.34 (t, *J* = 7.9 Hz, 2H), 7.22 – 7.12 (m, 5H), 6.60 (ddd, *J* = 20.1, 12.1, 8.0 Hz, 3H), 5.86 (dd, *J* = 3.3, 1.5 Hz, 2H), 3.98 – 3.91 (m, 1H), 3.06

(ddd, *J* = 24.3, 13.9, 8.0 Hz, 2H), 2.74 (ddd, *J* = 27.1, 13.9, 6.4 Hz, 2H). <sup>13</sup>C NMR (101 MHz, CDCl<sub>3</sub>) δ 203.3, 147.5, 145.9, 139.5, 137.5, 137.4, 133.3, 132.8, 129.0, 128.5, 128.4, 128.1, 126.3, 122.0, 109.4, 108.2, 100.8, 50.7, 38.2, 37.9.

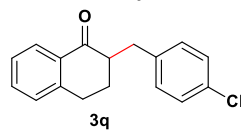
**2-Benzyl-3,4-dihydronaphthalen-1(2H)-one (3p):** According to the procedure described in section 2.5.1,



the mentioned product obtained as colorless liquid (50.2 mg, 85%); <sup>1</sup>H NMR (400 MHz, CDCl<sub>3</sub>) δ 8.07 (dd, *J* = 7.9, 1.0 Hz, 1H), 7.46 (td, *J* = 7.5, 1.4 Hz, 1H), 7.33 – 7.29 (m, 3H), 7.25 – 7.21 (m, 4H), 3.50 (dd, *J* = 13.7, 3.9 Hz, 1H),

2.96-2.91 (m, 2H), 2.79 – 2.72 (m, 1H), 2.65 (dd, *J* = 13.7, 9.6 Hz, 1H), 2.13 – 2.08 (m, 1H), 1.84 – 1.74 (m, 1H). <sup>13</sup>C NMR (101 MHz, CDCl<sub>3</sub>) δ 199.38, 144.02, 139.99, 133.26, 132.42, 129.25, 128.70, 128.38, 127.52, 126.60, 126.10, 49.43, 35.63, 28.60, 27.62.

**2-(4-chlorobenzyl)-3,4-dihydronaphthalen-1(2H)-one (3q):** According to the procedure described in



section 2.5.1, the mentioned product obtained as colorless liquid ( 61.6 mg, 91%); <sup>1</sup>H NMR (400 MHz, CDCl<sub>3</sub>) δ 8.05-8.03 (m, 1H), 7.47- 7.43 (m, 1H), 7.32- 7.26 (m, 3H), 7.24- 7.14 (m, 3H), 3.43- 3.39 (m, 1H), 2.97- 2.90 (m,

2H), 2.73- 2.61(m, 2H) , 2.11-2.02 (m, 1H), 1.81 - 1.71 (m, 1H). <sup>13</sup>C NMR (101 MHz, CDCl<sub>3</sub>) δ 199.09, 143.93, 138.63, 133.25, 132.40, 130.59, 128.69, 127.40, 126.59, 49.23, 35.20, 28.83, 27.72.

## 2.9 Results and discussion

The scanning electron microscopy (SEM) image revealed the homogeneously dispersed polyhedral crystals of MnPhen@ZIF with a particle size of ~600 nm (Figure 2.1a-2.1c).

Transmission electron microscopy (TEM) further confirmed the polyhedral morphology (Figure 2.11d-2.1f).

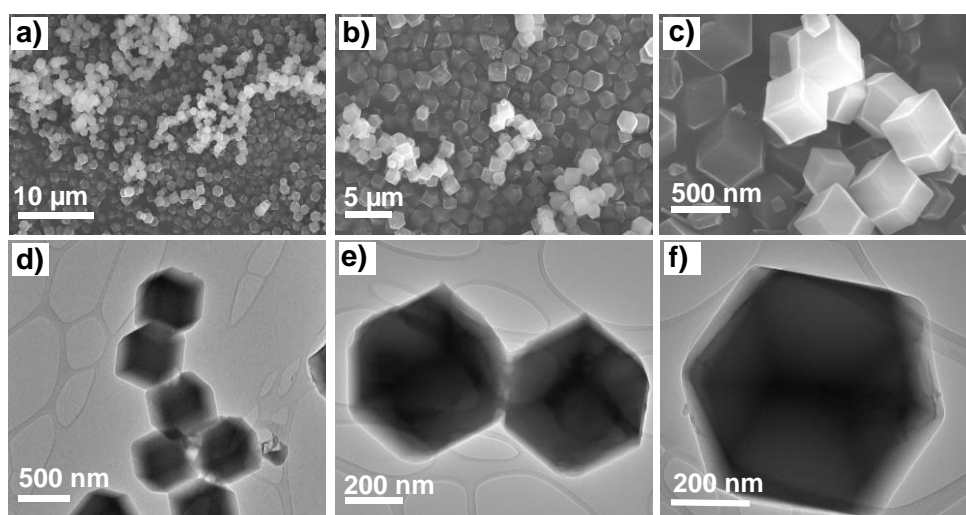


**Figure 2.1** a)-c) SEM images at different scale bars; d)-f) TEM images of the as synthesized MnPhen@ZIF catalyst.

The powder X-ray diffraction (PXRD) pattern of MnPhen@ZIF matched well with that of pristine ZIF-8, which established the phase purity (Figure 2.2). Additionally, the absence of MnPhen's distinctive diffraction peaks in MnPhen@ZIF suggests that MnPhen is not present on MOF surfaces and probably encapsulated in ZIF-8 pores.

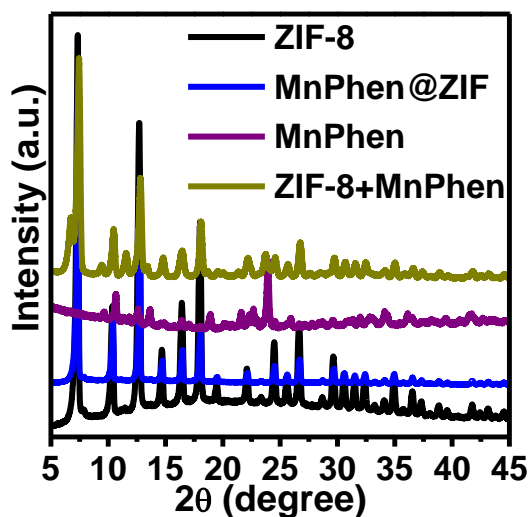


**Figure 2.2** PXRD patterns of ZIF-8, MnPhen@ZIF, MnPhen, and a mixture of ZIF-8 with MnPhen.

Brunauer–Emmett–Teller (BET) measurements suggested a decrease in the surface area of MnPhen@ZIF in comparison with that of ZIF-8, which is expected because of the encapsulation of the MnPhen complex into ZIF-8 pores (Figure 2.3). The solid-state UV-

vis spectrum of MnPhen@ZIF showed a broad peak in between 250 and 300 nm, which can be assigned to the encapsulated MnPhen complexes (Figure 2.4) [165].

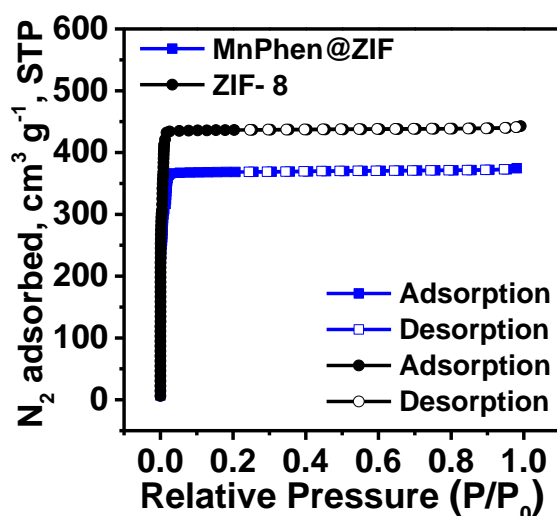


**Figure 2.3** N<sub>2</sub> sorption isotherms of ZIF-8 (black) and Mnphen@ZIF (blue), recorded at 77 K. Filled and open circles represent adsorption and desorption, respectively.

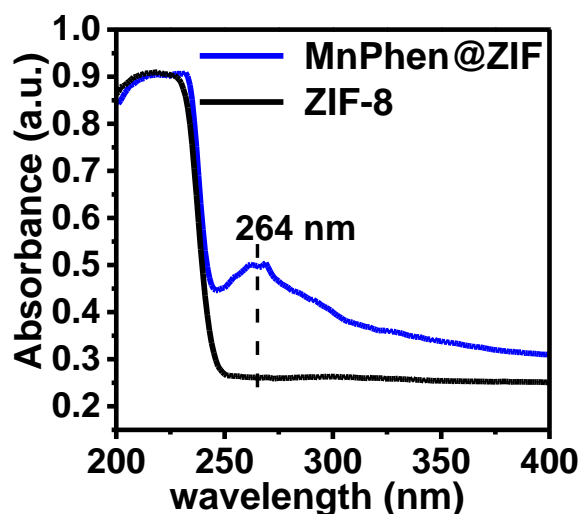


**Figure 2.4** Solid state UV-Vis spectra of ZIF-8 and MnPhen@ZIF.

High angle annular dark field scanning transmission electron microscopy (HAADF-STEM) and energy dispersive spectroscopy (EDS) elemental mapping established the presence of homogeneously dispersed Mn ions in MnPhen@ZIF (Figure 2.5).

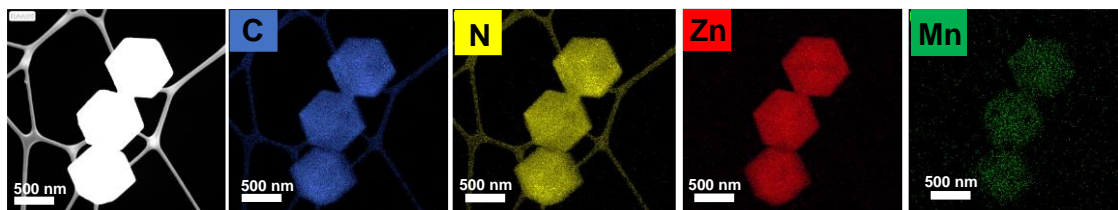


**Figure 2.5** Dark-field HAADF-STEM image of MnPhen@ZIF with the corresponding elemental mappings.

X-ray photoelectron spectroscopy (XPS) revealed weak Mn 2p peaks, which intensified after Ar-sputtering. This suggests that Mn is mostly available inside the crystals and not on the surface (Figure 2.6).

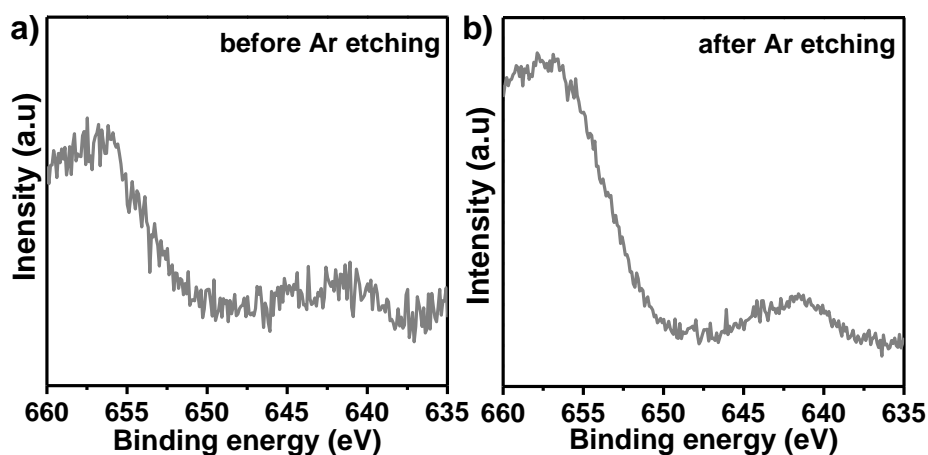


**Figure 2.6** Mn 2p XPS spectra of MnPhen@ZIF a) before Ar-etching (left), and b) after Ar etching (right). This Ar-sputtering suggests the presence of more Mn in the bulk of MnPhen@ZIF crystals.

Additionally, the color of MnPhen@ZIF is white similar to that of pure ZIF-8. This further strengthens the fact that the MnPhen complex is encapsulated into ZIF-8 (Figure 2.7).

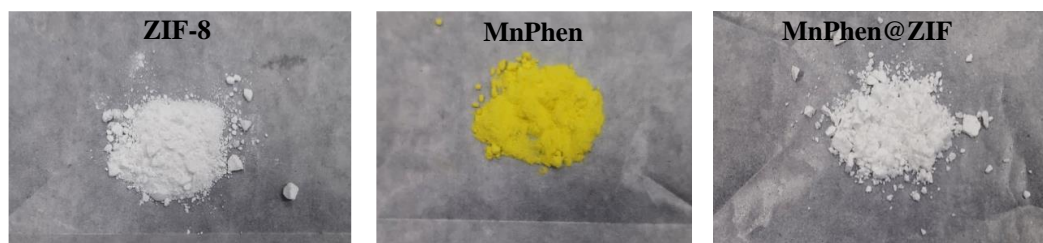
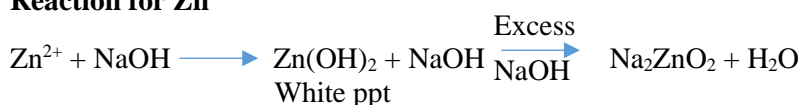


**Figure 2.7** Physical appearance of pure ZIF-8, manganese phenanthroline complex (MnPhen) and as-synthesized catalyst MnPhen@ZIF.

We also performed a Mn–NaOH test with MnPhen@ZIF, which did not give a positive result which might be because of Mn–Phen encapsulation; however, the addition of an acid, which destroyed the MOF structure, provided a positive result suggesting that the MnPhen complex is immobilized into ZIF-8 pores (Figure 2.8) [166]. Inductively coupled plasma optical emission spectroscopy (ICP-OES) suggested the presence of 0.8 wt% Mn in MnPhen@ZIF.

**Reaction for Zn<sup>2+</sup>**



**Reaction for Mn<sup>2+</sup>**

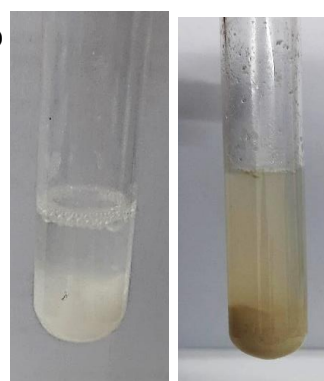
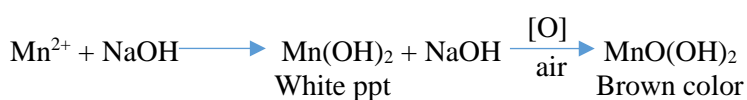


**Figure 2.8** Physical appearances of Mn-NaOH test for MnPhen@ZIF a) without, and b) with acid.

We initiated our investigation by reacting propiophenone 1a with benzyl alcohol 2a in the presence of Mnphen@ZIF and t-BuOK, which produced branched ketone 3a in 82% isolated yield (Table 2.1, entry 1). The application of Mnphen@ZIF, having a MnCl<sub>2</sub> and phen ligand ratio of 1 : 2, reduced the product yield (Table 2.1, entry 2). Different bases, KOH or K<sub>2</sub>CO<sub>3</sub>, did not further improve the catalytic performance (Table 2.1, entries 3 and 4). MnCl<sub>2</sub> was found to be the most suitable salt for the synthesis of Mnphen@ZIF (Table 2.1, entries 5 and 6). In the absence of a Mn-complex or base, product conversion was significantly reduced. ZIF-8 alone was found to be active but with lower selectivity (Table 2.1, entries 7 and 8). In order to confirm the significance of the MnPhen complex in Mnphen@ZIF, a bimetallic covalently substituted catalyst, Mn-ZIF-8, was also synthesized and tested for ketone alkylation. However, only a 52% yield of 3a was obtained



(Table 2.1, entry 9). A homogeneous system using MnPhen alone, with respect to 0.8 wt% Mn, yielded only 35% of 3a (Table 2.1, entry 10).

**Table 2.1** Optimization of reaction conditions<sup>a</sup>.

Reaction scheme: Propiophenone (1a) + Benzyl alcohol (2a)  $\xrightarrow[\text{toluene, 140 }^\circ\text{C, 24h}]{\text{MOF Catalyst (50mg), t-BuOK (1.0 equiv.)}}$  2-phenylpropan-1-one (3a) + 1-phenylpropan-2-ol (3a')

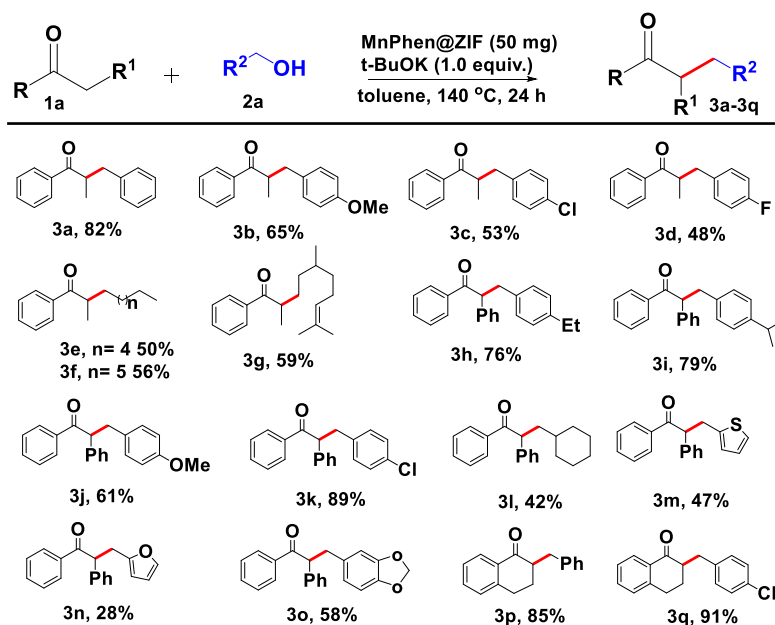
entry	Mn-salt	Mn-salt : Phen	MOF used	Catalyst Name	Base	GC-Yield (%)	
						3a	3a'
1	MnCl <sub>2</sub>	1:1	ZIF-8	MnPhen@ZIF	t-BuOK	91(82) <sup>b</sup>	8
2	MnCl <sub>2</sub>	1:2	ZIF-8	MnPhen(1:2)@ZIF	t-BuOK	57	11
3	MnCl <sub>2</sub>	1:1	ZIF-8	MnPhen@ZIF	KOH	66	3
4	MnCl <sub>2</sub>	1:1	ZIF-8	MnPhen@ZIF	K <sub>2</sub> CO <sub>3</sub>	61	4
5	Mn(OAc) <sub>2</sub>	1:1	ZIF-8	Mn(OAc) <sub>2</sub> Phen@ZIF	t-BuOK	70	5
6	Mn(OAc) <sub>2</sub>	1:2	ZIF-8	Mn(OAc) <sub>2</sub> Phen(1:2)@ZIF	t-BuOK	51	15
7	-	-	ZIF-8	ZIF-8	t-BuOK	41	19
8	MnCl <sub>2</sub>	1:1	ZIF-8	MnPhen@ZIF	No base	5	0
9	-	-	Mn-ZIF-8	Mn-ZIF-8	t-BuOK	52	10
10 <sup>c</sup>	MnCl <sub>2</sub>	1:1	-	MnPhen	t-BuOK	35	6

<sup>a</sup>Reaction conditions: propiophenone 1a (0.25 mmol), benzyl alcohol 2a (0.3125 mmol) catalyst (50 mg corresponding to 2.72 mol% Mn), base (0.25 mmol), and toluene (2.0 mL) in a 25 mL round bottom flask under an Ar atmosphere at 140 °C in an oil bath for 24 h reaction time. <sup>b</sup> Isolated yield. <sup>c</sup> 0.007 mmol of MnCl<sub>2</sub> was used corresponding to 0.8 wt% Mn present in 50 mg of MnPhen@ZIF.

Considering the optimized conditions presented in Table 2.1, various methylene ketones were reacted with a series of functionalized alcohols to synthesize branched ketones in excellent yields. For instance, propiophenone efficiently reacted with benzyl alcohols bearing electron-donating and electron-withdrawing groups and yielded 48–82% of branched ketones 3a–3g (Table 2.2). Replacing propiophenone with more hindered 1,2-diphenylethanone resulted in up to 89% yield of the desired gem-di-substituted ketones 3h–3o (Table 2.2). It can be seen that heterocyclic alcohols are also viable coupling partners delivering di-substituted ketones with good to moderate yields (Table 2.2, 3m–3o).

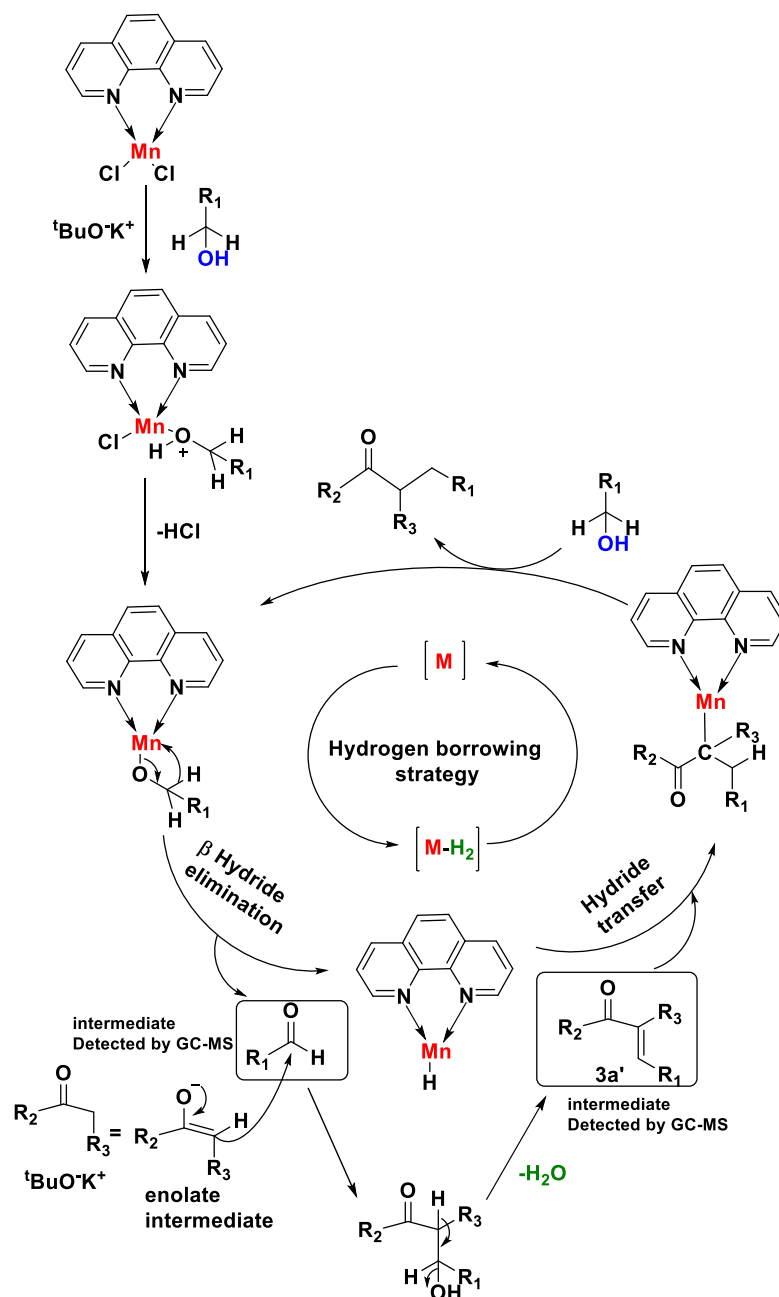
Interestingly,  $\alpha$ -tetralone provided the desired alkylated products 3p–3q with 85% and 91% yields, respectively (Table 2.2).

**Table 2.2** MnPhen@ZIF catalysed alkylation of ketones with alcohols<sup>a,b</sup>.



Reaction conditions: a Propiophenone 1a (0.25 mmol), benzyl alcohol 2a (0.3125 mmol), MnPhen@ZIF (50 mg), t-BuOK (0.25 mmol), toluene (2.0 mL) in a 25 mL round bottom flask under Ar atmosphere at 140 °C in an oil bath for 24 h reaction time. b Isolated yield.

Next, we conducted preliminary mechanistic studies for the Mn-catalysed process following the hydrogen borrowing strategy (Scheme 2.3) [157-158]. Reaction intermediates, aldehydes and enone 3a'' as shown in Scheme 2.3 were detected using gas chromatography-mass spectrometry (GC-MS).



**Scheme 2.3** Proposed mechanism for the Mn-catalyzed alkylation of ketones.

A water displacement experiment revealed 0.68 mmol of H<sub>2</sub> generation during the reaction (Figure 2.9). In a 15 mL oven dried Schlenk tube, propiophenone (0.25 mmol), benzylalcohol (0.3125 mmol), MnPhen@ZIF (50 mg), t-BuOK (0.25 mmol), toluene (2.0 mL) were mixed and flushed three times whole set up with Ar. Then gas burette was connected as mentioned in Figure 2.9. Then it was heated at 140 °C in an oil bath until

the production of H<sub>2</sub> gas ceased. The procedure was repeated three times to get more accurate results.



**Figure 2.9** The set-up made for the measurement of generated H<sub>2</sub> gas in the reaction.

**Calculation:**

Total volume of water displaced  $V = 17.1 \text{ ml} / 0.0171 \text{ L}$

Vapor pressure of water at 298K  $P_{\text{H}_2\text{O}} = 23.7695 \text{ Torr}$

Atmospheric pressure at 298K  $P_{\text{atm}} = 758.3124 \text{ Torr}$

Pressure of H<sub>2</sub> gas,

$P_{\text{H}_2} = P_{\text{atm}} - P_{\text{H}_2\text{O}} = (758.3124 - 23.7695) \text{ Torr} = 734.5429 \text{ Torr}$

Since  $P_{\text{H}_2} * V = n_{\text{H}_2} * R * T$

or  $n_{\text{H}_2} = P_{\text{H}_2} * V / R * T$

$$= 734.5429 \text{ Torr} * 0.0171 \text{ L} / 62.3635 \text{ L Torr K}^{-1} \text{ mol}^{-1} * 298\text{K}$$

$$= 0.0006758 \text{ mol}$$

$$= 0.68 \text{ mmol}$$

GC further confirmed that the collected gas is H<sub>2</sub> having a retention time of 0.54 min (Figure 2.10).

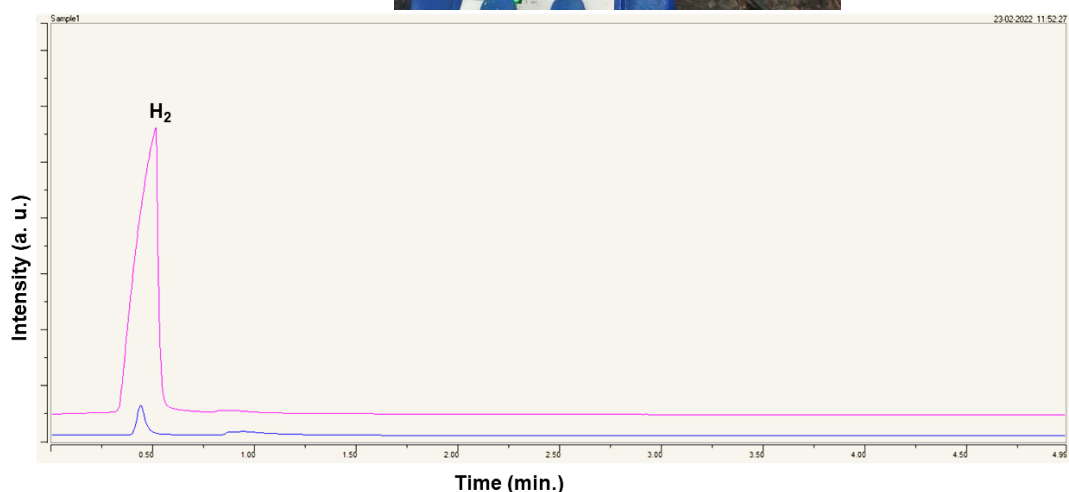
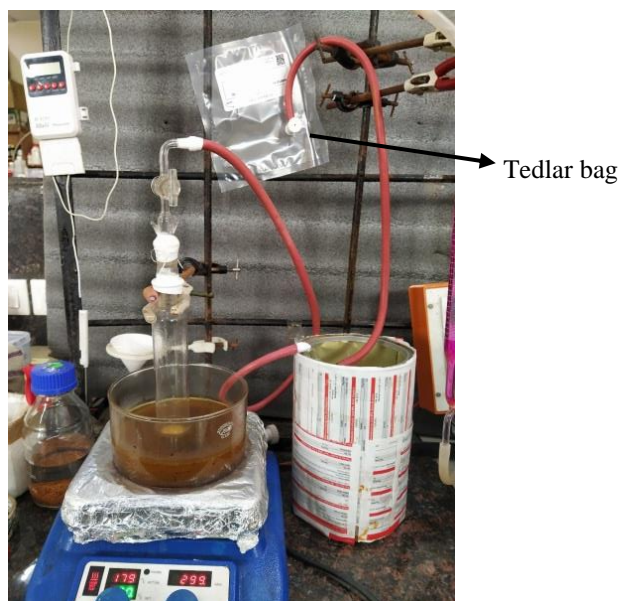
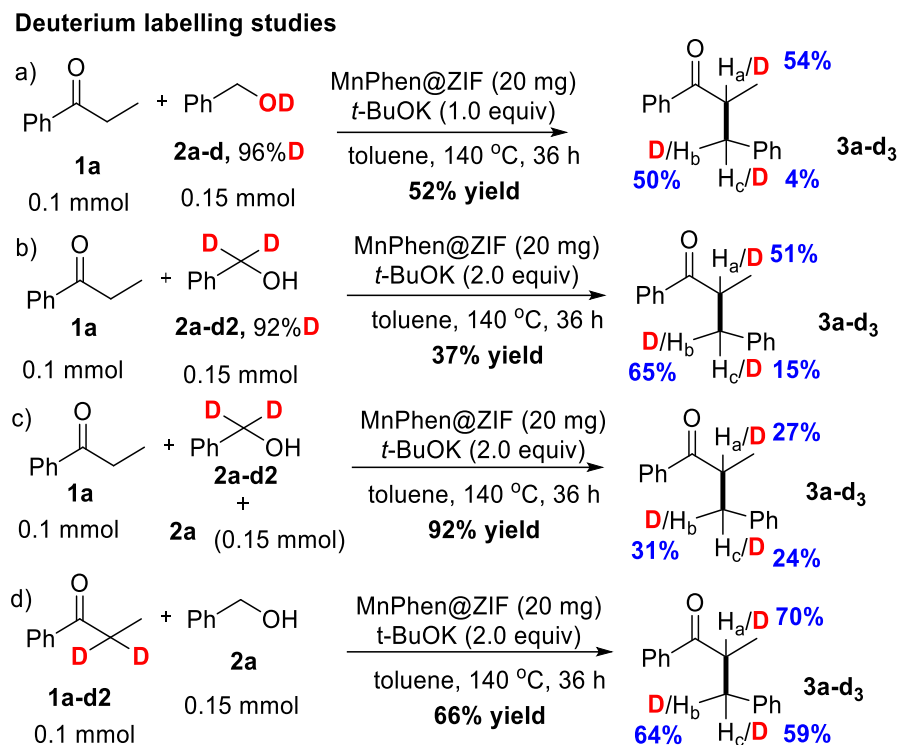


**Figure 2.10** The set-up made for the collection of generated  $\text{H}_2$  gas in the reaction (conditioned were same as mentioned in section 5) (above). Gas chromatographs of the collected gas in reaction mentioned as blue line, which has same retention time as pure  $\text{H}_2$  shown in pink line (below).

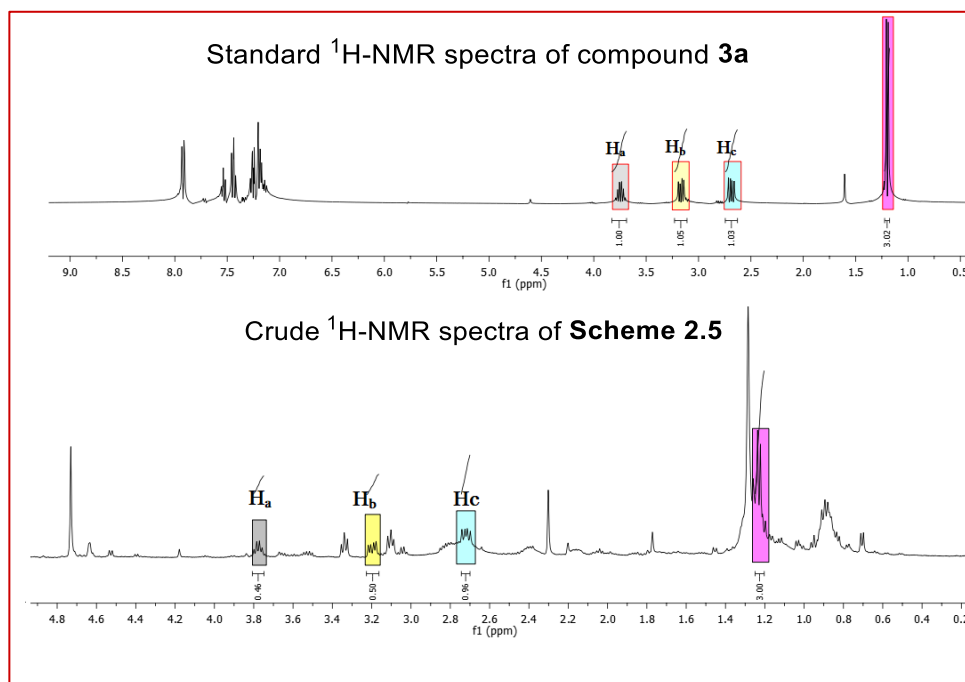
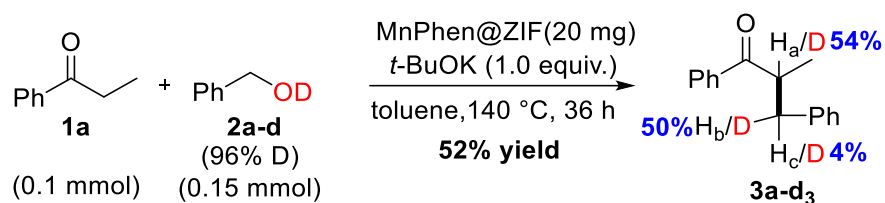
In addition, a deuterium labelling experiment of propiophenone 1a with 2a-d under standard catalytic conditions resulted in a branched ketone in 52% yield with 54–50% deuterium incorporation at the  $\alpha$ - and  $\beta$ -positions, respectively, as confirmed by  $^1\text{H}$  NMR and GC-MS analyses (Scheme 2.4a and Scheme 2.5). Similarly, the reaction of 1a with 2a-d<sub>2</sub> produced a 51–65% deuterium incorporated product (Scheme 2.4b and Scheme 2.6). Furthermore, the reaction with a 1:1 mixture of 2a-d<sub>2</sub> and 2a-d<sub>1</sub> yielded the desired ketones in 66–92% yields with 24–31% deuterium incorporation (Scheme 2.4c and Scheme 2.7). However, the reaction of 1a-d<sub>2</sub> with 2a produced a 59–70% deuterium labelled

product (Scheme 2.4d and Scheme 2.8). All these H/D scrambled products in deuterium labelling experiments together with the detection of intermediates and H<sub>2</sub> strongly support that the mechanism involves the borrowing hydrogen process [167].



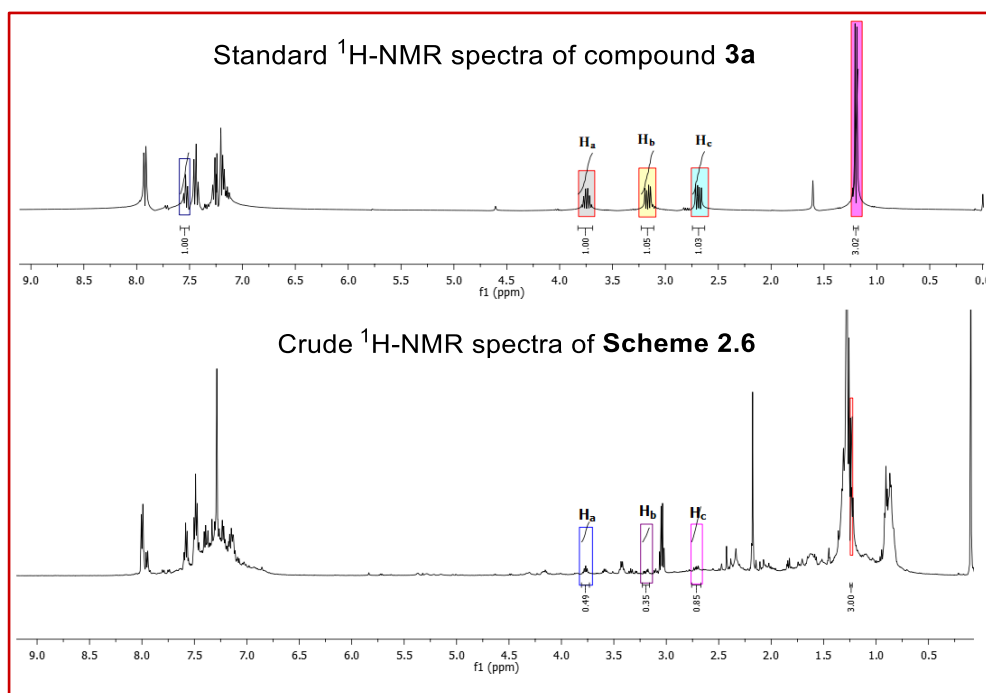
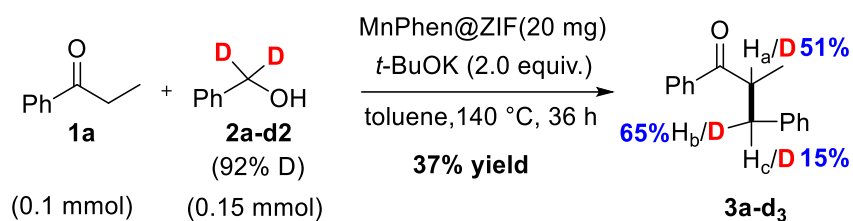
**Scheme 2.4** Reaction conditions: propiophenone 1a (0.1 mmol), benzyl alcohol 2a (0.15 mmol), MnPhen@ZIF (20 mg), t-BuOK 1.0 equiv. for (a) and 2.0 equiv. for (b)–(d), toluene (2 mL) under an Ar atmosphere, a Schlenk tube used under an Ar atmosphere, 140 °C, 36 h time.

**Scheme 2.5** Deuterium labelling experiments between 1a with 2a-d.



		Deuterium incorporation in H <sub>a</sub> Position	Deuterium in in Deuterium incorporation in H <sub>b</sub> Position	Deuterium in Deuterium incorporation in H <sub>c</sub> Position	
Signal (ppm)	δ	1.2 [d, CH <sub>3</sub> , (3H)]	3.77 (1H)	3.19 (1H)	2.71 (1H)
Integral Value		3.0	0.46	0.50	0.96
Calculated ratio			(1-0.46)×100 = 54%	(1-0.50)×100 = 50%	(1-0.96)×100 = 4%

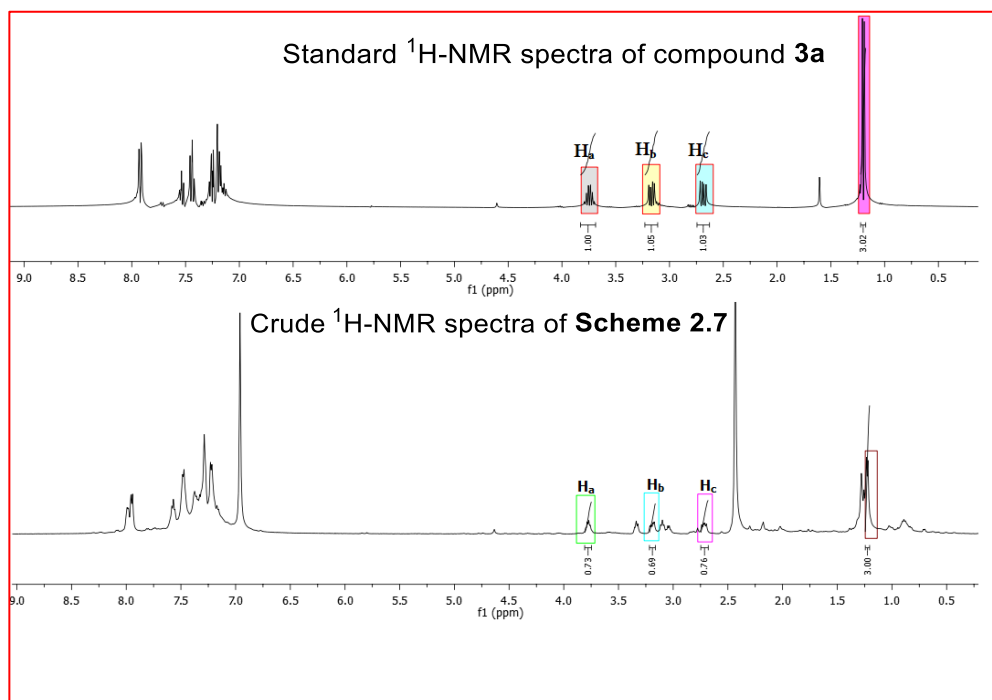
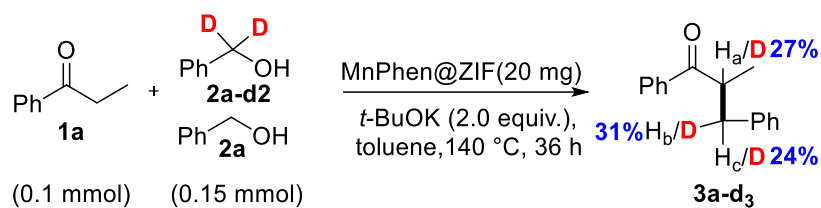
**Scheme 2.6** Deuterium labelling experiments between 1a with 2a-d<sub>2</sub>.



		Deuterium in- corporation in H <sub>a</sub> Position	Deuterium in- corporation in H <sub>b</sub> Position	Deuterium in- corporation in H <sub>c</sub> Po- sition
<b>Signal δ (ppm)</b>	1.2 [d, CH <sub>3</sub> , (3H)]	3.77 (1H)	3.19 (1H)	2.71 (1H)
<b>Integral Value</b>	3.0	0.49	0.35	0.85
<b>Calculated ra- tio</b>		(1-0.49)×100 = <b>51%</b>	(1-0.35)×100 = <b>65%</b>	(1-0.85)×100 = <b>15%</b>

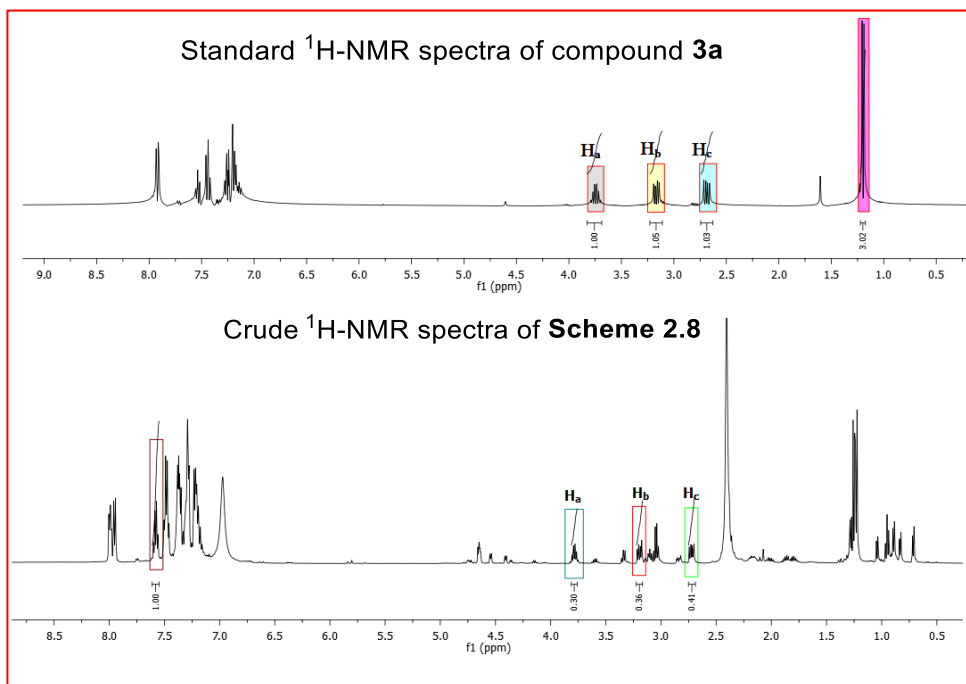
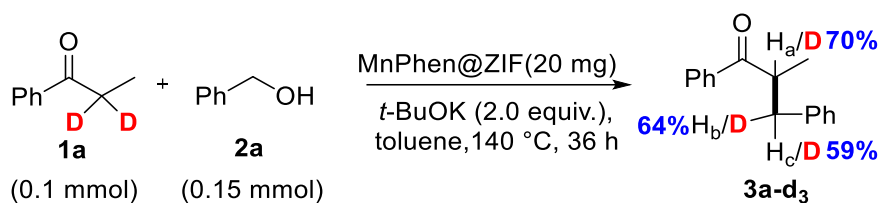


**Scheme 2.7** Deuterium labelling experiments between 1a with mixture of 2a & 2a-d<sub>2</sub>.



		Deuterium in- corporation in H <sub>a</sub> Position	Deuterium in- corporation in H <sub>b</sub> Position	Deuterium in- corporation in H <sub>c</sub> Position
<b>Signal δ (ppm)</b>	1.2 [d, CH <sub>3</sub> , (3H)]	3.77 (1H)	3.19 (1H)	2.71 (1H)
<b>Integral Value</b>	3.0	0.73	0.69	0.76
<b>Calculated ratio</b>		(1-0.73)×100 = 27%	(1-0.69)×100 = 31%	(1-0.76)×100 = 24%

**Scheme 2.8** Deuterium labelling experiments between 1a-d<sub>2</sub> with 2a.



			Deuterium incorporation in H <sub>a</sub> Position	Deuterium incorporation in H <sub>b</sub> Position	Deuterium incorporation in H <sub>c</sub> Position
Signal (ppm)	$\delta$	7.54 [m, <i>p</i> -Ar-H, (1H)]	3.77 (1H)	3.19 (1H)	2.71 (1H)
Integral Value		1.0	0.30	0.36	0.41
Calculated ratio			(1-0.30)×100 = <b>70%</b>	(1-0.36)×100 = <b>64%</b>	(1-0.41)×100 = <b>59%</b>

MnPhen@ZIF was found to be a good performing heterogeneous catalyst with significant retention of its original catalytic activity (Figure 2.11).

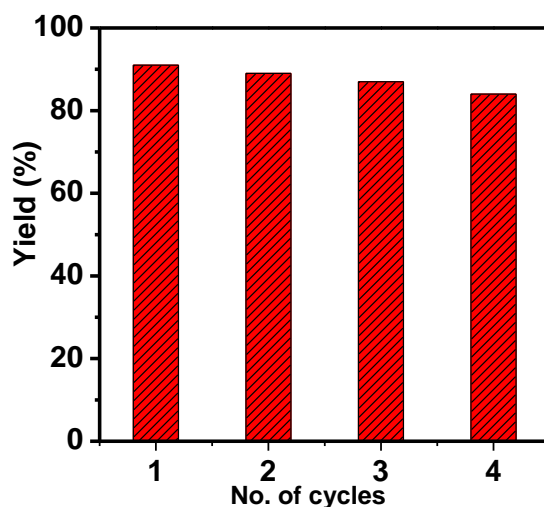


**Figure 2.11** Recyclability test of MnPhen@ZIF for the synthesis of 2-Methyl-1,3-diphenylpropan-1-one (3a).

Moreover, the used catalyst was examined. TEM images revealed the retention of the size and shape of most of the MnPhen@ZIF nanocrystals (Figure 2.12a-2.12c). Although, a few broken or surface-etched crystals were observed in the sample.

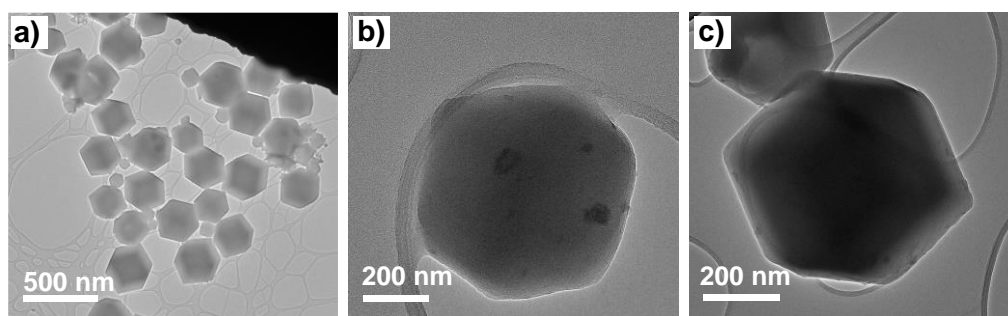


**Figure 2.12** a)-c) TEM images of MnPhen@ZIF after catalysis.

BET and PXRD analyses of the used MnPhen@ZIF catalyst suggested a decrease in the surface area and retention of crystallinity, respectively (Figure 2.13a, 2.13b). However, the pore size distribution (PSD) derived from Figure 2.13a suggested an increase in pore size (Figure 2.13c). The broadening of the peak in the range of 1.2–1.6 nm indicates the generation of larger pore sizes after catalysis. The formation of such defects is known for MOF systems, which might be favourable for the transportation of reactants and

products. EDS elemental mapping further confirmed the homogeneous distribution of atomic manganese within the crystals and eliminated the probability of formation of metal aggregates during the catalysis process (Figure 2.14).

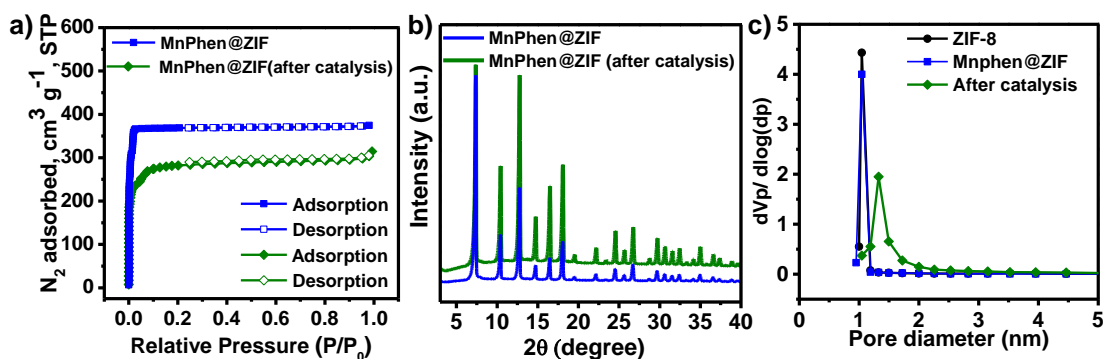


**Figure 2.13** a)  $N_2$  adsorption–desorption curves b) PXRD patterns of MnPhen@ZIF before and after catalysis, c) Pore size distribution of ZIF-8, MnPhen@ZIF (before catalysis), and MnPhen@ZIF (after catalysis).

**Table 2.3** Pore size and pore volume of MnPhen@ZIF and supporting catalysts.

Catalyst	Average pore size (nm)	Average pore volume ( $\text{cm}^3 \text{g}^{-1}$ )
ZIF-8	1.21	0.68
MnPhen@ZIF (before catalysis)	1.20	0.66
MnPhen@ZIF (after catalysis)	1.47	0.52

Furthermore, inductively coupled plasma-optical emission spectrometry (ICP-OES) measurements of the reaction filtrate revealed the presence of the Zn element, which is due to the formation of point defects within the MOF frameworks. However, we did not observe any Mn leaching within the reaction filtrate that might be because of the nature of the coordinated ligand Phen, which strongly get stabilized within the ZIF-8 cavities via supramolecular interactions and prevent Mn from leaching into the solution. The hot

filtration method was tested using a hot frit to separate out the solid catalysts at ~2 h time, and a reaction using the filtrate was continuously run for 24 h. Figure 2.15 shows that the reaction did not proceed in the absence of MnPhen@ZIF, and the product yield remains unaltered. This concluded that MnPhen@ZIF catalyzes the reaction and is solely responsible for the catalytic activity.

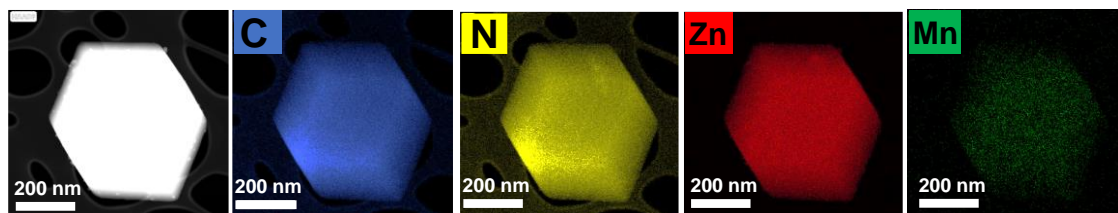


**Figure 2.14** HAADF-STEM image of used MnPhen@ZIF with the corresponding elemental mapping of C, N, Zn and Mn.

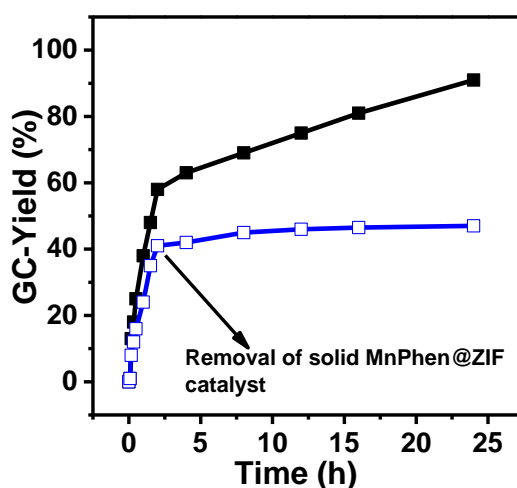


**Figure 2.15** Hot filtration test indicating no further formation of branched ketone product 3a after removal of solid MnPhen@ZIF catalyst. Black line curve is product formation vs time plot till completion of the reaction (24 h), while blue curve is for second batch of reaction where catalyst was removed by hot filtration at the time of ~2 h.

Also, thermogravimetric analysis (TGA) suggested that MnPhen@ZIF is stable at the experimental reaction temperature, i.e., 140 °C (Figure 2.16).

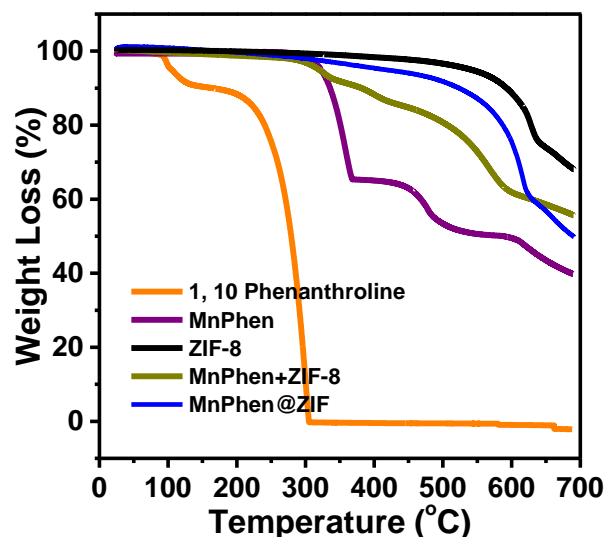


**Figure 2.16** A comparison of TGA curves of as-synthesized catalyst MnPhen@ZIF, a mixture of MnPhen+ZIF-8 complex, pristine ZIF-8, MnPhen complex, and Phen ligand itself. This data suggests that MnPhen@ZIF and its encapsulated Mn-complex is stable under experimental catalytic reaction temperature ie; at 140 °C.

ZIF-8 is a microporous MOF and its catalytic activity is largely explained on the basis of Lewis acidic or basic sites present on its external surfaces [168-170]. This might be the reason that pristine ZIF-8 alone produced 41% of branched ketone (Table 2.1, entry 7). Therefore, the encapsulated MnPhen complex plays an important role in obtaining higher yield and selectivity. Comparison of the ammonia-temperature programmed desorption (NH<sub>3</sub>-TPD) profiles of fresh and used catalysts revealed a greater integrated peak for the latter (Figure 2.17). This confirmed that more low coordinated metal sites (Lewis acidic sites) are generated during the catalytic reactions.

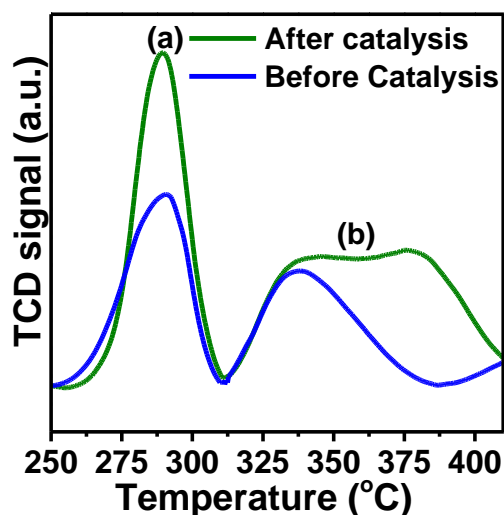


**Figure 2.17** NH<sub>3</sub>-TPD profiles for MnPhen@ZIF before and after catalysis.

**Table 2.4** Lewis acidity calculation from NH<sub>3</sub> TPD.

MnPhen@ZIF	Acidity (mmol/g)
<b>Before catalysis</b>	a) 9.51
	b) 8.17
<b>After catalysis</b>	a) 16.69
	b) 21.92

Moreover, the XPS spectra of the used catalyst also showed a higher intensity of O 1s peaks, corresponding to Zn coordinated OH/OH<sub>2</sub> (Figure 2.18). The generation of Zn–OH/ OH<sub>2</sub> sites is because of the breaking of the Zn-imidazolate bonds of ZIF-8 during the reactions and the formation of larger size cavities, as observed above in BET and PSD measurements. Such a pore enlargement is expected to facilitate the transportation of reactants and products during reactions.

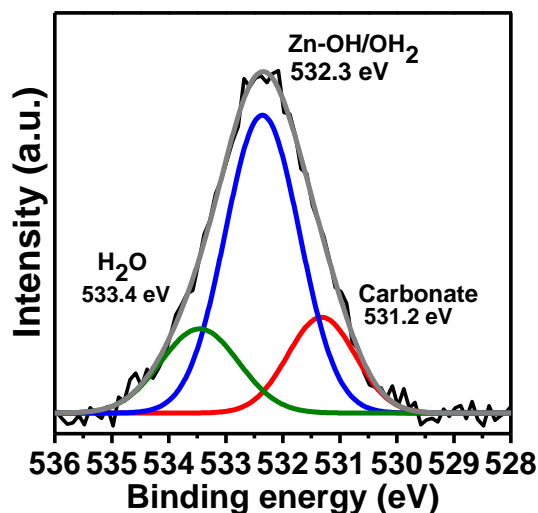


**Figure 2.18** O 1s XPS spectrum of MnPhen@ZIF after catalysis.

Next, kinetics studies were performed to determine the rate and order of the reaction (Figure 2.19a). First order kinetics was observed with respect to 1a considering a steady state approximation for 2a. In addition, although ZIF-8 itself shows good catalytic activity, the presence of MnPhen affects the catalytic activity of MnPhen@ZIF a lot in terms of either product selectivity or the rate of product formation. MnPhen@ZIF provided ~50% of product 3a in the initial 1.5 h, while ZIF-8 provided <10% only (Figure 2.19b).

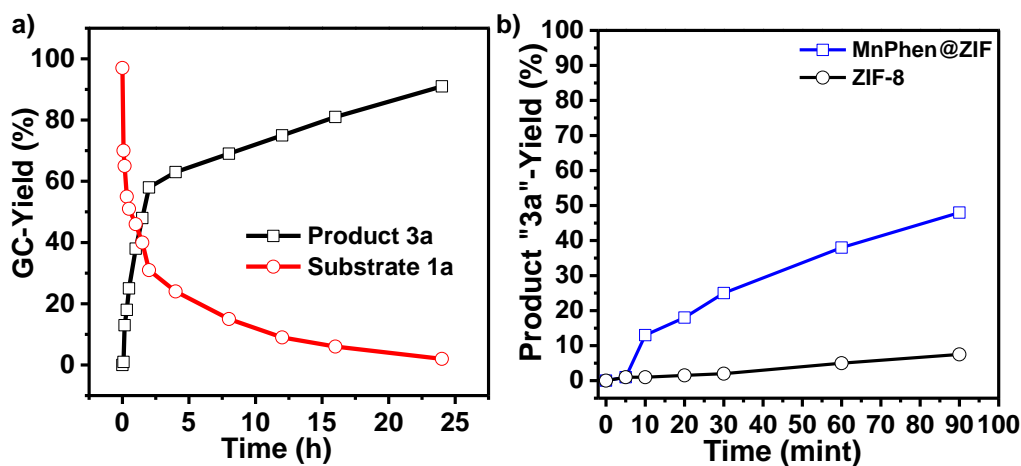


**Figure 2.19** a) Formation of product 3a and decrease in concentration of 1a with reaction time in presence of catalyst MnPhen@ZIF, b) Comparison of product 3a formation with respect to initial period of time in presence of catalyst MnPhen@ZIF and ZIF-8.



## **2.10 Conclusion**

In conclusion, we have developed an Earth-abundant Mn-based heterogeneous catalyst, using the method of immobilization of a homogeneous MnPhen complex into MOF pores, for the selective synthesis of branched ketones. Mechanistic studies, controlled deuterium labelling experiments, and kinetics studies demonstrated the hydrogen borrowing strategy, releasing water and hydrogen as byproducts, for di-substituted ketones.

This page was intentionally left blank.

## **Chapter 3: Carbon Nanofibers Coated With MOF-Derived Carbon Nanostructures For Vanadium Redox Flow Batteries With Enhanced Electrochemical Activity And Power Density**

### **3.1 Abstract**

A unique synthetic approach has been introduced where nanostructurally grown zinc layered double hydroxide on graphitic carbon felt (CF) is converted into a zeolitic imidazolate framework (ZIF-8), and then, subsequent carbonization resulted in a N/O-functionalized porous carbon electrode (N,O/CF). Because of the presence of N/O-containing functional groups and deposition of ZIF-8-derived nanoporous carbon on the CF, the N,O/CF is found to be highly hydrophilic in nature with a large surface area. Cyclic voltammetry measurements with N,O/CF suggest the fast electrochemical kinetics of V(IV)  $\leftrightarrow$  V(V) reactions. Polarization curves and electrochemical impedance spectroscopy measurements of the vanadium redox flow battery (VRFB) assembly illustrate the significant decrease in charge transfer resistance at electrode surfaces. At 50 mL/min electrolyte flow rate, N,O/CF delivers energy efficiencies of 83.11 and 76.66% at current densities of 40 and 80 mA/cm<sup>2</sup>, respectively. The values are 82.59 and 76.39%, respectively, at 100 mL/min, showing the negligible effect of the flow rate. The power density of VRFBs at various electrolyte flow rates is also presented, which increases with increasing flow rates and is higher for N,O/CF ( $\sim$ 821 mW/cm<sup>2</sup>) than for bare CF (606 mW/cm<sup>2</sup>). The stability test confirms the retention of energy, voltage, and coulombic efficiencies after recycling of the electrode. The above-mentioned findings of improved performance of VRFBs with employing the N,O/CF electrode are a cumulative effect of enhanced nanoporosity, an increased number of catalytic active sites, high wettability, and low charge transfer resistance.

## 3.2 Introduction

Depletion of fossil fuels, environmental pollution, and energy crisis has engendered the higher utilization of renewable and sustainable energy such as solar or wind energy, etc [171–174]. To meet the growing demand, large-scale energy devices, which must be safe and cost-effective, are required to store the energy harvested from different energy sources, to use it for various applications and to connect with the grid [175–178]. Among available storage technologies, the application of redox flow batteries (RFBs) has been rising with great assurance [179–185]. In RFBs, energy storage and power generation are decoupled. The choice of flexibility in design, high safety, and long-life cycle make vanadium redox flow batteries (VRFB) a promising device [186–190]. They utilize vanadium ions, which exist in four different oxidation states. During the charging process, at the positive side, V(IV) oxidizes to V(V), whereas at the negative side, V(III) converts into V(II); reverse reactions occur during discharging. The electrolytes in the battery are separated by an acidic, cation exchange membrane. The reaction involving V(V)/V(IV) interconversion is sluggish which limits the efficiency of the VRFB system [190]. Thus, the electrodes supporting electrochemical conversion play a crucial role in determining the power density and energy efficiency of the VRFB system by providing active sites for vanadium redox reactions [191–193].

Graphite felt and carbon paper, which are commonly used as electrodes in VRFBs, show poor electrochemical activity, leading to limited power and current outputs. To address this issue, structural engineering and surface modifications are suggested to design new carbon electrodes [194–196]. Although absorption of active species such as metals, metal oxides, and metal nitrides on the felt support is used in the electrode development, their high-cost, instability, and poor electronic conductivity inhibit application in the battery system [197–204]. Structural engineering involves designing nanoporous structures to

decorate complex interfaces [205–209]. A sacrificial template is used to introduce nanopores on graphite felt, resulting in an improved energy efficiency.<sup>37</sup> Similarly, a wood-derived carbon electrode is used, which improves the battery performance due to the presence of aligned channels and large pores [208]. A graphene hybrid electrode or nanoporous platelet carbon grown on carbon felt is also used as electrode materials for improving the VRFB system [209]. Very recently,  $\text{LaBO}_3$  ( $B = \text{V}, \text{Cr}, \text{Mn}$ ) perovskites have been demonstrated for superior electrochemical kinetics toward vanadium redox reactions in VRFBs [210].

The surface modification approach involves the covalent adhering of functional groups, such as  $-\text{OH}$ ,  $-\text{COOH}$ , and  $\text{C}=\text{O}$ , on the electrode surfaces [211,212]. Similarly, electrode surfaces can be decorated with nonmetal heteroatoms such as nitrogen, phosphorus, and sulfur atoms [213-215]. With this functionalization, the hydrophilicity of the carbon electrode is greatly enhanced, and most importantly, favorable edge sites and defects are incorporated in the felt carbon structures, which significantly enhance the vanadium redox reaction kinetics [216]. In addition, surface functionalization enhances the electrode stability and the electrical conductivity, which are essential for electrochemical reactions. For example, graphene nanowall-incorporated carbon felt is found to be excellent in vanadium redox reaction activity owing to the presence of exposed graphene edge sites [217]. N-doped carbon spheres decorated on graphite felt or polypyrrole-derived N-doped graphite felt exhibit high electrochemical activity in the battery [217,218]. Similarly, N/P or N/S dual-doped carbon electrodes have also been proven to be excellent electrodes for VRFBs [218-221]. Despite the great efforts in electrode development for VRFBs, more work is needed to establish a correlation between surface functionalization and properties of the developed electrodes.

Metal–organic frameworks (MOFs) are porous coordination polymers and are known for their high surface area, tunable porosity, and multifunctional applications [222–229]. MOF derived carbons have emerged as high-performance electrode materials for energy storage devices [230-234]. These carbon materials often show large surface area and high porosity like their parent MOFs. Additionally, by controlling the carbonization temperatures, the structure and surface chemistry of the carbon materials can be tuned to optimize the conductivity, active sites, and charge transfer processes beneficial for catalytic electrochemical redox reactions [235,236]. Recently, MOF-derived materials such as zirconium oxide porous carbon nanocomposites [237], nanoporous platelet carbons grown on carbon felt [238], and N-doped carbon nanotubes [239] have been demonstrated as high-performance positive/negative electrodes in VRFBs.

Herein, we present a unique approach to fabricate a nanoporous N and O-decorated carbon electrode using high temperature carbonization of the ZIF-8 film, made up of highly porous zinc-imidazolate MOF, directly grown on the surfaces of commercial graphitic carbon felt (CF) with the help of layered zinc hydroxide sheets (Zn-LDH). Dual heteroatom functionalization increases the hydrophilicity and thus the wettability of the as-synthesized N,O/CF electrode surfaces. N,O/CF shows lower charge transfer resistance and better electrochemical activity for vanadium redox reactions in comparison to bare CF that is used generally. Also, it delivers a high energy efficiency and power density of VRFBs at varying current densities and electrolyte flow rates.

### **3.3 Experimental**

#### **3.3.1 Chemicals**

Zinc nitrate hexahydrate ( $\text{Zn}(\text{NO}_3)_2 \cdot 6\text{H}_2\text{O}$ ), AR grade, 2-methylimidazole, hexamethylene tetramine (HMTA), sulfuric acid 98%, methanol (MeOH), and hydrogen peroxide 6% (w/v) ( $\text{H}_2\text{O}_2$ ) were purchased from SD Fine-Chem Limited. Vanadyl (IV) sulfate 97% ( $\text{VOSO}_4 \cdot x\text{H}_2\text{O}$ ) and vanadium oxide ( $\text{V}_2\text{O}_3$ ) were purchased from Sisco Research

Laboratories Pvt. Ltd. and Alfa-Aesar, respectively. Graphite felt was purchased from Fuel Cell Store; the Nafion 117 membrane was supplied by Alfa Aesar.

### 3.3.2 Synthesis

**3.3.2.1 Synthesis of Zn-LDH/CF:** First, commercial graphitic carbon felt (Bare CF) of 5 cm<sup>2</sup> area was pretreated at 450 °C for 5 h in argon to remove any amorphous carbon deposited on the surfaces. The treated carbon felt was then soaked in a 20 mL methanol solution of 1.90 g of zinc nitrate hexahydrate and 0.5 g of HMTA. The mixture was transferred into a 25 mL autoclave and solvothermally heated at 90 °C for 24 h with a heating rate of 1 °C/min. After cooling to room temperature, the carbon felt was washed with methanol several times and dried under vacuum at 60 °C for 4 h. The dried sample was named as Zn-LDH/CF.

**3.3.2.2 Synthesis of ZIF-8/CF:** The above-mentioned as-synthesized Zn-LDH/CF was soaked in a 15 mL methanol solution of 2- methylimidazole (2 g) for 24 h, which allowed the growth of ZIF-8 nanocrystals on the surfaces of the carbon felt. The whitish material was separated from the solution and washed with methanol thoroughly. It was dried under vacuum at 60 °C for 4 h and designated as ZIF-8/CF.

**3.3.2.3 Synthesis of N,O/CF:** The as-synthesized ZIF-8/CF was carbonized at 1000 °C for 4 h under an argon flow (50 mL/min) with a heating rate of 5 °C min<sup>-1</sup>. The resultant dark-black material was then treated with 10% H<sub>2</sub>SO<sub>4</sub> at 80 °C for 6 h to remove any excess zinc. Subsequent washing with water and vacuum drying resulted in N,O/CF.

### 3.4 Materials Characterization

Scanning electron microscopy (SEM) measurements were performed employing a JEOL JXA 8230 operated at 20 kV. Transmission electron microscopy (TEM) images were acquired using a Talos F200S G2 TEM operated at 200 kV, equipped with an in-colum

energy dispersive X-ray spectrometer (EDS) and a CMOS camera detector. X-ray photoelectron spectroscopy (XPS) was performed on a Thermo Fisher Scientific (K-Alpha) equipped with an Al K $\alpha$  source (10 kV, 10 mA) having attached with an ion source (EX06). X-ray diffraction (XRD) studies were performed on a PANalytical diffractometer using a Cu K $\alpha$  source ( $\lambda = 1.5405 \text{ \AA}$ ) with  $2^\circ/\text{min}$  scan rate and a step size of  $0.05^\circ$ . The Brunauer–Emmett–Teller (BET) surface area of electrodes after activation at  $150^\circ\text{C}$  under vacuum for 6 h was measured using  $\text{N}_2$  as an adsorbate at liquid nitrogen temperature ( $77 \text{ K}$ ). The BET equation used here for calculation of surface area is  $P/V_a(P_0 - P) = 1/V_m C + (C - 1)P/(V_m C)P_0$ . BET surface area calculations for samples were calculated using software provided within the BELSORP MAX II, the equipment used for measuring  $\text{N}_2$  adsorption and desorption isotherms. Isotherm points chosen to calculate the BET surface area were subject to the three consistency criteria detailed by Walton and Snurr [240]. First, the pressure range selected should have values of  $P/V_a(P_0 - P)$ , increasing with  $P/P_0$ . Second, the points used to calculate the BET surface area must be linear with an upward slope. Third, the line they form must have a positive y-intercept. Water adsorption capacity of both N,O/CF and bare CF electrodes, using degassed DI water, was also measured at  $25^\circ\text{C}$  employing a BELSORP Max. For this, the electrode samples were pretreated at  $150^\circ\text{C}$  for 4 h. Degassing of DI water was accomplished by sequentially freezing in liquid nitrogen and heating using hot water. Raman spectra were recorded with a Princeton instruments (Acton Spectra Pro-2500i) using a 532 nm DPSS laser (laser quantum gem with a power of 50 mW). A slow motion camera, Phantom AMETEK (VEO 640L), was used to examine the wettability of electrodes.



### 3.5 Electrochemical measurements

Cyclic voltammetry (CV) studies were performed on an electrochemical workstation (CHI604E, CH Instruments). A typical three-electrode system was used for measuring CVs in 0.5 M VOSO<sub>4</sub> + 1 M H<sub>2</sub>SO<sub>4</sub> electrolyte, where Pt mesh was employed as a counter electrode (5 cm<sup>2</sup>), with Ag/AgCl as a reference electrode and bare CF or N,O/CF as a working electrode. The working electrode was dipped up to a surface area of 0.12 cm<sup>2</sup>. The scan rate was fixed at 5 mV/s, and five cycles were performed. Data of the third cycle were reported. A single cell of the VRFB was assembled as per the protocol provided in the literature [241]. The cell was constructed with two interdigitated flow fields, two 5 mm-thick gaskets with a cavity of 5 cm<sup>2</sup> to place electrodes, two copper current collectors, and two end plates as shown in Figure 3.13. A bare CF or N,O/CF with a size of 5 cm<sup>2</sup> was used as both an anode and cathode, separated with a Nafion 117 membrane. A 857 redox flow cell test system (Scribner Associates, Inc.) was employed to evaluate the performance of the VRFB, employed with bare CF and N,O/CF electrodes alternatively. Before starting the measurements, the battery assembly was tested for leakage by varying flow rates of distilled water and, subsequently, with 4 M H<sub>2</sub>SO<sub>4</sub>. This step helps in removing impurities from the assembly and in hydration of the membrane. The required V(II) and V(V) oxidation states of vanadium in the corresponding negative and positive tanks were obtained by two-step electrochemical charging of starting solution of 1 M VOSO<sub>4</sub> + 4 M H<sub>2</sub>SO<sub>4</sub>. All electrochemical measurements were performed by continuously purging the electrolyte tanks with nitrogen gas. Polarization curves of the battery were obtained by pumping positive and negative electrolytes in the corresponding sides of the cell at four flow rates: 30, 50, 80, and 120 mL/min. Potential was measured during discharging the solution for 30 s at a fixed current density. The applied current density was increased by a step of 5 mA/cm<sup>2</sup> until the potential reaches zero, i.e., limiting

current density. Electrochemical impedance spectroscopy (EIS) measurements of the fully charged solution at the above-mentioned four flow rates were performed by varying the frequency from 10 kHz to 0.001 Hz. The obtained highfrequency response was used to get iR-free polarization curves. Voltage efficiency (VE), energy efficiency (EE), and coulombic efficiency (CE) of the battery were calculated from charge–discharge curves using the following equations

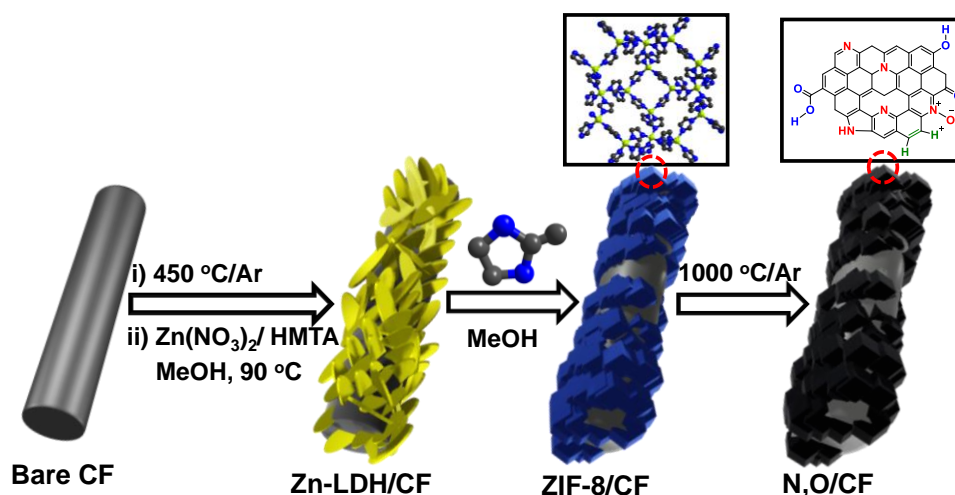
$$VE = \frac{\text{Average discharge voltage (V)}}{\text{Average charge voltage (V)}} \times 100 \%$$

$$CE = \frac{\text{Discharge capacity (A.h)}}{\text{Charge capacity (A.h)}} \times 100 \%$$

$$EE = \frac{\text{Charge energy (W.h)}}{\text{Discharge energy (W.h)}} \times 100 \%$$

### 3.6 Results and discussion

The schematic diagram for the synthesis of the N,O/CF electrode is presented in Scheme 3.1.



**Scheme 3.1** Schematic representation of the synthesis of N,O/CF from bare CF.

The SEM image of bare CF revealed a smooth and clean surface and have a nanofibrous structure (Figure 3.1), whereas Zn-LDH/CF has uniformly coated layered zinc hydroxide nanoflakes on CF (Figures 3.2).

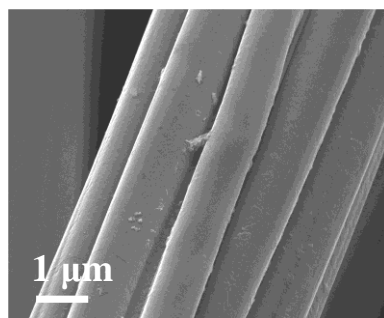


**Figure 3.1** SEM images of bare CF.

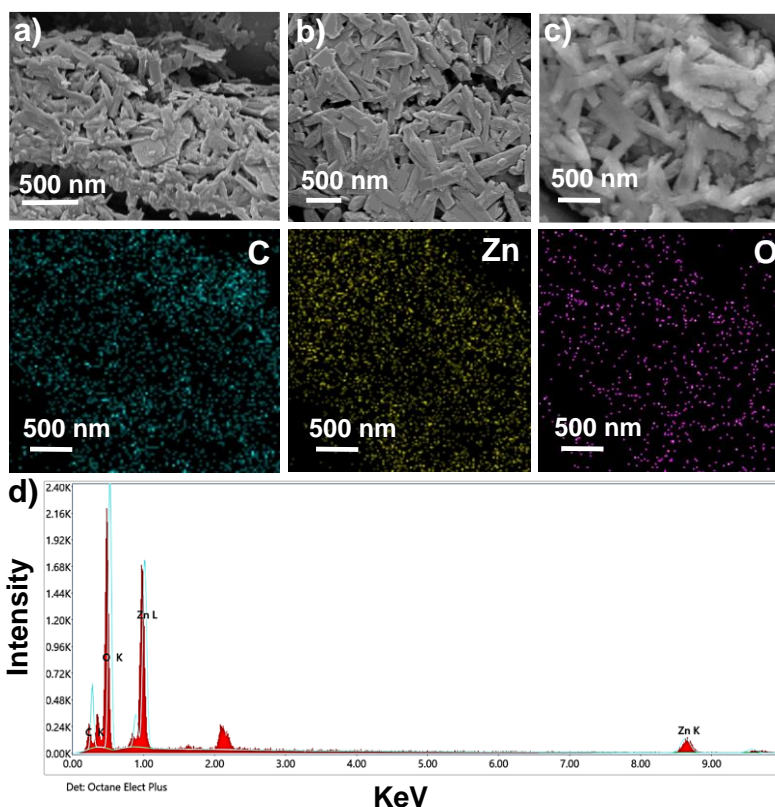


**Figure 3.2** SEM images of a-b) Zn-LDH/CF. c) SEM image of Zn-LDH/CF with corresponding elemental mappings (C, Zn, O). d) EDX spectrum of Zn-LDH/CF (The peak at ~2.2 eV is from Au coating).

After the treatment of Zn-LDH/CF with 2-methylimidazole, a homogeneous growth of ZIF-8 nanocrystals on CF can be seen in ZIF-8/CF (Figure 3.3). SEM images further revealed that these deposited ZIF-8 nanocrystals are tightly bounded to the CF surfaces. Subsequent carbonization of ZIF-8/CF at 1000 °C under an argon atmosphere resulted in N and O-functionalized carbon electrode, N,O/CF. The SEM image of N,O/CF showed porous and rough surfaces, where the deposited ZIF-8 is converted into nanoporous

carbon structures (Figure 3.4a,b). Interestingly, a tightly bound ZIF-8-derived porous carbon film can be seen on the CF surfaces (Figure 3.4c). The carbon film has a typical interconnected polyhedral structure and grown homogeneously all over the CF [242]. As the zinc metal boiling point is  $\sim 910^{\circ}\text{C}$ , after pyrolyzing at  $1000^{\circ}\text{C}$ , carbon-reduced zinc was evaporated, generating the nanopores within carbon structures. As a precaution, we also treated N,O/CF with acid to remove zinc (if any) before characterization and electrochemical measurements. N,O/CF was physically more flexible and dark black, whereas bare CF was hard and grayish (Figure 3.5).

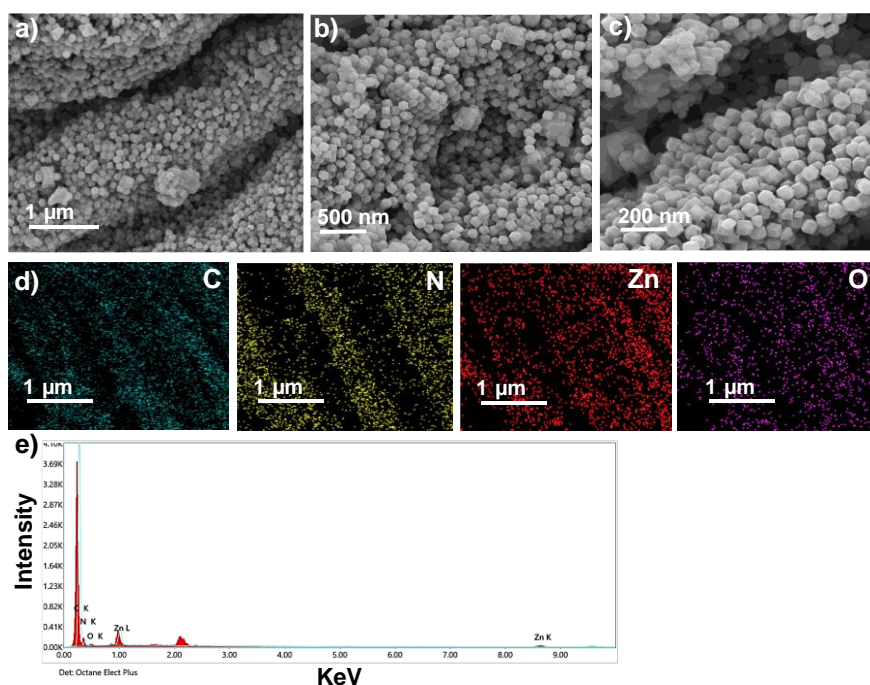


**Figure 3.3** a-c) SEM images of ZIF-8/CF at different resolutions. d) Corresponding EDX elemental mappings (C, Zn, N, O). e) EDX spectrum of ZIF-8/CF (The extra peak at  $\sim 2.2$  eV is from Au coating).

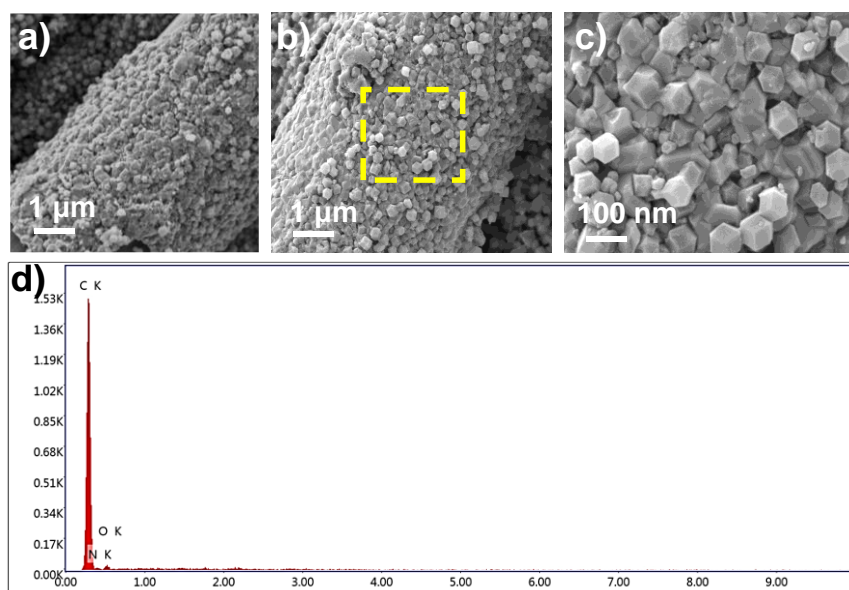


**Figure 3.4** a)-b) SEM images of as-synthesized N,O/CF. c) High-resolution SEM image of the area highlighted in yellow in b).

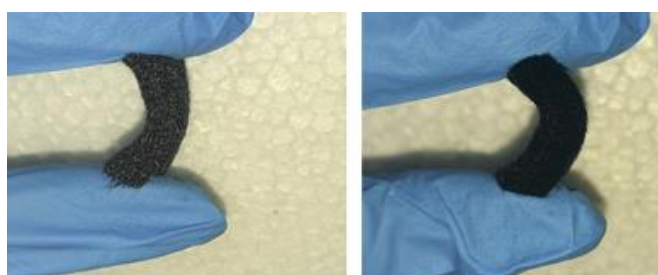


**Figure 3.5** Digital photographs of bare CF (left) and as-synthesized N,O/CF (right).

No zinc or zinc oxide nanoparticles were observed in TEM images of N,O/CF (Figures 3.6). Figure 3.6a-c further verifies the SEM observation that the ZIF-8-derived carbon is present in the form of a film with interconnected polyhedral carbons and is porous in nature. EDX elemental mapping of N,O/CF reveals only the presence of C, N, and O elements (Figure 3.6e). EDX analysis suggests that N,O/CF contains 6.6 wt % of N and 12.6 wt % of O, which are sufficiently high values to be a good hydrophilic carbon electrode.

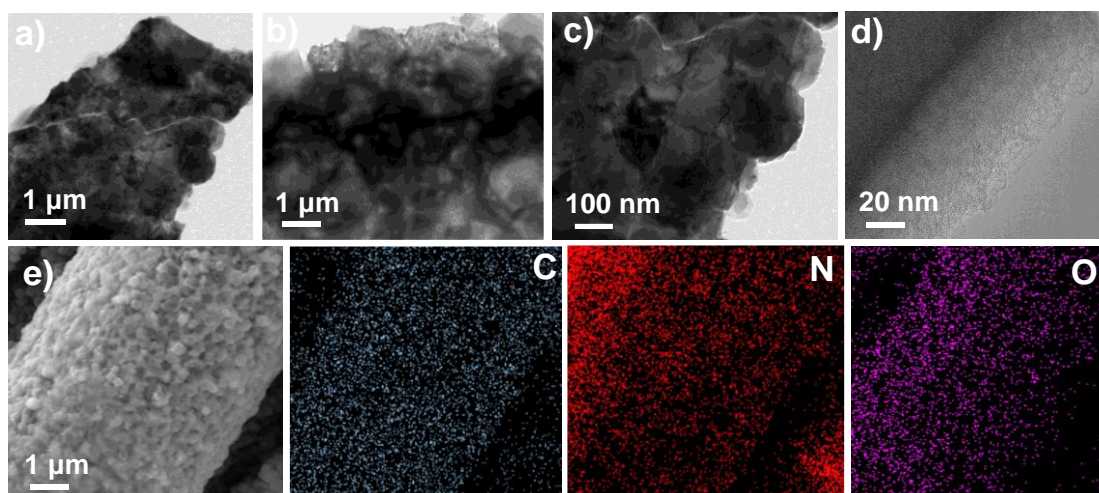


**Figure 3.6** a)-d) TEM images of N,O/CF. (e) SEM image of N,O/CF with the corresponding elemental mappings C, N, and O.

XRD pattern of Zn-LDH/CF reveal the major presence of layered zinc double hydroxide, although some amount of zinc oxide was also detected (Figure 3.7a). After growing the ZIF-8, that of the resulting ZIF-8/CF well matched with the XRD pattern of the simulated ZIF-8. This suggests that most of the Zn-LDH was converted into ZIF-8, although some amount of Zn-LDH was still left in the sample. After carbonization of ZIF-8/CF in an Ar atmosphere at 1000 °C, the obtained sample N,O/CF shows only two XRD peaks at around 25.2 and 44°, which correspond to the (002) and (110) planes of graphitic carbon. This suggests that N,O/CF is made up of carbon materials and free of any metal nanoparticles, further validating the TEM observations. Raman spectra reveal two notable peaks at 1345 and 1590  $\text{cm}^{-1}$ , assigned to D- and G-bands of graphitic carbon, respectively (Figure 3.7b). The ratio of relative peak intensities of D- and G-bands in N,O/CF is 0.87, which is lower in comparison to that of bare CF (1.02). This suggests that N,O/CF has a more ordered graphitic structure than that of bare CF. The higher degree of graphitization of N,O/CF also suggests it to be a better electronically-conductive and corrosion-resistant electrode for electrocatalysis [217].

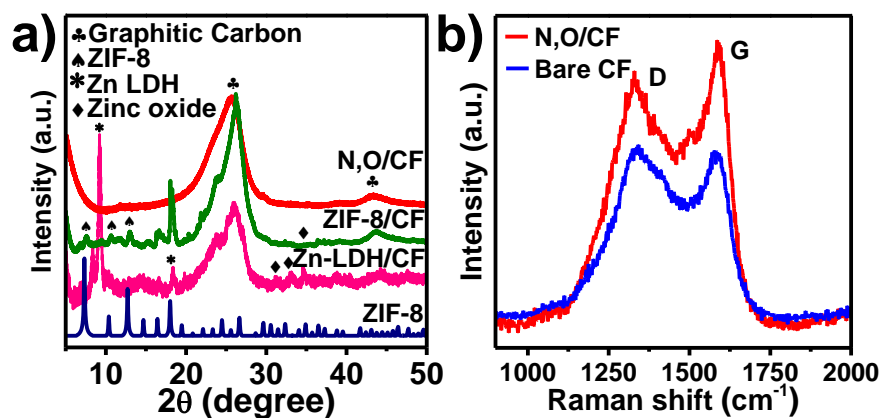


**Figure 3.7** a) PXRD patterns, (b) Raman spectra of N,O/CF and bare CF.

The estimated BET surface area from N<sub>2</sub> adsorption–desorption curve analysis reveals enhancement from 1.80 to 190 m<sup>2</sup>/g (Figure 3.8a). The pore size distribution of N,O/CF demonstrates both microporosity and mesoporosity in N,O/CF with a pore volume of 0.125 cm<sup>3</sup>/g, which is missing in bare CF (Figure 3.8b). Higher pore volume and larger surface area are expected to provide higher catalytic active sites and their access to the electrolyte.

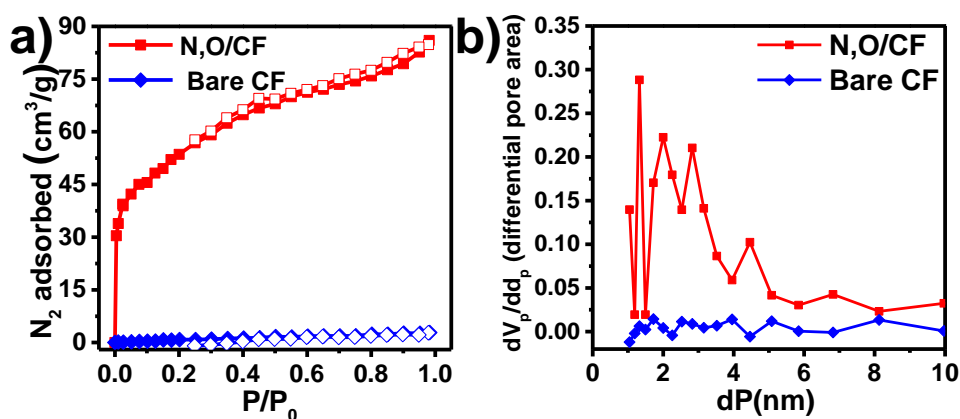


**Figure 3.8** a) N<sub>2</sub> adsorption–desorption isotherms of bare CF and N,O/CF, (b) Pore size distribution of bare CF and N,O/CF calculated from their corresponding N<sub>2</sub> sorption isotherms.

The XPS analysis conducted on the N,O/CF electrode to find the chemical composition and to determine the types of functional groups suggests the presence of carbon, nitrogen, and oxygen elements only. C 1s peaks indicate the presence of C–N bonds and C–OH

species together with delocalized C=C bonds (Figure 3.9a). The deconvoluted N 1s peaks at 398.7, 399.9, 401.1, and 402.3 eV correspond to pyridinic N, pyrrolic N, graphitic N, and oxidic N, respectively (Figure 3.9b). O 1s mainly consists of –OH, –COOH, and –C=O functional groups (Figure 3.9c). Conclusively, the XPS results clearly illustrate the successful decoration of CF with nitrogen and oxygen functional groups, with domination of pyridinic/pyrrolic nitrogen and –OH groups.

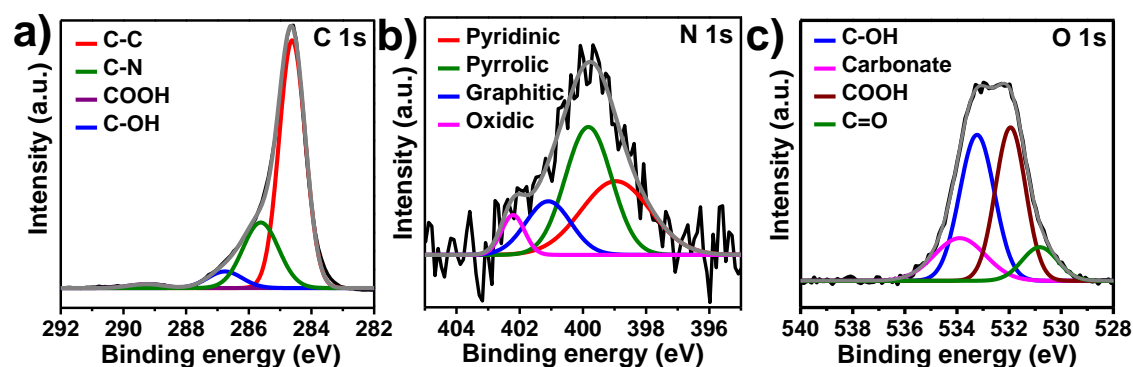


**Figure 3.9** XPS of a) C 1s, b) N 1s, and c) O 1s of N,O/CF.

Surface functionalization with nitrogen and oxygen also helped in improving the hydrophilic nature of N,O/CF, resulting in faster uptake of the electrolyte and its distribution in the nanoporous spaces of the electrode. The hydrophilic nature of N,O/CF was diagnosed using a surface wettability test, which suggests that the residence time of the water droplet on the N,O/CF surface is very small and the droplet gets absorbed within the pores immediately, while the water droplet on bare CF remains there for an appreciable amount of time (Figure 3.10).

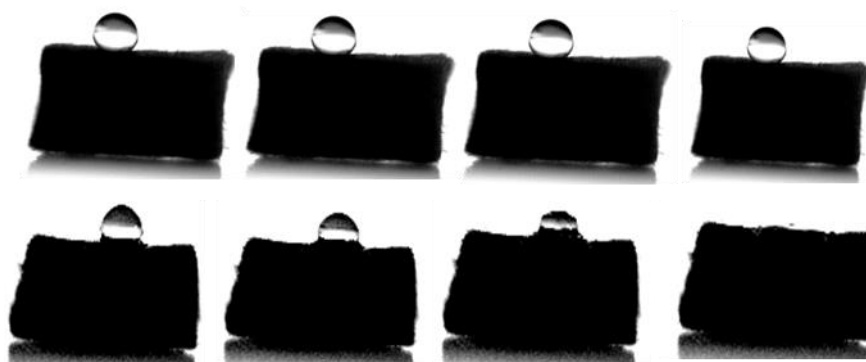




**Figure 3.10** Wettability test of bare CF (up) and N,O/CF (down) using a slow motion camera; pictures captured within a gap of milliseconds.

Furthermore, the water adsorption capacity of N,O/CF was measured and found approximately five times higher than that of bare CF (Figure 3.11). These findings clearly suggest that nano structuring CF with N- and O-decorated carbons helps in introducing hydrophilic characteristics in the electrode, which is desirable for its high-performance electro-chemical activity.

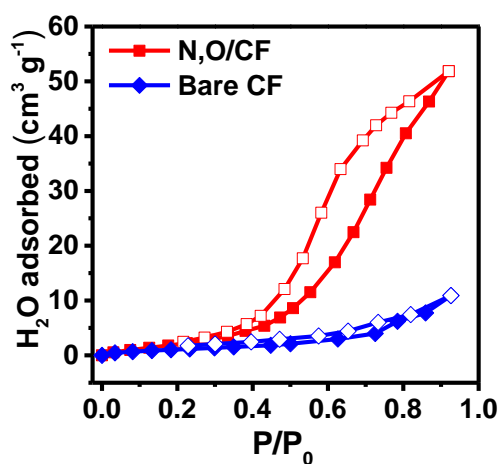


**Figure 3.11** H<sub>2</sub>O adsorption–desorption isotherms of bare CF and N,O/CF.

### 3.6.1 Electrochemical and Flow Battery Test

CV measurements of bare CF and N,O/CF electrodes in 0.5 M VOSO<sub>4</sub> + 1 M H<sub>2</sub>SO<sub>4</sub> illustrate two current peaks; for the former, they are at potentials of 0.36 and 1.25 V and for the latter, they are at 0.58 and 1.10 V, respectively (Figure 3.12a). These potentials are associated with oxidation and reduction reactions for interconversion, V(IV) ↔ V(V). The difference between peak potentials,  $\Delta E_p$ , for bare CF and N,O/CF is 0.89 and 0.52 V, respectively, comparable to the reported values [242]. The onset potentials for bare CF and N,O/CF are 0.93 and 0.87 V, respectively. A comparison of the highest anodic peak current densities illustrates that the value is ~3 times higher for N,O/CF (574 mA/cm<sup>2</sup>) than that for bare CF (190 mA/cm<sup>2</sup>). The evaluated ratio of anodic and cathodic peak currents for N,O/CF is closer to 1, while it is higher than 1 for bare CF. Similarly,

CV spectra with bare CF and N,O/CF were measured in 0.01 M  $V_2O_3$  in 1 M  $H_2SO_4$  to determine the oxidation and reduction potentials for the  $V(II) \leftrightarrow V(III)$  redox couple (Figure 3.12b). Again, a larger anodic and cathodic current was observed for N,O/CF in comparison with bare CF. The measured  $\Delta E_p$  value for N,O/CF was found to be 260 mV, which is much lower than that for bare CF (440 mV). These  $\Delta E_p$  values, onset potential, current density, and the ratio of peak current densities clearly conclude that the electrochemical reactions are more facile at the N,O/CF electrode, resulting from its highly electrochemically active surfaces [243]. The enhanced electrochemical activity of N,O/CF is directly related to N doping and O functionalization, stemming from its improved electrical conductivity, increased number of catalytic active sites for oxidation and reduction of vanadium species, and enhanced wettability.

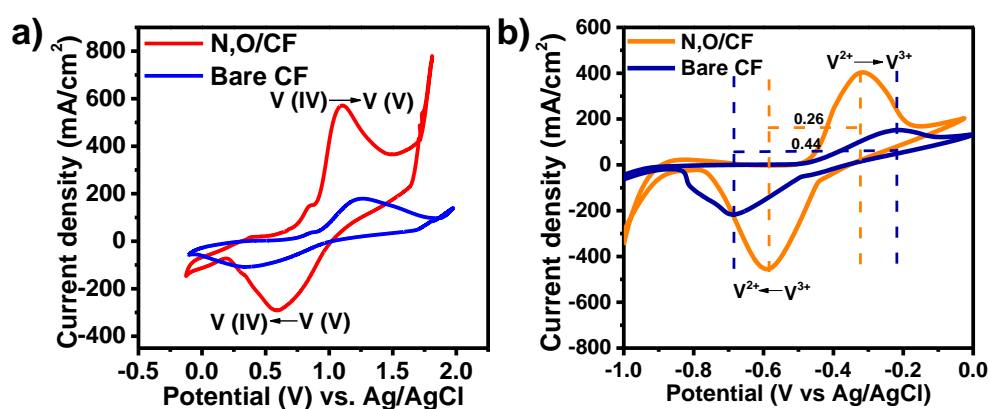


**Figure 3.12** a) Cyclic voltammetry in 0.5 M  $VOSO_4 + 1.0 M H_2SO_4$  at a scan rate 5 mV/s, b) Cyclic voltammograms of bare CF and N,O/CF using 0.01 M  $V_2O_3$  in 1M  $H_2SO_4$  with scan rate of 5 mV/s.

The performance of battery assembly, employed with N,O/CF as both the anode and cathode with an interdigitated flow path (Figures 3.13 and 3.14), was examined using our flow battery workstation (Figure 3.15). For comparison, similar experiments were also performed using the bare CF electrode.

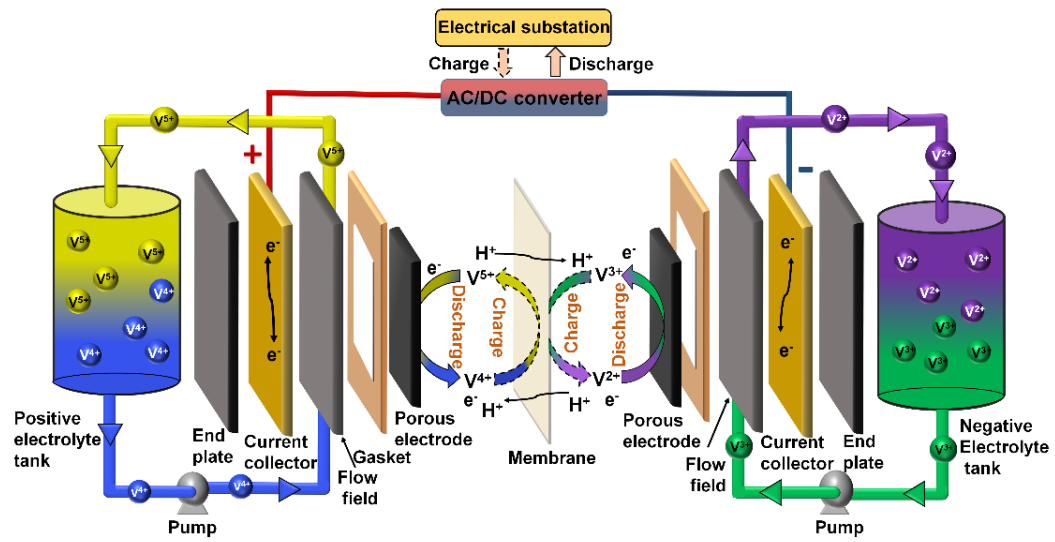


**Figure 3.13** Schematic representation of vanadium redox flow battery (VRFB).

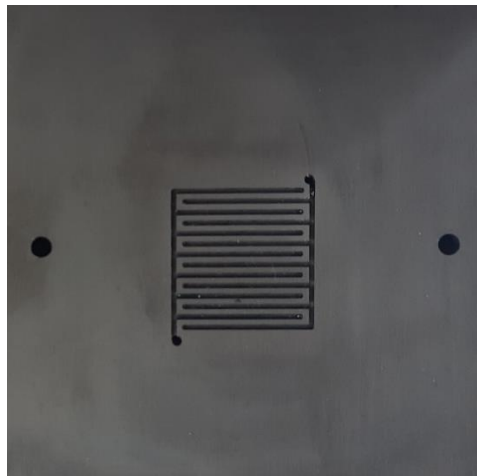


**Figure 3.14** The digital image of interdigitated flow field plate used in our VRFB experiments.

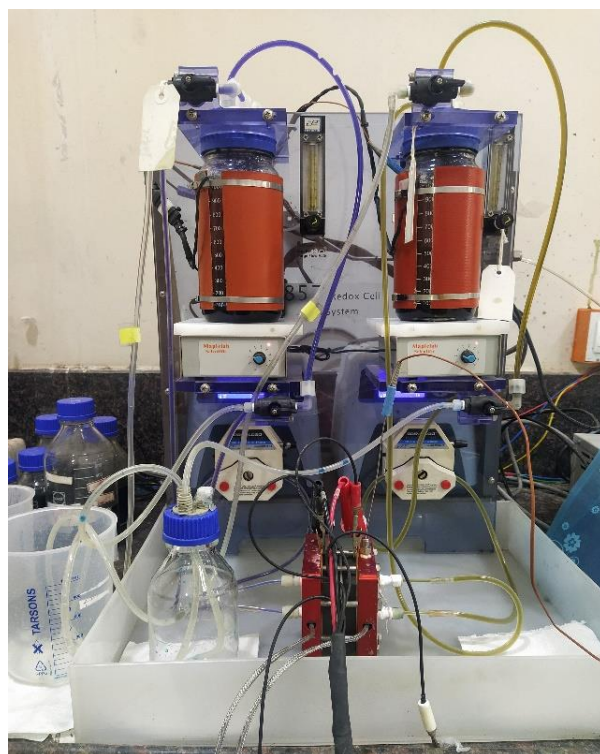


**Figure 3.15** The vanadium redox flow battery workstation used for measurements.

After accomplishing the two-step charging procedure, polarization curves of the battery were obtained by varying the electrolyte flow rates and are presented in Figure 3.16. These figures also show the power density variation, which was evaluated from potential and current density. The average open-circuit potential (OCP) values are  $\sim 1.525$  V using bare CF, which is similar to that reported in the literature [241], and 1.60 V for the N,O/CF electrode. The higher potential value clearly indicates that higher energy can be stored in the electrolyte using the modified electrode.

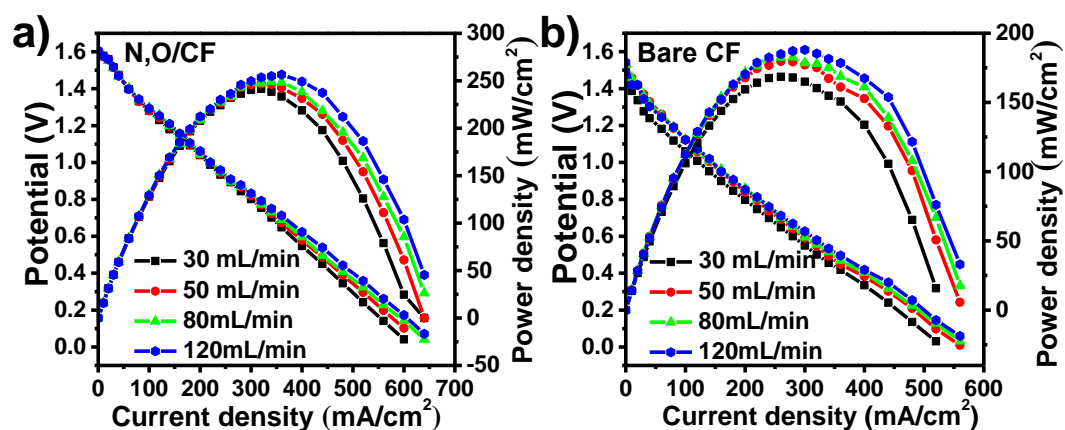


**Figure 3.16** a) N,O/CF and b) bare CF at electrolyte flow rates of 30, 50, 80, and 120 mL/min in the VRFB.

The trend of potential drop with increasing current density is almost similar for both the electrodes (Figure 3.17). Due to the higher potential of the battery at any withdrawn current density, N,O/CF helps achieve higher power density. Polarization curves are a characteristic of an energy device. Loss of potential from the OCP value is due to kinetic, ohmic, and mass transfer resistances, stemming from slow kinetics at the catalyst surface, ionic resistance of membrane and electronic resistance of battery components, and the concentration gradient of electroactive species. EIS measurements, performed by varying electrolyte flow rates, were used to decouple and estimate these resistances. Results for N,O/CF and bare CF electrodes are presented as Nyquist plots in Figure 3.18 a,b. A depressed semicircle for bare CF indicates that charge transfer resistance at one electrode is high enough to overwhelm the resistance at the other electrode, while two partially overlapping depressed semicircles for N,O/CF are a result of comparable charge transfer resistance at both the anode and cathode. The value at the leftmost intercept of a circle on the Z axis approximates the ohmic resistance of the membrane. To extract values for these resistances, an equivalent electrical circuit was modeled by fitting the obtained Nyquist plot using inbuilt Zview software. The circuit parameters  $R_s$ ,  $R_{CT}$ , and CPE are ohmic resistance, charge transfer resistance, and constant phase element, respectively,

and their values are presented in Tables 3.1 and 3.2 for N,O/CF and bare CF, respectively. Results show that the values of  $R_s$  are in the range of 0.36–0.38  $\Omega$  for both N,O/CF and bare CF, almost invariant with the type of the electrode and flow rate. The lower area of the membrane (5  $\text{cm}^2$ ) leads to higher  $R_s$  values than those previously reported [241]. The cumulative value of two charge transfer resistances,  $R_{CT1}$  and  $R_{CT2}$ , for N,O/CF is lower than that for bare CF; for example, at 30 mL/min, the resultant  $R_{CT}$  for the former is  $0.34 + 0.22 = 0.56\Omega$ , which is much lower than 24.36  $\Omega$ , the value for the latter. This concludes that N,O/CF has better charge transfer kinetics than that of bare CF. The CPE values  $<1$  for these electrodes at all electrolyte flow rates indicate the pseudocapacitive nature at the electrode–electrolyte interface, stemming from double layer formation. In conclusion, a mixed resistive and capacitive behavior is present in both N,O/CF and bare CF.

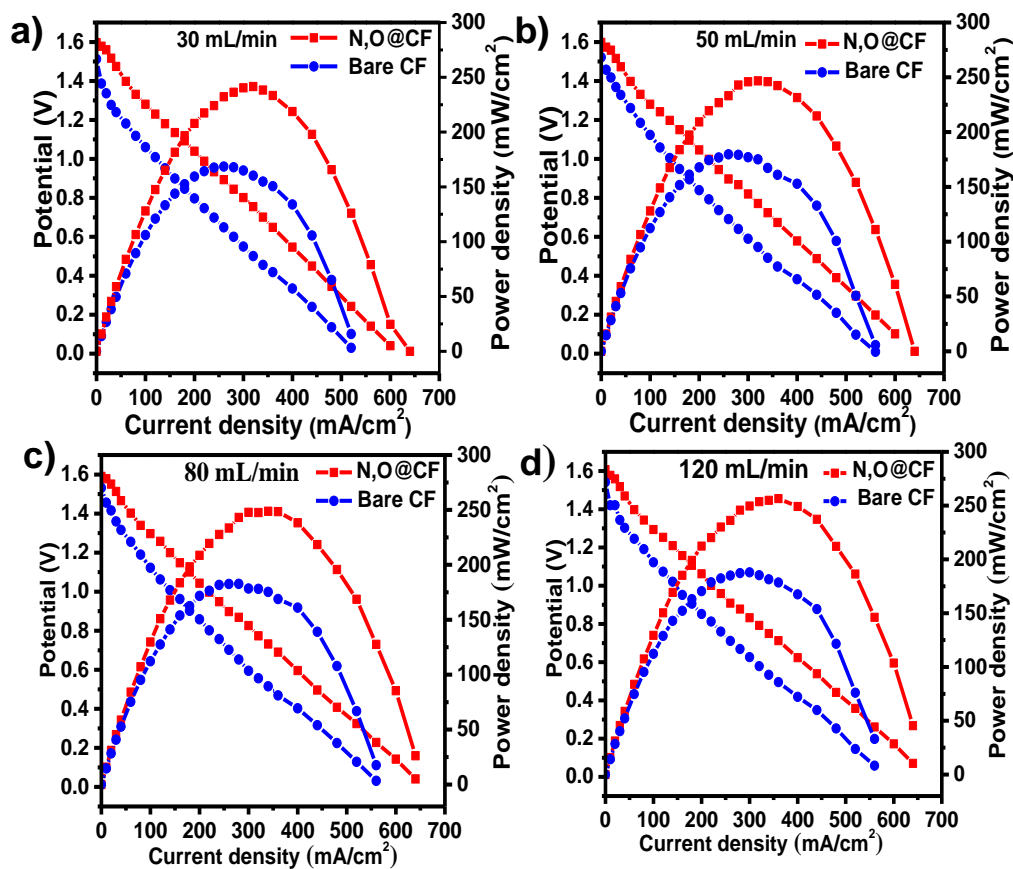


**Figure 3.17** Comparative study of polarization and power density curves for the VRFB system with bare CF and as-synthesized N,O/CF at electrolyte flow rates (a) 30, (b) 50, (c) 80, and (d) 120 mL/min.

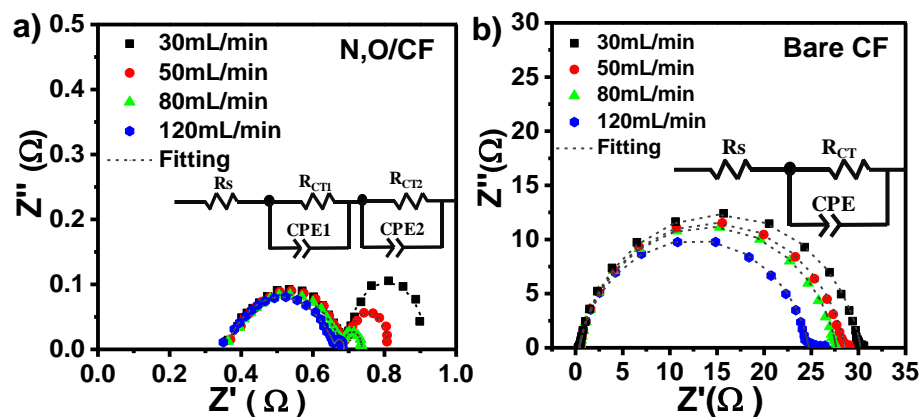


**Figure 3.18** Electrochemical impedance spectroscopy and equivalent circuits for a) N,O/CF and b) bare CF.

**Table 3.1** Equivalent circuit parameters for N,O/CF after fitting EIS.

Equivalent circuit parameters	Flow rate (mL/min)			
	30 mL/min	50 mL/min	80 mL/min	120 mL/min
$R_s$	0.36	0.37	0.36	0.35
$R_{CT1}$	0.34	0.33	0.32	0.31
$R_{CT2}$	0.22	0.12	0.05	0.02
CPE1-T	0.03	0.03	0.04	0.04
CPE1-P	0.63	0.63	0.61	0.61
CPE2-T	40.63	40.53	61.36	98.92
CPE2-P	0.96	0.96	1.02	1.15

**Table 3.2** Equivalent circuit parameters for bare CF after fitting EIS.

Equivalent circuit parameters	Flow rate (mL/min)			
	30 ml/min	50 ml/min	80 ml/min	120 ml/min
$R_s$	0.38	0.40	0.39	0.37
$R_{CT}$	24.36	27.24	28.19	29.87
CPE-T	0.00	0.00	0.00	0.00
CPE-P	0.87	0.87	0.87	0.88

The obtained  $R_s$  values from EIS results are used to obtain  $iR$ -free polarization curves, eliminating the effect of membrane resistance and showing the effect of kinetic and mass transfer resistances, the former dominating at low current density, while the latter at higher values. The resulting polarization curves (Figure 3.19 a, b) at all flow rates of electrolytes are closely following each other, suggesting a very little effect of increasing flow rates. The polarization curves of N,O/CF further illustrate that the increasing flow rate has a little effect on the potential drop. At 120 mL/min, the highest current density values of 640 and 560 mA/cm<sup>2</sup> were achieved for N,O/CF and bare CF, respectively (Figure 3.19 a, b). The  $iR$ -free power density of the VRFB at various electrolyte flow rates is also presented in the figures. The power density increases with increasing flow rates and is more prominent for N,O/CF (up to ~821 mW/cm<sup>2</sup> at 120 mL/min) than for bare CF (up to ~606 mW/cm<sup>2</sup> at 120 mL/min).



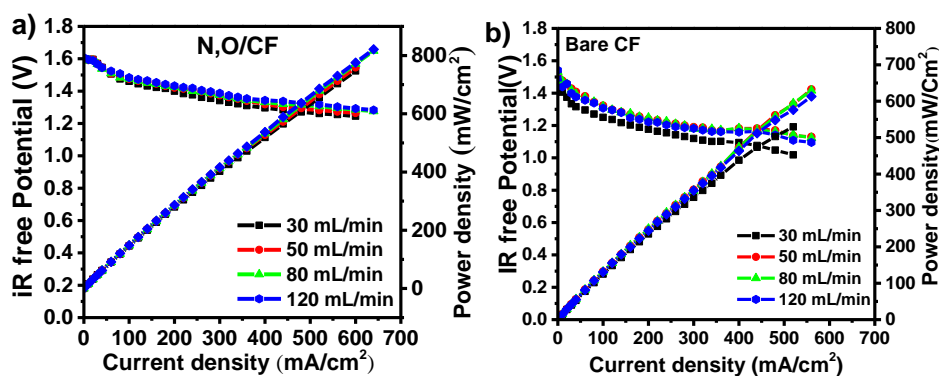


**Figure 3.19** iR-corrected polarization and power density curves of a) N,O/CF and b) bare CF.

A comparative study of polarization plots at the same flow rates suggests that the cell potential decreases less sharply for N,O/CF with increasing current density (Figure 3.20).

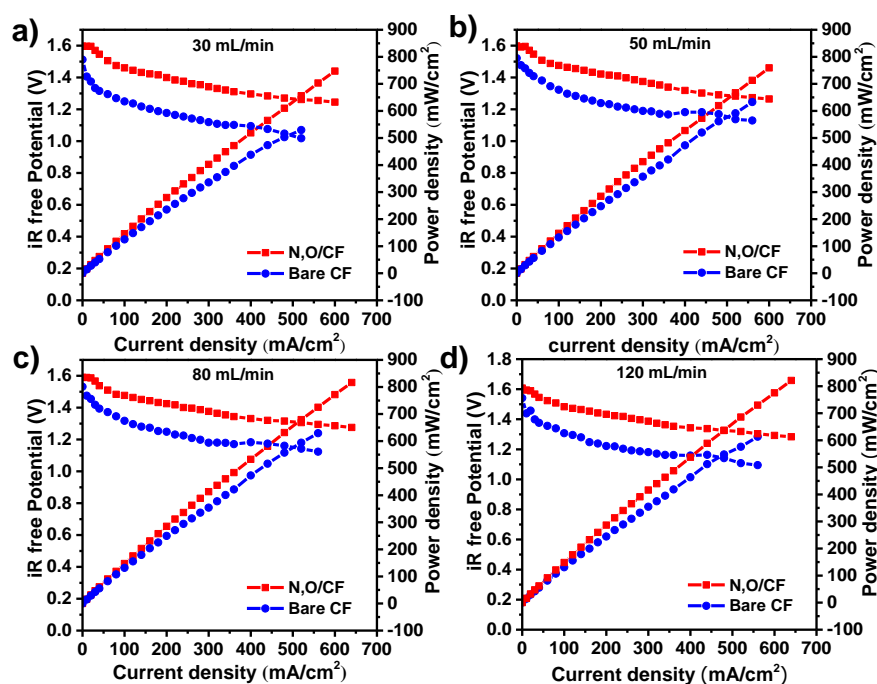


**Figure 3.20** Comparative study of polarization and power density curves with iR correction for VRFB system with bare CF and as-synthesized N,O/CF at electrolyte flow rates a) 30, b) 50, c) 80, and d) 120 mL/min.

The loss in potential at an applied current (or current density) is calculated by OCP-cell potential and is presented in Figure 3.21, where OCP is measured at zero current. Results show a lower potential loss or potential penalty using the modified electrodes. This implies that favorable active sites are present in excess on the surface of N,O/CF, which

help in withdrawing current at lower overpotential, and the increased hydrophilicity of the electrode allows electrolytes to access the active sites, reducing the mass transfer resistance [188].

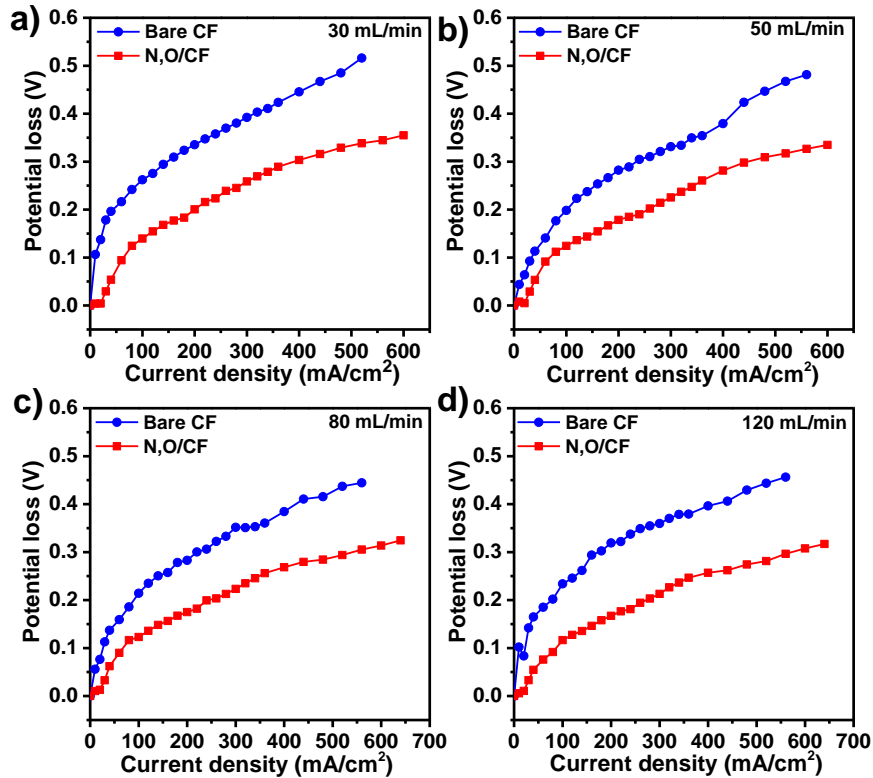


**Figure 3.21** Comparative study of potential loss from OCP for VRFB system with bare CF and N,O/CF at electrolyte flow rates (a) 30, (b) 50, (c) 80, and (d) 120 mL/min.

The performance of the electrodes was further analyzed by obtaining charging–discharging curves at two flow rates, 50 and 100 mL/min, and at current densities 40 and 80 mA/cm<sup>2</sup>. Results are presented in Figure 3.22 a, b. Longer discharging time was observed for N,O/CF in comparison to that of bare CF (Figure 3.23). Also, the effect of increasing electrolyte flow rates was minimal for N,O/CF, while for bare CF, the performance was much improved at a higher flow rate. Summarized values of VE, EE, and CE for both N,O/CF and bare CF at different electrolyte flow rates and current densities are provided in Tables 3.3 and 3.4. Results show that at 40 mA/cm<sup>2</sup>, by increasing the flow rate from 50 to 100 mL/min, the values of VE and EE do not appreciably change: VE = ~86% and

EE = ~83%. These efficiencies are higher than those upon using bare CF as an electrode; the effect of the flow rate is also evident. At 50 mL/min, VE and EE are 67.01 and 64.92%, and at 100 mL/min, values increase to 76.33 and 73.56%, respectively.

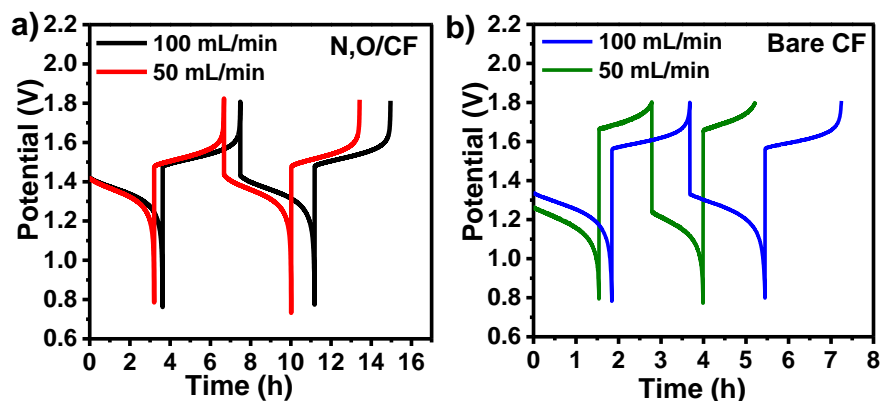


**Figure 3.22** Charging–discharging measurement of the battery employed with a) N,O/CF and b) bare CF at 40 mA/cm<sup>2</sup> current density with flow rates of 50 and 100mL/min.

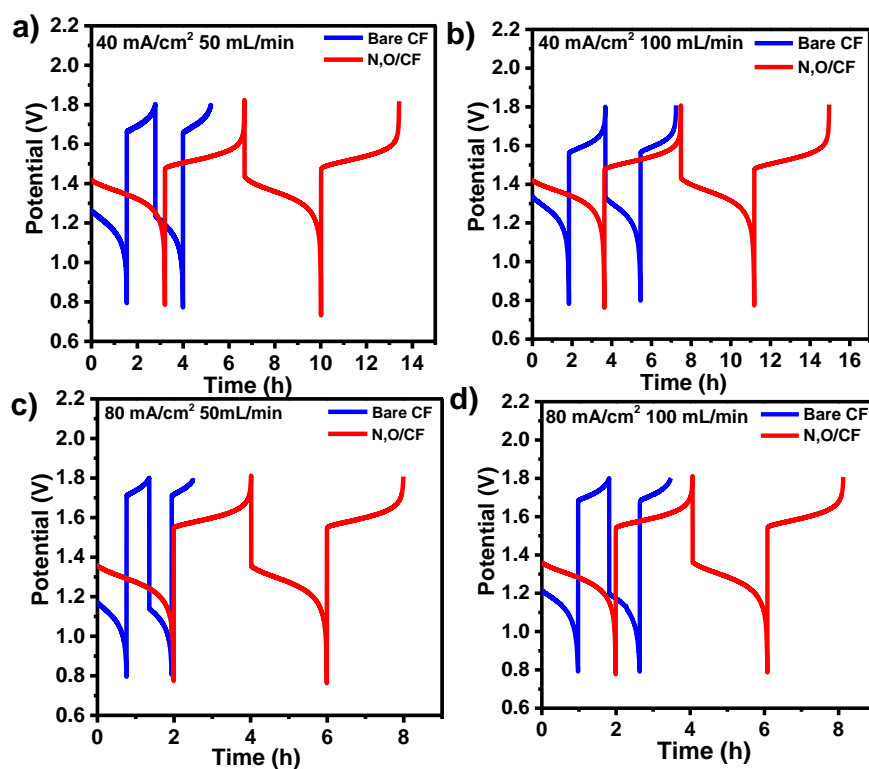


**Figure 3.23** Comparative study of charge-discharge curve of VRFB with N,O/CF and bare CF at a) 50 mL/min & b) 100 mL/min at 40 mA/cm<sup>2</sup>; c) 50 mL/min & d) 100 mL/min at 80 mA/cm<sup>2</sup>.

**Table 3.3** VE, CE, EE at 40 mA/cm<sup>2</sup> at different flow rates for bare CF and N,O/CF.

Materials	50mL/min			100mL/min		
	Voltage efficiency (%)	Energy efficiency (%)	Columbic efficiency (%)	Voltage efficiency (%)	Energy efficiency (%)	Columbic efficiency (%)
<b>N,O /CF</b>	86.36	83.11	96.24	86.31	82.59	95.68
<b>Bare CF</b>	67.01	64.92	96.87	76.33	73.56	96.37

**Table 3.4** VE, CE, EE at 80 mA/cm<sup>2</sup> at different flow rates for bare CF and N,O/CF.

Materials	50mL/min			100mL/min		
	Voltage efficiency (%)	Energy efficiency (%)	Coloumbicefficiency (%)	Voltage efficiency (%)	Energy efficiency (%)	Columbic efficiency (%)
<b>N,O/CF</b>	77.98	76.66	97.53	78.70	76.39	97.50
<b>Bare CF</b>	60.79	59.94	98.60	64.06	63.0	98.34

With increasing current density from 40 to 80 mA/cm<sup>2</sup> at a fixed electrolyte flow rate (100 mL/min), both VE and EE values, extracted from Figure 3.24 a,b decrease to 78.70 and 76.39%, respectively (Table 3.4). Results are similar for the bare CF electrode. This is expected at higher current density owing to the larger polarization and increased electrolyte diffusion resistances [244]. Considering CE values in both cases, irrespective of the flow rate or current density, the slightly lower efficiency value for N,O/CF in comparison to bare CF may be due to the longer charge–discharge time and some side reactions, such as water splitting, at nitrogen-doped sites [244]. Notably, the above-

mentioned 97% CE was retained for N,O/CF. The above-mentioned findings imply that N,O/CF can be utilized at lower electrolyte flow rates, which will lower the operating cost of a VRFB.

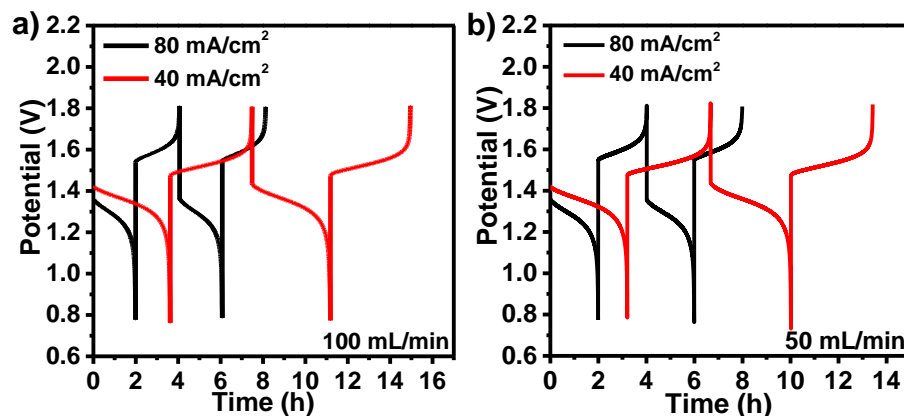


**Figure 3.24** Charging–discharging test of the VRFB with N,O/CF using it as both the anode and cathode at current densities of 40 and 80 mA/cm<sup>2</sup> with a) flow rates of 100 mL/min and b) 50 mL/min.

To examine the electrochemical stability of N,O/CF, a charging–discharging experiment was performed for longer cycles at 40 mA/cm<sup>2</sup> with 100 mL/min flow rate (Figure 3.25 a). The N,O/CF electrode retains its efficiencies and maintains discharge capacity (Figure 3.25 b, c). This also confirms the improved reversibility of vanadium redox reactions at the active sites of N,O/CF. As reported in the literature, active sites for vanadium redox couples have covalently bonded oxygen and nitrogen functional groups on the surfaces of carbon electrodes. In comparison to the bare CF, such functional groups are present in a large number on N,O/CF. Thus, its outer and inner surfaces both are highly active for electrochemical kinetics in the VRFB. A schematic illustration of the redox reaction mechanism for the V(V)/V(IV) redox couple on oxygen and nitrogen functional groups is shown in Figure 3.26.

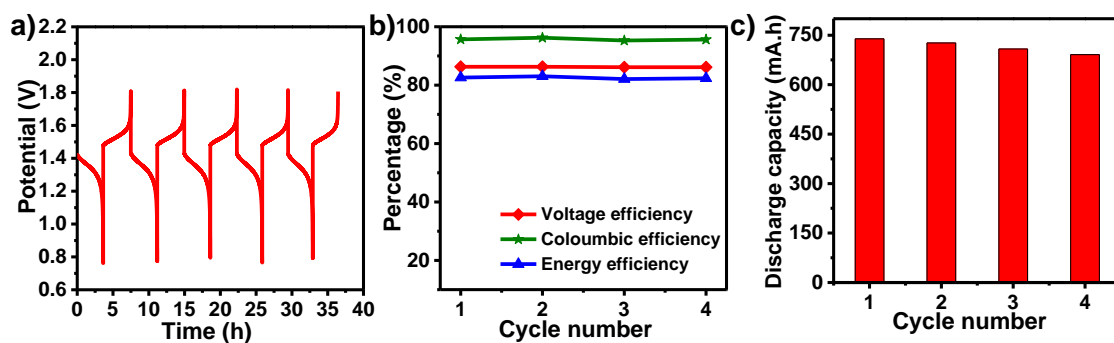


**Figure 3.25** a) Charging–discharging test performed at 40 mA/cm<sup>2</sup> for four cycles with a flow rate of 100 mL/min to show the electrochemical stability. b) Voltage, energy, and coulombic efficiencies calculated for four cycles mentioned in (3.24a). c) Discharge capacity plotted as a function of the cycle number for N,O/CF.

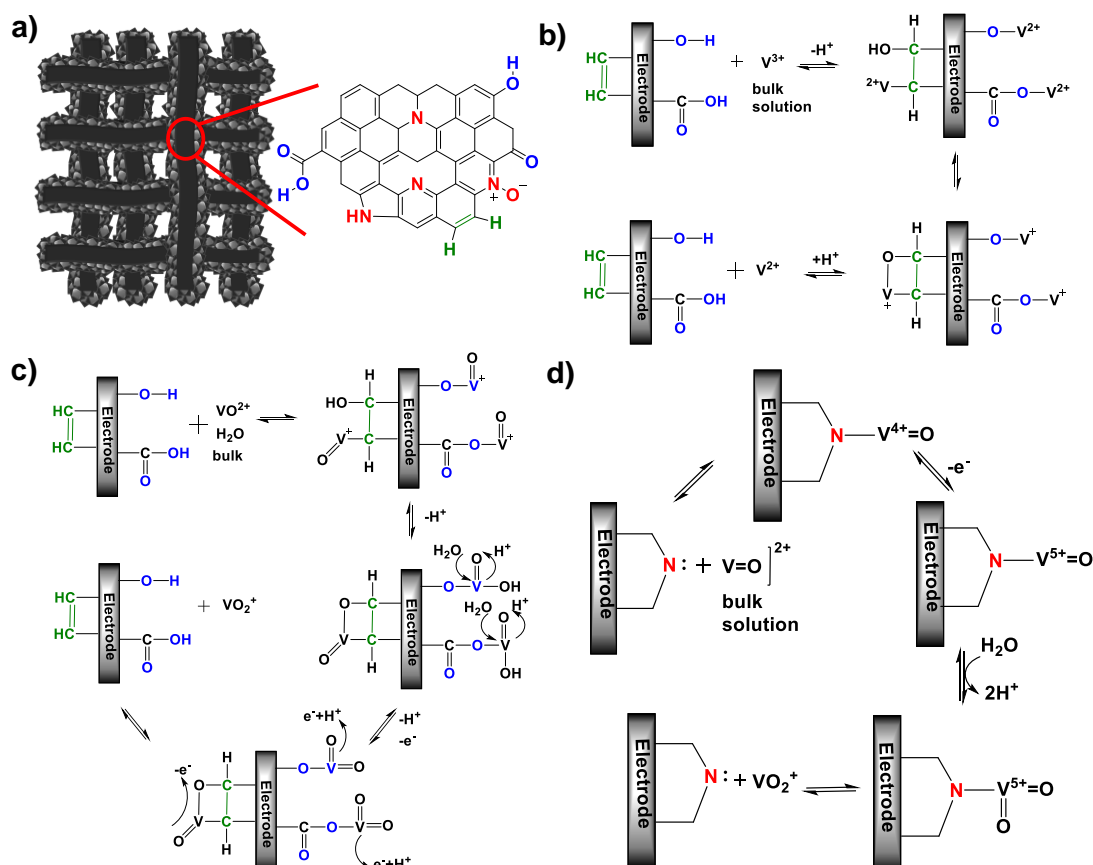


**Figure 3.26** The proposed surface structure of N, O/CF; Reaction mechanism for, b) V<sup>2+</sup>/V<sup>3+</sup> and c) VO<sub>2</sub><sup>+</sup>/VO<sub>2</sub><sup>2+</sup> redox couples at oxygen functional group active sites, d) Reaction mechanism for VO<sub>2</sub><sup>+</sup>/VO<sub>2</sub><sup>2+</sup> redox couple at nitrogen functional group active sites.

The morphology of the N,O/CF electrode was also inspected after the charge–discharge recycling test to examine any changes in its porous fibrous structures. The SEM-EDX elemental mapping suggests the retention of the structure with a homogeneous distribution of nitrogen and oxygen functional groups (Figure 3.27a). XPS results reveal more developed oxygen functional groups on the surfaces of the positive electrode after charge–discharge cycle tests (Figures 3.27 b-d). The presence of more such functional groups on the electrode surfaces is also favorable for the higher electro-chemical kinetics and retention of energy efficiency in VRFBs.

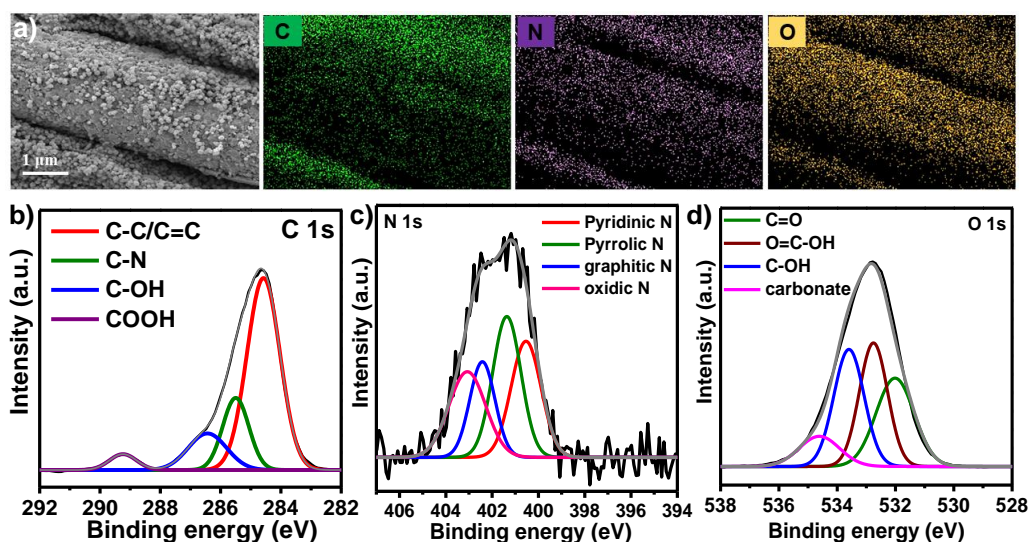


**Figure 3.27** a) SEM image and corresponding elemental mappings of N,O/CF after VRFB charge- discharge stability test, b) XPS spectra of C, N, O of N,O/CF after VRFB charge-discharge stability test.

**Table 3.5** Comparison of performance of N,O/CF in VRFB with literature.

<b>Electrode</b>	<b>Peak Power density (mW/cm<sup>2</sup>)</b>	<b>Current density (mA/cm<sup>2</sup>)</b>	<b>Voltage efficiency (%)</b>	<b>Energy efficiency (%)</b>	<b>Ref.</b>
N,O/CF	821	40 80	86.31 78.70	82.59 76.39	This work
CPC13(Activated carbon paper-WO <sub>3</sub> )	540	-	-	-	245
NSGF	404	-	-	-	246
Biomass derived activated carbon	438	-	-	-	247
1NP-CP	349	-	-	-	248
CNF/CNT-700	-	100	67.5	65.6	249
N-doping	-	40 (70)	84.88 (75.63)	82.6 (74.50)	250
Turbostratic carbon	-	10	-	84	251
MWCNT	-	70	76.1	75	252
SWCNT	-	20	96.8	89.3	253
Graphene Oxide	-	20	-	81.8	254
Mesoporous carbon	-	10	92.6	85	255
N-doped CNT	-	10	94.7	77	256
CNF	-	30	87.8	83.3	257
Wood derived carbon	-	40	-	75.44	258
Ir	-	60	87.2	58.5	259



Mn <sub>3</sub> O <sub>4</sub>	-	40	90.2	77	260
Ta <sub>2</sub> O <sub>5</sub> nano-particles	-	80	78.10	73.13	261
H-W <sub>18</sub> O <sub>49</sub> NWs-GF	-	40	90.40	81.74	262
Nb-WO <sub>3</sub>	-	80	-	78.10	263

**Table 3.6** Comparison of performance of N,O/CF in VRFB with literature considering peak potential values.

Material	$\Delta E_p = E_{pa} - E_{pc}$ (mV)	$\Delta E_p = E_{pa} - E_p$ (mV)	References
	V(IV) $\longleftrightarrow$ V(V)	V(II) $\longleftrightarrow$ V(III)	
N,O/CF	520	260	This Work
CPC13	180	510	245
NSGF	293	222	246.
C200	147	242	247
1NP-CP	142		248
CNF/CNT-700	136.12	615.07	249
NGF-900	400	250	250
Turbostratic Carbon	360	-	251
MWCNTs	204.2	-	252
SWCNTs	190	90	253
Graphene oxide	108	55	254
Mesoporous carbon	280	550	255
CNF	414	-	257
Wood derived carbon	540	350	258
Ir modified	260	-	259
Mn <sub>3</sub> O <sub>4</sub>	560	600	260

Ta <sub>2</sub> O <sub>5</sub>	450	-	261
H-CeO <sub>2</sub> NWs-GF	510	-	262
Nb-WO <sub>3</sub>	620	-	263
m-NCNT	109	-	264
PCP-800	~320	-	265
ZrO <sub>2</sub> @C	254	~220	266

### 3.7 Conclusion

Aiming to enhance the electrochemical kinetics in vanadium redox flow batteries (VRFBs), a highly nanoporous nitrogen and oxygen-functionalized graphitic carbon felt electrode, N,O/CF, has been developed through directly growing a nanostructured ZIF-8 film with the help of formation of layered zinc double hydroxide nanoflakes on the carbon felt and subsequent calcination at higher temperature. Analytical techniques, such as SEM, TEM, BET, XRD, XPS, and Raman spectroscopy, have been used to examine the surface characteristics of the nanoporous structure and functionalization of the electrode. Results show that ZIF-8 film-derived carbons are homogeneously distributed over the surface and are wrapped around the fibers of the CF. The BET surface area increases from 1.8 to 190 m<sup>2</sup>/g, having micro- to mesopores, thus providing a larger area for the catalytic sites for the reactions. The presence of C, N, and O elements was confirmed from XPS analysis by unearthing the existence of functional groups (-OH, -COOH, and C=O) and bonds (C-N, C-OH, and C=C), illustrating successful decoration with these functional groups. The doping helps in achieving hydrophilic characteristics of the electrode. The performance of the VRFB, employed with the as-synthesized nanostructured electrode and bare carbon felt, was examined by CV, polarization curves, and charge-discharge cycles. CV results show the improved electrochemical activities of the N,O/CF. Findings are supported by the lower charge transfer resistance determined by EIS. EIS measurements were employed to estimate kinetic, ohmic, and mass transfer

resistances of the VRFB. If the contribution of ohmic loss is subtracted, employing the synthesized electrode, the maximum attained power density of the battery is found to be  $\sim 821 \text{ mW/cm}^2$ , which is 1.35 times higher than using bare CF. The energy efficiency of the battery operating at an electrolyte flow rate of 50 mL/min is 83.11 and 76.66% at current densities of 40 and 80 mA/cm<sup>2</sup>, respectively. The values change slightly to 82.59 and 76.39%, respectively, at 100 mL/min, indicating the negligible effect of the flow rate on the efficiency, stemming from the improved wettability of the electrode. A coulombic efficiency of  $>96\%$  is attained. A comparison chart of the performance of N,O/CF with the literature reports is presented in Table 3.5. Although this study was accomplished on 5 cm<sup>2</sup> electrode surface area, the presented strategy for N and O decoration is easily scalable. Future work will be targeted on the development of larger VRFB assembly, aimed at an application employing the electrode synthesized by the presented scheme.

This page was intentionally left blank.

## **Chapter 4: Dual Single-Atomic Co–Mn Sites In Metal–Organic-Framework-Derived N-Doped Nanoporous Carbon For Electrochemical Oxygen Reduction**

### **4.1 Abstract**

Synthesizing dual single-atom catalysts (DSACs) with atomically isolated metal pairs is a challenging task but can be an effective way to enhance the performance for electrochemical oxygen reduction reaction (ORR). Herein, well-defined DSACs of Co–Mn, stabilized in N-doped porous carbon polyhedra (named CoMn/NC), are synthesized using high-temperature pyrolysis of a Co/Mn-doped zeolitic imidazolate framework. The atomically isolated Co–Mn site in CoMn/NC is recognized by combining microscopic as well as spectroscopic techniques. CoMn/NC exhibited excellent ORR activities in alkaline ( $E_{1/2} = 0.89$  V) as well as in acidic ( $E_{1/2} = 0.82$  V) electrolytes with long-term durability and enhanced methanol tolerance. Density functional theory (DFT) suggests that the Co–Mn site is efficiently activating the O–O bond via bridging adsorption, decisive for the  $4e^-$  oxygen reduction process. Though the Co–Mn sites favor  $O_2$  activation via the dissociative ORR mechanism, stronger adsorption of the intermediates in the dissociative path degrades the overall ORR activity. Our DFT studies conclude that the ORR on Co–Mn site mainly occurs via bridging side-on  $O_2$  adsorption following thermodynamically and kinetically favorable associative mechanistic pathways with a lower overpotential and activation barrier. CoMn/NC performed excellently as a cathode in a proton exchange membrane (PEM) fuel cell and rechargeable Zn–air battery with high peak power densities of 970 and 176  $mW\ cm^{-2}$ , respectively. This work provides the guidelines for the rational design and synthesis of nonprecious DSACs for enhancing the ORR activity as well as the robustness of DSACs

and suggests a design of multifunctional robust electrocatalysts for energy storage and conversion devices.

## 4.2 Introduction

A proton exchange membrane (PEM) fuel cell is an innovative sustainable energy conversion technology that can provide a continuous electrical supply utilizing H<sub>2</sub> as feed to meet the world's growing demand for energy [267]. The fuel cell consists of two electrodes: anode and cathode. H<sub>2</sub> is oxidized at the anode while an oxygen reduction reaction (ORR) proceeds at the cathode. The core of this technology is the membrane electrode assembly (MEA), which can be fabricated by pressing a commercial Nafion membrane between anode and cathode catalysts [268]. Together with fuel cell technologies, zinc–air batteries (ZABs) have also emerged as the most desirable future storage devices due to their advantages in terms of safe operation, environmental friendliness, and economic viability, as well as their high theoretical energy densities [269]. The practical performances of rechargeable ZABs, which are controlled by the effective bifunctional activities of the electrocatalysts at the air cathode, are used to assess their efficiency [270]. At the air cathode, an oxygen evolution reaction (OER) and ORR occur during the charging and discharging processes, respectively. The implementation of both these energy technologies has been stymied by the sluggish ORR, for which the expensive Pt and its alloys have been examined as the best leading-edge catalysts. However, degradation of these catalysts over a period of time has hindered its long-term applications [271,272]. Therefore, for successful implementation of these energy storage and conversion technologies into the market, continuous efforts are needed to substitute Pt-based ORR catalysts with nonprecious-metal-based ORR catalysts [273,274].

In recent times, single-atom catalysts (SACs) have emerged as attractive heterogeneous catalysts owing to their maximum active metal-utilization efficiency [275-

282]. These materials have been excellently utilized for various kinds of catalytic reactions, especially electrocatalysis [283-287]. Transition metals (Fe, Co, Ni), usually atomically stabilized by N-doped carbons, are the most widely studied SACs [288-292]. They have been well established due to their high ORR activities [293,294]. However, geometric configurations of SACs and electron density at the active metal centers are the most important factors deciding the catalytic performance [295-306]. In other words, the O<sub>2</sub> adsorption type, the O–O bond length, and the mechanistic pathway are highly involved in determining the ORR activity. Compared to SACs, dual single-atom catalysts (DSACs) can not only tune the electronic structure of active metal sites but also provide a different path for the adsorption and activation of O<sub>2</sub> [307-312]. Reports suggest that O<sub>2</sub> preferentially interacts with SACs through either end-on or side-on models, while DSACs allow the formation of an – O–O– bridging model. The bridging model on DSACs favors the cleavage of the O–O bond and thus results in a favorable 4e<sup>-</sup> transfer process. In a recent example, Fe–Zn DSACs with a specific separation of ~3 Å demonstrated high ORR activity in acidic electrolyte via a direct O–O cleavage pathway, favoring an unconventional dissociative ORR mechanism [307]. Similarly, Pt–Fe DSACs demonstrated excellent ORR activity in alkaline electrolyte owing to the bridging mode adsorption of O<sub>2</sub> between Pt and Fe (Pt–O–O–Fe) [308]. Fe–Mn DSACs are also found to be effective in promoting \*O–OH dissociation and hence accelerate the ORR process significantly [309]. Furthermore, Fe–Co DSACs have been reported to have a high ORR activity in acidic electrolyte, resulting from facile activation of the O–O bond, attributed to strong binding of O<sub>2</sub> on dual metal sites [310]. At present, different DSACs are proposed, and diversity in the geometry and metal coordination environment significantly challenge us to establish the correct structure–activity relationship experimentally and theoretically.

Metal–organic frameworks (MOFs) are porous materials made up of periodic arrangement of metal ions and organic linkers within their framework structures [313]. Because of the presence of tunable organic and metal moieties, MOFs are considered attractive precursors for the fabrication of various SACs or dual metal atom catalysts [314-316]. Herein, we report atomically dispersed Co–Mn DSACs anchored on nanostructured N-doped porous carbon polyhedra synthesized via controlled carbonization of a Co/Mn-doped ZIF-8 MOF. The as-synthesized catalyst, denoted CoMn/NC, exhibited excellent ORR activity with positive half-wave potentials ( $E_{1/2}$ ) of 0.89 and 0.82 V (vs RHE) in alkaline and acidic electrolytes, respectively. CoMn/NC showed superior methanol tolerance and high ORR durability, outperforming the commercial Pt/C catalyst. Density functional theory (DFT) reveals that the bridging mode of the O<sub>2</sub> adsorption on the Co–Mn dual site is more favorable than end-on adsorption. A strong binding of O<sub>2</sub> via a bridging mode at Co–Mn favors a thermodynamically dissociative ORR pathway. The calculated onset potentials for Co–Mn sites exhibited values of 0.40 and 0.72 V (vs RHE) for dissociative and associative ORR pathways, respectively, suggesting a favorable associative ORR mechanism. Furthermore, CoMn/NC performed well as a cathode in a proton exchange membrane (PEM) fuel cell with a peak power density of 970 mW cm<sup>-2</sup>. The catalyst also showed significant OER activity under alkaline conditions. Utilizing its bifunctional oxygen electrode activity, a high power density of 176 mW cm<sup>-2</sup> with long-term cycling stability is achieved with CoMn/NC in an aqueous rechargeable ZAB.

## 4.3 Experimental

### 4.3.1 Materials:

All the reagents were purchased commercially and used without further purifications. Zinc acetate dihydrate (98%) and cobalt acetate tetrahydrate (98.5%) were purchased from Molychem. 2-methylimidazole (98%) was purchased from Avra. Manganese



acetate tetrahydrate (98%), sulphuric acid (97%), Methanol (99%) were purchased from SDFCL. KOH (85%) was acquired from Azytus. Ethanol, 20 wt% platinum on graphitized carbon, 5% Nafion™ 117 solution, cobalt phthalocyanine and manganese phthalocyanine, Zn foil of 0.25mm thickness (99.99%) were purchased from Sigma-Aldrich. Iridium (IV) oxide powder 99% was purchased from Alfa aesar. Nafion 212 membrane, ELAT LT 1400 were purchased from Fuel Cell store. High purity Ar (99.999%) and O<sub>2</sub> (99.999%) gases were acquired from Sigma-Gases New Delhi and used for high temperature carbonization and electrolyte purging processes.

#### **4.3.2 Physicochemical characterizations:**

PANalytical diffractometer using Cu K $\alpha$  source ( $\lambda = 1.5405 \text{ \AA}$ ) was used to analyse powder X-ray diffraction (PXRD) with 2°/min scan rate and 0.05 steps. The instrument was operated at 30 kV and a current of 10 mA. N<sub>2</sub> sorption isotherms were recorded by using BELSORP MAX II sorption analyser at liquid N<sub>2</sub> temperature (77K). Prior to measurements, samples were degassed under vacuum at 120 °C for 12 h. The specific surface area and pore size distribution were evaluated by Brunauer-Emmett-Teller (BET) method and Barrett-Joyner Halenda (BJH) model, respectively. The pore volume was calculated by adsorption amount of N<sub>2</sub> at a relative pressure of 0.99 bar. Xray photoelectron spectroscopy (XPS) were acquired on a Thermo Fisher Scientific (K-Alpha) Xray photoelectron spectrometer using an Al K $\alpha$  source (10 kV, 10 mA) equipped with ion source (EX06). Scanning electron microscopic (SEM) images were acquired using JEOL (JXA-8230) at 20 kV. 200 kV Talos F200S G2 transmission electron microscope combined with column energy dispersive X-ray spectrometer (EDS) and a CMOS Camera 4K x 4K detector were used for Transmission Electron Microscopy (TEM) measurements. High Resolution high-angle annular dark-field scanning transmission electron microscopy (HAADF-STEM) measurement was taken on a JEM-ARM200F instrument at 200 kV.

PERKIN ELMER OPTIMA 5300 DV ICP-OES was used for the determination of metal contents in samples. Raman spectroscopy measurements were carried out on the Princeton instruments (Acton spectra pro-2500i) with the help of 532 nm DPSS Laser (laser quantum gem with a power of 50 mW). X-ray Absorption Spectroscopy (XAS) measurements, which comprises of both X-ray Near Edge Structure (XANES) and Extended X-ray Absorption Fine Structure (EXAFS) techniques, have been carried out to probe the local structure of CoMn/NC at Mn and Co K-edges. Co and Mn foil, Co-phthalocyanine (CoPc) and Mn-phthalocyanine (MnPc) were used as reference samples. The XAS measurements have been carried out at the Energy-Scanning EXAFS beamline (BL-9) at the Indus-2 Synchrotron Source (2.5 GeV, 100 mA) at Raja Ramanna Centre for Advanced Technology (RRCAT)-Indore, India [317,318]. This beamline operates in the energy range of 4 KeV to 25 KeV. The beamline optics consists of a Rh/Pt coated collimating meridional cylindrical mirror and the collimated beam reflected by the mirror is monochromatized by a Si(111) ( $2d = 6.2709 \text{ \AA}$ ) based double crystal monochromator (DCM). The second crystal of DCM is a sagittal cylinder used for horizontal focusing while a Rh/Pt coated bendable post mirror facing down is used for vertical focusing of the beam at the sample position. Rejection of the higher harmonics content in the X-ray beam is performed by detuning the second crystal of DCM. In the present case, XAS measurements have been performed in the fluorescent mode for the samples and in the transmission mode for the standards. For the transmission measurement, three ionization chambers (300 mm length each) have been used for data collection, one ionization chamber for measuring incident flux ( $I_0$ ), second one for measuring transmitted flux ( $I_t$ ) and the third ionization chamber for measuring XAS spectrum of a reference metal foil for energy calibration. Appropriate gas pressure and gas mixtures have been chosen to achieve 10-20% absorption in first ionization chamber and 70-90% absorption in second

ionization chamber to improve the signal to noise ratio. For measurements in the fluorescence mode, the sample is placed at  $45^\circ$  to the incident X-ray beam, and a fluorescence detector is placed at right angle to the incident X-ray beam to collect the signal. One ionization chamber detector is placed prior to the sample to measure the incident flux and fluorescence detector measures the fluorescence intensity. The spectrum was obtained as a function of energy by scanning the monochromator over the specified range. Pellets were made using catalyst or reference powder samples for recording absorption spectra. Sample powder was mixed homogeneously with cellulose powder in appropriate proportion and pressed into a 15 mm diameter disc. The amount of the sample was estimated such that to get a reasonable edge jump at a particular absorption edge of the element to be probed. Spectra were collected at the Mn and Co K-edge in transmission mode and were calibrated against the reference spectrum of metallic Mn and Co. Data were processed using Demeter software. Metallic Mn and Co foil standards were used as reference for energy calibration and was measured simultaneously with experimental samples. The set of EXAFS data analysis programme available within Demeter software package have been used for EXAFS data analysis. This includes background reduction and Fourier transform to derive the  $\chi(R)$  versus R spectra from the absorption spectra (using ATHENA software), generation of the theoretical EXAFS spectra starting from an assumed crystallographic structure and finally fitting of experimental data with the theoretical spectra using ARTEMIS software [319]. For EXAFS fitting using DFT optimized structure, spectrum was calibrated against the reference spectra and aligned to the first peak in the smoothed first derivative of the absorption spectrum, the background noise was removed, and the spectra were processed to obtain a normalized unit edge step.

### **4.3.3 Synthesis:**

**4.3.3.1 Synthesis of CoMn-ZIF:** Typically, zinc acetate dihydrate (10 mmol), cobalt acetate tetrahydrate (1 mmol), and manganese acetate tetrahydrate (2 mmol) were dissolved in methanol (290 mL) by using a single conical flask. At the same time in another beaker, 2-methylimidazole (148 mmol) was also dissolved in 290 mL of methanol. A metal solution was added to the linker solution with continuous stirring for 2 h. Subsequently, it was kept for 24 h without stirring to grow the Co-/Mn-doped ZIF-8 nanocrystals. The solid precipitate was collected by centrifugation and washed several times with methanol to give CoMn-ZIF. It was then dried under a vacuum at 80 °C overnight for further use.

**4.3.3.2 Synthesis of Mn-ZIF:** Mn-substituted ZIF-8 (Mn-ZIF) was synthesized similar to the procedure following the synthesis of CoMn-ZIF without using manganese acetate tetrahydrate.

**4.3.3.3 Synthesis of Co-ZIF:** Mn-substituted ZIF-8 (Co-ZIF) was synthesized similar to procedure following the synthesis of CoMn-ZIF without using cobalt acetate tetrahydrate.

**4.3.3.4 Synthesis of CoMn/NC:** The as-obtained light purple nanocrystals of CoMn-ZIF were carbonized using a tubular furnace at 950 °C for 4 h under a continuous flow of Ar gas having an outlet bubbling flow rate of 1 bubble s<sup>-1</sup>. The ramping rate to reach the maximum temperature was 2 °C min<sup>-1</sup>. After cooling to room temperature, the black solid was treated with a 10% H<sub>2</sub>SO<sub>4</sub> solution at 70 °C for 16 h. Subsequent centrifugation and washing with plenty of deionized water led to a black solid. It was further treated at 70 °C under vacuum for further use and designated as our main catalyst, CoMn/NC.

**4.3.3.5 Synthesis of CoMn/NC800:** CoMn/NC800 was synthesized similar to procedure following the synthesis of CoMn/NC using carbonization temperature as 800 °C.

**4.3.3.6 Synthesis of CoMn/NC700:** CoMn/NC700 was synthesized similar to procedure following the synthesis of CoMn/NC using carbonization temperature as 700 °C.

**4.3.3.7 Synthesis of Co/NC:** Co/NC was synthesized similar to procedure following the synthesis of CoMn/NC using Co-ZIF as the carbonization precursor.

**4.3.3.8 Synthesis of Mn/NC:** Mn/NC was synthesized similar to procedure following the synthesis of CoMn/NC using Mn-ZIF as the carbonization precursor.

#### **4.3.4 Electrochemical measurements:**

All the electrochemical measurements were performed on a Biologic VSP-128 electrochemical workstation using a conventional three-electrode setup, consisting of a rotating disk electrode (RDE) having a glassy-carbon geometric diameter of 3 mm as the working electrode, Pt mesh as the counter electrode, and Ag/AgCl (3 M KCl) as the reference electrode using either 0.1 M KOH or 0.5 M H<sub>2</sub>SO<sub>4</sub> electrolyte. The catalyst ink was made by dispersing 5 mg of the catalyst in 490 μL of ethanol, 490 μL of deionized water along with 20 μL of 5% Nafion 117 solution, followed by ultrasonication for 15 min to get a homogeneous suspension. The ink was deposited on a precleaned GC electrode to maintain a catalyst mass loading of 0.320 mg cm<sup>-2</sup> and dried at room temperature (for 3–4 h) to yield a thin film. All the ORR activities of catalysts were measured on a RDE or rotating ring disk electrode (RRDE) at room temperature using 0.1 M KOH or 0.5 M H<sub>2</sub>SO<sub>4</sub> electrolyte saturated with O<sub>2</sub> for 30 min. All the catalyst-deposited electrodes were preconditioned by cyclically sweeping the potential in the potential range of 1.2–0.0 V vs the reversible hydrogen electrode (RHE) at a scan rate of 100 mV s<sup>-1</sup> until reproducible cyclic voltammograms (CV) were obtained. Linear sweep voltammograms (LSVs) were recorded at a scan rate of 5 mV s<sup>-1</sup>. Before each RDE measurement, the catalyst was

scanned in Ar-saturated electrolyte, and the obtained background voltammogram was subtracted from the measured voltammogram in the O<sub>2</sub>-saturated electrolyte. The Tafel plots were extracted from the recorded LSVs. All reported potentials were corrected for the resistance of the electrolyte (iR drop). Electrochemical impedance spectroscopy (EIS) was performed at 1.05 V vs RHE. The frequency ranged from 100000 to 0.1 Hz, and the applied voltage was 5 mV. The EIS was fitted to an equivalent circuit using BioLogic software, where R<sub>s</sub> is the series resistance and R<sub>ct</sub> is the charge transfer resistance. Fitted results provide the R<sub>s</sub> and R<sub>ct</sub> values. All the experimental data were taken with respect to Ag/AgCl and converted into a standard reversible hydrogen electrode (RHE) potential by using the formula

$$E_{\text{RHE}} (\text{V}) = E_{\text{Ag/AgCl}} (3\text{MKCl}) (\text{V}) + (0.0591 \times \text{pH}) + 0.210 \text{ V} \dots \dots \dots (1)$$

The number of electrons and JK value was evaluated on the basis of the Koutecky–Levich (K-L) equation:

$$\frac{1}{J} = \frac{1}{J_k} + \frac{1}{J_L} \quad (2)$$

$$\frac{1}{J} = \frac{1}{J_k} + \frac{1}{B\sqrt{\omega}} \quad (3)$$

$$B = 0.62 nFC_0D_0^{2/3} \nu^{-1/6} \quad (4)$$

$$J_K = nFkC_0 \quad (5)$$

where J is the measured current density, J<sub>k</sub> and J<sub>L</sub> are kinetic and diffusion-limiting current densities, respectively, ω is the angular velocity in units of rad s<sup>-1</sup> (ω = 2πN, where N the is rotation speed), n is the overall number of electrons transferred during the oxygen reduction reaction, F is the Faraday constant (F = 96485 C mol<sup>-1</sup>), C<sub>0</sub> is the saturated concentration of O<sub>2</sub> (1.2 × 10<sup>-6</sup> mol cm<sup>-3</sup>), D<sub>0</sub> is the diffusion coefficient constant of O<sub>2</sub> in electrolyte (1.9 × 10<sup>-5</sup> cm<sup>2</sup> s<sup>-1</sup>), ν is the kinetic viscosity of the electrolyte (0.01 cm<sup>2</sup> s<sup>-1</sup>), and k is the electron transfer rate constant. From the slope and intercept of the

following K-L plots, we analyzed  $n$  and  $J_K$ , respectively. RRDE measurements were conducted to investigate hydrogen peroxide formation ( $H_2O_2\%$ ) during the ORR. GC disk and Pt ring (RRDE) electrodes were employed in the RRDE measurements. The disk area of the RRDE (glassy carbon) was  $0.1256 \text{ cm}^2$ , while the area of the ring (Pt) was  $0.1884 \text{ cm}^2$ . The catalyst loading on the disk was  $0.304 \text{ mg cm}^{-2}$ . Disk and ring currents were recorded with a scan rate of  $5 \text{ mV s}^{-1}$  in both  $0.1 \text{ M KOH}$  and  $0.5 \text{ M H}_2\text{SO}_4$  solutions. The  $H_2O_2$  yield and the electron transfer number ( $n$ ) of the samples were calculated using the formulas:

$$H_2O_2(\%) = 200 \times \frac{\frac{I_r}{N}}{I_d + \frac{I_r}{N}} \quad (6)$$

$$n = 4 \times \frac{I_d}{I_d + \frac{I_r}{N}} \quad (7)$$

where  $I_d$ ,  $I_r$ , and  $N$  correspond to the disk current, ring current, and collection efficiency of the Pt ring ( $N = 40\%$ ), respectively. The electrochemical active surface area (ECSA) was estimated from the double-layer capacitance ( $C_{dl}$ ), which was determined from the non-Faradaic potential region: i.e.,  $1.03\text{--}1.13 \text{ V}$  (vs RHE) in  $0.1 \text{ M KOH}$  solution. For  $C_{dl}$  calculations, a cyclic voltammetry study was carried out at different scan rates ( $5, 10, 20, 30, 40, 50 \text{ mV s}^{-1}$ ) and then  $(j_a - j_c)/2$  was plotted against the scan rate at  $1.08 \text{ V}$  vs RHE, where  $j_a$  is the anodic current density and  $j_c$  is the cathodic current density. The slope of the above profiles corresponds to  $C_{dl}$ . Then using the following equation, we calculated ECSA:

$$ECSA = \frac{C_{dl}}{C_s} \quad (8)$$

Here  $C_s$  is the specific capacitance, which was evaluated from the smooth surface of the materials under a specific electrochemical condition. We determined a temperature of

0.04 mF cm<sup>-2</sup>. The durability of CoMn/NC for the ORR, deposited on an RDE, was examined by chronoamperometry at a potential of 0.82 V (vs RHE) and 0.89 V (vs RHE) in 0.5 M H<sub>2</sub>SO<sub>4</sub> and 0.1 M KOH, respectively, using continuous electrode rotation at 900 rpm throughout the measurement. An O<sub>2</sub> flow was maintained over the surface of the electrolyte during the experiment. A methanol tolerance test was conducted via injecting 3 mL of methanol in the electrolytic solution at 700 s.

#### **4.3.5 Proton exchange membrane fuel cell (PEMFC) testing**

CoMn/NC and Pt/C were tested as oxygen electrodes (cathodes) in a Membrane Electrode Assembly (MEA) under a fuel cell environment. The catalyst ink (prepared as described above with ~25 wt % of Nafion) was brush-painted on the microporous layer (MPL) side of commercially available ELAT LT 1400 (Teflon-treated carbon cloth with MPL applied to one side of the cloth). Following this, two catalyst-coated gas diffusion layers (GDL) were prepared, one with CoMn/NC for cathodic side (loading ~1.0 mg cm<sup>-2</sup>) and another one with 20 wt % Pt/C (loading 0.5 mg cm<sup>-2</sup>) for the anodic side. A Nafion 212 membrane with a defined active geometric area of ~5.0 cm<sup>2</sup> was inserted between these catalyst-loaded GDLs, by hot pressing at 100 °C for 5 min, resulting in our 5-layered MEA. A single cell with single-serpentine flow channels was assembled as shown in Figures S23 and S24 and evaluated in our electrochemical workstation. The cell was standardly conditioned at 0.4 V, 100% relative humidity, and 70 °C until a steady-state current was achieved. H<sub>2</sub> and O<sub>2</sub> (flowing rate 200 mL min<sup>-1</sup>) were used as anode and cathode feeds, respectively. The back pressure during the cell tests was 1.0 bar. PEMFC voltammograms were recorded in a current control mode, and then the corresponding power density (W cm<sup>-2</sup>) was calculated.



Catalyst loadings: with CoMn/NC 1.0 mg cm<sup>-2</sup> CoMn/NC at the cathode and 0.5 mg cm<sup>-2</sup> Pt/C at the anode; with Pt/C 0.5 mg cm<sup>-2</sup> Pt/C at the cathode and 0.5 mg cm<sup>-2</sup> Pt/C at the anode.

#### **4.3.6 Fabrication and testing of Zn–Air battery**

We fabricated a homemade rechargeable Zn–air battery (ZAB) and tested its overall performance. First, the catalyst ink was made by dispersing 10 mg of catalyst in 100 μL of ethanol and 100 μL of deionized water along with 40 μL of 5% Nafion 117 solution, followed by ultrasonication for 15 min to get a homogeneous suspension. The ink was drop-casted on the microporous layer (MPL) side of commercially available ELAT LT 1400 to maintain a catalyst mass loading of 1 mg cm<sup>-2</sup> and dried at room temperature. The support worked as a current collector at the air cathode. Following this, another set with a 20 wt % Pt/C+ IrO<sub>2</sub> mixture (1:1) was fabricated. For the anode, cleaned and polished zinc foil of 0.25 mm thickness was utilized. The effective surface area of the electrodes exposed to the electrolyte was 1 cm<sup>2</sup>. The electrolyte was chosen as a mixed solution of 6 M KOH and 0.2 M zinc acetate to promote a reversible zinc-based electrochemical reaction at the anode. Battery testing was accomplished at room temperature with a Biologic VSP-128 electrochemical workstation.

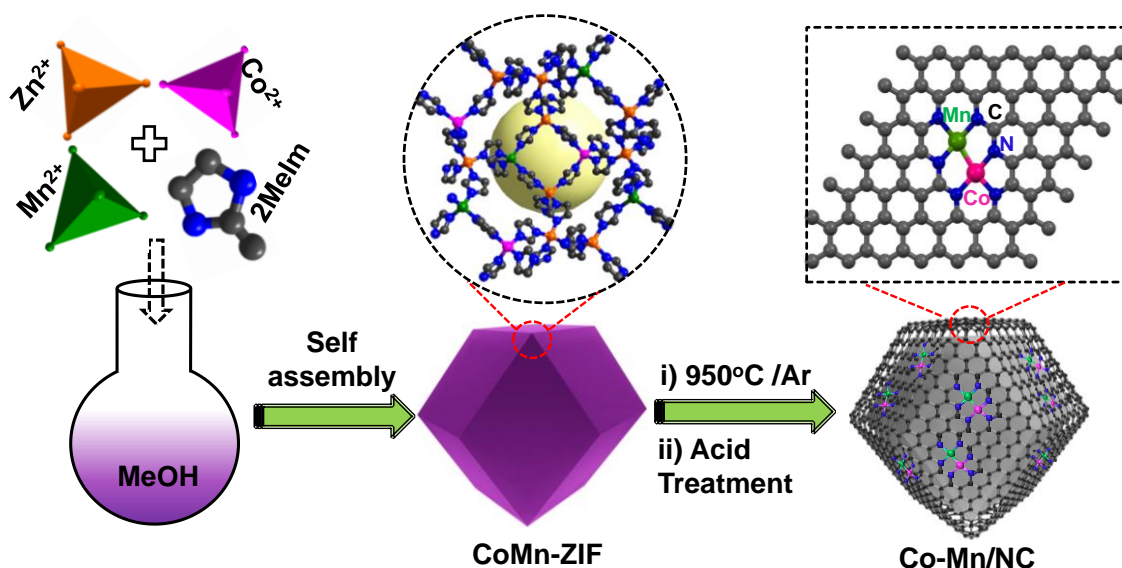
#### **4.3.7 Density functional theory (DFT) calculations**

The spin-polarized calculations were performed at density functional theory (DFT) by using the plane-wave method as implemented in Vienna Ab Initio Simulation Package (VASP) [320]. The exchange-correlation energy was considered by the generalized gradient approximation method (GGA) parameterized by the Perdew-Burke Ernzerhof (PBE) [321]. The projector augmented wave potential (PAW) was used to treat the ion-electron interactions. The Grimme's DFT-D2 empirical correction method was applied for describing the effect of van der Waals interactions [322]. To account for the on-site

coulomb repulsion and improve the description of the localized d-electrons of the transition metals namely Mn, Co, Hubbard correction parameter U-term (DFT+U) was used with U values 5.0 and 4.0 eV respectively for Mn and Co as suggested by earlier studies [323-325]. In all computations, the kinetic energy cut off is set to be 500 eV in the plane-wave expansion. All the structures were fully relaxed (lattice constant and atomic position) using the conjugated gradient method and the convergence threshold was set to be  $10^{-4}$  eV in energy and 0.01 eV/Å in force. For geometry optimization, the Brillouin zone was sampled using a  $5 \times 5 \times 1$  Monkhorst-Pack k-point mesh. The climbing image nudged elastic band method (CI-NEB) was used to calculate activation barriers and six intermediate images were considered along the minimum energy path (MEP) to search for transition states for the intermediate states toward O<sub>2</sub> hydrogenation [326]. For all the pathways, the activation barriers ( $\Delta E^\ddagger$ ) were calculated using the following equations:  $\Delta E^\ddagger = E_{TS} - E_{IS}$  and  $\Delta E = E_{FS} - E_{IS}$ ; where IS, TS and FS correspond to the initial state, transition state, and final state, respectively. To avoid the spurious interactions between the neighboring slabs, a vacuum layer of 20 Å is used in the direction perpendicular to the surfaces (along the Z-direction) and the nearest distance between the two adsorbed molecules in the adjacent supercell is  $\sim 14$  Å.

#### 4.4 Results and discussion

Scheme 4.1 represents the synthetic procedure for CoMn/NC. First, Co-/Mn-doped ZIF-8 was synthesized by simultaneous addition of all three metal precursors Zn(OAc)<sub>2</sub>·2H<sub>2</sub>O, Co(OAc)<sub>2</sub>·4H<sub>2</sub>O, and Mn(OAc)<sub>2</sub>·4H<sub>2</sub>O into a methanolic solution of 2-methylimidazole (2-MeIm) linker at room temperature. When the Zn/Co/Mn mass ratios were 1/0/0, 1/0.1/0, 1/0/0.2, and 1/0.1/0.2, the resulting samples were named ZIF-8, Co-ZIF, Mn-ZIF, and CoMn-ZIF, respectively.



**Scheme 4.1** Schematic representation for the synthesis of the CoMn/NC catalyst.

PXRD patterns verified the phase purity of all synthesized MOF materials, matching with ZIF-8 simulated crystal structures (Figure 4.1). The BET surface area of CoMn-ZIF was found to be  $2210 \text{ m}^2 \text{ g}^{-1}$ , compared to Co-ZIF ( $1920 \text{ m}^2 \text{ g}^{-1}$ ) and Mn-ZIF ( $1950 \text{ m}^2 \text{ g}^{-1}$ ) (Figure 4.2 and Table 4.1).

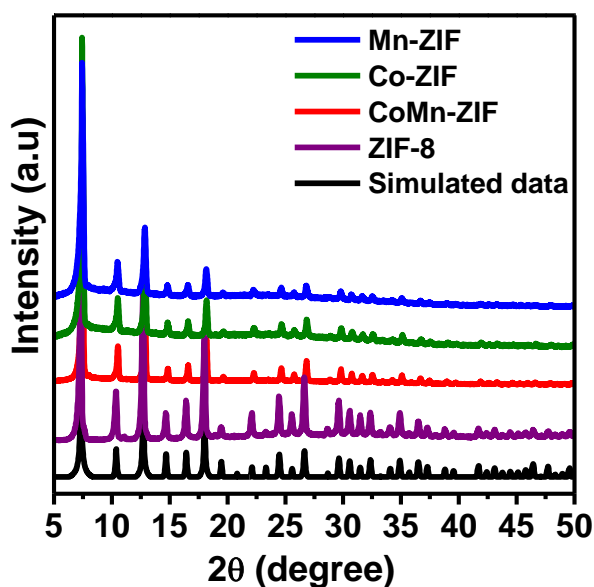


**Figure 4.1** PXRD patterns of simulated ZIF-8, as-synthesized ZIF-8, CoMn-ZIF, Co-ZIF and MnZIF.

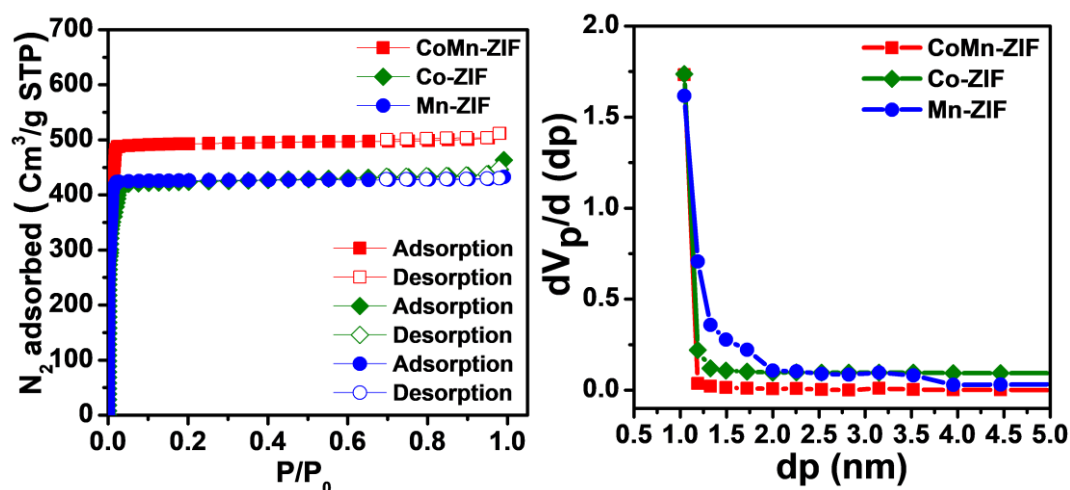


**Figure 4.2** N<sub>2</sub> sorption isotherms (left) and their corresponding BJH pore size distribution (right) of CoMn-ZIF, Co-ZIF and Mn-ZIF.

**Table 4.1** Comparison of surface area, average pore size and total pore volume for CoMn-ZIF, Co-ZIF and Mn-ZIF.

Sample Name	BET surface area (m <sup>2</sup> /g)	Average pore size (nm)	Pore volume (cm <sup>3</sup> /g)
CoMn-ZIF	2210	1.21	0.79
Co-ZIF	1920	1.22	0.71
Mn-ZIF	1950	1.22	0.75

SEM of CoMn-ZIF showed its typical zeolitic polyhedral morphology of ~300 nm size (Figure 4.3 a-c) with a narrow size distribution. The corresponding EDS elemental mapping further verified the continuous distribution of Co and Mn atoms within the ZIF-8 crystals (Figure 4.3 d). The result was confirmed by X-ray photo electron spectroscopy (XPS) (Figure 4.3 e).

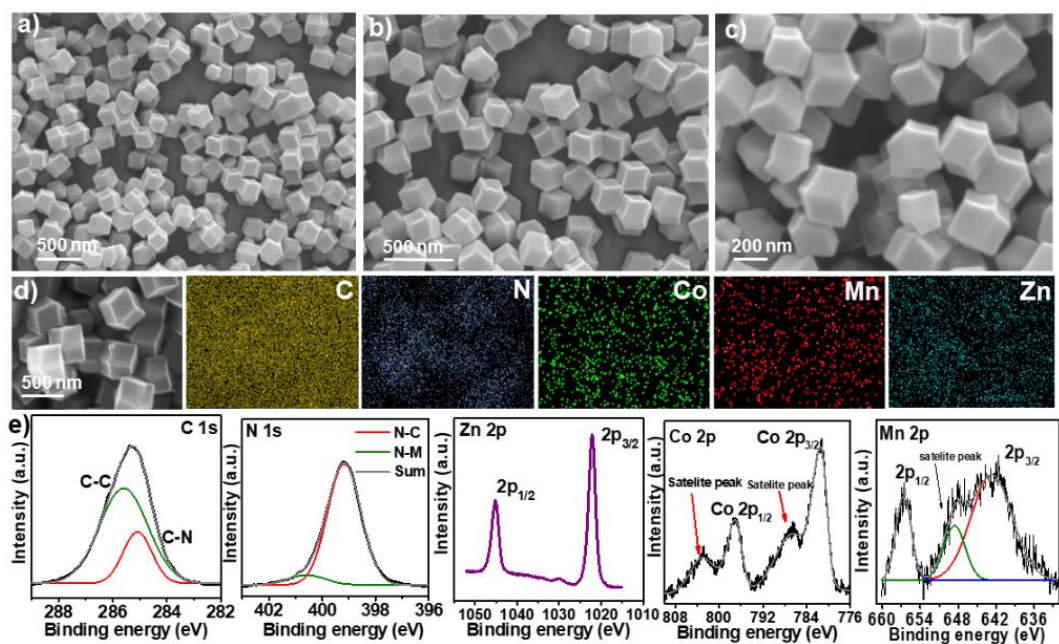


**Figure 4.3** SEM images of a-c) CoMn-ZIF at different scale bars. d) SEM image with corresponding EDS elemental mappings of CoMn-ZIF. e) High-resolution XPS spectra of C 1s, N 1s, Zn 2p, Co 2p, and Mn 2p acquired from CoMn-ZIF.

After the successful formation of CoMn-ZIF, it was subjected to carbonization at 950 °C for 4 h under an Ar atmosphere. Subsequent acid treatment led to Co–Mn DSAC sites anchored on N-doped porous carbon, denoted CoMn/NC. The Zn species present in CoMn-ZIF would be evaporated, as carbon-reduced Zn metal has a relatively low boiling point (~907 °C) [327]. This strategy prevented the agglomeration of Co and Mn metals and facilitated the separation of SACs or Co–Mn DSACs, embedded into a porous carbon structure [328]. Similarly, the supporting carbon materials NC, Co/NC, and Mn/NC were obtained under similar reaction conditions by calcination of the corresponding MOFs ZIF-8, Co-ZIF, and Mn-ZIF. Materials obtained by carbonization of CoMn-ZIF at 700 and 800 °C are named CoMn/NC700 and CoMn/NC800, respectively. Scanning electron microscopy (SEM) images revealed a polyhedral morphology of CoMn/NC particles with the size of ~300 nm, similar to that observed for CoMn-ZIF (Figure 4.4a). The particles were not agglomerated and were highly dispersed. Transmission electron microscopy (TEM) further confirmed this size and shape (Figure 4.4 b,c). High-resolution

TEM (HR-TEM) images suggested that CoMn/NC has a porous and graphitic carbon structure having the absence of any metal aggregates (Figure 4.4 d). No metal clusters or nanoparticles were detected, which was further verified by a diffuse selected area electron diffraction (SAED) pattern (inset in Figure 4.5 f). An aberration-corrected high-angle annular dark-field scanning TEM (HAADF-STEM) image of CoMn/NC revealed the presence of many SAC sites, uniformly dispersed in the carbon structure (Figure 4.4 e). Many encircled dual white dots, which can be seen in Figure 4.4 e, confirmed the formation of dual metal sites. The distance between two white dots was statistically measured to be close to 2.5 Å, suggesting a bonding interaction between two metal atoms (Figure 4.4 f). The corresponding EDS elemental mappings suggested the homogeneous distribution of Co and Mn atoms over all N-doped carbon polyhedra of CoMn/NC (Figure 4.4 g). Electron energy-loss spectroscopy (EELS) of a selected area of two white dots in the HAADF-STEM image of CoMn/NC confirmed the existence of Co–Mn DSAC sites (Figure 4.6). Additional SEM and HR-TEM images of CoMn/NC from different regions are shown in Figure 4.5. All of these data validate the successful embedding of DSAC sites into N-doped carbons.

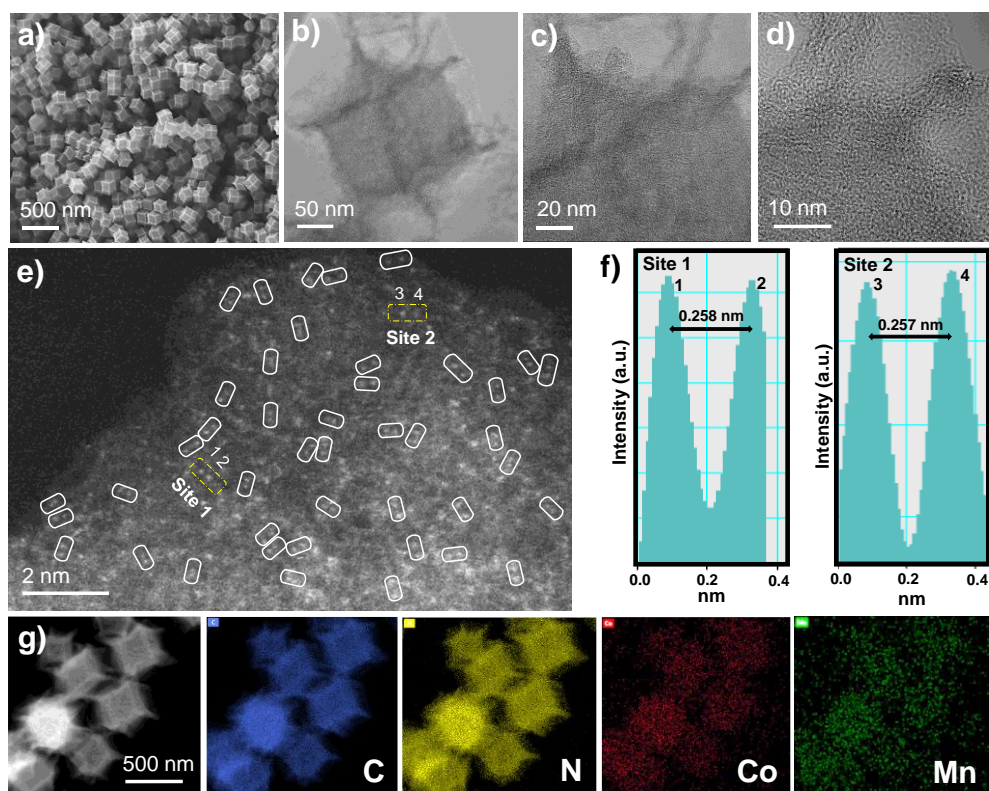


**Figure 4.4** a) Schematic representation for the synthesis of the CoMn/NC catalyst. b) SEM. c, d) TEM, e) HR-TEM, and f) high-resolution HAADF-STEM image of CoMn/NC. g) Intensity profiles obtained from two sites, site 1 and site 2, in (f). h) HAADF-STEM image of CoMn/NC with the corresponding C, N, Co and Mn EDX elemental mappings. The white encircled two white dots in (f) correspond to the dual single-metal sites.

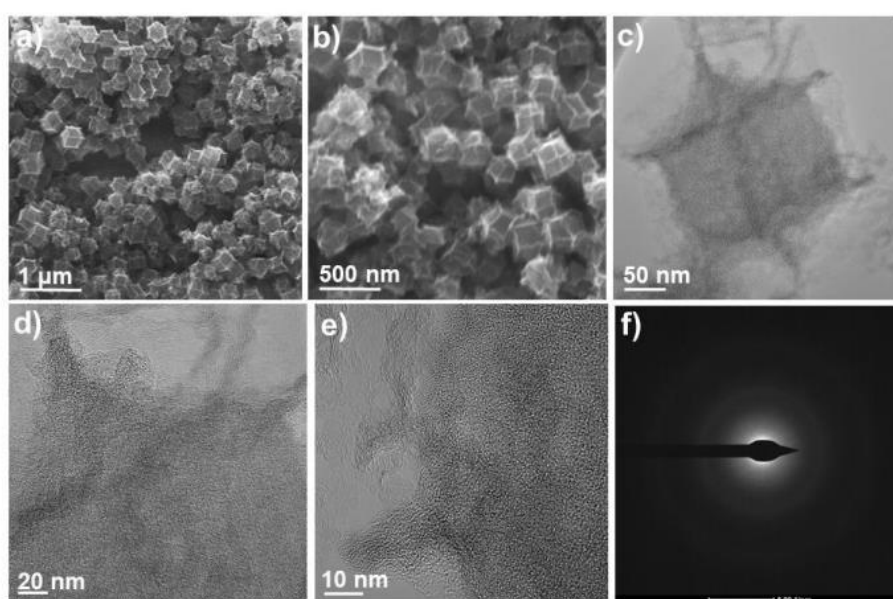


**Figure 4.5** a-b) SEM images of CoMn/NC. c-e) TEM images of CoMn/NC at different scale bars. f) SAED pattern of CoMn/NC, revealing absence of any metallic nanoparticle.

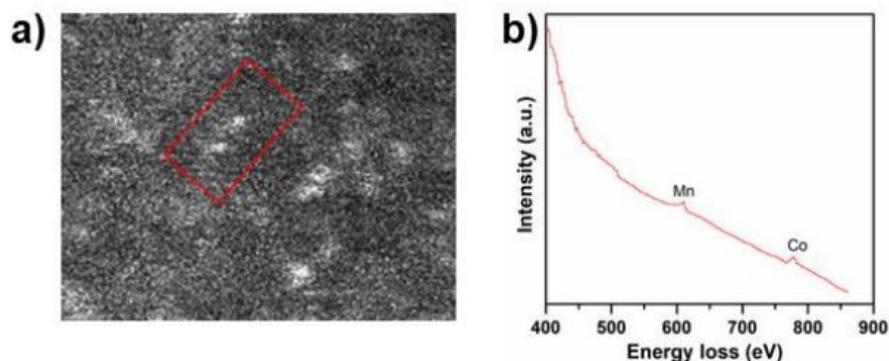


**Figure 4.6** a) HAADF-STEM image of CoMn/NC showing encircled a single Co-Mn pair as two white dots and b) corresponding EELS spectrum.

The supporting samples NC, Co/NC, Mn/NC, CoMn/ NC700, and CoMn/NC800 were also synthesized and characterized using SEM, TEM, HR-TEM, SAED, and EDS elemental mappings (Figures 4.7–4.10). As expected, no metal was found in the NC sample. In the case of Co/NC, Mn/NC, CoMn/NC700, and CoMn/NC800, no metal clusters were seen, suggesting that Co/Mn metals are mostly present in the form of atomic (SAC) structures.



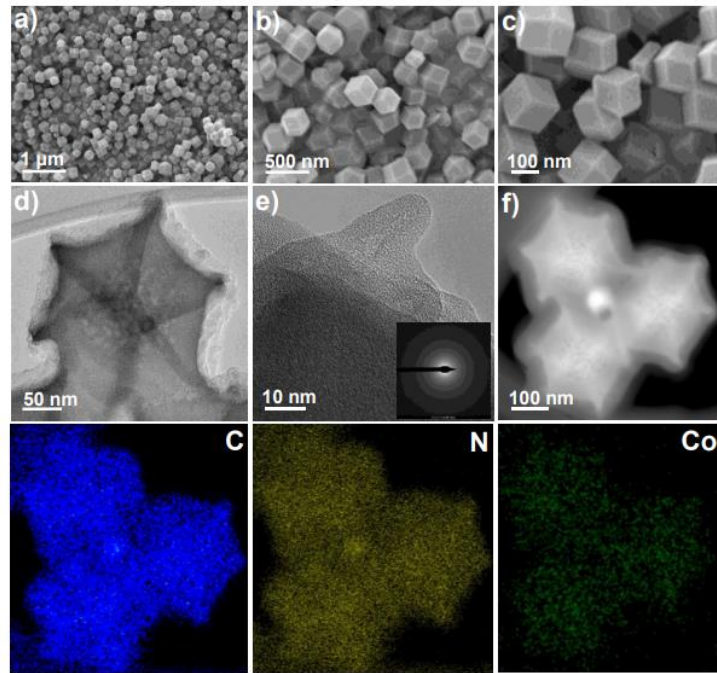


**Figure 4.7** a-c) SEM images of Co/NC at different scale bars. d) TEM image of single polyhedron of Co/NC. e) High-resolution TEM image of Co/NC and corresponding SAED pattern. f) HAADF-STEM image and corresponding EDX elemental mappings of carbon (blue), nitrogen (yellow), and cobalt (green) of Co/NC.

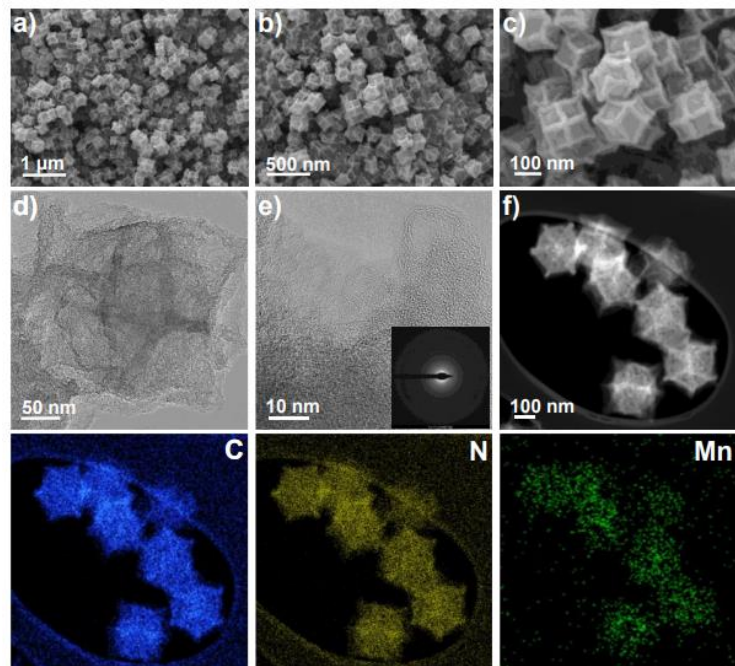


**Figure 4.8** a-c) SEM images of Mn/NC at different scale bars. d) TEM image of single polyhedron of Mn/NC. e) High-resolution TEM image of Mn/NC and corresponding SAED pattern. f) HAADF STEM image of Mn/NC and corresponding EDX elemental mappings of carbon (blue), nitrogen (yellow), and manganese (green).

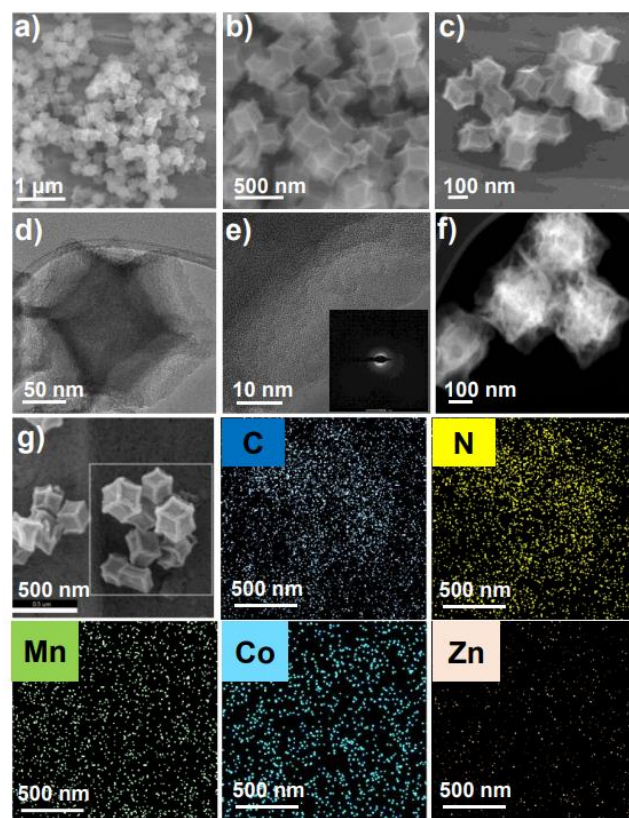


**Figure 4.9** a-c) SEM images of CoMn/NC700 at different scale bars. d) TEM image of single polyhedron of CoMn/NC700. e) High-resolution TEM image of CoMn/NC700 and corresponding SAED pattern. f) STEM image of CoMn/NC700. g) SEM image with corresponding EDX elemental mappings of carbon (blue), nitrogen (yellow), manganese (green), cobalt (greenish blue), and zinc (grey).

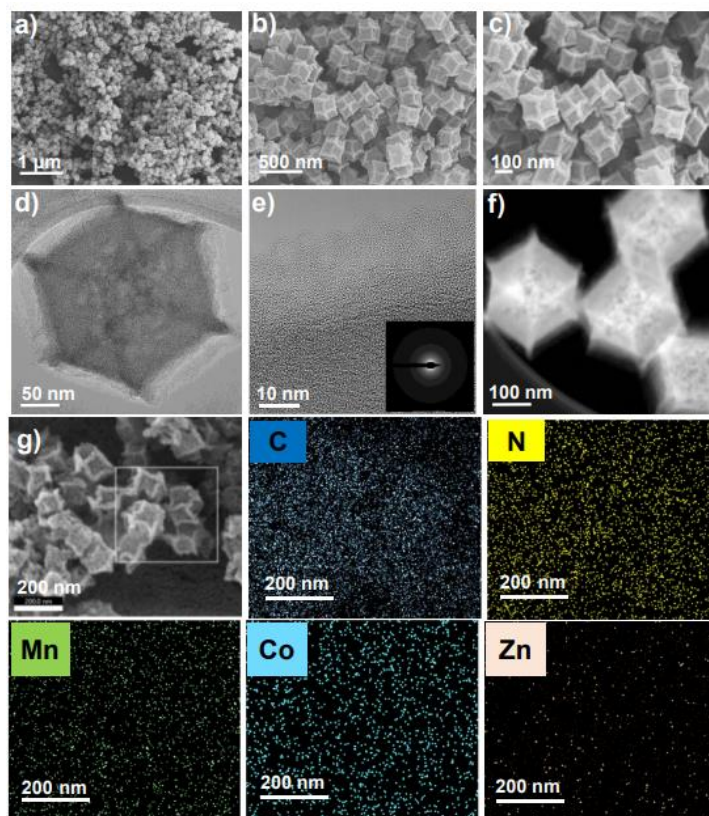


**Figure 4.10** a-c) SEM images of CoMn/NC800 at different scale bars. d) TEM image of single polyhedron of CoMn/NC800. e) High-resolution TEM image of CoMn/NC800 and corresponding SAED pattern. f) STEM image of CoMn/NC800. g) SEM image with corresponding EDX elemental mappings of carbon (blue), nitrogen (yellow), manganese (green), cobalt (greenish blue), and zinc (grey).

PXRD patterns of CoMn/NC exhibited two broad peaks at  $26.3^\circ$  and  $43.4^\circ$ , which represent the carbon (002) and (101) planes, respectively (Figure 4.11 a). No extra PXRD peaks were observed, suggesting the absence of any metal nanoparticles in the CoMn/NC sample and strengthening the microscopic findings. It seems that an acid-washing step during CoMn/NC synthesis is necessary to achieve the desired DSACs, as this step removes the metallic clusters from the sample (Figure 4.11 b). Similar PXRD patterns were also observed for NC, Co/NC, Mn/NC, CoMn/NC700, and CoMn/NC800 with no metal aggregation.

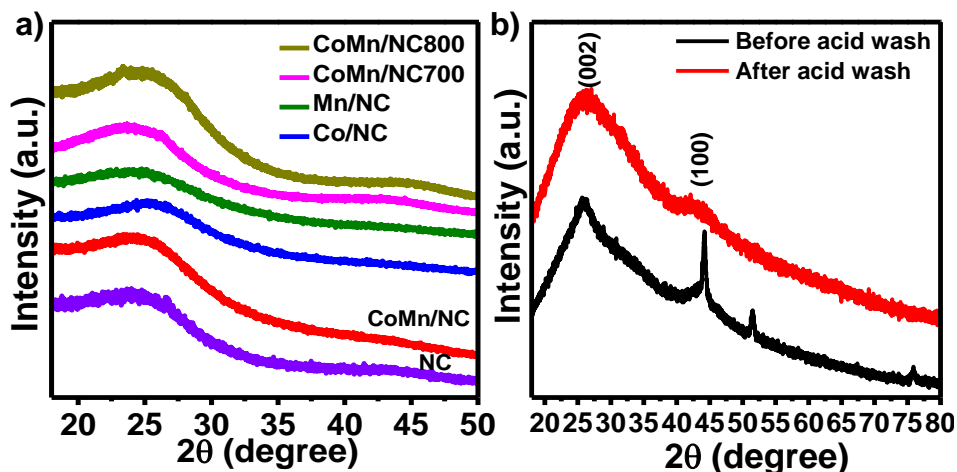


**Figure 4.11** a) PXR patterns, b) Powder X-ray diffraction (PXR) patterns of CoMn/NC before and after acid (10%  $\text{H}_2\text{SO}_4$ ) wash. Two sharp peaks shown in sample (before acid wash) correspond to metallic nanoparticles. These two peaks disappeared in sample (after acid wash), confirming the absence of any metallic or metal oxide nanoparticles within CoMn/NC.

CoMn/NC was further evaluated by Raman spectroscopy, which revealed two Raman bands at  $1588$  and  $1340\text{ cm}^{-1}$ , assigned to the G (ordered graphitic carbon) and D (disordered carbon) bands, respectively (Figure 4.12 a). The relative intensity ratio of D and G bands ( $I_D/I_G$ ) is lower for CoMn/NC than for NC, indicating a higher degree of graphitization in the former. Furthermore, the Raman spectrum of CoMn/NC over a broader Raman shift ( $500\text{--}3000\text{ cm}^{-1}$ ) showed no additional peaks, confirming the absence of any metal oxide in the sample (Figure 4.12 b). Moreover, samples synthesized at lower carbonization temperatures, CoMn/NC700 and CoMn/NC800, showed higher  $I_D/I_G$  ratios, as expected.

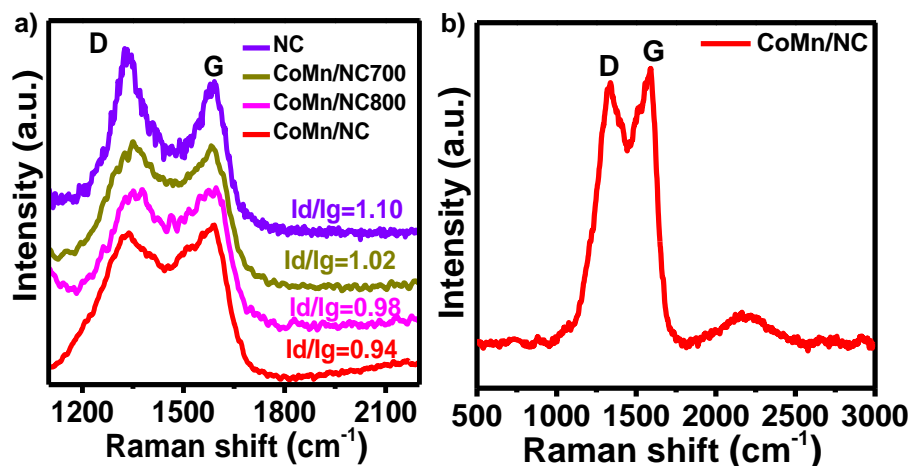


**Figure 4.12** a) Raman spectrum of CoMn/NC and other supporting catalysts, b) Raman spectra of CoMn/NC in wider Raman shift range from 500 to 3000  $\text{cm}^{-1}$ .

The porous nature and specific surface area of CoMn/NC were studied by an  $\text{N}_2$  adsorption isotherm (Figure 4.13 a). It showed significantly increased  $\text{N}_2$  uptake at low pressure with a small hysteresis at higher pressure. This indicates that CoMn/NC has both micro- as well as mesopores in its framework structure. CoMn/NC possesses a high BET surface area of  $1160 \text{ m}^2 \text{ g}^{-1}$  with a pore volume of  $1.04 \text{ cm}^3 \text{ g}^{-1}$ . Notably, NC, Co/NC, and Mn/NC also have comparable specific surface areas, although CoMn/NC700 and CoMn/NC800 showed lower values of  $684$  and  $854 \text{ m}^2 \text{ g}^{-1}$ , respectively. This porous structure was further confirmed by pore size distribution curves showing micropores mainly centered at  $\sim 1.2\text{--}1.3 \text{ nm}$  (Figure 4.13 b). Several mesopores, with a larger size of  $2 \text{ nm}$ , were also observed in a significant ratio. The large surface area and porosity of CoMn/NC are expected to facilitate the access of reactants to active metal sites and thus will enhance the kinetics of electrocatalytic reactions [329].

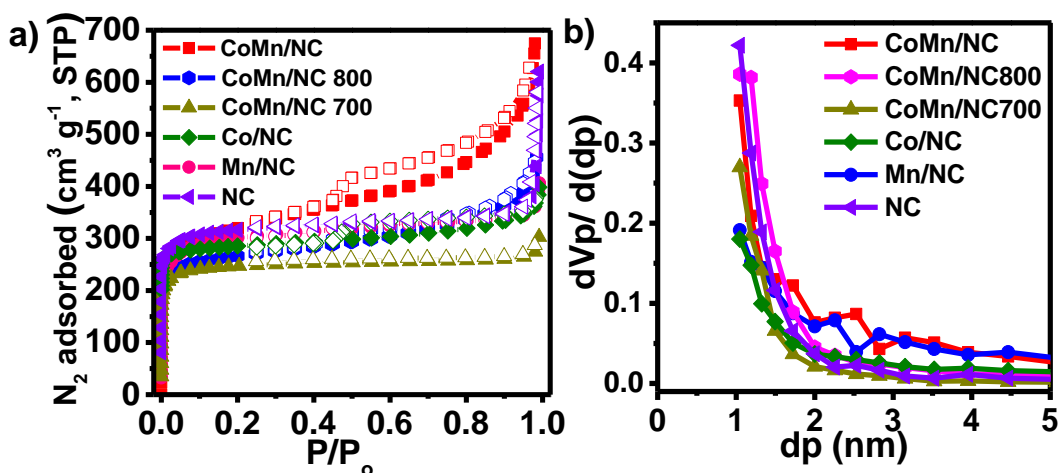


**Figure 4.13** a)  $N_2$ -sorption isotherms of CoMn/NC and supporting catalysts, b) Pore size distribution of CoMn/NC and supporting samples derived from figure a.

XPS was then explored to determine the surface chemical composition of CoMn/NC. It confirmed the existence of C, N, Co, and Mn elements. The N 1s spectrum of CoMn/NC revealed the presence of pyridinic, pyrrolic, and graphitic N at binding energies of 398.1, 400.2, and  $\sim 400.9$  eV, respectively (Figure 4.14 a) [293]. Pyridinic N is mostly known as anchoring sites for SACs stabilization [301]. Therefore, N atoms coordinated with single Co and Mn atoms were also observed at 399.4 eV [330]. The Co 2p spectrum of CoMn/NC showed two major peaks at 779.8 and 796.1 eV, attributed to N-coordinated Co  $2p_{3/2}$  and Co  $2p_{1/2}$ , respectively (Figure 4.14 b). Similarly, the Mn 2p spectrum showed two peaks at 641.4 and 654.5 eV, attributed to N-coordinated Mn  $2p_{3/2}$  and Mn  $2p_{1/2}$ , respectively (Figure 4.14 c). These XPS results reveal that Co and Mn atoms are mostly coordinated with the surrounding N atoms. The absence of any peak intensity corresponding to the Zn 2p spectrum suggests that CoMn/NC is free from Zn impurity (Figure 4.15 a). Similarly, N-coordinated Mn and N-coordinated Co are present in XPS spectra of Mn/NC and Co/NC, respectively (Figure 4.16). Using the XPS survey of CoMn/NC, the surface atomic percentage of all the elements present in the catalyst is summarized in Table 4.2 (Figure 4.15 b). Moreover, inductively coupled plasma-optical emission spectrometry (ICP-OES) suggested 1.1 and 0.6 wt % of Co and Mn in the CoMn/NC catalyst,

respectively. No traceable amount of Zn was found during ICP-OES analysis of CoMn/NC.

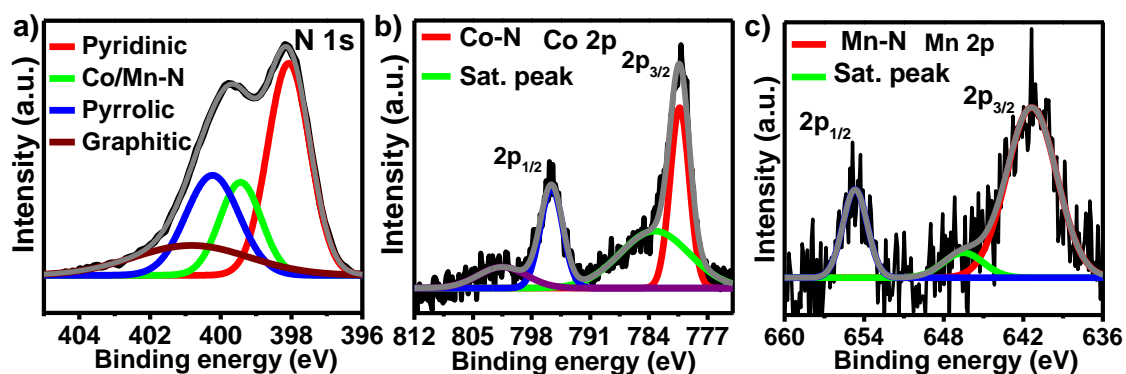


**Figure 4.14** High-resolution XPS spectra of a) N 1s, b) Co 2p, and c) Mn 2p of CoMn/NC.

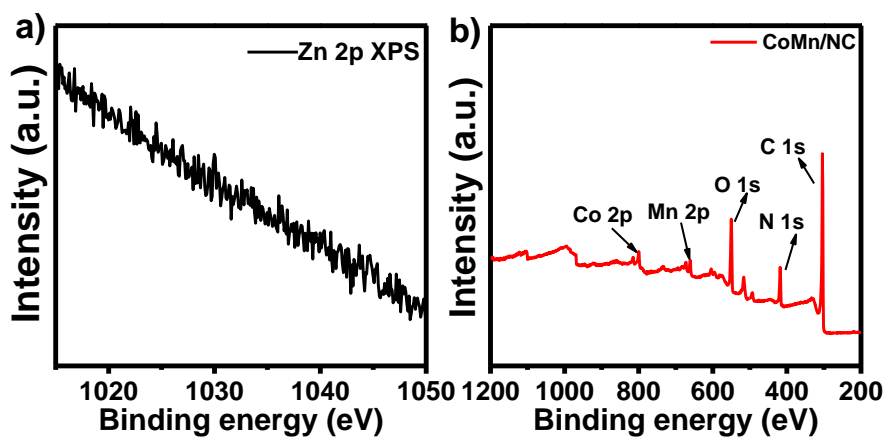


**Figure 4.15** a) Zn 2p XPS spectrum of CoMn/NC, b) XPS survey of CoMn/NC.

**Table 4.2** Element content distribution for CoMn/NC from XPS analysis.

CoMn/NC	Elements in atomic%
C 1s	78.26%
N 1s	10.29 %
O 1s	8.17 %
Co 2p	1.36 %
Mn 2p	1.06 %

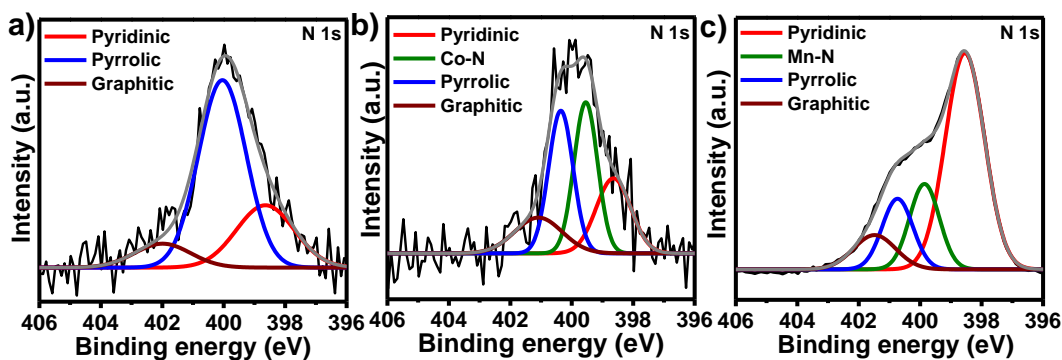


**Figure 4.16** N 1s XPS spectra of a) NC, b) Co/NC, c) Mn/NC.

Furthermore, to recognize the chemical and coordination structures of Co and Mn atoms in CoMn/NC, synchrotron X-ray absorption spectroscopy (XAS) measurements were used. The near-edge absorption energy of the Co K-edge X-ray absorption near-edge structure (XANES) has a lower value than that for cobalt phthalocyanine (Co-pc) and a higher value than that for Co foil, indicating that the valence state of Co in CoMn/NC exists between  $\text{Co}^0$  and  $\text{Co}^{2+}$  (Figure 4.17 a). Co-pc was chosen as a reference sample for XAS measurement, as it has a square-planar  $\text{CoN}_4$  geometry with  $\text{Co}^{2+}$  valence state. Furthermore, the Co K-edge extended X-ray absorption fine structure (EXAFS) spectrum of CoMn/NC gave two peaks at  $\sim 1.4$  and  $2.1 \text{ \AA}$ , which were attributed to the nearest Co–N and nearest Co–Mn coordination, respectively (Figure 4.17 b). The first major peak at  $1.4 \text{ \AA}$ , seen in both CoMn/NC and Co-pc, suggests that a confined Co–N coordination exists in CoMn/NC. The second peak at  $2.1 \text{ \AA}$  confirms the existence of Co–metal (Co–Mn) bonds in CoMn/NC, which are absent in Co-pc. This validates the existence of Co–Mn dual sites in CoMn/NC, in accord with the recently reported dual metal sites [296]. Simultaneously, the Mn K-edge XANES spectrum showed an edge position located between those of Mn foil and manganese phthalocyanine (Mn-pc), which indicates that the chemical state of Mn in CoMn/NC is located between  $\text{Mn}^0$  and  $\text{Mn}^{2+}$  (Figure 4.17 d). Similar results were obtained from Mn K-edge XANES and EXAFS spectra of CoMn/NC. A major peak at  $1.4 \text{ \AA}$ , which is present in both CoMn/NC and Mn-pc, can



be assigned to an Mn–N scattering path, while a peak for Mn–metal (Mn–Co) coordination can also be seen (Figure 4.17 e). Density functional theory (DFT) studies were performed to conclude the possible dual Co–Mn–N model based on the collected Fourier transform  $k^2$ -weighted  $\chi(k)$ -function curves (Figure 4.17 c, f). The calculated Co–Mn length matched well with the experimental value of 2.5 Å, which further verified the existence of dual Co–Mn sites. In addition, the fitting results of CoMn/NC revealed Co–N and Mn–N coordination numbers close to 3 (3.1 and 3.2, respectively), suggesting the presence of a possible CoN<sub>3</sub>–MnN<sub>3</sub> coordination geometry (Tables 4.3 & 4.4). Furthermore, the second scattering path, Co–Mn or Mn–Co, was best fitted close to 1, suggesting a possible Co–Mn bond in the form of a CoN<sub>3</sub>–MnN<sub>3</sub> environment. These results corroborate the successful synthesis of atomically dispersed Co–Mn dual sites in CoMn/NC, as shown in Figure 4.18, which can have different electronic structures and favor the electrocatalytic reactions. It is important to note here that in general three methods are used to produce DSACs with a direct metal–metal bond: (i) a two-solvent route, where one metal is present at the node and second metal is confined within MOF cavities and then subsequent carbonization to the required temperature is carried out, (ii) a wet-chemistry route, where dual metal precipitation by organic ligands results in DSACs after carbonization, and (iii) direct calcination of metal-dimer precursors. Herein, although both the metals Co and Mn are present at the ZIF-8 nodes, there is the possibility that the Mn complex may also be confined within the cavities of the MOF. This is possible, as Co<sup>2+</sup> reacts with 2-methylimidazole very quickly, likely to be present at the nodes (ZIF-67 is an example), while reaction of Mn<sup>2+</sup> with the linker is slow and may not have sufficient time to come into the picture of the ZIF framework [293]. This competitive reaction nature of two metals with linkers produces case (i) as described above, and thus, dual single-metal atoms are obtained instead of randomly distributed single-atom catalysts.

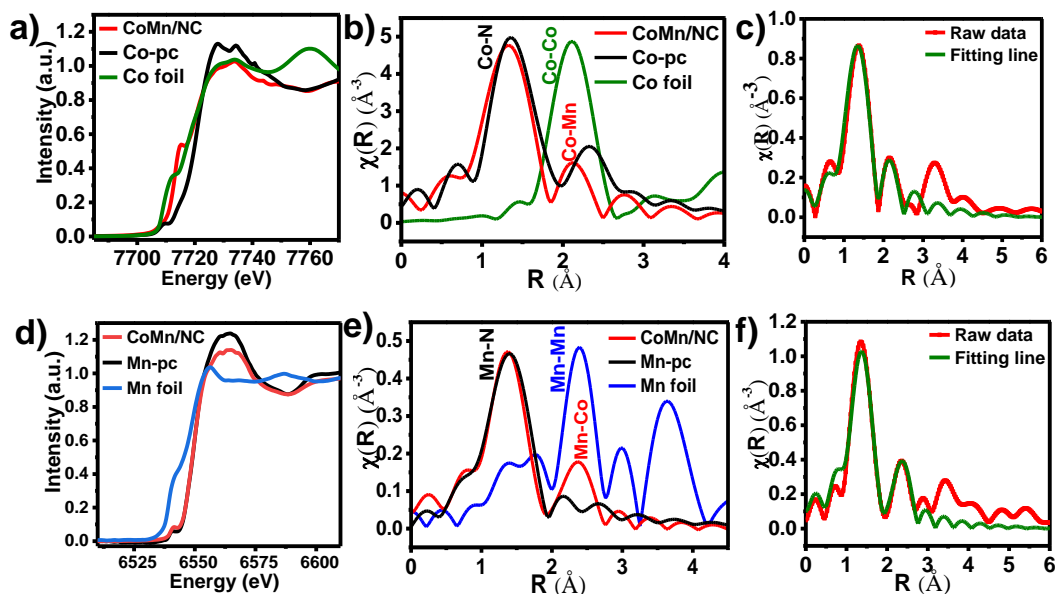


**Figure 4.17** XAS analysis: at Co K-edge, a) normalized XANES spectra of CoMn/NC along with Co-pc (cobalt phthalocyanine) and Co foil, b)  $k^3$ -weighted EXAFS spectra of Co K-edge, and c) EXAFS fitting curve of CoMn/NC at R-space. XAS analysis: at Mn K-edge, d) normalized XANES spectra of CoMn/NC along with Mn-pc (manganese phthalocyanine) and Co foil, e)  $k^3$ -weighted EXAFS spectra of Mn K-edge, f) EXAFS fitting curve of CoMn/NC at R-space.

**Table 4.3** Bond length, coordination number and disorder factors obtained by EXAFS fitting at Co K- edge.

Scattering Path	Parameter	Co-pc	CoMn/NC
Co-N	R (Å)	$1.89 \pm 0.01$	$1.90 \pm 0.01$
	N	$4.0 \pm 0.1$	$3.1 \pm 0.12$
	$\sigma^2$ (Å <sup>2</sup> )	0.0011	0.001
Co-Mn	R (Å)		$2.57 \pm 0.01$
	N		$1.0 \pm 0.01$
	$\sigma^2$ (Å <sup>2</sup> )		0.001

**Table 4.4** Bond length, coordination number and disorder factors obtained by EXAFS fitting at Mn K- edge.

Scattering Path	Parameter	Mn-pc	CoMn/NC
Mn-N	R (Å)	$1.94 \pm 0.01$	$1.92 \pm 0.01$
	N	$4.0 \pm 0.1$	$3.2 \pm 0.12$
	$\sigma^2$ (Å <sup>2</sup> )	0.003	0.001
Mn-Co	R (Å)		$2.56 \pm 0.01$
	N		$1.0 \pm 0.02$
	$\sigma^2$ (Å <sup>2</sup> )		0.001

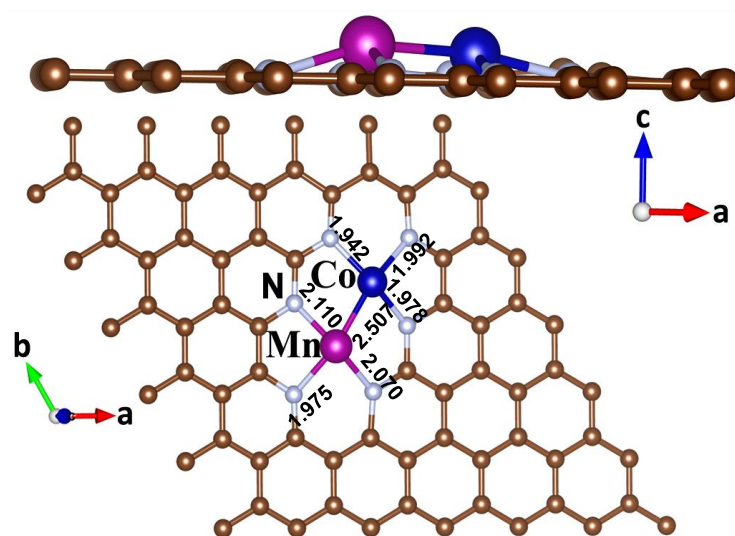


**Figure 4.18** Proposed atomic model of the Co–Mn dual active site present in CoMn/NC with bond length values (Å) using DFT methods.

The ORR performance of CoMn/NC was evaluated in an O<sub>2</sub>-saturated 0.1 M KOH solution using a rotating disk electrode (RDE). Cyclic voltammetry (CV) showed a great reduction peak at 0.82 V, confirming that CoMn/NC has impressive ORR electrocatalytic activity (Figure 4.19).

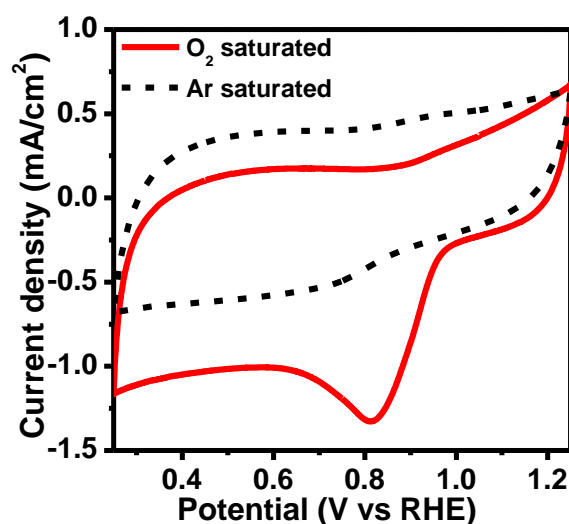


**Figure 4.19** CV curves of CoMn/NC in Ar- and O<sub>2</sub>-saturated 0.1 M KOH acquired at scan rate of 50 mV/s.

The linear sweep voltammetry (LSV) measurements suggested that CoMn/NC has good ORR performance, having onset ( $E_{\text{onset}}$ ) and half-wave potentials ( $E_{1/2}$ ) of 0.98 and 0.89

V, respectively, close to those of Pt/C (1.01 and 0.88 V) (Figure 4.20 a). The  $E_{1/2}$  value of CoMn/NC is higher than those of Co/NC (0.83 V) and Mn/NC (0.82 V) (Figure 4.20 b).

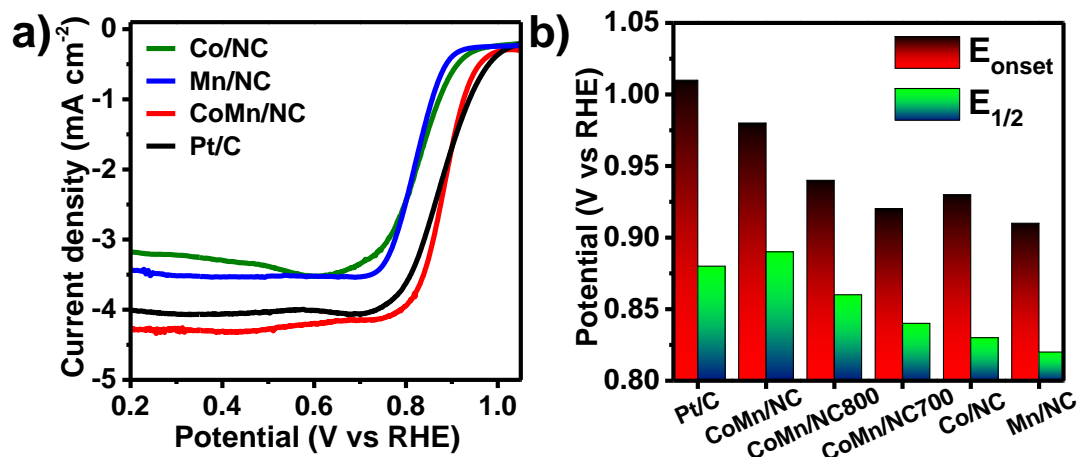


**Figure 4.20** Electrochemical ORR performance in 0.1 M KOH. a) LSV curves of CoMn/NC, Co/NC, Mn/NC, and Pt/C catalysts with a sweep rate of 5 mV/s and a rotation rate of 900 rpm, b)  $E_{onset}$  and  $E_{1/2}$  of CoMn/NC, Pt/C, and supporting catalysts.

The  $e^-$  transfer number ( $n$ ) of CoMn/NC was estimated from the LSVs (Figure 4.21 a) using the Koutecky–Levich (K-L) equation, giving a value of 3.97 at 0.8 V (vs RHE), confirming the direct  $4e^-$  transfer ORR process. The  $n$  value and  $H_2O_2$  yield were further calculated with a rotating ring-disk electrode (RRDE), which gave  $\sim 4$  and  $<2\%$ , respectively, over the potential range of 0.8–0.2 V, revealing near-complete removal of unrequired  $H_2O_2$  formation (Figure 4.21 b).

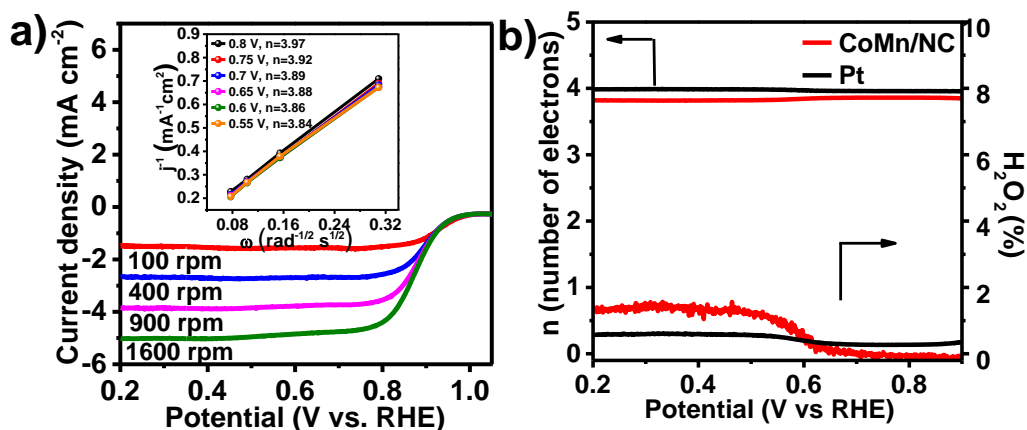


**Figure 4.21** a) Polarization curves of CoMn/NC at different rotation speeds. The inset shows the corresponding K-L plots with  $e^-$  transfer number ( $n$ ) at different potentials, b)  $H_2O_2$  yield and  $n$  values for CoMn/NC and Pt/C, calculated from RRDE measurements.

Moreover, a Tafel plot showed a smaller slope value of  $86 \text{ mV dec}^{-1}$  for CoMn/NC, close to that of Pt/C ( $\sim 90 \text{ mV dec}^{-1}$ ) and better than those of Co/NC ( $113 \text{ mV dec}^{-1}$ ) and Mn/NC ( $118 \text{ mV dec}^{-1}$ ) (Figure 4.22).

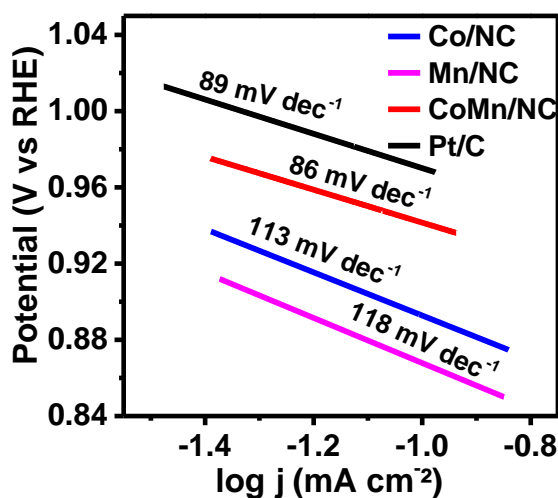


**Figure 4.22** Tafel slopes of CoMn/NC and other supporting catalysts in 0.1 M KOH.

The catalysts synthesized at 700 and 800 °C, CoMn/NC700 and CoMn/NC800, respectively, also showed noticeable ORR activity (Figure 4.23).

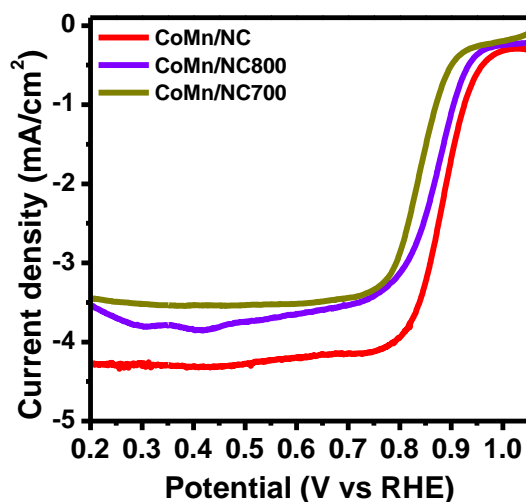


**Figure 4.23** ORR linear sweep voltammograms (LSVs) of CoMn/NC, CoMn/NC700, and CoMn/NC800 in 0.1 M KOH acquired at scan rate of 5 mV/s.

Interestingly, supporting catalysts also favored the 4e<sup>-</sup> transfer ORR process (Figure 4.24 and Tables 4.5–4.8).

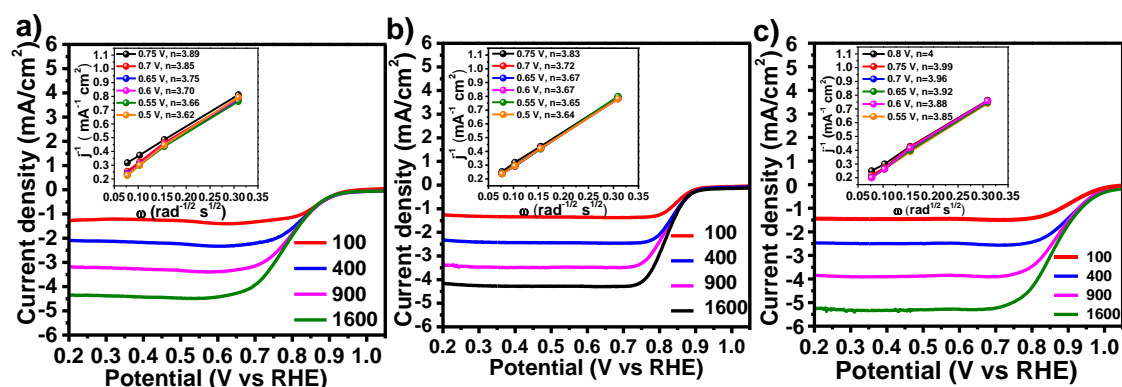


**Figure 4.24** RDE polarization curves for a) Co/NC, b) Mn/NC, and c) Pt/C in 0.1 M KOH acquired at scan rate of 5 mV/s. Inset figures are corresponding K-L plots with e-transfer numbers at different potentials.

**Table 4.5** A summary of kinetic parameters derived from the K-L plots of CoMn/NC in 0.1 M KOH.

E/ V vs RHE	Slope of K-L plot	n	Intercept	J <sub>k</sub> (mA/cm <sup>2</sup> )
0.8	2.175	3.97	0.0567	17.64
0.75	2.202	3.92	0.044	22.73
0.7	2.219	3.89	0.0435	22.98
0.65	2.227	3.88	0.0387	25.87

**Table 4.6** A summary of kinetic parameters derived from the K-L plots of Pt/C in 0.1 M KOH.

E/ V vs RHE	Slope of K-L plot	n	Intercept	$J_k$ (mA/cm <sup>2</sup> )
0.8	2.161	4	0.0927	10.78
0.75	2.166	3.99	0.0898	11.13
0.7	2.179	3.96	0.0764	13.08
0.65	2.206	3.92	0.0757	13.21

**Table 4.7** A summary of kinetic parameters derived from the K-L plots of Co/NC in 0.1 M KOH.

E/ V vs RHE	Slope of K-L plot	n	Intercept	$J_k$ (mA/cm <sup>2</sup> )
0.75	2.220	3.89	0.1465	6.82
0.7	2.245	3.85	0.0943	10.66
0.65	2.305	3.75	0.0705	14.18
0.6	2.233	3.70	0.0684	14.61

**Table 4.8** A summary of kinetic parameters derived from the K-L plots of Mn/NC in 0.1 M KOH.

E/ V vs RHE	Slope of K-L plot	n	Intercept	$J_k$ (mA/cm <sup>2</sup> )
0.75	2.256	3.83	0.088	11.34
0.7	2.325	3.72	0.064	15.53
0.65	2.355	3.67	0.053	18.82
0.6	2.355	3.67	0.054	18.42

The Nyquist plots of electrochemical impedance spectroscopy (EIS) revealed that CoMn/NC has a smaller semicircle diameter than Co/NC or Mn/NC, suggesting a lower charge transfer resistance ( $R_{ct}$ ) for the former (Figure 4.25 a). These observations suggest that CoMn/NC has better ORR kinetics and a more favorable charge-transfer process. Moreover, to get the intrinsic activity of total active sites, the double-layer capacitance ( $C_{dl}$ ) was determined, as  $C_{dl}$  is mostly correlated to the electrochemical surface area

(ECSA). As shown in Figure 4.25 b and Figure 4.26, CoMn/NC has much larger  $C_{dl}$  value (13.47 mF cm<sup>-2</sup>) than Co/NC (9.29 mF cm<sup>-2</sup>) or Mn/NC (7.43 mF cm<sup>-2</sup>), suggesting that the Co–Mn pair is significantly involved as a catalytically active site for ORR activity. This was further confirmed by the much higher kinetic current density ( $J_k$ ) measured for CoMn/NC (22.73 mAcm<sup>-2</sup>) in comparison to Pt/C (11.12 mA cm<sup>-2</sup>), Co/NC (6.82mA cm<sup>-2</sup>), and Mn/NC (11.34 mA cm<sup>-2</sup>) (Figure 4.27).

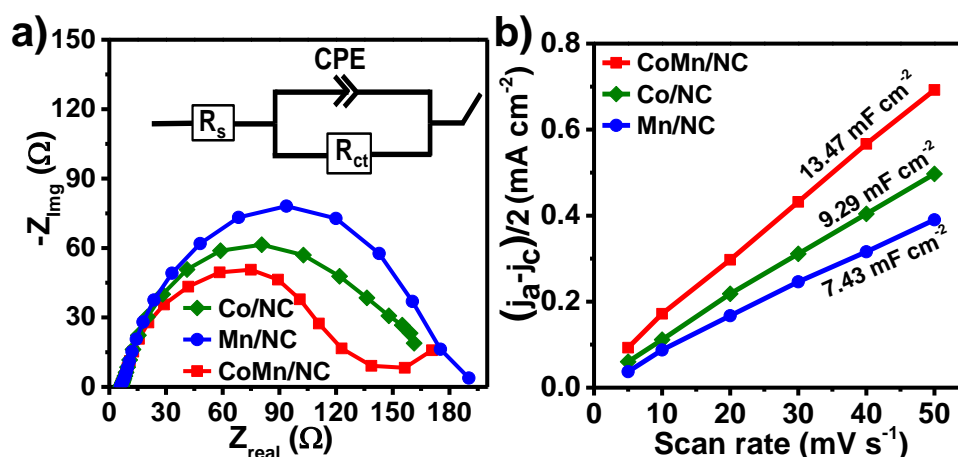


**Figure 4.25** a) Nyquist plots, and b) electrochemical double-layer capacitance ( $C_{dl}$ ) of CoMn/NC and supporting catalysts.

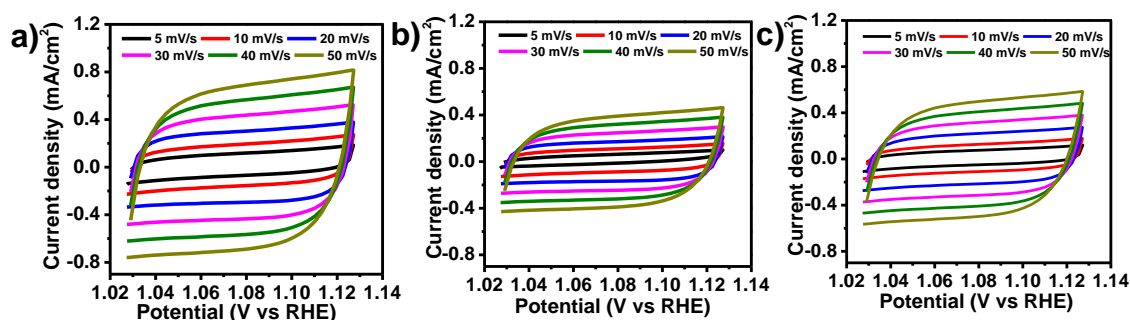


**Figure 4.26** Cyclic voltammograms for a) CoMn/NC, b) Mn/NC, c) Co/NC in 0.1 M KOH at different electrochemical scan rates 5, 10, 20, 30, 40, 50 mV/s within potential window 1.03-1.13 V (vs RHE) (non-faradaic region).



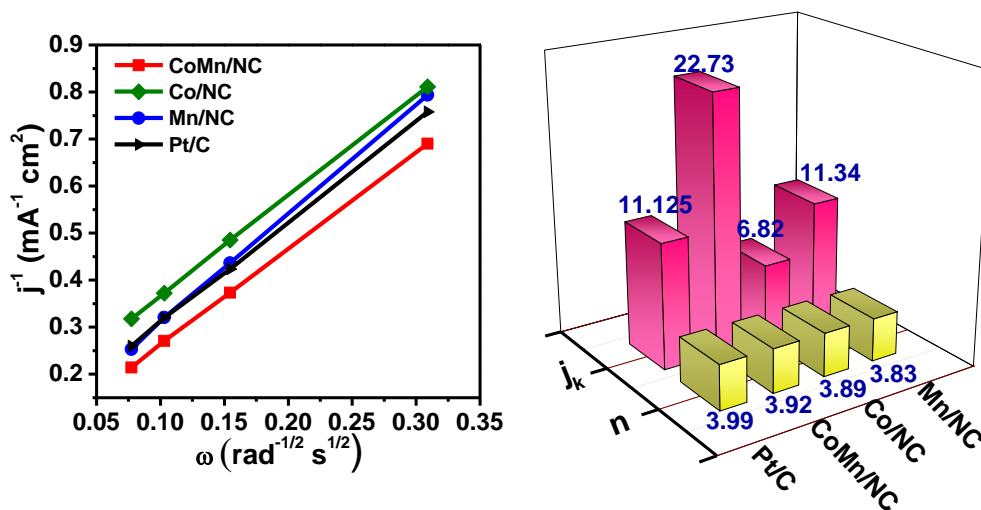


**Figure 4.27** Comparative plots for K-L analysis (left) and derived rate limiting currents ( $j_k$ ) & number of e- transfer ( $n$ ) (right) for ORR in 0.1 M KOH using CoMn/NC, Co/NC, Mn/NC, and Pt/C at 0.75 V vs RHE.

Unlike the Pt/C catalyst, CoMn/NC showed tolerance to methanol (Figure 4.28 a). Notably, CoMn/NC demonstrated a better long-term stability than Pt/C, as can be seen in chronoamperometry measurements (Figure 4.28 b), showing a small decay in E1/2 (14 mV) (Figure 4.28 c & d). Considering the longer period of the stability test, CoMn/NC showed a maintained relative current percentage of 86.8% after 72 h of continuous operation (Figure 4.28 e). In addition, a cyclic voltammetry (CV) study suggested minimal potential loss even after 10000 cycles (Figure 4.28 f). These findings well illustrate the superior ORR performance of CoMn/NC.

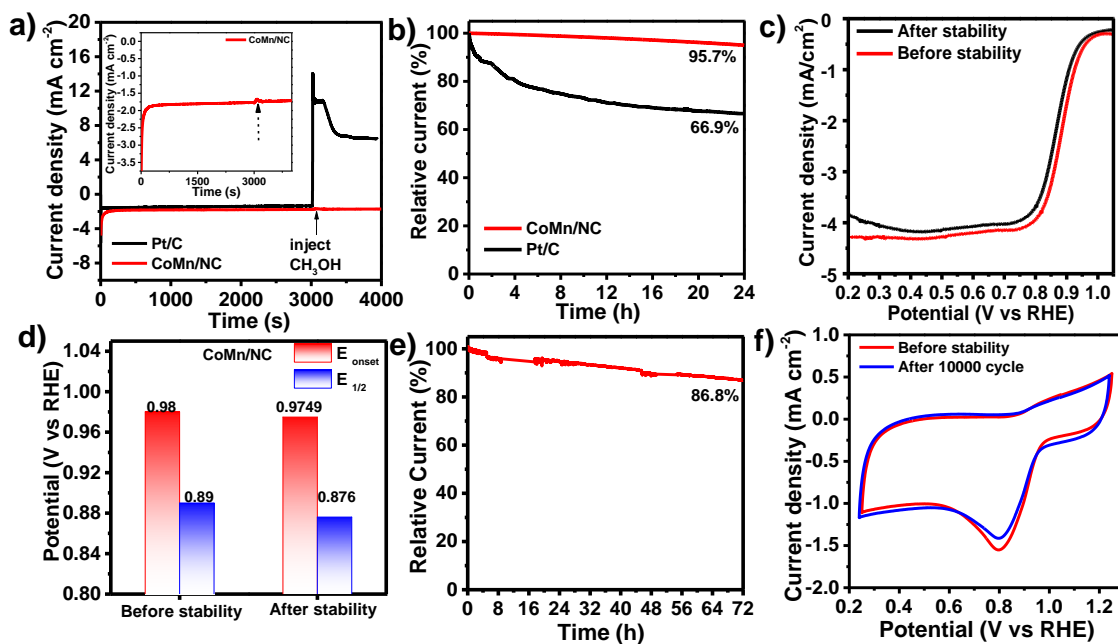


**Figure 4.28** a) Comparison of methanol tolerances of CoMn/NC and Pt/C at 0.86 V (vs RHE). Methanol was injected into the electrolyte at 3000 s, b) Chronoamperometric durability test for CoMn/NC and Pt/C at 0.89 V (vs RHE), c) ORR LSVs of CoMn/NC before and after stability test with continuous run for 24 h at a constant potential of 0.89 V (vs RHE) with electrode rotation of 900 rpm in 0.1 M KOH solution, d) comparison of  $E_{\text{onset}}$  and  $E_{1/2}$  of CoMn/NC before and after stability test, e) Chronoamperometric ORR stability test of CoMn/NC with continuous run for 72 h at a constant potential of 0.89 V (vs RHE) with electrode rotation of 900 rpm in 0.1 M KOH solution, and f) ORR cyclic voltammetry curves of CoMn/NC before and after 10,000 cycles.

The ORR activity of CoMn/NC was further assessed in an  $\text{O}_2$ -saturated 0.5 M  $\text{H}_2\text{SO}_4$  solution (Figure 4.29 a). CoMn/NC exhibited good catalytic activity in an acidic electrolyte as well, having  $E_{\text{onset}}$  and  $E_{1/2}$  values of 0.90 and 0.82 V, respectively, comparable to those of commercial Pt/C (Figure 4.29 b). The CoMn/NC ORR performance was found to be superior among all supporting catalysts (Figure 4.29 a and Figure 4.29 c).

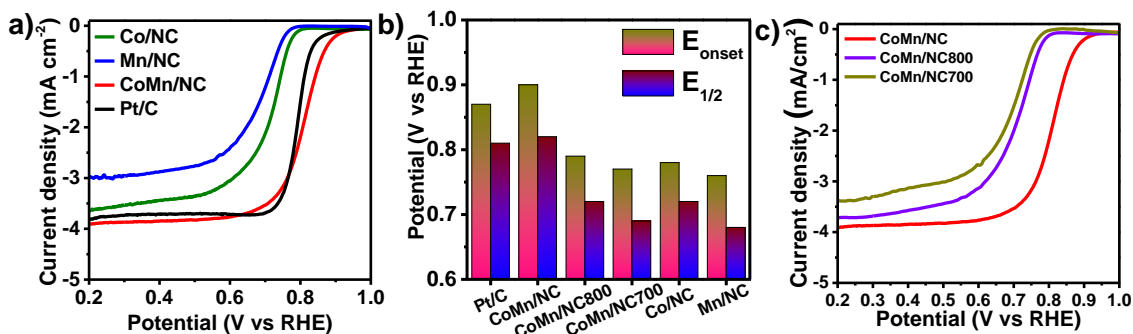


**Figure 4.29** Electrochemical ORR performance in 0.5 M  $\text{H}_2\text{SO}_4$ . a) LSV curves for CoMn/NC, Co/NC, Mn/NC, and Pt/C catalysts with a sweep rate of 5 mV/s and a rotation

rate of 900 rpm, b) Onset potentials and half-wave potentials ( $E_{1/2}$ ) of CoMn/NC, Pt/C, and supporting catalysts, c) ORR LSVs of CoMn/NC, CoMn/NC700 and CoMn/NC800 in 0.5 M  $H_2SO_4$  acquired at scan rate of 5 mV/s.

The K-L plot derived from the RDE curves at different electrode rotations revealed an  $n$  value of 3.97 at 0.7 V (vs RHE) (Figure 4.30 a and Figure 4.31). The RRDE measurements further demonstrate that  $n$  and the  $H_2O_2$  yield is  $\sim 4$  and  $< 1\%$ , respectively, agreeing with the  $n$  value achieved from the K-L plot (Figure 4.30 b). These results suggest that CoMn/NC catalyzes the oxygen reduction solely via  $4e^-$  transfer in acidic electrolyte, like in alkaline electrolyte.

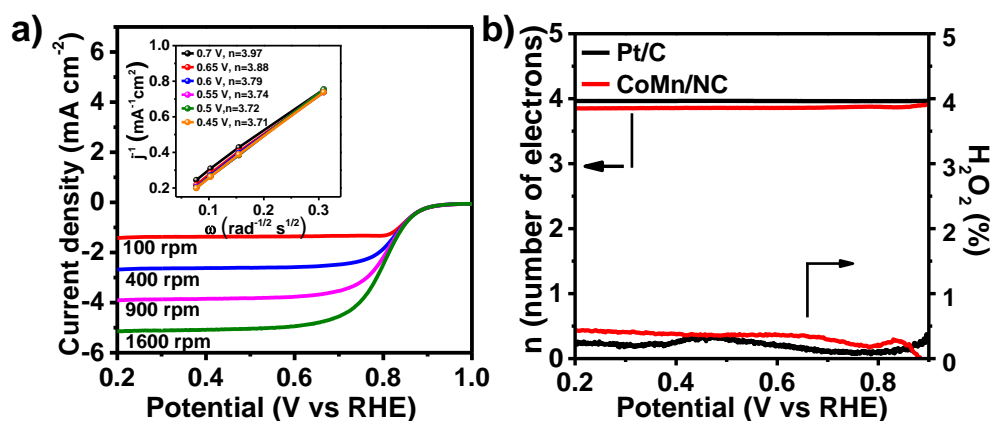


**Figure 4.30** Comparative plots for K-L analysis (left) and derived rate limiting currents (jk) & number of  $e^-$  transfer ( $n$ ) (right) for ORR in 0.1 M KOH using CoMn/NC, Co/NC, Mn/NC, and Pt/C at 0.75 V vs RHE.

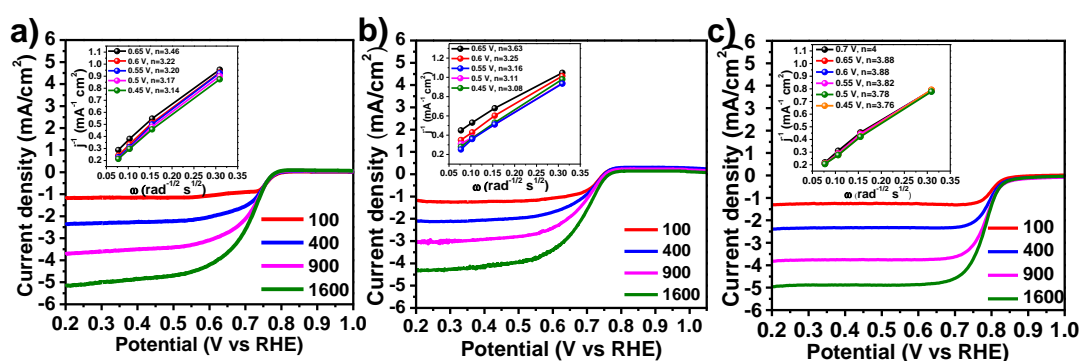


**Figure 4.31** RDE polarization curves of a) Co/NC, b) Mn/NC and c) Pt/C in 0.5 M  $H_2SO_4$  solution acquired at scan rate of 5 mV/s. Inset figures are corresponding K-L plots with  $e^-$  transfer numbers at different potentials.

A comparison of Tafel slope values of CoMn/NC ( $95.7 \text{ mV dec}^{-1}$ ) with respect to Pt/C ( $96.8 \text{ mV dec}^{-1}$ ) confirms the faster ORR kinetics of the former (Figure 4.32 a).

Considering the metal contents, the mass activity for CoMn/NC was found to be much higher than that of Pt/C (Figure 4.32 b). Faster kinetics was further confirmed by a much higher  $J_k$  value measured for CoMn/NC ( $19.20 \text{ mA cm}^{-2}$ ) in comparison to Pt/C ( $9.99 \text{ mA cm}^{-2}$ ), Co/NC ( $5.48 \text{ mA cm}^{-2}$ ), and Mn/NC ( $3.19 \text{ mA cm}^{-2}$ ) (Figure 4.32 c and Tables 4.9–4.12).

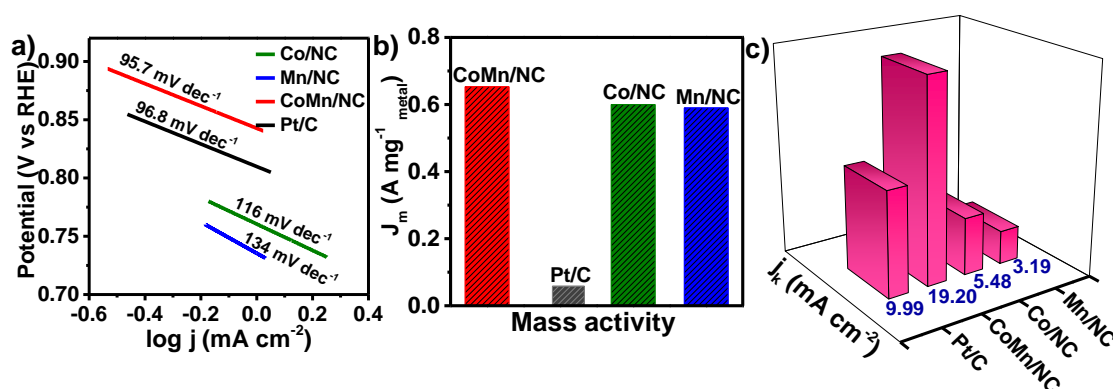


**Figure 4.32** a) Tafel slopes, b) mass activities, and c)  $J_k$  values of CoMn/NC and supporting catalysts.

**Table 4.9** Summary of kinetic parameters derived from the K-L plots of CoMn/NC in  $0.5 \text{ M H}_2\text{SO}_4$ .

E/ V vs RHE	Slope of K-L plot	n	Intercept	$J_k$ (mA/cm <sup>2</sup> )
0.7	2.178	3.97	0.08302	12.04
0.65	2.231	3.88	0.05206	19.21
0.6	2.285	3.79	0.03515	28.45
0.55	2.312	3.74	0.02707	36.94

**Table 4.10** Summary of kinetic parameters derived from the K-L plots of Pt/C in  $0.5 \text{ M H}_2\text{SO}_4$ .

E/ V vs RHE	Slope of K-L plot	n	Intercept	$J_k$ (mA/cm <sup>2</sup> )
0.7	2.158	4.0	0.12107	8.26
0.65	2.224	3.88	0.1001	9.99
0.6	2.23	3.88	0.09211	10.85
0.55	2.265	3.82	0.08949	11.17

**Table 4.11** Summary of kinetic parameters derived from the K-L plots of Co/NC in 0.5 M H<sub>2</sub>SO<sub>4</sub>.

E/ V vs RHE	Slope of K-L plot	n	Intercept	J <sub>k</sub> (mA/cm <sup>2</sup> )
0.65	2.498	3.46	0.1822	5.49
0.6	2.688	3.22	0.0955	10.48
0.55	2.7017	3.20	0.0741	13.50
0.5	2.724	3.17	0.0591	16.92

**Table 4.12** Summary of kinetic parameters derived from the K-L plots of Mn/NC in 0.5 M H<sub>2</sub>SO<sub>4</sub>.

E/ V vs RHE	Slope of K-L plot	n	Intercept	J <sub>k</sub> (mA/cm <sup>2</sup> )
0.65	2.376	3.63	0.3127	3.19
0.6	2.658	3.25	0.1920	5.20
0.55	2.735	3.16	0.089	11.17
0.5	2.775	3.11	0.0805	12.42

In addition, CoMn/NC demonstrated high ORR durability, as confirmed by a chronoamperometry test (Figure 4.33 a and Figure 4.33 b) with minimal E<sub>1/2</sub> potential loss (Figure 4.33 c). All these results imply that CoMn/NC is an excellent electrocatalyst for the ORR in an acidic electrolyte as well, where Co–Mn dual sites favor the rate-limiting O<sub>2</sub> activation processes. Comparison lists of the ORR performance of CoMn/NC with those of known different non-precious-metal electrocatalysts in acid and base are given in Tables 4.13 and 4.14.

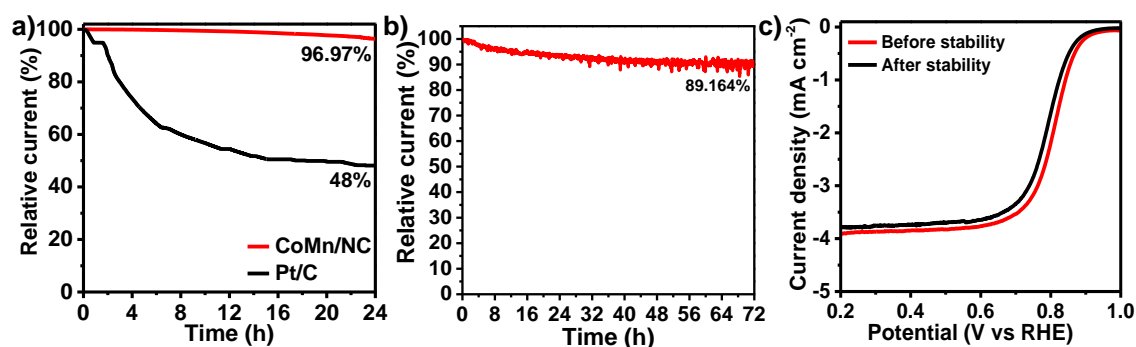


**Figure 4.33** a) Chronoamperometric durability test for CoMn/NC and Pt/C at 0.82 V (vs RHE), b) Chronoamperometric ORR stability test of CoMn/NC with continuous run for 72 h at a constant potential of 0.82 V (vs RHE) with electrode rotation of 900 rpm in 0.5 M H<sub>2</sub>SO<sub>4</sub> solution, c) LSV curves of CoMn/NC before and after the durability test.

Considering the good ORR activity of CoMn/NC in an acidic electrolyte, first-principles DFT calculations using the Vienna ab initio Simulation Package (VASP) were performed. We calculated the potential energy surface of the ORR by optimizing a structure with Co–Mn DSACs sites encapsulated in N-doped graphene. The relative stability of the CoN<sub>3</sub>–MnN<sub>3</sub> pair was found to be –0.27 eV: i.e., CoN<sub>3</sub>–MnN<sub>3</sub> is comparatively 0.27 eV more stable than the corresponding homonuclear structures (CoN<sub>3</sub>–CoN<sub>3</sub> and MnN<sub>3</sub>–MnN<sub>3</sub>) (Figure 4.34).

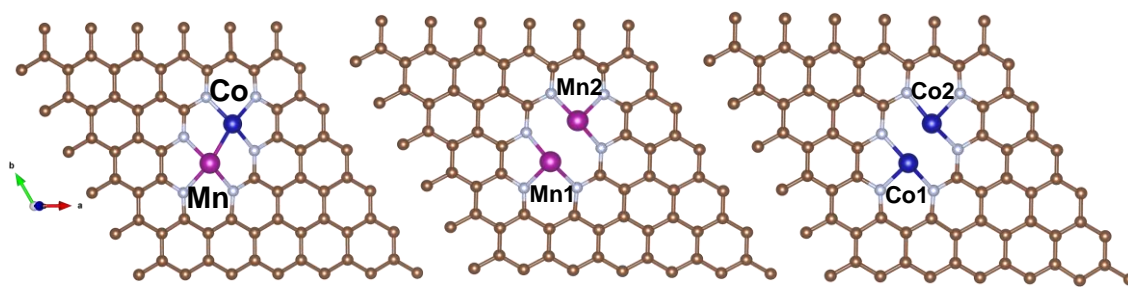


**Figure 4.34** Optimized geometries of CoN<sub>3</sub>–MnN<sub>3</sub>, MnN<sub>3</sub>–MnN<sub>3</sub>, and CoN<sub>3</sub>–CoN<sub>3</sub> DSAC models.

Besides, to further confirm the aptness of the CoN<sub>3</sub>–MnN<sub>3</sub> structural model, we considered other possible CoN<sub>x</sub>C<sub>y</sub>–MnN<sub>x</sub>C<sub>y</sub> models (where x, y, x', and y' = 0–3) and calculated their relative stability energies compared to that of the CoN<sub>3</sub>–MnN<sub>3</sub> model (Figures 4.35 and 4.36). The relative stability study vividly exhibits that all the other possible CoN<sub>x</sub>C<sub>y</sub>–MnN<sub>x</sub>C<sub>y</sub> models are considerably unstable with positive relative stability energy

compared to  $\text{CoN}_3\text{-MnN}_3$  and establishes that  $\text{CoN}_3\text{-MnN}_3$  is the most stable structural model of the synthesized catalyst. The higher relative stability of the  $\text{CoN}_3\text{-MnN}_3$  model compared to its other possible analogues further strengthens our consideration of the  $\text{CoN}_3\text{-MnN}_3$  coordination environment of the synthesized catalyst to decisively establish its structure–property relationship. Optimization of the geometry further assisted us in understanding the role of Co–Mn dual sites and the reaction mechanism in the ORR process at the atomic level.

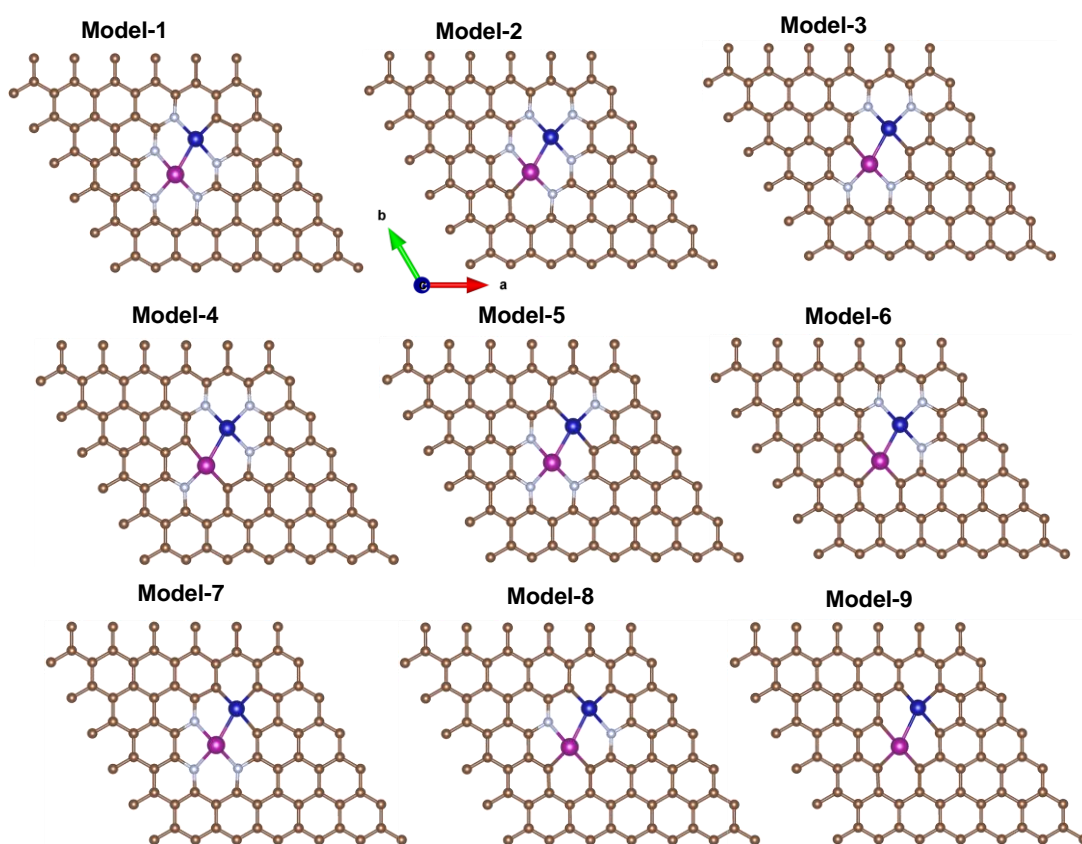


**Figure 4.35** Optimized structures of various possible  $\text{CoN}_x\text{C}_y\text{-MnN}_x\text{C}_y'$  atomic models (where  $x, y, x'$  and  $y' = 0\text{-}3$ ) (blue = Co, pink = Mn, grey = N, and brown = C).

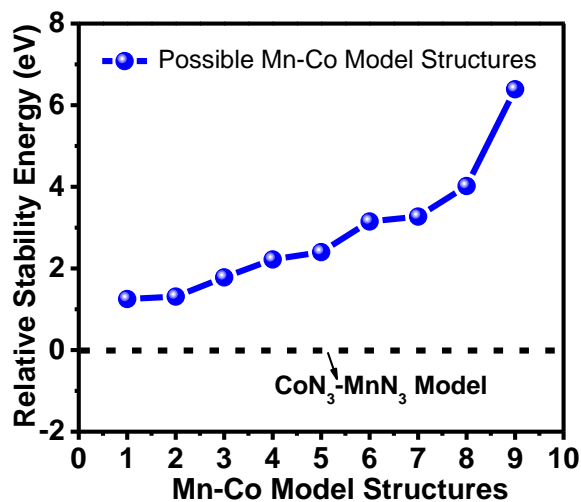


**Figure 4.36** Relative stability of various possible  $\text{CoN}_x\text{C}_y\text{-MnN}_x\text{C}_y'$  structures (where  $x, y, x'$  and  $y' = 0\text{-}3$ ) with respect to the  $\text{CoN}_3\text{-MnN}_3$  model.

Considering the  $4e^-$  transfer process, after the initial adsorption of  $\text{O}_2$  on an Co–Mn site, the ORR can occur via a (i) dissociative or (ii) associative reaction mechanism. In the former, direct splitting of an O–O bond occurs first and then hydrogenation of O atom and the next elementary steps proceed. In the latter, the mechanism first involves hydrogenation of  $\text{O}_2$  followed by O–OH bond dissociation and other reaction steps. An associative mechanism is most common with SACs, as a dissociative mechanism is greatly hindered by the high activation barrier for  $\text{O}_2$  dissociation [331]. We expect that Co–Mn DSAC sites can greatly facilitate an uncommon dissociative ORR mechanism. In our initial finding, it was observed that  $\text{O}_2$  binds preferentially to the Co–Mn site via a bridging mode rather than an end-on mode (Figure 4.37). Further extending the  $\text{O}_2$  bridging mode on the Co–Mn site suggested a stronger  $\text{O}_2$  interaction via a dissociative pathway. The  $\text{O}_2$  binding energy is found to be  $-2.93$  eV with significant lengthening of the O–O bond from 1.22 to 3.34 Å. This facilitates the cleavage of the O–O bond. In contrast, the associative reaction path involves an  $\text{O}_2$  binding energy of  $-2.30$  eV with an O–O bond lengthening upon adsorption on the Co–Mn site from 1.22 to 1.38 Å. This suggests that



Co–Mn dual sites thermodynamically favor the cleavage of the O–O bond via an O<sub>2</sub> bridging and dissociative mechanistic pathway.

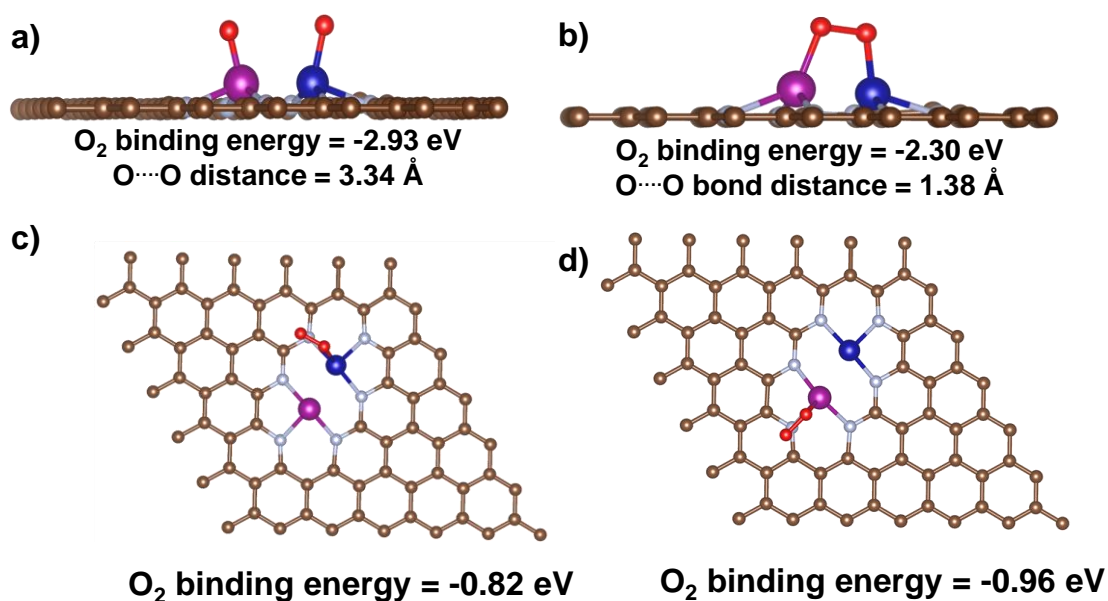


**Figure 4.37** O<sub>2</sub> activation (bridge mode) on the Co–Mn active site in a) dissociative pathways and b) associative pathways, c) O<sub>2</sub> activation (end on) on one of the metal atoms of Co–Mn active site considering associative path at c) Co atom and d) Mn atom. DFT calculation further added that side on adsorption is more favourable over end on.

At zero cell potential ( $U = 0$  V vs RHE), the free energy diagram consists of a downhill process for both the dissociative and associative paths, suggesting all ORR elementary reaction steps are exothermic in nature (Figure 4.38 a, b). At the equilibrium thermodynamic potential ( $U_0 = 1.23$  V vs RHE), some of the elementary reactions in both reaction mechanisms are endothermic and thus thermodynamically unfavorable on Co–Mn sites. However, the limiting potentials ( $U_L$ ) for dissociative and associative pathways were calculated as 0.40 and 0.72 V (vs RHE), respectively, showing that at these potentials all the elementary steps proceed spontaneously. The ORR efficacy of an electrocatalyst can be determined from its overpotential ( $\eta_{\text{theo}} = U_0 - U_L$ ): the lower the overpotential, the higher the catalytic activity. Hence, it can be concluded that even though O<sub>2</sub> activation is facilitated in the dissociative pathway, the overall ORR process on the Mn–Co site is thermodynamically more favorable via an associative reaction mechanism with lower

overpotential compared to the dissociative mechanism. This is due to the stronger adsorption of ORR intermediates on the Mn–Co sites for the dissociative pathway, eventually deteriorating ORR activity.

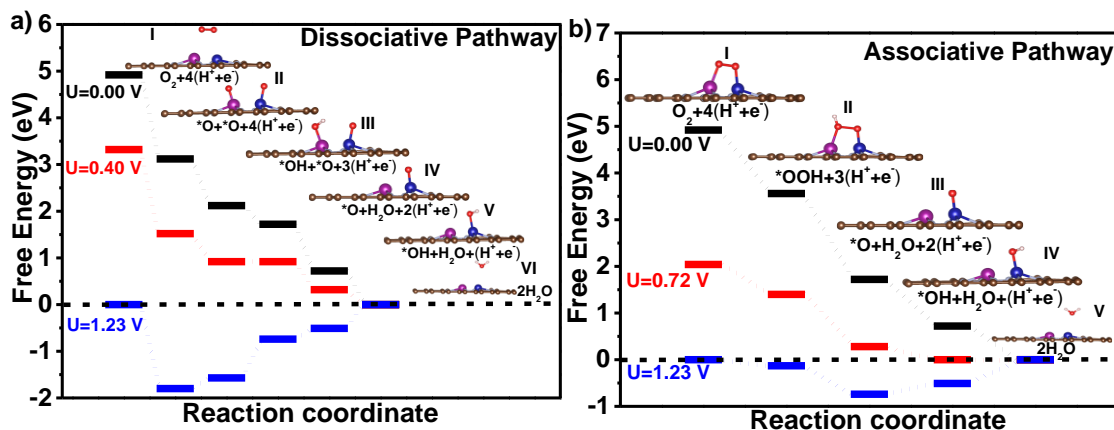


**Figure 4.38** Free energy diagrams for the ORR at Co–Mn DSAC sites for a) dissociative mechanisms and b) associative mechanisms. Elementary reaction steps are shown inside the free energy diagrams.

A kinetic study reveals that the activation energy for the rate-limiting reaction step for the dissociative pathway ( $\text{*O}_2 \rightarrow \text{O}^* + \text{O}^*$ ) was found to be quite large, 1.24 eV (Figure 4.39 a), while for the associative reaction pathway ( $\text{*O}_2 + \text{H}^* \rightarrow \text{O-OH}^*$ ) this value was 0.79 eV (Figure 4.39 b), indicating the kinetic feasibility of the associative over the dissociative pathway. The initial, transition state, and final geometries for all elementary reaction steps are shown in Figure 4.39 a, b. These calculations suggest that because of the high energy barrier for the rate-limiting step, the Co–Mn site may kinetically follow the associative reaction mechanism over the dissociative one. Hence, we conclude that Co–Mn DSAC sites favor the associative ORR mechanism both thermodynamically and kinetically. Therefore, the DFT study unveils that the presence of Mn–Co DSAC sites favors the activation of the O–O bond from 1.22 Å in the gas phase to 1.38 Å in the adsorbed state, resulting in the facile cleavage of  $\text{O}_2$  to enhance ORR activity. Moreover, Mn–Co sites accelerate the ORR reaction kinetics by reducing the activation barrier for the rate-limiting  $\text{O}_2$  activation step by providing two anchoring active sites favoring

metal–oxygen bond formation. This is due to both the accessibility of Mn–Co DSAC sites and a strong synergistic interaction among them. These findings are in good agreement with previously reported Ni–Co, Ni–Fe, and Fe–Co DSACs [297,310,330]. Hence, the theoretical study based on DFT highlights the requirement of a synergistic interaction among the dual single-metal atom sites to substantially improve the ORR activity favoring the metal–metal path in DSACs with multinary active sites.

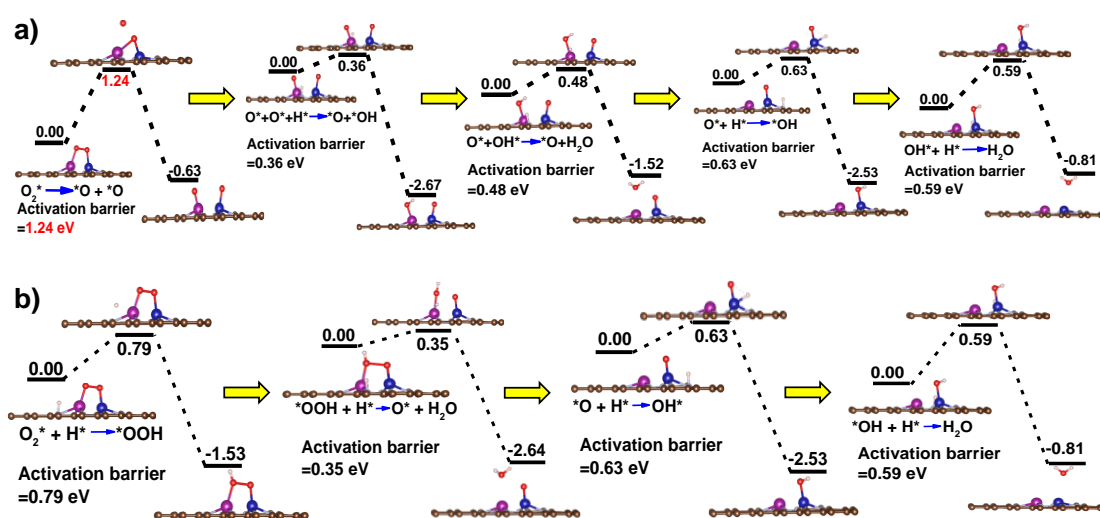


**Figure 4.39** Kinetic aspects of the ORR pathway on Co–Mn DSAC sites in the a) dissociative approach and b) associative approach.

Furthermore, the CoMn/NC performance was tested as the cathode catalyst in a PEM fuel cell. The anode was chosen to be Pt/C. Schematic diagrams of the PEM fuel cell (Figure 4.40 a) and 5-layered membrane electrode assembly with our PEM fuel cell stack are shown in Figures 4.41 and 4.42.

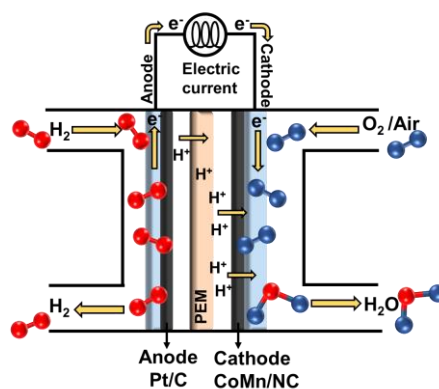


**Figure 4.40** Schematic diagram of a PEM fuel cell.

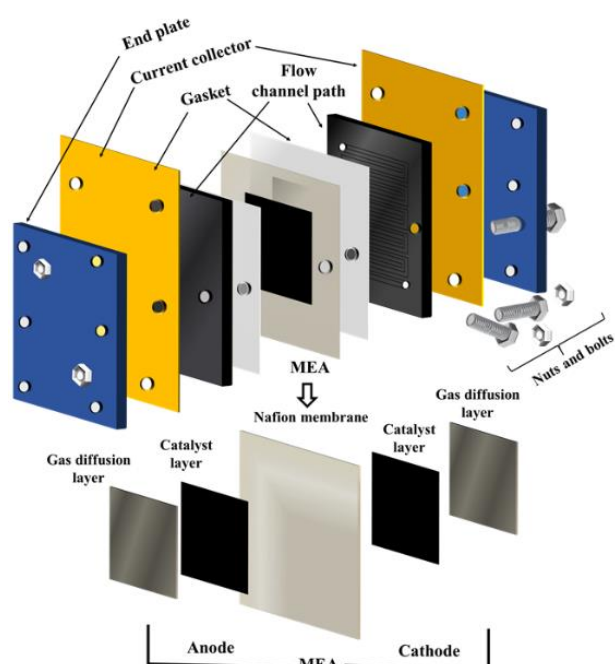


**Figure 4.41** A schematic diagram for single PEM fuel cell assembly showing 5-layered MEA.

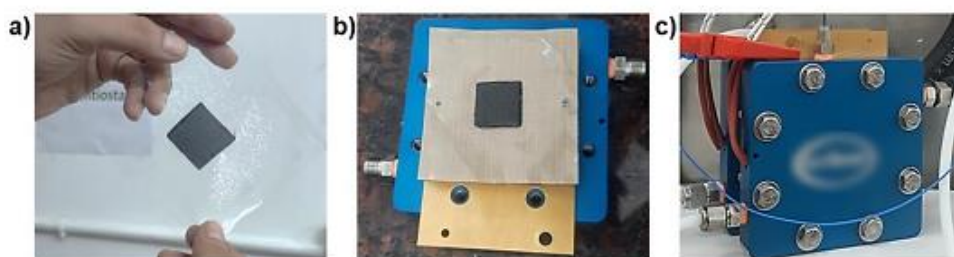


**Figure 4.42** Physical appearance of MEA and single cell PEM fuel cell assembly progress.

With  $O_2$  as oxidant, the cell had an open circuit voltage (OCP) value of 0.98 V, validating the high intrinsic ORR activity under fuel cell conditions (Figure 4.43 a). The cell delivered maximum current and power densities of  $2.24 \text{ A cm}^{-2}$  and  $970 \text{ mW cm}^{-2}$ , respectively, at a back pressure of 0.1 MPa. The cell performance was comparable with that of Pt/C with negligible current loss after  $\sim 24$  h of continuous operation (Figure 4.43 b). Under more practical  $H_2$ /air fuel cell conditions, CoMn/NC as a cathode reached a kinetic current of  $\sim 920 \text{ mA cm}^{-2}$  with a peak power density of  $390 \text{ mW cm}^{-2}$  (Figure 4.43 c).

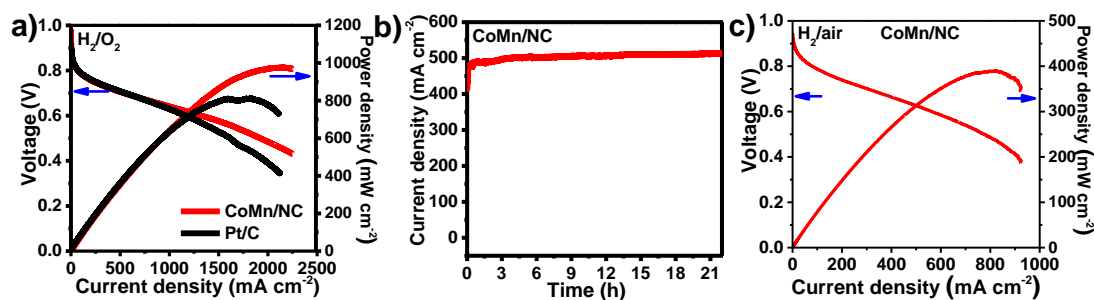


**Figure 4.43** a) Polarization curves and corresponding power densities of CoMn/NC and Pt/C under H<sub>2</sub>/O<sub>2</sub> fuel cell conditions, b) Stability test of CoMn/NC as a cathode in a fuel cell at 0.65 V, c) Polarization curve and corresponding power density of CoMn/NC in H<sub>2</sub>/air fuel cell.

Interestingly, CoMn/NC was found to be quite active for the OER, delivering 10 mA cm<sup>-2</sup> anodic current density in 0.1 M KOH at an overpotential of only 0.30 V (Figure 4.44). The overvoltage between ORR and OER ( $\Delta E$ ), calculated from  $E_{1/2}$  for the ORR and potential at 10 mA cm<sup>-2</sup> for the OER, established good reversibility for CoMn/NC (0.64 V) as compared to Pt/C + IrO<sub>2</sub> (0.79 V).

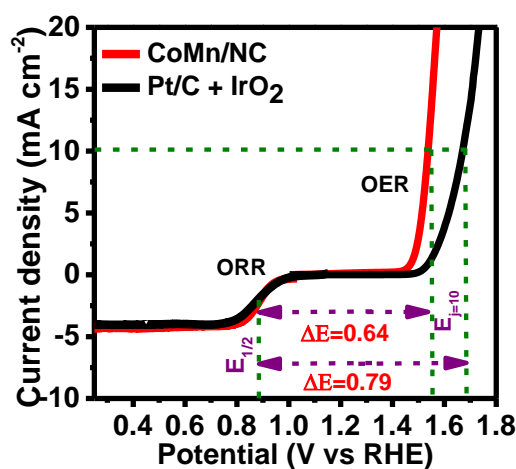


**Figure 4.44** Bifunctional ORR/OER characteristics of CoMn/NC and the Pt/C + IrO<sub>2</sub> couple showing LSVs for both the ORR and the OER, acquired in 0.1 M KOH at a scan rate of 5 mV s<sup>-1</sup>.

Considering this amazing ORR/OER bifunctionality, a homemade Zn–air battery (ZAB) was constructed by employing CoMn/NC as an air cathode. Figure 4.45 a depicts the construction of a rechargeable two-electrode liquid cell employing CoMn/NC or Pt/C + IrO<sub>2</sub> modified on a gas diffusion layer as the cathode and a metallic Zn plate as the anode

counterpart. The cell was filled with an aqueous electrolyte consisting of 6.0 M KOH and 0.2 M Zn(CH<sub>3</sub>COO)<sub>2</sub>. CoMn/NC exhibited a very stable open circuit voltage (OCP) of 1.487 V (Figure 4.45 b). The device delivered an impressive peak power density of 176 mW cm<sup>-2</sup> with CoMn/NC (Figure 4.45 c), outperforming the Pt/C + IrO<sub>2</sub> couple (144 mW cm<sup>-2</sup>). The ZAB driven by CoMn/NC was found to have a much greater discharge current density and a reduced charge–discharge voltage gap compared to Pt/C + IrO<sub>2</sub> (Figure 4.45 d). CoMn/NC possesses voltage gaps of 0.27 V at 25 mA cm<sup>-2</sup>, 0.53 V at 50 mA cm<sup>-2</sup>, and 0.82 V at 100 mA cm<sup>-2</sup>, much lower than those of the Pt/C + IrO<sub>2</sub> couple, 0.75 V at 25 mA cm<sup>-2</sup>, 0.88 V at 50 mA cm<sup>-2</sup>, and 1.12 V at 100 mA cm<sup>-2</sup> current density. We then tested the stability of the catalyst at different discharge current densities (10, 20, 30, and 40 mA cm<sup>-2</sup>), and it holds its potential nicely even after 10 h of operation (Figure 4.45 e). To check the long-term durability, CoMn/NC showed a stable performance with minimal voltage loss after 30 h of use at a current density of 40 mA cm<sup>-2</sup> (Figure 4.45 f). To further assess the rechargeability of CoMn/NC-based ZAB, the cycle stability was determined using a galvanostatic discharge–charge measurement with a duration of 20 min per cycle (10 min for charging and 10 min for discharging) at a current density of 5 mA cm<sup>-2</sup> (Figure 4.45 g). Interestingly, CoMn/NC showed a favorable low voltage gap of 0.59 V (discharge voltage 1.47 V, charge voltage 2.06 V) with a voltage efficiency of 70.69%, while Pt/C + IrO<sub>2</sub> showed a voltage gap of 0.7 V. After ~24 h of cycling performance, CoMn/NC showed a modest increase in the voltage gap (0.61 V) with negligible change in voltage efficiency, while for Pt/C, the voltage gap increases after 14 h up to 0.85 V. The battery displayed a strong cycle performance over 30 h even at a high current density of 20 mA cm<sup>-2</sup> with a cycle duration of 2 h (Figure 4.45 h). All of these results conclude that the CoMn/NC catalyst has a high potential to be a good candidate to serve as a cathode in both PEM fuel cells and ZABs.

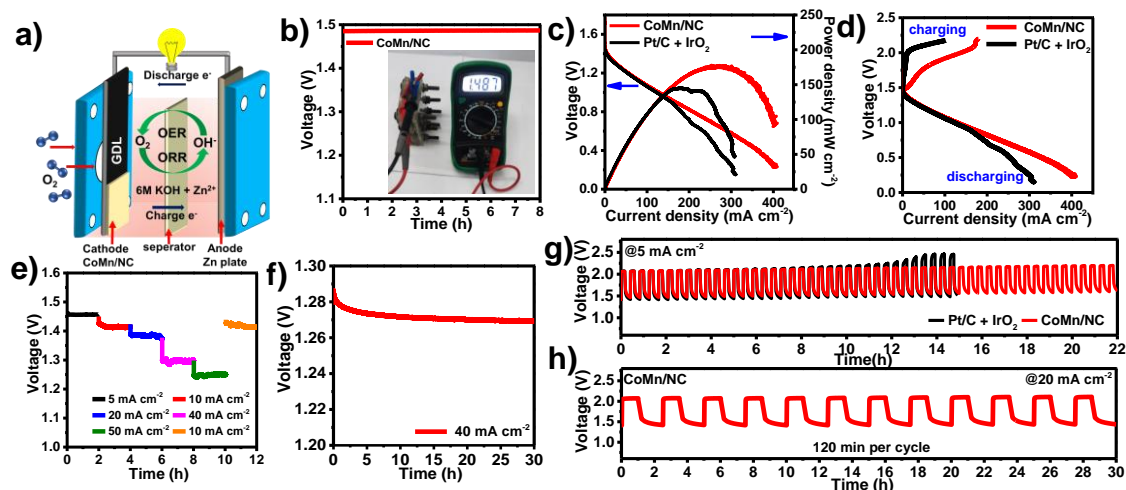


**Figure 4.45** a) Schematic diagram of a homemade liquid cell-based rechargeable ZAB. Performance of ZAB using CoMn/NC as the ORR/OER oxygen electrode: b) open circuit voltage, c) discharge polarization curves and corresponding power density curves showing a comparison with the Pt/C + IrO<sub>2</sub> couple, d) charge–discharge polarization curves showing a comparison with the Pt/C + IrO<sub>2</sub> system, e) repeating discharge curves at various current densities, f) long-time discharge at a fixed current density 40 mA cm<sup>-2</sup>, g) cycling performance at 5 mA cm<sup>-2</sup> current density and 20 min duration per cycle, and h) cycling performance with a cycle duration of 2 h at higher current density of 20 mA cm<sup>-2</sup>.

**Table 4.13** Comparison of ORR activities of CoMn/NC with various reported nonprecious electrocatalysts under alkaline conditions.

Catalysts	Electrolyte	E (V) Onset Potential (vs RHE)	E <sub>1/2</sub> (V) Half-Wave Potential (vs RHE)	References
CoMn/NC	0.1 M KOH	0.98	0.89	This work
(Fe,Co)/CNT	0.1 M KOH	1.15	0.954	332
CoNi-SAs/NC	0.1 M KOH	0.88	0.76	333
Zn/CoN-C	0.1 M KOH	1.004	0.861	334
Fe, Mn, N-FGC	0.1 M KOH	1.03	0.89	335
NCAG/Fe-Co	0.1 M KOH	1.04	0.89	336
Fe-NiNC-50	0.1 M KOH	1.0	0.84	337
FeZnNC	0.1 M KOH	0.965	0.873	338
Co <sub>2</sub> /Fe-N@CHC	0.1 M KOH	1.03	0.95	339
Ni <sub>0.7</sub> Cu <sub>0.3</sub> -N-C	0.1 M KOH	0.872	0.783	340
(Fe,Co SAs-PNCF)	0.1 M KOH	1.04	0.93	341
Fe <sub>1</sub> Co <sub>3</sub> -NC1100	0.1 M KOH	1.05	0.877	342

CNS <sub>FeZnN</sub>	0.1 M KOH	0.95	0.84	343
Fe, Mn-N/C-900	0.1 M KOH	-	0.904	344
NiN <sub>4</sub> /GHSs/FeN <sub>4</sub>	0.1 M KOH	0.93	0.83	345
PtFeNC	0.1 M KOH	1.05	0.895	346
Fe,Co-SA/Cs	0.1 M KOH	0.96	0.86	347
Fe/Mn-N <sub>x</sub> -C	0.1 M KOH	1.02	0.88	348
Fe-Co DSAC	0.1 M KOH	-	0.86	349
FeMn-DSAC	0.1 M KOH	1.04	0.92	350
CoFe-N-C	0.1 M KOH	1.04	0.897	351
CoFe@C	0.1 M KOH	-	0.886	352
MnCo-N-C	0.1 M KOH	-	0.89	353

**Table 4.14** Comparison of ORR activities of CoMn/NC with various reported nonprecious electrocatalysts under acidic conditions.

Catalysts	Electrolyte	E (V) Onset Potential (vs RHE)	E <sub>1/2</sub> (V) Half-Wave Potential (vs RHE)	Refer- ences
<b>CoMn/NC</b>	<b>0.5 M H<sub>2</sub>SO<sub>4</sub></b>	<b>0.90</b>	<b>0.82</b>	<b>This work</b>
(Fe,Co)/NC	0.1 M HClO <sub>4</sub>	1.06	0.863	354
Zn/CoN-C	0.5 M H <sub>2</sub> SO <sub>4</sub>	0.940	0.851	334
FeCoN <sub>5</sub> P <sub>1</sub>	0.5 M H <sub>2</sub> SO <sub>4</sub>	0.853	0.771	355
Au-Co	0.1 M HClO <sub>4</sub>	-	0.82	356
FeNi-N <sub>6</sub>	0.1 M HClO <sub>4</sub>	-	0.8	357
FeMn-DSAC	0.5 M H <sub>2</sub> SO <sub>4</sub>	-	0.79	350
FeTMPPCl derived Fe-N-C	0.5 M H <sub>2</sub> SO <sub>4</sub>	0.790	0.668	358
Fe-N-C	0.5 M H <sub>2</sub> SO <sub>4</sub>	0.83	0.68	359
Cr/N/C	0.1 M HClO <sub>4</sub>	-	0.773	360
CoFe@C	0.5 M H <sub>2</sub> SO <sub>4</sub>	-	0.698	352
MnCo-N-C	0.5 M H <sub>2</sub> SO <sub>4</sub>	-	0.80	353
Ru-N/G-750	0.1 M HClO <sub>4</sub>	0.89	0.75	361
Mn-NC-sec- ond	0.5 M H <sub>2</sub> SO <sub>4</sub>	-	0.80	362
Fe-N/P-C- 700	SACs	0.89	0.72	363



**Table 4.15** Comparison of potential difference of CoMn/NC catalyst with previously reported dual single-atom based bifunctional electrocatalysts.

Catalysts	Potential @ 10 mA cm <sup>-2</sup> (vs RHE) OER	E <sub>1/2</sub> (V) Half-Wave Potential (vs RHE) ORR	ΔE (V vs RHE)	References
<b>CoMn/NC</b>	<b>1.53</b>	<b>0.89</b>	<b>0.64</b>	<b>This Work</b>
CoNi-SAs/NC	1.57	0.76	0.81	333
NCAG/Fe-Co	1.52	0.89	0.64	336
Fe-NiNC-50	1.57	0.84	0.73	337
Fe <sub>1</sub> Co <sub>3</sub> -NC1100	1.58	0.877	0.70	342
Ni-N <sub>4</sub> /GHSs/Fe-N <sub>4</sub>	1.62	0.83	0.79	345
(Fe,Co)-SA/CS	1.59	0.86	0.73	347
FeMn-DSAC	1.63	0.92	0.72	350
CoFe-N-C	1.59	0.89	0.69	351
Fe,Co,N-C	1.64	0.90	0.74	364
Fe,Mn/N-C	1.62	0.928	0.692	365
FeCo-DACs/NC	1.60	0.877	0.723	366
Ru-Co DAC	1.498	0.895	0.603	367

## 4.5 Conclusion

In summary, we have successfully demonstrated the dual single-atom Co–Mn sites dispersed in MOF-derived N-doped nanoporous carbon, named CoMn/NC, for a highly efficient electrochemical ORR in both alkaline and acidic electrolytes. The presence of the Co–Mn site is confirmed by the combination of microscopic images, spectroscopic measurements, and theoretical calculations. DFT suggests that adsorbed bridging O<sub>2</sub> gets activated more on the Mn–Co site in the dissociative pathway. But the overall ORR preferably proceeds via both a thermodynamically and kinetically favorable associative mechanistic pathway. This is due to the moderate adsorption of ORR intermediates in the associative path compared to the dissociative path, where relatively stronger adsorption of the intermediates results in the degradation of ORR activity. Furthermore, CoMn/NC as a cathode catalyst exhibited promising performance in a PEM fuel cell under both H<sub>2</sub>/O<sub>2</sub> and H<sub>2</sub>/air feeding conditions. As a bifunctional ORR/OER catalyst, CoMn/NC

delivered a high power density for a rechargeable Zn–air battery. These performances demonstrate the applicability for the practical use of CoMn/NC. This work highlights an attractive dual single-atom site for fundamental research and provides insights for designing advanced DSAC-based electrocatalysts.

## **Chapter 5: NiO Nanoclusters Supported On Atomically Dispersed Ni single Atom at Mesoporous Carbon Cages For Oxygen Evolution Reaction and Quasi-Solid-State Zn-air Batteries With An Organohydrogel Electrolyte.**

### **5.1 Abstract**

we introduce a quasi-solid-state Zinc-Air Battery (ZAB) exhibiting prolonged cycle life and robust stability over a wide temperature range. Our method involves the fabrication of a unique nanostructure through a silica-mediated Metal-Organic Framework (MOF) templated approach. This structure comprises a mesoporous concave carbon cage with elongated edges, facilitating efficient mass transport, and exposing catalytically active sites for oxygen redox reactions. The incorporation of NiO nanoclusters onto isolated nickel atom sites (Ni-N-C) enhances catalytic activity for both Oxygen Evolution Reaction (OER) and Oxygen Reduction Reaction (ORR). Through Density Functional Theory (DFT) calculations, we investigated the role of NiN<sub>4</sub> and cubic NiO in decorating NiN<sub>4</sub> sites, elucidating the mechanism of OER at the atomic level. Our analysis revealed an augmentation of Ni d-orbitals near the Fermi level, promoting H<sub>2</sub>O molecule absorption and subsequent intermediates. The OER activity at Ni of the NiO site surpassed that of the Ni single site of NiN<sub>4</sub>. Furthermore, we improved interfacial stability and low-temperature tolerance of the battery electrolyte by modifying the H-bond network with DMSO and Zn (BF<sub>4</sub>)<sub>2</sub>. This approach enables high-rate cycling at 25 °C and broad temperature adaptability (-70 to 70 °C), providing valuable insights for the advancement of quasi-solid-state ZAB technology.

## 5.2 Introduction

Zinc-air batteries (ZABs) have garnered significant attention due to their high theoretical energy density, environmental friendliness, and the abundance of zinc anode [368-370]. However, achieving high-rate operation and robust performance it faces two critical challenges: (1) finding suitable bifunctional O<sub>2</sub> electrocatalysts for the air cathode and, (2) ensuring electrochemical interface stability [371,372]. The kinetics of the O<sub>2</sub> reduction/evolution reactions (ORR/OER) at the air cathode significantly influence the discharging/charging process but suffer from sluggish kinetics, resulting in substantial overpotentials. Although precious metals such as Pt for ORR and Ru/Ir oxides for OER have been employed to enhance O = O bond cleavage and formation processes, still there remains a pressing need for durable and highly efficient electrocatalysts [373-377]. Hence, significant attentions have been paid for investigating active, durable, and cost-effective first-row transition-metal oxides (MOs) with comparable oxygen evolution reaction (OER) performance [378-385]. In this regard, Nickel-based materials particularly nickel oxides have emerged as promising candidates, prompting extensive research to enhance their performance further [386-391]. Besides this, it has been observed that integrating active materials with functional supports has proven effective in enhancing the activity of oxygen evolution reaction (OER) catalysts [392-398]. For instance, Dai et al. demonstrated that anchoring cobalt oxide nanoparticles (NPs) onto nitrogen-doped graphene led to improved OER activity [399]. Single atom catalysts (SACs), particularly those comprising isolated transition metals integrated into carbon-based matrices, have emerged as a focal point in electrocatalyst research due to their exceptional atom utilization efficiency, versatile control over metal atoms and coordination, as well as their high conductivity and cost-effectiveness [400-401]. Among SACs, M-N-C materials, featuring either iron (Fe), cobalt (Co), Nickel (Ni) have been derived as highly promising catalysts for

oxygen reduction reaction (ORR). The active sites within these materials are attributed to central metal ions stabilized by nitrogen functional groups on carbonaceous surfaces and they exhibit unique interactions with oxygen molecules and intermediates. These distinctive characteristics of M-N-C materials indicate their potential as catalyst supports in theory but they are suffering due to low metal loading [402]. Furthermore, the catalytic efficacy of M-N-C materials for reversible O<sub>2</sub> redox kinetics fundamentally hinges on the distribution of d-band electrons of the chosen metal atoms, as the hybridization interaction between the metal's d orbitals and the adsorbate's p orbitals dictates adsorption and reaction dynamics [403]. Additionally, for achieving high-rate zinc-air batteries (ZABs) requires both readily accessible atomic metal active sites and rapid charge transfer. This can be accomplished through the design of an electrocatalyst featuring a hierarchical porous nanoarchitecture. However, it is crucial to note that single-atom metal sites, particularly those that are not exposed or embedded within dense carbon matrix remain inactive and limiting their utilization and mass transport through catalyst layers [404]. In 2006, Dodelet et al. proposed that mesopores in the catalyst could improve the utilization of Fe-N<sub>x</sub> moieties by creating channels to previously inaccessible sites [405]. Thus engineering the catalyst morphology to maximize metal sites exposure at the three-phase boundary (catalyst-electrolyte-oxygen) is seen as a promising approach for improving mass transport and catalytic activity [406-408]. Despite research endeavors have been devoted to increase metal site density, maximizing their utilization as true catalytically active sites remains a formidable challenge, representing the primary bottleneck in single-atom catalysis [409]. Metal-organic frameworks (MOFs) offer potential as templates for constructing porous functional materials, including carbon-decorated single-atom catalysts [410]. However, direct pyrolysis of MOFs often results in aggregated or collapsed or micropore dominated structures, limiting the creation of catalytically active sites [411-

413]. So, there is a need for innovative synthesis approaches to generate structures with increased three-phase boundaries/interfaces and highly exposed desired catalytically active sites to enable rapid catalysis. Moreover, efforts to design flexible aqueous ZABs have focused on achieving both robust electrochemical performance and mechanical resilience. Despite advancements, traditional sandwich-stacked configurations are prone to performance degradation under external deformation, unlike the cohesive all-in-one structure which ensures continuous loading and ions-transfer capacity, thereby enhancing stability. Solid and quasi-solid-state electrolytes play pivotal roles in these advanced ZAB designs [414-417]. Hydrogel electrolytes show promise as semi-solid electrolyte options [418-421]. However, their high-water content leads to freezing at subzero temperatures, hindering ion mobility, electrolyte-electrode interface wettability, and flexibility [422,423]. Also, conventional alkaline hydrogel electrolytes often induce Zn anode passivation, limiting Zn plating/stripping reversibility and cycling capability. Addressing this, modifications to the  $\text{Zn}^{2+}$  solvation sheath and reduction of water activity may enhance Zn plating/stripping reversibility [424-426]. Developing anti-freezing hydrogel electrolytes that maintain compatibility under extreme conditions remains an underexplored area for both high-rate and temperature-adaptive ZABs. Wang et al. investigated that dimethyl sulfoxide (DMSO) organic solvent possessing significant polarity, serves as an additive to adjust the hydrogen bonding network in aqueous electrolytes [427]. But it has been observed that addition of organic solvent reduces ionic conductivity of hydrogel electrolyte. In addition to this organic solvent, anions possessing high electronegativity were also incorporated into the hydrogel electrolytes to lower the freezing point [428-429]. However, at extremely subzero temperature both are not able to meet the practical demand. Herein, to solve the above-mentioned problems, we present a quasi-solid-state ZAB which showed long cycle span and robust stability across a wide temperature range.

Firstly, using a silica-mediated MOF templated approach, we create a mesoporous concave carbon cage with more stretched edges where NiO small nanocluster is homogeneously distributed over isolated nickel atom sites (Ni-N-C). The resulting nanostructures increase elongated edges to facilitate mass transport and expose catalytically active Ni sites for efficient O<sub>2</sub> redox reactions. Along with that, the synergistic interaction between NiO nanocluster and Ni-N-C boosts the catalytic activity for both OER/ORR. DFT calculations were utilized to examine into the role of NiN<sub>4</sub> and cubic NiO in decorating NiN<sub>4</sub> sites, as well as the mechanism of the Oxygen Evolution Reaction (OER) at the atomic level. Density of states analysis indicated enhancement of availability of Ni d-orbitals near the Fermi level in NiO decorated on NiN<sub>4</sub> sites which further facilitating H<sub>2</sub>O molecule absorption and subsequent intermediates. The OER activity at Ni of the NiO site surpassed that of the Ni single site of NiN<sub>4</sub>. Additionally, by modifying the H-bond network of the organohydrogel electrolyte with DMSO and Zn (BF<sub>4</sub>)<sub>2</sub>, we enhance interfacial stability and low-temperature tolerance of the battery by breaking the H bonding network between water molecules. Our approach achieves high-rate cycling at 25 °C and broad temperature adaptability (-70 to 70 °C), offering insights for further quasi-solid-state ZAB advancements.

## **5.3 Experimental**

### **5.3.1 Materials**

All the reagents were purchased commercially and used without further purifications. Zinc acetate dihydrate (98%), Nickel acetate tetrahydrate (98%), High purity Acrylamide (99%), Potassium persulphate K<sub>2</sub>S<sub>2</sub>O<sub>8</sub> (98%) and DI water were purchased from Molychem. 2-methylimidazole (98%) was purchased from Avra. Cetyltrimethylammonium bromide, Sodium hydroxide pellets, Hydrogen fluoride, Dimethyl sulphoxide (98%), Sulphuric acid (97%), Methanol (99%) were purchased from SDFCL. Potassium

hydroxide (85%) was acquired from Azytus. *tert*-butyl alcohol (99%) were purchased from TCI. Nickel (II) acetylacetonate (95%), ethanol, 20 wt% Platinum on graphitized carbon, 5% Nafion<sup>TM</sup> 117 solution, Nickel phthalocyanine and Nickel oxide, Zn foil of 0.25mm thickness (99.99%), Nickel foam, Zinc tetrafluoroborate hydrate were purchased from Sigma-Aldrich. Iridium (IV) oxide powder 99% was purchased from Alfa aesar. N,N-methylenebisacrylamide (MBAA, Crosslinker) was purchased from SRL (99.5%). ELAT LT 1400 (GDL, Toray TGP-H-06) was purchased by a fuel cell store. High purity Ar (99.999%), 10% Ar/H<sub>2</sub> and O<sub>2</sub> (99.999%) gases were acquired from Sigma-Gases New Delhi and used for high temperature carbonization and electrolyte purging processes.

### 5.3.2 Physicochemical characterization

PANalytical diffractometer using Cu K $\alpha$  source ( $\lambda = 1.5405 \text{ \AA}$ ) was used to analyse powder X-ray diffraction (PXRD) with 2°/min scan rate and 0.05 steps. The instrument was operated at 30 kV and a current of 10 mA. The FT-IR data were analyzed in ATR mode by the Perkin Elmer Spectrum Two instrument. N<sub>2</sub> sorption isotherms were recorded by using BELSORP MAX II sorption analyser at liquid N<sub>2</sub> temperature (77K). Prior to measurements, samples were degassed under vacuum at 120 °C for 12 h. The specific surface area and pore size distribution were evaluated by Brunauer-Emmett-Teller (BET) method and Barrett-Joyner Halenda (BJH) model, respectively. The pore volume was calculated by adsorption amount of N<sub>2</sub> at a relative pressure of 0.99 bar. X-ray photoelectron spectroscopy (XPS) were acquired on a Thermo Fisher Scientific (K-Alpha). X-ray photoelectron spectrometer using an Al K $\alpha$  source (10 kV, 10 mA) equipped with ion source (EX06). UPS was performed on a SPECS Leybold EA11 MCD electron spectrometer and the base pressure in the measurement chamber is in the range of 5\*10<sup>-10</sup> mbar. The spectrometer is equipped with a He discharge lamp for UPS (He II at  $h\nu = 40.82 \text{ eV}$ ).



EPR spectra were conducted on a benchtop spectrometer Bruker EMXnano with x band. Scanning electron microscopic (SEM) images were acquired using JEOL (JXA-8230) at 20 kV. 200 kV Talos F200S G2 transmission electron microscope combined with column energy dispersive X-ray spectrometer (EDS) and a CMOS Camera 4K x 4K detector were used for Transmission Electron Microscopy (TEM) measurements. High Resolution high-angle annular dark-field scanning transmission electron microscopy (HAADF-STEM) measurement was taken on a JEM-ARM200F instrument at 200 kV. PERKIN ELMER OPTIMA 5300 DV ICP-OES was used for the determination of metal contents in samples. Raman spectroscopy measurements were carried out on the Princeton instruments (Acton spectra pro-2500i) with the help of 532 nm DPSS Laser (laser quantum gem with a power of 50 mW). The stretchable properties of gel electrolyte were investigated Utilizing the Tinius Olsen H5KL UTM machine in the Generic Compression-Stress vs. Strain method. The freezing point of the gel electrolyte was characterized by a DSC (Hitachi, DSC7020 instrument)) under the N<sub>2</sub> atmosphere with a cooling rate of 5 °C min<sup>-1</sup>.

### **5.3.3 Synthetic methods**

**5.3.3.1. Synthesis of ZIF-8:** The synthesis of ZIF-8 nanocrystals was based on a previous procedure with few modifications. Typically, Zn(OAc)<sub>2</sub>.2H<sub>2</sub>O (3.80 g) was dissolved in 500 ml of methanol. A mixture of 2-methylimidazole (21.04 g) with 500 ml methanol was added to the above solution with vigorous stirring for 2 h and kept at rest for 24 h. The product was separated by centrifugation and washed 2 to 3 times with methanol and dried at 80°C under vacuum for final collection. The resulting powder was further activated at 120°C under vacuum for 12 h prior to use.

**5.3.3.2. Synthesis of ZIF-8@SiO<sub>x</sub>:** For the synthesis of ZIF-8@SiO<sub>x</sub>, the above synthesized ZIF-8 was dispersed in 120 ml of methanol followed by addition of 120 ml

D.I. water, and then 6 ml of an aqueous cetyltrimethylammonium bromide (CTAB) solution (25mg/ml) and 10 ml of an aqueous NaOH solution (6 mg/ml) were added. Tetraethyl orthosilicate (TEOS) (1.2 ml in 6 ml of methanol) was injected into the above solution. The mixture was kept at stirring for 2 h and collected by centrifugation followed by washing several times with ethanol. The final powder was dried at 100°C in vacuum for 12 h for further use and marked as ZIF-8@SiO<sub>x</sub>.

**5.3.3.3. Synthesis of Ni/ZIF-8:** The synthesis of Ni/ZIF-8 was done by dissolving 200 mg of Ni(CH<sub>3</sub>COO)<sub>2</sub>·4H<sub>2</sub>O into 50 ml of methanol followed by addition of activated ZIF-8 powder (600 mg). The mixture was slowly stirred for 12 h for obtaining desired product which was further washed with methanol several times and dried at 60°C to obtain final powder.

**5.3.3.4 Synthesis of Ni/ZIF-8@SiO<sub>x</sub>:** For the synthesis of Ni/ZIF-8@SiO<sub>x</sub>, the as-synthesized Ni/ZIF-8 was dispersed in 120 ml of methanol followed by addition of 120 ml D.I. water, and then 6 ml of an aqueous cetyltrimethylammonium bromide (CTAB) solution (25mg/ml) and 10 ml of an aqueous NaOH solution (6 mg/ml) were added. Tetraethyl orthosilicate (TEOS) (1.2 ml in 6 ml of methanol) was injected into the above solution. The mixture was kept at stirring for 2 h and collected by centrifugation followed by washing several times with ethanol. The final powder was dried at 100°C in vacuum for 12 h for further use and marked as Ni/ZIF-8@SiO<sub>x</sub>.

### **5.3.3.5 Synthesis of MOF derived catalysts:**

**5.3.3.5.1 Synthesis of NiO/Ni-SACs/mNC1000:** The as-obtained nanocrystals of Ni/ZIF-8@SiO<sub>x</sub> were then carbonized using a tubular furnace at 1000°C for 4 h under continuous flow of 10% Ar/H<sub>2</sub> gas having outlet bubbling flow rate of 1 bubble sec<sup>-1</sup>.

The ramping rate to reach the maximum temperature was  $5\text{ }^{\circ}\text{C min}^{-1}$ . After cooling down to room temperature the resultant black carbon powder was washed with 12% HF and dilute HCl solution,  $\text{H}_2\text{O}$  and Methanol and dried at  $60^{\circ}\text{C}$  under Vacuum for further use and designated as our main catalyst NiO/Ni-SACs/mNC1000.

**5.3.3.5.2 Synthesis of NiO/Ni-SACs/mNC900:** NiO/Ni-SACs/mNC-900 was synthesized similar to procedure following the synthesis of NiO/Ni-SACs/mNC-1000 using carbonization temperature as  $900\text{ }^{\circ}\text{C}$ .

**5.3.3.5.3 Synthesis of mNC1000:** mNC1000 was synthesized similar to the procedure following the synthesis of NiO/Ni-SACs/mNC-1000 using ZIF-8@ $\text{SiO}_x$  as the carbonization precursor.

**5.3.3.5.4 Synthesis of Ni-SACs/NC1000:** To obtain only Ni-SACs on nitrogen doped carbon we followed our previous reported synthetic procedure. The as-obtained nanocrystals of Ni/ZIF-8 were carbonized using a tubular furnace at  $1000\text{ }^{\circ}\text{C}$  for 4 h under continuous flow of dilute  $\text{H}_2$  gas having outlet bubbling flow rate of 1 bubble  $\text{sec}^{-1}$ . The ramping rate to reach the maximum temperature was  $5\text{ }^{\circ}\text{C min}^{-1}$ . After cooling to room temperature, the black solid was treated with 10%  $\text{H}_2\text{SO}_4$  solution at  $70\text{ }^{\circ}\text{C}$  for 16 h. Subsequent centrifugation and washing with plenty of de-ionized water led to the black solid. It was further treated at  $70\text{ }^{\circ}\text{C}$  under vacuum for further use and designated as Ni-SACs/NC1000.

**5.3.3.5.5 Synthesis of NC1000:** NC1000 was synthesized similar to the procedure following the synthesis of Ni-SACs/NC1000 using only ZIF-8 as the carbonization precursor.

**5.3.3.6 Synthesis of NiO NPs:** In a typical procedure, 0.13 g (0.50 mmol) of nickel (II) acetylacetonate ( $\text{Ni}(\text{acac})_2$ ) was added to 14 mL of tert-butanol (0.147 mol) and formed a turbid light green suspension. Then the reaction mixture was stirred for 10 min and transferred into a Teflon autoclave. The autoclaves were kept at 210 °C in a laboratory oven for 24 h. The as-prepared powders then collected by centrifugation & were dried in air at 60 °C in a laboratory oven.

### **5.3.3.7 Synthesis of the hydrogel electrolytes:**

**5.3.3.7.1 Synthesis of the PAM hydrogel electrolyte (PAM-h):** Free radical polymerization approach has been adopted for the synthesis of the stretchable gel electrolyte. Here, initiators help to encourage the creation of free radicals and start the process of polymerization. For the synthesis of PAM hydrogel electrolyte 4 g of acrylamide (AM), 4 mg of N,N'-methylenebisacrylamide (MBAA, Crosslinking agent), and 10 mg of potassium persulfate ( $\text{K}_2\text{S}_2\text{O}_8$ , Initiator) were dissolved in 10 mL of Milli-Q water and keep in vigorous stirring for 1h. The resultant solution was then poured into a transparent box. Then the box was sealed with tape and placed in an oven at 70 °C for 12 h. The as-prepared PAM hydrogel named as PAM-h was immersed in the 6 M KOH + 0.2 M Zn (OAc) $_2$ ·6H $_2$ O electrolyte for 72 h before use.

### **5.3.3.7.2 Synthesis of the PAM organohydrogel electrolyte (PAM-dh):**

PAM organohydrogel was synthesized similar to procedure following the synthesis of PAM-h using 5 mL of Milli-Q water and 5 ml dimethyl sulphoxide (DMSO).

### **5.3.3.7.3 Synthesis of the metal salt treated PAM hydrogel electrolyte**

**(PAM-zh):** Metal salt treated PAM hydrogel was synthesized similar to procedure following the synthesis of PAM-h using 5 mL of Milli-Q water and 20 mg of zinc tetrafluoroborate hydrate ( $\text{Zn}(\text{BF}_4)_2 \cdot x\text{H}_2\text{O}$ ).

#### 5.3.3.7.4 Synthesis of the metal salt treated PAM organohydrogel elec-

**trolyte (PAM-zdh):** Metal salt treated PAM organohydrogel was synthesized similar to procedure following the synthesis of PAM-h using 5 mL of Milli-Q water and 5 ml DMSO and 20 mg of zinc tetrafluoroborate hydrate ( $\text{Zn}(\text{BF}_4)_2 \cdot x\text{H}_2\text{O}$ ).

#### 5.3.4 d band center calculations

The center of d-band was calculated according to Eq. S1. Surface valence band photoemission spectra were corrected by subtracting the Shirley background. For the accurate comparison of all valence-band spectra, the upper level of integration of background subtraction was set at the 10.0 eV bonding energy position throughout all valence-band spectra [430-432].

$$\mu = \frac{\int N(\varepsilon)\varepsilon d\varepsilon}{\int N(\varepsilon)d\varepsilon} \quad \dots\dots\dots (\text{S1})$$

where  $N(\varepsilon)$  is the DOS.  $\mu$  is the center of d-band.  $\varepsilon$  is the bonding energy.

#### 5.3.5 Electrochemical measurements

The electrochemical measurements for HER, OER, and ORR were performed by using a traditional 3-electrode setup connected with VSP 128 bi-potentiostat (BioLogic). The reference, working, and counter electrodes were Hg/HgO, glassy carbon, and graphitic rod electrodes (graphitic rod for ORR, Pt mesh for OER), respectively. All potentials were normalized to values in relation to the reversible hydrogen electrode. To make catalyst ink, 5 mg of catalyst was mixed with DI water (490  $\mu\text{l}$ ), ethanol (490  $\mu\text{l}$ ), and Nafion 5% (20  $\mu\text{l}$ ) then sonicated for 20 minutes at room temperature. Afterwards, a specific volume of catalyst ink was dropped onto the pre-cleaned surface of the working electrode, equivalent to 0.210  $\text{mg cm}^{-2}$ . The electrodes were held to dry in the air prior to testing of electrochemical activity. Before performing linear sweep voltammograms

(LSVs) ( $5 \text{ mV s}^{-1}$ ) at room temperature, electrodes were preconditioned by taking repeating cyclic voltammograms (CVs) in desired potential range. All OER were tested in Ar-saturated solution of 1 M KOH. The ORR measurements were tested in 0.1M KOH at  $5 \text{ mV sec}^{-1}$  in  $\text{O}_2$ -saturated solution. For ORR, LSVs were recorded at different electrode rotation speeds (100-2500 rpm). The Tafel slope values for OER, and ORR were extracted from the kinetic region of performed LSVs. The electrochemical active surface area (ECSA) was calculated by taking CV scans at different scan rates in a non-Faradaic region. The obtained current density is assumed to be due to charging in the non-Faradaic region. Then, the difference in current density variation ( $J_a - J_c$ ) vs RHE were plotted against the scan rate.  $C_{dl}$  was collected from its slope. Finally, ECSA was obtained by dividing the slope value by specific capacitance ( $C_s$ ), generally  $C_s$  value is  $0.035 \text{ mF cm}^{-2}$  was used for catalyst surface. Electrochemical impedance spectroscopy (EIS) was performed in the frequency range from 1,00,000 to 0.01 Hz at  $5 \text{ mV s}^{-1}$  scan rate. EIS fitting circuit model provides the  $R_s$  (series resistance) and  $R_{ct}$  (charge transfer resistance) values, which are analyzed by in-built Biologic software.

For RDE measurements, the kinetic current density and number of electron transfer were analyzed by using the Koutecky-Levich equation:

$$\frac{1}{J} = \frac{1}{J_L} + \frac{1}{J_k} = \frac{1}{B\omega^{1/2}} + \frac{1}{J_k} \dots\dots\dots(S2)$$

$$B = 0.62nFC_0D_0^{2/3}V^{1/6} \text{ and } J_k = nFkC_0 \dots\dots\dots(S3)$$

Where,  $J$  is the measured current density,  $J_k$  and  $J_L$  are the kinetic and limiting current densities,  $\omega$  is the angular velocity of the disk in the unit of  $\text{rad s}^{-1}$ ,  $n$  is the total transfer number of electrons in oxygen reduction reaction,  $F$  is the Faraday constant ( $96485 \text{ C/mol}$ ),  $C_0$  is the bulk concentration of oxygen ( $1.2 \times 10^{-6} \text{ mol cm}^{-3}$ ),  $D_0$  is the diffusion

coefficient of O<sub>2</sub> (1.9 x 10<sup>-5</sup> cm<sup>2</sup> s<sup>-1</sup>), and V is the kinematic viscosity of the electrolytic solution (0.01cm<sup>2</sup> s<sup>-1</sup>), and k is the rate constant for electron transfer.

The area of glassy carbon (disc electrode) and Pt (ring) of rotating ring disc electrode (RRDE) was 0.1256 cm<sup>2</sup> and 0.18853 cm<sup>2</sup>. The electron transfer number (n) and H<sub>2</sub>O<sub>2</sub> production yield percent were calculated by the following equations:

$$n = 4 \times \frac{I_D}{I_D + \frac{I_R}{N}} \dots\dots\dots(S4)$$

$$H_2O_2(\%) = 200 \times \frac{\frac{I_R}{N}}{I_D + \frac{I_R}{N}} \dots\dots\dots (S5)$$

Where, I<sub>D</sub> is disc current, I<sub>R</sub> is ring current and N is the ring collection efficiency of Pt ring (0.41).

### 5.3.5.1 TOF calculations for OER

TOF for OER was calculated using the catalyst-modified disc electrode (RRDE), subject to a potential ramp over a specified potential range in which OER occurs considerably, while the ring electrode was held at a constant cathodic potential adequate to reduce the O<sub>2</sub> developed from the disc electrode. The used equation for TOF calculation is:

$$TOF = i_R / A \times F \times n \times N_{CL} \times \Gamma \dots\dots\dots (S6)$$

Where, i<sub>R</sub>, A, F, n, N<sub>CL</sub>, and Γ, represent the ring current, area of the electrode, Faraday constant, the number of electrons transferred to produced one molecule of the product, collection efficiency of RRDE electrode, and surface concentration or accurate number of active sites catalyzing the reaction (m<sup>-2</sup>), respectively.

### 5.3.5.2 Faradaic efficiency calculations for OER

FE for OER was calculated via RRDE electrode using formula,

$$F. E. = I_r/N \times I_d \quad \dots\dots\dots (S7)$$

Where,  $I_r$  and  $I_d$  stand for ring current and disc current, respectively.  $N$  is the current collection efficiency for Pt ring (0.41).

### 5.3.6 Fabrication of quasi-solid-state Zn-air battery (ZABs)

Quasi-solid-state Zn-air battery was assembled using PAM modified hydrogel solid electrolyte. The as-prepared hydrogels were immersed in the 6 M KOH + 0.2 M Zn (OAc)<sub>2</sub>·6H<sub>2</sub>O electrolyte for 72 h before use. A clean Zn foil (0.2 mm thickness) was used as an anode. The air electrode (cathode) was made by dropping catalyst ink onto a flexible GDL with loading of 1.5 mg cm<sup>-2</sup>. The battery was tested at different temperatures ranging from ice cold conditions to room temperature. All battery data tested with with VSP 128 bi-potentiostat (BioLogic).

### 5.3.7 Electrolytic cell measurements

Two electrode water electrolysis device was assembled using NiO/Ni-SACs/mNC1000 as OER catalyst and Pt/C as HER catalyst. A homogeneous ink of NiO/Ni-SACs/mNC1000 was uniformly coated on nickel foam to generate an electrode with 1.2 mg cm<sup>-2</sup> catalyst loading. The electrochemical activity was tested by taking voltammograms in Ar-saturated solution at 5 mV s<sup>-1</sup>. The theoretical amount of generated H<sub>2</sub> and O<sub>2</sub> gas was calculated by using Faraday's Law:

$$n = (I \times t)/(z \times F) \quad (S8)$$

where  $n$  is no. of moles,  $I$  is current (A),  $t$  is time (s) and  $Z$  is no. of electrons transferred in the reaction (for HER,  $Z = 2 e^-$  and for OER,  $Z = 4e^-$ ), and  $F$  is the Faraday constant ( $F = 96487 C$ ). Whereas, the experimentally generated gas was measured from the water displacement method using Dalton's law,  $P_{total} = P_{gas} + P_{water}$ , the water vapor pressure



( $P_{H_2O}$ ) is 23.6955 torr and atmospheric pressure ( $P_{atm}$ ) under same condition is 758.3124 torr. Number of moles of generated gas was measured by water displacement method using  $PV = nRT$  relation, where  $V$  is volume of produced gas ( $H_2/O_2$ ),  $R$  is the gas constant ( $8.3144 \text{ L}\cdot\text{kPa}\cdot\text{K}^{-1}\cdot\text{mol}^{-1}$ ),  $T$  is the temperature (298 K). The Faradaic efficiency was evaluated using following equation:

$$\text{Faradaic efficiency} = \frac{\text{Experimental mmol of gas}}{\text{Theoretical mmol of gas}} \times 100 \quad (\text{S9})$$

\*\*\* Generally, all electrochemical data were measured at least three times. All experimental electrochemical values reported in this manuscript were taken from single experiments.

#### 5.4 Binding energy calculations

We have performed Density functional theory for binding energy calculations of the gel electrolytes using Gaussian 16 software. We have used B3LYP function with basis set 6-311+g (d,p). First, we have optimized the geometries and then calculated counterpoise corrected energy. The binding energy  $E_b$  can be calculated according to the following equation:

$$E_b = E_{total} - \sum E_{component} \quad (\text{S10})$$

where  $E_{total}$  is the total energy,  $E_{component}$  is the energy of each component. The higher absolute value of  $E_b$  indicates stronger interactions.

#### 5.5 Density functional theory (DFT) calculations

Spin-polarized density functional theory (DFT) calculations were conducted using the Vienna Ab initio Simulation Package (VASP) code [433]. The projector augmented wave (PAW) scheme [434,435] was employed to describe all atoms, and the exchange-correlation effects were corrected using generalized gradient approximations (GGA) with PBE functions [436]. A consistent energy cutoff of 500 eV was applied for all calculations.

The electronic convergence criterion was set at  $10^{-6}$  eV, and the final residual forces on each atom in optimized structures were maintained below  $0.01$  eV/Å. To prevent interactions between periodic images of the NiN<sub>4</sub>-graphene monolayer, a minimum vacuum length of  $20$  Å was maintained in the z-direction. For the geometry optimization of the NiN<sub>4</sub>-graphene monolayer, a Monkhorst-Pack  $2 \times 2 \times 1$  k-point grid was utilized. The Gibbs free energy changes for each electron transfer reaction were calculated using the computational standard hydrogen electrode (CHE) model, developed by Nørskov et al. [436], defined as:

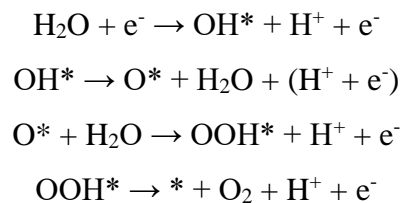
$$\Delta G = \Delta H + \Delta ZPE - T\Delta S + G_{\text{pH}}$$

Here,  $\Delta H$ ,  $T$ ,  $\Delta S$ , and  $\Delta ZPE$  denote the change in enthalpy from the DFT calculation, temperature, change in entropy, and change in zero-point energy of the reaction, respectively.  $G_{\text{pH}}$  is the correction of the free energy due to variations in the concentration of  $\text{H}^+$  and is defined as [437]:

$$G_{\text{pH}} = k_{\text{B}}T \times \ln[\text{H}^+]$$

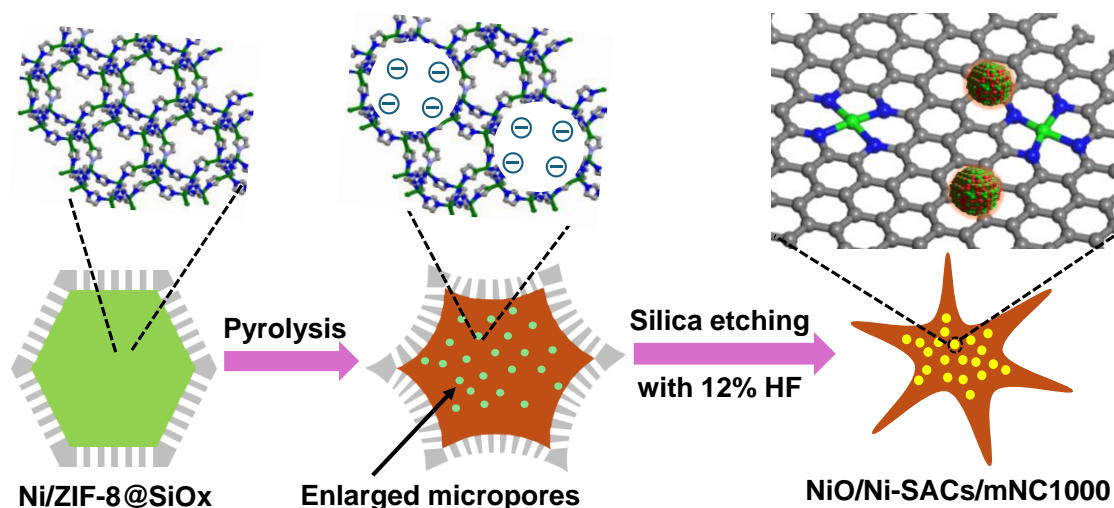
In this study, we considered  $\text{pH} = 0$ , and the temperature parameter for each calculation step was set to  $298.15$  K. The entropy for free gas molecules were obtained from the NIST database, while those for the adsorbed species were computed from the vibrational frequencies of the adsorbed intermediates. Therefore, only vibrational entropy was considered for the calculation of change in entropy ( $\Delta S$ ) for the adsorbed species. The mechanisms underlying the oxygen evolution reaction (OER) in both acidic and basic medium can be described as follows:

OER in acidic medium:



## 5.6 Results and discussion

As presented in Scheme 5.1, three step procedure was employed to synthesize NiO/Ni-SACs/mNC1000 with concave shaped morphology and largely enhanced mesoporosity. First, Nickel acetate was encapsulated within the nanocavities of zeolitic imidazolate framework-8 (ZIF-8) which named as Ni/ZIF-8. Next, a thin silicon oxide ( $\text{SiO}_x$ ) layer was deposited onto the surface of Ni/ZIF-8. Finally, the resulting Ni/ZIF-8@SiO<sub>x</sub> was subjected to calcination at 1000 °C under 10% Ar/H<sub>2</sub> atmosphere followed by treatment with 12% HF and diluted HCl to remove SiO<sub>x</sub> shell and any loosely bounded metal nanoparticles.



**Scheme 5.1** Schematic representation for the synthesis of NiO/Ni-SACs/mNC1000.

The uniform coating of silica over Ni/ZIF-8 was analyzed by different analytical techniques. Powder X-ray diffraction pattern (PXRD) suggests that phase purity or crystallinity of Ni/ZIF-8@SiO<sub>x</sub> or ZIF-8@SiO<sub>x</sub> were retained even after coating of respective MOFs with silica (Figure 5.1).

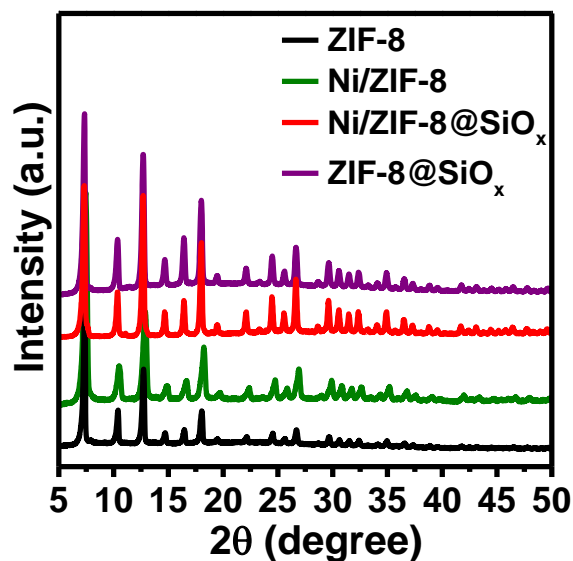


**Figure 5.1** PXRD pattern of ZIF-8, Ni/ZIF-8, Ni/ZIF-8@SiO<sub>x</sub>, ZIF-8@SiO<sub>x</sub>.

The presence of the SiO<sub>x</sub> coating was further verified through Fourier transform infrared spectroscopy (FTIR) analysis (Figure 5.2). As mentioned in Figure 5.2, Ni/ZIF-8@SiO<sub>x</sub> showed a prominent broad peak at 1061.12 cm<sup>-1</sup> which indicate the presence of Si-O-Si bonds.

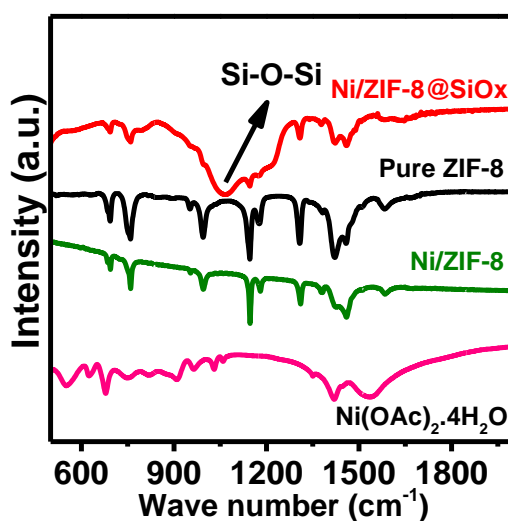


**Figure 5.2** FT-IR analysis of Ni(OAc)<sub>2</sub>.4H<sub>2</sub>O, ZIF-8, Ni/ZIF-8, Ni/ZIF-8@SiO<sub>x</sub>.

Furthermore, reductions in specific surface area for Ni/ZIF-8@SiO<sub>x</sub> (542 m<sup>2</sup> g<sup>-1</sup>) as compared to ZIF-8 (1840 m<sup>2</sup> g<sup>-1</sup>), Ni/ZIF-8 (1800 m<sup>2</sup> g<sup>-1</sup>), calculated from the N<sub>2</sub>

adsorption/desorption isotherm experiments, suggested that the MOFs were partially filled with the guest species (Figure 5.3).

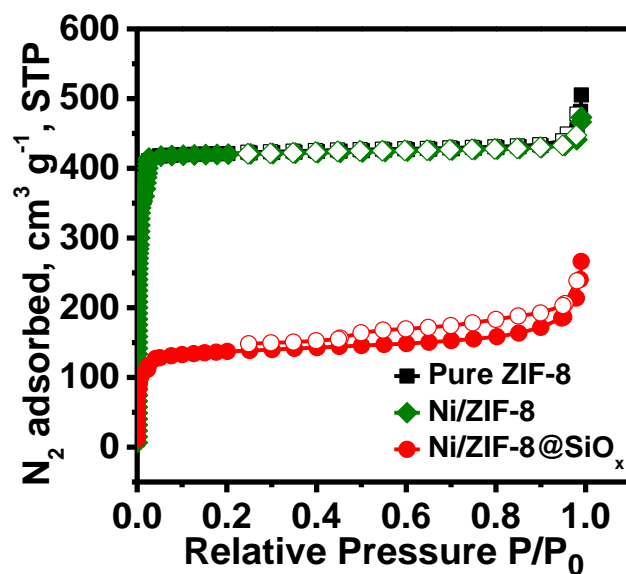


**Figure 5.3** N<sub>2</sub> adsorption-desorption isotherm of pure ZIF-8, Ni/ZIF-8, Ni/ZIF-8@SiO<sub>x</sub>. Additionally, scanning electron microscopy (SEM), transmission electron microscopy (TEM), and high-angle annular dark-field scanning transmission electron microscopy (HAADF-STEM) and its corresponding elemental mapping analysis again provided conclusive evidence affirming the effective synthesis of Ni/ZIF-8@SiO<sub>x</sub> where SiO<sub>x</sub> is uniformly coated over Ni-ZIF-8 surface which comprised of polyhedral morphology & particle size ~250 nm (Figure 5.4-5.6).

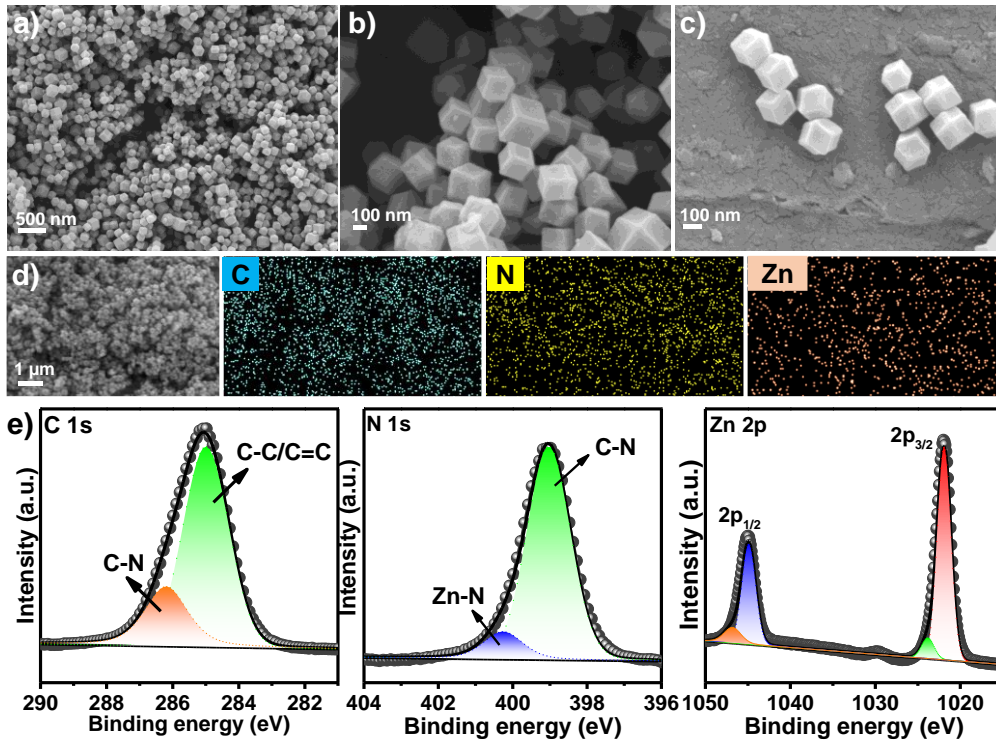


**Figure 5.4** a)-c) SEM images of ZIF-8 at different scale bars. d) SEM image with corresponding EDS elemental mappings of ZIF-8. e) XPS spectra of C1s, N1s, Zn 2p, acquired from ZIF-8.

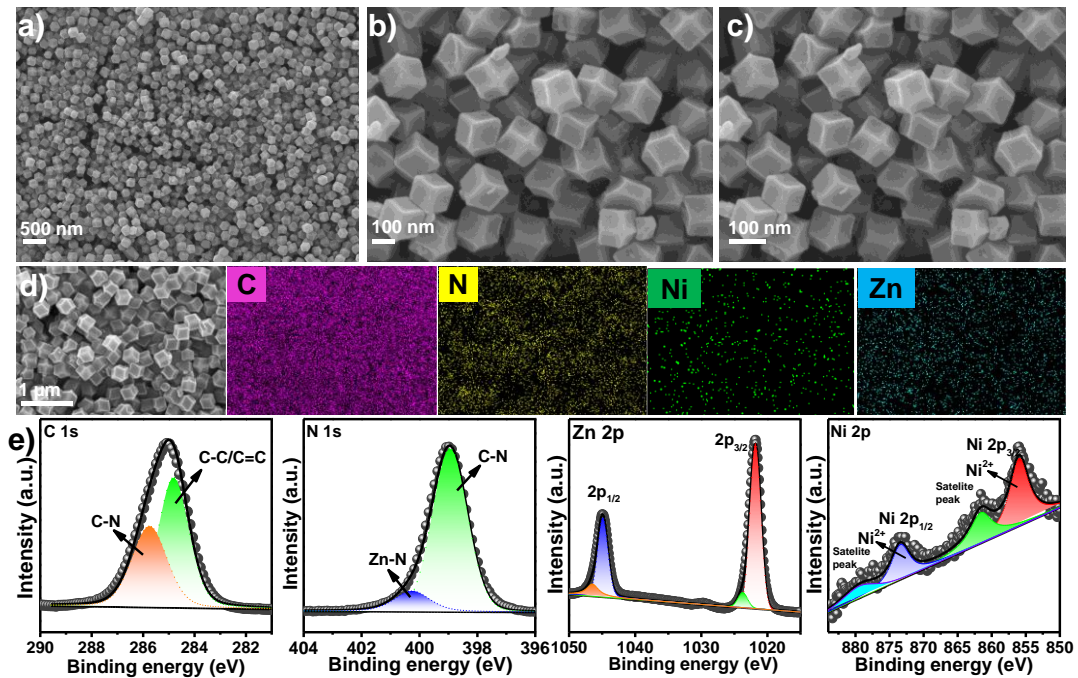


**Figure 5.5** a)-c) SEM images of Ni/ZIF-8 at different scale bars. d) SEM image with corresponding EDS elemental mappings of Ni/ZIF-8. e) XPS spectra of C1s, N1s, Zn 2p, Ni 2p acquired from Ni/ZIF-8.

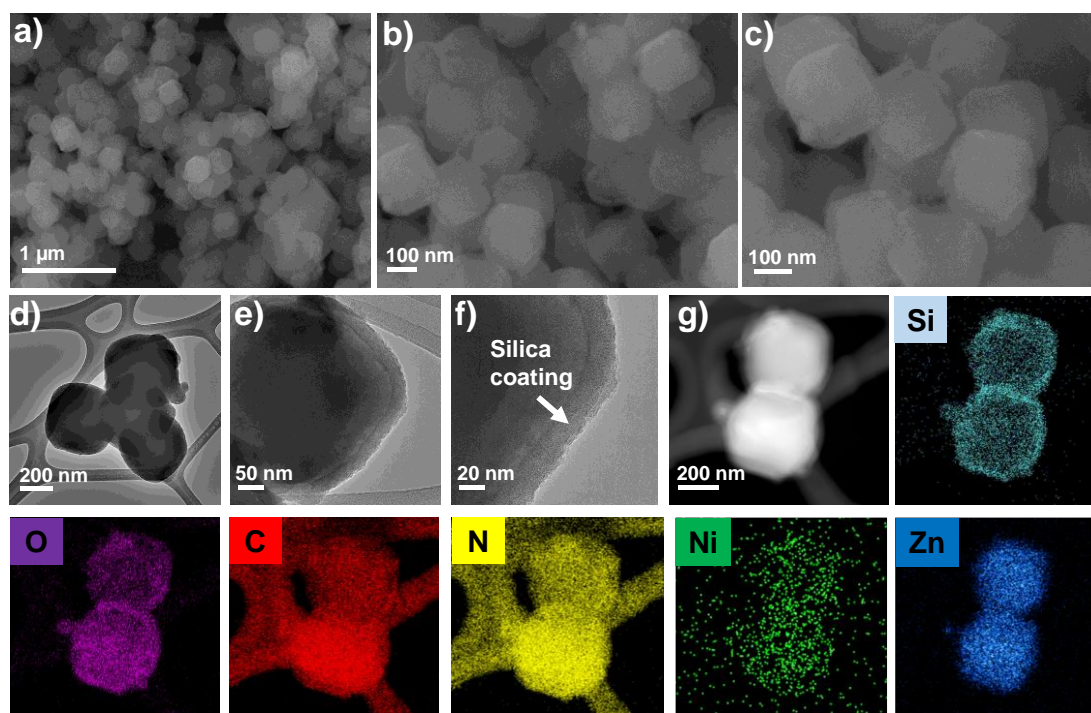


**Figure 5.6** a)-c) SEM images of Ni/ZIF-8@SiO<sub>x</sub> at different scale bars. d)-f) HR-TEM images of Ni/ZIF-8@SiO<sub>x</sub>. g) HAADF-STEM image and its corresponding EDX elemental mapping of Silicon (cyan), Oxygen (purple), Carbon (red), Nitrogen (yellow), Nickel (green), Zinc (blue).

We then performed X-ray photo electron spectroscopy (XPS) to confirm the presence of all the elements in Ni/ZIF-8@SiO<sub>x</sub> such as carbon (C), nitrogen (N), silicon (Si), oxygen (O), zinc (Zn) & nickel (Ni) (Figure 5.7). Due to the coating of silica we did not get any peak corresponding to the Ni 2p.

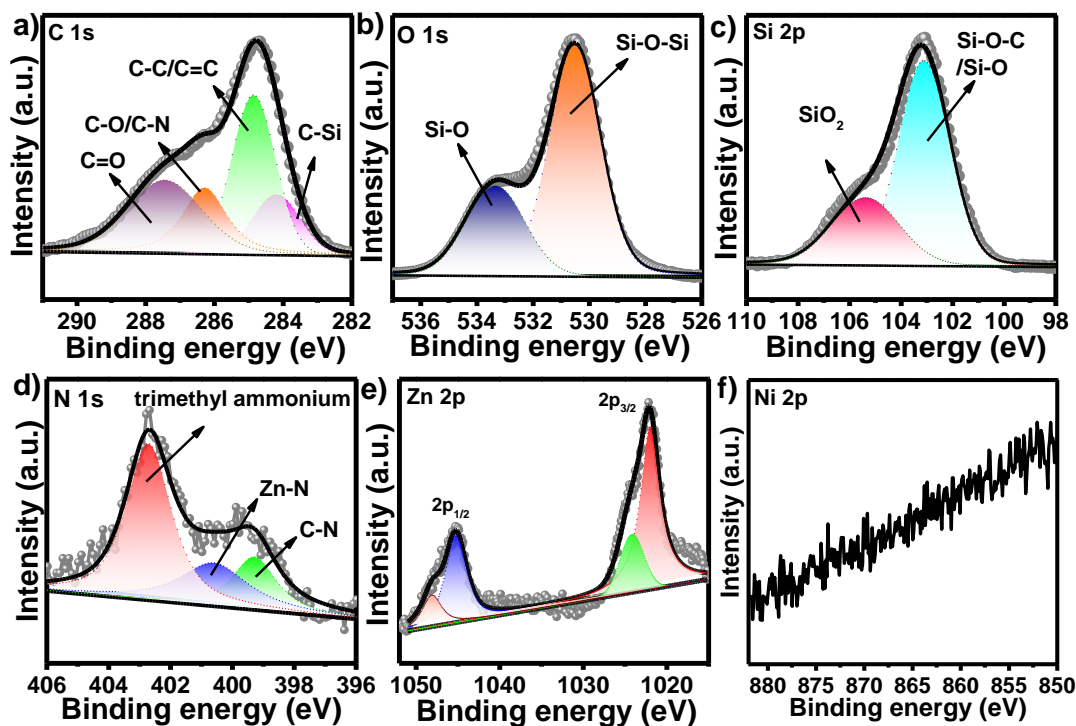


**Figure 5.7** High resolution XPS spectra of C1s, O1s, Si 2p, N1s, Zn 2p, Ni 2p acquired from Ni/ZIF-8@SiO<sub>x</sub>.

Now, after treatment of this silica coated Ni/ZIF-8 at higher temperature and removal of SiO<sub>x</sub> shell, we further then characterized it. The SEM image (Figure 5.8 a) of the Ni/ZIF-8@SiO<sub>x</sub>-derived material (NiO/Ni-SACs/mNC1000), carbonized at 1000°C, illustrates the complete transformation of each individual polyhedral nanocrystal into concave-shaped stretched-edge mesoporous carbon cages, with a particle size of approximately 200 nm. TEM measurements provided additional endorsement of the formation of this unique carbon structure (Figure 5.8 b). Furthermore, HR-TEM images depicted that very small NiO nanoclusters encapsulated within the carbon matrix (Figure 5.8 c), a finding corroborated by a diffuse selected area electron diffraction (SAED) pattern (inset in Figure 5.8 c). The approximate size of the NiO nanoclusters to be <2 nm. In addition, an aberration-corrected HAADF-STEM image of NiO/Ni-SACs/mNC1000 also showcased the presence of tiny metallic nanoclusters (Figure 5.8 d), along with numerous white dots corresponding to single atomic sites (Figure 5.8 e), uniformly dispersed throughout the



carbon structure. We then calculated the crystal lattice spacing of nanoclusters obtained from HR-TEM images (Figure 5.8 f). The spacing value of 0.241 nm well matched with (111) plane of NiO which again validates the above-mentioned fact (Figure 5.8 g). The HAADF-STEM image & its corresponding EDS elemental mappings revealed the uniform dispersion of Ni and O atoms across all N-doped carbon nano structures of NiO/Ni-SACs/mNC1000 (Figure 5.8 h).

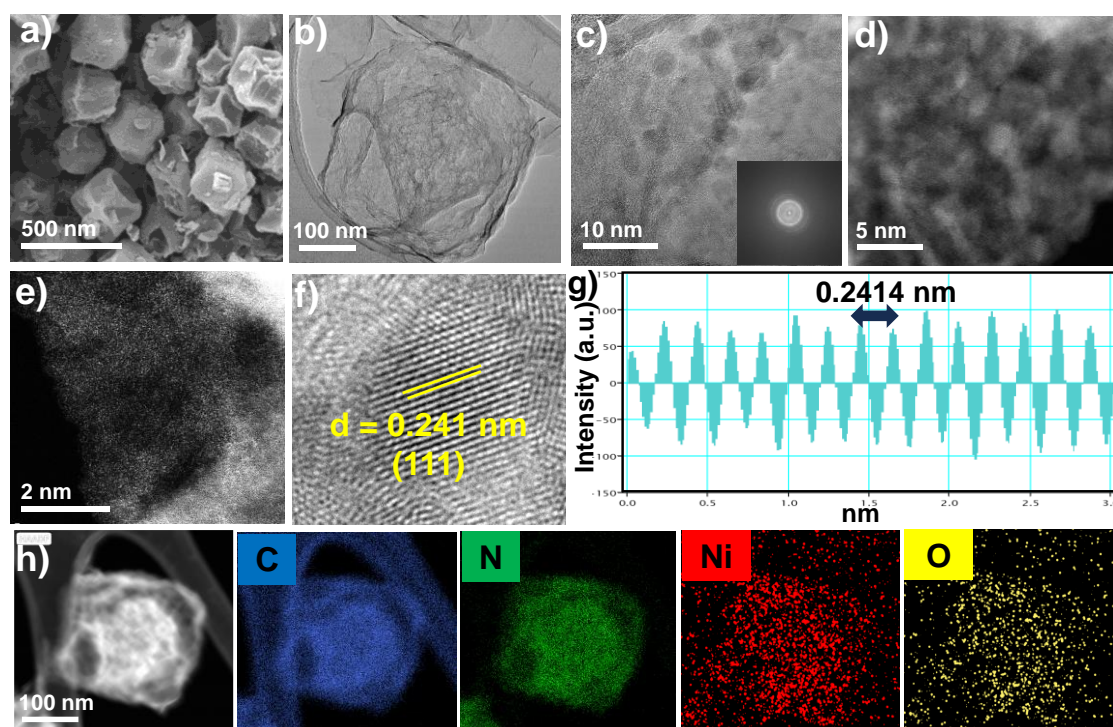


**Figure 5.8** a) SEM images of NiO/Ni-SACs/mNC1000. b) TEM images of NiO/Ni-SACs/mNC900. c) HR-TEM images where small NiO nanoclusters distributed over carbon (inset is the SAED pattern of NiO/Ni-SACs/mNC900). d)-e) High resolution HAADF-STEM images. f) d spacing calculations from corresponding fringes of NiO nanoclusters. g) Intensity profiles of the nanoclusters. h) HAADF-STEM image and its corresponding EDX elemental mapping of Carbon (blue), Nitrogen (green), Nickel (red), Oxygen (yellow).

Conclusively, all these findings strongly suggest the coupling of Ni-N-C with very small NiO nanoclusters which exist on concave shaped stretched edge mesoporous carbon cages. For comparison, we have prepared other supporting materials (Figure 5.9-S11) also. We carbonized Ni/ZIF-8@SiO<sub>x</sub> at 900 °C which denoted as NiO/Ni-SACs/mNC900. Further characterization by SEM, HR-TEM, HAADF-STEM &

elemental mapping showed that NiO/Ni-SACs/mNC900 also possesses concave shaped mesoporous carbon nanostructures (Figure 5.9 a-d) and small NiO nanoclusters again distributed homogeneously all over the carbon which confirmed by crystal lattice spacing and SAED pattern (Figure 5.9 f-g).

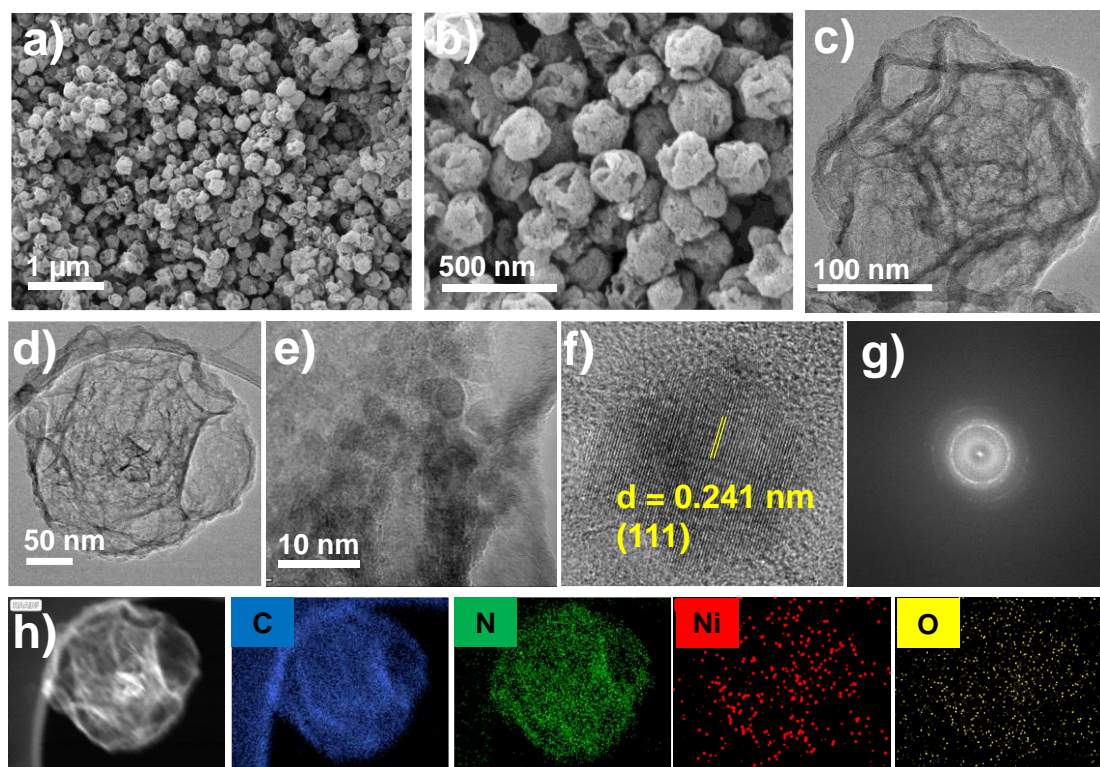


**Figure 5.9** a)-b) SEM images of NiO/Ni-SACs/mNC900 at different scale bars. c)-d) TEM images of NiO/Ni-SACs/mNC900. e) HR-TEM images where small NiO nanoclusters distributed over carbon. f) d spacing calculations from corresponding fringes of NiO nanoclusters. g) SAED pattern of NiO/Ni-SACs/mNC900. h) HAADF-STEM image and its corresponding EDX elemental mapping of Carbon (blue), Nitrogen (green), Nickel (red), Oxygen (yellow).

Similar nanostructured carbon has been examined when we calcined only ZIF-8@SiO<sub>x</sub> as depicted in Figure 5.10 a-d (i.e., in absence of Ni). Several mesopores were created there & absence of any metallic nanoclusters here again verified by HR-TEM analysis and SAED pattern Figure 5.10 e-f.

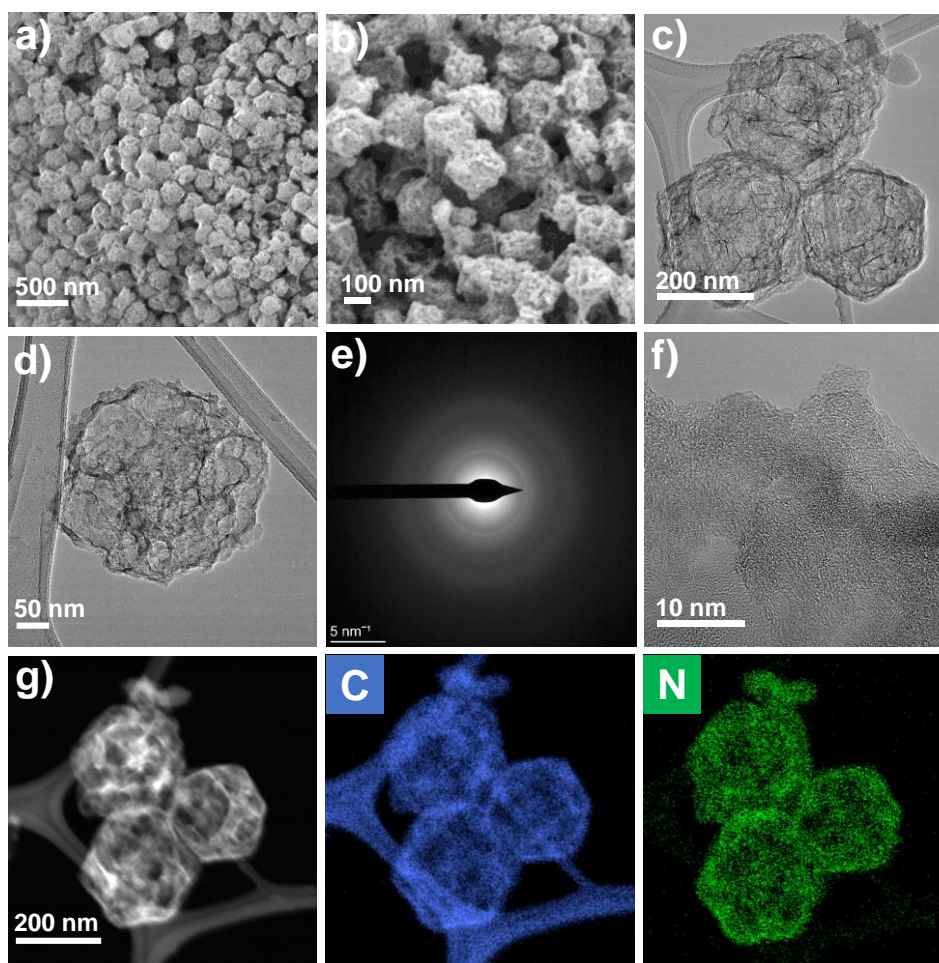


**Figure 5.10** a)-b) SEM images of mNC1000 at different scale bars. c)-d) TEM images of mNC1000. e) SAED pattern of mNC1000. f) HR-TEM images where no metallic particles or clusters are present. g) HAADF-STEM image and its corresponding EDX elemental mapping of Carbon (blue), Nitrogen (green).

Now to check whether this distinctive morphology of carbon is occurring for silica coating or not, we then synthesized Ni-SACs/NC1000 by carbonizing only Ni/ZIF-8 (without silica coated sample) at 1000 °C followed by acid washing with 10% H<sub>2</sub>SO<sub>4</sub> at 80 °C. Ni-SACs/NC1000 maintained the original dodecahedral morphology of ZIF-8 precursors, as illustrated in Figure 5.11 a-d. In addition to this, HR-TEM and its corresponding SAED pattern suggests the nonexistence of any metallic nanoparticles throughout the carbon matrix (Figure 5.11 e-f). Although EDS elemental mapping implies the presence of Ni that means Ni is present as single atomic form (Figure 5.11 g).

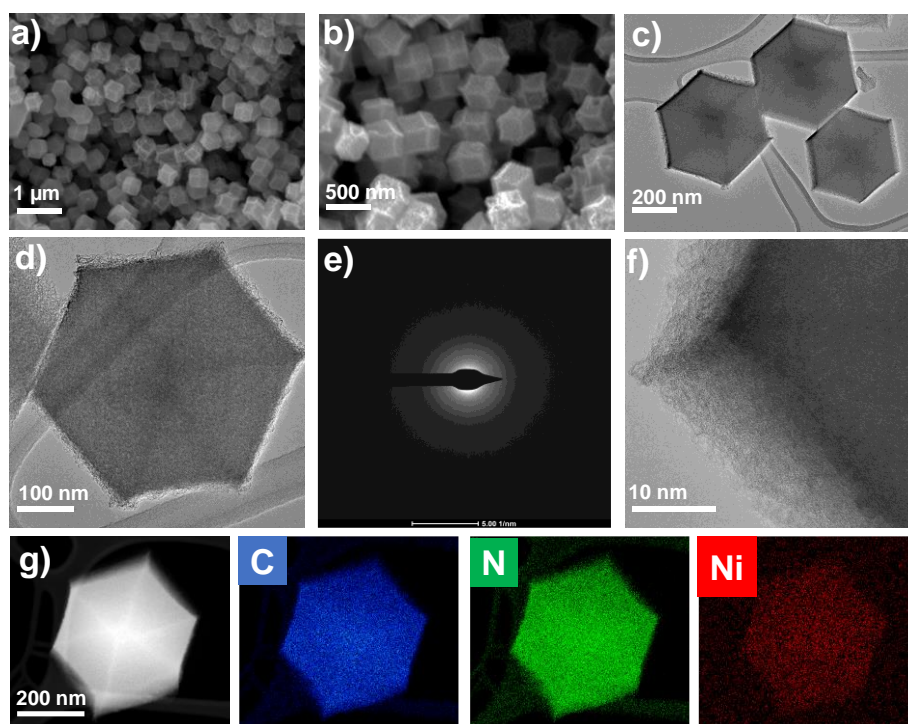


**Figure 5.11** a)-b) SEM images of Ni-SACs/NC1000 at different scale bars. c)-d) TEM images of Ni-SACs/NC1000. e) SAED pattern of Ni-SACs/NC1000. f) HR-TEM images where no metallic particles or clusters are present. g) HAADF-STEM image and its corresponding EDX elemental mapping of Carbon (blue), Nitrogen (green), Nickel (Ni).

So Based on these controlled experiments, we can say here the  $\text{SiO}_x$ -coating step plays a crucial role in shaping the distinctive stretched edge concave morphology after calcination which help to improve the mass transfer kinetics. During controlled thermal transformation, solitary MOFs i.e., without coating undergo isotropic shrinking, forming solid dodecahedral carbons. However, MOFs with an external  $\text{SiO}_x$ -coated layer exhibit anisotropic thermal shrinkage due to  $\text{SiO}_x$ -induced outward adsorption forces, as validated by thermogravimetric analysis (TGA) (Figure 5.12).

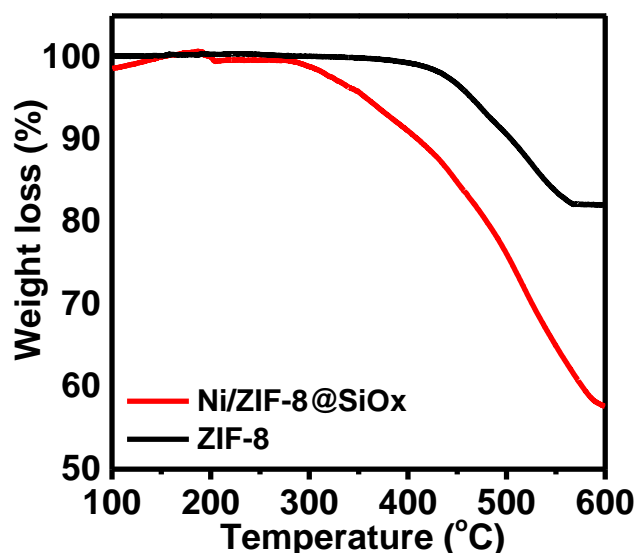


**Figure 5.12** TGA of ZIF-8 and Ni/ZIF-8@SiOx at a ramp rate of 10 °C min<sup>-1</sup> under an N<sub>2</sub> flow.

While the edge fringes of ZIF-8 are preserved, the planar faces of the dodecahedron collapse during pyrolysis, as demonstrated by thermal stress analysis in Figure 5.13 [438]. Simultaneously, during the pyrolytic conditions some amount of Ni<sup>2+</sup> is reduced by resulting N-doped carbons and bonds with neighboring atoms, forming catalytically active Ni-N-C sites doped within concave shaped mesoporous carbons while some Ni<sup>2+</sup> formed ultra small NiO nanoclusters which is tightly bounded with Ni-N-C and remained stable even after acid treatment.

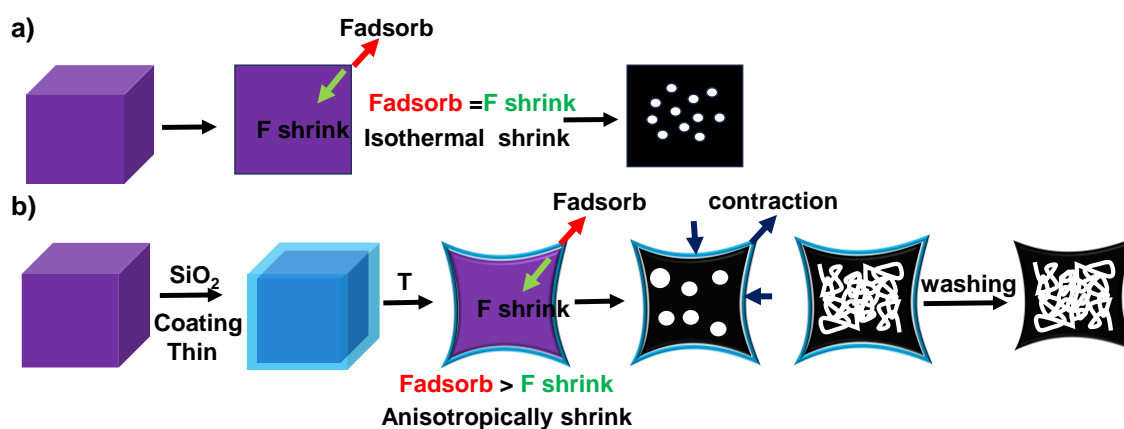


**Figure 5.13** Schematic illustration of the synthesis process of mesoporous carbon cages with more stretched edges.

The PXRD pattern of NiO/Ni-SACs/mNC1000 exhibited only two peaks at  $25.44^\circ$  and  $44.5^\circ$ , corresponding primarily to the 002 and 100 planes of graphitic carbon, respectively (Figure 5.14). Notably, no peak corresponding to metallic nanoclusters was observed, may be due to their very small particle size. Similar PXRD patterns were observed for NiO/Ni-SACs/mNC900 and other supporting materials.

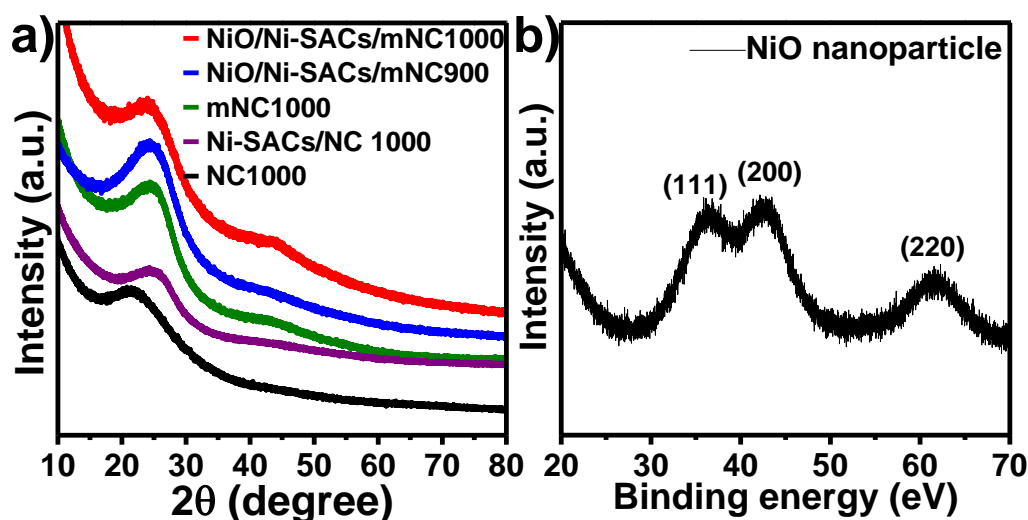


**Figure 5.14** a) PXRD of as synthesis NiO/Ni-SACs/mNC1000 and other supporting catalysts. b) PXRD of as synthesized NiO nanoparticles.

But further characterization through Raman scattering analysis revealed two observable peaks at  $464.6$  and  $917.7\text{ cm}^{-1}$  in NiO/Ni-SACs/mNC1000 and NiO/Ni-SACs/mNC900, attributed to Ni-O lattice vibrations (Figure 5.15) [439]. Additionally, no metallic oxide peak was observed for Ni-SACs/NC1000, validating the presence of Ni solely in atomic form. NiO/Ni-SACs/mNC1000 displayed two additional Raman peaks at  $1347.3$  and  $1590\text{ cm}^{-1}$ , attributed to the disordered carbon (D band) and graphitic carbon (G band), respectively. We compare the Raman intensity ratio of D band and G band for all the materials. The lower  $I_d/I_g$  value (0.942) of NiO/Ni-SACs/mNC1000 as compared to Ni-SACs/NC1000 (1.04) and other supporting materials indicates higher degree of graphitization.

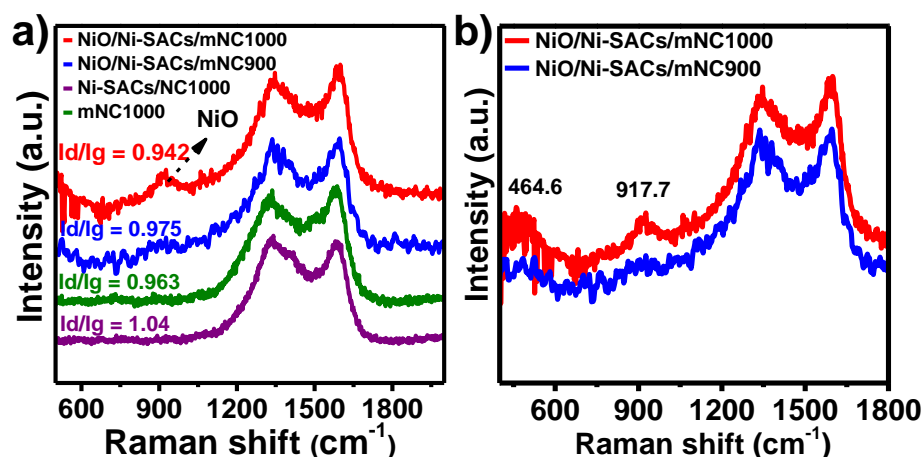


**Figure 5.15** a) Comparison of Raman spectra of as synthesized NiO/Ni-SACs/mNC1000 with all other supporting catalysts. b) Raman spectra of NiO/Ni-SACs/mNC1000 and NiO/Ni-SACs/mNC900 in a wide range.

Moreover, a prominent electron paramagnetic resonance (EPR) signal confirms the abundance of defects within the catalysts (Figure 5.16). Electronic behavior analysis via EPR spectroscopy at room temperature revealed a  $g$ -value of 2.17 for both NiO/Ni-SACs/mNC1000 and Ni-SACs/NC900 samples. Notably, the EPR signal intensity of NiO/Ni-SACs/mNC1000, where Ni single atoms are coupled with NiO, was more than 8 times higher than that of the sole Ni single-atom catalyst, indicative of an electron-rich structure because of the presence of NiO nanoclusters [427, 440, 441].

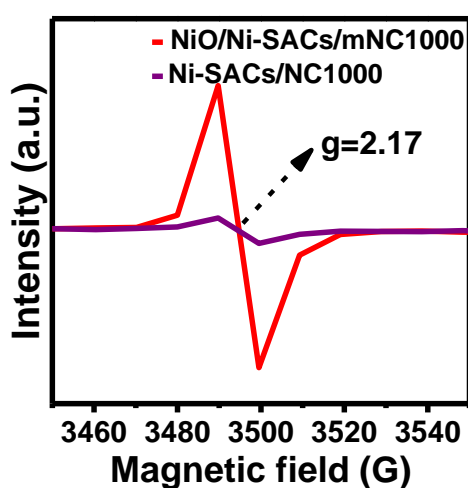


**Figure 5.16** Electron paramagnetic resonance (EPR) spectra measured at 292 K.

The chemical state and elemental composition of the catalysts were thoroughly investigated using X-ray photoelectron spectroscopy. As depicted in Figure 5.17, the Ni single-atom catalyst displayed a prominent peak at 856.54 eV in Ni 2p<sub>3/2</sub>, primarily corresponding to the Ni (II) state, consistent with the binding energy of Ni (II) in nickel phthalocyanine [442]. We also have studied Ni 2p XPS of pure NiO nanoparticles and it showed a characteristic peak at 854.37 eV in Ni 2p<sub>3/2</sub> region [443]. Nevertheless, the Ni 2p<sub>3/2</sub> spectra of NiO/Ni-SACs/mNC1000 exhibited two strong peaks: one associated with Ni-N or NiO in the range of 854.53 eV, and another at 856.23 eV attributed to Ni (II). Similar observations were made for NiO/Ni-SACs/mNC900, displaying two peaks at 854.53 eV and 856.12 eV corresponding to Ni-N/NiO and Ni (II), respectively. Strikingly, in both NiO/Ni-SACs/mNC1000 and NiO/Ni-SACs/mNC900, the binding energies of Ni (II) shifted to lower binding energies compared to the sole Ni single-atom catalyst, while the binding energies of NiO/Ni-N shifted to higher binding energies as compared to pure NiO nanoparticles. These findings demonstrate that Ni-N-C exhibit a stronger electron coupling effect, facilitating electron transfer from NiO nanoparticles to Ni single-atom catalysts, thus resulting the presence of low-valence Ni single atoms and higher valence NiO.



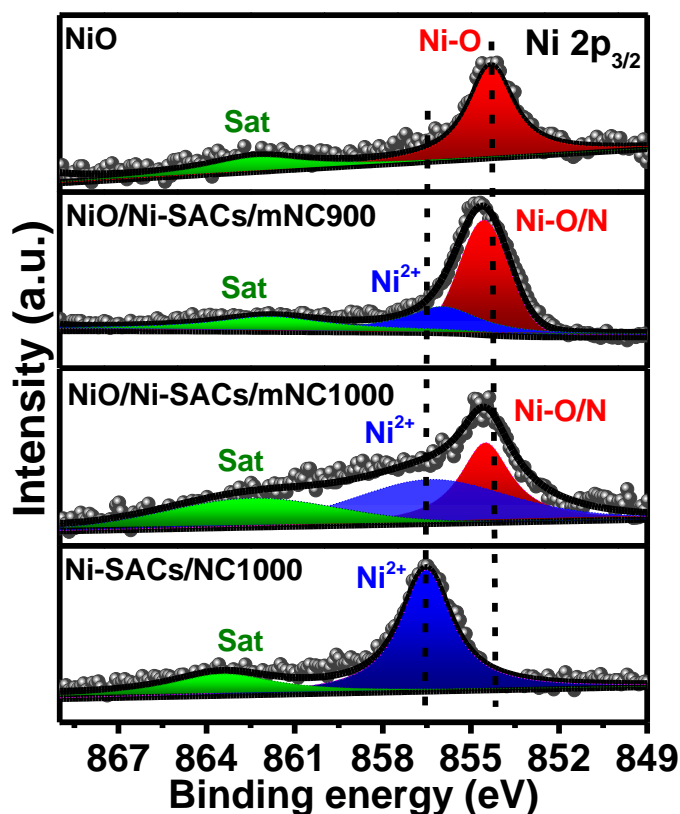


**Figure 5.17** Comparison of XPS Ni 2p spectra of NiO/Ni-SACs/mNC1000 with other supporting catalysts.

Furthermore, the deconvolution of N 1s XPS spectra for NiO/Ni-SACs/mNC1000 revealed four types of N characteristic peaks: pyridinic (398.43 eV), pyrrolic (400.42 eV), graphitic (401.17 eV), and metal-coordinated N (399.46 eV) (Figure 5.18). Among all pyridinic N being the predominant species, serving as anchoring sites for stabilizing the SACs within the carbon structure and as active sites for enhanced O<sub>2</sub> redox reaction kinetics [444]. Additionally, an upshift in peak positions for Metal-N, pyridinic N, and pyrrolic N species was observed for both NiO/Ni-SACs/mNC1000 and NiO/Ni-SACs/mNC900 compared to Ni-SACs/NC1000, indicative of a strong binding between Ni and N due to electron transfer from NiO nanoclusters to Ni single atoms.

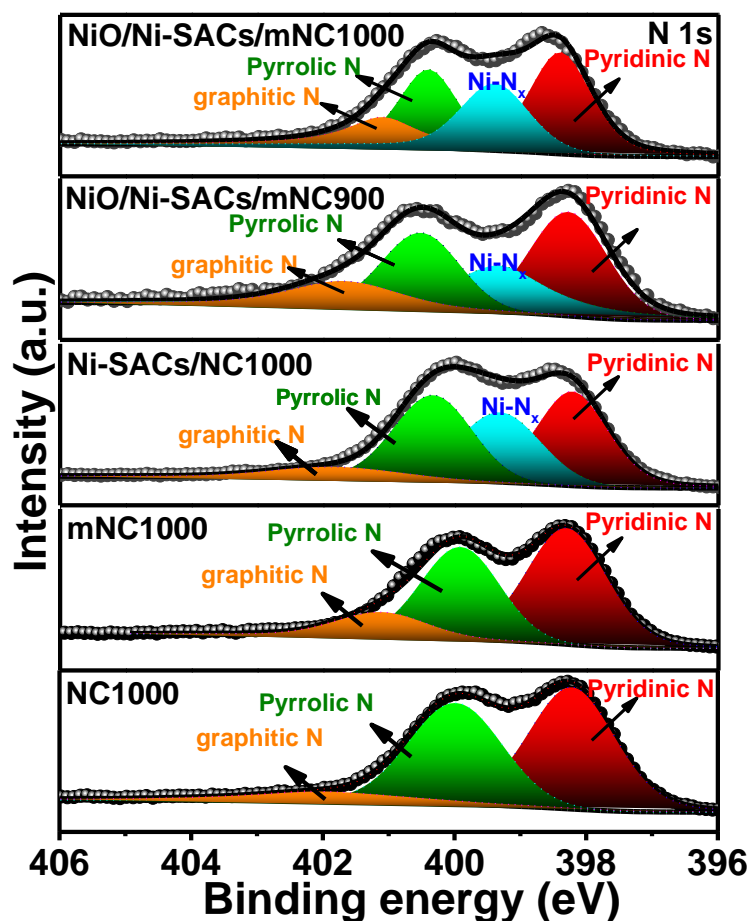


**Figure 5.18** Comparison of XPS N 1s spectra of NiO/Ni-SACs/mNC1000 with other supporting catalysts.

The oxygen signal of as-synthesized pure NiO nanoparticles revealed two lattice-bound oxygen components, Ni<sup>II</sup>-O and Ni<sup>III</sup>-O, at 529.3 and 530.58 eV, respectively (Figure 5.19). The oxygen component at higher binding energies (532.20 eV) was associated with deficient, interstitial, and peroxo-like species, known as oxygen vacancies (O<sub>v</sub>). It has been reported that oxygen vacancies also contribute to enhance the OER activity. Similarly, the same phenomenon was observed for both NiO/Ni-SACs/mNC1000 and NiO/Ni-SACs/mNC900. In both cases, three peaks were observed in the range of 529.4-529.5 eV, 530.8-531.1 eV, and 532.5-532.76 eV, corresponding to Ni<sup>II</sup>-O, Ni<sup>III</sup>-O, and O<sub>v</sub>, respectively. However, Ni<sup>II</sup>-O was predominantly present, while the other two peaks were less intensified, possibly due to the formation of the NiO nanoclusters after higher temperature treatment [445].

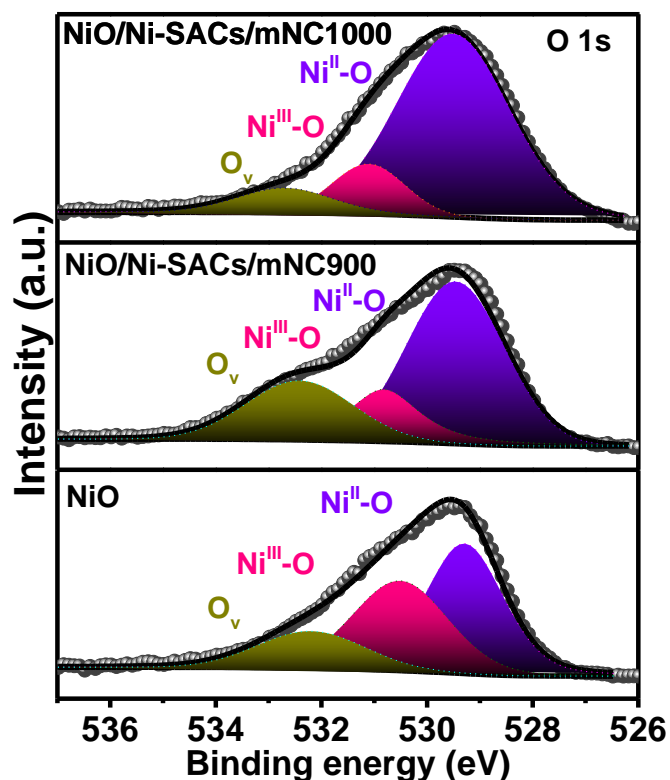


**Figure 5.19** Comparison of XPS O 1s spectra of NiO/Ni-SACs/mNC1000 and NiO/Ni-SACs/mNC900 with pure NiO nanoparticles.

Besides it, we conducted an examination of the d band structure of Ni using ultraviolet photoelectron spectroscopy (UPS). The complete photoemission spectra obtained for NiO/Ni-SACs/mNC1000 and Ni-SACs/NC100 were acquired with an ultraviolet source of He I (21.22 eV). The obtained photoemission spectrum was referenced to the Fermi level ( $E_f$ ) as zero eV. By identifying the cut-off energy value, the work function ( $\Phi$ ) value can be determined. The coupling of NiO with Ni-N-C resulted in a  $\Phi$  value of 4.486 eV (the difference between He (I) and  $E_{\text{cut-off}}$ ), which is lower than that of only Ni-N-C (5.07 eV), as depicted in Figure 5.20 a. A low work function value also denotes that NiO/Ni-SACs/mNC1000 are capable of facilitating charge transfer at the interface. Additionally, the shift of near Fermi level signals can be ascribed to the change in the electronic structure of Ni single atoms on the surface of N-doped mesoporous carbon. The position of Ni-SACs/NC100 exhibits an increase in binding energy compared to NiO/Ni-

SACs/mNC1000 (away from the Fermi level). According to the d band theory, the downshifted d band of only Ni single atom catalyst (grey curve) corresponds to a weakened adsorption strength [446,447]. To delve deeper into this electron interaction, surface valence band photoemission spectra (VBS) of NiO/Ni-SACs/mNC1000 and Ni-SACs/NC1000 were collected using XPS (see Figure 5.20 b). The findings reveal that the d band center relative to the Fermi level ( $E-E_f$ , calculated using Eq. S1 mentioned in section 2.1) exhibit an upward shift from Ni-SACs/NC1000 (4.667) to NiO/Ni-SACs/mNC1000 (4.248). Concurrently, the upward shift of the d band center contributes to a decrease in the electron filling in the antibonding orbital, thereby enhancing the binding affinity between Ni and oxygenated species. It is widely acknowledged that the interaction between the adsorbed valence state and the transition metal d state results in the formation of distinct bonding and antibonding orbitals [448,449]. The bonding states, located well below  $E_f$ , are fully occupied, whereas the electron occupancy of the antibonding states is contingent upon the energy states relative to  $E_f$ , influencing bond strength. Consequently, the introduction of NiO leads to the d electron contribution from NiO to Ni single atoms, causing an upward shift of the d band center toward  $E_f$ . This, in turn, prompts a reduction in electron occupancy in antibonding states, strengthening the interaction between adsorbate and surface. Collectively, these findings indicate that the synergistic interplay between Ni-N-C and NiO enhanced the reversible  $O_2$  redox reaction.

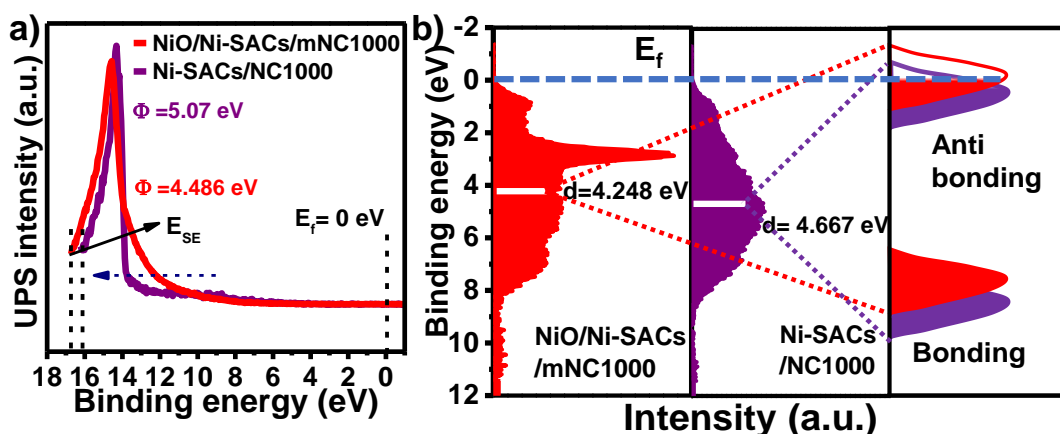


**Figure 5.20** a) UPS He I spectra b) Valence band spectra (The white bar shows d-band center) of NiO/Ni-SACs/mNC1000 and Ni-SACs/NC1000.

The  $N_2$  sorption isotherms of NiO/Ni-SACs/mNC1000 revealed characteristic type-IV isotherms (Figure 5.21), with a specific surface area ( $S_{BET}$ ) of  $2369 \text{ m}^2 \text{ g}^{-1}$  and a pore volume ( $V_p$ ) of  $11.4 \text{ cm}^3 \text{ g}^{-1}$ , markedly larger than those of Ni-SACs/NC1000 ( $S_{BET} = 868.3 \text{ m}^2 \text{ g}^{-1}$ ,  $V_p = 0.45 \text{ cm}^3 \text{ g}^{-1}$ ) (refer to Table 5.1). Additionally, NiO/Ni-SACs/mNC1000 exhibited hierarchical pores with a combination of micro and mesopores (as depicted in Figure 5.22). Even similar thing we observe i.e., the formation of meso and micropore and enhancement of surface area for mNC1000 ( $S_{BET} = 2120 \text{ m}^2 \text{ g}^{-1}$ ,  $V_p = 2.592 \text{ cm}^3 \text{ g}^{-1}$ ).

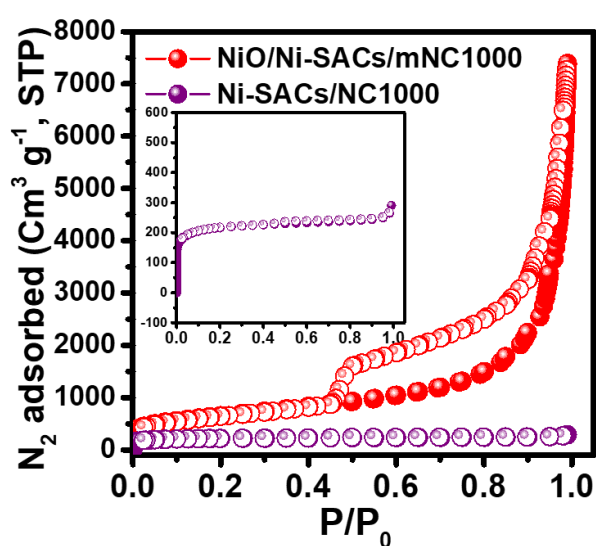


**Figure 5.21** N<sub>2</sub> adsorption desorption isotherm comparison between NiO/Ni-SACs/mNC1000 and Ni-SACs/NC1000.

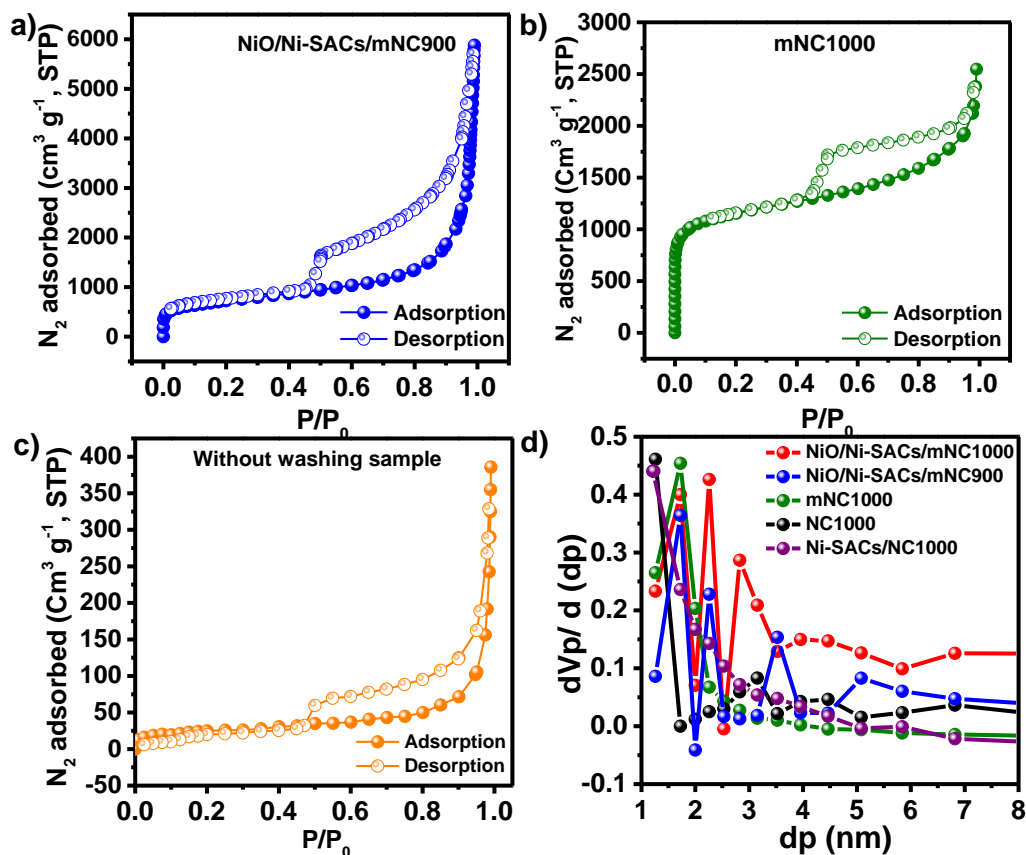


**Figure 5.22** a)-c) N<sub>2</sub> adsorption desorption isotherms of NiO/Ni-SACs/mNC900, mNC1000 & without washed sample of NiO/Ni-SACs/mNC1000 respectively. D) BJH analysis for pore size distribution of NiO/Ni-SACs/mNC1000 and all other supporting catalysts.

**Table 5.1** Surface texture characteristics of the NiO/Ni-SACs/mNC1000, NiO/Ni-SACs/mNC900, mNC1000, Ni-SACs/NC1000, NC1000 (a-b) BET method, (c) BJH method.

Catalyst	Specific surface area (m <sup>2</sup> g <sup>-1</sup> )(a)	Total pore volume (cm <sup>3</sup> g <sup>-1</sup> ) (b)	Average pore diameter (nm) (c)
NiO/Ni-SACs/mNC1000	2369.7	11.4	15.603
NiO/Ni-SACs/mNC900	1824.6	5.68	14.089
mNC1000	2120	2.592	8.1913
Ni-SACs/NC1000	868.3	0.4498	2.1247
Without wash sample of NiO/Ni-SACs/mNC1000	101.16	0.5835	12.997

These findings indicate that during pyrolysis, SiO<sub>x</sub>-coating can induce inward carbon migration to the exterior, leading to the formation of numerous meso/micropores on the walls. Such concave shaped morphology with elongated edges results in a substantial increase in external surface area, while the in-situ generated meso/micropores can be found on the walls of NiO/Ni-SACs/mNC1000.

The electrocatalytic OER performance of NiO/Ni-SACs/mNC1000 and its supporting catalysts was measured in basic electrolytes using a standard three-electrode setup. Cyclic voltammetry (CV) was conducted in 1 M KOH at room temperature, with a scan rate of 10 mV/s (Figure 5.23). We observed the oxidation (Ni<sup>2+</sup> to Ni<sup>3+</sup>) & reduction peak (Ni<sup>3+</sup> to Ni<sup>2+</sup>) corresponding to NiO nanoclusters present in NiO/Ni-SACs/mNC1000. Potentials were adjusted to the reversible hydrogen electrode (RHE) scale [450].

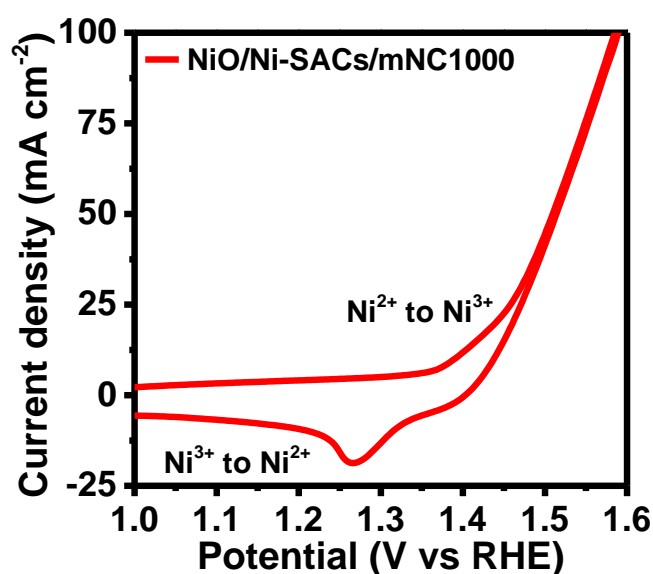


**Figure 5.23** Cyclic voltammetry study of NiO/Ni-SACs/mNC1000 catalyst in 1 M KOH solution at scan rate 10 mV/s.

Linear sweep voltammetry (LSV) studies mentioned in Figure 5.24 illustrate that NiO/Ni-SACs/mNC1000 exhibited higher current density and low OER onset potential (1.467 V vs. RHE) compared to NiO/Ni-SACs/mNC900 (1.494 V), Ni-SACs/mNC1000 (1.536 V), mNC1000 (1.569 V) & IrO<sub>2</sub> (1.589 V). Moreover, the overpotential required

to achieve a current density of  $10 \text{ mA cm}^{-2}$  is commonly used as a benchmark to estimate the OER catalyst's activity. NiO/Ni-SACs/mNC1000 required small overpotential values of 0.296 to reach a current density of  $10 \text{ mA cm}^{-2}$  (Figure 5.24 b). Nevertheless, Ni-SACs/NC1000 necessitated overpotentials of 0.38 mV to achieve the same. This emphasizes the importance of the coexistence of NiO with Ni single atoms which synergistically improving the overall OER performance of NiO/Ni-SACs/mNC1000. A comparison of overpotential required to deliver a current density of  $10 \text{ mA cm}^{-2}$  for various catalysts in 1 M KOH electrolytes is illustrated in Figure 5.24 b.

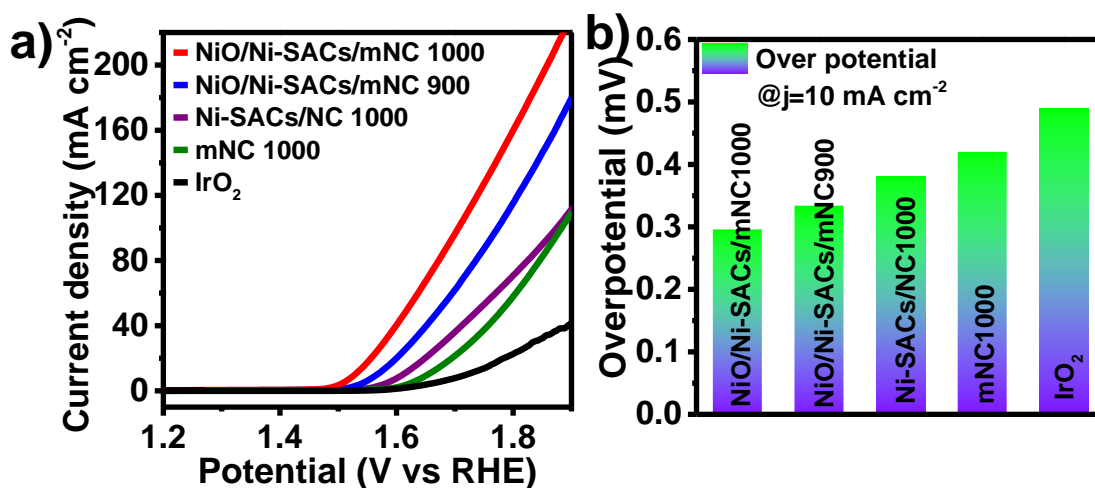


**Figure 5.24** a) Linear sweep voltammetry study of NiO/Ni-SACs/mNC1000 and other supporting catalysts in 1 M KOH solution at scan rate 5mV/s. b) Bar graph corresponding to comparison of overpotential for different catalysts required to achieve  $10 \text{ mA cm}^{-2}$ .

Tafel slope values extracted from corresponding LSV curves for NiO/Ni-SACs/mNC1000 ( $73.59 \text{ mV dec}^{-1}$ ), Ni-SACs/NC1000 ( $102.28 \text{ mV dec}^{-1}$ ), NiO/Ni-SACs/mNC900 ( $76.96 \text{ mV dec}^{-1}$ ) in 1 M KOH are depicted in Figure 5.25. Notably, NiO/Ni-SACs/mNC1000 exhibited smaller Tafel slope values, indicating superior OER activity.



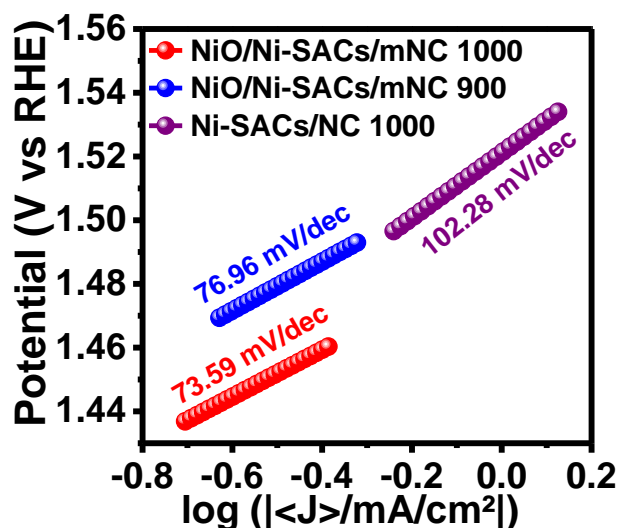


**Figure 5.25** Tafel plots of NiO/Ni-SACs/mNC1000 and other supporting catalysts.

The Nyquist plot of NiO/Ni-SACs/mNC1000 illustrates a smaller semi-circle compared to Ni-SACs/NC1000, indicating faster reaction kinetics and favorable charge-transfer resistance ( $R_{ct}$ ) with values of  $2.835 \Omega$  for former while  $4.55 \Omega$  for the later, respectively (Figure 5.26 a). An equivalent electrical circuit model, obtained through fitting the Nyquist plots, suggests a parallel model for the OER kinetics, where  $R_1$  represents solution resistance,  $CPE_1$  and  $CPE_2$  are two constant phase elements associated with double layer capacitance at the solid-electrolyte interfaces caused by charge-transfer resistance at low ( $R_2$ ) and high frequencies ( $R_3$ ), respectively (Figure 5.26 b&c).

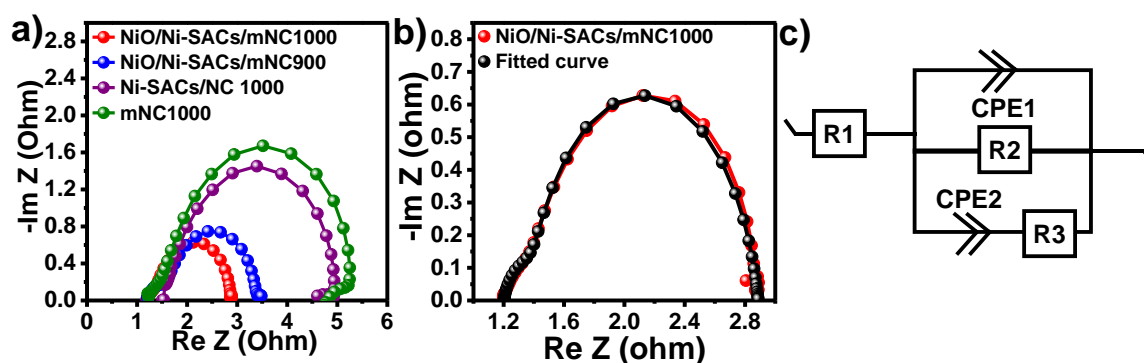


**Figure 5.26** a) Comparison of Nyquist plots of NiO/Ni-SACs/mNC1000 and other supporting catalysts for OER in 1M KOH. b) & c) Fitting of the Nyquist plot and its corresponding equivalent circuit model used for OER kinetics.

Furthermore, double layer capacitance ( $C_{dl}$ ) and electrochemical active surface area (ECSA) were calculated by measuring cyclic voltammetry (CV) with different scan rates ranging from 20 to 120  $\text{mV s}^{-1}$  in a non-faradaic potential region (Figure 5.27 & Figure 5.28). In 1 M KOH solution, the  $C_{dl}$  value for NiO/Ni-SACs/mNC1000 ( $22.96 \text{ mF cm}^{-2}$ ) surpasses that of Ni-SACs/NC1000 ( $14.34 \text{ mF cm}^{-2}$ ), NiO/Ni-SACs/mNC900 ( $21.84 \text{ mF cm}^{-2}$ ), and  $\text{IrO}_2$  ( $2.14 \text{ mF cm}^{-2}$ ). A larger  $C_{dl}$  value directly correlates with the electrochemical surface area (ECSA), suggesting the presence of more effective or exposed catalytic active sites for NiO/Ni-SACs/mNC1000, resulting in excellent OER performance.

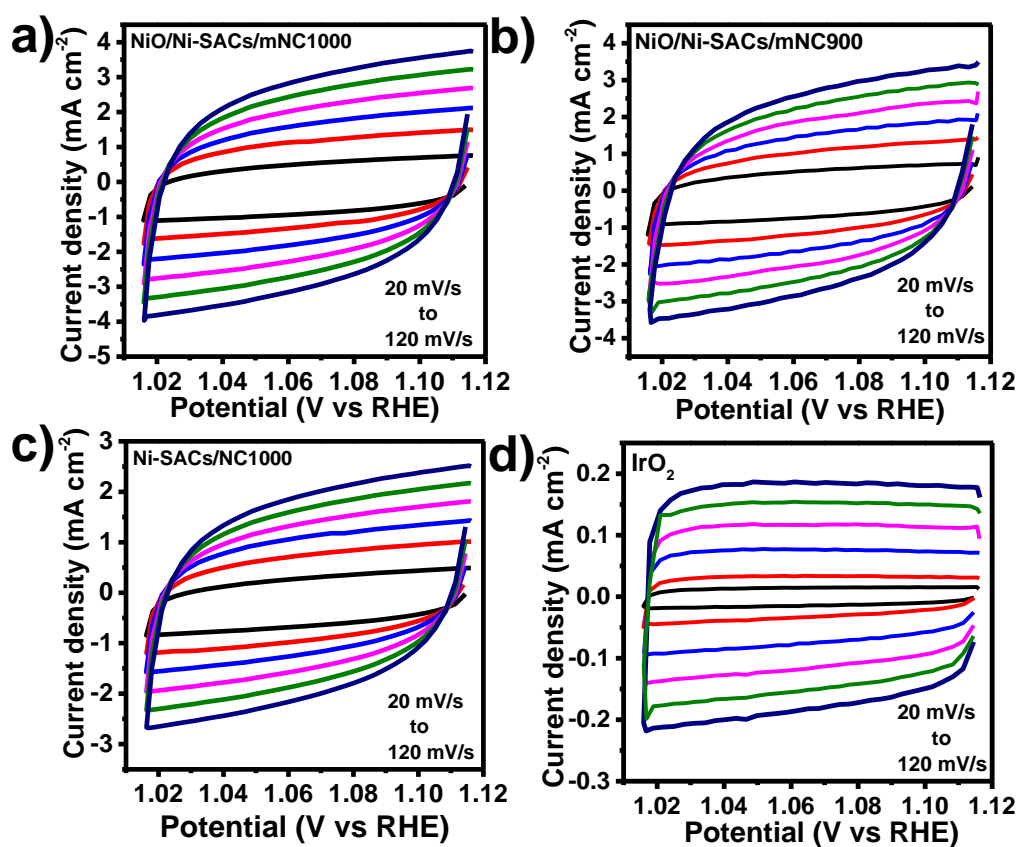


**Figure 5.27** CV curves of (a) NiO/Ni-SACs/mNC1000, (b) NiO/Ni-SACs/mNC900, (c) Ni-SACs/NC1000 and (d)  $\text{IrO}_2$  in a potential range of 1.028 to 1.128 V vs. RHE at different scan rate in 1 M KOH.

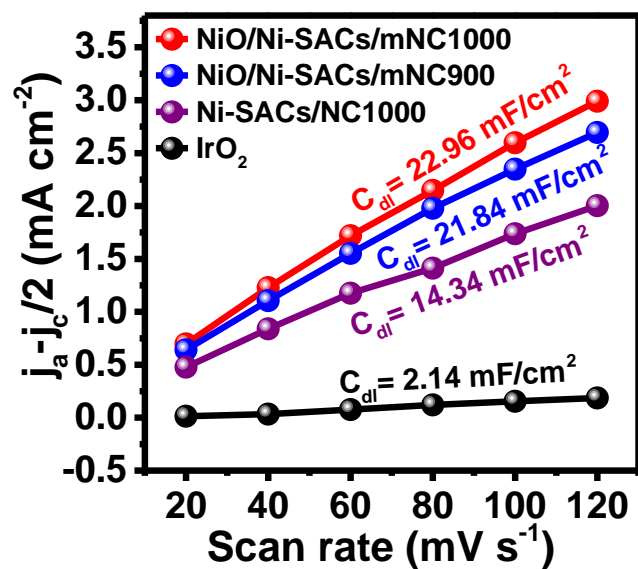


**Figure 5.28** Electrochemical double-layer capacitance ( $C_{dl}$ ) of NiO/Ni-SACs/mNC1000 and supporting catalysts.

Long-term OER stability of NiO/Ni-SACs/mNC1000 in 1 M KOH electrolytes was assessed using chronoamperometric tests at different current density (5,10,15, 20, 25 mA cm<sup>-2</sup>) and the catalyst demonstrated stable performance for approximately 50 hours without any significant loss. As demonstrated in Figure 5.29 a even after 50 h operation when we go back to 10 mA cm<sup>-2</sup> the catalyst holds its potential nicely. The LSVs before and after the stability test remained almost identical (Figure 5.29 b). From all of these results, it is evident that synergistic interaction between NiO and Ni single atom catalyst not only boosts OER activity but also provides robustness to the catalyst for long-term applications.

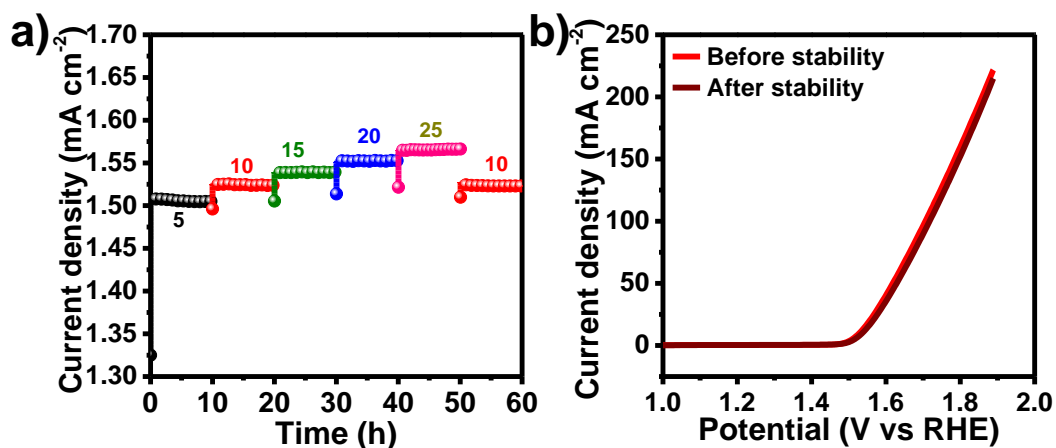


**Figure 5.29** a) Chronopotentiometric durability test of NiO/Ni-SACs/mNC1000 at different current densities (5, 10, 15, 20, 25 mA cm<sup>-2</sup>). b) LSV before and after stability test.

Through rotating ring disc electrode (RRDE) measurements, Faradaic efficiency (F.E.) and turnover frequency (TOF) were determined for NiO/Ni-SACs/mNC1000 & Ni-SACs/NC1000 (Figure 5.30 a & b) using the equation S6 & S7. NiO/Ni-SACs/mNC1000 showed F.E. 95.99% at 1.7 V. In contrast, the NiO-free catalyst (Ni-SACs/NC1000) exhibited lower value of only 63.45%. We then compared the calculated TOF and F.E. at different overpotentials 350 mV, 400 mV & 450 mV etc. NiO/Ni-SACs/mNC1000 demonstrated TOF values 8385 s<sup>-1</sup> whereas NiO-free catalyst showed 3272 s<sup>-1</sup>. The higher TOF value of NiO/Ni-SACs/mNC1000 indicates greater intrinsic activity compared to the Ni-SACs/NC1000 catalyst. These findings establish NiO/Ni-SACs/mNC1000 as an outstanding OER electrocatalyst for alkaline water electrolysis.

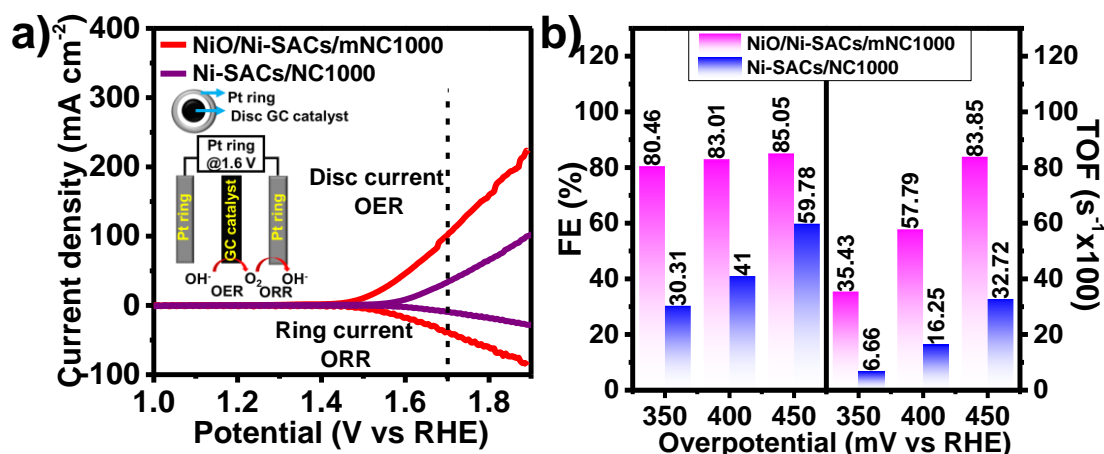


**Figure 5.30** a) RRDE current-potential response of NiO/Ni-SACs/mNC1000 and Ni-SACs/NC1000 catalysts for OER in O<sub>2</sub>-saturated 1.0 M KOH. b) TOF and FE calculated for OER considering different overpotential values, catalyzed by NiO/Ni-SACs/mNC1000 and Ni-SACs/NC1000.

Moreover, the outstanding OER activity exhibited by NiO/Ni-SACs/mNC1000 prompted the assembly of a 2-electrode alkaline water electrolytic cell for overall water splitting (Figure 5.31 a). NiO/Ni-SACs/mNC1000 coated Ni foam were selected as the anode and Pt/C coated Ni foam used as cathode, with a catalyst loading of 1.2 mg cm<sup>-2</sup> for each. The cell operated at a voltage of 1.58 V to achieve a current density of 10 mA cm<sup>-2</sup>, comparable to the Pt/C + IrO<sub>2</sub> couple (1.78 V) (Figure 5.31 b).

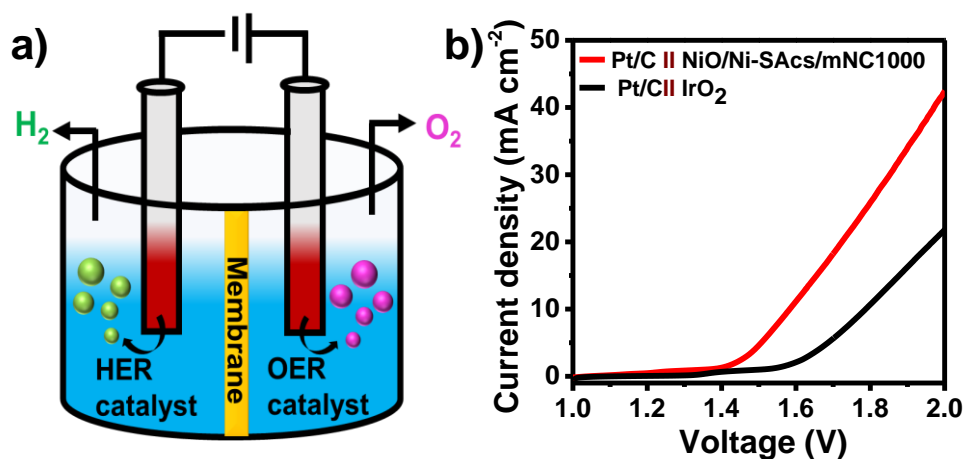


**Figure 5.31** a) Schematic illustration of water splitting electrochemical cell. b) LSV curves of NiO/Ni-SACs/mNC1000 + Pt/C where Pt/C used as cathode and NiO/Ni-

SACs/mNC1000 used as anode and compare with conventional catalyst mixture Pt/C + IrO<sub>2</sub>.

Motivated by the OER properties of the catalyst, we further explored the multifunctional capability of NiO/Ni-SACs/mNC1000 via performing its electrochemical ORR activity measurements. Utilizing a three-electrode setup with a rotating disk electrode (RDE) and O<sub>2</sub>-saturated 0.1 M KOH as the electrolyte. The linear sweep voltammetry (LSV) results indicate that NiO/Ni-SACs/mNC1000 exhibits excellent ORR performance, with onset ( $E_{\text{onset}}$ ) and half-wave potentials ( $E_{1/2}$ ) of 0.967 and 0.885 V, respectively, closely resembling those of Pt/C (1.01 and 0.92 V) (refer to 5.32 a). Moreover, the  $E_{1/2}$  value of NiO/Ni-SACs/mNC1000 surpasses that of NiO free catalyst Ni-SACs/NC1000 (0.85 V) (refer to Figure 5.32 b). All these results suggests the benefits of the coupling of NiO with Ni single atom catalyst on concave shaped stretched edge structure in enhancing the mass transport of reactants.

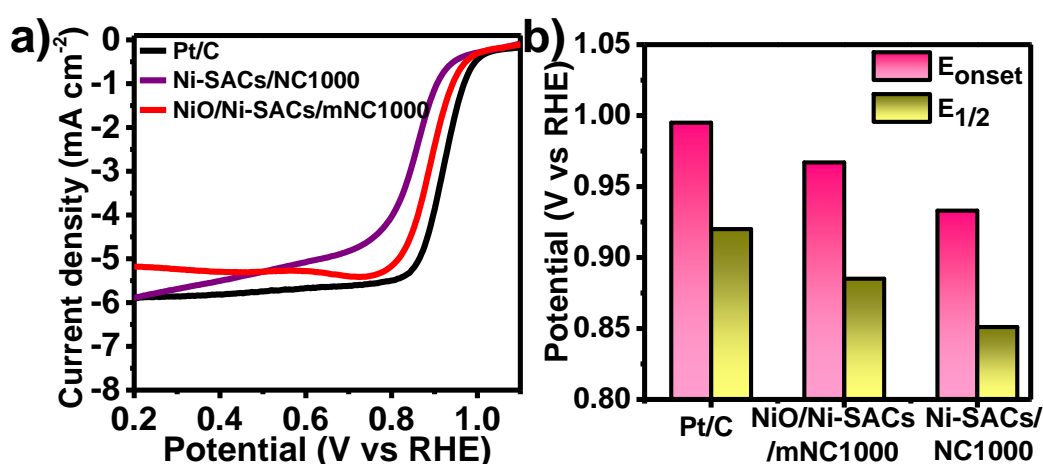


**Figure 5.32** Electrochemical ORR performance in 0.1 M KOH. a) LSV curves of NiO/Ni-SACs/mNC1000, Ni-SACs/NC1000, Pt/C with a sweep rate of 5 mV/s and a rotation rate of 900 rpm. (b)  $E_{\text{onset}}$  and  $E_{1/2}$  of NiO/Ni-SACs/mNC1000, Pt/C, and supporting catalysts.

DFT calculations were conducted to gain deeper insights into the involvement of Ni single atom catalysts i.e., NiN<sub>4</sub> and cubic NiO decorating NiN<sub>4</sub> sites, as well as the reaction

mechanism during the Oxygen Evolution Reaction (OER) process at the atomic level.

The optimised structures are illustrated in Figures 5.33 and 5.34.

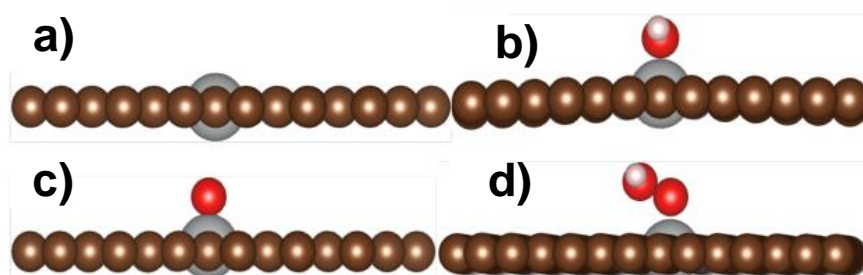


**Figure 5.33** The optimized structure for a) Ni-N<sub>4</sub> and b) OH, c) O, and d) OOH adsorbed on Ni-N<sub>4</sub>.

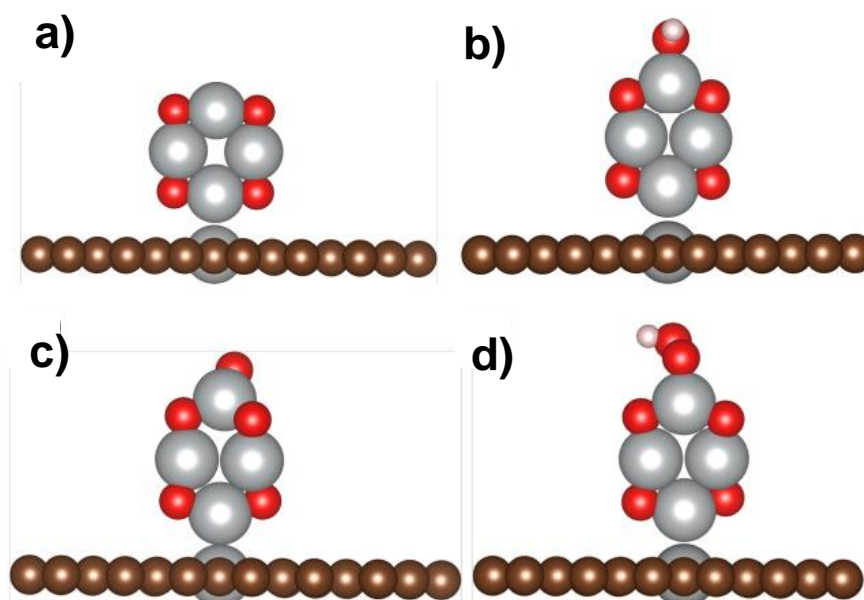


**Figure 5.34** The optimized structure for a) Ni-NiO-N<sub>4</sub> and b) OH, c) O, and d) OOH adsorbed on Ni-NiO-N<sub>4</sub>.

The calculated density of states (Figure 5.35 a & b) reveals an increased presence of Ni d-orbitals near the Fermi level in NiO decorated on NiN<sub>4</sub> sites. In contrast, no d-orbital states are observed near Fermi in the case of NiN<sub>4</sub>. These available d-orbital states notably facilitate the absorption of H<sub>2</sub>O molecules and subsequent intermediates. The absorption of H<sub>2</sub>O at the NiO side of NiO decorated on NiN<sub>4</sub> site is 0.577 eV higher than at

NiN<sub>4</sub> (without NiO) site. Correspondingly, the calculated d-band center exhibits an upward shift of 0.34 eV. This upward shift promotes the adsorption of active intermediates, leading to an enhancement in the reactivity of active sites. The OER process at NiN<sub>4</sub> site, Ni single atom initially adsorbs OH, and the \*OH species then interacts with a hydroxyl radical to produce \*O and a water molecule. Continuing the process, \*O combines with OH<sup>-</sup> to produce \*OOH, which eventually forms O<sub>2</sub> while interacting with OH<sup>-</sup>, thereby producing H<sub>2</sub>O. We then calculated the Gibbs free energy to determine the theoretical onset potential, which was found to be 2.14 V, as demonstrated in Figure 5.35 c & d. The rate-determining step in this mechanism was identified as the splitting of \*OH to \*O. Continuing our investigation, we explored the OER mechanism on a Ni single atom catalyst and on NiO of NiO-NiN<sub>4</sub>. The theoretical onset potentials were found to be 2.25 V and 1.89 V, respectively. Notably, the rate-determining step for the OER on NiO shifted to the formation of O<sub>2</sub> from \*OOH. The OER at Ni of the NiO site exhibited higher activity compared to the Ni single site of NiN<sub>4</sub>.



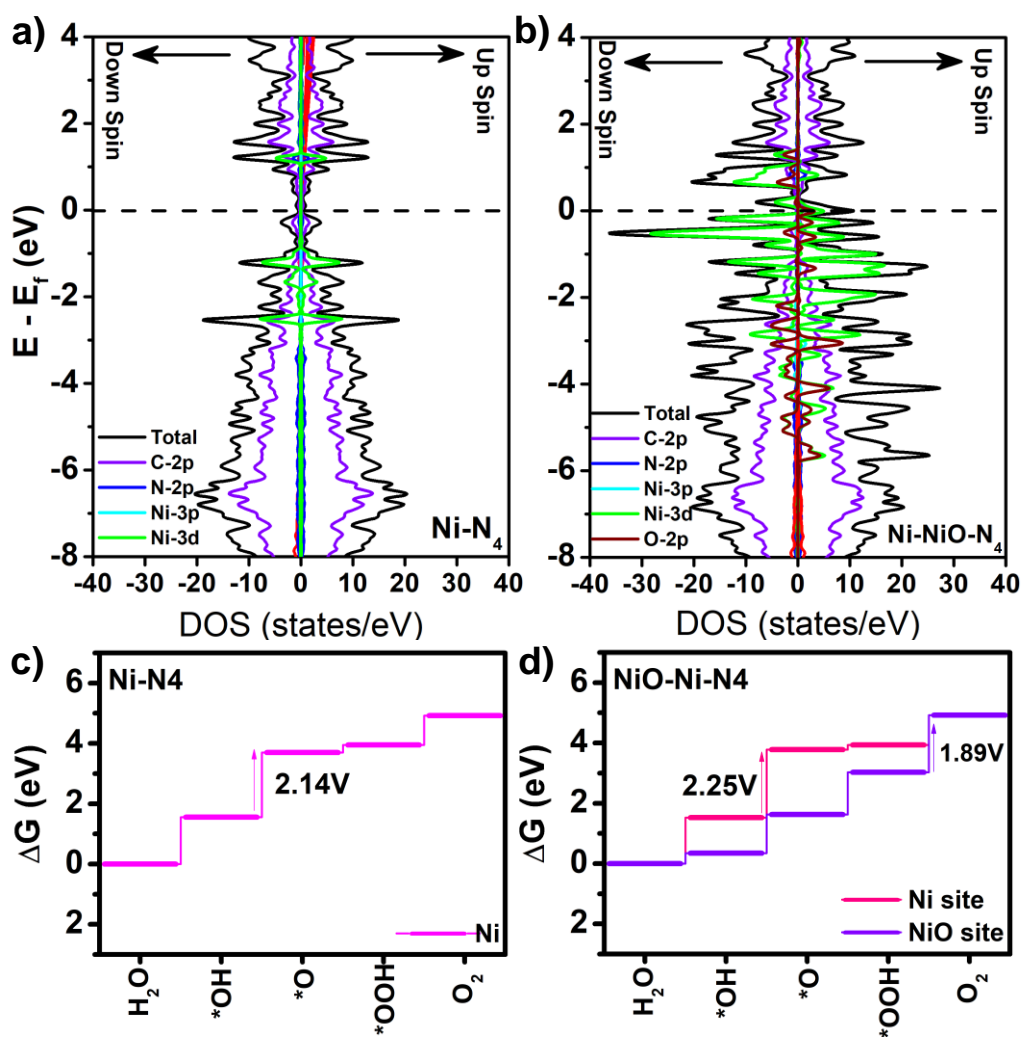


**Figure 5.35** DOS of (a) Ni-N<sub>4</sub> and (b) Ni-NiO-N<sub>4</sub>. The Fermi energy (E<sub>F</sub>) is at zero. Calculated free energy diagram for OER on c) Ni-N<sub>4</sub> and (b)Ni-NiO-N<sub>4</sub> at zero applied potential (U = 0).

Encouraged by the exceptional bifunctional OER/ORR capabilities, we proceeded to fabricate a more challenging solid-state ZAB comprising a gas diffusion layer (GDL) coated with NiO/Ni-SACs/NC1000 as the air cathode, a polished zinc foil serving as the anode and a hydrogel electrolyte dipped into 6 M KOH + 0.2 M Zn(OAc)<sub>2</sub>·6H<sub>2</sub>O. Initially, we synthesized and investigated the physicochemical properties of polyacrylamide (PAM) hydrogel denoted as PAM-h. The quasi-solid-state ZABs utilizing NiO/Ni-SACs/mNC1000 at cathodes with PAM hydrogel electrolyte exhibited open circuit voltage ~1.361 V (Figure 5.36).



**Figure 5.36** Photograph displaying measured open-circuit voltage of ~1.361 V using PAM-h electrolyte for NiO/Ni-SACs/mNC1000.

However, achieving high-rate performance remained challenging due to the formation of dense Zn dendrites and the disruption of the Zn|hydrogel electrolyte interface due to large amount of free water molecule. Therefore, it was essential to modify the intrinsic properties of the hydrogel electrolyte to address these challenges and achieve high-rate capability under ambient conditions. Here we have added DMSO and  $\text{Zn}(\text{BF}_4)_2$  during the synthesis of PAM-h and named as PAM-zdh. We have given a photograph of as synthesized PAM-zdh hydrogel (Figure 5.37)

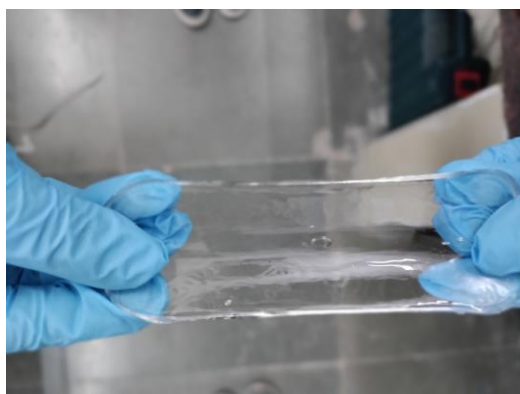


**Figure 5.37** photograph of PAM-zdh electrolyte.

For comparison we also have prepared only DMSO treated hydrogel (PAM-dh) and only metal salt treated hydrogel (PAM-zh). PAM-zdh showed good stretchability (Figure 5.38 a). To evaluate the compatibility between the Zn anode and the organohydrogel electrolyte, Zn|Zn symmetric cells were constructed. The Zn|Zn symmetric cell with the PAM-

zdh electrolyte exhibited lower polarization during plating/stripping cycles compared to the PAM-h indicating a stable electrochemical interface (Figure 5.38 b). Furthermore, PXRD patterns revealed weaker intensity of formed Zn dendrites (ZnO) when using the PAM-zdh as compared to other supporting electrolytes (Figure 5.38 c). So, it can be said that, DMSO which known as a favorable H-bond acceptor, forming a robust H-bond network with water molecules thereby reconstructing the solvation sheath structure of  $\text{Zn}^{2+}$  along with that due to the considerable electronegativity of F atoms,  $\text{BF}_4^-$  anions engage with water molecules through O-H $\cdots$ F interactions, displacing the O-H $\cdots$ O bonds between water molecules. Moreover, considering the practical demand for rechargeable batteries in cold regions and highlands, there is a need to develop low-temperature quasi-solid-state ZABs. The slow ion transport in low-temperature ( $\leq 0\text{ }^\circ\text{C}$ ) environments limits the depth of discharge and leads to low critical current densities. To address this challenge, the temperature-tolerance abilities of the PAM-zdh electrolyte were further investigated using differential scanning calorimetry (DSC). DSC findings indicate that the solid-liquid transitions of PAM-zdh hydrogel electrolytes vary significantly. Typically, the ice melting process exhibits a distinct endothermic peak, while the glass transition presents a noticeable step. During the heating process, significant endothermic peaks are observed in PAM-h, PAM-dh, PAM-zh. But for PAM-zdh, these endothermic peaks diminish, and only glass transition peaks are evident in hydrogel electrolytes, indicating a reduction in free water content. The results revealed anti-freezing and thermally stable properties for the synthesized PAM-zdh electrolyte (Figure 5.38 d).

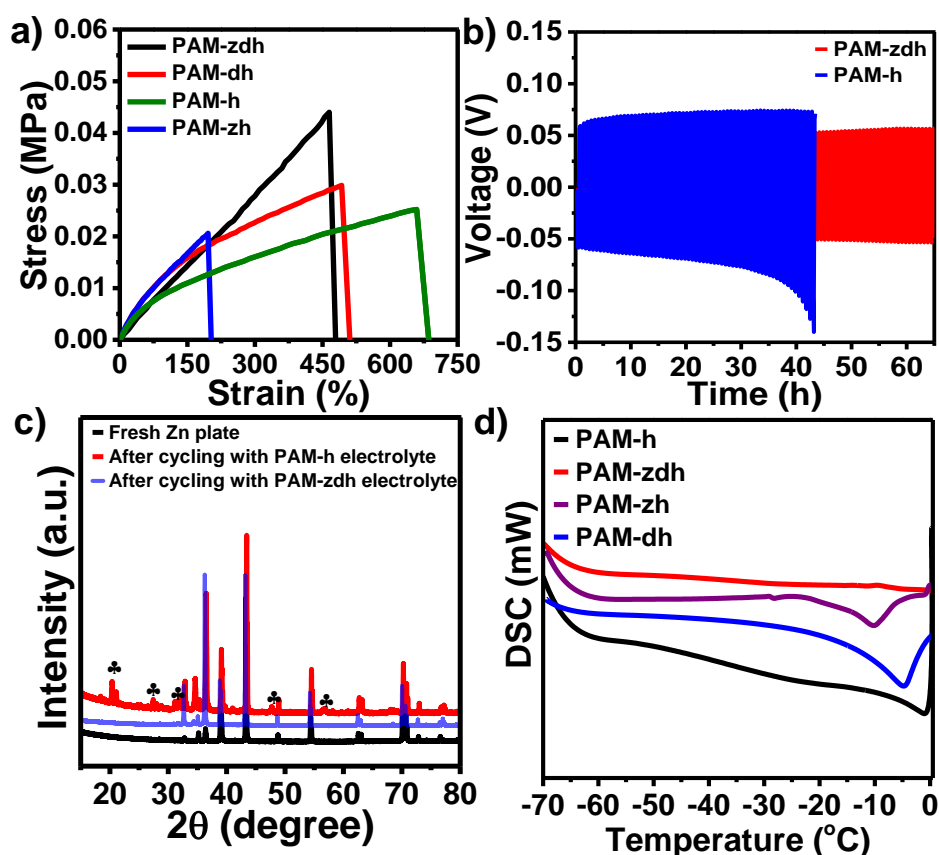


**Figure 5.38** a) Tensile stress-strain curve of PAM-h, PAM-dh, PAM-zh, PAM-zdh. b) Cycling performance of the symmetric Zn || Zn cells employing PAM hydrogel electrolyte and PAM organohydrogel electrolyte at  $5 \text{ mA cm}^{-2}$ . c) XRD patterns of various Zn samples. It suggests that the discharging and charging/discharging products are  $\text{Zn(OH)}_2$  and  $\text{ZnO}$ , respectively. d) DSC curves of PAM-h, PAM-dh, PAM-zh, PAM-zdh.

To further verify our understanding, we have calculated binding energy ( $E_b$ ). The binding energy ( $E_b$ ) quantifies the strength of interaction between different components. A lower  $E_b$  value signifies a stronger interaction. For instance, the  $E_b$  values for PAM- $\text{H}_2\text{O}$  (-33.855 kcal/mol), PAM-DMSO- $\text{H}_2\text{O}$  (-168.797 kcal/mol), PAM- $\text{Zn(BF}_4)_2$ - $\text{H}_2\text{O}$  (-502 kcal/mol) and PAM- $\text{Zn(BF}_4)_2$ -DMSO- $\text{H}_2\text{O}$  (-766 kcal/mol) are lower than that of  $\text{H}_2\text{O}$ - $\text{H}_2\text{O}$  (-5.85 kcal/mol) (Figure 5.39). Essentially, the stronger  $E_b$  of PAM- $\text{Zn(BF}_4)_2$ -DMSO- $\text{H}_2\text{O}$  signifies the hydrogel electrolyte's stronger ability to disrupt the hydrogen bonds between water molecules and to resist freezing in low-temperature environments.

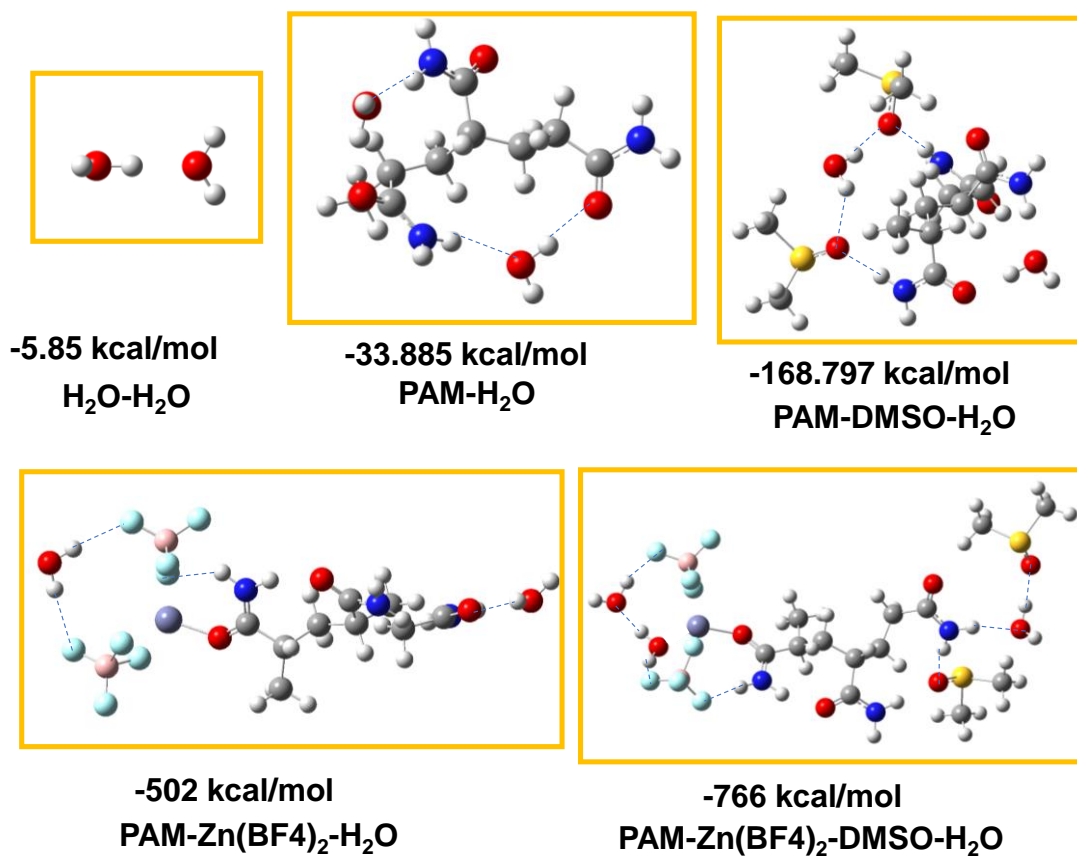


**Figure 5.39** The binding energy between H<sub>2</sub>O, PAM-H<sub>2</sub>O, PAM-DMSO-H<sub>2</sub>O, PAM-Zn(BF<sub>4</sub>)<sub>2</sub>-H<sub>2</sub>O and PAM-DMSO-Zn(BF<sub>4</sub>)<sub>2</sub>-H<sub>2</sub>O obtained by DFT simulation using Gaussian.

We then further tested quasi solid state ZABs with NiO/Ni-SACs/mNC1000 using as cathode and PAM-zdh as electrolyte. In comparison, a blend of 20% commercial Pt/C and IrO<sub>2</sub> in equal proportions was also evaluated as a cathode. The NiO/Ni-SACs/mNC1000 based battery exhibits a consistent open-circuit voltage (OCV) of 1.45 V, Similar to that of Pt/C + IrO<sub>2</sub> (Figure 5.40).

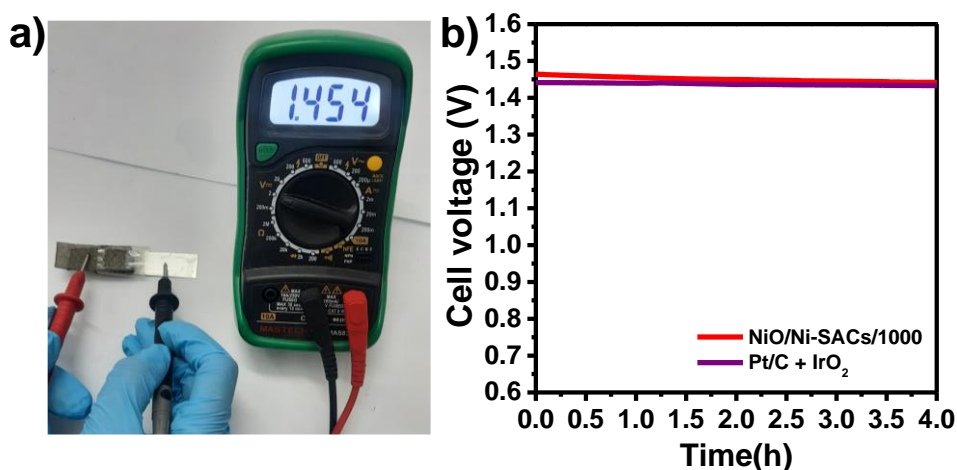


**Figure 5.40** a) Photograph displaying measured open-circuit voltage of ~1.454 V, and b) open circuit voltage of 1.454 and 1.446 V using PAM-zdh electrolyte for NiO/Ni-SACs/mNC1000 and Pt/C+IrO<sub>2</sub> couple, respectively.

The minimal voltage difference between discharge-charge polarization curves and the corresponding power density of the NiO/Ni-SACs/mNC1000 based ZAB yields a peak power density of 123.2 mW cm<sup>-2</sup>, significantly higher than that of Pt/C + IrO<sub>2</sub> based ZAB (96.51 mW cm<sup>-2</sup>), indicating excellent rechargeable capability of NiO/Ni-SACs/mNC1000 based ZAB (Figure 5.41 a). Demonstratively, a series connection of two Zn-air batteries can power red light-emitting diodes (LEDs) for several hours (Figure 5.41 b). NiO/Ni-SACs/mNC1000 showed higher specific capacity 451.89 mA.h.g<sup>-1</sup> as compared to Pt/C + IrO<sub>2</sub> (279.82 mA.h.g<sup>-1</sup>) (Figure 5.41 c). The long-term rechargeability of NiO/Ni-SACs/mNC1000 based solid ZAB was evaluated through galvanostatic discharge-charge cycling at a current density of 20 mA cm<sup>-2</sup> with 60 minutes per cycle (30 minutes discharging and 30 minutes charging) (Figure 5.41 d). After prolonged cycling for up to 65 hours, minimum loss in voltaic efficiency was observed for NiO/Ni-SACs/mNC1000 based solid ZAB, whereas the voltage gap sharply increased after ~25 hours for Pt/C + IrO<sub>2</sub> based solid ZAB. Long-term cycling performance analysis also reveals that the NiO/Ni-SACs/mNC1000 based battery maintains a low discharge-charge voltage gap compared to the Pt/C + IrO<sub>2</sub> based battery (Figure 5.41 d). Moreover, with

NiO/Ni-SACs/mNC1000 ZAB demonstrates stable discharge voltages under various current densities (Figure 5.41 e). We have tested the experiment three times and it maintained its discharge voltage nicely. After the ~65 h operation, we have shown here the gel electrolyte interface and Zn foil (Figure 5.41 f). Then We have checked the cycling performance of ZAB at different current densities from 10 mA cm<sup>-2</sup> (Figure 5.41 g) to high current densities 60 mA cm<sup>-2</sup> (Figure 5.41 h) & 100 mA cm<sup>-2</sup> (Figure 5.41 i). To further verify the deformation of ZAB we have tested charging discharging cycle test at different bending conditions 0°, 45°, 90°, & 180°. It showed negligible change in voltage gap (Figure 5.41 j). At ice cold condition (Figure 5.41 k), the assembled quasi-solid-state ZABs exhibited the charging/discharging cycles at 2 mA cm<sup>-2</sup> for 50 hours which demonstrated robust durability of the battery. These results affirm NiO/Ni-SACs/mNC1000 as an outstanding bifunctional OER/ORR oxygen electrode and PAM-zdh a suitable electrolyte for long-term rechargeable liquid Zn-air batteries.

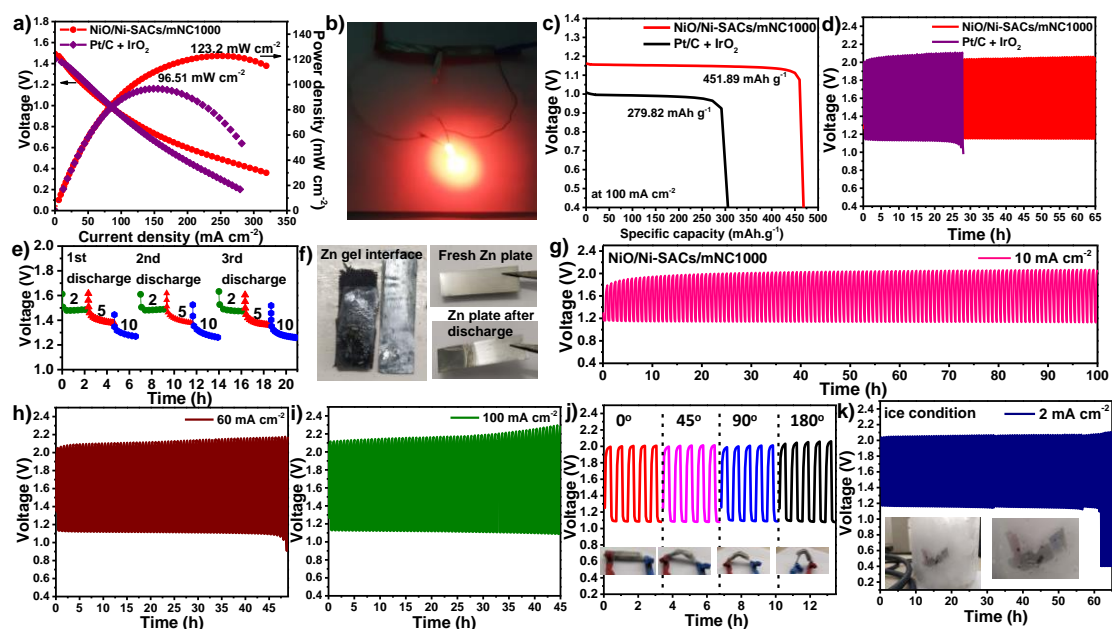


**Figure 5.41** a) Polarization curves and corresponding power densities of NiO/Ni-SACs/mNC1000 and Pt/C + IrO<sub>2</sub> as cathode using PAM-zdh electrolyte for single solid-state ZAB. b) Photograph of a lighted LED powered via connecting two ZABs in a series.

c) Comparison of specific capacity between NiO/Ni-SACs/mNC1000 and Pt/C + IrO<sub>2</sub>. d) Comparison of galvanostatic discharge-charge cycling performance of rechargeable solid-state ZAB at a constant discharge-charge current density of 20 mA cm<sup>-2</sup> with a cycle duration of 1h for NiO/Ni-SACs/mNC1000 and Pt/C + IrO<sub>2</sub>. e) Repeating discharge curves three time at various current densities (2, 5, 10 mA cm<sup>-2</sup>). f) Photograph of Zn-gel interface, fresh Zn plate and Zn plate after long term discharge. g) Charging discharging stability of the battery at with NiO/Ni-SACs/mNC1000 at 10 mA cm<sup>-2</sup> for 110h. Cycling stability at higher current densities h) 60 mA cm<sup>-2</sup> & i) 100 mA cm<sup>-2</sup>. j) Stability test of the battery at different bending conditions. k) Battery performance at ice cold condition: charging discharging test at 2 mA cm<sup>-2</sup>.

## 5.7 Conclusion

In summary, we present a highly active and durable non-precious metal-based bifunctional OER/ORR electrocatalyst, NiO/Ni-SACs/mNC1000. This catalyst comprises well-dispersed single Ni atoms (Ni-N<sub>4</sub>) and small NiO nanoclusters embedded within nitrogen-doped concave shaped mesoporous carbon cage with stretched edges synthesized using silica templated method. NiO/Ni-SACs/mNC1000 demonstrates the ability to achieve a current density of 10 mA cm<sup>-2</sup> at a low cell voltage of 1.58 V in a two-electrode alkaline electrolytic cell. Furthermore, we showcase the performance of the catalyst in quasi-solid rechargeable Zn-air batteries. Additionally, we established a anti freezing gel electrolyte by modifying PAM hydrogel with the addition of DMSO a H bond acceptor and metal salt Zn (BF<sub>4</sub>)<sub>2</sub> additives. Using as synthesized PAM-zdh quasi solid ZAB showed outstanding performance at wider temperature range. DFT calculations reveal a synergistic interaction between Ni-N<sub>4</sub> and NiO small nanoclusters, favoring the Gibbs free energy for O<sub>2</sub> evolution. Notably, the presence of NiO nanoclusters enhances the availability of d orbitals which facilitates the adsorption of water and other intermediates and improve the OER kinetics. This study not only introduces a novel synthetic strategy for designing advanced single-atom catalyst-based electrocatalysts but also underscores the significance of incorporating small quantities of metal oxide nanoclusters in



enhancing electrocatalytic activity and robustness. This work opens avenues for the design of multifunctional and robust electrocatalysts for long-term O<sub>2</sub> evolution applications.

This page was intentionally left blank.

## Chapter 6: Summary And Future Directions

The design and synthesis of MOF composites and MOF derivatives are included in this thesis study for their use in organic transformation reactions and electrochemical energy conversion and storage devices, respectively. To diminish worries about organic transformations, environmentally friendly methods are essential. Overuse of hazardous catalysts leads to ecological imbalance and health risks. Heterogeneous catalysis is a promising method for removing contaminants from organic reactions that are generated by dangerous compounds used as catalysts. One can envision a path toward greener catalytic practices with the advancement of cutting-edge technology. Heterogeneous catalysts have gained substantial attraction in organic transformation due to homogeneous catalysts' inability to be isolated, reused, and subject to temperature instability. The development of MOF composites has brought the prospect of their implementation as solid catalysts in industrial settings one step closer to reality. So motivated by these unique properties of MOF, we have designed a earth abundant, cost effective, easily synthesis, reusable catalyst by using an encapsulation technique that involved nano-confinement of a homogenous Mn-phenanthroline complex inside ZIF-8 pores. The as prepared catalyst for the very first time used for  $\alpha$ -alkylation of ketones with alcohols which provide a path for direct access to branch di substituted ketones. Here we involve the hydrogen borrowing catalysis, mainly occur under harsh basic conditions, under which the majority of recognized MOFs quickly deteriorate and are unsuitable for heterogeneous catalysis. Nevertheless, the process of encapsulating metal complexes in MOF pores in situ is still relatively new. Further research is required in this area, including the synthesis of novel, extremely stable MOFs under challenging circumstances and window pore size tuning to allow for the entry of big molecules.

With the rapid depletion of fossil fuels and severe environmental issues, developing sustainable energy conversion and storage (ECS) technology to power our future society is critical. Electrocatalysis plays a pivotal role for most of the ECS systems like water electrolyzers, flow batteries, fuel cell, Zn-air battery. But electrocatalysts typically have significant overpotentials and slow kinetics, which require a lot of excess energy. The limited lifetime and high cost of the catalysts also limit their broad and large-scale usage. In this regard MOF derived nanostructured materials emerged as a promising candidate.

MOF derived single atom catalysts provide a solution towards the leaching problem of active sites or instability under highly robust conditions. It has been reported that utilizing SACs as a catalyst has the benefit of stabilizing metals within carbon structures very firmly and preventing metal leakage during the reaction process and ease of mechanistic study. SAC also offers maximum metal utilization efficiency, which results in increased catalytic activity. However, there are some major drawbacks of MOF derived SACs. Among all low metal loading is a big challenge in most of the cases. So we have developed a dual single atom catalyst from MOF by linking SACs with second metals in the form of SACs. It not only reinforces the catalyst's performance for ORR in a synergistic manner, but it will also adjust the electronic structure of the metal sites, resulting in high selectivity and the suppression of any potential Fenton reactions at the electrode. The catalyst exhibited remarkable activity and durability for both proton exchange membrane fuel cell and Zn-air battery. Notably, the electrical and coordinating structures in dual atom catalysts (DACs) are still being debated. It could be owing to various synthesis processes or metal-specific characteristics. In this context, there is a rising recognition of the significance of dual-atom configuration engineering and application-oriented DAC design. This opens the door to future prospects for DAC development.

For the real application of those catalysts at industrial level most of the time we coated the catalyst ink on a 3D support such as nickel foam, carbon cloth or carbon paper by using nafion binder. Uses of this nafion binder hinders the catalyst's application at high current density or also blocks the active sites. So, we have developed a method for direct growth of ZIF-8 into carbon felt and after pyrolysis we got nitrogen, oxygen functionalized porous carbon strongly bounded to carbon felt surface. The as synthesized catalyst showed good performance for vanadium redox flow battery.

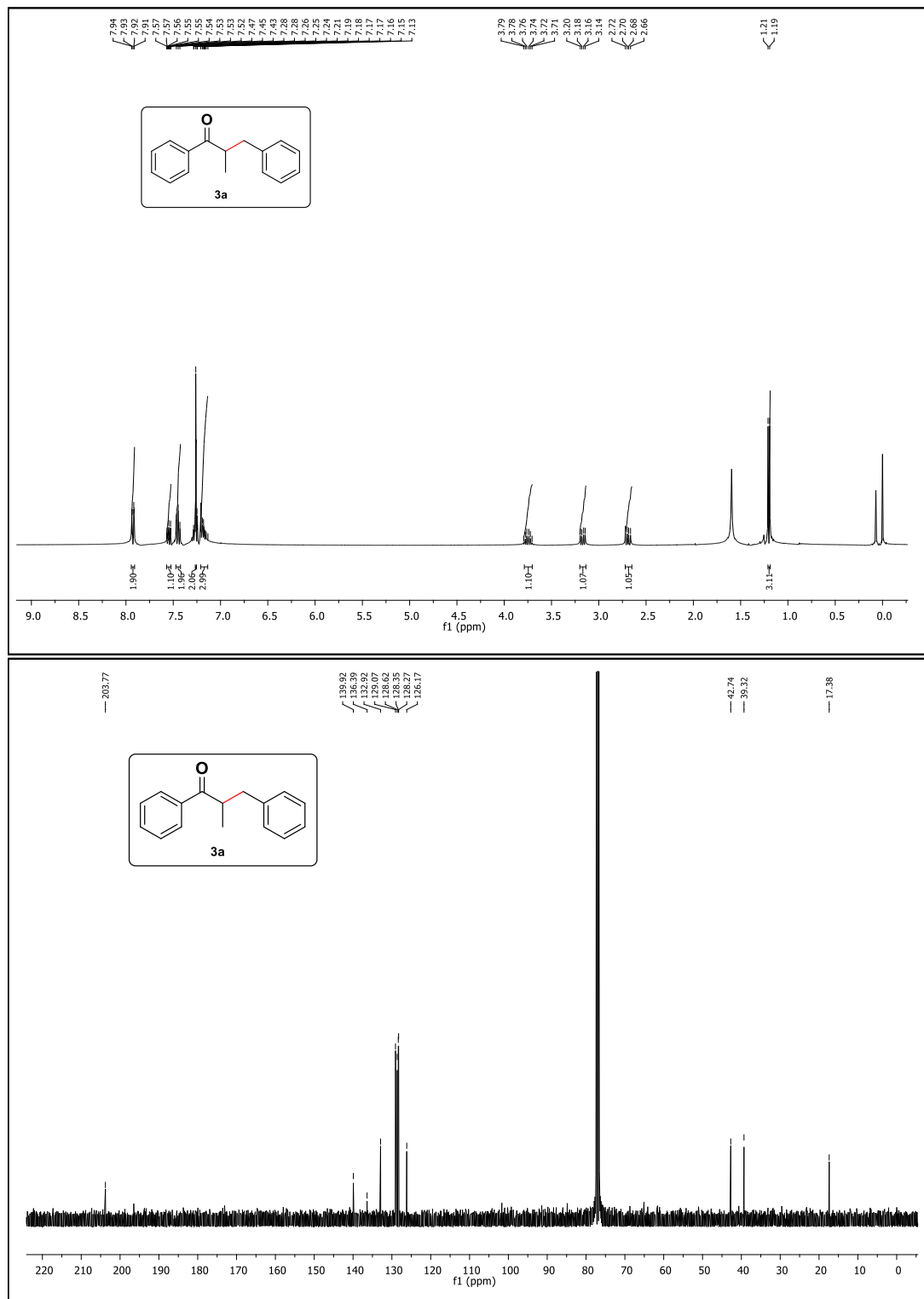
So further exploration needed to develop nonprecious, easily scalable MOF derived nanostructured materials with defined active sites which can be used for high current density and long-term stability with minimum dissolution of active sites and also to establish structure activity correlation more precisely. Other heterogeneous catalytic reaction can also be explored with these MOF composites or MOF derivatives.

The aforementioned issues and future plans necessitate collaborative efforts from professionals of various sectors like inorganic, organic, engineering, and material science. We believe that our work will help the scientific community improve life in some way!

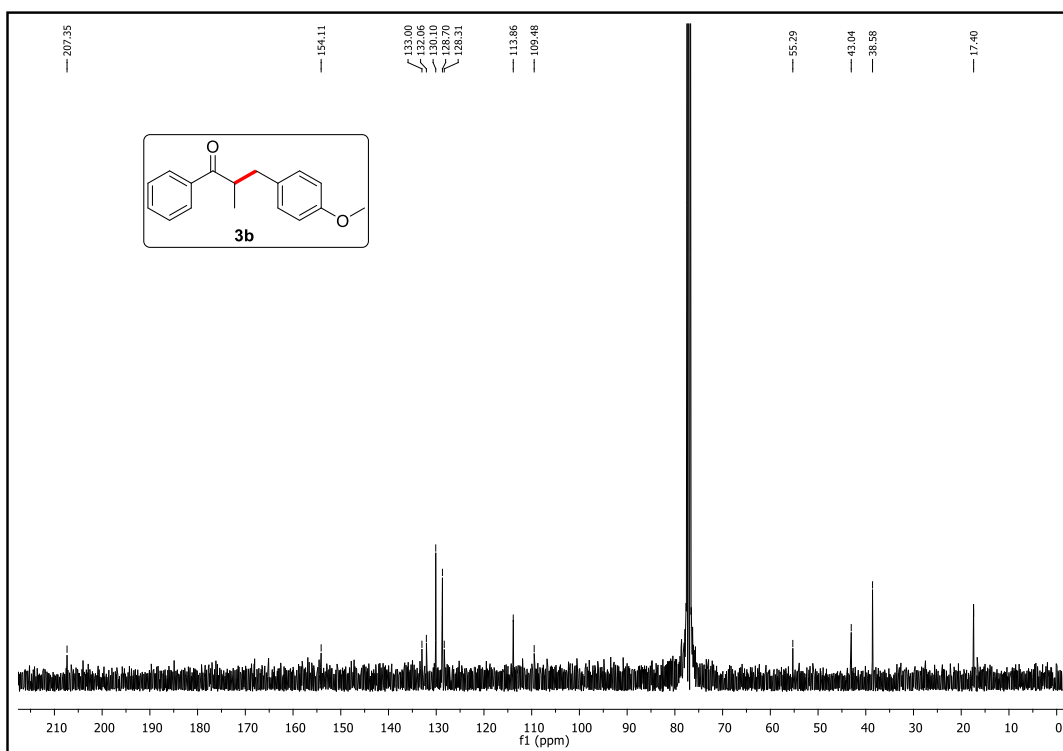
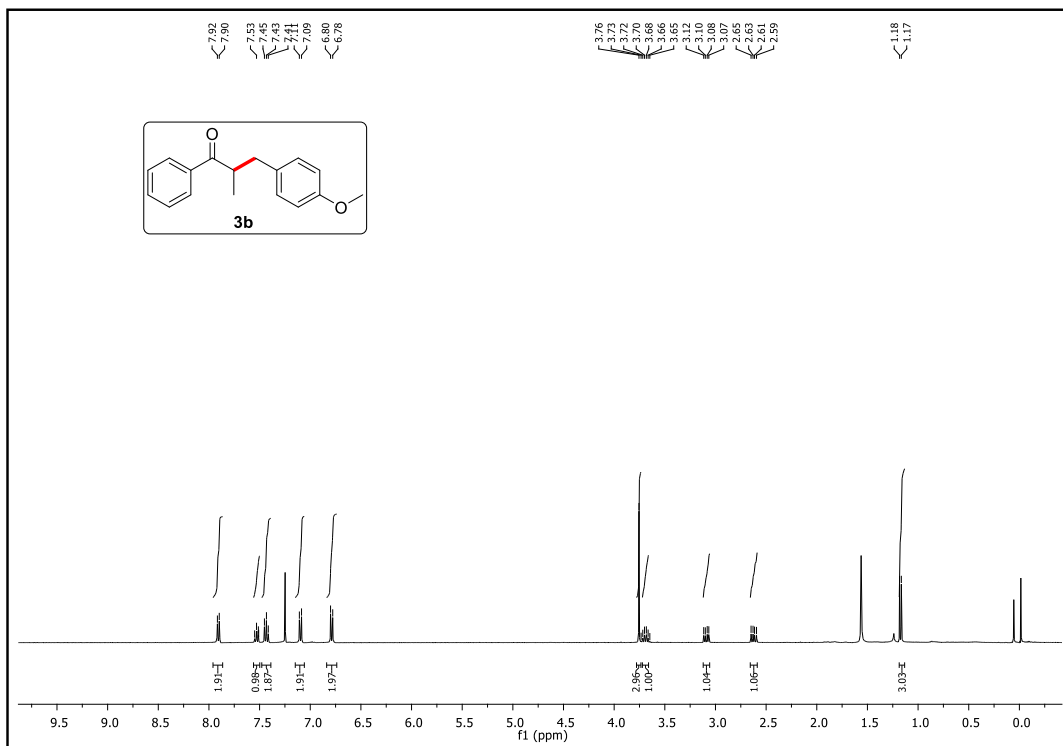
## Appendix Section

### Copies of $^1\text{H}$ NMR & $^{13}\text{C}$ NMR spectra:

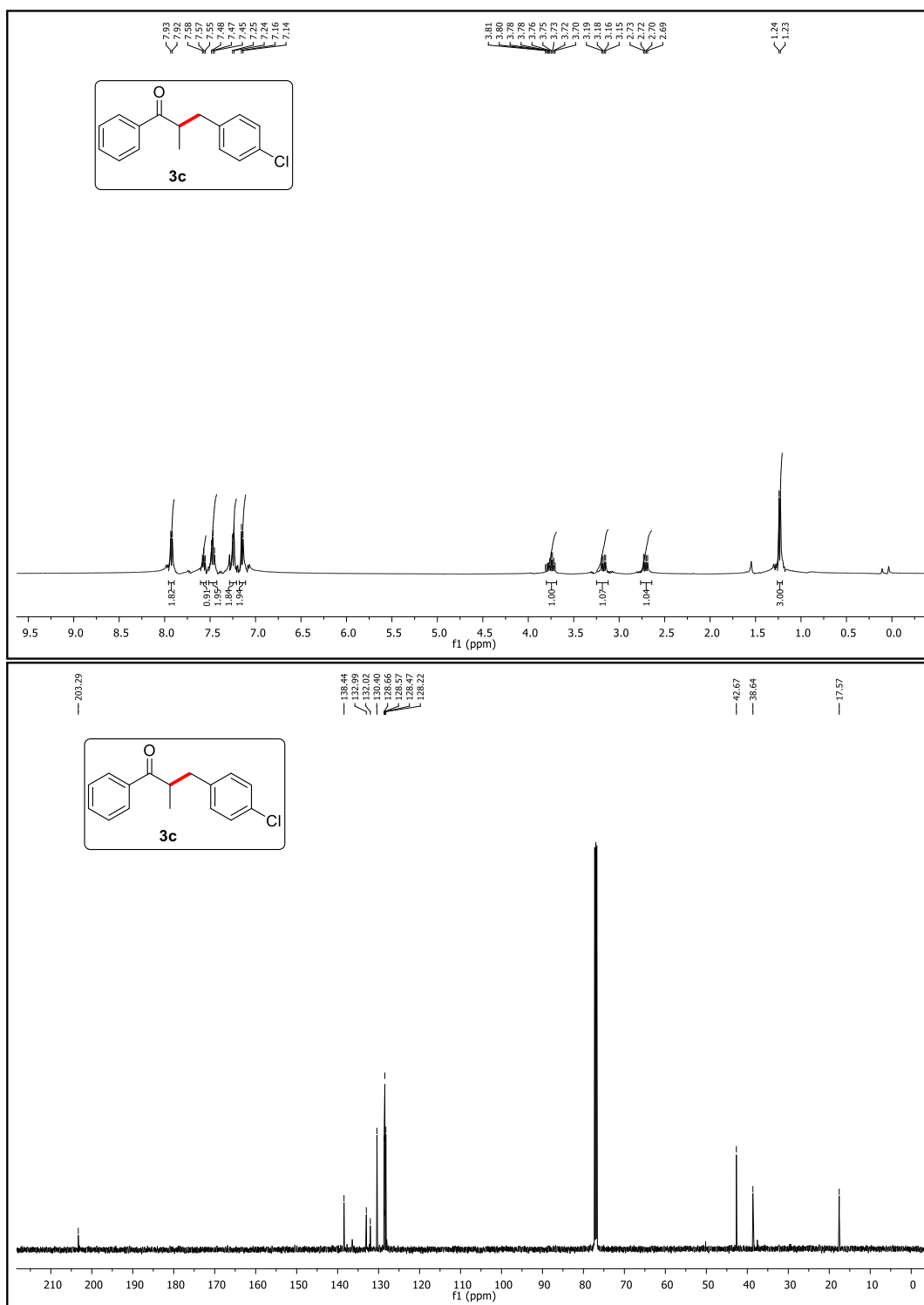
2-Methyl-1,3-diphenylpropan-1-one:



**3-(4-Methoxyphenyl)-2-methyl-1-phenylpropan-1-one:**

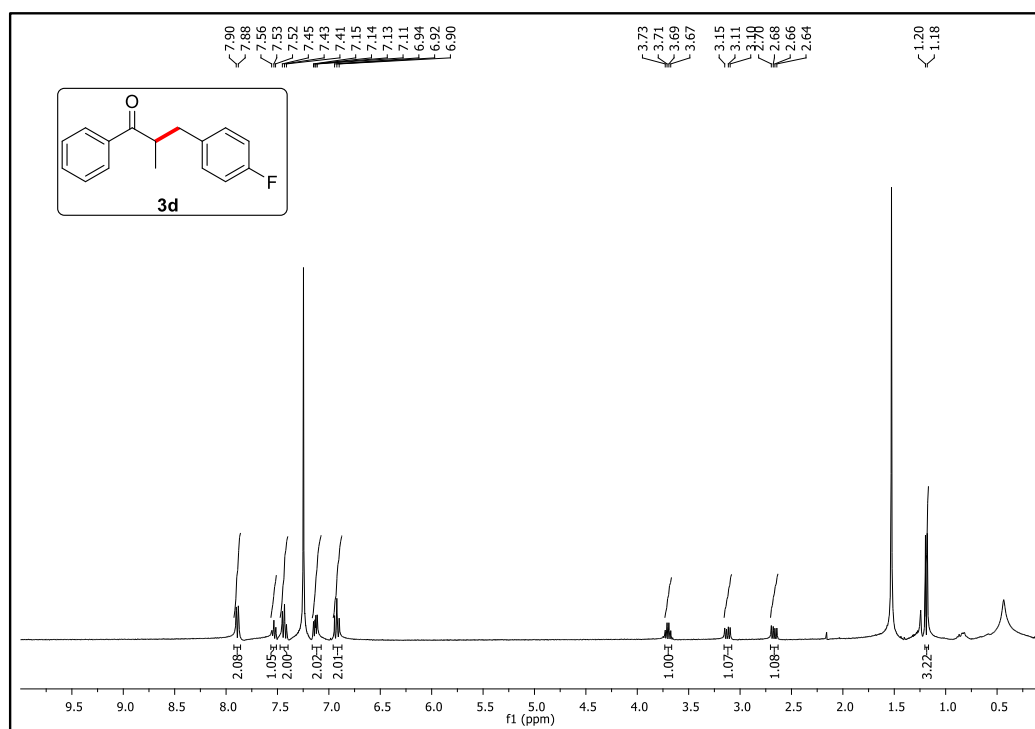


3-(4-Chlorophenyl)-2-methyl-1-phenylpropan-1-one:

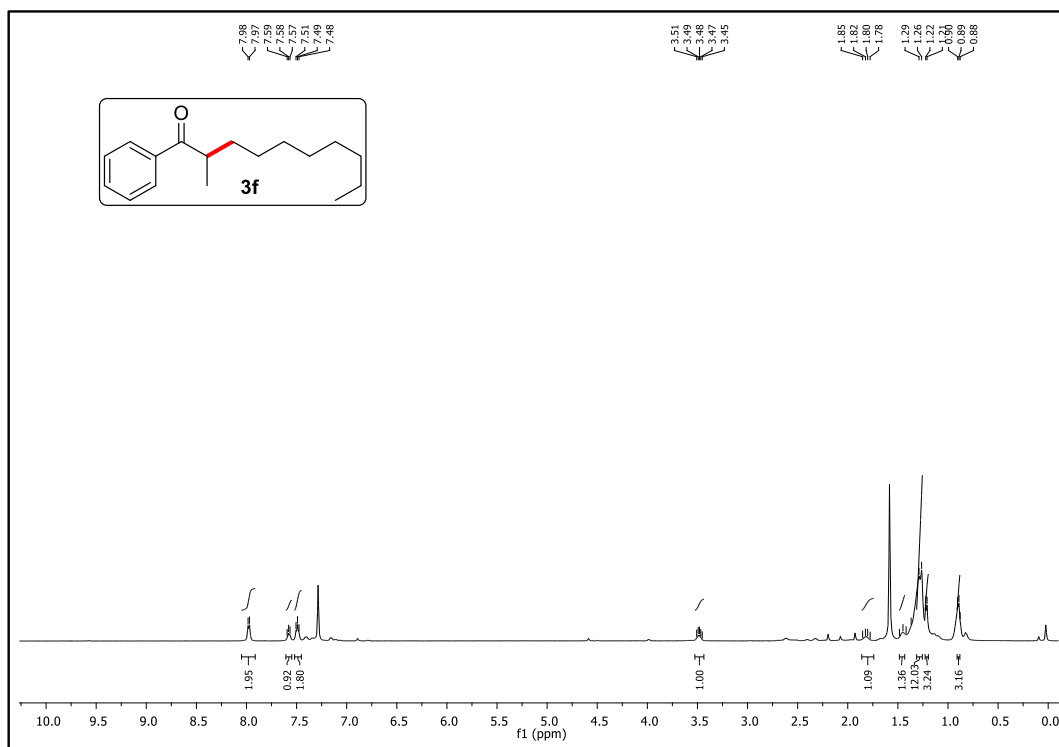




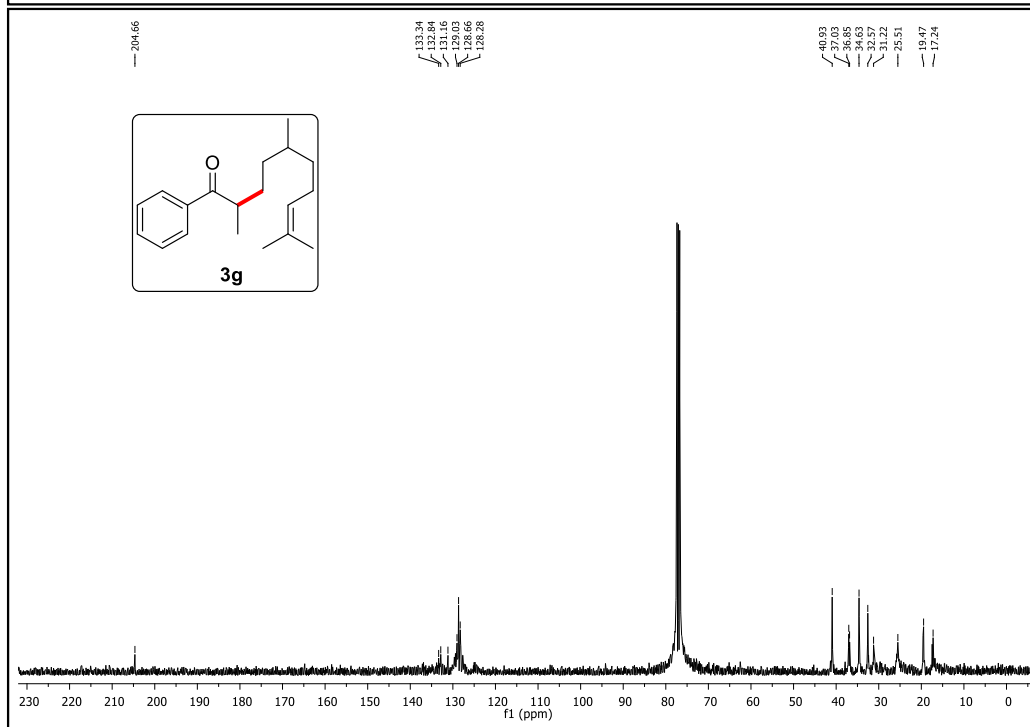
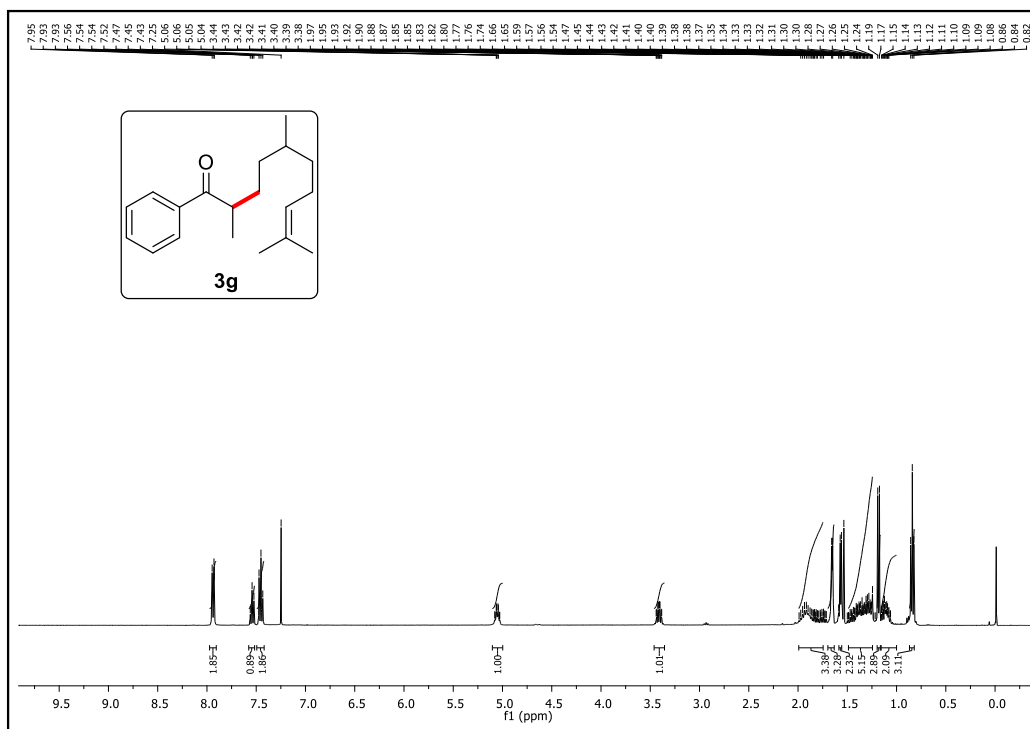
**3-(4-Fluorophenyl)-2-methyl-1-phenylpropan-1-one:**



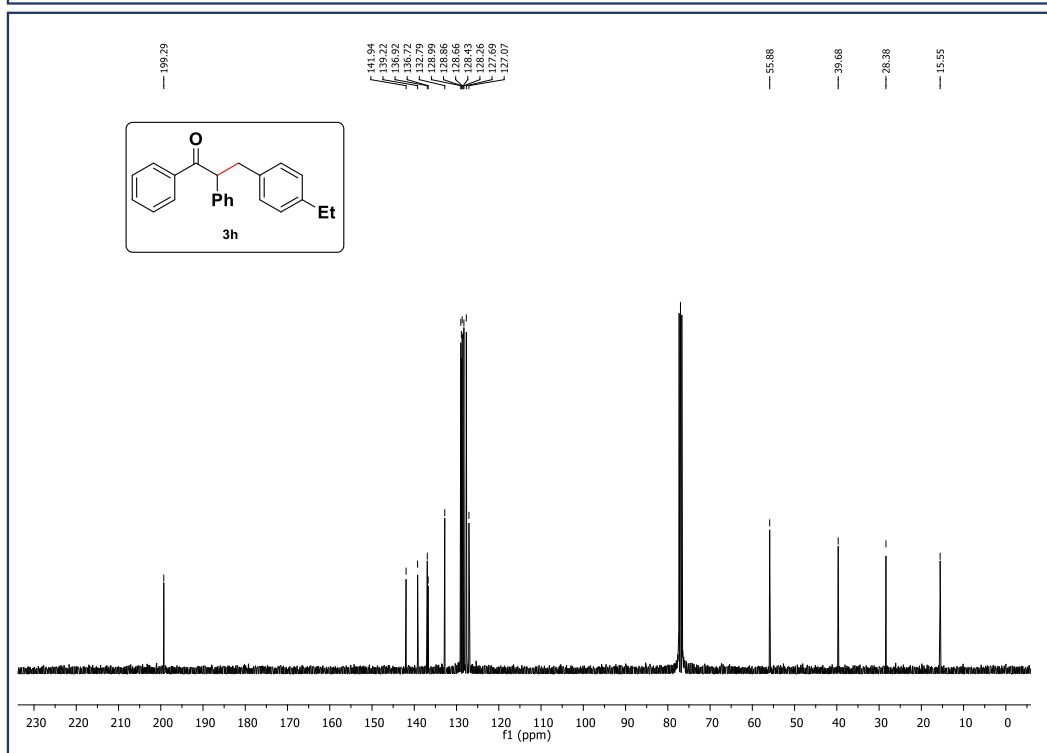
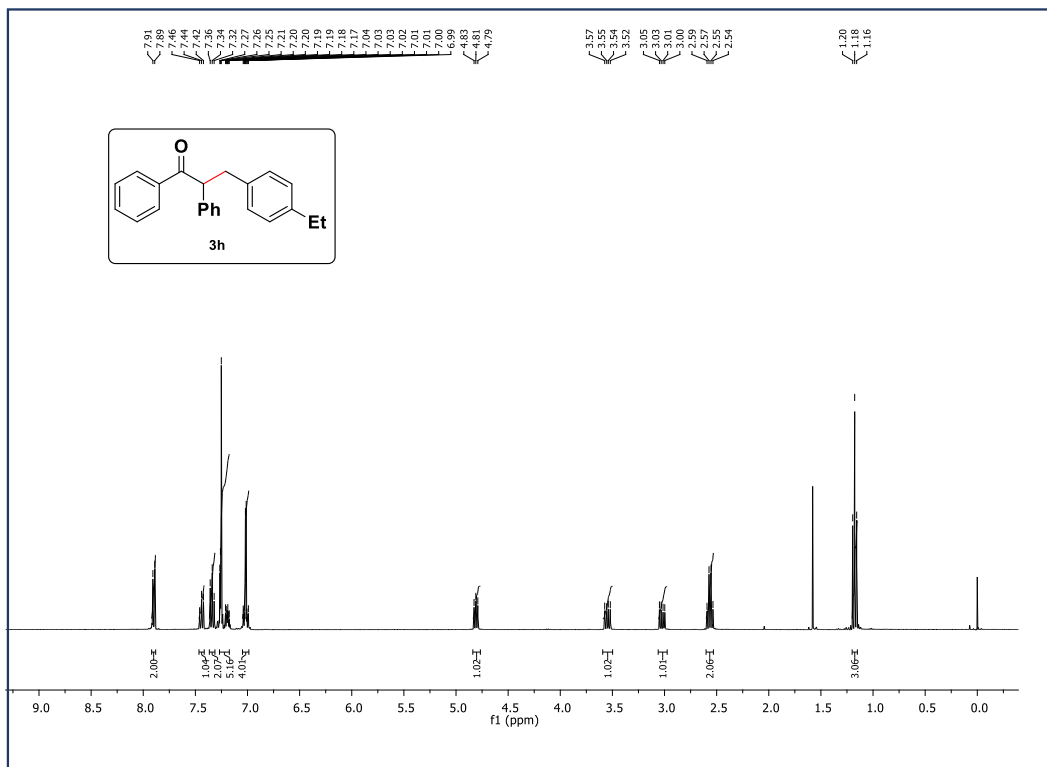
2-methyl-1-phenyldecan-1-one:



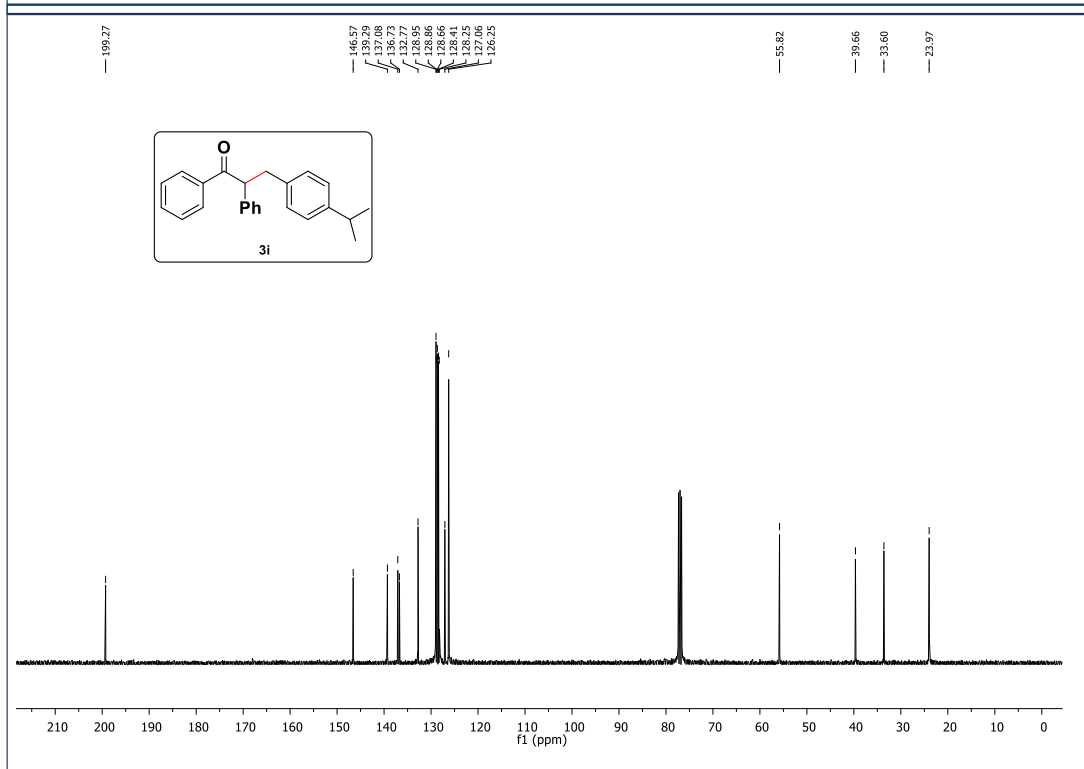
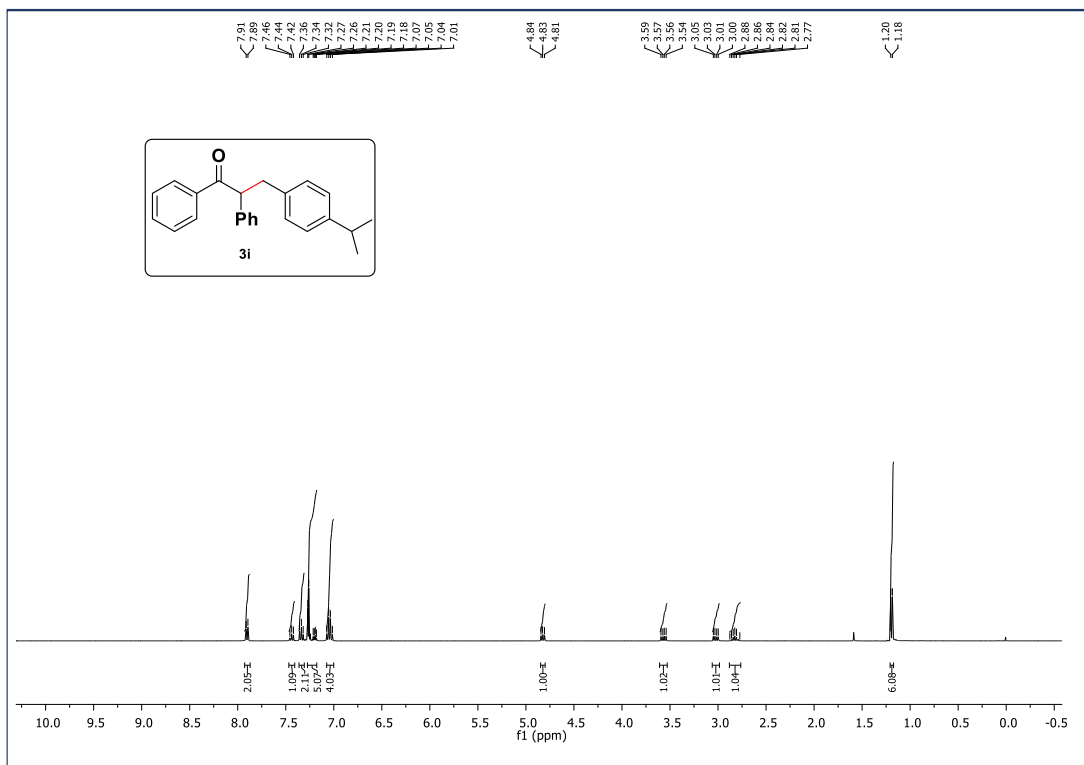
2,5,9-Trimethyl-1-phenyldec-8-en-1-one:



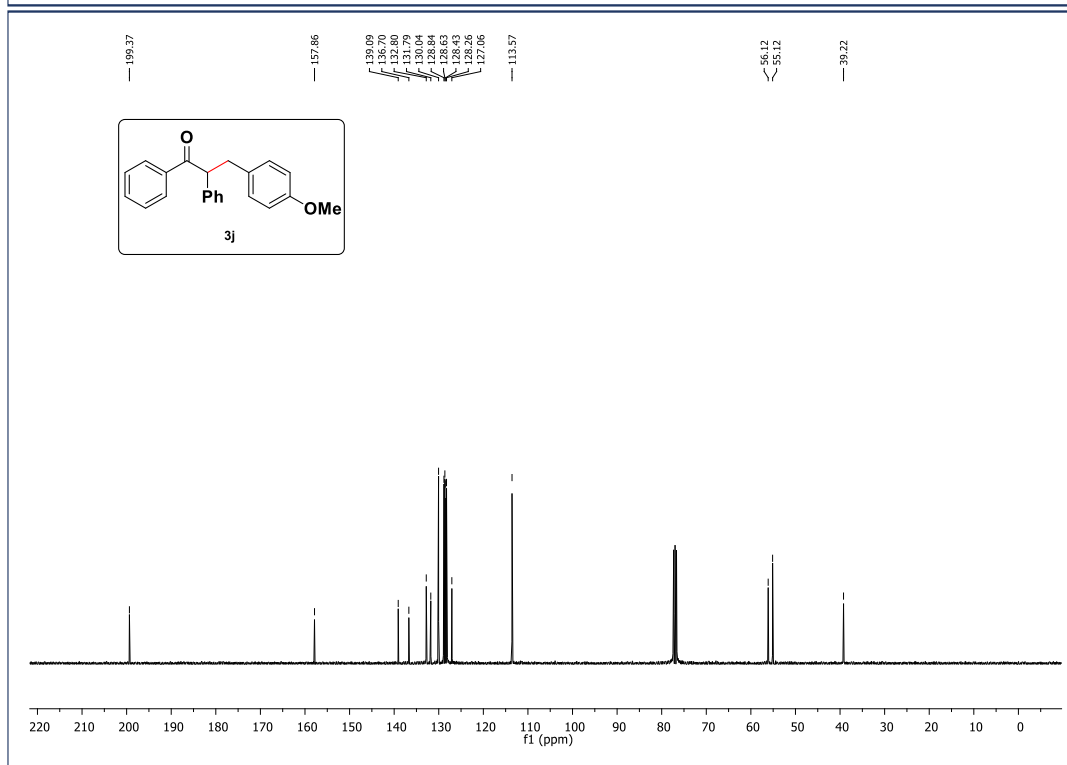
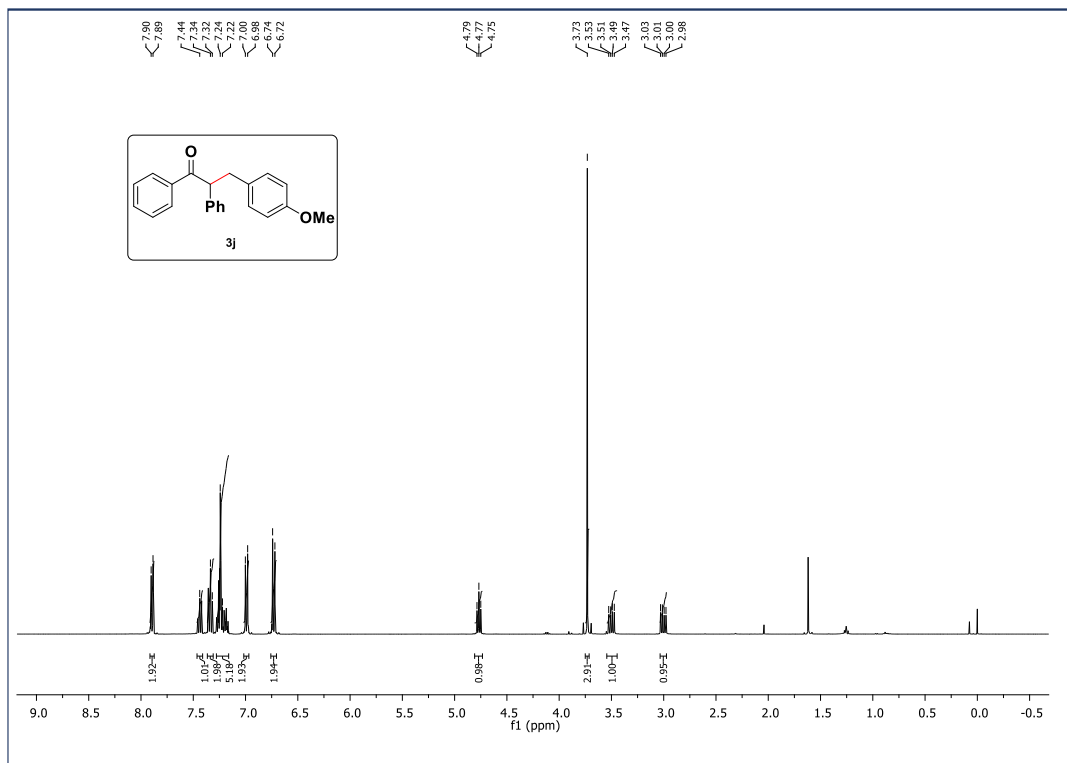
**4-ethylphenyl)-1,2-diphenylpropan-1-one:**



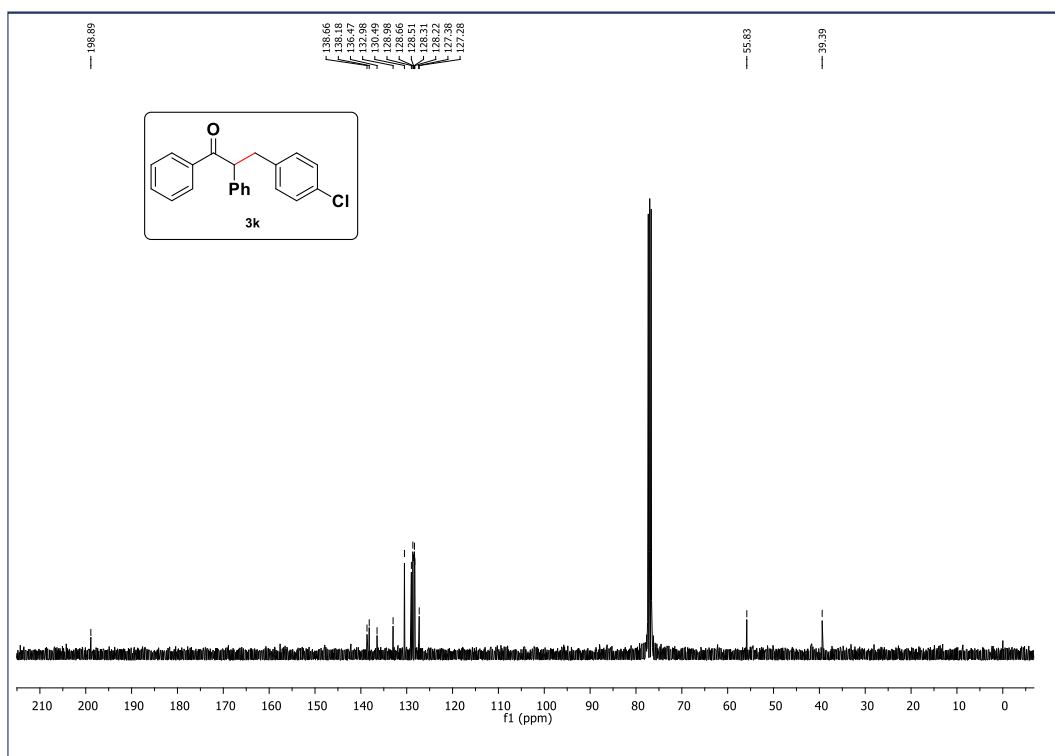
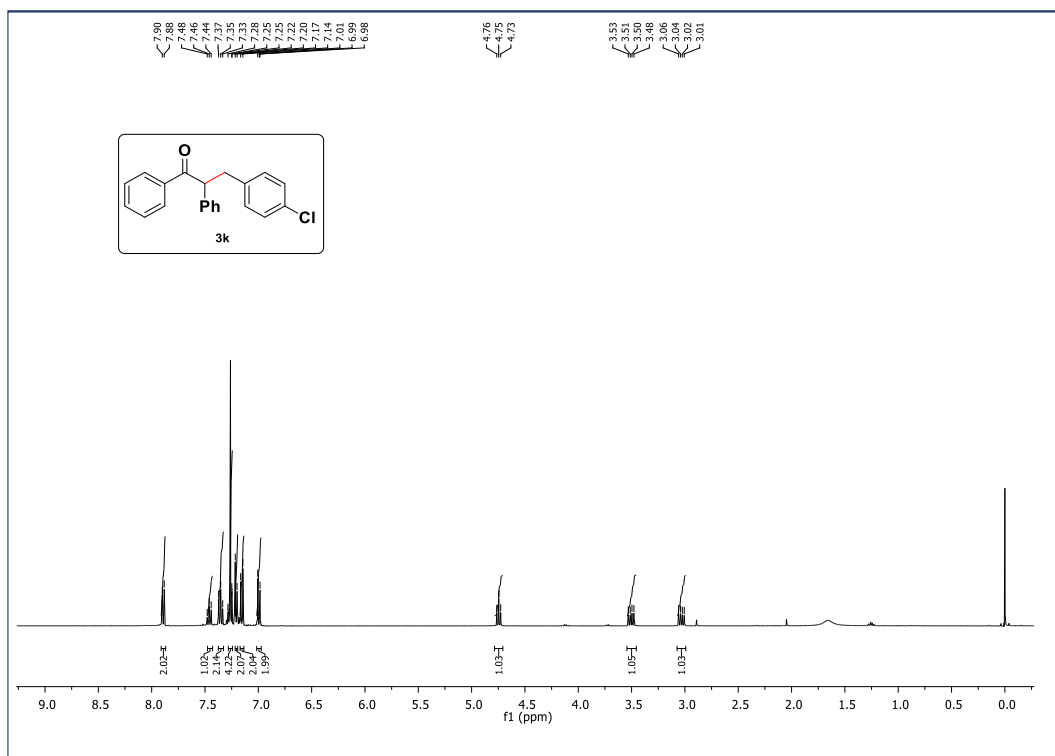
3-(4-isopropylphenyl)-1,2-diphenylpropan-1-one:



3-(4-methoxyphenyl)-1,2-diphenylpropan-1-one:



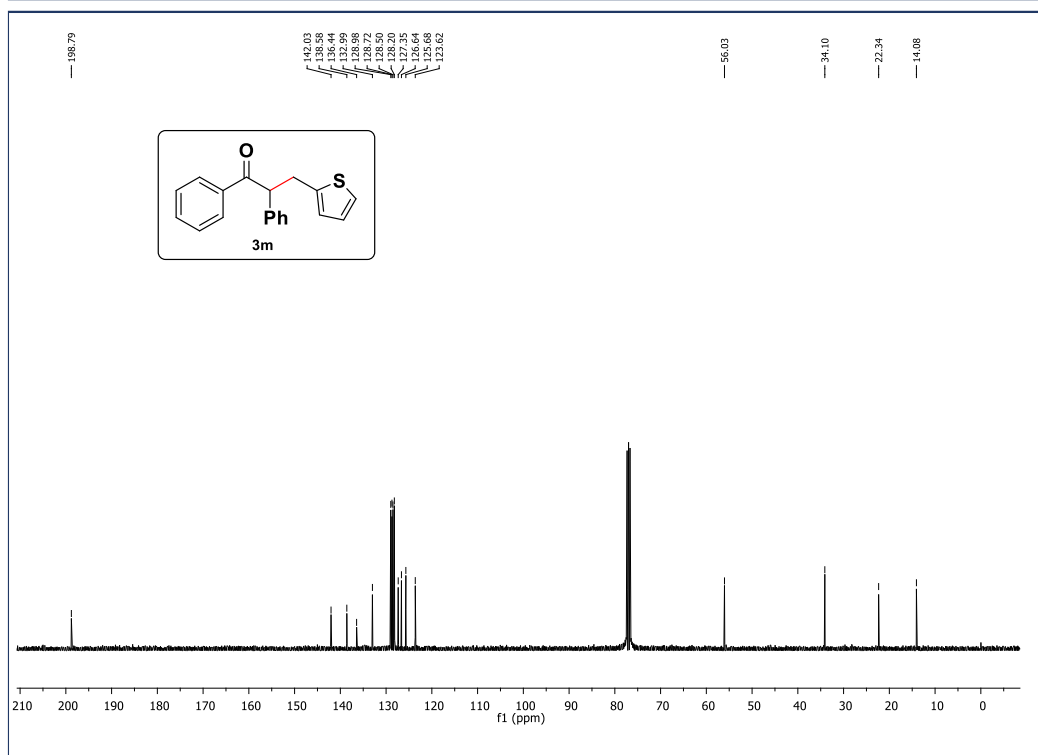
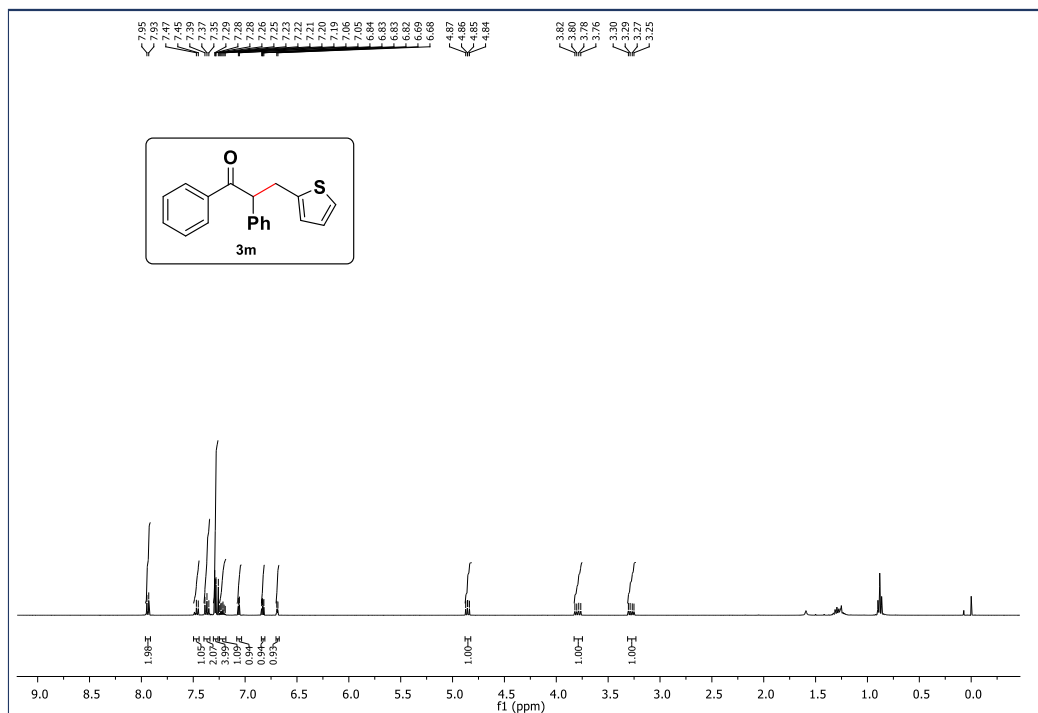
**3-(4-chlorophenyl)-1,2-diphenylpropan-1-one:**



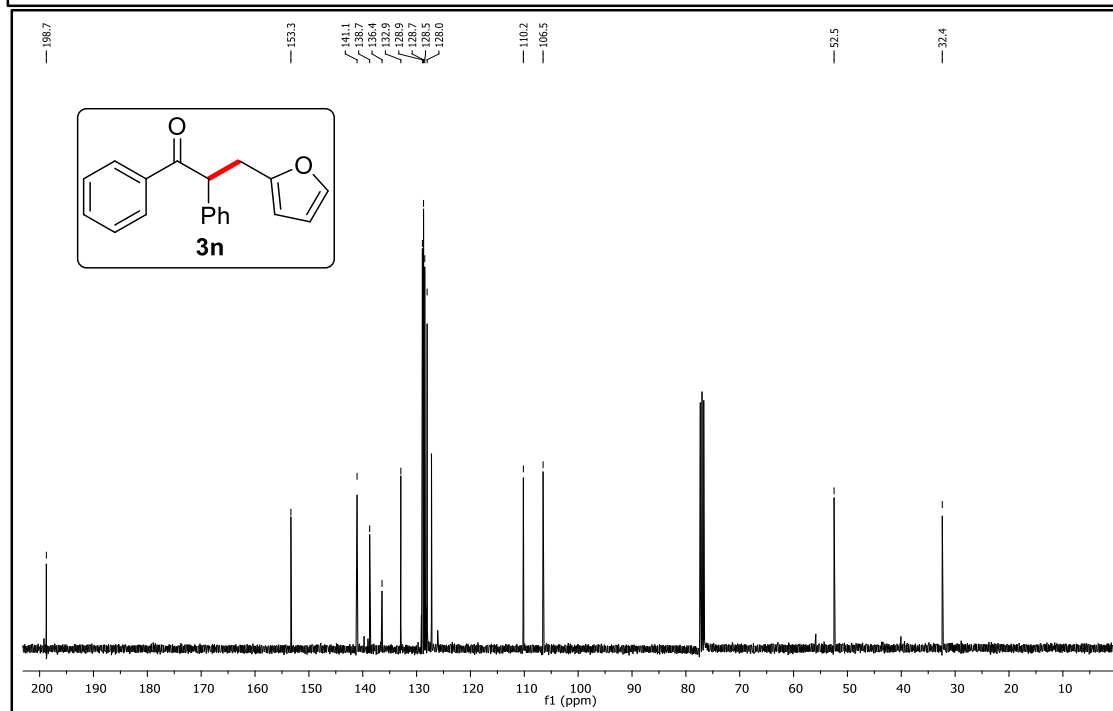
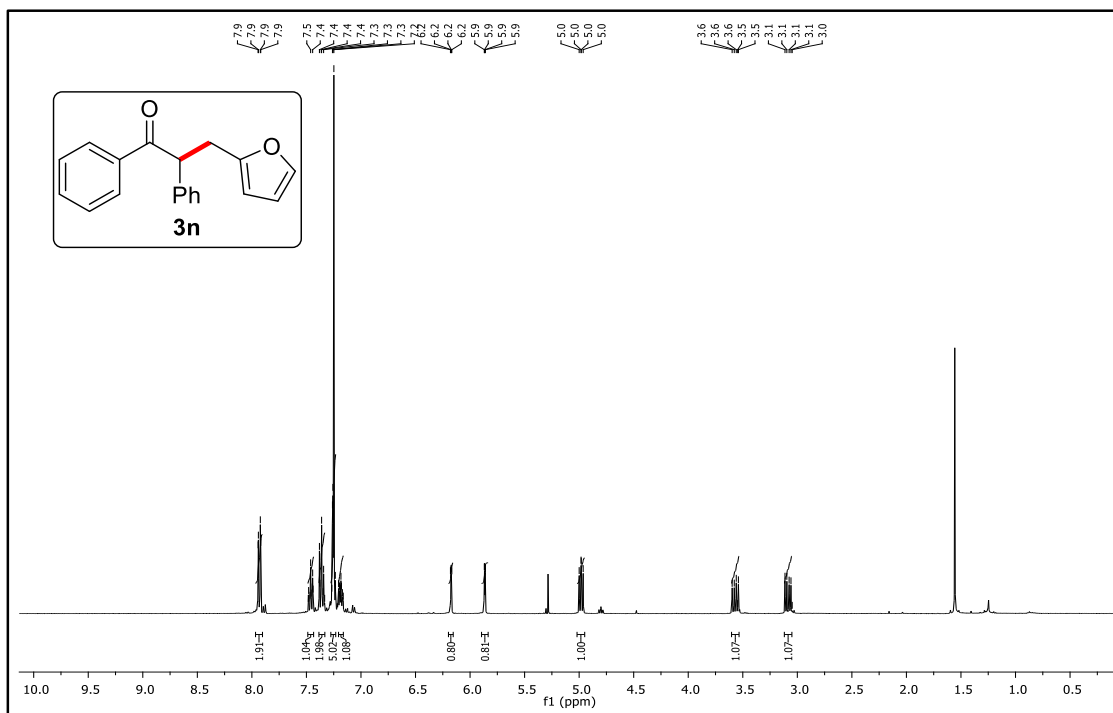




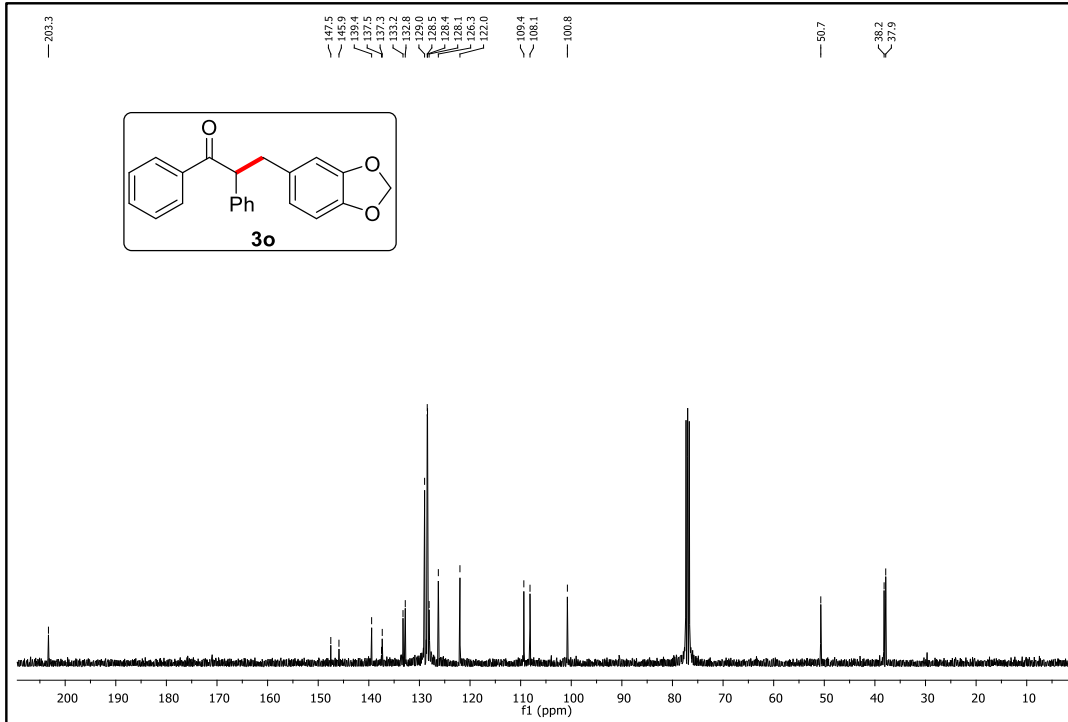
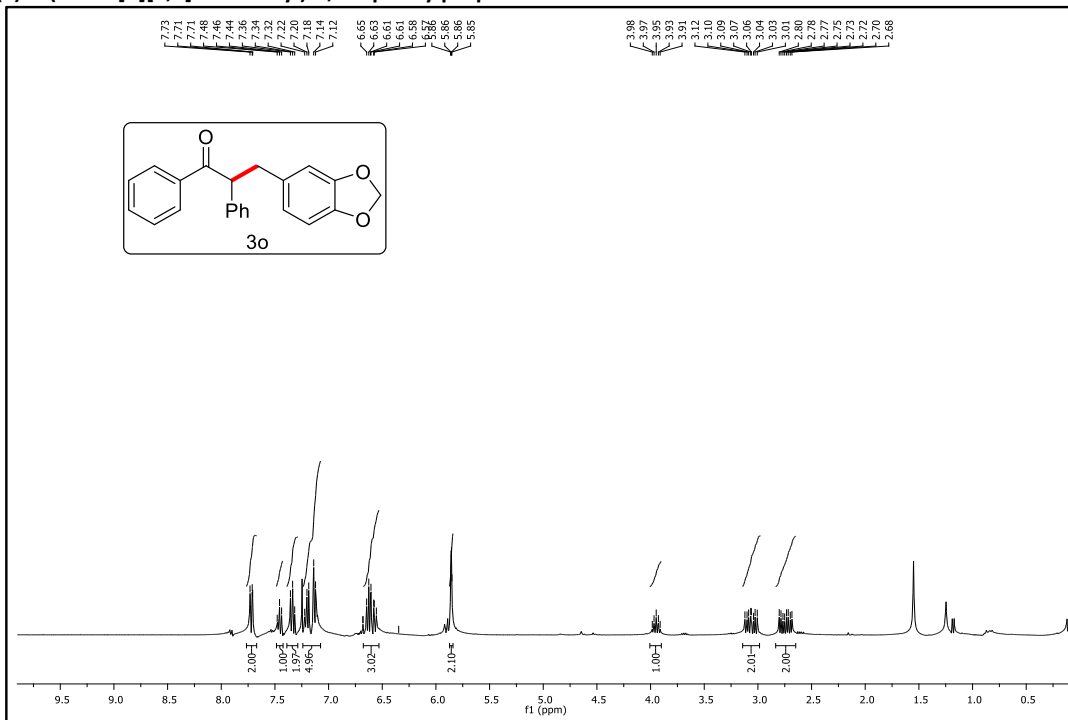
1,2-diphenyl-3-(thiophen-2-yl)propan-1-one:



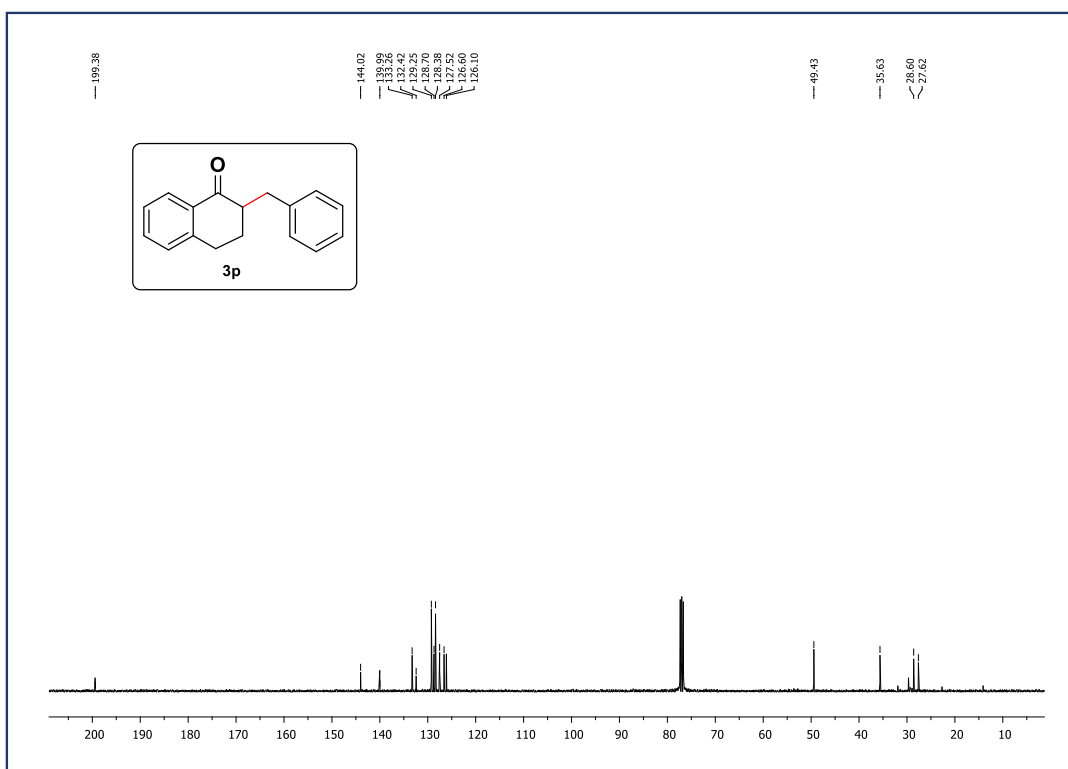
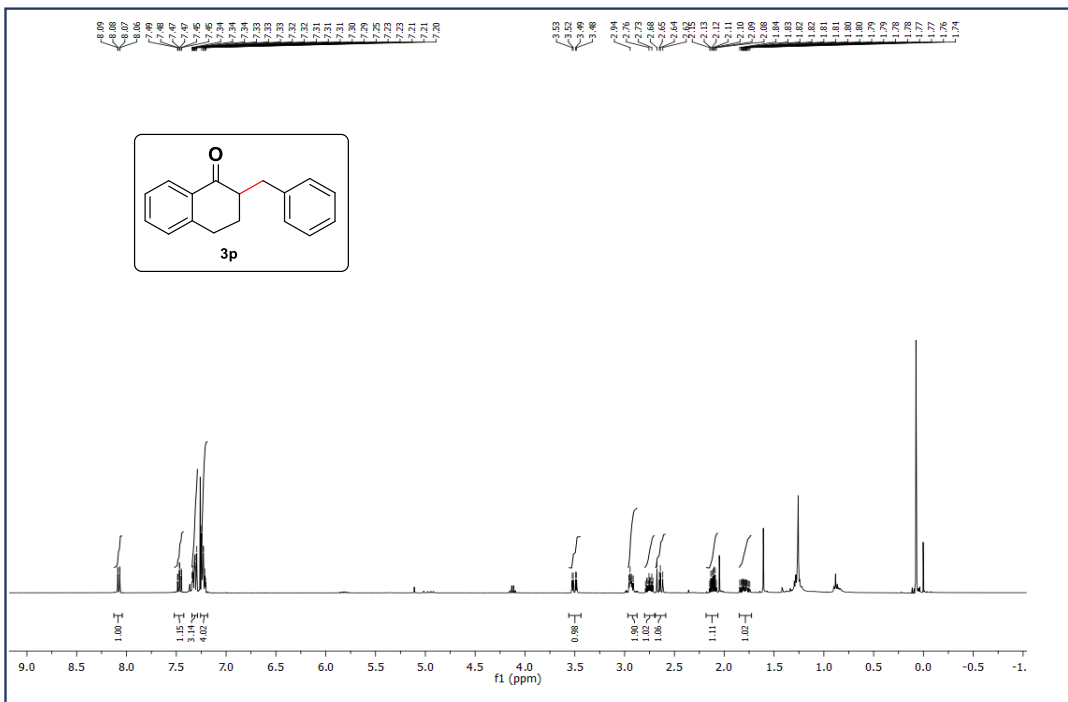
**((S)-3-(furan-2-yl)-1,2-diphenylpropan-1-one:**



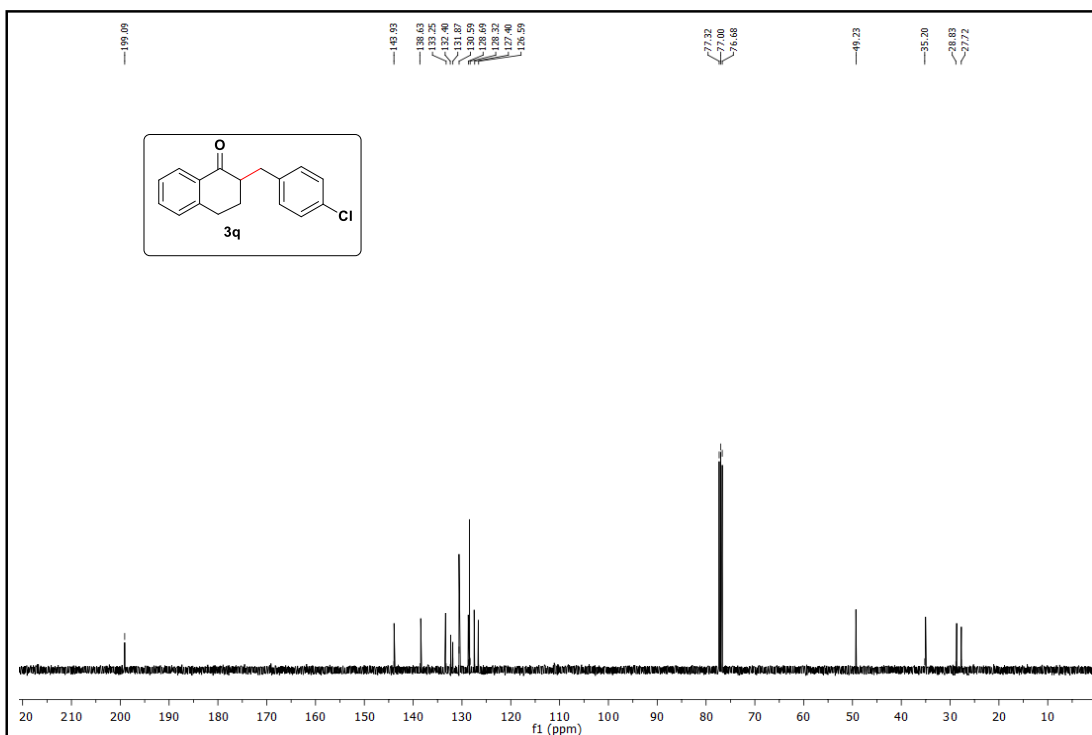
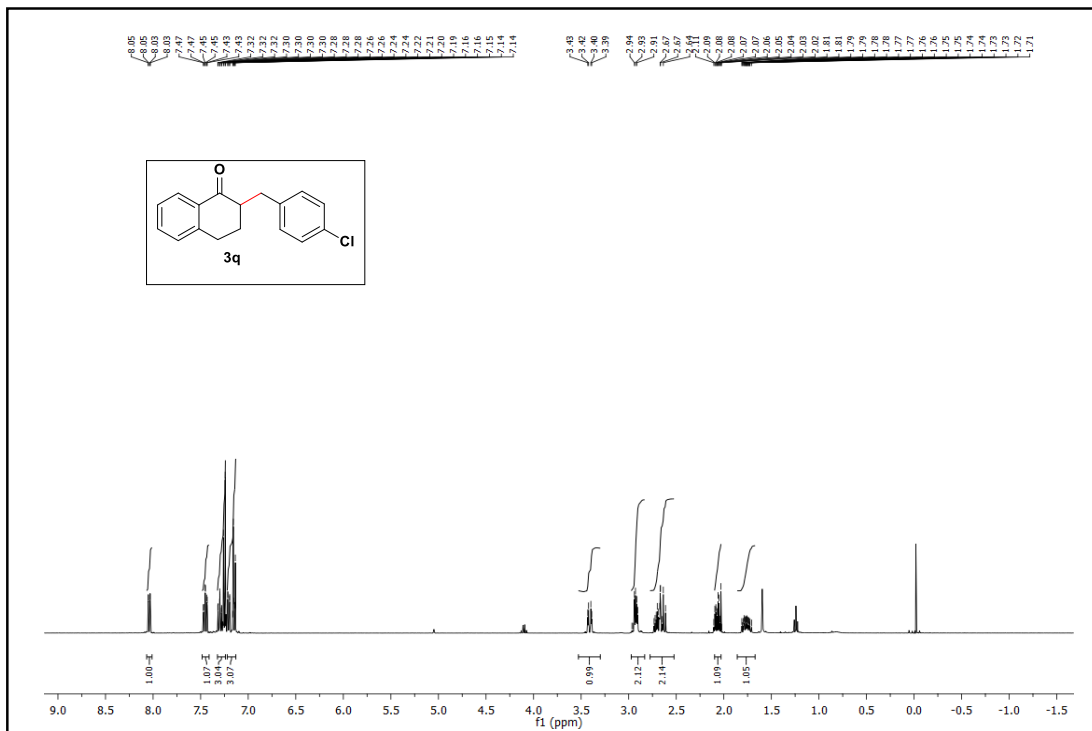
(S)-3-(benzo[d][1,3]dioxol-5-yl)-1,2-diphenylpropan-1-one :



**2-Benzyl-3,4-dihydronaphthalen-1(2H)-one:**



2-(4-chlorobenzyl)-3,4-dihydronaphthalen-1(2H)-one (3q)



This Page was intentionally left blank

## References

- [1] Paul T. Anastas, Mary M. Kirchhoff, Tracy C. Williamson, "Catalysis as a foundational pillar of green chemistry", *Appl. Catal. A Gen.* **221**(1-2), pp. 3-13 (2001).
- [2] Christophe Copÿret, Mathieu Chabanas, Romain Petroff Saint-Arroman, Jean-Marie Basset, "Homogeneous and Heterogeneous Catalysis: Bridging the Gap through Surface Organometallic Chemistry", *Angew. Chem. Int. Ed.* **42**(2), pp. 156-181 (2003).
- [3] Jens Hagen, "Economic Importance of Catalysts. In Industrial Catalysis, A Practical Approach", *Wiley Chapter 17*, pp. 459–462 (2015).
- [4] Mark E. Davis, "Ordered porous materials for emerging applications", *Nature* **417**, pp. 813-821 (2002).
- [5] Jihong Yu, Avelino Corma, Yi Li, "Functional Porous Materials Chemistry", *Adv. Mater.* **32**(44), pp. 2006277 (2020).
- [6] Carmine Colella, Alessandro F. Gualtieri, "Cronstedt's zeolite", *Microporous Mesoporous Mater.* **105**(3), pp. 213–221 (2007).
- [7] Reema Narayan, Usha Y. Nayak, Ashok M. Raichur, Sanjay Garg, "Mesoporous Silica Nanoparticles: A Comprehensive Review on Synthesis and Recent Advances", *Pharmaceutics* **10**(3), pp. 118 (2018).
- [8] Guillaume Maurin, Christian Serre, Andrew Cooper, Gérard Férey, "The new age of MOFs and of their porous-related solids", *Chem. Soc. Rev.* **46**(11), pp. 3104–3107 (2017).
- [9] Christian S Diercks, Omar M Yaghi, "The atom, the molecule, and the covalent organic framework", *Science* **355**(6328), pp. 11585 (2017).
- [10] Ralph Freund, Orysia Zaremba, Giel Arnauts, Rob Ameloot, Grigorii Skorupskii, Mircea Dincă, Anastasiya Bavykina, Jorge Gascon, Aleksander Ejsmont, Joanna Goscianska, Markus Kalmutzki, Ulrich Lächelt, Evelyn Ploetz, Christian S. Diercks, Stefan Wuttke, "The Current Status of MOF and COF Applications", *Angew. Chem. Int. Ed.* **60**(45), pp. 23975-24001(2021).
- [11] Sharath Kandambeth, Kaushik Dey, Rahul Banerjee, "Covalent Organic Frameworks: Chemistry beyond the Structure", *J.Am.Chem.Soc.* **141**(5), pp. 1807–1822 (2019).
- [12] Hiroyasu Furukawa, Kyle E. Cordova, Michael O'Keeffe, Omar M. Yaghi, "The Chemistry and Applications of Metal-Organic Frameworks" *Science* **341**(6149), pp. 1230444 (2013).
- [13] Omar M. Yaghi, Michael O'Keeffe, Nathan W. Ockwig, Hee K. Chae, Mohamed Eddaoudi, Jaheon Kim "Reticular Synthesis and the Design of New Materials" *Nature* **423**(6941), pp. 705–714 (2003).

- [14] Susumu Kitagawa, Ryo Kitaura, Shin-ichiro Noro, “Functional Porous Coordination Polymers”, *Angew. Chem. Int. Ed.* **43**(18), pp. 2334–2375 (2004).
- [15] Cho Rong Kim, Takashi Uemura, Susumu Kitagawa, “Inorganic Nanoparticles in Porous Coordination Polymers”, *Chem. Soc. Rev.* **45**(14), pp. 3828–3845 (2016).
- [16] Zhenqiang Wang, Seth M. Cohen, “Post synthetic Modification of Metal-Organic Frameworks”, *Chem. Soc. Rev.* **38**(5), pp. 1315–1329 (2009).
- [17] Mohamed Eddaoudi, Jaheon Kim, Nathaniel Rosi, David Vodak, Joseph Wachter, Michael O’Keeffe, Omar M. Yaghi, “Systematic Design of Pore Size and Functionality in Isoreticular MOFs and Their Application in Methane Storage”, *Science* **295**(5554), pp. 469-472 (2002).
- [18] Hiroyasu Furukawa, Nakeun Ko, Yong Bok Go, Naoki Aratani, Sang Beom Choi, Eunwoo Choi, A. Özgür Yazaydin, Randall Q. Snurr, Michael O’Keeffe, Jaheon Kim, Omar M. Yaghi, “Ultrahigh Porosity in Metal-Organic Framework”, *Science* **329** (5990), pp. 424–428 (2010).
- [19] K. Mark Thomas, “Adsorption and Desorption of Hydrogen on Metal-Organic Framework Materials for Storage Applications: Comparison with Other Nanoporous Materials”, *Dalt. Trans.* **9**, pp. 1487–1505 (2009).
- [20] Priscilla Rocío-Bautista, Iván Taima-Mancera, Jorge Pasán, Verónica Pino, “Metal-Organic Frameworks in Green Analytical Chemistry”, *Separations* **6**(3), pp. 33 (2019).
- [21] Vadia Foziya Yusuf, Naved I. Malek, Suresh Kumar Kailasa, “Review on Metal–Organic Framework Classification, Synthetic Approaches, and Influencing Factors: Applications in Energy, Drug Delivery, and Wastewater Treatment”, *ACS Omega* **7**(49), pp. 44507–44531(2022).
- [22] Colm Healy, Komal M. Patil, Benjamin H. Wilson, Lily Hermanspahn, Nathan C. Harvey-Reid, Ben I. Howard, Carline Kleinjan, James Kolien, Fabian Payet, Shane G. Telfer, Paul E. Kruger, Thomas D. Bennett, “The Thermal Stability of Metal-Organic Frameworks”, *Coord. Chem. Rev.* **419**, pp. 213388 (2020).
- [23] Karen Leusa, Thomas Bogaerts, Jeroen De Deckera, Hannes Depauwa, Kevin Hendrickxa, Henk Vrielinck, Veronique Van Speybroeck, Pascal Van Der Voort “Systematic Study of the Chemical and Hydrothermal Stability of Selected “Stable” Metal Organic Frameworks”, *Microporous Mesoporous Mater.* **226**, pp. 110–116 (2016).
- [24] Kranthi Kumar Gangu, Suresh Maddila, Sreekantha B. Jonnalagadda, “The pioneering role of metal–organic framework-5 in ever-growing contemporary applications – a review”, *RSC Adv.* **12**(22), pp.14282 (2022).



- [25] Harrison D. Lawson, S. Patrick Walton, Christina Chan, “Metal–Organic Frameworks for Drug Delivery: A Design Perspective”, *ACS Appl. Mater. Interfaces* **13** (6), pp. 7004–7020 (2021).
- [26] Dongxiao Li, Anurag Yadav, Hong Zhou, Kaustav Roy, Pounraj Thanasekaran, Chengkuo Lee, “Advances and Applications of Metal-Organic Frameworks (MOFs) in Emerging Technologies: A Comprehensive Review”, *Global Challenges*. **8**(2), pp. 2300244(2024).
- [27] Yuan-Biao Huang, Jun Liang, Xu-Sheng Wang, Rong Cao, “Multifunctional metal–organic framework catalysts: synergistic catalysis and tandem reactions”, *Chem. Soc. Rev.* **46**(1), pp. 126-157(2017).
- [28] Yu-Zhen Chen, Rui Zhang, Long Jiao, Hai-Long Jiang, “Metal–organic framework-derived porous materials for catalysis”, *Coord. Chem. Rev.* **362**, pp. 1-23 (2018).
- [29] Jingwen Chen, Xiaoling Chen, Zhiguo Zhang\*, Zongbi Bao, Huabin Xing, Qiwei Yang, Qilong Ren, “MIL-101(Cr) as a synergistic catalyst for the reduction of imines with trichlorosilane”, *Mol. Catal.* **445**, pp. 163–169 (2018).
- [30] Sadegh Rostamnia, Hassan Alamgholiloo, Xiao Liu, “Pd-grafted open metal site copper-benzene-1,4-dicarboxylate metal organic frameworks (Cu-BDC MOF’s) as promising interfacial catalysts for sustainable Suzuki coupling”, *J. Colloid. Interface. Sci.* **469**, pp. 310–317 (2016).
- [31] David J. Tranchemontagne, Jose´ L. Mendoza-Corte´s, Michael O’Keeffe, Omar M. Yaghi “Secondary building units, nets and bonding in the chemistry of metal–organic frameworks”, *Chem. Soc. Rev.* **38**(5), pp. 1257–1283 (2009).
- [32] Mikhail Meilikhov, Kirill Yussenko, Roland A. Fischer, “Turning MIL-53(Al) redox-active by functionalization of the bridging OH-group with 1,1'-ferrocenediyl-dimethylsilane”, *J. Am. Chem. Soc.* **131**(28), pp. 9644–9645 (2009).
- [33] Kuntal Manna, Pengfei Ji, Zekai Lin, Francis X. Greene, Ania Urban, Nathan C. Thacker, Wenbin Lin, “Chemoselective single-site Earth-abundant metal catalysts at metal–organic framework nodes”, *Nat Commun* **7**(1), pp. 12610 (2016).
- [34] Xingjie Wang, Xuan Zhang, Peng Li, Ken-ichi Otake, Yuexing Cui, Jiafei Lyu, Matthew D. Krzyaniak, Yuanyuan Zhang, Zhanyong Li, Jian Liu, Cassandra T. Buru, Timur Islamoglu, Michael R. Wasielewski, Zhong Li, and Omar K. Farha, “Vanadium catalyst on isostructural transition metal, lanthanide, and actinide based metal–organic frameworks for alcohol oxidation” *J. Am. Chem. Soc.* **141**(20), pp. 8306–8314 (2019).
- [35] Yong-Sheng Wei, Mei Zhang, Ruqiang Zou, Qiang Xu, “Metal–Organic Framework-Based Catalysts with Single Metal Sites” *Chem. Rev.* **120**(21), pp. 12089–12174 (2020).
- [36] Pengfei Ji, Takahiro Sawano, Zekai Lin, Ania Urban, Dean Boures, Wenbin Lin, “Cerium-Hydride Secondary Building Units in a Porous Metal–Organic Framework

for Catalytic Hydroboration and Hydrophosphination”, *J. Am. Chem. Soc.* **138**(45), pp. 14860–14863 (2016).

- [37] Ryo Kitaura, Goro Onoyama, Hirotohi Sakamoto, Ryotaro Matsuda, Sin-ichiro Noro, Susumu Kitagawa, “Immobilization of a Metallo Schiff Base into a Microporous Coordination Polymer”, *Angew. Chem. Int. Ed.* **43**(20), pp. 2684–2687 (2004).
- [38] Suntao Wu, Liyu Chen, Biaolin Yin, Yingwei Li, ““Click” post-functionalization of a metal–organic framework for engineering active single-site heterogeneous Ru(III) catalysts”, *Chem. Commun.* **51**(48), pp. 9884–9887 (2015).
- [39] Honghan Fei, Matthew D. Sampson, Yeob Lee, Clifford P. Kubiak, Seth M. Cohen, “Photocatalytic CO<sub>2</sub> Reduction to Formate Using a Mn(I) Molecular Catalyst in a Robust Metal–Organic Framework”, *Inorg. Chem.* **54**(14), pp. 6821–6828 (2015).
- [40] Honghan Fei, JaeWook Shin, Ying Shirley Meng, Mario Adelhardt, Jörg Sutter, Karsten Meyer, Seth M. Cohen, “Reusable Oxidation Catalysis Using Metal-Monocatecholato Species in a Robust Metal–Organic Framework”, *J. Am. Chem. Soc.* **136**(13), pp. 4965–4973 (2014).
- [41] Stephan Hermes, Marie-Katrin Schröter, Rochus Schmid, Lamma Khodeir, Martin Muhler, Arno Tissler, Richard W. Fischer, Roland A. Fischer, “Metal@MOF: Loading of Highly Porous Coordination Polymers Host Lattices by Metal Organic Chemical Vapor Deposition”, *Angew. Chem. Int. Ed.* **44**(38), pp. 6237–6241 (2005).
- [42] Young Kyu Hwang, Do-Young Hong, Jong-San Chang, Sung Hwa Jung, You-Kyong Seo, Jinheung Kim, Alexandre Vimont, Marco Daturi, Christian Serre, Gerard Ferey, “Amine Grafting on Coordinatively Unsaturated Metal Centers of MOFs: Consequences for Catalysis and Metal Encapsulation”, *Angew. Chem., Int. Ed.* **47**(22), pp. 4144–4148 (2008).
- [43] Tamao Ishida, Megumi Nagaoka, Tomoki Akita, Masatake Haruta, “Deposition of Gold Clusters on Porous Coordination Polymers by Solid Grinding and Their Catalytic Activity in Aerobic Oxidation of Alcohols” *Chem. - Eur. J.* **14**(28), pp. 8456–8460 (2008).
- [44] Arshad Aijaz, Abhi Karkamkar, Young Joon Choi, Nobuko Tsumori, Ewa Rönnebro, Tom Autrey, Hiroshi Shioyama, Qiang Xu, “Immobilizing Highly Catalytically Active Pt Nanoparticles Inside the Pores of Metal–Organic Framework: A Double Solvents Approach”, *J. Am. Chem. Soc.* **134**(34), pp. 13926–13929 (2012).
- [45] Yongxin Liu, Shan Wang, Xiaohu Wu, Yihu Zhao, Yuping Lu, Yanshuang Zhang, Guohai Xu, Jiali Zhang, Zanru Guo, Xi Chen, “Cu<sub>2</sub>O/Au@HKUST-1 Hollow Nanostructures: One-Pot Synthesis and Catalysis Evaluation”, *Microporous Mesoporous Mater.* **279**, pp. 228–233 (2019).

- [46] Liangmin Ning, Shengyun Liao, Xuguang Liu, Pengfei Guo, Zhenya Zhang, Haigang Zhang, Xinli Tong “A Regulatable Oxidative Valorization of Furfural with Aliphatic Alcohols Catalyzed by Functionalized Metal–Organic Frameworks Supported Au Nanoparticles”, *J. Catal.* **364**, pp. 1–13 (2018).
- [47] Bo Li, Jian-Gong Ma, Peng Cheng, “Silica-Protection-Assisted Encapsulation of Cu<sub>2</sub>O Nanocubes into a Metal–Organic Framework (ZIF-8) To Provide a Composite Catalyst”, *Angew. Chem. Int. Ed.* **57**(23), pp. 6834–6837 (2018).
- [48] Sora Choi, Moonhyun Oh, “Well-Arranged and Confined Incorporation of PdCo Nanoparticles within a Hollow and Porous Metal–Organic Framework for Superior Catalytic Activity”, *Angew. Chem., Int. Ed.* **58**(3), pp. 866–871(2019).
- [49] Arshad Aijaz, Abhi Karkamkar, Young Joon Choi, Nobuko Tsumori, Ewa Rönnebro, Tom Autrey, Hiroshi Shioyama, Qiang Xu, “Immobilizing Highly Catalytically Active Pt Nanoparticles inside the Pores of Metal–Organic Framework: A Double Solvents Approach” *J. Am. Chem. Soc.* **134** (34), pp. 13926-13929 (2012).
- [50] Guang Lu, Shaozhou Li, Zhen Guo, Omar K. Farha, Brad G. Hauser, Xiaoying Qi, Yi Wang, Xin Wang, Sanyang Han, Xiaogang Liu, Joseph S. DuChene, Hua Zhang, Qichun Zhang, Xiaodong Chen, Jan Ma, Say Chye Joachim Loo, Wei D. Wei, Yanhui Yang, Joseph T. Hupp, Fengwei Huo, “Imparting functionality to a metal–organic framework material by controlled nanoparticle encapsulation”, *Nature Chem* **4**(4), pp. 310–316 (2012).
- [51] Bo Li, Jian-Gong Ma, Peng Cheng, “Silica-Protection-Assisted Encapsulation of Cu<sub>2</sub>O Nanocubes into a Metal–Organic Framework (ZIF-8) To Provide a Composite Catalyst”, *Angew. Chem. Int. Ed.* **57**(23), pp. 6834–6837 (2018).
- [52] Mohamed H. Alkordi, Yunling Liu, Randy W. Larsen, Jarrod F. Eubank, Mohamed Eddaoudi, “Zeolite-like Metal–Organic Frameworks as Platforms for Applications: On Metalloporphyrin-Based Catalysts”, *J. Am. Chem. Soc.* **130**(38), pp. 12639–12641(2008).
- [53] Zhenzhen Zhou, Xiao Liu, Jian-Gong Ma, Peng Cheng, “MOF-Incorporated Binuclear N-Heterocyclic Carbene-Cobalt Catalyst for Efficient Conversion of CO<sub>2</sub> to Formamides”, *ChemSusChem* **15**(19), pp. e2022013 (2022).
- [54] Qihao Yang, Qiang Xu, Hai-Long Jiang, “Metal–organic frameworks meet metal nanoparticles: synergistic effect for enhanced catalysis”, *Chem. Soc. Rev.* **46**(15), pp. 4774-4808 (2017).
- [55] Jiewei Liu, Lianfen Chen, Hao Cui, Jianyong Zhang, Li Zhang, Cheng-Yong Su, “Applications of metal–organic frameworks in heterogeneous supramolecular catalysis”, *Chem. Soc. Rev.* **43**(16), pp. 6011-6061 (2014).
- [56] Long Jiao, Yang Wang, Hai-Long Jiang, Qiang Xu, “Metal–Organic Frameworks as Platforms for Catalytic Applications” *Adv. Mater.* **30**(37), pp.1703663 (2017).

- [57] Hai-Long Jiang, Bo Liu, Ya-Qian Lan, Kentaro Kuratani, Tomoki Akita, Hiroshi Shioyama, Fengqi Zong, Qiang Xu, “From Metal–Organic Framework to Nanoporous Carbon: Toward a Very High Surface Area and Hydrogen Uptake”, *J. Am. Chem. Soc.* **133**(31), pp. 11854–11857 (2011).
- [58] Bo Liu, Hiroshi Shioyama, Tomoki Akita, Qiang Xu, “Metal-Organic Framework as a Template for Porous Carbon Synthesis”, *J. Am. Chem. Soc.* **130**(16), pp. 5390–5391(2008).
- [59] Zixu Tao, Teng Wang, Xiaojuan Wang, Jie Zheng, Xingguo Li, “MOF-Derived Noble Metal Free Catalysts for Electrochemical Water Splitting”, *ACS Appl. Mater. Interfaces* **8**(51), pp. 35390–35397 (2016).
- [60] Tianjie Qiu, Zibin Liang, Wenhan Guo, Hassina Tabassum, Song Gao, and Ruqiang Zou, “Metal–Organic Framework-Based Materials for Energy Conversion and Storage”, *ACS Energy Lett.* **5**(2), pp. 520–532 (2020).
- [61] Seung Jae Yang, Taehoon Kim, Ji Hyuk Im, Yern Seung Kim, Kunsil Lee, Haesol Jung, Chong Rae Park, “MOF-Derived Hierarchically Porous Carbon with Exceptional Porosity and Hydrogen Storage Capacity”, *Chem. Mater.* **24**(3), pp. 464–470 (2012).
- [62] Shengqian Ma, Gabriel A. Goenaga, Ann V. Call, Di-Jia Liu, “Cobalt Imidazolate Framework as Precursor for Oxygen Reduction Reaction Electrocatalysts”, *Chem. - Eur. J.* **17**, pp. 2063– 2067 (2011).
- [63] Soumen Dutta, Zhiming Liu, HyukSu Han, Arindam Indra, Taeseup Song, “Electrochemical Energy Conversion and Storage with Zeolitic Imidazolate Framework Derived Materials: A Perspective”, *ChemElectroChem* **5**, pp. 3571–3588 (2018).
- [64] Varsha M. V., Gomathi Nageswaran, Lavanya Jothi, Ravi Sankar A, “Review—Recent Advances in Metal Organic Framework Derived Carbon Materials for Electrocatalytic Applications”, *J. Electrochem. Soc.* **169**(3), pp. 036503 (2022).
- [65] Qiongyi Xie, Hong Ou, Qingyun Yang, Xiaoming Lin, Akif Ze, Kang Li, Xinli Chen, Guozheng Ma, “A review on metal–organic framework-derived anode materials for potassium-ion batteries”, *Dalton Trans.* **50**(28), pp. 9669-9684 (2021).
- [66] Xu Zhang, An Chen, Ming Zhong, Zihe Zhang, Xin Zhang, Zhen Zhou, Xian-He Bu, “Metal–Organic Frameworks (MOFs) and MOF-Derived Materials for Energy Storage and Conversion”, *Electrochem. Energ. Rev.* **2**(1), pp. 29–104 (2019).
- [67] Xing-Chen Xie, Ke-Jing Huang, Xu Wu, “Metal–organic framework derived hollow materials for electrochemical energy storage”, *J. Mater. Chem. A* **6**(16), pp. 6754-6771 (2018).
- [68] Jincan Ren, Yalan Huang, He Zhu, Binghao Zhang, Hekang Zhu, Shenghui Shen, Guoqiang Tan, Feng Wu, Hao He, Si Lan, Xinhui Xia, Qi Liu, “Recent progress on MOF-derived carbon materials for energy storage”, *Carbon Energy* **2**(2), pp. 176–202(2020).

- [69] Pingping Zhao, Xing Hua, Wei Xu, Wei Luo, Shengli Chen, Gongzhen Cheng, “Metal–organic framework-derived hybrid of Fe<sub>3</sub>C nanorod-encapsulated, N-doped CNTs on porous carbon sheets for highly efficient oxygen reduction and water oxidation”, *Catal. Sci. Technol.* **6**(16), pp. 6365-6371 (2016).
- [70] Yiqiong Yang, Han Dong, Yin Wang, Chi Heb, Yuxin Wang, Xiaodong Zhang, “Synthesis of octahedral like Cu-BTC derivatives derived from MOF calcined under different atmosphere for application in CO oxidation”, *J. Solid State Chem.* **258**, pp. 582–587 (2018).
- [71] Ye-Chuang Han, Meng-Li Liu, Li Sun, Xu-Cheng Li, Yonggang Yao, Chao Zhang, Song-Yuan Ding, Hong-Gang Liao, Li Zhang, Feng Ru Fan, Martin Moskovits, Zhong Qun Tian, “A general strategy for overcoming the trade-off between ultrasmall size and high loading of MOF-derived metal nanoparticles by millisecond pyrolysis”, *Nano Energy* **97**, pp. 107125 (2022).
- [72] Xiaowen Sun, Hui Huang, Chaopeng Wang, Yingying Liu, Tong Liang Hu, Xian-He Bu, “Effective Co<sub>x</sub>S<sub>y</sub> HER Electrocatalysts Fabricated by In-Situ Sulfuration of a Metal–Organic Framework”, *ChemElectroChem* **5**(23), pp. 3639– 3644 (2018).
- [73] Jing Tang, Rahul R. Salunkhe, Jian Liu, Nagy L. Torad, Masataka Imura, Shuhei Furukawa, Yusuke Yamauchi, “Thermal conversion of core–shell metal–organic frameworks: A new method for selectively functionalized nanoporous hybrid carbon”, *J. Am. Chem. Soc.* **137**, (4), pp. 1572–1580 (2015).
- [74] Pradip Pachfule, Dhanraj Shinde, Mainak Majumder, Qiang Xu, “Fabrication of carbon nanorods and graphene nanoribbons from a metal–organic framework”, *Nature Chem* **8**(7), pp. 718–724 (2016).
- [75] Hao Bin Wu, Bao Yu Xia, Le Yu, Xin-Yao Yu, Xiong Wen (David) Lou, “Porous molybdenum carbide nano-octahedrons synthesized via confined carburization in metal-organic frameworks for efficient hydrogen production”, *Nat. Commun.* **6**(1), pp. 6512 (2015).
- [76] Zewen Zhuang, Yu Wang, Cong-Qiao Xu, Shoujie Liu, Chen Chen, Qing Peng, Zhongbin Zhuang, Hai Xiao, Yuan Pan, Siqi Lu, Rong Yu, Weng-Chon Cheong, Xing Cao, Konglin Wu, Kaiian Sun, Yu Wang, Dingsheng Wang, Jun Li, Yadong Li, “Three-dimensional open nano-netcage electrocatalysts for efficient pH-universal overall water splitting”. *Nat Commun.* **10**(1), pp. 4875 (2019).
- [77] Peiqun Yin, Tao Yao, Yuen Wu, Lirong Zheng, Yue Lin, Wei Liu, Huanxin Ju, Junfa Zhu, Xun Hong, Zhaoxiang Deng, Gang Zhou, Shiqiang Wei, Yadong Li, “Single Cobalt Atoms with Precise N-Coordination as Superior Oxygen Reduction Reaction-Catalysts”, *Angew. Chem. Int. Ed.* **55** (36), pp.10800–10805 (2016).
- [78] Lu Shang, Huijun Yu, Xing Huang, Tong Bian, Run Shi, Yufei Zhao, Geoffrey I. N. Waterhouse, Li-Zhu Wu, Chen-Ho, Tierui Zhang, “Well-Dispersed ZIF-Derived Co,N-Co-doped Carbon Nanoframes through Mesoporous-Silica-Protected

Calcination as Efficient Oxygen Reduction Electrocatalysts”, *Adv. Mater.*, 28 (8), pp. 1668-1674 (2016).

- [79] Yuanjun Chen, Shufang Ji, Shu Zhao, Wenxing Chen, Juncai Dong, Weng-Chon Cheong, Rongan Shen, Xiaodong Wen, Lirong Zheng, Alexandre I. Rykov, Shichang Cai, Haolin Tang, Zhongbin Zhuang, Chen Chen, Qing Peng, Dingsheng Wang, Yadong Li, “Enhanced oxygen reduction with single-atomic-site iron catalysts for a zinc-air battery and hydrogen-air fuel cell”, *Nat Commun* **9**(1), pp. 5422 (2018).
- [80] Vlad Pascanu, Greco González Miera, A. Ken Inge, Belén Martín-Matute, “Metal–Organic Frameworks as Catalysts for Organic Synthesis: A Critical Perspective”, *J. Am. Chem. Soc.* **141**(18), pp. 7223–7234 (2019).
- [81] Kranthi Kumar Gangu, Sreekantha B. Jonnalagadda, “A Review on Metal-Organic Frameworks as Congenial Heterogeneous Catalysts for Potential Organic Transformations”, *Front. Chem* **9**, pp. 2296-2646 (2021).
- [82] Naved Akhtar, Manav Chauhan, Bharti Rana, Chhaya Thadhani, Rahul Kalita, Wahida Begum, Biplab Ghosh, Kuntal Manna, “Selective Reduction of Nitro Compounds by Organosilanes Catalyzed by a Zirconium Metal-Organic Framework Supported Salicylaldehyde-Cobalt(II) Complex”, *ChemPlusChem* pp. e20230052 (2023).
- [83] Palani Elumalai, Hind Mamlouk, Wubulikasimu Yiming, Liang Feng, Shuai Yuan, Hong-Cai Zhou, Sherzod T. Madrahimov, “Recyclable and Reusable Heteroleptic Nickel Catalyst Immobilized on Metal–Organic Framework for Suzuki–Miyaura Coupling”, *ACS Appl. Mater. Interfaces* **10**(48), pp. 41431–41438(2018).
- [84] Hyunho Noh, Yuexing Cui, Aaron W. Peters, Dale R. Pahls, Manuel A. Ortuño, Nicolaas A. Vermeulen, Christopher J. Cramer, Laura Gagliardi, Joseph T. Hupp, Omar K. Farha, “An Exceptionally Stable Metal–Organic Framework Supported Molybdenum (VI) Oxide Catalyst for Cyclohexene Epoxidation”, *J. Am. Chem. Soc.* **138**(44), pp. 14720–14726 (2016).
- [85] Yu-Zhen Chen, Yu-Xiao Zhou, Hengwei Wang, Junling Lu, Takeyuki Uchida, Qiang Xu, Shu-Hong Yu, Hai-Long Jiang, “Multifunctional PdAg@MIL-101 for One-Pot Cascade Reactions: Combination of Host–Guest Cooperation and Bimetallic Synergy in Catalysis”, *ACS Catal.* **5**(4), pp. 2062–2069 (2015).
- [86] Justus Masa, Corina Andronescu, Wolfgang Schuhmann, “Electrocatalysis as the Nexus for Sustainable Renewable Energy: The Gordian Knot of Activity, Stability, and Selectivity”, *Angew. Chem. Int. Ed.* **59**(36), pp. 15298 – 15312 (2020).
- [87] Bruce Dunn, Haresh Kamath, Jean-Marie Tarascon, “Electrical energy storage for the grid: A battery of choices”, *Science* **334** (6058), pp. 928–935 (2011).
- [88] Zhi Wei Seh, Jakob Kibsgaard, Colin F. Dickens, Ib Chorkendorff, Jens K. Nørskov, Thomas F. Jaramillo, “Combining theory and experiment in electrocatalysis: Insights into materials design”, *Science* **355**(6321), pp. ead4998 (2017).

- [89] Martin Winter, Ralph J. Brodd, “What are batteries, fuel cells, and supercapacitors?”, *Chem. Rev.* **104**(10), pp. 4245–4270 (2004).
- [90] Tianjie Qiu, Zibin Liang, Wenhan Guo, Hassina Tabassum, Song Gao, Ruqiang Zou, “Metal–Organic Framework-Based Materials for Energy Conversion and Storage”, *ACS Energy Lett.* **5**(2), pp. 520–532 (2020).
- [91] Xue Feng Lu, Yongjin Fang, Deyan Luan, Xiong Wen David Lou, “Metal–Organic Frameworks Derived Functional Materials for Electrochemical Energy Storage and Conversion: A Mini Review”, *Nano Lett.* **21**(4), pp. 1555–1565 (2021).
- [92] Yan Li, Xinfu Wei, Lisong Chen, Jianlin Shi, “Electrocatalytic hydrogen production trilogy”, *Angew. Chem. Int. Ed.* **60**(36), pp. 19550–19571 (2021).
- [93] Bo You, Yujie Sun, “Innovative Strategies for Electrocatalytic Water Splitting”, *Acc. Chem. Res.* **51**(7), pp. 1571–1580 (2018).
- [94] Kai Zeng, Dongke Zhang, “Recent progress in alkaline water electrolysis for hydrogen production and applications”, *Prog. Energy Combust. Sci.* **2010**, **36**(3), pp. 307–326 (2010).
- [95] Yan Jiao, Yao Zheng, Mietek Jaroniec, Shi Zhang Qiao, “Design of electrocatalysts for oxygen- and hydrogen-involving energy conversion reactions”, *Chem. Soc. Rev.* **44**(8), pp. 2060–2086 (2015).
- [96] Charles C. L. McCrory, Suho Jung, Ivonne M. Ferrer, Shawn M. Chatman, Jonas C. Peters, Thomas F. Jaramillo, “Benchmarking Hydrogen Evolving Reaction and Oxygen Evolving Reaction Electrocatalysts for Solar Water Splitting Devices”, *J. Am. Chem. Soc.* **137**(13), pp. 4347–4357 (2015).
- [97] Bo Liu, Hiroshi Shioyama, Tomoki Akita, Qiang Xu, “Metal-Organic Framework as a Template for Porous Carbon Synthesis”, *J. Am. Chem. Soc.* **130**(16), pp. 5390–5391 (2008).
- [98] Yuan Pan, Kaian Sun, Shoujie Liu, Xing Cao, Konglin Wu, Weng-Chon Cheong, Zheng Chen, Yu Wang, Yang Li, Yunqi Liu, Dingsheng Wang, Qing Peng, Chen Chen, Yadong Li, “Core–Shell ZIF-8@ZIF-67-Derived CoP Nanoparticle-Embedded N-Doped Carbon Nanotube Hollow Polyhedron for Efficient Overall Water Splitting”, *J. Am. Chem. Soc.* **140**(7), pp. 2610–2618 (2018).
- [99] Megan E. Scofield, Haiqing Liu, Stanislaus S. Wong, “A concise guide to sustainable PEMFCs: recent advances in improving both oxygen reduction catalysts and proton exchange membranes”, *Chem. Soc. Rev.* **44**(16), pp. 5836–5860 (2015).
- [100] Sazali, Norazlianie, Wan Norharyati Wan Salleh, Ahmad Shahir Jamaludin, Mohd Nizar Mhd Razali, “New Perspectives on Fuel Cell Technology: A Brief Review” *Membranes* **10**(5), pp. 99 (2020).

- [101] Shankhamala Kundu, Tharamani Chikka Nagaiah, Wei Xia, Yuemin Wang, Stefan Van Dommele, Johannes Hendrik Bitter, Monika Santa, Guido Grundmeier, Michael Bron, Wolfgang Schuhmann, Martin Muhler “Electrocatalytic Activity and Stability of Nitrogen-Containing Carbon Nanotubes in the Oxygen Reduction Reaction”, *J. Phys. Chem. C* **113**(32), pp. 14302-14310 (2009).
- [102] Ambarish Kulkarni, Samira Siahrostami, Anjali Patel, Jens K. Nørskov, “Understanding Catalytic Activity Trends in the Oxygen Reduction Reaction”, *Chem. Rev.* **2018**, **118**(5), pp. 2302-2312 (2018).
- [103] Xiaoming Ge, Afriyanti Sumboja, Delvin Wu, Tao An, Bing Li, F. W. Thomas Goh, T. S. Andy Hor, Yun Zong, Zhaolin Liu, “Oxygen Reduction in Alkaline Media: From Mechanisms to Recent Advances of Catalysts”, *ACS Catal.* **5**(8), pp. 4643-4667 (2015).
- [104] John A. Keith, Timo Jacob “Theoretical Studies of Potential-Dependent and Competing Mechanisms of the Electrocatalytic Oxygen Reduction Reaction on Pt (111)”, *Angew. Chem. Int. Ed.* **49**(49), pp. 9521-9525 (2010).
- [105] Srijib Das, Souvik Ghosh, Tapas Kuila, Naresh Chandra Murmu, Aniruddha Kundu, “Fundamentals of Oxygen Reduction Reaction”, Encyclopedia. Available online: <https://encyclopedia.pub/entry/26657> (accessed on 29 November 2023).
- [106] Liu Yang, Xiaofei Zeng, Wenchuan Wang, Dapeng Cao, “Recent progress in MOF-derived, heteroatom-doped porous carbons as highly efficient electrocatalysts for oxygen reduction reaction in fuel cells”, *Adv. Funct. Mater.* **28**(7), pp. 1704537 (2018).
- [107] Shaofang Fu, Chengzhou Zhu, Junhua Song, Dan Du, Yuehe Lin, “Metal-Organic Framework-Derived Non-Precious Metal Nanocatalysts for Oxygen Reduction Reaction”, *Adv. Energy Mater.* **7**(19), pp. 1700363 (2017).
- [108] Zhengju Zhu, Huajie Yin, Yun Wang, Cheng-Hao Chuang, Lei Xing, Mengyang Dong, Ying-Rui Lu, Gilberto Casillas-Garcia, Yonglong Zheng, Shan Chen, Yuhai Dou, Porun Liu, Qilin Cheng, Huijun Zhao, “Coexisting Single-Atomic Fe and Ni Sites on Hierarchically Ordered Porous Carbon as a Highly Efficient ORR Electrocatalyst”, *Adv. Mater.* **32**(42), pp. 2004670 (2020).
- [109] Jilei Liu, Jin Wang, Chaohe Xu, Hao Jiang, Chunzhong Li, Lili Zhang, Jianyi Lin, Ze Xiang Shen, “Advanced Energy Storage Devices: Basic Principles, Analytical Methods, and Rational Materials Design”, *Adv. Sci.* **5**(1), pp. 1700322 (2018).
- [110] Xiayue Fan, Bin Liu, Jie Liu, Jia Ding, Xiaopeng Han, Yida Deng, Xiaojun Lv, Ying Xie, Bing Chen, Wenbin Hu, Cheng Zhong, “Battery Technologies for Grid-Level Large-Scale Electrical Energy Storage”, *Trans. Tianjin Univ.* **26**(2), pp. 92–103 (2020)
- [111] Jie Zhang, Qixing Zhou, Yawen Tang, Liang Zhang, Yanguang Li, “Zinc–air batteries: are they ready for prime time?”, *Chem. Sci.* **10**(39), pp. 8924-8929 (2019).



- [112] Hao-Fan Wang, Qiang Xu, “Materials design for rechargeable metal-air batteries”, *Matter* **1**(3), pp. 565–595 (2019).
- [113] Junxing Han, Xiaoyi Meng, Liang Lu, Juanjuan Bian, Zhipeng Li, Chunwen Sun, “Single-Atom Fe-Nx-C as an Efficient Electrocatalyst for Zinc–Air Batteries”, *Adv. Funct. Mater.* **29**(41), pp. 1808872 (2019).
- [114] Bruce Dunn, Haresh Kamath, Jean-Marie Tarascon, “Electrical Energy Storage for the Grid: A Battery of Choices”, *Science*, **334**(6058), pp. 928-935 (2011).
- [115] Zhenguo Yang, Jianlu Zhang, Michael C. W. Kintner-Meyer, Xiaochuan Lu, Daiwon Choi, John P. Lemmon, Jun Liu, “Electrochemical Energy Storage for Green Grid”, *Chem. Rev.* **111**(5), pp. 3577–3613 (2011).
- [116] Robert M. Darling, Kevin G. Gallagher, Jeffrey A. Kowalski, Seungbum Ha, Fikile R. Brushett, “Pathways to low-cost electrochemical energy storage: a comparison of aqueous and nonaqueous flow batteries”, *Energy Environ. Sci.* **7**(11), pp. 3459 (2014)
- [117] Qixing Wu, Xiangyang Zhang, Yunhui Lv, Liyu Lin, Yao Liu, Xuelong Zhou, “Bio-inspired multiscale-pore-network structured carbon felt with enhanced mass transfer and activity for vanadium redox flow batteries”, *J. Mater. Chem. A*, **6**(41), pp. 20347 (2018).
- [118] Ki Jae Kim, Min-Sik Park, Young-Jun Kim, Jung Ho Kim, Shi Xue Dou, M. Skyllas-Kazacos, “A technology review of electrodes and reaction mechanisms in vanadium redox flow batteries”, *J. Mater. Chem. A* **3**(33), pp. 16913 (2015).
- [119] Ke Gong, Fei Xu, Jonathan B. Grunewald, Xiaoya Ma, Yun Zhao, Shuang Gu, Yushan Yan, “All-Soluble All-Iron Aqueous Redox-Flow Battery”, *ACS Energy Lett.* **1**(1), pp. 89–93 (2016).
- [120] Lei Zhang, Junpei Yue, Qi Deng, Wei Ling, Chun-Jiao Zhou, Xian-Xiang Zeng, Congshan Zhou, Xiong-Wei Wu, YuPing Wu “Preparation of a porous graphite felt electrode for advance vanadium redox flow batteries”, *RSC Adv.* **10**(23), pp. 13374-13378 (2020).
- [121] Yingqiao Jiang, Gang Cheng, Yuehua Li, Zhangxing He, Jing Zhu, Wei Meng, Lei Dai, Ling Wang, “Promoting vanadium redox flow battery performance by ultra-uniform ZrO<sub>2</sub>@C from metal-organic framework”, *Chem. Eng. J.* **415**, pp. 129014 (2021).
- [122] Susumu Kitagawa, Ryo Kitaura, Shin-ichiro Noro, “Functional Porous Coordination-Polymers”, *Angew. Chem., Int. Ed.* **43**(18), pp. 2334–2375 (2004).
- [123] Omar M. Yaghi, Michael O’Keeffe, Nathan W. Ockwig, Hee K. Chae, Mohamed Eddaoudi, Jaheon Kim, “Reticular synthesis and the design of new materials”, *Nature* **423**(6941), pp. 705 (2003).

- [124] Hong-Cai Zhou, Jeffrey R. Long, Omar M. Yaghi, “Introduction to Metal–Organic Frameworks”, *Chem. Rev.* **112**(2), pp. 673-674 (2012).
- [125] Yuanjing Cui, Bin Li, Huajun He, Wei Zhou, Banglin Chen, Guodong Qian, “Metal–Organic Frameworks as Platforms for Functional Materials”, *Acc. Chem. Res.* **49**(3), pp. 483–493 (2016).
- [126] Yong-Sheng Wei, Mei Zhang, Ruqiang Zou, Qiang Xu, “Metal–Organic Framework-Based Catalysts with Single Metal Sites”, *Chem. Rev.* **120**(21), pp. 12089–12174 (2020).
- [127] Hong Jiang, Wenqiang Zhang, Xing Kang, Ziping Cao, Xu Chen, Yan Liu, Yong Cui, “Topology-Based Functionalization of Robust Chiral Zr-Based Metal–Organic Frameworks for Catalytic Enantioselective Hydrogenation”, *J. Am. Chem. Soc.* **142**(21), pp. 9642–9652 (2020).
- [128] Dandan Li, Hai-Qun Xu, Long Jiao, Hai-Long Jiang, “Metal-organic frameworks for catalysis: State of the art, challenges, and opportunities”, *EnergyChem* **1**(1), pp. 100005 (2019).
- [129] Jun-Sheng Qin, Shuai Yuan, Christina Lollar, Jiandong Pang, Ali Alsalmeh, Hong-Cai Zhou, “Stable metal–organic frameworks as a host platform for catalysis and biomimetics”, *Chem. Commun.* **54**(34), pp. 4231-4249 (2018).
- [130] Adeel H. Chughtai, Nazir Ahmad, Hussein A. Younus, A. Laypkovc, Francis Verpoort, “Metal–organic frameworks: versatile heterogeneous catalysts for efficient catalytic organic transformations”, *Chem. Soc. Rev.* **44**(19), pp. 6804-6849 (2015).
- [131] A. Corma, H. García, and F. X. Llabrés i Xamena, “Engineering Metal Organic Frameworks for Heterogeneous Catalysis”, *Chem. Rev.* **110**(8), pp. 4606–4655 (2010).
- [132] P. Mialane, C. Mellot-Draznieks, P. Gairola, M. Duguet, Y. Benseghir, O. Oms, A. Dolbecq, “Heterogenisation of polyoxometalates and other metal-based complexes in metal–organic frameworks: from synthesis to characterization and applications in catalysis”, *Chem. Soc. Rev.* **50**(10), pp. 6152-6220 (2021).
- [133] Vlad Pascanu, Greco González Miera, A. Ken Inge, Belén Martín-Matute, “Metal–Organic Frameworks as Catalysts for Organic Synthesis: A Critical Perspective”, *J. Am. Chem. Soc.* **141**(18), pp. 7223-7234 (2019).
- [134] Pilar García-García, Maike Muller, Avelino Corma, “MOF catalysis in relation to their homogeneous counterparts and conventional solid catalysts”, *Chem. Sci.* **5**(8), pp. 2979-3007 (2014).
- [135] Fabian Kallmeier, Beata Dudzic, Torsten Irrgang, Rhet Kempe, “Manganese-Catalyzed Sustainable Synthesis of Pyrroles from Alcohols and Amino Alcohols” *Angew. Chem. Int. Ed.* **56**(25), pp. 7261-7265 (2017).

- [136] Amanda W. Stubbs, Luca Braglia, Elisa Borfecchia, Randall J. Meyer, Yuriy Román-Leshkov, Carlo Lamberti, Mircea Dincă, “Selective Catalytic Olefin Epoxidation with Mn<sup>II</sup>-Exchanged MOF-5”, *ACS Catal.* **8**(1), pp. 596-601 (2018).
- [137] Yu Fu, Yanglong Guo, Yun Guo, Yunsong Wang, Li Wang, Wangcheng Zhan, Guanzhong Lu, “In situ assembly of ultrafine Mn<sub>3</sub>O<sub>4</sub> nanoparticles into MIL-101 for selective aerobic oxidation”, *Catal. Sci. Technol.* **7**(18), pp. 4136-4144 (2017).
- [138] Chao Zou, Tianfu Zhang, Ming-Hua Xie, Lijun Yan, Guo-Qiang Kong, Xiu-Li Yang, An Ma, Chuan-De Wu, “Four Metalloporphyrinic Frameworks as Heterogeneous Catalysts for Selective Oxidation and Aldol Reaction” *Inorg. Chem.* **52**(7), pp. 3620-3626 (2013).
- [139] Xiu-Li Yang, Ming-Hua Xie, Chao Zou, Yabing He, Banglin Chen, Michael O’Keeffe, Chuan-De Wu, “Porous Metalloporphyrinic Frameworks Constructed from Metal 5,10,15,20-Tetrakis(3,5-biscarboxylphenyl)porphyrin for Highly Efficient and Selective Catalytic Oxidation of Alkylbenzenes”, *J. Am. Chem. Soc.* **134**(25), pp. 10638-10645 (2012).
- [140] Mohamed H. Alkordi, Yunling Liu, Randy W. Larsen, Jarrod F. Eubank, Mohamed Eddaoudi, “Zeolite-like Metal–Organic Frameworks as Platforms for Applications: On Metalloporphyrin-Based Catalysts”, *J. Am. Chem. Soc.* **130**(38), pp. 12639-12641 (2008).
- [141] Cheng Huang, Rui Liu, Wenyu Yang, Yunpeng Li, Jinsong Huang, Hongjun Zhu, “Enhanced catalytic activity of MnCo-MOF-74 for highly selective aerobic oxidation of substituted toluene”, *Inorg. Chem. Front.* **5**(8), pp. 1923-1932 (2018).
- [142] Jingwen Chen, Minda Chen, Biying Zhang, Renfeng Nie, Ao Huang, Tian Wei Goh, Alexander Volkov, Zhiguo Zhang, Qilong Rena, Wenyu Huang, “Allylic oxidation of olefins with a manganese-based metal–organic framework”, *Green Chem.* **2019**, **21**(13), pp. 3629-3636 (2019).
- [143] Abraham M. Shultz, Omar K. Farha, Debashis Adhikari, Amy A. Sarjeant, Joseph T. Hupp, SonBinh T. Nguyen, “Selective Surface and Near-Surface Modification of a Noncatenated, Catalytically Active Metal–Organic Framework Material Based on Mn(salen) Struts”, *Inorg. Chem.* **2011**, **50**(8), pp. 3174-3176 (2011).
- [144] So-Hye Cho, Baoqing Ma, SonBinh T. Nguyen, Joseph T. Hupp, Thomas E. Albrecht-Schmitt, “A metal–organic framework material that functions as an enantioselective catalyst for olefin epoxidation” *Chem. Commun.* **24**, pp. 2563-2565 (2006).
- [145] Mohammad Rasel Mian, Unjila Afrin, Majed S. Fataftah, Karam B. Idrees, Timur Islamoglu, Danna E. Freedman, Omar K. Farha, “Control of the Porosity in Manganese Trimer-Based Metal–Organic Frameworks by Linker Functionalization”, *Inorg. Chem.* **59**(12), pp. 8444-8450 (2020).
- [146] Yansong Jiang, Jianing Xu, Ziqian Zhu, Changwei Jiang, Lin Ma, Hui Wang, Li Wang, Yong Fan, “Manganese-organic framework assembled by 5-((4'-(tetrazol-5"-yl) benzyl) oxy) isophthalic acid: A solvent-free catalyst for the formation of carbon–carbon bond”, *Inorg. Chim. Acta* **510**, pp. 119735 (2020).

- [147] Amarajothi Dhakshinamoorthy, Abdullah M. Asiri, Hermenegildo Garcia, "Metal-organic frameworks catalyzed C-C and C-heteroatom coupling reactions", *Chem. Soc. Rev.* **44**(7), pp.1922-1947 (2015).
- [148] JunZo Otera, "Modern Carbonyl Chemistry", Wiley-VCH, Weinheim, 2000.
- [149] Takashi Kuwahara, Takahide Fukuyama, Ilhyong Ryu, "RuHCl(CO)(PPh<sub>3</sub>)<sub>3</sub>-Catalyzed  $\alpha$ -Alkylation of Ketones with Primary Alcohols", *Org. Lett.* **14**(18), pp. 4703-4705 (2012).
- [150] María L. Buil, Miguel A. Esteruelas, Juana Herrero, Susana Izquierdo, Isidro M. Pastor, Miguel Yus, "Osmium Catalyst for the Borrowing Hydrogen Methodology:  $\alpha$ -Alkylation of Arylacetonitriles and Methyl Ketones", *ACS Catal.* **3**(9), pp. 2072-2075 (2013).
- [151] X. Yu, Q. Y. Wang, Q. J. Wu, D. W. Wang, "Rhodium-catalyzed alkylation of ketones and alcohols with alcohols" *Russ. J. Gen. Chem.* **86**(1), pp. 178-183 (2016).
- [152] Kazuhiko Taguchi, Hideto Nakagawa, Tomotaka Hirabayashi, Satoshi Sakaguchi, Yasutaka Ishii, "An Efficient Direct  $\alpha$ -Alkylation of Ketones with Primary Alcohols Catalyzed by [Ir(cod)Cl]<sub>2</sub>/PPh<sub>3</sub>/KOH System without Solvent", *J. Am. Chem. Soc.* **126**(1), pp. 72-73 (2004).
- [153] Patrick Piehl, Miguel Pena-Lopez, Anna Frey, Helfried Neumann, Matthias Beller, "Hydrogen autotransfer and related dehydrogenative coupling reactions using a rhenium(I) pincer catalyst", *Chem. Commun.* 2017, **53**(22), pp. 3265-3268
- [154] Guoqi Zhang, Jing Wu, Haisu Zeng, Shu Zhang, Zhiwei Yin, Shengping Zheng, "Cobalt-Catalyzed  $\alpha$ -Alkylation of Ketones with Primary Alcohols", *Org. Lett.* **19**(5), pp. 1080-1083 (2017).
- [155] Miguel Pena-López, Patrick Piehl, Saravanakumar Elangovan, Helfried Neumann, Matthias Beller, "Manganese-Catalyzed Hydrogen-Autotransfer C-C Bond Formation:  $\alpha$ -Alkylation of Ketones with Primary Alcohols", *Angew. Chem. Int. Ed.* **55**(48), pp. 14967-14971 (2016).
- [156] Di Shen, Darren L. Poole, Camilla C. Shotton, Anne F. Kornahrens, Mark P. Healy, Timothy J. Donohoe, "Hydrogen-Borrowing and Interrupted-Hydrogen-Borrowing Reactionsof Ketones and Methanol Catalyzed by Iridium" *Angew. Chem., Int. Ed.* **54**(5), pp. 1642-1645 (2015).
- [157] Feng Li, Juan Ma, and Nana Wang, " $\alpha$ -Alkylation of Ketones with Primary Alcohols Catalyzed by a Cp\*Ir Complex Bearing a Functional Bipyridonate Ligand", *J. Org. Chem.* **79**(21), pp. 10447-10455 (2014).
- [158] Christoph Schleppehorst, Biplab Maji, Frank Glorius, "Ruthenium-NHC Catalyzed  $\alpha$ -Alkylation of Methylene Ketones Provides Branched Products through Borrowing Hydrogen Strategy", *ACS Catal.* **6**(7) pp. 4184-4188 (2016).

- [159] Francisco Alonso, Paola Riente, Miguel Yus, "Alcohols for the  $\alpha$ -Alkylation of Methyl Ketones and Indirect Aza-Wittig Reaction Promoted by Nickel Nanoparticles" *Eur. J. Org. Chem.* **2008**(29), pp. 4908-4914 (2008).
- [160] Min Serk Kwon, Namdu Kim, Seong Hyeok Seo, In Soo Park, Ravi Kumar Cheedra, Jaiwook Park, "Recyclable Palladium Catalyst for Highly Selective  $\alpha$  Alkylation of Ketones with Alcohols" *Angew. Chem., Int. Ed.* **44**(42), pp. 6913-6915 (2005).
- [161] Lalit Mohan Kabadwal, Jagadish Das, Debasis Banerjee, "Mn (II)-catalysed alkylation of methylene ketones with alcohols: direct access to functionalized branched products", *Chem. Commun.* **54**(100), pp. 14069-14072 (2018).
- [162] Jagadish Das, Khushboo Singh, Mari Vellakkaran and Debasis Banerjee, "Nickel-Catalyzed Hydrogen-Borrowing Strategy for  $\alpha$ -Alkylation of Ketones with Alcohols: A New Route to Branched gem-Bis(alkyl) Ketones", *Org. Lett.* **20**(18), pp. 5587-5591 (2018).
- [163] Sourajit Bera, Lalit Mohan Kabadwal, Debasis Banerjee, "Recent advances in transition metal-catalyzed (1,n) annulation using (de)-hydrogenative coupling with alcohols", *Chem. Commun.* **57**(77), pp. 9807-9819 (2021).
- [164] Lalit Mohan Kabadwal, Sourajit Bera and Debasis Banerjee, "Recent advances in sustainable organic transformations using methanol: expanding the scope of hydrogen-borrowing catalysis", *Org. Chem. Front.* **8**(24), pp. 7077-7096 (2021).
- [165] Shadab, Gargi Dey, Motahar SK, Debasis Banerjee, Arshad Aijaz, "Heterogenizing a Homogeneous Nickel Catalyst Using Nanoconfined Strategy for Selective Synthesis of Mono- and 1,2-Disubstituted Benzimidazoles", *Inorg. Chem.* **60**(21), pp.16042-16047 (2021).
- [166] María de la Luz Perez-Arredondo, María del Refugio Gonzalez-Ponce, Gabriela Ana Zanor, Juan Antonio Ramirez Vazquez, Jose J.N. Segoviano-Garfias, "Complex formation equilibria of 2,2'-bipyridyl and 1,10-phenanthroline with manganese(II) in methanol", *Kar. Int. J. Modn. Sci.* **1**(3), pp. 178-186 (2015).
- [167] M. Haniti S. A. Hamid, C. Liana Allen, Gareth W. Lamb, Aoife C. Maxwell, Hannah C. Maytum, Andrew J. A. Watson, Jonathan M. J. Williams, "Ruthenium-Catalyzed N-Alkylation of Amines and Sulfonamides Using Borrowing Hydrogen Methodology", *J. Am. Chem. Soc.* **131**(5), pp. 1766-1774 (2009).
- [168] Wei Gong, Yan Liu, Haiyang Li, Yong Cui, "Metal-organic frameworks as solid Brønsted acid catalysts for advanced organic transformations", *Coord. Chem. Rev.* **420**, pp. 213400 (2020).
- [169] Bibimaryam Mousavi, Zhixiong Luo, Suphot Phatanasri, Wei Su, Tingting Wang, Somboon Chaemchuen, Francis Verpoort, "One-Step Synthesis of 2,5-Bis(chloromethyl)-1,4-dioxane from Epichlorohydrin Using ZIF-8, Taking Advantage of Structural Defects", *Eur. J. Inorg. Chem.* **2017**(42), pp. 4947-4954 (2017).

- [170] Uyen P. N. Tran, Ky K. A. Le, Nam T. S. Phan, “Expanding Applications of Metal–Organic Frameworks: Zeolite Imidazolate Framework ZIF-8 as an Efficient Heterogeneous Catalyst for the Knoevenagel Reaction”, *ACS Catal.* **1**(2), pp. 120–127 (2011).
- [171] Jinlong Gong, Can Li, Michael R. Wasielewski, “Advances in Solar Energy Conversion”, *Chem. Soc. Rev.* **48**(7), pp. 1862–1864 (2019).
- [172] Bruce Dunn, Haresh Kamath, Jean-Marie Tarascon, “Electrical Energy Storage for the Grid: A Battery of Choices”, *Science* **334**(6058), pp. 928–935 (2011).
- [173] Zhenguo Yang, Jianlu Zhang, Michael C. W. Kintner-Meyer, Xiaochuan Lu, Daiwon Choi, John P. Lemmon, Jun Liu “Electrochemical Energy storage for Green Grid”, *Chem. Rev.* **111**(5), pp. 3577–3613 (2011).
- [174] Timothy R. Cook, Dilek K. Dogutan, Steven Y. Reece, Yogesh Surendranath, Thomas S. Teets, Daniel G. Nocera, “Solar Energy Supply and Storage for the Legacy and Nonlegacy Worlds”, *Chem. Rev.* **110**(11), pp. 6474–6502 (2010).
- [175] Turgut M. Gur, “Review of Electrical Energy Storage Technologies, Materials and Systems: Challenges and Prospects for Large-Scale Grid Storage”, *Energy Environ. Sci.* **11**(10), pp. 2696–2767 (2018).
- [176] Sameer Hameer, Johannes L. van Niekerk, “A Review of Large Scale Electrical Energy Storage”, *Int. J. Energy Res.* **39**(9), pp. 1179–1195 (2015).
- [177] Dongyao Zhang, Chuanchang Li, Niangzhi Lin, Baoshan Xie, Jian Chen, “Mica-Stabilized Polyethylene Glycol Composite Phase Change Materials for Thermal Energy Storage”, *Int. J. Miner., Metall. Mater.* **29**(1), pp. 168–176 (2022).
- [178] Shengkui Zhong, Xiaoping Zhang, Jiequn Liu, Yulei Sui, “Study on  $x\text{LiVPO}_4\text{F} \cdot y\text{Li}_3\text{V}_2(\text{PO}_4)_3/\text{C}$  Composite for High-Performance Cathode Material for Lithium-Ion Batteries”, *Front. Chem.* **8**, pp. 361 (2020).
- [179] Zhejun Li, Yi-Chun Lu, “Material Design of Aqueous Redox Flow Batteries: Fundamental Challenges and Mitigation Strategies”, *Adv. Mater.* **32**(47), pp. 2002132 (2020).
- [180] Yanxin Yao, Zengyue Wang, Zhejun Li, Yi-Chun Lu, “A Dendrite-Free Tin Anode for High-Energy Aqueous Redox Flow Batteries”, *Adv. Mater.* **33**(15), pp. 2008095 (2021).
- [181] Mike L. Perrya, Adam Z. Weber, “Advanced Redox-Flow Batteries”, *J. Electrochem. Soc.* **163**, pp. A5064–A5067 (2016).
- [182] Grigorii L. Soloveichik, “Flow Batteries: Current Status and Trends”, *Chem. Rev.* 2015, **115**(20), pp. 11533–11558 (2015).
- [183] Robert M. Darling, Kevin G. Gallagher, Jeffrey A. Kowalski, Seungbum Ha, Fikile R. Brushett “Pathways to Low-Cost Electrochemical Energy Storage: A Comparison

- of Aqueous and Non-aqueous Flow Batteries”, *Energy Environ. Sci.* **7**(11), pp. 3459–3477 (2014).
- [184] Wei Wang, Qingtao Luo, Bin Li, Xiaoliang Wei, Liyu Li, Zhenguo Yang, “Recent Progress in Redox Flow Battery Research and Development”, *Adv. Funct. Mater.* **23**(8), pp. 970–986 (2013).
- [185] Puiki Leung, Xiaohong Li, Carlos Ponce de Leon, Leonard Berlouis, C. T. John Low, Frank C. Walsh, “Progress in Redox Flow Batteries, Remaining Challenges and Their Applications in Energy Storage”, *RSC Adv.* **2**(27), pp. 10125–10156 (2012).
- [186] Xinyou Ke, Joseph M. Prael, J. Iwan D. Alexander, Jesse S. Wainright, Thomas A. Zawodzinski, Robert F. Savinell “Rechargeable Redox Flow Batteries: Flow fields, Stacks and Design Considerations”, *Chem. Soc. Rev.* **47**(23), pp. 8721–8743 (2018).
- [187] Minjoon Park, Jaechan Ryu, Wei Wang, Jaephil Cho “Material Design and Engineering of Next-Generation Flow Battery Technologies”, *Nat. Rev. Mater.* **2**(1), pp. 16080 (2017).
- [188] Gareth Kear, Akeel A. Shah, Frank C. Walsh “Development of the All-Vanadium Redox Flow Battery for Energy Storage: A Review of Technological, Financial and Policy Aspects”, *Int. J. Energy Res.* **36**(11), pp. 1105–1120 (2012).
- [189] Liyu Li, Soowhan Kim, Wei Wang, M. Vijayakumar, Zimin Nie, Baowei Chen, Jianlu Zhang, Guanguang Xia, Jianzhi Hu, Gordon Graff, Jun Liu, Zhenguo Yang, “A Stable Vanadium Redox-Flow Battery with High Energy Density for Large Scale Energy Storage”, *Adv. Energy Mater.* **1**(3), pp. 394–400 (2011).
- [190] S. Zhong, M. Skyllas-Kazacos, “Electrochemical Behaviour of Vanadium (V)/ Vanadium (IV) Redox Couple at Graphite Electrodes”, *J. Power Sources* **39**(1), pp. 1–9 (1992).
- [191] Qixing Wu, Xiangyang Zhang, Yunhui Lv, Liyu Lin, Yao Liu, Xuelong Zhou, “Bio-Inspired Multiscale-Pore Network Structured Carbon Felt with Enhanced Mass Transfer and Activity for Vanadium Redox Flow Batteries”, *J. Mater. Chem. A* **6**(41), pp. 20347–20355 (2018).
- [192] Ki Jae Kim, Min-Sik Park, Young-Jun Kim, Jung Ho Kim, Shi Xue Dou, M. Skyllas-Kazacos, “A Technology Review of Electrodes and Reaction Mechanisms in Vanadium Redox Flow Batteries. *J. Mater. Chem. A.* **3**(33), 16913–16933 (2015).
- [193] S. Zhong, C. Padeste, M. Kazacos, M. Skyllas-Kazacos, “Comparison of The Physical, Chemical and Electrochemical Properties of Rayon- and Polyacrylonitrile-based Graphite felt Electrodes”, *J. Power Sources* **45**(1), pp. 29–41 (1993).
- [194] Yang Zhao, Erin E. Taylor, Xudong Hu, Brian Evanko, Xiaojun Zeng, Hengbin Wang, Ryohji Ohnishi, Takaki Tsukazaki, Jian-Feng Li, Nicholas P. Stadie, Seung Joon Yoo, Galen D. Stucky, Shannon W. Boettcher, “What Structural Features Make Porous Carbons work for Redox-Enhanced Electrochemical Capacitors? A fundamental Investigation”, *ACS Energy Lett.* **6**(3), pp. 854–861 (2021).

- [195] Lei Zhang, Junpei Yue, Qi Deng, Wei Ling, Chun-Jiao Zhou, Xian-Xiang Zeng, Congshan Zhou, Xiong-Wei Wu, YuPing Wu, "Preparation of a Porous Graphite Felt Electrode for Advance Vanadium Redox Flow Batteries", *RSC Adv.* **10**(23), pp. 13374–13378 (2020).
- [196] Tao Liu, Xianfeng Li, Chi Xu, Huamin Zhang "Activated Carbon Fiber Paper Based Electrodes with High Electrocatalytic Activity for Vanadium Flow Batteries with Improved Power Density", *ACS Appl. Mater. Interfaces* **9**(5), pp. 4626–4633 (2017).
- [197] Yang Lv, Chunmei Yang, Haining Wang, Jin Zhang, Yan Xiang, Shanfu Lu "Antimony-Doped Tin Oxide as an Efficient Electrocatalyst Toward the  $\text{VO}^{2+}/\text{VO}_2^+$  Redox Couple of the Vanadium Redox Flow Battery", *Catal. Sci. Technol.* **10**(8), pp. 2484–2490 (2020).
- [198] Xian Xie, Yan Xiang, Walid A. Daoud, "MoO<sub>3</sub>- Deposited Graphite Felt for High Performance Vanadium Redox- Flow Batteries", *ACS Appl. Energy Mater.* **3**(11), pp. 10463–10476 (2020).
- [199] Sheeraz Mehboob, Ghulam Ali, Hyun-Jin Shin, Jinyeon Hwang, Saleem Abbas, Kyung Yoon Chung, Heung Yong Ha, "Enhancing the Performance of All Vanadium Redox Flow Batteries by Decorating Carbon Felt Electrodes with SnO<sub>2</sub> Nanoparticles", *Appl. Energy* **229**, pp. 910– 921 (2018).
- [200] Haipeng Zhou, Yi Shen, Jingyu Xi, Xinpeng Qiu, Liquan Chen "ZrO<sub>2</sub>-Nanoparticle Modified Graphite Felt: Bifunctional Effects on Vanadium Flow Batteries", *ACS Appl. Mater. Interfaces* 2016, **8**(24), pp. 15369–15378 (2016).
- [201] Bin Li, Meng Gu, Zimin Nie, Xiaoliang Wei, Chongmin Wang, Vincent Sprenkle, Wei Wang, "Nanorod Niobium Oxide as Powerful Catalysts for an All Vanadium Redox Flow Battery", *Nano Lett.* **14**(1), pp. 158–165 (2014).
- [202] Bin Li, Meng Gu, Zimin Nie, Yuyan Shao, Qingtao Luo, Xiaoliang Wei, Xiaolin Li, Jie Xiao, Chongmin Wang, Vincent Sprenkle, Wei Wang, "Bismuth Nanoparticle Decorating Graphite Felt as a High-Performance Electrode for an All-Vanadium Redox Flow Battery", *Nano Lett.* **13**(3), pp. 1330–1335 (2013).
- [203] Ki Jae Kim, Min-Sik Park, Jae-Hun Kim, Uk Hwang, Nam Jin Lee, Goojin Jeong, Young-Jun Kim, "Novel Catalytic Effect of Mn<sub>3</sub>O<sub>4</sub> for All Vanadium Redox Flow Batteries", *Chem. Commun.* **48**(44), pp. 5455–5457 (2012).
- [204] Bianting Sun, M. Skyllas-Kazakos, M. "Chemical Modification and Electrochemical Behaviour of Graphite Fibre in Acidic Vanadium Solution" *Electrochim. Acta* **36**(3-4), pp. 513–517 (1991).
- [205] Lei Zhang, Qiang Ma, Jun-Ping Hu, Jun Liu, Qi Deng, Pan Ning, Congshan Zhou, Xiongwei Wu, Yuping Wu, "Enhancing the Catalytic Kinetics of Electrodes by using a Multi-Dimensional Carbon Network for Applications in Vanadium Redox Flow Batteries", *ChemElectroChem.* **7**(4), pp. 1023– 1028 (2020).



- [206] Yang Yang, Xiao Sun, Zheng Cheng, Alolika Mukhopadhyay, Avi Natan, Chao Liu, Daxian Cao, Hongli Zhu “Functionalized Well-Aligned Channels Derived from Wood as a Convection- Enhanced Electrode for Aqueous Flow Batteries”, *ACS Appl. Energy Mater.* **3**(7), pp. 6249– 6257 (2020).
- [207] Miaolun Jiao, Tao Liu, Chaoji Chen, Meng Yue, Glenn Pastel, Yonggang Yao, Hua Xie, Wentao Gan, Amy Gong, Xianfeng Li, Liangbing Hu, “Holey Three-Dimensional Wood Based Electrode for Vanadium Flow Batteries”, *Energy Storage Mater.* **27**, pp. 327–332 (2020).
- [208] Yuchen Liu, Yi Shen, Lihong Yu, Le Liu, Feng Liang, Xinping Qiu, Jingyu Xi, “Holey Engineered Electrodes for Advanced Vanadium Flow Batteries”, *Nano Energy* **43**, pp. 55–62 (2018).
- [209] Guangjian Hu, Minghua Jing, Da-Wei Wang, Zhenhua Sun, Chuan Xu, Wencai Ren, Hui-Ming Cheng, Chuanwei Yan, Xinzhuang Fan, Feng Li, “A Gradient Bi-Functional Graphene-Based Modified Electrode for Vanadium Redox Flow Batteries” *Energy Storage Mater.* **13**, pp. 66–71 (2018).
- [210] Yingqiao Jiang, Ziheng Liu, Yanrong Lv, Ao Tang, Lei Dai, Ling Wang, Zhangxing He, “Perovskite Enables High Performance Vanadium Redox Flow battery”, *Chem. Eng. J.* **443**, pp.136341 (2022).
- [211] Zhen Jiang, Vitaly Alexandrov “Electrocatalytic Activity of Oxygen Functionalized Carbon Electrodes for Vanadium Redox Flow Batteries from Free-Energy Calculations”, *ACS Appl. Energy Mater.* **3**(8), pp. 7543–7549 (2020).
- [212] Alolika Mukhopadhyay, Yang Yang, Yifan Li, Yong Chen, Hongyan Li, Avi Natan, Yuanyue Liu, Daxian Cao, Hongli Zhu, “Mass Transfer and Reaction Kinetic Enhanced Electrode for High-Performance Aqueous Flow Batteries”, *Adv. Funct. Mater.* **29**(43), pp.1903192 (2019).
- [213] Peng Huang, Wei Ling, Hang Sheng, Yan Zhou, Xiaopeng Wu, Xian-Xiang Zeng, Xiongwei Wu, Yu-Guo Guo, “Heteroatom-doped Electrodes for All-Vanadium Redox Flow Batteries with Ultralong Lifespan”, *J. Mater. Chem. A* **6**(1), pp. 41–44 (2018).
- [214] H. R. Jiang, W. Shyy, L. Zeng, R. H. Zhang, T. S. Zhao, “Highly Efficient and Ultra-Stable Boron-Doped Graphite Felt Electrodes for Vanadium Redox Flow Batteries” *J. Mater. Chem. A* **6**(27), pp. 13244–13253 (2018).
- [215] Shuangyin Wang, Xinsheng Zhao, Thomas Cochell, Arumugam Manthiram, “Nitrogen Doped Carbon Nanotube/Graphite Felts as Advanced Electrode Materials for Vanadium Redox Flow Batteries”, *J. Phys. Chem. Lett.* **3**(16), pp. 2164–2167 (2012).
- [216] Minjoon Park, In-Yup Jeon, Jaechan Ryu, Jong-Beom Baek, Jaephil Cho, “Exploration of the Effective Location of Surface Oxygen Defects in Graphene-Based Electrocatalysts for All-Vanadium Redox-Flow Batteries”, *Adv. Energy Mater.* **5**(5), pp.1401550 (2015).

- [217] Wenyue Li, Zhenyu Zhang, Yongbing Tang, Haidong Bian, Tsz-Wai Ng, Wenjun Zhang, Chun-Sing Lee “Graphene-Nanowall-Decorated Carbon Felt with Excellent Electrochemical Activity Toward VO<sub>2</sub> +/VO<sub>2</sub><sup>+</sup> couple for All Vanadium Redox Flow Battery”, *Adv. Sci.* **3**(4), pp. 1500276 (2016).
- [218] Lantao Wu, Yi Shen, Lihong Yu, Jingyu Xi, Xinping Qiu “Boosting Vanadium Flow Battery Performance by Nitrogen-doped Carbon Nanospheres Electrocatalyst”, *Nano Energy* **28**, pp. 19–28 (2016).
- [219] Sangki Park, Hansung Kim, “Fabrication of Nitrogen-Doped Graphite Felts as Positive Electrodes using Polypyrrole as a Coating Agent in Vanadium Redox Flow Batteries”, *J. Mater. Chem. A* **3**(23), pp.12276– 12283 (2015).
- [220] Chulsang Youn, Wook Ahn, Shin Ae Song, Kiyong Kim, Ju Young Woo, Sung Nam Lim, “High-Power Vanadium Redox Flow Battery Based on N-S- Dual Functionalized Graphite Felt”, *J. Electrochem. Soc.* **167**(11), pp.110530 (2020).
- [221] Wei Ling, Qi Deng, Qiang Ma, Hong-Rui Wang, Chun-Jiao Zhou, Jian-Kai Xu, Ya-Xia Yin, Xiong-Wei Wu, Xian-Xiang Zeng, Yu-Guo Guo, “Hierarchical Carbon Micro/Nanonetwork with Superior Electrocatalysis for High-Rate and Endurable Vanadium Redox Flow Batteries” *Adv. Sci.* **5**(12), pp.1801281 (2018).
- [222] Hao Jiang, Dalal Alezi, Mohamed Eddaoudi “A Reticular Chemistry Guide for The Design of Periodic Solids”, *Nat. Rev. Mater.* **6**(6), pp. 466–487 (2021).
- [223] Yuanjing Cui, Bin Li, Huajun He, Wei Zhou, Banglin Chen, Guodong Qian, “Metal-organic Framework as Platform for Functional Materials”, *Acc. Chem. Res.* **49**(3), pp. 483–493 (2016).
- [224] Hong-Cai Zhou, Jeffrey R. Long, Omar M. Yaghi, “Introduction to Metal-Organic Frameworks” *Chem. Rev.* **112**(2), pp. 673–674 (2012).
- [225] Hai-Long Jiang, Qiang Xu, “Porous Metal-Organic Frameworks as Platforms for Functional Applications”, *Chem. Commun.* **47**(12), pp. 3351–3370 (2011).
- [226] Jun-Dong Yi, Duan-Hui Si, Ruikuan Xie, Qi Yin, Meng-Di Zhang, Qiao Wu, Guo-Liang Chai, Yuan-Biao Huang, Rong Cao “Conductive Two-Dimensional Phthalocyanine-based Metal-Organic Framework Nanosheets for efficient Electroreduction of CO<sub>2</sub>” *Angew. Chem., Int. Ed.* **60**(31), pp. 17108–17114 (2021).
- [227] Gilbert C. Walker, Sai Sriharsha M. Konda, Tapas Kumar Maji, Kirk S. Schanze “Preface to the “Metal-Organic Frameworks: Fundamental Study and Applications” Joint Virtual Issue”, *Langmuir* **36**(49), pp. 14901–14903 (2020).
- [228] A. Schneemann, V. Bon, I. Schwedler, I. Senkovska, S. Kaskel, R. A. Fischer, “Flexible Metal-Organic Frameworks”, *Chem. Soc. Rev.* **43**(16), pp. 6062–6096 (2014).
- [229] Yang Song, Pengchao Ruan, Caiwang Mao, Yuxin Chang, Ling Wang, Lei Dai, Peng Zhou, Bingan Lu, Jiang Zhou, Zhangxing He “Metal-Organic Frameworks

- Functionalized Separators for Robust Aqueous Zinc-Ion Batteries”, *Nano-Micro Lett.* **14**, pp. 218 (2022)
- [230] Rahul R. Salunkhe, Yusuf V. Kaneti, Yusuke Yamauchi, “Metal-Organic Framework-Derived Nanoporous Metal Oxides toward Supercapacitor Applications: Progress and Prospects”, *ACS Nano* **11**(6), pp. 5293– 5308 (2017).
- [231] Bao Yu Xia, Ya Yan, Nan Li, Hao Bin Wu, Xiong Wen (David) Lou, Xin Wang, “A Metal-Organic Framework-Derived Bifunctional Oxygen Electrocatalyst” *Nat. Energy* **1**(1), pp. 15006 (2016).
- [232] Wei Xia, Asif Mahmood, Ruqiang Zou, Qiang Xu “Metal-Organic Framework and Their Derived Nanostructures for Electrochemical Energy Storage and Conversion” *Energy Environ. Sci.* **8**(7), pp 1837– 1866 (2015).
- [233] Tian Yi Ma, Sheng Dai, Mietek Jaroniec, Shi Zhang Qiao “Metal–Organic Framework Derived Hybrid  $\text{Co}_3\text{O}_4$ -Carbon Porous Nanowire Arrays as Reversible Oxygen Evolution Electrodes” *J. Am. Chem. Soc.* **136**(39), pp. 13925–13931 (2014).
- [234] Seung Jae Yang, Taehoon Kim, Ji Hyuk Im, Yern Seung Kim, Kunsil Lee, Haesol Jung, Chong Rae Park, “MOF-Derived Hierarchically Porous Carbon with Exceptional Porosity and Hydrogen Storage Capacity” *Chem. Mater.* **24**(3), pp. 464–470 (2012).
- [235] Xue Feng Lu, Yongjin Fang, Deyan Luan, Xiong Wen David Lou, “Metal–Organic Frameworks Derived Functional Materials for Electrochemical Energy Storage and Conversion: A Mini Review”, *Nano Lett.* **21**(4), pp. 1555– 1565 (2021).
- [236] Lide Oar-Arteta, Tim Wezendonk, Xiaohui Sun, Freek Kapteijn, Jorge Gascon “Metal Organic Frameworks as Precursors for the Manufacture of Advanced Catalytic Materials”, *Mater. Chem. Front.* **1**(9), pp. 1709– 1745 (2017).
- [237] Yingqiao Jiang, Gang Cheng, Yuehua Li, Zhangxing He, Jing Zhu, Wei Meng, Lei Dai, Ling Wang, “Promoting Vanadium Redox Flow Battery Performance by Ultra-Uniform  $\text{ZrO}_2$ @C from Metal-Organic Framework”, *Chem. Eng. J.* **415**, pp. 129014 (2021).
- [238] Yang Li, Lianbo Ma, Zhibin Yi, Yunhe Zhao, Jiatao Mao, Shida Yang, Wenqing Ruan, Diwen Xiao, Nauman Mubarak, Junxiong Wu, Tian-Shou Zhao, Qing Chen, Jang-Kyo Kim, “Metal-Organic Framework-Derived Carbon as a Positive Electrode for High-Performance Vanadium Redox Flow Batteries” *J. Mater. Chem. A* **9**(9), pp. 5648–5656 (2021).
- [239] Chanho Noh, Chang Soo Lee, Won Seok Chi, Yongjin Chung, Jong Hak Kim, Yongchai Kwon “Vanadium Redox Flow Battery Using Electrocatalyst Decorated with Nitrogen-Doped Carbon Nanotubes Derived from Metal-Organic Frameworks”, *J. Electrochem. Soc.* **165**(7), pp. A1388–A1399 (2018).

- [240] Krista S. Walton, Randall Q. Snurr, “Applicability of the BET Method for Determining Surface Areas of Microporous Metal-Organic Frameworks” *J. Am. Chem. Soc.* **129**(27), pp. 8552–8556 (2007).
- [241] Harsh Sharma, Milan Kumar, “Enhancing power density of a vanadium redox flow battery using modified serpentine channels”, *J. Power Sources* **494**, pp. 229753 (2021).
- [242] Bo Liu, Hiroshi Shioyama, Tomoki Akita, Qiang Xu “Metal-Organic Framework as a Template for Porous Carbon Synthesis”, *J. Am. Chem. Soc.* **130**(16), pp. 5390–5391 (2008).
- [243] Charles Tai-Chieh Wan, Diego López Barreiro, Antoni Forner-Cuenca, Jack-William Barotta, Morgan J. Hawker, Gang Han, Hyun-Chae Loh, Admir Masic, David L. Kaplan, Yet-Ming Chiang, Fikile R. Brushett, Francisco J. Martin-Martinez, Markus J. Buehler, “Exploration of Biomass-Derived Activated Carbons for Use in Vanadium Redox Flow Batteries”, *ACS Sustainable Chem. Eng.* **8**(25), pp. 9472–9482 (2020).
- [244] Zhangxing He, Lang Shi, Junxi Shen, Zhen He, Suqin Liu, “Effects of Nitrogen Doping on The Electrochemical Performance of Graphite Felts for Vanadium Redox Flow Batteries” *Int. J. Energy Res.* **39**(5), pp. 709– 716 (2015).
- [245] Tao Liu, Xianfeng Li, Chi Xu, Huamin Zhang “Activated Carbon Fiber Paper Based Electrodes with High Electrocatalytic Activity for Vanadium Flow Batteries with Improved Power Density”, *ACS Appl. Mater. Interface* **9**(5), pp. 4626-4633 (2017).
- [246] Chulsang Youn, Wook Ahn, Shin Ae Song, Kiyoung Kim, Ju Young Woo, Sung Nam Lim “High-Power Vanadium Redox Flow Battery Based on N-S-Dual Functionalized Graphite Felt” *J. Electrochem. Soc.* **167**(11), pp. 110530 (2020).
- [247] Charles Tai-Chieh Wan, Diego López Barreiro, Antoni Forner-Cuenca, Jack-William Barotta, Morgan J. Hawker, Gang Han, Hyun-Chae Loh, Admir Masic, David L. Kaplan, Yet-Ming Chiang, Fikile R. Brushett, Francisco J. Martin-Martinez, Markus J. Buehler, “Exploration of Biomass-derived Activated Carbons for Use in Vanadium Redox Flow Batteries. *ACS Sustainable Chem. Eng.* **8**(25), pp. 9472-9482 (2020).
- [248] Saleem Abbas, Sheeraz Mehboob, Hyun-Jin Shin, Oc Hee Han, Heung Yong Ha, “Highly Functionalized Nanoporous Thin Carbon Paper Electrodes for High Energy Density of Zero-gap Vanadium Redox Flow Battery”, *Chemical Engineering Journal* **378**, pp. 122190 (2019).
- [249] Minjoon Park, Yang-jae Jung, Jungyun Kim, Ho il Lee, Jeaphil Cho, “Synergistic Effect of Carbon Nanofiber/Nanotube Composite Catalyst on Carbon Felt Electrode for High-Performance All-Vanadium Redox Flow Battery”, *Nano Lett.* **13**(10), pp. 4833-4839 (2013).
- [250] Zhangxing He, Lang Shi, Junxi Shen, Zhen He, Suqin Liu, “Effects of Nitrogen Doping on the Electrochemical Performance of Graphite Felts for Vanadium Redox Flow Batteries”, *Int. J. Energy Res.* 2015, **39**(5), pp. 709-716 (2015).

- [251] Rudra Kumar, Thiruvolu Bhuvana, Ashutosh Sharma “Tire Waste Derived Turbostratic Carbon as an Electrode for a Vanadium Redox Flow Battery”, *ACS Sustainable Chem. Eng.* **6**(7), pp. 8238-8246 (2018).
- [252] Wenyue Li, Jianguo Liu, Chuanwei Yan, “Multi-walled Carbon Nanotubes Used as an Electrode Reaction Catalyst for  $\text{VO}_2^+/\text{VO}^{2+}$  for a Vanadium Redox Flow Battery”, *Carbon* **49**(11), pp. 3463-3470 (2011).
- [253] Wenyue Li, Jianguo Liu, Chuanwei Yan, “The Electrochemical Catalytic Activity of Single-walled Carbon Nanotubes towards  $\text{VO}_2^+/\text{VO}^{2+}$  and  $\text{V}^{3+}/\text{V}^{2+}$  Redox pairs for an all Vanadium Redox Flow Battery” *Electrochim. Acta.* **79**, pp.102-108 (2012).
- [254] Wenyue Li, Jianguo Liu, Chuanwei Yan, “Reduced Graphene oxide with Tunable C/O ratio and its activity towards Vanadium Redox Pairs for an all Vanadium Redox Flow Battery”, *Carbon* **55**, pp. 313- 320 (2013).
- [255] Mani Ulaganathan, Akshay Jain, Vanchiappan Aravindan, Sundaramurthy Jayaraman, Wong Chui Ling, Tuti Mariana Lim, Madapusi P. Srinivasan, Qingyu Yan, Srinivasan Madhavi, “Bio-mass Derived Mesoporous Carbon as Superior Electrode in all Vanadium Redox Flow Battery with Multicouple Reactions”, *J. Power Sources* **274**, pp. 846- 850 (2015).
- [256] Shuangyin Wang, Xinsheng Zhao, Thomas Cochell, Arumugam Manthiram, “Nitrogen-Doped Carbon Nanotube/Graphite Felts as Advanced Electrode Materials for Vanadium Redox Flow Batteries”, *J. Phys. Chem. Lett.* **3**(16), pp. 2164-2167 (2012).
- [257] Zhangxing He, Lei Liu, Chao Gao, Zhi Zhou, Xinxing Liang, Ying Lei, Zhen He, Suqin Liu “Carbon Nanofibers Grown on the Surface of Graphite Felt by Chemical Vapour Deposition for Vanadium Redox Flow Batteries”, *RSC Adv.* **3**(43), pp. 19774-19777 (2013).
- [258] Miaolun Jiao, Tao Liu, Chaoji Chen, Meng Yue, Glenn Pastel, Yonggang Yao, Hua Xie, Wentao Gan, Amy Gong, Xianfeng Li, Liangbing Hu, “Holey Three-Dimensional Wood Based Electrode for Vanadium Flow Batteries”, *Energy Storage Mater.* **27**, pp. 327–332 (2020).
- [259] W.H. Wang, X.D. Wang “Investigation of Ir-Modified Carbon Felt as the Positive Electrode of an All-Vanadium Redox Flow Battery”, *Electrochim. Acta* **52**(24), pp. 6755-6762 (2007).
- [260] Ki Jae Kim, Min-Sik Park, Jae-Hun Kim, Uk Hwang, Nam Jin Lee, Goojin Jeong, Young-Jun Kim, “Novel Catalytic Effect of  $\text{Mn}_3\text{O}_4$  for All Vanadium Redox Flow Batteries”, *Chem. Commun.* **48**(44), pp. 5455–5457 (2012).
- [261] Anteneh Wodaje Bayeh, Daniel Manaye Kabtamu, Yu-Chung Chang, Guan-Cheng Chen, Hsueh-Yu Chen, Guan-Yi Lin, Ting-Ruei Liu, Tadele Hunde Wondimu, Kai-Chin Wang, Chen-Hao Wang “ $\text{Ta}_2\text{O}_5$  Nanoparticle-Modified Graphite Felt as a High-Performance Electrode for a Vanadium Redox Flow Battery” *ACS Sustainable Chem. Eng.* **6**(3), pp. 3019-3028 (2018).

- [262] Anteneh Wodaje Bayeh, Guan-Yi Lin, Yu-Chung Chang, Daniel Manaye Kabtamu, Guan-Cheng Chen, Hsueh-Yu Chen, Kai-Chin Wang, Yao-Ming Wang, Tai-Chin Chiang, Hsin-Chih Huang, Chen-Hao Wang, “Oxygen-Vacancy-Rich Cubic CeO<sub>2</sub> Nanowires as Catalysts for Vanadium Redox Flow Batteries”, *ACS Sustainable Chem. Eng.* **8**(45), pp. 16757-16765 (2020).
- [263] Daniel Manaye Kabtamu, Jian-Yu Chen, Yu-Chung Chang, Chen-Hao Wang, “Electrocatalytic Activity of Nb doped Hexagonal WO<sub>3</sub> Nanowire-Modified Graphite Felt as a Positive Electrode for Vanadium Redox Flow Batteries”, *J. Mater. Chem. A.* **4**(29), pp. 11472-11480 (2016).
- [264] Chanhoh Noh, Chang Soo Lee, Won Seok Chi, Yongjin Chung, Jong Hak Kim, Yongchai Kwon “Vanadium Redox Flow Battery Using Electrocatalyst Decorated with Nitrogen-Doped Carbon Nanotubes Derived from Metal-Organic Frameworks”, *J. Electrochem. Soc.* **165**(7), pp. A1388–A1399 (2018).
- [265] Yang Li, Lianbo Ma, Zhibin Yi, Yunhe Zhao, Jiatao Mao, Shida Yang, Wenqing Ruan, Diwen Xiao, Nauman Mubarak, Junxiong Wu, Tian-Shou Zhao, Qing Chen, Jang-Kyo Kim, “Metal-Organic Framework-Derived Carbon as a Positive Electrode for High-Performance Vanadium Redox Flow Batteries” *J. Mater. Chem. A* **9**(9), pp. 5648–5656 (2021).
- [266] Yingqiao Jiang, Gang Cheng, Yuehua Li, Zhangxing He, Jing Zhu, Wei Meng, Lei Dai, Ling Wang, “Promoting Vanadium Redox Flow Battery Performance by Ultra-Uniform ZrO<sub>2</sub>@C from Metal-Organic Framework”, *Chem. Eng. J.* **415**, pp. 129014 (2021).
- [267] Mark K. Debe, “Electrocatalyst Approaches and Challenges for Automotive Fuel Cells”, *Nature* **486**(7401), pp. 43–51 (2012).
- [268] Brian C. H. Steele, Angelika Heinzl, “Materials for Fuel-Cell Technologies” *Nature* **414**(6861), pp. 345–352 (2001).
- [269] Jie Zhang, Qixing Zhou, Yawen Tang, Liang Zhang, Yanguang Li, “Zinc–Air Batteries: Are They Ready for Prime Time?”, *Chem. Sci.* **10**(39), pp. 8924–8929 (2019).
- [270] Zequan Zhao, Xiayue Fan, Jia Ding, Wenbin Hu, Cheng Zhong, Jun Lu, “Challenges in Zinc Electrodes for Alkaline Zinc–Air Batteries: Obstacles to Commercialization”, *ACS Energy Lett.* **4**(9), pp. 2259–2270 (2019).
- [271] Xin Gong, Shanshan Liu, Chuying Ouyang, Peter Strasser, Ruizhi Yang, “Nitrogen- and Phosphorus-Doped Biocarbon with Enhanced Electrocatalytic Activity for Oxygen Reduction”, *ACS Catal.* **5**(2), pp. 920–927 (2015).
- [272] Yao Nie, Li Li, Zidong Wei, “Recent Advancements in Pt and Pt-free Catalysts for Oxygen Reduction Reaction”, *Chem. Soc. Rev.* **44**(8), pp. 2168–2201 (2015).
- [273] Yong-Sheng Wei, Mei Zhang, Ruqiang Zou, Qiang Xu “Metal–Organic Framework-Based Catalysts with Single Metal Sites”, *Chem. Rev.* **120**(21), pp.12089–12174 (2020).

- [274] Frédéric Jaouen, Eric Proietti, Michel Lefèvre, Régis Chenitz, Jean-Pol Dodelet, Gang Wu, Hoon Taek Chung, Christina Marie Johnston, Piotr Zelenay “Recent Advances in Non-Precious Metal Catalysis for Oxygen-Reduction Reaction in Polymer Electrolyte Fuel Cells”, *Energy Environ. Sci.* **4**(1), pp. 114–130 (2011).
- [275] Qi Zhang, Mi Peng, Zirui Gao, Wendi Guo, Zehui Sun, Yi Zhao, Wu Zhou, Meng Wang, Bingbao Mei, Xian-Long Du, Zheng Jiang, Wei Sun, Chao Liu, Yifeng Zhu, Yong-Mei Liu, He-Yong He, Zhen Hua Li, Ding Ma, Yong Cao “Nitrogen-Neighbored Single-Cobalt Sites Enable Heterogeneous Oxidase-Type Catalysis” *J. Am. Chem. Soc.* **145**(7), pp. 4166–4176 (2023).
- [276] Manoj B. Gawande, Paolo Fornasiero, Radek Zbořil, “Carbon-Based Single-Atom Catalysts for Advanced Applications”, *ACS Catal.* **10**(3), pp. 2231–2259 (2020).
- [277] Aiqin Wang, Jun Li, Tao Zhang, “Heterogeneous Single-Atom Catalysis”, *Nat. Rev. Chem.* **2**(6), pp. 65–81 (2018).
- [278] Selina K. Kaiser, Zupeng Chen, Dario Faust Akl, Sharon Mitchell, Javier Pérez-Ramírez, “Single-Atom Catalysts Across the Periodic Table” *Chem. Rev.* **120**(21), pp. 11703–11809 (2020).
- [279] Jérémie D. A. Pelletier, Jean-Marie Basset, “Catalysis by Design: Well-Defined Single-Site Heterogeneous Catalysts”, *Acc. Chem. Res.* **49**(4), pp. 664–677 (2016).
- [280] Sharon Mitchell, Evgeniya Vorobyeva, Javier Pérez-Ramírez, “The Multifaceted Reactivity of Single-Atom Heterogeneous Catalysts”, *Angew. Chem., Int. Ed.* **57**(47), pp. 15316–15329 (2018).
- [281] Jun Li, Maria Flytzani Stephanopoulos, Younan Xia “Introduction: Heterogeneous Single-Atom Catalysis”, *Chem. Rev.* **120**(21), pp. 11699–11702 (2020).
- [282] Long Jiao, Juntong Zhu, Yan Zhang, Weijie Yang, Siyuan Zhou, Aowen Li, Chenfan Xie, Xusheng Zheng, Wu Zhou, Shu-Hong Yu, Hai-Long Jiang “Non-Bonding Interaction of Neighboring Fe and Ni Single-Atom Pairs on MOF-Derived N-Doped Carbon for Enhanced CO<sub>2</sub> Electroreduction”, *J. Am. Chem. Soc.* **143**(46), pp. 19417–19424 (2021).
- [283] Chengzhou Zhu, Shaofang Fu, Qiurong Shi, Dan Du, Yuehe Lin “Single-Atom Electrocatalysts” *Angew. Chem., Int. Ed.* **56**(45), pp. 13944–13960 (2017).
- [284] Yuxuan Wang, Hongyang Su, Yanghua He, Ligui Li, Shangqian Zhu, Hao Shen, Pengfei Xie, Xianbiao Fu, Guangye Zhou, Chen Feng, Dengke Zhao, Fei Xiao, Xiaojing Zhu, Yachao Zeng, Minhua Shao, Shaowei Chen, Gang Wu, Jie Zeng, Chao Wang, “Advanced Electrocatalysts with Single-Metal-Atom Active Sites”, *Chem. Rev.* **120**(21), pp. 12217–12314 (2020).
- [285] Quanchen Feng, Xingli Wang, Malte Klingenhof, Marc Heggen, Peter Strasser, “Low-Pt NiNC-Supported PtNi Nanoalloy Oxygen Reduction Reaction Electrocatalysts-In Situ Tracking of the Atomic Alloying Process”, *Angew. Chem., Int. Ed.* **61**(36), pp. e202203728 (2022).

- [286] Xiang Ao, Wei Zhang, Bote Zhao, Yong Ding, Gyutae Nam, Luke Soule, Ali Abdelhafiz, Chundong Wang, Meilin Liu, “Atomically Dispersed Fe-N-C Decorated with Pt-Alloy Core-Shell Nanoparticles for Improved Activity and Durability towards Oxygen Reduction”, *Energy Environ. Sci.* **13**(9), pp. 3032–3040 (2020).
- [287] Bowen Liu, Ruohan Feng, Michael Busch, Sihong Wang, Haofei Wu, Pan Liu, Jiajun Gu, Ashkan Bahadoran, Daiju Matsumura, Takuya Tsuji, Di Zhang, Fang Song, Qinglei Liu, “Synergistic Hybrid Electrocatalysts of Platinum Alloy and Single-Atom Platinum for an Efficient and Durable Oxygen Reduction Reaction” *ACS Nano* **16**(9), pp. 14121–14133 (2022).
- [288] Wen-Jie Jiang, Lin Gu, Li Li, Yun Zhang, Xing Zhang, Lin-Juan Zhang, Jian-Qiang Wang, Jin-Song Hu, Zidong Wei, Li-Jun Wan, “Understanding the High Activity of Fe-N-C Electrocatalysts in Oxygen Reduction: Fe/Fe<sub>3</sub>C Nanoparticles Boost the Activity of Fe-N<sub>x</sub>”, *J. Am. Chem. Soc.* **138**(10), 3570–3578 (2016).
- [289] Chang-Xin Zhao, Bo-Quan Li, Jia-Ning Liu, Qiang Zhang, “Intrinsic Electrocatalytic Activity Regulation of M–N–C Single-Atom Catalysts for Oxygen Reduction Reaction”, *Angew. Chem. Int. Ed.* **60**(9), pp. 4448–4463 (2021).
- [290] Chengzhang Wan, Xiangfeng Duan, Yu Huang, “Molecular Design of Single-Atom Catalysts for Oxygen Reduction Reaction”, *Adv. Energy Mater.* **10**(14), pp. 1903815 (2020).
- [291] Chun-Chao Hou, Lianli Zou, Liming Sun, Kexin Zhang, Zheng Liu, Yinwei Li, Caixia Li, Ruqiang Zou, Jihong Yu, Qiang Xu, “Single-Atom Iron Catalysts on Overhang-Eave Carbon Cages for High-Performance Oxygen Reduction Reaction”, *Angew. Chem. Int. Ed.* **59**(19), pp. 7384–7389 (2020).
- [292] Peiqun Yin, Tao Yao, Yuen Wu, Lirong Zheng, Yue Lin, Wei Liu, Huanxin Ju, Junfa Zhu, Xun Hong, Zhaoxiang Deng, Gang Zhou, Shiqiang Wei, Yadong Li, “Single Cobalt Atoms with Precise N-Coordination as Superior Oxygen Reduction Reaction Catalysts”, *Angew. Chem. Int. Ed.* **55**(36), pp. 1–7 (2016).
- [293] Jiazhan Li, Mengjie Chen, David A. Cullen, Sooyeon Hwang, Maoyu Wang, Boyang Li, Kexi Liu, Stavros Karakalos, Marcos Lucero, Hanguang Zhang, Chao Lei, Hui Xu, George E. Sterbinsky, Zhenxing Feng, Dong Su, Karren L. More, Guofeng Wang, Zhenbo Wang, Gang Wu, “Atomically Dispersed Manganese Catalysts for Oxygen Reduction in Proton-Exchange Membrane Fuel cells”, *Nat. Catal.* **1**(12), pp. 935–945 (2018).
- [294] Xiaohong Xie, Cheng He, Boyang Li, Yanghua He, David A. Cullen, Evan C. Wegener, A. Jeremy Kropf, Ulises Martinez, Yingwen Cheng, Mark H. Engelhard, Mark E. Bowden, Miao Song, Teresa Lemmon, Xiaohong S. Li, Zimin Nie, Jian Liu, Deborah J. Myers, Piotr Zelenay, Guofeng Wang, Gang Wu, Vijay Ramani, Yuyan Shao, “Performance Enhancement and Degradation Mechanism Identification of a Single-Atom Co-N-C Catalyst for Proton Exchange Membrane Fuel Cells”, *Nat. Catal.* **3**(12), pp. 1044–1054 (2020).



- [295] Jing Wang, Wei Liu, Gan Luo, Zhijun Li, Chao Zhao, Haoran Zhang, Mengzhao Zhu, Qian Xu, Xiaoqian Wang, Changming Zhao, Yunteng Qu, Zhengkun Yang, Tao Yao, Yafei Li, Yue Lin, Yuen Wu, Yadong Li “Synergistic Effect of Well-Defined Dual Sites Boosting the Oxygen Reduction Reaction”, *Energy Environ. Sci.* **11**(12), pp. 3375–3379 (2018).
- [296] Ziyang Lu, Bo Wang, Yongfeng Hu, Wei Liu, Yufeng Zhao, Ruouo Yang, Zhiping Li, Jun Luo, Bin Chi, Zheng Jiang, Minsi Li, Shichun Mu, Shijun Liao, Jiujun Zhang, Xueliang Sun “An Isolated Zinc–Cobalt Atomic Pair for Highly Active and Durable Oxygen Reduction”, *Angew. Chem. Int. Ed.* **58**(9), pp. 2622–2626 (2019).
- [297] Xiaopeng Han, Xiaofei Ling, Deshuang Yu, Dengyu Xie, Linlin Li, Shengjie Peng, Cheng Zhong, Naiqin Zhao, Yida Deng, Wenbin Hu, “Atomically Dispersed Binary Co–Ni Sites in Nitrogen-Doped Hollow Carbon Nanocubes for Reversible Oxygen Reduction and Evolution”, *Adv. Mater.* **31**(49), pp. 1905622 (2019).
- [298] Shipeng Gong, Changlai Wang, Peng Jiang, Lin Hu, Hu Lei, Qianwang Chen, “Designing Highly Efficient Dual-Metal Single-Atom Electrocatalysts for Oxygen Reduction Reaction Inspired by Biological Enzyme System. *J. Mater. Chem. A* **6**(27), 13254–13262 (2018).
- [299] Subhajit Sarkar, Ashmita Biswas, Taniya Purkait, Manisha Das, Navpreet Kamboj, Ramendra Sundar Dey, “Unravelling the Role of Fe–Mn Binary Active Sites Electrocatalyst for Efficient Oxygen Reduction Reaction and Rechargeable Zn–Air Batteries” *Inorg. Chem.* **59**(7), pp. 5194–5205 (2020).
- [300] Diyang Zhang, Wenxing Chen, Zhi Li, Yuanjun Chen, Lirong Zheng, Yue Gong, Qiheng Li, Rongan Shen, Yunhu Han, Weng-Chon Cheong, Lin Gu, Yadong Li, “Isolated Fe and Co Dual Active Sites on Nitrogen-Doped Carbon for Highly Efficient Oxygen Reduction Reaction”, *Chem. Commun.* **54**(34), pp. 4274–4277 (2018).
- [301] Subhajit Sarkar, Ashmita Biswas, Erakulan E Siddharthan, Ranjit Thapa, Ramendra Sundar Dey, “Strategic Modulation of Target-Specific Isolated Fe,Co Single-Atom Active Sites for Oxygen Electrocatalysis Impacting High Power Zn–Air Battery”, *ACS Nano* **16**(5), pp. 7890–7903 (2022).
- [302] Mengjie Liu, Hoje Chun, Tsung-Cheng Yang, Sung Jun Hong, Chia-Min Yang, Byungchan Han, Lawrence Yoon Suk Lee, “Tuning the Site-to-Site Interaction in Ru–M (M = Co,Fe, Ni) Diatomic Electrocatalysts to Climb up the Volcano Plot of Oxygen Electroreduction”, *ACS Nano* **16**(7), pp. 10657–10666 (2022).
- [303] Ming Liu, Na Li, Shoufu Cao, Xuemin Wang, Xiaoqing Lu, Lingjun Kong, Yunhua Xu, Xian-He Bu, “A Pre-Constrained Metal Twins” Strategy to Prepare Efficient Dual-Metal-Atom Catalysts for Cooperative Oxygen Electrocatalysis”, *Adv. Mater.* **34**(7), pp. 2107421 (2022).
- [304] Hongwei Zhang, Xindie Jin, Jong-Min Lee, Xin Wang, “Tailoring of Active Sites from Single to Dual Atom Sites for Highly Efficient Electrocatalysis”, *ACS Nano* **16**(11), pp. 17572–17592 (2022).

- [305] Gege Yang, Jiawei Zhu, Pengfei Yuan, Yongfeng Hu, Gan Qu, Bang-An Lu, Xiaoyi Xue, Hengbo Yin, Wenzheng Cheng, Junqi Cheng, Wenjing Xu, Jin Li, Jinsong Hu, Shichun Mu, Jia-Nan Zhang, “Regulating Fe-spin State by Atomically Dispersed Mn-N in Fe-N-C Catalysts with High Oxygen Reduction Activity”, *Nat. Commun.* **12**(1), pp. 1734 (2021).
- [306] Junhong Fu, Jinhu Dong, Rui Si, Keju Sun, Junying Zhang, Mingrun Li, Nana Yu, Bingsen Zhang, Mark G. Humphrey, Qiang Fu, Jiahui Huang, “Synergistic Effects for Enhanced Catalysis in a Dual Single-Atom Catalyst”, *ACS Catal.* **11**(4), pp. 1952–1961 (2021).
- [307] Yuhan Xie, Xin Chen, Kaian Sun, Jinqiang Zhang, Wei-Hong Lai, Hao Liu, Guoxiu Wang, “Direct Oxygen-Oxygen Cleavage through Optimizing Interatomic Distances in Dual Single-atom Electrocatalysts for Efficient Oxygen Reduction Reaction”, *Angew. Chem. Int. Ed.* **62**(17), pp. e202301833 (2023).
- [308] Wanlin Zhou, Hui Su, Weiren Cheng, Yuanli Li, Jingjing Jiang, Meihuan Liu, Feifan Yu, Wei Wang, Shiqiang Wei, Qinghua Liu “Regulating the Scaling Relationship for High Catalytic Kinetics and Selectivity of the Oxygen Reduction Reaction”, *Nat. Commun.* **13**(1), pp. 6414 (2022).
- [309] Tingting Cui, Yun-Peng Wang, Tong Ye, Jiao Wu, Zhiqiang Chen, Jiong Li, Yongpeng Lei, Dingsheng Wang, Yadong Li, “Engineering Dual Single-Atom Sites on 2D Ultrathin N-doped Carbon Nanosheets Attaining Ultra-Low-Temperature Zinc Air Battery”, *Angew. Chem., Int. Ed.* **61**(12), pp. e202115219 (2022).
- [310] Jing Wang, Zhengqing Huang, Wei Liu, Chunran Chang, Haolin Tang, Zhijun Li, Wenxing Chen, Chunjiang Jia, Tao Yao, Shiqiang Wei, Yuen Wu, Yadong Li, “Design of N-Coordinated Dual-Metal Sites: A Stable and Active Pt-Free Catalyst for Acidic Oxygen Reduction Reaction”, *J. Am. Chem. Soc.* **139**(48), pp. 17281–17284 (2017).
- [311] Yaodan Zhou, Wen Yang, Wellars Utetiwabo, Yi-Meng Lian, Xue Yin, Lei Zhou, Peiwen Yu, Renjie Chen, Shaorui Sun, “Revealing of Active Sites and Catalytic Mechanism in N-Coordinated Fe, Ni Dual-Doped Carbon with Superior Acidic Oxygen Reduction than Single-Atom Catalyst”, *J. Phys. Chem. Lett.* **11**(4), pp. 1404–1410 (2020).
- [312] Yan Xu, Wenyuan Li, Long Chen, Wenzhang Li, Wenhui Feng, Xiaoqing Qiu, “Regulating the N-Coordination Structure of Fe–Fe Dual Sites as the Electrocatalyst for the O<sub>2</sub> Reduction Reaction in Metal–Air Batteries”, *Inorg. Chem.* **62**(13), pp. 5253–5261 (2023).
- [313] Hong-Cai Zhou, Jeffrey R. Long, Omar M. Yaghi, “Introduction to Metal–Organic Frameworks”, *Chem. Rev.* **112**(2), pp. 673–674 (2012).
- [314] Haigen Huang, Kui Shen, Fengfeng Chen, Yingwei Li, “Metal–Organic Frameworks as a Good Platform for the Fabrication of Single-Atom Catalysts. *ACS Catal.* **10**(12), pp. 6579–6586 (2020).

- [315] Chun-Chao Hou, Hao-Fan Wang, Caixia Li, Qiang Xu “From Metal–Organic Frameworks to Single/Dual-atom and Cluster Metal Catalysts for Energy Applications”, *Energy Environ. Sci.* **13**(6), pp. 1658-1693 (2020).
- [316] Siru Chen, Ming Cui, Zehao Yin, Jiabin Xiong, Liwei Mi, Yanqiang Li, “Single-Atom and Dual-Atom Electrocatalysts Derived from Metal Organic Frameworks: Current Progress and Perspectives”, *ChemSusChem* **14**(1), pp. 73–93 (2021).
- [317] A. K. Poswal, A. Agrawal, A. K. Yadav, C. Nayak, S. Basu, S. R. Kane, C. K. Garg, D. Bhattacharyya, S. N. Jha, N. K. Sahoo “Commissioning and first results of scanning type EXAFS beamline (BL-09) at INDUS-2 synchrotron source”, *AIP Conference Proceedings* **1591**(1), pp. 649-651 (2014).
- [318] S. Basu, C. Nayak, A. K. Yadav, A. Agrawal, A. K. Poswal, D. Bhattacharyya, S. N. Jha, N K Sahoo “A comprehensive facility for EXAFS measurements at the INDUS-2 synchrotron source at RRCAT, Indore, India”, *Journal of Physics: Conference Series* **493**, pp. 012032 (2014).
- [319] M. Newville, B. Ravel, D. Haskel, J.J. Rehr, E.A. Stern, Y. Yacoby, “Analysis of multiple scattering XAFS data using theoretical standards”, *Physica B: Condensed Matter* **208-209**, pp. 154-156 (1995).
- [320] G. Kresse, J. Hafner, “Ab initio molecular dynamics for liquid metals”, *Phys. Rev. B* **47**(1), pp. 558 (1993).
- [321] John P. Perdew, Kieron Burke, Matthias Ernzerhof, “Generalized gradient approximation made simple”, *Phys. Rev. Lett.* **77**(7), pp. 3865 (1996).
- [322] Stefan Grimme, “Semiempirical GGA-type density functional constructed with a long-range dispersion correction”, *J. Comput. Chem.* **27**(15), pp. 1787-1799 (2006).
- [323] Rajkumar Jana, Chandra Chowdhury, Ayan Datta, “Transition-metal phosphorus trisulfides and its vacancy defects: emergence of a new class of anode material for Li-ion batteries”, *ChemSusChem* **13**(15), pp. 3855-3864 (2020).
- [324] Rajkumar Jana, Chandra Chowdhury, Ayan Datta, “Deciphering the Role of Substitution in Transition-Metal Phosphorous Trisulfide (100) Surface: A Highly Efficient and Durable Pt-free ORR Electrocatalyst”, *ChemPhysChem* **23**(15), pp. e202200013 (2022).
- [325] Rajkumar Jana, Ayan Datta, Sudip Malik, “Tuning intermediate adsorption in structurally ordered substituted PdCu<sub>3</sub> intermetallic nanoparticles for enhanced ethanol oxidation reaction”, *Chem. Commun.* **57**(37), pp. 4508-4511 (2021).
- [326] Graeme Henkelman, Hannes Jónsson, “Improved tangent estimate in the nudged elastic band method for finding minimum energy paths and saddle points”, *J. Chem. Phys.* **113**(22), pp. 9978-9985 (2000).
- [327] Hai-Long Jiang, Bo Liu, Ya-Qian Lan, Kentaro Kuratani, Tomoki Akita, Hiroshi Shioyama, Fengqi Zong, Qiang Xu, “From Metal–Organic Framework to

Nanoporous Carbon: Toward a Very High Surface Area and Hydrogen Uptake”, *J. Am. Chem. Soc.* **133**(31), 11854–11857 (2011).

- [328] Peiqun Yin, Tao Yao, Yuen Wu, Lirong Zheng, Yue Lin, Wei Liu, Huanxin Ju, Junfa Zhu, Xun Hong, Zhaoxiang Deng, Gang Zhou, Shiqiang Wei, Yadong Li, “Single Cobalt Atoms with Precise N-Coordination as Superior Oxygen Reduction Reaction Catalysts”, *Angew. Chem. Int. Ed.* **55**(36), pp. 1–7 (2016).
- [329] Chi Zhang, Lei Wang, Chuan-De Wu “Stabilization of Transition Metal Heterojunctions Inside Porous Materials for High-Performance Catalysis”, *Dalton Trans.* **52**(26), pp. 8834–8849 (2023).
- [330] Wenhao Ren, Xin Tan, Wanfeng Yang, Chen Jia, Shumao Xu, Kaixue Wang, Sean C Smith, Chuan Zhao, “Isolated Diatomic Ni-Fe Metal–Nitrogen Sites for Synergistic Electroreduction of CO<sub>2</sub>”, *Angew Chem. Int. Ed.* **58**(21), pp. 6972–6976 (2019).
- [331] Adhitya Gandaryus Saputro, Apresio Kefin Fajrial, Arifin Luthfi Maulana, Fadjar Fathurrahman, Mohammad Kemal Agusta, Fiki Taufik Akbar, Hermawan Kresno Dipojono, “Dissociative Oxygen Reduction Reaction Mechanism on the Neighboring Active Sites of a Boron-Doped Pyrolyzed Fe–N–C Catalyst”, *J. Phys. Chem. C* **124**(21), pp. 11383–11391 (2020).
- [332] Jing Wang, Wei Liu, Gan Luo, Zhijun Li, Chao Zhao, Haoran Zhang, Mengzhao Zhu, Qian Xu, Xiaoqian Wang, Changming Zhao, Yunteng Qu, Zhengkun Yang, Tao Yao, Yafei Li, Yue Lin, Yuen Wu, Yadong Li “Synergistic Effect of Well-Defined Dual Sites Boosting the Oxygen Reduction Reaction”, *Energy Environ. Sci.* **11**(12), pp. 3375–3379 (2018).
- [333] Xiaopeng Han, Xiaofei Ling, Deshuang Yu, Dengyu Xie, Linlin Li, Shengjie Peng, Cheng Zhong, Naiqin Zhao, Yida Deng, Wenbin Hu, “Atomically Dispersed Binary Co-Ni Sites in Nitrogen-Doped Hollow Carbon Nanocubes for Reversible Oxygen Reduction and Evolution”, *Adv. Mater.* **31**(49), pp. 1905622 (2019).
- [334] Ziyang Lu, Bo Wang, Yongfeng Hu, Wei Liu, Yufeng Zhao, Ruouo Yang, Zhiping Li, Jun Luo, Bin Chi, Zheng Jiang, Minsi Li, Shichun Mu, Shijun Liao, Jiujun Zhang, Xueliang Sun “An Isolated Zinc–Cobalt Atomic Pair for Highly Active and Durable Oxygen Reduction”, *Angew. Chem. Int. Ed.* **58**(9), pp. 2622–2626 (2019).
- [335] Subhajit Sarkar, Ashmita Biswas, Taniya Purkait, Manisha Das, Navpreet Kamboj, Ramendra Sundar Dey, “Unravelling the Role of Fe–Mn Binary Active Sites Electrocatalyst for Efficient Oxygen Reduction Reaction and Rechargeable Zn-Air Batteries” *Inorg. Chem.* **59**(7), pp. 5194–5205 (2020).
- [336] Yang Chen, Shengqiang Hu, Forrest Nichols, Frank Bridges, Shuting Kan, Ting He, Yi Zhang, Shaowei Chen, “Carbon Aerogels with Atomic Dispersion of Binary Iron–Cobalt Sites as Effective Oxygen Catalysts for Flexible Zinc-Air batteries”, *J. Mater. Chem. A.* **8**(23), 11649–11655 (2020).
- [337] Xiaofeng Zhu, Detao Zhang, Chih-Jung Chen, Qingran Zhang, Ru-Shi Liu, Zhenhai Xia, Liming Dai, Rose Amal, Xunyu Lu, “Harnessing interplay of Fe-Ni atom pairs

- embedded in nitrogen-doped carbon for bifunctional oxygen electrocatalysis”, *Nano Energy* **71**, pp. 104597 (2020).
- [338] Shiliu Yang, Xiaoyi Xue, Chenchen Dai, Xinhe Liu, Quanzhou Yin, Jiabiao Lian, Yan Zhao, Yongfeng Bu, Guochun Li, “Zinc-Iron Bimetallic-Nitrogen Doped Porous Carbon Microspheres as Efficient Oxygen Reduction Electrocatalyst for Zinc Air Batteries”, *Appl. Surf. Sci.* **546**, pp. 148934 (2021).
- [339] Zhe Wang, Xiaoyan Jin, Chao Zhu, Yipu Liu, Hua Tan, Ruiqi Ku, Yongqi Zhang, Liujiang Zhou, Zheng Liu, Seong-Ju Hwang, Hong Jin Fan, “Atomically Dispersed Co<sub>2</sub>-N<sub>6</sub> and Fe-N<sub>4</sub> Costructures Boost Oxygen Reduction Reaction in Both Alkaline and Acidic Media”, *Adv. Mater.* **33**(49), pp. 2104718 (2021).
- [340] Hao Hu, Jia-Hao Liang, Zhao-Yang Zu, Jian-Li Mi, Bei-Bei Xiao, Peng Zhang “Ni/Cu Regulating Nitrogen-Doped Porous Carbon as Electrocatalyst for Oxygen Reduction Reaction”, *ChemistrySelect* **6**(27), pp. 6949–6956 (2021).
- [341] Min Jiang, Fei Wang, Fan Yang, Hao He, Jian Yang, Wei Zhang, Jiayan Luo, Jiao Zhang, Chaopeng Fu, “Rationalization on High-Loading Iron and Cobalt Dual Metal Single Atoms and Mechanistic Insight into the Oxygen Reduction Reaction”, *Nano Energy* **93**, pp. 106793 (2022).
- [342] Yuting He, Xiaoxuan Yang, Yunsong Li, Liting Liu, Shengwu Guo, Chengyong Shu, Feng Liu, Yongning Liu, Qiang Tan, Gang Wu “Atomically Dispersed Fe-Co Dual Metal Sites as Bifunctional Oxygen Electrocatalysts for Rechargeable and Flexible Zn-Air Batteries” *ACS Catal.* **12**(2), pp. 1216–1227 (2022).
- [343] Chenchen Dai, Quanzhou Yin, Mingsheng Yang, Guochun Li, Jiabiao Lian, Yan Zhao, Yongfeng Bu, Mingjun Hu, Shiliu Yang, “Gradually Anchoring N and Fe, Zn Atoms on Monodispersed Carbon Nanospheres: Their Contribution to the Oxygen Reduction Reaction under Analogous Structure”, *Ind. Eng. Chem. Res.* **61**(22), pp. 7513–7522 (2022).
- [344] Shipeng Gong, Changlai Wang, Peng Jiang, Lin Hu, Hu Lei, Qianwang Chen, “Designing Highly Efficient Dual-Metal Single-Atom Electrocatalysts for Oxygen Reduction Reaction Inspired by Biological Enzyme System. *J. Mater. Chem. A* **6**(27), 13254–13262 (2018).
- [345] Jiangyue Chen, Hao Li, Chuang Fan, Qingwei Meng, Yawen Tang, Xiaoyu Qiu, Gengtao Fu, Tianyi Ma, “Dual Single-Atomic Ni-N<sub>4</sub> and Fe-N<sub>4</sub> Sites Constructing Janus Hollow Graphene for Selective Oxygen Electrocatalysis. *Adv. Mater.* **32**(30), pp. 2003134 (2020).
- [346] Xiongwei Zhong, Shulong Ye, Jun Tang, Yuanmin Zhu, Duojie Wu, Meng Gu, Hui Pan, Baomin Xu “Engineering Pt and Fe Dual-metal Single Atoms Anchored on Nitrogen-Doped Carbon with High Activity and Durability towards Oxygen Reduction Reaction for Zinc-air Battery”, *Appl. Catal. B.* **286**, pp. 119891 (2021).

- [347] Vishal Jose, Huimin Hu, Eldho Edison, William Manalastas Jr., Hao Ren, Pinit Kidkhunthod, Sivaramapanicker Sreejith, Anjali Jayakumar, Jean Marie Vianney Nsanzimana, Madhavi Srinivasan, Jinho Choi, Jong-Min Lee, “Modulation of Single Atomic Co and Fe Sites on Hollow Carbon Nanospheres as Oxygen Electrodes for Rechargeable Zn–Air Batteries”, *Small Methods* **5**(2), pp. 2000751 (2020).
- [348] Zhe Chen, Xiaobin Liao, Congli Sun, Kangning Zhao, Daixin Ye, Jiantao Li, Gang Wu, Jianhui Fang, Hongbin Zhao, Jiujun Zhang, “Enhanced Performance of Atomically Dispersed Dual-site Fe-Mn Electrocatalysts through Cascade Reaction Mechanism”, *Appl. Catal. B.* **288**, pp.120021 (2021).
- [349] Yunyan Wu, Caichao Ye, Lei Yu, Yifan Liu, Jiangfeng Huang, Jiabao Bi, Liang Xue, Jingwen Sun, Juan Yang, Wenqing Zhang, Xin Wang, Pan Xiong, Junwu Zhu “Soft Template-Directed Interlayer Confinement Synthesis of A Fe-Co Dual Single-Atom Catalyst For Zn-Air Batteries”, *Energy Storage Materials.* **45**, pp. 805–813 (2022).
- [350] TingtingCui, Yun-PengWang, TongYe, JiaoWu, Zhiqiang Chen, JiongLi, Yongpeng Lei, DingshengWang, Yadong Li, “Engineering Dual Single-Atom Sites on 2D Ultrathin N-doped Carbon Nanosheets Attaining Ultra-Low-Temperature Zinc Air Battery”, *Angew. Chem., Int. Ed.* **61**(12), pp. e202115219 (2022).
- [351] Xuyan Zhou, Jiaojiao Gao, Yixuan Hu, Zeyu Jin, Kailong Hu, Kolan Madhav Reddy, Qunhui Yuan, Xi Lin, Hua-Jun Qiu “Theoretically Revealed and Experimentally Demonstrated Synergistic Electronic Interaction of CoFe Dual-Metal Sites on N-doped Carbon for Boosting Both Oxygen Reduction and Evolution Reactions”, *Nano Lett.* **22**(8), pp. 3392–3399 (2022).
- [352] Ruo Zhao, Zibin Liang, Song Gao, Ce Yang, Bingjun Zhu, Junliang Zhao, Chong Qu, Ruqiang Zou, Qiang Xu, “Puffing up Energetic Metal-organic Frameworks to Large Carbon Networks with Hierarchical Porosity and Atomically Dispersed Metal Sites. *Angew. Chem., Int. Ed.* **57**(7), pp. 1–6 (2018).
- [353] Guojie Chao, Yizhe Zhang, Longsheng Zhang, Wei Zong, Nan Zhang, Tiantian Xue, Wei Fan, Tianxi Liu, Yi Xie “Nitrogen-coordinated Single-atom Catalysts with Manganese and Cobalt sites for Acidic Oxygen Reduction”, *J. Mater. Chem. A* **10**(11), pp. 5930–5936 (2022).
- [354] Jing Wang, Zhengqing Huang, Wei Liu, Chunran Chang, Haolin Tang, Zhijun Li, Wenxing Chen, Chunjiang Jia, Tao Yao, Shiqiang Wei, Yuen Wu, Yadong Li, “Design of N-Coordinated Dual-Metal Sites: A Stable and Active Pt-Free Catalyst for Acidic Oxygen Reduction Reaction”, *J. Am. Chem. Soc.* **139**(48), pp. 17281–17284 (2017).
- [355] Yinuo Wang, Xin Wan, Jieyuan Liu, Wenwen Li, Yongcheng Li, Xu Guo, Xiaofang Liu, Jiaxiang Shang, Jianglan Shui, “Catalysis Stability Enhancement of Fe/Co Dual-atom Site via Phosphorus Coordination for Proton Exchange Membrane Fuel cell”, *Nano Res.* **15**(4), pp. 3082–3089 (2022).

- [356] Fanpeng Kong, Rutong Si, Ning Chen, Qi Wang, Junjie Li, Geping Yin, Meng Gu, Jiajun Wang, Li-Min Liu, Xueliang Sun “Origin of Hetero-Nuclear Au-Co Dual Atoms for Efficient Acidic Oxygen Reduction”, *Appl. Catal., B.* **301**, pp. 120782 (2022).
- [357] Yaodan Zhou, Wen Yang, Wellars Utetiwabo, Yi-Meng Lian, Xue Yin, Lei Zhou, Peiwen Yu, Renjie Chen, Shaorui Sun, “Revealing of Active Sites and Catalytic Mechanism in N-Coordinated Fe, Ni Dual-Doped Carbon with Superior Acidic Oxygen Reduction than Single-Atom Catalyst”, *J. Phys. Chem. Lett.* **11**(4), pp. 1404–1410 (2020).
- [358] Stephan Wagner, Hendrik Auerbach, Claudia E. Tait, Ioanna Martinaiou, Shyam C. N. Kumar, Christian Kgbel, Ilya Sergeev, Hans-Christian Wille, Jan Behrends, Juliusz A. Wolny, Volker Schgnemann, Ulrike I. Kramm, “Elucidating the Structural Composition of an Fe–N–C Catalyst by Nuclear- and Electron-Resonance Techniques”, *Angew. Chem., Int. Ed.* **58**(31), pp. 10486–10492 (2019).
- [359] Ulrike I. Kramm, Iris Herrmann-Geppert, Jan Behrends, Klaus Lips, Sebastian Fiechter, Peter Bogdanoff “On an Easy Way To Prepare Metal–Nitrogen Doped Carbon with Exclusive Presence of MeN<sub>4</sub>-type Sites Active for the ORR” *J. Am. Chem. Soc.* **138**(2), pp. 635–640 (2016).
- [360] Ergui Luo, Hao Zhang, Xian Wang, Liqin Gao, Liyuan Gong, Tuo Zhao, Zhao Jin, Junjie Ge, Zheng Jiang, Changpeng Liu, Wei Xing, “Single-Atom Cr–N<sub>4</sub> Sites Designed for Durable Oxygen Reduction Catalysis in Acid Media”, *Angew. Chem., Int. Ed.* **58**(36), pp. 12469–12475 (2019).
- [361] Chenhao Zhang, Junwei Sha, Huilong Fei, Mingjie Liu, Sadegh Yazdi, Jibo Zhang, Qifeng Zhong, Xiaolong Zou, Naiqin Zhao, Haisheng Yu, Zheng Jiang, Emilie Ringe, Boris I. Yakobson, Juncai Dong, Dongliang Chen, James M. Tour, “Single-Atomic Ruthenium Catalytic Sites on Nitrogen-Doped Graphene for Oxygen Reduction Reaction in Acidic Medium”, *ACS Nano* **11**(7), pp. 6930–6941 (2017).
- [362] Jiazhan Li, Mengjie Chen, David A. Cullen, Sooyeon Hwang, Maoyu Wang, Boyang Li, Kexi Liu, Stavros Karakalos, Marcos Lucero, Hanguang Zhang, Chao Lei, Hui Xu, George E. Sterbinsky, Zhenxing Feng, Dong Su, Karren L. More, Guofeng Wang, Zhenbo Wang, Gang Wu, “Atomically Dispersed Manganese Catalysts for Oxygen Reduction in Proton-Exchange Membrane Fuel cells”, *Nat. Catal.* **1**(12), pp. 935–945 (2018).
- [363] Kai Yuan, Dirk Lützenkirchen-Hecht, Longbin Li, Ling Shuai, Yizhe Li, Rui Cao, Ming Qiu, Xiaodong Zhuang, Michael K. H. Leung, Yiwang Chen, Ullrich Scherf, “Boosting Oxygen Reduction of Single Iron Active Sites via Geometric and Electronic Engineering: Nitrogen and Phosphorus Dual Coordination”, *J. Am. Chem. Soc.* **142**(5), pp. 2404–2412 (2020).
- [364] Subhajit Sarkar, Ashmita Biswas, Erakulan E Siddharthan, Ranjit Thapa, Ramendra Sundar Dey, “Strategic Modulation of Target-Specific Isolated Fe,Co Single-Atom

Active Sites for Oxygen Electrocatalysis Impacting High Power Zn–Air Battery”, *ACS Nano* **16**(5), pp. 7890–7903 (2022).

- [365] Gege Yang, Jiawei Zhu, Pengfei Yuan, Yongfeng Hu, Gan Qu, Bang-An Lu, Xiaoyi Xue, Hengbo Yin, Wenzheng Cheng, Junqi Cheng, Wenjing Xu, Jin Li, Jinsong Hu, Shichun Mu, Jia-Nan Zhang, “Regulating Fe-spin State by Atomically Dispersed Mn-N in Fe-N-C Catalysts with High Oxygen Reduction Activity”, *Nat. Commun.* **12**(1), pp. 1734 (2021).
- [366] Ming Liu, Na Li, Shoufu Cao, Xuemin Wang, Xiaoqing Lu, Lingjun Kong, Yunhua Xu, Xian-He Bu, “A Pre-Constrained Metal Twins” Strategy to Prepare Efficient Dual-Metal-Atom Catalysts for Cooperative Oxygen Electrocatalysis”, *Adv. Mater.* **34**(7), pp. 2107421 (2022).
- [367] Mengjie Liu, Hoje Chun, Tsung-Cheng Yang, Sung Jun Hong, Chia-Min Yang, Byungchan Han, Lawrence Yoon Suk Lee, “Tuning the Site-to-Site Interaction in Ru–M (M = Co, Fe, Ni) Diatomic Electrocatalysts to Climb up the Volcano Plot of Oxygen Electroreduction”, *ACS Nano* **16**(7), pp. 10657–10666 (2022).
- [368] Kunze Wu, Lei Zhang, Yifei Yuan, Linxin Zhong, Zhongxin Chen, Xiao Chi, Hao Lu, Zehong Chen, Ren Zou, Tingzhen Li, Chengyu Jiang, Yongkang Chen, Xinwen Peng, Jun Lu, “An iron-decorated carbon aerogel for rechargeable flow and flexible Zn-air batteries”, *Adv. Mater.* **32**(32), pp. 2002292 (2020).
- [369] Sambhaji S. Shinde, Jin Young Jung, Nayantara K. Wagh, Chi Ho Lee, Dong-Hyung Kim, Sung-Hae Kim, Sang Uck Lee, Jung-Ho Lee, “Ampere-hour-scale zinc-air pouch cells”, *Nat. Energy* **6**(6), pp. 592–604 (2021).
- [370] Yongpeng Lei, Qichen Wang, Shengjie Peng, Seeram Ramakrishna, Dou Zhang, Kechao Zhou, “Electrospun inorganic nanofibers for oxygen electrocatalysis: design, fabrication, and progress”, *Adv. Energy Mater.* **10**(45), pp. 1902115 (2020).
- [371] Botao Hu, Aijian Huang, Xuejiang Zhang, Zheng Chen, Renyong Tu, Wei Zhu, Zhongbin Zhuang, Chen Chen, Qing Peng, Yadong Li, “Atomic Co/Ni dual sites with N/P-coordination as bifunctional oxygen electrocatalyst for rechargeable zinc-air batteries”, *Nano Res.* **14**(10), pp. 3482–3488 (2021).
- [372] Tang Tang, Wen-Jie Jiang, Xiao-Zhi Liu, Jun Deng, Shuai Niu, Bin Wang, Shi-Feng Jin, Qiang Zhang, Lin Gu, Jin-Song Hu, Li-Jun Wan, “Metastable rock salt oxide-mediated synthesis of high-density dual-protected M@NC for long-life rechargeable zinc-air batteries with record power density”, *J. Am. Chem. Soc.* **142**(15), pp. 7116–7127 (2020).
- [373] Wei Sun, Fei Wang, Bao Zhang, Mengyi Zhang, Verena Küpers, Xiao Ji, Claudia Theile, Peter Bieker, Kang Xu, Chunsheng Wang, Martin Winter, “A rechargeable zinc-air batteries based on zinc peroxide chemistry”, *Science* **371**(6524), pp. 46–51 (2021).
- [374] Mingchuan Luo, Zhonglong Zhao, Yelong Zhang, Yingjun Sun, Yi Xing, Fan Lv, Yong Yang, Xu Zhang, Sooyeon Hwang, Yingnan Qin, Jing-Yuan Ma, Fei Lin, Dong



- Su, Gang Lu, Shaojun Guo, “PdMo bimetallic for oxygen reduction catalysis”, *Nature* **574**(7776), pp. 81–85 (2019).
- [375] S. Trasatti, “Electrocatalysis in the anodic evolution of oxygen and chlorine”, *Electrochim. Acta* **29**(11), pp. 1503-1512 (1984).
- [376] S. Ardizzone, G. Fregonara, S. Trasatti, ““Inner” and “outer” active surface of RuO<sub>2</sub> electrodes”, *Electrochim. Acta* **35**(1), pp. 263-267 (1990).
- [377] Youngmin Lee, Jin Suntivich, Kevin J May, Erin E Perry, Yang Shao-Horn “Synthesis and activities of rutile IrO<sub>2</sub> and RuO<sub>2</sub> nanoparticles for oxygen evolution in acid and alkaline solutions”, *J. Phys. Chem. Lett.* **3**(3), pp. 399–404 (2012).
- [378] Yelena Gorlin, Thomas F. Jaramillo, “A Bifunctional Nonprecious Metal Catalyst for Oxygen Reduction and Water Oxidation”, *J. Am. Chem. Soc.* **132**(39), pp. 13612-13614 (2010).
- [379] Tse-Luen Wee, Benjamin D. Sherman, Devens Gust, Ana L. Moore, Thomas A. Moore, Yun Liu, Juan C. Scaiano, “Photochemical Synthesis of a Water Oxidation Catalyst Based on Cobalt Nanostructures”, *J. Am. Chem. Soc.* **133**(42), pp. 16742-16745 (2011).
- [380] D. Kwabena Bediako, Benedikt Lassalle-Kaiser, Yogesh Surendranath, Junko Yano, Vittal K. Yachandra, Daniel G. Nocera, “Structure–Activity Correlations in a Nickel–Borate Oxygen Evolution Catalyst”, *J. Am. Chem. Soc.* **134**(15), pp. 6801-6809 (2012).
- [381] Lena Trotochaud, James K. Ranney, Kerisha N. Williams, and Shannon W. Boettcher, “Solution-Cast Metal Oxide Thin Film Electrocatalysts for Oxygen Evolution”, *J. Am. Chem. Soc.* **134**(41), pp. 17253-17261 (2012).
- [382] Boon Siang Yeo, Alexis T. Bell, “Enhanced Activity of Gold-Supported Cobalt Oxide for the Electrochemical Evolution of Oxygen”, *J. Am. Chem. Soc.* **133**(14), pp. 5587-5593 (2011).
- [383] Alexis Grimaud, Kevin J. May, Christopher E. Carlton, Yueh-Lin Lee, Marcel Risch, Wesley T. Hong, Jigang Zhou, Yang Shao-Horn, “Double perovskites as a family of highly active catalysts for oxygen evolution in alkaline solution”, *Nat. Commun.* **4**(1), pp. 2439 (2013).
- [384] Feng Jiao, Heinz Frei, “Nanostructured Cobalt Oxide Clusters in Mesoporous Silica as Efficient Oxygen-Evolving Catalysts”, *Angew. Chem. Int. Ed.* **48**(10), pp. 1841-1844 (2009).
- [385] Sheng Chen, Jingjing Duan, Mietek Jaroniec, Shi Zhang Qiao, “Three-Dimensional N-Doped Graphene Hydrogel/NiCo Double Hydroxide Electrocatalysts for Highly Efficient Oxygen Evolution”, *Angew. Chem. Int. Ed.* **52**(51), pp. 13567-13570 (2013).

- [386] Boon Siang Yeo, Alexis T. Bell, “In Situ Raman Study of Nickel Oxide and Gold-Supported Nickel Oxide Catalysts for the Electrochemical Evolution of Oxygen”, *J. Phys. Chem. C* **116**(15), pp. 8394-8400 (2012).
- [387] Ram Subbaraman, Dusan Tripkovic, Kee-Chul Chang, Dusan Strmcnik, Arvydas P. Paulikas, Pussana Hirunsit, Maria Chan, Jeff Greeley, Vojislav Stamenkovic, Nenad M. Markovic, “Trends in activity for the water electrolyser reactions on 3d M(Ni,Co,Fe,Mn) hydr(oxy)oxide catalysts”, *Nat. Mater.* **11**(6), pp. 550-557 (2012).
- [388] B. V. Tilak, P. W. T. Lu, J. E. Colman, S. Srinivasan, “Comprehensive Treatise of Electrochemistry”, *Springer* **2**, pp. 1-104 (1981).
- [389] Kim Kinoshita, “Electrochemical Oxygen Technology”, *Wiley-Interscience* 1992.
- [390] Michael J Kenney, Ming Gong, Yanguang Li, Justin Z Wu, Ju Feng, Mario Lanza, Hongjie Dai, “High-performance silicon photoanodes passivated with ultrathin nickel films for water oxidation”, *Science* **342**(6160), pp. 836-840 (2013).
- [391] Rodney D L Smith, Mathieu S Prévot, Randal D Fagan, Zhipan Zhang, Pavel A Sedach, Man Kit Jack Siu, Simon Trudel, Curtis P Berlinguette, “Photochemical Route for Accessing Amorphous Metal Oxide Materials for Water Oxidation Catalysis”, *Science* **340**(6128), pp. 60-63 (2013).
- [392] Yongye Liang, Yanguang Li, Hailiang Wang, Hongjie Dai, “Strongly Coupled Inorganic/Nanocarbon Hybrid Materials for Advanced Electrocatalysis”, *J. Am. Chem. Soc.* **135**(6), pp. 2013-2036 (2013).
- [393] Shaojun Guo, Sen Zhang, Liheng Wu, Shouheng Sun, “Co/CoO Nanoparticles Assembled on Graphene for Electrochemical Reduction of Oxygen”, *Angew. Chem. Int. Ed.* **51**(47), pp. 11770-11773 (2012).
- [394] Changbin Zhang, Fudong Liu, Yanping Zhai, Hiroko Ariga, Nan Yi, Yongchun Liu, Kiyotaka Asakura, Maria Flytzani-Stephanopoulos, Hong He, “Alkali-Metal-Promoted Pt/TiO<sub>2</sub> Opens a More Efficient Pathway to Formaldehyde Oxidation at Ambient Temperatures”, *Angew. Chem. Int. Ed.* **51**(38), pp. 9628-9632 (2012).
- [395] Xiaoyan Liu, Ming-Han Liu, Yi-Chia Luo, Chung-Yuan Mou, Shawn D. Lin, Hongkui Cheng, Jin-Ming Chen, Jyh-Fu Lee, Tien-Sung Lin, “Strong Metal-Support Interactions between Gold Nanoparticles and ZnO Nanorods in CO Oxidation”, *J. Am. Chem. Soc.* **134**(24), pp. 10251-10258 (2012).
- [396] Ming Gong, Yanguang Li, Hailiang Wang, Yongye Liang, Justin Z. Wu, Jigang Zhou, Jian Wang, Tom Regier, Fei Wei, and Hongjie Dai, “An Advanced Ni-Fe Layered Double Hydroxide Electrocatalyst for Water Oxidation”, *J. Am. Chem. Soc.* **135**(23), pp. 8452-8455 (2013).
- [397] Min-Rui Gao, Yun-Fei Xu, Jun Jiang, Ya-Rong Zheng, Shu-Hong Yu, “Water Oxidation Electrocatalyzed by an Efficient Mn<sub>3</sub>O<sub>4</sub>/CoSe<sub>2</sub> Nanocomposite”, *J. Am. Chem. Soc.* **134**(6), pp. 2930-2933 (2012).

- [398] Y. Gorlin, C. J. Chung, J. D. Benck, D. Nordlund, L. Seitz, T. C. Weng, D. Sokaras, B. M. Clemens, T. F. Jaramillo, *J. Am. Chem. Soc.* 2014, 136, 4920
- [399] Yongye Liang, Yanguang Li, Hailiang Wang, Jigang Zhou, Jian Wang, Tom Regier, Hongjie Dai, “Co<sub>3</sub>O<sub>4</sub> nanocrystals on graphene as a synergistic catalyst for oxygen reduction reaction”, *Nat. Mater.* **10**(10), pp. 780-786 (2011).
- [400] Bingzhang Lu, Qiming Liu, Shaowei Chen, “Electrocatalysis of Single-Atom Sites: Impacts of Atomic Coordination”, *ACS Catal.* **10**(14), pp. 7584-7618 (2020).
- [401] Chang-Xin Zhao, Bo-Quan Li, Jia-Ning Liu, Qiang Zhang “Intrinsic Electrocatalytic Activity Regulation of M–N–C Single-Atom Catalysts for Oxygen Reduction Reaction”, *Angew. Chem. Int. Ed.* **60**(9), pp 4448–4463 (2021).
- [402] Jiazhan Li, Chang Chen, Lekai Xu, Yu Zhang, Wei Wei, Erbo Zhao, Yue Wu, Chen Chen, “Challenges and Perspectives of Single-Atom-Based Catalysts for Electrochemical Reactions”, *JACS Au.* **3**(3), pp. 736–755 (2023).
- [403] Xilin Zhang, Zhansheng Lu, Zongxian Yang, “The mechanism of oxygen reduction reaction on CoN<sub>4</sub> embedded graphene: A combined kinetic and atomistic thermodynamic study”, *Int. J. Hydrogen Energy* **41**(46), pp. 21212–21220 (2016).
- [404] Chun-Chao Hou, Lianli Zou, Liming Sun, Kexin Zhang, Zheng Liu, Yinwei Li, Caixia Li, Ruqiang Zou, Jihong Yu, Qiang Xu, “Single-Atom Iron Catalysts on Overhang-Eave Carbon Cages for High-Performance Oxygen Reduction Reaction”, *Angew. Chem. Int. Ed.* **59**(19), pp. 7384 –7389 (2020).
- [405] Xin Wan, Xiaofang Liu, Yongcheng Li, Ronghai Yu, Lirong Zheng, Wensheng Yan, Hui Wang, Ming Xu, Jianglan Shui, “Fe–N–C electrocatalyst with dense active sites and efficient mass transport for high-performance proton exchange membrane fuel cells”, *Nat. Catal.* **2**(3), pp. 259–268 (2019).
- [406] Long Jiao, Hai-Long Jiang, “Metal-Organic-Framework-Based Single-Atom Catalysts for Energy Applications”, *Chem* **5**(4), pp. 786-804 (2019).
- [407] De-Shan Bin, Zi-Xiang Chi, Yutao Li, Ke Zhang, Xinzheng Yang, Yong-Gang Sun, Jun-Yu Piao, An-Min Cao, Li-Jun Wan, “Controlling the Compositional Chemistry in Single Nanoparticles for Functional Hollow Carbon Nanospheres”, *J. Am. Chem. Soc.* **139**(38), pp. 13492-13498 (2017).
- [408] Yong-Gang Sun, Jun-Yu Piao, Lin-Lin Hu, De-Shan Bin, Xi-Jie Lin, Shu-Yi Duan, An-Min Cao, Li-Jun Wan, “Controlling the Reaction of Nanoparticles for Hollow Metal Oxide Nanostructures”, *J. Am. Chem. Soc.* **140**(29), pp. 9070-9073 (2018).
- [409] Yan Jiao, Yao Zheng, Kenneth Davey, Shi-Zhang Qiao, “Activity origin and catalyst design principles for electrocatalytic hydrogen evolution on heteroatom-doped graphene”, *Nat. Energy* **1**(10), pp. 16130 (2016).
- [410] Chun-Chao Hou, Qiang Xu, “Metal–Organic Frameworks for Energy”, *Adv. Energy Mater.* **9**(13), pp. 1801307 (2019).

- [411] Ruo Zhao, Zibin Liang, Song Gao, Ce Yang, Bingjun Zhu, Junliang Zhao, Chong Qu, Ruqiang Zou, Qiang Xu, “Puffing Up Energetic Metal–Organic Frameworks to Large Carbon Networks with Hierarchical Porosity and Atomically Dispersed Metal Sites”, *Angew. Chem. Int. Ed.* **58**(7), pp. 1975-1979 (2019).
- [412] Yanghua He, Sooyeon Hwang, David A. Cullen, M. Aman Uddin, Lisa Langhorst, Boyang Li, Stavros Karakalos, A. Jeremy Kropf, Evan C. Wegener, Joshua Sokolowski, Mengjie Chen, Debbie Myers, Dong Su, Karren L. More, Guofeng Wang, Shawn Litster, Gang Wu, “Highly active atomically dispersed Co/N fuel cell cathode catalysts derived from surfactant-assisted MOFs: carbon-shell confinement strategy”, *Energy Environ. Sci.* **12**(1), pp. 250-260 (2019).
- [413] Xiao Xia Wang, Mark T. Swihart, Gang Wu, “Achievements, challenges and perspectives on cathode catalysts in proton exchange membrane fuel cells for transportation”, *Nat. Catal.* **2**(7), pp. 578-589 (2019).
- [414] Z. Yuan, M. Yao, N. Zhang, S. Wang, X. Rui, Q. Zhang, Z. Niu, *Sci. China Mater.* **64**, pp. 2182-2192 (2021).
- [415] Rui Wang, Minjie Yao, Shuo Huang, Jinlei Tian, Zhiqiang Niu, “Sustainable Dough-Based Gel Electrolytes for Aqueous Energy Storage Devices”, *Adv. Funct. Mater.* **31**(14), pp. 2009209 (2021).
- [416] Zifeng Wang, Hongfei Li, Zijie Tang, Zhuoxin Liu, Zhaoheng Ruan, Longtao Ma, Qi Yang, Donghong Wang, Chunyi Zhi, “Hydrogel Electrolytes for Flexible Aqueous Energy Storage Devices”, *Adv. Funct. Mater.* **28**(48), pp. 1804560 (2018).
- [417] Canpeng Li, Xuesong Xie, Hui Liu, Pinji Wang, Canbin Deng, Bingan Lu, Jiang Zhou, Shuquan Liang, “Integrated ‘all-in-one’ strategy to stabilize zinc anodes for high-performance zinc-ion batteries”, *Natl. Sci. Rev.* **2022**, **9**(3), pp. nwab177 (2022).
- [418] Siyuan Zhao, Yayu Zuo, Tong Liu, Shuo Zhai, Yawen Dai, Zengjia Guo, Yang Wang, Qijiao He, Lingchao Xia, Chunyi Zhi, Jinhye Bae, Keliang Wang, Meng Ni, “Multi-Functional Hydrogels for Flexible Zinc-Based Batteries Working under Extreme Conditions”, *Adv. Energy Mater.* **11**(34), pp. 2101749 (2021).
- [419] Chaonan Gu, Xiao-Qiao Xie, Yujia Liang, Jingjing Li, Hai Wang, Kaifang Wang, Junpeng Liu, Mengke Wang, Yunfei Zhang, Manxing Li, Huajie Kong, Chun-Sen Liu, “Small molecule-based supramolecular-polymer double-network hydrogel electrolytes for ultra-stretchable and waterproof Zn–air batteries working from –50 to 100 °C”, *Energy Environ. Sci.* **14**(8), 4451-4462 (2021).
- [420] Qi Liu, Anran Zhao, Xuexia He, Qi Li, Jie Sun, Zhibin Lei, Zong-Huai Liu, “Full-Temperature All-Solid-State  $Ti_3C_2T_x$ /Aramid Fiber Supercapacitor with Optimal Balance of Capacitive Performance and Flexibility” *Adv. Funct. Mater.* **31**(22), pp. 2010944 (2021).
- [421] M. H. J. Huang, X. Wu, S. Liang, J. Zhou, *Chin. J. Inorg. Chem.* **38**, pp. 1451 (2022)

- [422] Hainan Gao, Ziguang Zhao, Yudong Cai, Jiajia Zhou, Wenda Hua, Lie Chen, Li Wang, Jianqi Zhang, Dong Han, Mingjie Liu, Lei Jiang, “Adaptive and freeze-tolerant heteronetwork organohydrogels with enhanced mechanical stability over a wide temperature range”, *Nat. Commun.* **8**(1), pp. 15911 (2017).
- [423] Xuting Jin, Li Song, Hongsheng Yang, Chunlong Dai, Yukun Xiao, Xinqun Zhang, Yuyang Han, Congcong Bai, Bing Lu, Qianwen Liu, Yang Zhao, Jiatao Zhang, Zhipan Zhang, Liangti Qu, “Stretchable supercapacitor at  $-30\text{ }^{\circ}\text{C}$ ”, *Energy Environ. Sci.* **14**(5), pp. 3075-3085 (2021).
- [424] Zengxia Pei, Ziwen Yuan, Chaojun Wang, Shenlong Zhao, Jingyuan Fei, Li Wei, Junsheng Chen, Cheng Wang, Rongjie Qi, Zongwen Liu, Yuan Chen, “A flexible rechargeable zinc-air batteries with excellent low temperature adaptability”, *Angew. Chem. Int. Ed.* **59**(12), pp. 4793–4799 (2020)
- [425] Chang-Xin Zhao, Jia-Ning Liu, Nan Yao, Juan Wang, Ding Ren, Xiang Chen, Bo-Quan Li, Qiang Zhang, “Can aqueous zinc-air batteries work at sub-zero temperatures?”, *Angew. Chem. Int. Ed.* **60**(28), pp. 15281–15285 (2021)
- [426] Qiu Zhang, Yilin Ma, Yong Lu, Lin Li, Fang Wan, Kai Zhang, Jun Chen, “Modulating electrolyte structure for ultralow temperature aqueous zinc batteries”, *Nat. Commun.* **11**(1), pp. 4463 (2020)
- [427] Qichen Wang, Qingguo Feng, Yongpeng Lei, Shuaihao Tang, Liang Xu, Yu Xiong, Guozhao Fang, Yuchao Wang, Peiyao Yang, Jingjing Liu, Wei Liu, Xiang Xiong, “Quasi-solid-state Zn-air batteries with an atomically dispersed cobalt electrocatalyst and organohydrogel electrolyte”, *Nat Commun* **13**(1), pp. 3689 (2022).
- [428] Nan Wang, Xiaoli Dong, Bingliang Wang, Zhaowei Guo, Zhuo Wang, Renhe Wang, Xuan Qiu, Yonggang Wang, “Zinc-Organic Battery with a Wide Operation-Temperature Window from  $-70$  to  $150\text{ }^{\circ}\text{C}$ ”, *Angew. Chem. Int. Ed.* **59**(34), pp. 14577-14583 (2020).
- [429] Wenjun Deng, Zhuqing Zhou, Yibo Li, Man Zhang, Xinran Yuan, Jun Hu, Zhengang Li, Chang Li, Rui Li, “High-Capacity Layered Magnesium Vanadate with Concentrated Gel Electrolyte toward High-Performance and Wide-Temperature Zinc-Ion Battery”, *ACS Nano* 2020, **14**(11), pp. 15776-15785 (2020).
- [430] Timo Hofmann, Ted H. Yu, Michael Folse, Lothar Weinhardt, Marcus Bär, Yufeng Zhang, Boris V. Merinov, Deborah J. Myers, William A. Goddard III, Clemens Heske, “Using Photoelectron Spectroscopy and Quantum Mechanics to Determine D-Band Energies of Metals for Catalytic Applications” *J. Phys. Chem. C.* **116**(45), pp. 24016-24026 (2012).
- [431] Zhiyan Chen, Yao Song, Jinyan Cai, Xusheng Zheng, Dongdong Han, Yishang Wu, Yipeng Zang, Shuwen Niu, Yun Liu, Junfa Zhu, Xiaojing Liu, Gongming Wang, “Tailoring the D-Band Centers Enables  $\text{Co}_4\text{N}$  Nanosheets to Be Highly Active for Hydrogen Evolution Catalysis”, *Angew. Chem. Int. Ed.* **57**(18), pp. 5076-5080 (2018).

- [432] Yang Lou, Jian Ma, Xiaoming Cao, Li Wang, Qiguang Dai, Zhenyang Zhao, Yafeng Cai, Wangcheng Zhan, Yanglong Guo, P. Hu, Guanzhong Lu, Yun Guo, “Promoting Effects of  $\text{In}_2\text{O}_3$  on  $\text{Co}_3\text{O}_4$  for Co Oxidation: Tuning  $\text{O}_2$  Activation and Co Adsorption Strength Simultaneously”, *ACS Catal.* **4**(11), pp. 4143-4152 (2014).
- [433] G Kresse, J Furthmüller, “Efficient iterative schemes for ab initio total-energy calculations using a plane-wave basis set”, *Phys. Rev. B* **54**(16), pp. 11169–11186 (1996).
- [434] P E Blöchl, “Projector augmented-wave method”, *Phys. Rev. B* **50**(24), pp. 17953–17979 (1994).
- [435] G. Kresse, D. Joubert “From ultrasoft pseudopotentials to the projector augmented-wave method”, *Phys. Rev. B* **59**(3), pp. 1758–1775 (1999).
- [436] JP Perdew, K Burke, M Ernzerhof, “Generalized Gradient Approximation Made Simple”, *Phys. Rev. Lett.* **77**(18), pp. 3865–3868 (1996).
- [437] J. K. Nørskov, J. Rossmeisl, A. Logadottir, L. Lindqvist, J. R. Kitchin, T. Bligaard, H. Jónsson, “Origin of the overpotential for oxygen reduction at a fuel-cell cathode”, *J.Phys. Chem. B* **108**(46), pp. 17886–17892 (2004).
- [438] Chaohai Wang, Jeonghun Kim, Jing Tang, Minjun Kim, Hyunsoo Lim, Victor Malgras, Jungmok You, Qiang Xu, Jiansheng Li, Yusuke Yamauchi, “New Strategies for Novel MOF-Derived Carbon Materials Based on Nanoarchitectures”, *Chem* **6**(1), pp. 19-40 (2020).
- [439] Meng-Lin Lu, Tzu-Yun Lin, Tong-Min Weng, Yang-Fang Chen, “Large enhancement of photocurrent gain based on the composite of a single n-type  $\text{SnO}_2$  nanowire and p-type NiO nanoparticles”, *Opt. Express* **19**(17), pp. 16266-16272 (2011).
- [440] Wenhao Ren, Xin Tan, Chen Jia, Anna Krammer, Qian Sun, Jiangtao Qu, Sean C. Smith, Andreas Schueler, Xile Hu, Chuan Zhao, “Electronic Regulation of Nickel Single Atoms by Confined Nickel Nanoparticles for Energy-Efficient  $\text{CO}_2$  Electroreduction”, *Angew. Chem. Int. Ed.* **61**(26), pp. e202203335 (2022).
- [441] Hong Bin Yang, Sung-Fu Hung, Song Liu, Kaidi Yuan, Shu Miao, Liping Zhang, Xiang Huang, Hsin-Yi Wang, Weizheng Cai, Rong Chen, Jiajian Gao, Xiaofeng Yang, Wei Chen, Yanqiang Huang, Hao Ming Chen, Chang Ming Li, Tao Zhang, Bin Liu, “Atomically dispersed Ni(I) as the active site for electrochemical  $\text{CO}_2$  reduction”, *Nat Energy* **3**(2), pp. 140–147 (2018)
- [442] Ramireddy Boppella, Muthu Austeria P, Yujin Kim, Eunhyo Kim, Inae Song, Yaeun Eom, D. Praveen Kumar, Mani Balamurugan, Eunji Sim, Do Hwan Kim, Tae Kyu Kim, “Pyrrolic N-Stabilized Monovalent Ni Single-Atom Electrocatalyst for Efficient  $\text{CO}_2$  Reduction: Identifying the Role of Pyrrolic–N and Synergistic Electrocatalysis”, *Adv. Funct. Mater.* **32**(35), pp. 2202351 (2022).
- [443] Ksenia Fominykh, Johann M. Feckl, Johannes Sicklinger, Markus Döblinger, Sebastian Böcklein, Jürgen Ziegler, Laurence Peter, Jiri Rathousky, Ernst-Wilhelm Scheidt, Thomas Bein, Dina Fattakhova-Rohlfing, “Ultrasmall Dispersible

Crystalline Nickel Oxide Nanoparticles as High-Performance Catalysts for Electrochemical Water Splitting”, *Adv. Funct. Mater.* **24**(21), pp. 3123–3129 (2014).

- [444] Zhe Wang, Chao Zhu, Hua Tan, Jan Liu, Lulu Xu, Yongqi Zhang, Yipu Liu, Xiaoxin Zou, Zheng Liu, Xuehong Lu, “Understanding the Synergistic Effects of Cobalt Single Atoms and Small Nanoparticles: Enhancing Oxygen Reduction Reaction Catalytic Activity and Stability for Zinc-Air Batteries”, *Adv. Funct. Mater.* **31**(45), pp. 2104735 (2021).
- [445] Hannes Radinger, Paula Connor, Sven Tengeler, Robert W. Stark, Wolfram Jaegermann, and Bernhard Kaiser, “Importance of Nickel Oxide Lattice Defects for Efficient Oxygen Evolution Reaction”, *Chem. Mater.* **33**(21), 8259–8266 (2021).
- [446] Kalpana Deevi, Venkata Subba Reddy Immareddy, “Synthesis and characterization of optically transparent nickel oxide nanoparticles as a hole transport material for hybrid perovskite solar cells”, *J Mater Sci: Mater Electron* **30**(6), pp. 6242–6248 (2019).
- [447] B. Hammer, J.K. Nørskov, “Theoretical surface science and catalysis—calculations and concepts”, *Adv. Catal.* **45**, pp. 71–129 (2000).
- [448] Changhong Zhan, Yong Xu, Lingzheng Bu, Huaze Zhu, Yonggang Feng, Tang Yang, Ying Zhang, Zhiqing Yang, Bolong Huang, Qi Shao, Xiaoqing Huang, “Subnanometer high-entropy alloy nanowires enable remarkable hydrogen oxidation catalysis”, *Nat Commun* **12**(1), pp. 6261 (2021).
- [449] Qianqian Song, Junqi Li, Beiyi Zhang, Hu Li, Xiaoxu Liu, “Controlling the D-band for improved oxygen evolution performance in Ni modulated ultrafine Co nanoparticles embedded in Nitrogen-doped carbon microspheres”, *J Colloid Interface Sci* **623** pp. 44–53 (2022).
- [450] Jun Wang, Kai Li, Hai-xia Zhong, Dan Xu, Zhong-li Wang, Zheng Jiang, Zhi-jian Wu, Xin-bo Zhang, “Synergistic Effect between Metal–Nitrogen–Carbon Sheets and NiO Nanoparticles for Enhanced Electrochemical Water-Oxidation Performance”, *Angew.Chem.Int.Ed.* **54**(36), pp. 10530–10534 (2015).

This page was intentionally left blank



## List of Publications

1. **Gargi Dey**, Shadab Saifi, Motahar Sk, A. S. K. Sinha, Debasis Banerjee, Arshad Aijaz, “Immobilizing a homogeneous manganese catalyst into MOF pores for  $\alpha$ -alkylation of methylene ketones with alcohols”, *Dalton Trans.* **51**(47), pp. 17973–17977 (2022).
2. **Gargi Dey**, Shadab Saifi, Harsh Sharma, Milan Kumar, Arshad Aijaz, “Carbon Nanofibers Coated with MOF-Derived Carbon Nanostructures for Vanadium Redox Flow Batteries with Enhanced Electrochemical Activity and Power Density”, *ACS Appl. Nano Mater.* **6**(10), pp. 8192–8201 (2023).
3. **Gargi Dey**, Rajkumar Jana, Shadab Saifi, Ravi Kumar, D. Bhattacharyya, Ayan Datta, A. S. K. Sinha, Arshad Aijaz, “Atomically Distributed Co-Mn Dual Sites in MOF-derived N-doped Nanoporous Carbon for Electrochemical Oxygen Reduction”, *ACS Nano* **17**(19), pp. 19155–19167 (2023).
4. **Gargi Dey**, Shadab Saifi, Renna Shakir, Diksha Saini, J. Karthikeyan, Arshad Aijaz, “NiO nanoclusters supported on atomically dispersed Ni single atom at Mesoporous Carbon Cages for Oxygen Evolution Reaction and Quasi-Solid-State Zn-air batteries with an Organohydrogel Electrolyte”, (2024). (Manuscript submitted).
5. **Gargi Dey**, Shadab, Arshad Aijaz, “Metal-Organic Framework Derived Nanostructured Bifunctional Electrocatalysts for Water Splitting”, *ChemElectroChem* **8**(20), pp. 1–23 (2021). (Review Paper).
6. Shadab Saifi, **Gargi Dey**, Renna Shakir, J. Karthikeyan, Ravi Kumar, D. Bhattacharyya, A.S.K. Sinha, Arshad Aijaz, Boosting the Performance of Tri-functional Electrocatalyst via Integrating Single-Co-Atom with Cr-Co Nanoparticle for Rechargeable Zn-Air Battery-Driven Hydrogen Evolution, *Inorg. Chem* 2024 (Manuscript just accepted).
7. Shadab Saifi, **Gargi Dey**, J. Karthikeyan, Ravi Kumar, D. Bhattacharyya, A.S.K. Sinha, Arshad Aijaz, “Coupling Single-Ni-Atom with Ni–Co Alloy Nanoparticle for Synergistically Enhanced Oxygen Reduction Reaction”, *Inorg. Chem.* **62**(21), pp. 8200–8209 (2023).
8. Shadab Saifi, **Gargi Dey**, J. Karthikeyan, A. S. K. Sinha, Arshad Aijaz, “MoS<sub>2</sub> and WS<sub>2</sub> Nanosheets Decorated on Metal–Organic Framework-Derived Cobalt/Carbon Nanostructures as Electrocatalysts for Hydrogen Evolution”, *ACS Appl. Nano Mater.* **5**(8), pp. 10696–10703 (2022).
9. Shadab Saifi, **Gargi Dey**, Motahar Sk, Debasis Banerjee, Arshad Aijaz, “Heterogenizing a Homogeneous Nickel Catalyst Using Nanoconfined Strategy for Selective Synthesis of Mono- and 1,2-Disubstituted Benzimidazoles”, *Inorg. Chem.* **60**(21), pp. 16042–16047 (2021).







## Conferences

1. **Gargi Dey**, Arshad Aijaz, “Heterogenization of non-precious homogeneous catalysts within MOF pores for borrowing hydrogen catalysis.”, CRSI-NSC-30: 30<sup>th</sup> CRSI National Symposium in Chemistry, JNU, New Delhi, India, February 3-5, 2023.
2. **Gargi Dey**, Arshad Aijaz, “Atomically dispersed Cobalt-Manganese pair active sites for electrochemical oxygen reduction reaction”, International Conference on Modern Trends in Inorganic Chemistry (MTIC XIX), BHU, Varanasi India, December 15-17, 2022.

**GARGI DEY**

PhD Rajiv Gandhi Institute of Petroleum Technology,  
Jais, Amethi, Uttar Pradesh, India, Pin-229304  
✉: pc19002@rgipt.ac.in, gargi.chakdaha@gmail.com  
☎: +91-9679316858, +91-7001735649  
📍 : 1188, K.B.M, Chakdaha, Nadia, West Bengal, India, Pin-741222

**ACADEMIC OUTLINE**

-  **PhD in Chemistry** (July 2019-To date)  
Department of Sciences & Humanities,  
Rajiv Gandhi Institute of Petroleum Technology, Uttar Pradesh, India.  
Thesis topic: MOF and their derivatives for heterogeneous catalysis.  
Thesis supervisor: Dr. Arshad Aijaz
-  **Project Assistant** (January 2019-June 2019)  
Department of Sciences & Humanities,  
RGIPT, U.P, India.  
Project topic: MOF derived nanostructured materials for electrocatalytic applications.  
Project supervisor: Dr. Arshad Aijaz
-  **Master of Science in Organic Chemistry, 81.44%** 2016-2018  
Department of Chemistry,  
University of Kalyani, West Bengal, India.  
Thesis topic: Synthesis of tetracyclic carbazole derivatives.  
Thesis supervisor: Prof. Shital Kumar Chattopadhyay
-  **Bachelor of Science in Chemistry, 70.63%** 2013-2016  
Department of Chemistry,  
Chakdaha College, West Bengal, India.
-  **Higher secondary Class XII in Science, 84.2%** 2012-2013  
W.B.C.H.S.E, Basanta Kumari Balika Vidyapith,  
Chakdaha, West Bengal, India.
-  **Secondary Class X, 85.13%** 2010-2011  
W.B.B. S.E, Basanta Kumari Balika Vidyapith,  
Chakdaha, West Bengal, India.

## RESEARCH EXPERIENCE

- Doctoral studies under the supervision of Dr. Arshad Aijaz, Department of Sciences and Humanities, Rajiv Gandhi Institute of Petroleum Technology (RGIPT), Uttar Pradesh, India (2019 -2024).

## TEACHING EXPERIENCE

- Teaching Assistant- to Dr. Arshad Aijaz (“Inorganic chemistry”- Undergraduate Level)
- Teaching Assistant- to Dr. Shikha Singh, (“Inorganic & Physical Chemistry” – Undergraduate Level).

## FELLOWSHIPS AND AWARDS

- Qualified CSIR-JRF-National Eligibility Test (2017 December).
- Qualified CSIR-JRF-National Eligibility Test (2018 December).
- Qualified CSIR-JRF-National Eligibility Test (2019 June).
- Research Teaching Assistantship, JRF RGIPT, Amethi 2019-2021.
- Research Teaching Assistantship, SRF RGIPT, Amethi 2021-2023.
- Qualified IIT-JAM (2016 February).
- Merit-cum-Mean Scholarship (2013-2018) under Government of West Bengal.
- DST Inspire Scholarship (2013-2016).

## PERSONAL INFORMATION

Parent Name	Mr. Nikhil Chandra Dey & Mrs. Sukla Dey
Nationality	Indian
Date of Birth	5 <sup>th</sup> April, 1995
Gender	Female
Marital Status	Unmarried
Languages	Bengali, English, Hindi,

## DECLARATION

I hereby declare that all the information mentioned above is true and correct to the best of my knowledge.

Thank you,

**Place:** Jais, Amethi

  
**Gargi Dey**